frontiers | Research Topics

Vertical coupling in the atmosphere-ionosphere-magnetosphere system

Edited by
Jaroslav Chum, Petra Koucka Knizova, Veronika Barta, Christina Arras, Dimitry Pokhotelov, Erich Becker, Christoph Jacobi, Han-Li Liu, Huixin Liu and Gunter Stober

Published in
Frontiers in Astronomy and Space Sciences

ISSN 1664-8714
ISBN 978-2-8325-4379-5
DOI 10.3389/978-2-8325-4379-5

About Frontiers

Frontiers is more than just an open access publisher of scholarly articles: it is a pioneering approach to the world of academia, radically improving the way scholarly research is managed. The grand vision of Frontiers is a world where all people have an equal opportunity to seek, share and generate knowledge. Frontiers provides immediate and permanent online open access to all its publications, but this alone is not enough to realize our grand goals.

Frontiers journal series

The Frontiers journal series is a multi-tier and interdisciplinary set of open-access, online journals, promising a paradigm shift from the current review, selection and dissemination processes in academic publishing. All Frontiers journals are driven by researchers for researchers; therefore, they constitute a service to the scholarly community. At the same time, the *Frontiers journal series* operates on a revolutionary invention, the tiered publishing system, initially addressing specific communities of scholars, and gradually climbing up to broader public understanding, thus serving the interests of the lay society, too.

Dedication to quality

Each Frontiers article is a landmark of the highest quality, thanks to genuinely collaborative interactions between authors and review editors, who include some of the world's best academicians. Research must be certified by peers before entering a stream of knowledge that may eventually reach the public - and shape society; therefore, Frontiers only applies the most rigorous and unbiased reviews. Frontiers revolutionizes research publishing by freely delivering the most outstanding research, evaluated with no bias from both the academic and social point of view. By applying the most advanced information technologies, Frontiers is catapulting scholarly publishing into a new generation.

What are Frontiers Research Topics?

Frontiers Research Topics are very popular trademarks of the *Frontiers journals series*: they are collections of at least ten articles, all centered on a particular subject. With their unique mix of varied contributions from Original Research to Review Articles, Frontiers Research Topics unify the most influential researchers, the latest key findings and historical advances in a hot research area.

Find out more on how to host your own Frontiers Research Topic or contribute to one as an author by contacting the Frontiers editorial office: frontiersin.org/about/contact

Vertical coupling in the atmosphere-ionosphere-magnetosphere system

Citation

Chum, J., Knizova, P. K., Barta, V., Arras, C., Pokhotelov, D., Becker, E., Jacobi, C., Liu, H.-L., Liu, H., Stober, G., eds. (2024). *Vertical coupling in the atmosphere-ionosphere-magnetosphere system*. Lausanne: Frontiers Media SA. doi: 10.3389/978-2-8325-4379-5

Table of contents

frontiers | Frontiers in Astronomy and Space Sciences

TYPE Editorial
PUBLISHED 16 January 2024
DOI 10.3389/fspas.2023.1359458

OPEN ACCESS

EDITED AND REVIEWED BY
Joseph E. Borovsky,
Space Science Institute (SSI), United States

*CORRESPONDENCE
Jaroslav Chum,
jachu@ufa.cas.cz

RECEIVED 21 December 2023
ACCEPTED 31 December 2023
PUBLISHED 16 January 2024

CITATION
Barta V, Chum J, Liu H-L, Pokhotelov D and Stober G (2024), Editorial: Vertical coupling in the atmosphere-ionosphere-magnetosphere system.
Front. Astron. Space Sci. 10:1359458.
doi: 10.3389/fspas.2023.1359458

Editorial: Vertical coupling in the atmosphere-ionosphere-magnetosphere system

Veronika Barta[1], Jaroslav Chum[2]*, Han-Li Liu[3], Dimitry Pokhotelov[4] and Gunter Stober[5]

[1]Institute of Earth Physics and Space Science (EPSS), Sopron, Hungary, [2]Institute of Atmospheric Physics CAS, Prague, Czechia, [3]High Altitude Observatory, National Center for Atmospheric Research, Boulder, CO, United States, [4]Institute of Physics, University of Greifswald, Greifswald, Germany, [5]Institute of Applied Physics and Oeschger Center for Climate Change Research, Microwave Physics, University of Bern, Bern, Switzerland

KEYWORDS

ionosphere, atmosphere, magnetosphere, vertical coupling, waves, disturbances, irregularities

Editorial on the Research Topic
Vertical coupling in the atmosphere-ionosphere-magnetosphere system

The Earth's ionosphere, a partly ionized plasma layer in the upper atmosphere extending from about 60 km to around 1,000 km, is not only a playground for many fascinating phenomena such as the aurorae or plasma bubbles, but also affects many technological systems: Ionosphere and Ionospheric perturbations affect the propagation of electromagnetic waves (precision and reliability of GNSS, over the horizon radars, radio communications), ionospheric currents cause changes in the geomagnetic field, leading to geomagnetically induced currents that pose a risk to power line transformers.

Ionospheric plasma is primarily generated by ionizing solar radiation. However, ionospheric dynamics and disturbances depend strongly on the interaction between the solar wind and the Earth's magnetosphere, which is tightly coupled to the ionosphere through field-aligned currents, electric fields, etc. In addition, the ionosphere is strongly linked to the neutral atmosphere, with which it partially merges and responds to processes that take place below in the neutral atmosphere. In particular, during geomagnetically quiet periods neutral atmosphere may account for 10%–15% of the ionospheric variability. Atmospheric gravity waves, generated by a variety of processes in lower atmosphere, are the key vertical coupling agent, transferring energy and momentum into middle/upper atmosphere and ionosphere. Atmospheric thermal tides, both migrating and non-migrating, are responsible for diurnal, semidiurnal and terdiurnal variabilities. There are also reports of multi-day variabilities, matching the periods of various planetary waves, though the origin of these variabilities is still debated. Changes in global atmospheric circulations, e.g., seasonal or caused by sudden stratospheric warmings, can influence middle/upper atmosphere and ionosphere. A downward coupling to lower atmosphere, due to atmospheric gravity waves being generated by Joule heating in the ionospheric E-region, has been also proposed.

Although the ionosphere has been studied for more than one hundred years, starting with the transatlantic transmission of radio signals, and the basic principles of ionospheric physics are well known, the relative role of various mechanisms and conditions that lead to the development of specific perturbations, instabilities and day-to-day variability needs to

be further investigated because of the complex interactions with the layers below and above it. The papers in this Research Topic attempt to describe and explain some of these processes.

Prikryl and Rušin explores statistical connections between the occurrence of heavy floods in Canada and arrivals of solar wind high-speed streams (HSSs) emitted for solar coronal holes. Solar wind observations are statistically compared to the meteorological reanalysis data. The enhanced auroral energy deposition during HSSs is proposed as a mechanism for the generation of downward propagating atmospheric gravity waves (AGWs). As AGWs reach lower atmosphere, they may excite the conditional instability in the troposphere, thus leading to excessive precipitation. This downward influence from solar wind to troposphere could be considered as a direct link between solar variability and climate variability or trends.

Maetschke et al. suggest the generation process of auroral spirals, that remains a subject of long controversy. The process is illustrated using satellite observations in the tail of the Earth's magnetosphere during a specific geomagnetic substorm. It is shown that a chain of Kelvin-Helmholtz-type vortices in the magnetic field was triggered, leading to energetic electron injections into the Earth's upper atmosphere. The resulting auroral spiral was detected by ground optical cameras located in Tromsø, Norway.

Liu et al. examines changes of the total electron content (TEC) in local Asian sector during the period of a stratospheric sudden warming that occurred in Antarctica in 2019. Various well-known multi-day atmospheric periodicities are examined to distinguish between possible solar wind and geomagnetic forcing from above and forcing from lower atmosphere. The results suggest even a low-level geomagnetic activity could have certain impact on middle atmosphere and it should not be ignored when studying meteorological impacts on the ionosphere.

Szárnya et al. reports multi-instrument observations of a fireball that was recorded on 17 November 2019. The meteoroid had a velocity of 71.18 km/s and originated from the source radiant of the Leonid meteor shower. The meteor was recorded by the Czech fireball network cameras, and the produced ionization column was observed with a digisonde and with the Continous Doppler Sounding (CDS) at Průhonice and Sopron station. The meteor trail ionization was visible for more than 20 min in the digisonde data and CDS.

Knížová et al. describes the ionospheric response to severe tropospheric events in central Europe in July 2021 using multi-instrument observation of the ionosphere and mesosphere by ionosonde, continuous Doppler sounding and OH airglow cameras. It is shown that in addition to acoustic gravity waves, spread F was also observed.

Ikani et al. discusses observation of ionospheric irregularities over Nigeria using the rate of change index (ROTI) of the total electron content measured by receivers of the global navigation satellite signals. Latitudinal differences were found across Nigeria. The highest occurrence rate was around the March equinox. The second, less pronounced peak of occurrence rate was around the September equinox.

Aa et al. deals with a multi-instrument analysis of equatorial plasma bubbles in the American sector under a geomagnetically quiet period on 07–10 December 2019. Large day-to-day variability was found, which better corresponds to the activity of atmospheric gravity waves providing the seeding perturbation than to the estimated growth rate of the Rayleigh-Taylor instability.

Resende et al. describes atypical and spreading Sporadic E-layers (Es) observed by digisonde at low-latitude Brazilian station Cachoeira Paulista (22.41°S, 45°W, dip 35°) from 2016 to 2018. The authors conclude that the spreading Es layer, mainly during quiet times, is not necessarily formed by the particle precipitation in the South Atlantic magnetic anomaly region, but probably due to the turbulent wind shear affecting the evolution of the Es layer.

Buzás et al. investigates the effect of solar flares on the absorption of radio waves in the ionosphere using European digisondes DPS-4D. Amplitude changes at frequencies of 2.5 and 4 MHz were compared with changes in the minimum measured frequency fmin and the signal-to-noise ratio (SNR). The authors conclude that a combination of these three methods seems to be an efficient approach to monitor the ionospheric response to solar flares.

Gasperini et al. studies tides and planetary waves combining ICON MIGHTI wind data over the height ranges 93–106 km and 200–270 km (with day and night coverage), and *in-situ* topside F-region ion densities from IVMs onboard ICON near 590 km and the SORTIE CubeSat near 420 km. The study highlights the importance of simultaneous satellite measurements to analyze ion-neutral interaction and coupling via waves in the thermosphere–ionosphere system.

Kotov and Bogomaz is an opinion article that discusses an unconfirmed hypothesis on hot hydrogen atoms in the upper ionosphere (the exobase), and concludes that the hydrogen temperature is most likely consistent with that of other species.

Maute et al. examines the behaviour of migrating atmospheric solar tides simulated by TIE-GCM global circulation model, driven by tides fitted to ICON observations via the Hough Mode Extension method. It demonstrates that the SW2 tide unexpectedly changes it is latitudinal structure at 250 km from two peaks at mid latitudes to one broad low latitude peak. Other migrating tides undergo similar variations as SW2. The changes in tidal dynamics lead to substantial deviations of NmF2 and O/N_2 values from general seasonal behaviour.

Molina and Scherliess investigated the variability of thermospheric zonal winds at a height of about 250 km by applying a correlation analysis to GOCE zonal wind observations. GOCE observations were analyzed from −50°S to 50°N covering the low and mid-latitudes at dusk and dawn and during geomagnetic quiet conditions around the summer and winter solstice. Due to the GOCE orbit, only nonmigrating tidal components are found in the spatial and temporal correlations.

Molina and Scherliess presents an analysis of thermospheric zonal winds at 260 km altitude obtained from GOCE accelerometer data recorded from 2009 to 2012 during geomagnetically quiet times. Due to the orbit of GOCE measurements are always obtained at dusk and dawn around 6 and 18 LT. The longitudinal variability is assessed using a Fourier decomposition for the wavenumbers 1 to 5. This study summarizes the inter-year variability and seasonal differences concerning the different wavenumbers. Furthermore, the resulting wave activity for each wavenumber is compared to the Climatological Tidal Model of the Thermosphere (CTMT).

Berényi et al. examines the dynamics of ionospheric total electron content as well as the height and the peak density of the F region during the two large geomagnetic storms of the solar cycle

24. Additionally, SWARM and TIMED satellite data are examined. A method is proposed for the monitoring of the storm-time evolution of various known anomalies in sub-auroral, auroral and polar cap regions. The extreme plasma depletion is detected in connection to the equatorward expansion of the midlatitutde ionospheric trough.

Martinez and Lu investigates the short-term variability of the ratio between atomic oxygen and molecular nitrogen (O/N_2) measured by the geostationary GOLD satellite payload for over 3 years under various geomagnetically active conditions. Strong correlations between O/N_2 ratios and geomagnetic activity are found at high latitudes, while at low latitudes there also weak correlations. Strong seasonal dependence of these correlations is also reported. It is suggested that during geomagnetically quiet time the variability of O/N_2 ratios is substantially controlled by the influence from the lower atmosphere.

Kotov et al. investigates the impact of exosphere hydrogen density on the ionosphere-plasmasphere system. Satellite measurements in the topside ionosphere and in the plasmasphere are compared to a model constrained by ionospheric observations at both ends of the magnetic field line. It demonstrates that a factor of 2.75 increase in the hydrogen density increases the simulated plasma density in the afternoon plasmasphere up to ~80% and in the nighttime topside ionosphere up to ~100%, causing major errors.

Da Silva et al. explores the variability of energetic electron precipitations from the Earth's radiation belts in the atmosphere over auroral regions and over the near-equatorial South American Magnetic Anomaly. The particular focus is on electron losses from the radiation belts due to wave-particle interactions with plasma hiss waves during a specific geomagnetic event in Sept. 2017, caused by a high speed solar stream. Resulting precipitations of energetic electrons are shown to be the dominant mechanism for triggering the sporadic E layers.

Sobhkhiz-Miandehi et al. analyzes 11-year dataset of sporadic E layers, detected at mid and low altitudes by satellite radio occultation, and compares to ground observations from six ionosondes. It is demonstrated that at least in 20% of all cases, the ionosonde detections do not agree with radio occultation data. The authors conclude that ground and satellite occultation data agree best during daytime and local summer, when the E region has higher plasma concentration.

Author contributions

VB: Writing–review and editing. JC: Writing–original draft, Writing–review and editing. H-LL: Writing–review and editing. DP: Writing–original draft, Writing–review and editing. GS: Writing–review and editing.

Conflict of interest

The authors declare that the research was conducted in the absence of any commercial or financial relationships that could be construed as a potential conflict of interest.

The author(s) declared that they were an editorial board member of Frontiers, at the time of submission. This had no impact on the peer review process and the final decision.

Publisher's note

frontiers | Frontiers in Astronomy and Space Sciences

TYPE Original Research
PUBLISHED 20 February 2023
DOI 10.3389/fspas.2023.1129279

OPEN ACCESS

EDITED BY
Christina Arras,
GFZ German Research Centre for Geosciences, Germany

REVIEWED BY
Juha Vierinen,
UiT The Arctic University of Norway, Norway
Andrés Calabia,
University of Alcalá, Spain

*CORRESPONDENCE
Benjamin C. Martinez,
ben8@clemson.edu

†These authors have contributed equally to this work and share first authorship

SPECIALTY SECTION
This article was submitted to Space Physics, a section of the journal Frontiers in Astronomy and Space Sciences

RECEIVED 21 December 2022
ACCEPTED 09 February 2023
PUBLISHED 20 February 2023

CITATION
Martinez BC and Lu X (2023), Quantifying day-to-day variability of O/N_2 and its correlation with geomagnetic activity using GOLD.
Front. Astron. Space Sci. 10:1129279.
doi: 10.3389/fspas.2023.1129279

Quantifying day-to-day variability of O/N_2 and its correlation with geomagnetic activity using GOLD

Benjamin C. Martinez*† and Xian Lu†

Department of Physics and Astronomy, Clemson University, Clemson, SC, United States

We quantify the short-term (<30 day) variability of column O/N_2 measured by GOLD from January 2019 to August 2022 for various geomagnetic activity conditions. We find enhanced variabilities at high latitudes during active (Kp ≥ 3.0) times and weak but statistically significant variabilities at low latitudes. For active times, the largest absolute variability of O/N_2 ratio is 0.14 and the largest relative variability is 20.6% at ~60.0°N in Fall, which are about twice those of quiet times. The variability at higher latitudes can be larger than that of lower latitudes by a factor of 5–8. We further quantify contributions of magnetospheric forcing to O/N_2 variability in the Ionosphere-Thermosphere region by correlating O/N_2 perturbations with Dst. During geomagnetic active times, positive correlations as large as +0.66 and negative correlations as large as −0.65 are found at high and low latitudes, respectively, indicative of storm-induced O and N_2 upwelling at high latitudes and down welling at low latitudes. During quiet times, correlations between O/N_2 perturbations and Dst become insignificant at all latitudes, implying a more substantial contribution from below. O/N_2 variabilities maximize in Fall and decrease towards Summer, while correlations maximize in Spring/Summer and decrease in Winter/Spring, which may be related to seasonal variations of geomagnetic activity and mean circulation.

KEYWORDS

day-to-day variability, GOLD, geomagnetic activity, auroral heating, O/N_2 ratio, general circulation

1 Introduction

The Ionosphere-Thermosphere (IT) environment is strongly coupled to the magnetosphere above and the regions of the lower atmosphere below (Rishbeth et al., 2000). During active times, the short-term variability of the IT region is dominated by forcing from above in the form of enhanced magnetospheric forcing related to geomagnetic storms and substorms. During quiet times, the short-term variability of the IT region is modulated primarily by *in-situ* generated tides and/or upward-propagating waves originating from the lower atmosphere (Richmond, 1979; Rishbeth, 1997; Immel et al., 2006; Oberheide et al., 2011; Oberheide et al., 2013). Even during quiet times, however, solar geomagnetic activity can still have a significant impact on IT preconditioning (Cai et al., 2020), and it can take as long as 2 days for the IT to return to pre-storm conditions after a strong or moderate geomagnetic disturbance (Richmond et al., 2003; Lu et al., 2015; Yao et al., 2016). This makes the accurate characterization of the day-to-day variability difficult because it requires that we disentangle the effects of the different forcings in order to understand the relative contributions of each.

Strong agreement between the observed climatology of the IT region and the modeled climatology [from models like the Thermosphere-Ionosphere-Electrodynamics General Circulation Model (TIEGCM), its predecessor the Thermosphere General Circulation Model (TGCM), and the Whole Atmosphere Community Climate Model with thermosphere and ionosphere eXtension (WACCM-X)] has been demonstrated since as early as 1981 (Dickinson et al., 1981; Richmond et al., 1992; Fesen et al., 2002; Qian et al., 2014; Liu et al., 2018), but the day-to-day variations are comparatively difficult to model/study and therefore less understood (Zhou et al., 2020, Zhou et al., 2021; Andoh et al., 2022). Many details of the state of the IT system can be captured by parameters such as the ratio of atomic Oxygen (O) to molecular Nitrogen (N_2) (O/N_2). The seasonal O/N_2 composition of the IT region depends, in particular, on global, vertical circulation in the ionosphere (Burns et al., 1995; Rishbeth et al., 2000; Qian et al., 2010; Luan et al., 2017; Li et al., 2022), the absorption of solar EUV during geomagnetic active periods, which changes the ratio *via* a combination of photodissociation and ionization processes (Kelley, 2009; Schmölter et al., 2020; Yu et al., 2020), and auroral heating-induced vertical winds which bring up atomic oxygen-poor air from the lower atmosphere (Hays et al., 1973).

The recently launched Global Observations of the Limb and Disk (GOLD) satellite provides full-disk ionospheric column O/N_2 as a Level 2 data product from a geostationary orbit centered over the mouth of the Amazon River basin (Eastes et al., 2017). GOLD is the first satellite to observe the IT region from a fixed, geostationary orbit, which allows for the unambiguous separation of spatial and temporal IT variability and therefore makes possible unprecedented analysis of the day-to-day variability of O/N_2. Recent studies have utilized GOLD O/N_2 and temperature measurements to study seasonal variations of O/N_2 as well as the response of O/N_2 to both strong and weak geomagnetic activity (Cai et al., 2020; Laskar et al., 2021; Qian et al., 2022), but the seasonal, short-term response to varying geomagnetic activity levels has not yet been studied systematically across the full, presently available GOLD O/N_2 dataset. Efforts to assimilate GOLD disk temperatures into whole atmosphere models have already led to significant improvements in model effective temperature root-mean square error (RMSE) (Laskar et al., 2021), and it should be possible to use GOLD O/N_2 in a similar fashion to improve the abilities of models to capture day-to-day IT variability.

2 Data and methodology

2.1 GOLD data and data selection

GOLD measures the ratio of the vertical column density of O relative N_2 defined at a standard reference N_2 depth of 10^{17} cm^{-2}. This reference depth is chosen to minimize uncertainty in O/N_2 as a function of 135.6 nm/LBH and is equivalent to ~4 nanobar, or ~160 km (Correira et al., 2021). The O/N_2 ratio is retrieved directly from dayside disk measurements of the OI-135.6 nm and N2-LBH band emission lines in the ~134–164 nm wavelength range. We use version 3 of the O/N_2 data product. The GOLD O/N_2 data product is not optimized for auroral latitudes, so we limit our analysis to ±60° lat. The observations have longitudinal coverage ranging from 113.5°W to 19.5°E.

The O/N_2 data from January 2019 to August 2022 and universal time (UTC) = ~14:00–15:00 are used for the current study. This UTC time range is chosen because the full footprint of GOLD is illuminated at this time and because GOLD scanned at a cadence of one full disk every half hour from 2019–2021, and every hour in 2022. We omit several days in which the data are unreliable for instrumental reasons. We omit the data from the days surrounding a Gyrating Yaw Mechanism (GYM) actuation. GYM actuations, which lead to abrupt changes in 135.6 nm radiance and therefore make standard deviations unreliable, were applied twice in 2019 (4/26/2019 and 10/10/2019), twice in 2020 (3/20/2020 and 8/11/2020), and three times in 2021 (2/8/2021, 6/12/2021, and 8/27/2021) to mitigate the effects of detector burn-in. To quantify the uncertainties associated with each data point, we add the random, system, and model uncertainties reported for the column O/N_2 data product in quadrature. We then omit all data points in which the uncertainties exceed 0.3.

For a particular UTC, there is a 2-D snapshot image of the O/N_2 provided by GOLD for each individual day. In order to spatially suppress the noise, we take the average O/N_2 ratio in a $10^{\circ} \times 10^{\circ}$ (longitude × latitude) grid box and attribute this value to the center grid, and we collect all the data from January 2019 to August 2022 to each grid box. In order to have enough data points for calculating the standard deviation with significance, we omit all grid points where less than half of the days had reliable data. This results in the removal of much of the equatorial region, where uncertainties are generally higher because of flat-field correction errors (see the GOLD instrument documentation, available at https://gold.cs.ucf.edu/).

2.2 Calculation of short-term day-to-day variability

After binning the data for each grid box each day, we have obtained a time series with a temporal resolution of 1 day. We apply a 30-day high-pass filter to the time series at each longitude-latitude grid point to obtain the perturbations with periods shorter than 30 days, which are defined as O/N_2 residuals hereinafter. After these perturbations are obtained, they are grouped together according to different seasons and their standard deviations (stds) are calculated. The seasonal and year-to-year variations are suppressed by the high-pass filter and therefore do not contribute to the std. The std is treated as a proxy for the day-to-day variability shorter than 30 days and longer than 2 days within a given season as a result of the temporal sampling (1 day) and filtering. Winter is defined as December, January, and February, Spring is defined as March, April, and May, Summer is defined as June, July, and August, and Fall/Autumn is defined as September, October, and November.

We consider all pre-screened data that fall into each season (~270–360 points) first, then we divide the data into two activity classes categorized by Kp indices. We consider two separate activity thresholds based on Kp: days in which the maximum Kp ≥ 3.0 or 2.0 are considered to be active days, and days in which the maximum Kp < 3.0 or 2.0 were considered to be quiet days. To account for relatively long (~24–48 h) IT recovery phases, we omit 1 day after each active day from the quiet day data. We use Kp to establish our quiet-time threshold to be consistent with, e.g., Cai et al. (2020). The stds are then calculated for these different groups of data (quiet,

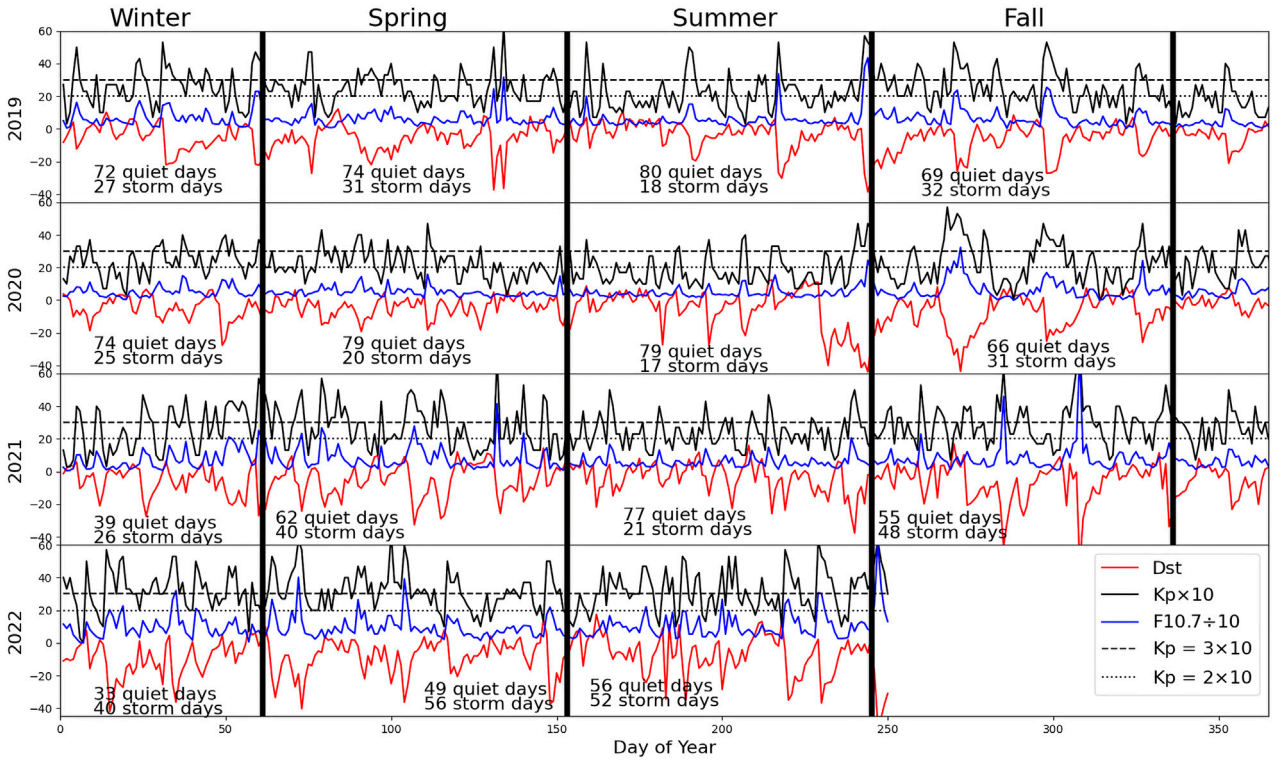

FIGURE 1
Solar and geomagnetic conditions for January 2019–August 2022. The solid black vertical lines divide the year into four seasons. Black, red, and blue lines show the daily maximum Kp, daily mean Dst (nT) and daily mean radio F10.7 (solar flux units). Dashed and dotted black lines show Kp = 3 and Kp = 2, respectively. The numbers in each box show the number of days with Kp ≥ 3.0 (storm days) and with Kp < 3.0 (quiet days). For viewing purposes, Kp index is multiplied by 10 and F10.7 is divided by 10.

active, and all) and used to represent the variability under each condition. Finally, we calculate a relative std by dividing the absolute std by the quiet-time mean O/N_2.

Geomagnetic conditions with the statistics of quiet and active days are summarized in Figure 1. In total, there are 440 active days (Kp ≥ 3.0) and 641 quiet days (Kp < 3.0). For the threshold of Kp = 2.0, there are 846 active days (Kp ≥ 2.0) and 220 quiet days (Kp < 2.0). Plotted Kp values are the daily maxima of 3-h Kp, and the reported Dst and F10.7 values are daily means. We choose daily maximum Kp as our quiet/active cutoff threshold in order to ensure that all days with any geomagnetic activity are considered active (using daily means could lead to misclassifications of days with short spikes of geomagnetic activity but low average Kp). We plot the solar F10.7 flux to show that our daily maximum Kp threshold is sufficient to account for periods of relatively high F10.7, and we show daily mean Dst because that value is used to track the O/N_2 response to geomagnetic activity by correlating it with O/N_2 residuals (see Section 3).

3 Observations and results

Figure 2 shows the full-disk absolute stds of O/N_2 perturbations as a proxy for the day-to-day variability with periods < 30 day in the IT region. Comparing different rows, variabilities are the strongest for Kp ≥ 3.0 (third row), with a maximum of 0.14 identified in Fall (Figure 2D3). Variabilities are the weakest during Kp < 2.0 (fourth row), with a maximum std of 0.07 also in Fall (Figure 2D4), which is about half of that in active time.

Figure 3 is the same as Figure 2 except for showing the relative stds of O/N_2 perturbations. Relative stds are also the strongest when strong activities are considered (Kp ≥ 3.0) and decrease gradually towards moderate strong (Kp ≥ 2.0), moderate weak (Kp < 3.0) and the weakest (Kp < 2.0) conditions. We focus on the relative stds for the discussion of variabilities. For the Kp ≥ 3.0 case (third row of Figure 3), the averaged relative std is 4.9% across all seasons and grid points, and this value is 3.7% for Kp < 2.0, which gives a 28% difference between variabilities during most active and quiet times.

Variability is enhanced at high latitudes which may be related to auroral heating. For Kp ≥ 3.0 (third row), the highest variability observed is 20.6% at (70°W, 60.0°N) in Fall (Figure 2D3) and the weakest variability is 2.4% at (12°E, 6°N) in Summer which differs by a factor of 8–9 between high and low latitude variability for this activity category. During quiet conditions (Kp < 3.0, second row), the high latitude variability enhancement is weakened but still observed. The maximum variability is found to be ~11.1% at a high latitude (70°W, 60°N) in Fall (Figure 3D2), which is about 4–5 times the minimum variability, that is, 2.4% at (8.0°E, 37°S) in Summer (Figure 3C2). The highest relative variability (20.6%) in active time is also about twice of that in quiet time (11.1%). The maximum and averaged variabilities for the various geomagnetic conditions and four seasons are plotted in Figures 6A, B.

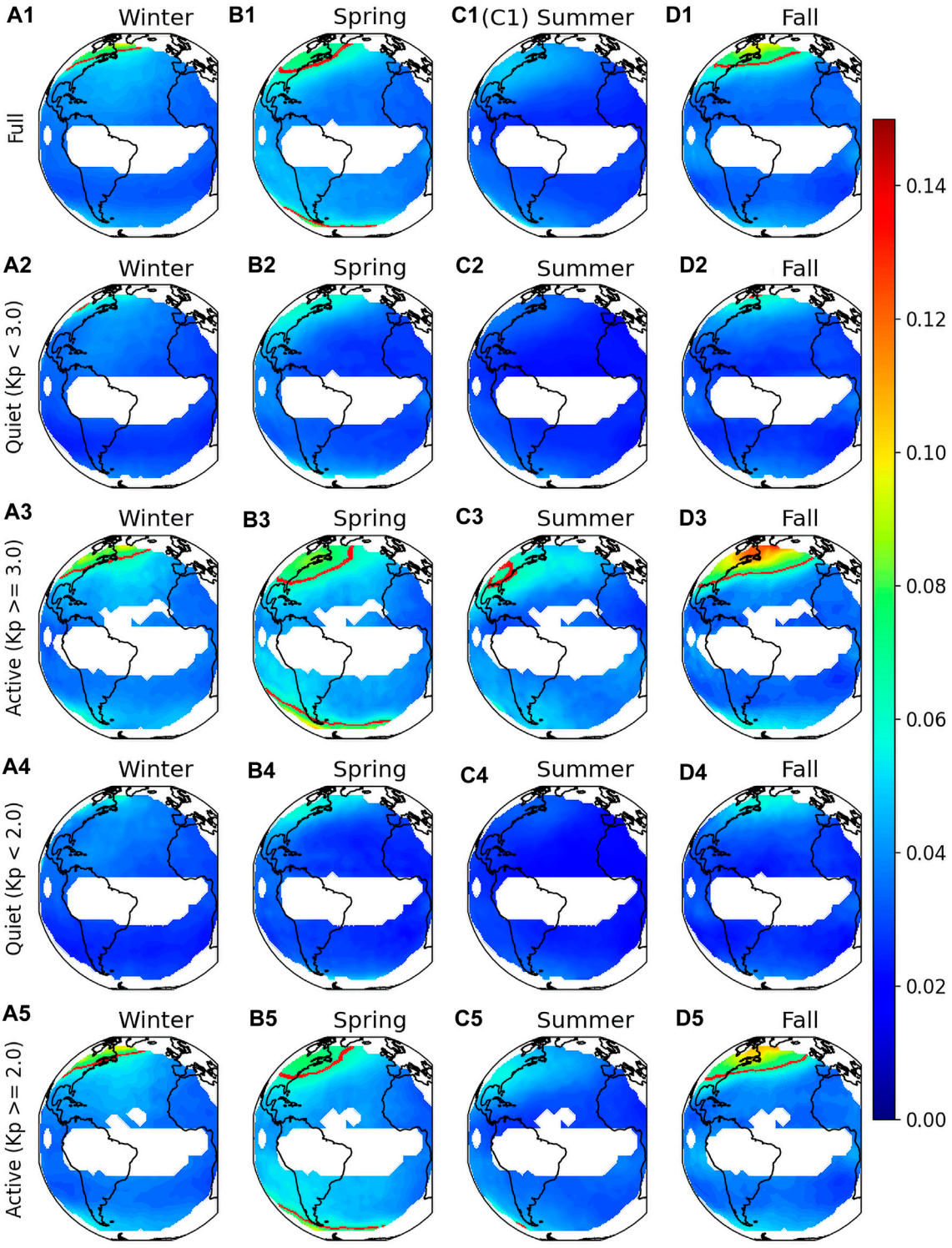

FIGURE 2
(A1–D1) Absolute stds of O/N_2 ratios for the four seasons using all reliable data. **(A2–D2)**, **(A3–D3)**, **(A4–D4)** and **(A5–D5)** are the same except for the stds calculated using data with Kp < 3.0, Kp ≥ 3.0, Kp < 2.0 and Kp ≥ 2.0, respectively. Blank areas are regions where more than half of the daily O/N_2 points had uncertainties exceeding 0.30. Red lines are the contours of 7.7%.

In addition to the obvious latitudinal dependence, the magnitude of O/N_2 variability and the extent of the high variability region at high northern latitudes also show a seasonal variation. The O/N_2 maxima for the full dataset (Figures 3A1–D1) are 16%, 14%, 12% and 9% in Fall, Winter, Spring and Summer, which decrease from Fall to Summer. Maximum O/N_2 variability

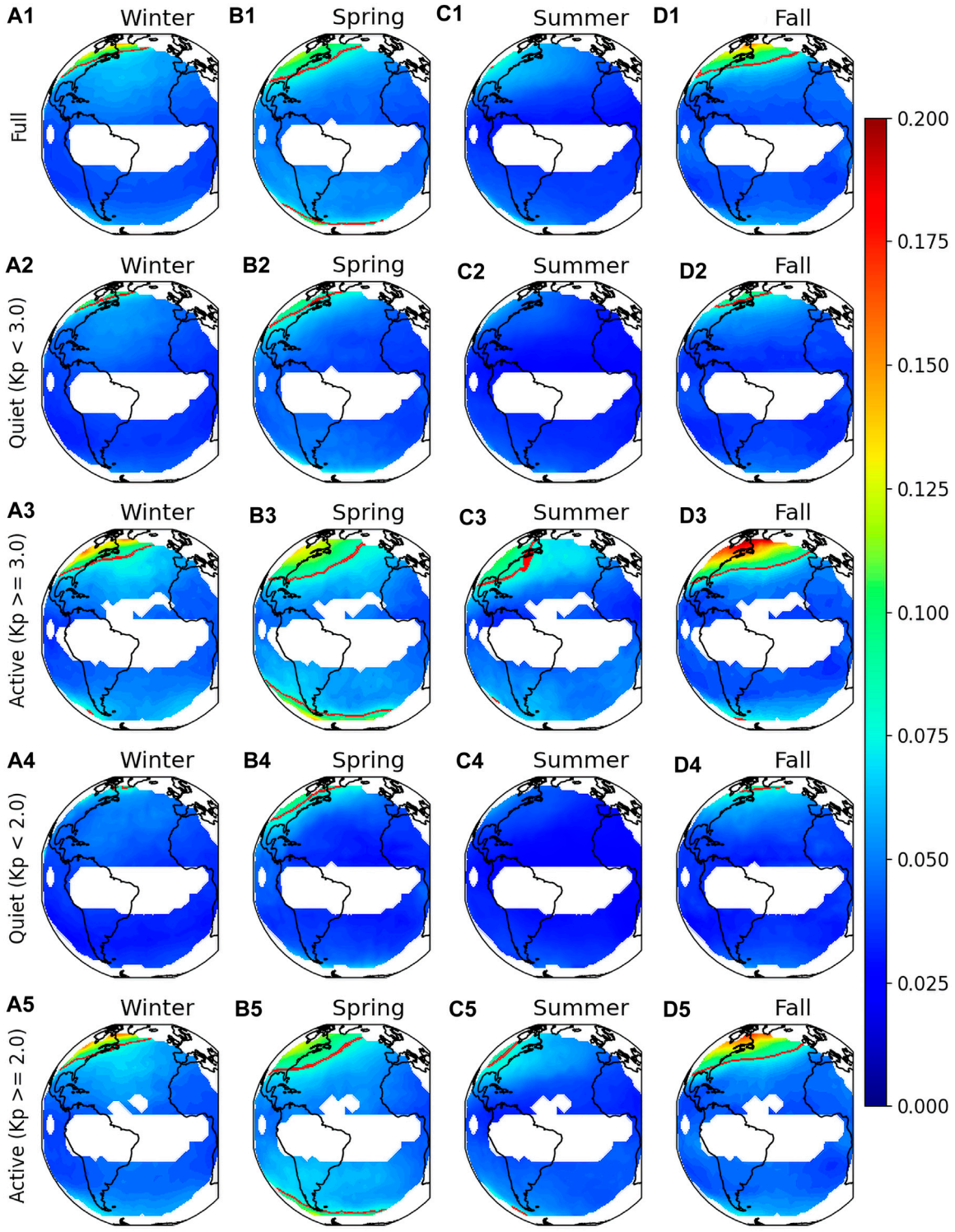

FIGURE 3
Same as Figure 2 except for relative stds. **(A1–D1)** are the relative stds of O/N_2 ratios for the four seasons using all reliable data. **(A2–D2)**, **(A3–D3)**, **(A4–D4)**, and **(A5–D5)** are the same except for the stds calculated using data with Kp < 3.0, Kp ≥ 3.0, Kp < 2.0, and Kp ≥ 2.0, respectively. Blank areas are regions where more than half of the daily O/N_2 points had uncertainties exceeding 0.30. Red lines are the contours of 7.7%.

also decreases from 21% to 11% from Fall to Summer for Kp ≥ 3.0. To quantify the extent of the high variability region which may be affected by aurora, we count all grid points where relative O/N_2 stds exceed 7.7% (red contours in Figure 3) and convert that number to a percentage of the full GOLD field of view (fov). For each set of geomagnetic conditions, the extent of the region of influence is at maximum during Fall and Spring and at minimum during Winter and Summer. As an example, 5.0%, 13%, 2.5%, and 11% of the

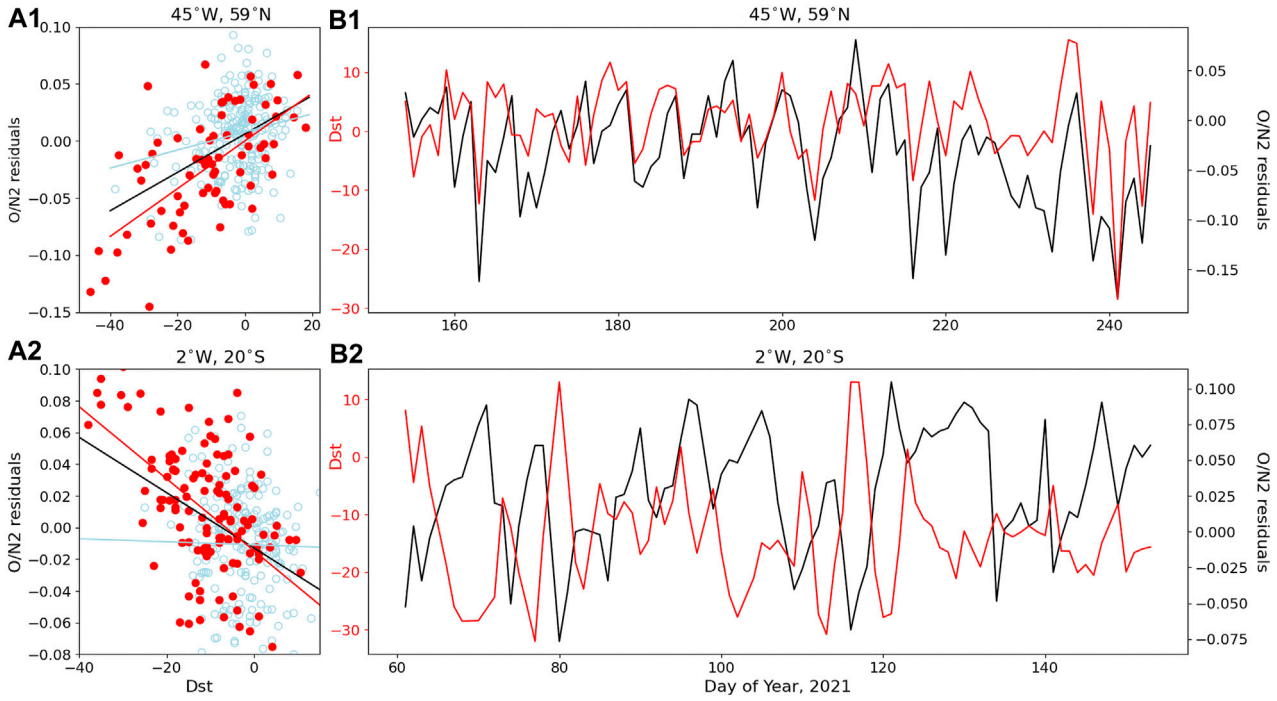

FIGURE 4
(A1,A2) O/N_2 residuals versus Dst (scattered points) and their corresponding linear fits (straight lines) at (45°W, 59°N), and (2°W, 20°S). Light blue and red colors represent quiet and storm-times. The solid black line in each panel is fitted to all data points. **(B1,B2)** O/N_2 residuals (black lines) and daily mean Dst (red lines) as a function of day of year at (45°W, 59°N), and (2°W, 20°N).

GOLD fov had relative O/N_2 stds > 7.7% for Winter, Spring, Summer, and Fall, respectively considering the full dataset. The extents of the high variability region for different geomagnetic conditions and four seasons are illustrated in Figure 6C. It should be noted that 3–4 years of GOLD O/N_2 data are used for this study: four Winters, Springs, and Summers and only three Falls. More data may help to better confirm the seasonal dependence.

From Figures 2, 3, variability increases with Kp index, which implies that magnetospheric forcing plays a role in the day-to-day variability of O/N_2, especially at high latitudes. In order to better quantify this contribution, we calculate the correlation between the time series of O/N_2 residuals and the Dst index. Figure 4 shows the correlation between these two parameters at (45°W, 59°N, a relatively high latitude region) during Summer and (2°W, 20°S, a relatively low latitude region) during Spring. The active-time data points (red in Figures 4A1, A2) are more tightly clustered than their quiet time (light blue) counterparts, and a linear fit shows a steep, positive (+0.66) correlation at (45°W, 59°N) and a steep negative (−0.65) correlation at (2°W, 20°S). In contrast, correlations are small when only quiet days are considered: +0.21 for (45°W, 59°N) and +0.07 for (2°W, 20°S). Magnitudes of the correlations decrease compared to active times when both quiet and active days are considered: they become +0.46 for (45°W, 59°N) and −0.38 for (2°W, 20°S). Figures 4B1, B2 show the time series of O/N_2 residuals overplotted with Dst indices (both quiet and storm times are considered). The correlation at high latitudes and the anti-correlation at low latitudes are apparent.

Shown in Figure 5 are the calculated correlation coefficients for each grid point in the GOLD fov for each season. Data gaps are present where correlations are determined to be insignificant based on a Student's *t*-test and its associated *p*-value. We keep correlations where the *p*-value is less than 0.05, which means that the significance level of the correlation is greater than 95%. Figures 5A1–D1 show correlation maps where all reliable data for both quiet and storm conditions are considered. Red regions indicate positive correlations, and blue regions indicate negative correlations. Since Dst decreases in response to enhanced geomagnetic activity, a positive correlation means that the O/N_2 ratio decreases as Dst decreases which corresponds to a storm-induced depletion in O/N_2. A negative correlation means O/N_2 ratio increases as Dst decreases, corresponding to a storm-induced enhancement in O/N_2.

By comparing different rows of Figure 5, which are grouped according to Kp, absolute correlations are the highest when large Kp values are considered (Kp ≥ 3.0, Figures 5A3–D3). Correlations as strong as +0.66 at (45°W, 59°N) and −0.65 at (2°W, 20°S) are observed during active time (Kp ≥ 3.0) in Summer (Figure 5C3). The highest correlations for Kp ≥ 2.0 are +0.55 at (45°W, 59°N) and −0.57 at (76°W, 55°S) in Summer (Figure 5C5). Maximum correlations for the full dataset (Figures 4A1–D1) are +0.47 at (72°W, 42°N) and −0.47 at (66°W, 54°S) during Summer (Figure 5C1). The maximum correlation and anti-correlation for the full dataset, and two active conditions are provided in Table 1.

There are very few significant correlations for quiet conditions (Kp < 3.0 and Kp < 2.0, Figures 5A2–D2, A4–D4) except for the quiet Summer. However, the region of significant correlation during Kp < 3.0 (Figure 5C2) shrinks significantly when only Kp < 2.0 is considered (Figure 5C4), which indicates that the threshold of Kp <

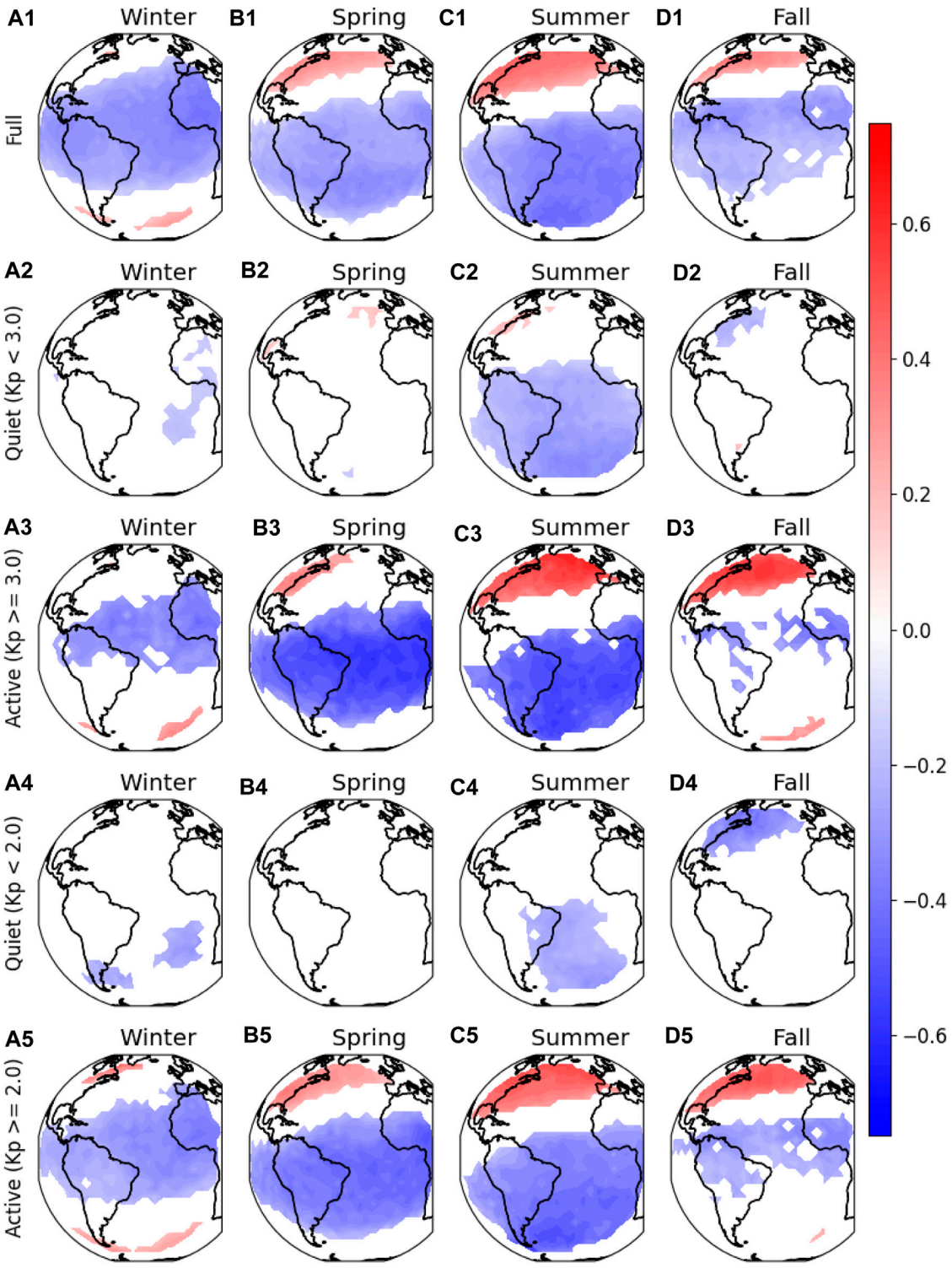

FIGURE 5
(A1–D1) Correlation maps between O/N_2 residuals and Dst indices for the four seasons. Data gaps are present where the significance level is less than 95%. **(A2–D2)** and **(A3–D3)** are the same except only for quiet time (with Kp < 3.0) and active (Kp ≥ 3.0) times. **(A4–D4)** and **(A5–D5)** are the same except for quiet time with Kp < 2.0 and Kp ≥ 2.0 times.

2.0 and the omission of 1 day after geomagnetic active days significantly reduces the contribution of magnetospheric forcing on IT variability. Cross-comparing Figures 2, 5, even though correlations are robust at both high and low latitudes during active times, variabilities are much larger at high latitudes, implying a more direct influence locally from aurora.

TABLE 1 The maximum correlation and largest anti-correlation for each season and activity class which includes active time data. The position of each correlation is given in parentheses.

	Winter	Spring	Summer	Fall
Full	0.3 (62.0°W, 54.0°N)	0.35 (81.0°W, 40.0°N)	0.47 (72.0°W, 42.0°N)	0.41 (70.0°W, 46.0°N)
	−0.45 (5.0°W, 11.0°N)	−0.39 (28.0°W, 27.0°S)	−0.47 (66.0°W, 54.0°S)	−0.39 (67.0°W, 10.0°N)
Kp ≥ 3.0	0.36 (6.0°E, 49.0°S)	0.39 (92.0°W, 37.0°N)	0.66 (45.0°W, 59.0°N)	0.61 (40.0°W, 42.0°N)
	−0.49 (5.0°W, 11.0°N)	−0.64 (39.0°W, 22.0°S)	−0.65 (2.0°W, 20.0°S)	−0.46 (18.0°W, 10.0°N)
Kp ≥ 2.0	0.48 (59.0°W, 60.0°N)	0.39 (92.0°W, 37.0°N)	0.55 (45.0°W, 59.0°N)	0.53 (36.0°W, 45.0°N)
	−0.46 (5.0°W, 11.0°N)	−0.51 (44.0°W, 1.0°S)	−0.57 (76.0°W, 55.0°S)	−0.4 (3.0°E, 11.0°N)

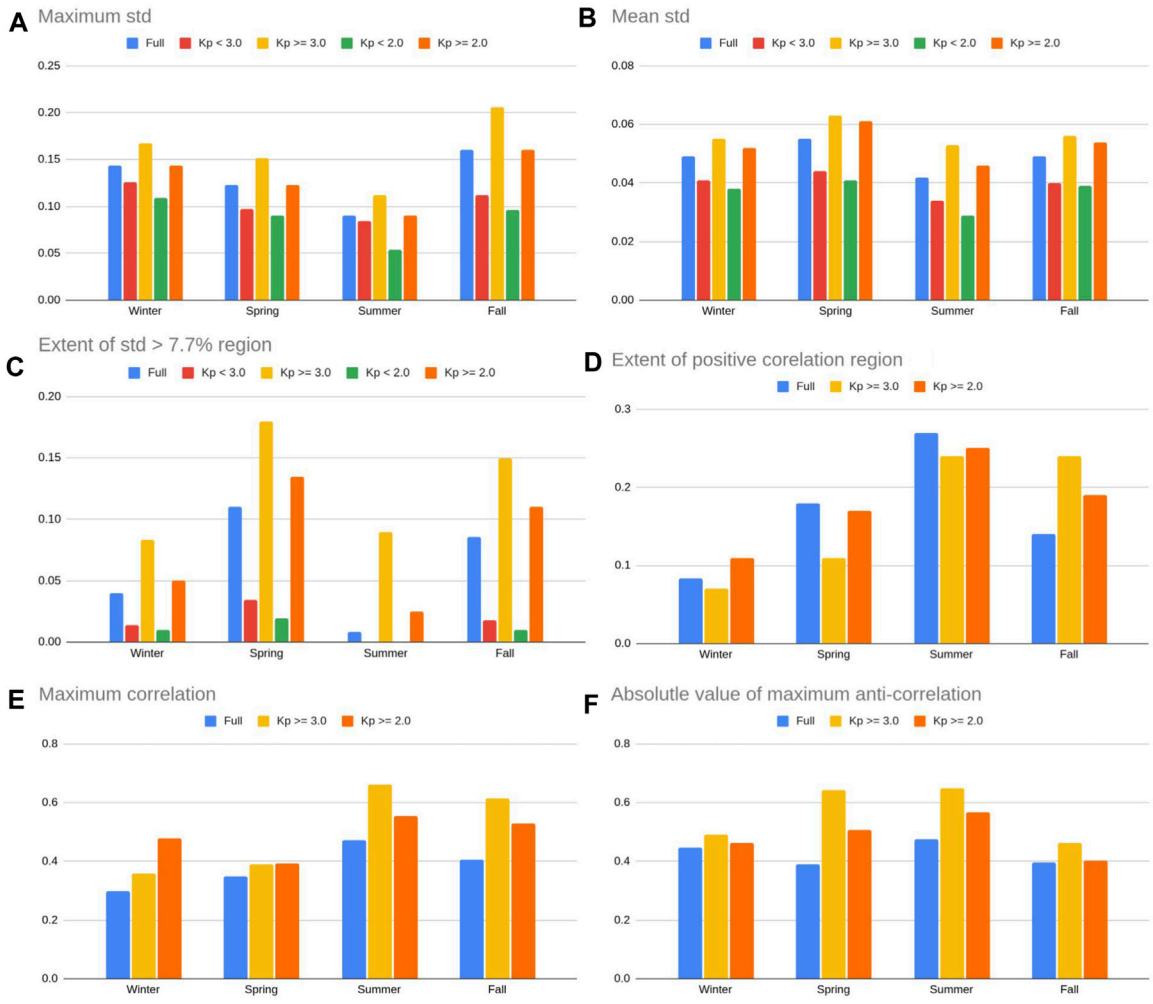

FIGURE 6
(A) Maximum and **(B)** mean standard deviation over the full disk for each season and each activity class. **(C)** Extent of the high variability region (relative stds ≥ 7.7%) as a percentage of the GOLD fov for each season and activity class. **(D)** Extent of the positive correlation region as a percentage of the GOLD fov. **(E)** Maximum positive correlation and **(F)** absolute value of maximum anti-correlation for each season and activity class.

Similar to the variability, the extent of the positive correlation region and the maximum correlation show apparent seasonal dependencies. The extent of the positive correlation region is smallest during Winter (8.3% of the GOLD fov) and largest during Summer (27% of the GOLD fov) for the full dataset (Figure 6D). Similar trends exist for Kp ≥ 3.0 and Kp ≥ 2.0 of the positive correlation regions, and for maximum correlation values (Figure 6E). For example, when all data points are considered, the maximum positive correlations are 0.30, 0.35, 0.41, and 0.47 for Winter, Spring, Fall, and Summer respectively. The absolute values

of largest anti-correlations for the three geomagnetic conditions (all data, Kp ≥ 3.0 and Kp ≥ 2.0) and four seasons are plotted in Figure 6F.

4 Discussion and summary

The dependence of variability and correlation on Kp index, and the statistically significant correlation with Dst index indicate that the day-to-day O/N_2 variabilities are strongly coupled to storm activities. Both auroral particle precipitation and Joule heating are enhanced during active times, with the auroral oval itself expanding and contracting with the activity level in a similar manner to the expansion and contraction of the high variability region (Figures 2, 3) and positive correlation region (Figure 5) observed at high latitudes. The fact that the high latitude enhancement in O/N_2 variability is present (albeit weakened) during quiet times indicates that forcing from above can still dominate at high latitudes, regardless of geomagnetic activity levels.

The correlation maps shown in Figure 5 reflect the storm-induced, global, thermospheric circulation patterns which influence the distribution of O and N_2. Joule heating causes the upwelling of N_2-rich air and O-depleted air from the lower atmosphere, which is then distributed over high and mid latitudes by neutral winds (Strickland et al., 2004; Zhang et al., 2004; Zhang et al., 2015). The high latitude, positive correlation regions in Figure 5 are indicative of this upwelling. The corresponding negative correlations at low latitudes can be explained by the storm induced change in global circulation which drives low latitude downwelling (Fuller-Rowell et al., 2002). The low latitude response required to maintain continuity of mass flow is both delayed and weakened relative to the high latitude response (Forbes, 2007), which explains the smaller variabilities at low latitudes seen in Figures 2, 3. Based on this interpretation, the correlation map for the storm-time matches very closely the accepted circulation patterns for O and N_2.

Luan et al. (2017) used data from the Global Ultraviolet Imager (GUVI) on board the TIMED (Thermosphere, Ionosphere, and Mesosphere, Energetics and Dynamics) satellite to obtain global maps of O/N_2. The group reported larger values of O/N_2 at high latitudes, which increased with increasing F10.7. They also reported significant longitudinal variations in O/N_2 at a particular LT. These results compliment our own work, which instead focuses on the day-to-day variability of O/N_2. Similar to the high latitude enhancement in mean O/N_2 reported by Luan et al. (2017), we report high latitude enhancements in the day-to-day variability of O/N_2 (Figures 2, 3). Luan et al. (2017) attributed the enhancement in mean O/N_2 to auroral heating, which agrees with our own conclusions about auroral heating as the source of enhanced variability in O/N_2.

Luan et al. (2017) also made use of TIE-GCM to further study the contribution of Joule heating to the observed O/N_2 latitude-longitudinal patterns. This study showed that stronger auroral precipitation causes a decrease in O/N_2 at high latitudes, which is consistent with the positive correlations between O/N_2 and Dst that we report at high latitudes (Figure 5). Our work demonstrates that geomagnetic activity not only changes the absolute values of O/N_2, it also contributes to the absolute and relative short-term temporal variability of O/N_2. This implies that O/N_2 changes more dramatically during storms and substorms.

The seasonal dependence of O/N_2 variability and O/N_2 residuals/Dst correlations may be partly explained by the seasonal dependence of auroral activity (Newell et al., 2010; Bower et al., 2022). O/N_2 variabilities are strongest during Fall and Winter and weakest during Summer, which is consistent with observations of stronger auroral hemispheric power (HP) during Winter months (Zheng et al., 2013). Although auroral activity is at a minimum during Summer months, geomagnetic active-time upper thermospheric winds are at a maximum during these months (Dhadly and Conde, 2017), which may cause N_2 rich and O poor air that has been brought up by upwelling to spread to lower latitudes. This may have the effect of increasing the auroral region of influence during Summer and enhancing the correlation, which is reflected in Figure 5.

In summary, the day-to-day (2–30 day) variability of GOLD O/N_2 column density has been quantified and its correlation with Dst has been evaluated for various geomagnetic conditions and seasons for the first time. The main findings include:

1. Variability is significantly enhanced at high latitudes and during active (Kp ≥ 3.0) times, during which the largest absolute and relative variabilities of O/N_2 ratio are found to be 0.14% and 21%, respectively, at ~60.0°N in Fall. Variabilities are the weakest during Summer. Small but statistically significant variabilities are also observed at low latitudes and during quiet (Kp < 3.0) times. The maximum variability at high latitude during quiet times can decrease to half of the that during active times. The variability at low latitudes is smaller than that at high latitudes by a factor of 5–8 in general.
2. The active-time (Kp > 3.0) O/N_2 residuals show the strongest positive correlation with Dst index at high latitude [+0.66 at (45°W, 59°N)] and strongest negative positive correlation at low latitude [−0.65 at (2°W, 20°S)] in Summer. Quiet-time correlation with Dst index is not statistically significant.
3. Correlations between Dst and O/N_2 residuals become insignificant across the GOLD fov when only quiet (Kp < 2.0) days are considered, which implies a more substantial contribution from forcing from below to the observed variability during quiet conditions.
4. O/N_2 variability and the correlation between Dst and O/N_2 residuals have apparent seasonal dependencies. O/N_2 variability is at a maximum during Fall and at minimum during Summer, whereas correlations are strongest during Summer and weakest during Winter.

This work has provided baseline/references for numerical models to capture the short-term variability of an important parameter (O/N_2) of the IT system. To further diagnose the contributions from each source and find quantitative explanations for the ways that chemistry, dynamics, and electrodynamics contribute to the observed variability, for instance geomagnetic origin versus lower-atmosphere forcing, we will involve model sensitivity runs in a future work.

Data availability statement

Publicly available datasets were analyzed in this study. This data can be found here: https://gold.cs.ucf.edu/data/search/.

Author contributions

BM and XL contributed to conceptualization, methodology, and writing. BM performed the analysis. XL contributed to funding acquisition, investigation, supervision, and review editing. All authors have read and agreed to the published version of the manuscript.

Funding

This work is supported by NASA 80NSSC22K0018, NNX17AG10G, 80NSSC22K1010, 80NSSCK19K0810, and NSF AGS-2149695 and CAREER-1753214, and AGS-2012994.

Acknowledgments

We are grateful for discussions with Jens Oberheide and Haonan Wu at Clemson University, Jintai Li at University of Alaska, Fairbanks, Richard Eastes and Quan Gan at LASP, University of Colorado Boulder, and Nick Pedatella at the High Altitude Observatory, NCAR.

Conflict of interest

The authors declare that the research was conducted in the absence of any commercial or financial relationships that could be construed as a potential conflict of interest.

Publisher's note

References

Andoh, S., Saito, A., and Shinagawa, H. (2022). Numerical simulations on day-to-day variations of low-latitude Es layers at Arecibo. *Geophys. Res. Lett.* 49, e2021GL097473. doi:10.1029/2021GL097473

Bower, G. E., Milan, S. E., Paxton, L. J., and Anderson, B. J. (2022). Occurrence statistics of horse collar aurora. *J. Geophys. Res. Space Phys.* 127, e2022JA030385. doi:10.1029/2022JA030385

Burns, A. G., Killeen, T. L., Carignan, G. R., and Roble, R. G. (1995). Large enhancements in the O/N2 ratio in the evening sector of the winter hemisphere during geomagnetic storms. *J. Geophys. Res.* 100 (A8), 14661–14671. doi:10.1029/94JA03235

Cai, X., Burns, A. G., Wang, W., Coster, A., Qian, L., Liu, J., et al. (2020). Comparison of GOLD nighttime measurements with total electron content: Preliminary results. *J. Geophys. Res. Space Phys.* 125, e2019JA027767. doi:10.1029/2019JA027767

Correira, J., Evans, J. S., Lumpe, J. D., Krywonos, A., Daniell, R., Veibell, V., et al. (2021). Thermospheric composition and solar EUV flux from the global-scale observations of the Limb and disk (GOLD) mission. *J. Geophys. Res. Space Phys.* 126, e2021JA029517. doi:10.1029/2021JA029517

Dhadly, M., and Conde, M. (2017). Trajectories of thermospheric air parcels flowing over Alaska, reconstructed from ground-based wind measurements. *J. Geophys. Res. Space Phys.* 122, 6635–6651. doi:10.1002/2017JA024095

Dickinson, R. E., Ridley, E. C., and Roble, R. G. (1981). A three-dimensional general circulation model of the thermosphere. *J. Geophys. Res.* 86 (A3), 1499–1512. doi:10.1029/JA086iA03p01499

Eastes, R. W., McClintock, W. E., Burns, A. G., Anderson, D. N., Andersson, L., Codrescu, M., et al. (2017). The global-scale observationsof the Limb and disk (GOLD) mission. *Space Sci. Rev.* 212 (1–2), 383–408. doi:10.1007/s11214-017-0392-2

Fesen, C. G., Hysell, D. L., Meriwether, J. M., Mendillo, M., Fejer, B. G., Roble, R. G., et al. (2002). Modeling the low-latitude thermosphere and ionosphere. *J. Atmos. Sol. Terr. Phys.* 64, 1337–1349. doi:10.1016/s1364-6826(02)00098-6

Forbes, J. M. (2007). Dynamics of the thermosphere. *J. Meteorol. Soc. Jpn.* 85B, 193–213. doi:10.2151/jmsj.85b.193

Fuller-Rowell, T. J., Millward, G. H., Richmond, A. D., and Codrescu, M. V. (2002). Storm-time changes in the upper atmosphere at low latitudes. *J. Atmos. Solar-Terrestrial Phys.* 64 (12–14), 1383–1391. doi:10.1016/s1364-6826(02)00101-3

Hays, P. B., Jones, R. A., and Rees, M. H. (1973). Auroral heating and the composition of the neutral atmosphere. *Planet. Space Sci.* 21 (4), 559–573. doi:10.1016/0032-0633(73)90070-6

Immel, T. J., Sagawa, E., England, S. L., Henderson, S. B., Hagan, M. E., Mende, S. B., et al. (2006). Control of equatorial ionospheric morphology by atmospheric tides. *Geophys. Res. Lett.* 33, L15108. doi:10.1029/2006GL026161

Kelley, M. C. (2009). *The earth's ionosphere: Plasma physics and electrodynamics, international geophysics series*, 43. Academic Press.

Laskar, F. I., Eastes, R. W., Codrescu, M. V., Evans, J. S., Burns, A. G., Wang, W., et al. (2021). Response of GOLD retrieved thermospheric temperatures to geomagnetic activities of varying magnitudes. *Geophys. Res. Lett.* 48, e2021GL093905. doi:10.1029/2021GL093905

Li, Z., Luan, X., Lei, J., and Ren, D. (2022). A simulation study on the variation of thermospheric O/N2 with solar activity. *J. Geophys. Res. Space Phys.* 127, e2022JA030305. doi:10.1029/2022JA030305

Liu, H.-L., Bardeen, C. G., Foster, B. T., Lauritzen, P., Liu, J., Lu, G., et al. (2018). Development and validation of the whole atmosphere community climate model with thermosphere and ionosphere extension (WACCM-X 2.0). *J. Adv. Model. Earth Syst.* 10, 381–402. doi:10.1002/2017MS001232

Lu, G., Hagan, M. E., Häusler, K., Doornbos, E., Bruinsma, S., Anderson, B. J., et al. (2015). Global ionospheric and thermospheric response to the 5 April 2010 geomagnetic storm: An integrated data-model investigation. *J. Geophys. Res. Space Phys.* 119 (10), 375. doi:10.1002/2014JA020555

Luan, X., Wang, W., Burns, A., and Dou, X. (2017). Solar cycle variations of thermospheric O/N2 longitudinal pattern from TIMED/GUVI. *J. Geophys. Res. Space Phys.* 122, 2605–2618. doi:10.1002/2016JA023696

Newell, P. T., Sotirelis, T., and Wing, S. (2010). Seasonal variations in diffuse, monoenergetic, and broadband aurora. *J. Geophys. Res.* 115, A03216. doi:10.1029/2009JA014805

Oberheide, J., Forbes, J. M., Zhang, X., and Bruinsma, S. L. (2011). Climatology of upward propagating diurnal and semidiurnal tides in the thermosphere. *J. Geophys. Res.* 116, A11306. doi:10.1029/2011JA016784

Oberheide, J., Mlynczak, M. G., Mosso, C. N., Schroeder, B. M., Funke, B., and Maute, A. (2013). Impact of tropospheric tides on the nitric oxide 5.3 µm infrared cooling of the low-latitude thermosphere during solar minimum conditions. *J. Geophys. Res. Space Phys.* 118, 7283–7293. doi:10.1002/2013JA019278

Qian, L., Burns, A. G., Emery, B. A., Foster, B., Lu, G., Maute, A., et al. (2014). "The NCAR TIE-GCM," in *Modeling the ionosphere–thermosphere system* Editors J. Huba, R. Schunk, and G. Khazanov doi:10.1002/9781118704417.ch7

Qian, L., Gan, Q., Wang, W., Cai, X., Eastes, R., and Yue, J. (2022). Seasonal variation of thermospheric composition observed by NASA GOLD. *J. Geophys. Res. Space Phys.* 127, e2022JA030496. doi:10.1029/2022JA030496

Qian, L., Solomon, S. C., and Mlynczak, M. G. (2010). Model simulation of thermospheric response to recurrent geomagnetic forcing. *J. Geophys. Res.* 115, A10301. doi:10.1029/2010JA015309

Richmond, A. D. (1979). Large-amplitude gravity wave energy production and dissipation in the thermosphere. *J. Geophys. Res.* 84 (5), 1880–1890. doi:10.1029/JA084iA05p01880

Richmond, A. D., Peymirat, C., and Roble, R. G. (2003). Long-lasting disturbances in the equatorial ionospheric electric field simulated with a coupled magnetosphere-ionosphere-thermosphere model. *J. Geophys. Res.* 108, 1118. doi:10.1029/2002ja009758

Richmond, A. D., Ridley, E. C., and Roble, R. G. (1992). A thermosphere/ionosphere general circulation model with coupled electrodynamics. *Geophys. Res. Lett.* 19 (6), 601–604. doi:10.1029/92GL00401

Rishbeth, H. (1997). Long-term changes in the ionosphere. *Adv. Space Res.* 20 (11), 2149–2155. doi:10.1016/S0273-1177(97)00607-8

Rishbeth, H., Müller-Wodarg, I. C. F., Zou, L., Fuller-Rowell, T. J., Millward, G. H., Moffett, R. J., et al. (2000). Annual and semiannual variations in the ionospheric F2-layer: II. Physical discussion. *Phys. Discuss. Ann. Geophys.* 18, 945–956. doi:10.1007/s00585-000-0945-6

Schmölter, E., Berdermann, J., Jakowski, N., and Jacobi, C. (2020). Spatial and seasonal effects on the delayed ionospheric response to solar EUV changes. *Ann. Geophys.* 38, 149–162. doi:10.5194/angeo-38-149-2020

Strickland, D. J., Meier, R. R., Walterscheid, R. L., Craven, J. D., Christensen, A. B., Paxton, L. J., et al. (2004). Quiet-time seasonal behavior of the thermosphere seen in the far ultraviolet dayglow. *J. Geophys. Res.* 109, A01302. doi:10.1029/2003JA010220

Yao, Y., Liu, L., Kong, J., and Zhai, C. (2016). Analysis of the global ionospheric disturbances of the March 2015 great storm. *J. Geophys. Res. Space Phys.* 121, 12,157–12,170. doi:10.1002/2016JA023352

Yu, T., Ye, H., Liu, H., Xia, C., Zuo, X., Yan, X., et al. (2020). Ionospheric F layer scintillation weakening as observed by COSMIC/FORMOSAT-3 during the major sudden stratospheric warming in january 2013. *J. Geophys. Res. Space Phys.* 125, e2019JA027721. doi:10.1029/2019JA027721

Zhang, B., Lotko, W., Brambles, O., Wiltberger, M., and Lyon, J. (2015). Electron precipitation models in global magnetosphere simulations. *J. Geophys. Res. Space Phys.* 120, 1035–1056. doi:10.1002/2014JA020615

Zhang, Y., Paxton, L. J., Morrison, D., Wolven, B., Kil, H., Meng, C.-I., et al. (2004). O/N2 changes during 1–4 october 2002 storms: IMAGE SI-13 and TIMED/GUVI observations. *J. Geophys. Res.* 109, A10308. doi:10.1029/2004JA010441

Zheng, L., Fu, S., Zong, Q., Parks, G., Wang, C., and Chen, X. (2013). Solar cycle dependence of the seasonal variation of auroral hemispheric power. *Chin. Sci. Bull.* 58 (4–5), 525–530. doi:10.1007/s11434-012-5378-6

Zhou, X., Liu, H., Lu, X., Zhang, R., Maute, A., Wu, H., et al. (2020). Quiet-time day-to-day variability of equatorial vertical E×B drift from atmosphere perturbations at dawn. *J. Geophys. Res. Space Phys.* 125. doi:10.1029/2020JA027824

Zhou, X., Yue, X., Liu, H., Lu, X., Wu, H., Zhao, X., et al. (2021). A comparative study of ionospheric day-to-day variability over wuhan based on ionosonde measurements and model simulations. *J. Geophys. Res. Space Phys.* 126. doi:10.1029/2020JA028589

frontiers | Frontiers in Astronomy and Space Sciences

TYPE Original Research
PUBLISHED 21 March 2023
DOI 10.3389/fspas.2023.1167245

OPEN ACCESS

EDITED BY
Jaroslav Chum,
Institute of Atmospheric Physics (ASCR), Czechia

REVIEWED BY
Tobias Verhulst,
Royal Meteorological Institute of Belgium, Belgium
Sampad Kumar Panda,
K L University, India

*CORRESPONDENCE
Ercha Aa,
aercha@mit.edu

SPECIALTY SECTION
This article was submitted to Space Physics, a section of the journal Frontiers in Astronomy and Space Sciences

RECEIVED 16 February 2023
ACCEPTED 09 March 2023
PUBLISHED 21 March 2023

CITATION
Aa E, Zhang S-R, Coster AJ, Erickson PJ and Rideout W (2023), Multi-instrumental analysis of the day-to-day variability of equatorial plasma bubbles.
Front. Astron. Space Sci. 10:1167245.
doi: 10.3389/fspas.2023.1167245

Multi-instrumental analysis of the day-to-day variability of equatorial plasma bubbles

Ercha Aa*, Shun-Rong Zhang, Anthea J. Coster, Philip J. Erickson and William Rideout

Haystack Observatory, Massachusetts Institute of Technology, Westford, MA, United States

This paper presents a multi-instrument observational analysis of the equatorial plasma bubbles (EPBs) variation over the American sector during a geomagnetically quiet time period of 07–10 December 2019. The day-to-day variability of EPBs and their underlying drivers are investigated through coordinately utilizing the Global-scale Observations of Limb and Disk (GOLD) ultraviolet images, the Ionospheric Connection Explorer (ICON) *in-situ* and remote sensing data, the global navigation satellite system (GNSS) total electron content (TEC) observations, as well as ionosonde measurements. The main results are as follows: 1) The postsunset EPBs' intensity exhibited a large day-to-day variation in the same UT intervals, which was fairly noticeable in the evening of December 07, yet considerably suppressed on December 08 and 09, and then dramatically revived and enhanced on December 10. 2) The postsunset linear Rayleigh-Taylor instability growth rate exhibited a different variation pattern. It had a relatively modest peak value on December 07 and 08, yet a larger peak value on December 09 and 10. There was a 2-h time lag of the growth rate peak time in the evening of December 09 from other nights. This analysis did not show an exact one-to-one relationship between the peak growth rate and the observed EPBs intensity. 3) The EPBs' day-to-day variation has a better agreement with that of traveling ionospheric disturbances and atmospheric gravity waves signatures, which exhibited relatively strong wavelike perturbations preceding/accompanying the observed EPBs on December 07 and 10 yet relatively weak fluctuations on December 08 and 09. These coordinate observations indicate that the initial wavelike seeding perturbations associated with AGWs, together with the catalyzing factor of the instability growth rate, collectively played important roles to modulate the day-to-day variation of EPBs. A strong seeding perturbation could effectively compensate for a moderate strength of Rayleigh-Taylor instability growth rate and therefore their combined effect could facilitate EPB development. Lacking proper seeding perturbations would make it a more inefficient process for the development of EPBs, especially with a delayed peak value of Rayleigh-Taylor instability growth rate.

KEYWORDS

equatorial plasma bubbles, Rayleigh-Taylor instability, day-to-day variation, TID/AGWs, GOLD-ICON, GNSS TEC

1 Introduction

Equatorial plasma bubbles (EPBs) are irregular plasma density depletion structures that are often observed at the nighttime equatorial and low-latitude ionospheric F-region, which have continued to be of long-standing research interest for decades due to their adverse impacts on navigation, communication, and radar systems (Hysell, 2000). The morphological features and dynamic variations of EPBs and associated plasma irregularities have been widely studied using a variety of ground-based and space-borne instruments/measurements, such as ionosonde (e.g., Booker and Wells, 1938; Cohen and Bowles, 1961; Abdu et al., 1982), coherent and incoherent scatter radars (e.g., Woodman and La Hoz, 1976; Hysell and Burcham, 2002; Jin et al., 2018; Rodrigues et al., 2018), all-sky airglow imagers (e.g., Mendillo and Baumgardner, 1982; Otsuka et al., 2002; Makela and Kelley, 2003; Martinis et al., 2015), space-based ultraviolet imagers (e.g., Kil et al., 2004; Aa et al., 2020a; Eastes et al., 2020; Karan et al., 2020), low-Earth orbiting satellites *in-situ* measurements (e.g., Burke et al., 2004; Stolle et al., 2006; Huang et al., 2012; Xiong et al., 2016; Aa et al., 2020b), as well as Global Navigation Satellite System (GNSS) total electron content (TEC) or scintillation observations (e.g., Valladares and Chau, 2012; Takahashi et al., 2015; Cherniak and Zakharenkova, 2016; Zakharenkova et al., 2016; Aa et al., 2018; Aa et al., 2019; Alfonsi et al., 2021; Vankadara et al., 2022). In addition, numerical simulations have also been utilized to analyze the onset condition and evolution process of EPBs (e.g., Retterer et al., 2005; Huba et al., 2008; Huba and Joyce, 2010; Yokoyama et al., 2014; Yokoyama, 2017; Huba and Liu, 2020).

It is generally accepted that EPBs are normally developed *via* the Rayleigh-Taylor (R-T) instability at the postsunset bottomside F-region with a steep vertical density gradient after the diminishing of the E-region. The generalized R-T instability growth rate can be expressed as a function of several flux-tube integrated variables (Sultan, 1996; Equation 26):

$$\gamma_{RT} = \frac{\sum_P^F}{\sum_P^E + \sum_P^F}\left(V_P - U_L^P - \frac{g_e}{\nu_{\text{eff}}}\right)K_F - R_T, \quad (1)$$

where $\sum_P^F$ and $\sum_P^E$ are the flux-tube integrated Pedersen conductivity in the F-region and E-region, respectively; V_P is the vertical **E×B** plasma drift due to zonal electric field **E** at the geomagnetic equator; U_L^P is the neutral wind perpendicular to **B** in the magnetic meridian plane weighted by Pedersen conductivity; g_e is the gravity acceleration (positive upward); ν_{eff} is the flux-tube integrated effective ion-neutral collision frequency; K_F is the altitudinal gradient of electron density in the F-region ($K_F = 1/N_e\ (\partial N_e/\partial h)$); R_T is the flux-tube integrated recombination rate. For more details, please refer to Sultan (1996).

The mathematical description of R-T instability has been largely used to help understand the longitudinal and seasonal variation of EPBs (e.g., Wu, 2015; Shinagawa et al., 2018). However, understanding and predicting EPBs' short-term variation, especially its complicated day-to-day variability, has always been a major challenge for the ionospheric community. In particular, EPBs can show unusual development on certain nights but suppression on other nights even under quiet geomagnetic conditions (e.g., Carter et al., 2014; Yamamoto et al., 2018; Abdu, 2019). Considering that the R-T instability growth rate is simultaneously influenced by various ionospheric/thermospheric parameters, the primary controlling drivers of the enigmatic day-to-day variability of EPBs are the following three factors.

1.1 Prereversal enhancement

The postsunet enhancement of eastward zonal electric field and upward plasma drift due to increased zonal wind and conductivity gradient, known as PRE (Farley et al., 1986; Heelis, 2004; Eccles et al., 2015), provides a favorable condition to facilitate the growth of the R-T instability by causing the postsunset rise (PSSR) of the equatorial F-layer to higher altitudes with lower ion-neutral collision frequency (e.g., Fejer et al., 1999; Sarudin et al., 2021). Along this line, some studies suggested that strong vertical plasma drift exceeding certain thresholds seems to conduct a systematic control on the development of EPBs. For example, Basu et al. (1996) and Anderson et al. (2004) indicated that the equatorial spread-F and scintillation could be generated when the postsunset upward E×B drift exceeds 20 m/s around solar minimum. In comparison, some other studies observed that strong equatorial plasma irregularities could occur near solar maximum when the postsunset upward E×B drift exceeds 50 m/s (e.g., Fejer et al., 1999; Whalen, 2001). Smith et al. (2016) suggested that the necessary PRE peak value that preceding equatorial spread-F development varies between 5 and 30 m/s across different seasons and solar activities. Moreover, a few statistical studies using satellite *in-situ* measurements have reported that the occurrence of EPBs is approximately proportional to the PRE magnitude, especially from a seasonal/longitudinal point of view (Su et al., 2008; Kil et al., 2009), and the irregularity occurrence probability becomes greater than 80% when the PRE is larger than 40 m/s (Huang and Hairston, 2015). Despite that the climatological correlation is strong, the PRE/PSSR does not always exhibit a clear day-to-day causal relationship with EPBs occurrence but shows large uncertainties (Abdu et al., 1983; Fukao et al., 2006). Moreover, it was found that local EPBs were not always effectively generated under large PRE/PSSR conditions (Saito and Maruyama, 2006, 2007), but could be sometimes triggered even without large upward plasma drift (Tsunoda et al., 2010; Smith et al., 2016). Thus, it seems that PRE itself is not sufficient to explain the quiet-time day-to-day occurrence/suppression of EPBs, and other geophysical factors such as instability seeding sources should also play an indispensable role.

1.2 Ionospheric large-scale wave structures associated with atmospheric gravity waves

Considering that the R-T instability originally plays a catalyzing role to boost the ionospheric perturbation structures, it would be an inefficient process that may take thousands of seconds if irregularities were to develop from merely noise-like background fluctuations (Huang and Kelley, 1996). Thus, initial seeding perturbations have also been proposed as a necessary prerequisite

for EPBs development to compensate for the otherwise modest strength of R-T instability, since the stronger magnitude of the initial perturbation, the less R-T instability growth rate is needed to amplify non-linearly the fluctuations into plasma bubbles (Retterer and Roddy, 2014). Many observational and theoretical studies have thus indicated that the development of EPBs could be closely related to a seeding precursor of large-scale wavelike electron density fluctuations and/or polarization electric field perturbations at the bottomside equatorial F-layer, which are potentially related to the presence of upward propagating AGWs from the lower atmosphere (e.g., Kelley et al., 1981; Singh et al., 1997; Tsunoda, 2005, 2015; Abdu et al., 2009; Krall et al., 2013; Huba and Liu, 2020). It is thought that AGWs with sufficient energy and vertical length can propagate into the ionosphere before being entirely dissipated, or that the primary waves may break into secondary waves which then subsequently reach ionospheric heights to cause traveling ionospheric disturbances (TIDs) (Vadas, 2007; Yizengaw and Groves, 2018). In particular, the occurrence of EPBs clusters are usually distributed quasi-periodically in longitude with inter-bubble distances of several hundred kilometers that are generally in agreement with the zonal wavelength of LSWS/TIDs (e.g., Röttger, 1973; Tsunoda and White, 1981; Takahashi et al., 2009; Makela et al., 2010; Taori et al., 2011; Aa et al., 2020a; Das et al., 2020). More importantly, it has been found that LSWS at the bottomside F-layer can provide not only the above-mentioned initial seeding density perturbations but also considerable upwelling of 50–100 km through large undulation of equatorial F-layer that directly contribute to an enhanced R-T growth rate (a.k.a., upwelling growth) (Tsunoda, 2010; Tsunoda et al., 2010). Thus, EPB patches are more likely triggered near each LSWS crest due to the large upwelling growth therein with elevated bottomside density gradient region, forming quasi-periodic distribution structures that are observed in ground-based and space-borne instruments (e.g., Takahashi et al., 2018; Eastes et al., 2020). Some studies suggested that the LSWS-related upwelling is comparable or even outweighs the PSSR to control EPBs development when PRE strength is weak (Tsunoda et al., 2018; Chou et al., 2020).

1.3 Neutral wind perturbation

Besides the predominant catalyzing effect of PRE and the seeding effect of AGWs as above-mentioned, EPBs' day-to-day variability might be partially complicated by the thermospheric neutral wind variation. For instance, the eastward thermospheric wind and the E layer conductivity longitudinal gradients after sunset could jointly control the PRE intensity and thereby influence the growth rate of R-T instability (Kudeki et al., 2007; Heelis et al., 2012; Abdu, 2019), although this might be more appropriate to be categorized into the PRE-related effect. On the other hand, the trans-equatorial wind tends to slightly decrease (increase) the low-latitude Pedersen conductivity in the upwind (downwind) side, thereby playing a destabilization (stabilization) role on the generalized R-T growth rate (Huba and Krall, 2013). The net effect is to increase the field-line integrated Pedersen conductivity and thereby suppressing the non-linear growth rate of the R-T instability (e.g., Maruyama, 1988; Mendillo et al., 2001; Krall et al., 2009). However, it should be noted that the trans-equatorial wind from summer to winter hemisphere is essentially a seasonal pattern, which are less likely subject to large day-to-day variability except when geomagnetic storms cause considerable equatorward neutral wind surge *via* Joule and auroral heating. During geomagnetic quiet time, the background neutral wind might be modulated by AGWs to cause ionospheric plasma density perturbation through wind components parallel and perpendicular to the geomagnetic field as follows: 1) The magnetic meridional wind perturbation (parallel components) due to AGWs move the plasma up and down along the field line *via* the neutral-drag effect, producing ionospheric height oscillation and density modulation though this process is not so effective around the equatorial region with small dip angles. 2) The zonal and vertical wind perturbations (perpendicular components) due to AGWs tend to create polarization electric fields (Tsunoda et al., 2010; Krall et al., 2013; Zhang et al., 2021) and modulate plasma density *via* E×B drift, which provides important seeding and undulation effects to facilitate EPB development as previously mentioned (e.g., Retterer and Roddy, 2014; Yokoyama et al., 2019). Thus, the short-term variability of EPBs associated with neutral wind perturbation could be intrinsically related to thermospheric waves.

Although significant progress on EPBs' mechanism has been obtained through those pioneering studies, our current knowledge is still limited regarding the relative importance of the concurrent or separate presence of these intertwined drivers in causing EPBs' large day-to-day variability, especially at a geomagnetically quiet time. Thus, in the present paper, we conducted a detailed event analysis of EPBs' day-to-day variability over the American sector during a geomagnetically quiet period of 07–11 December 2019, through coordinately utilizing multi-instrumental ground-based and space-borne observations, including the Global-scale Observations of Limb and Disk (GOLD) measurements, the Ionospheric Connection Explorer (ICON) data, the global navigation satellite system (GNSS) total electron content (TEC) observation, as well as ionosonde measurements. In particular, we found that the EPBs' activity exhibited a considerably large day-to-day variation around the same postsunset time periods through the selected period. We also conducted an in-depth analysis of potential drivers by calculating the R-T instability growth rate and examining the possible background seeding perturbations, which motivated this study as a good opportunity to advance the current understanding of EPBs' enigmatic day-to-day variability.

2 Instruments and data description

The GOLD ultraviolet spectrometers observe Earth's airglow emissions between 134 and 160 nm through the disk, limb, and stellar occultation measurements from a geostationary orbit at 47.5°W longitude, which has an unparalleled merit of imaging the American region with an unchanged field-of-view for extended time periods (Eastes et al., 2017, 2019). In this study, we use the GOLD nighttime disk images of OI 135.6 nm emission with ~100 km (longitude) by 50 km (latitude) resolution, which provides continuous time-evolving maps in the early evening hours that can unambiguously specify the spatial-temporal variation of low-

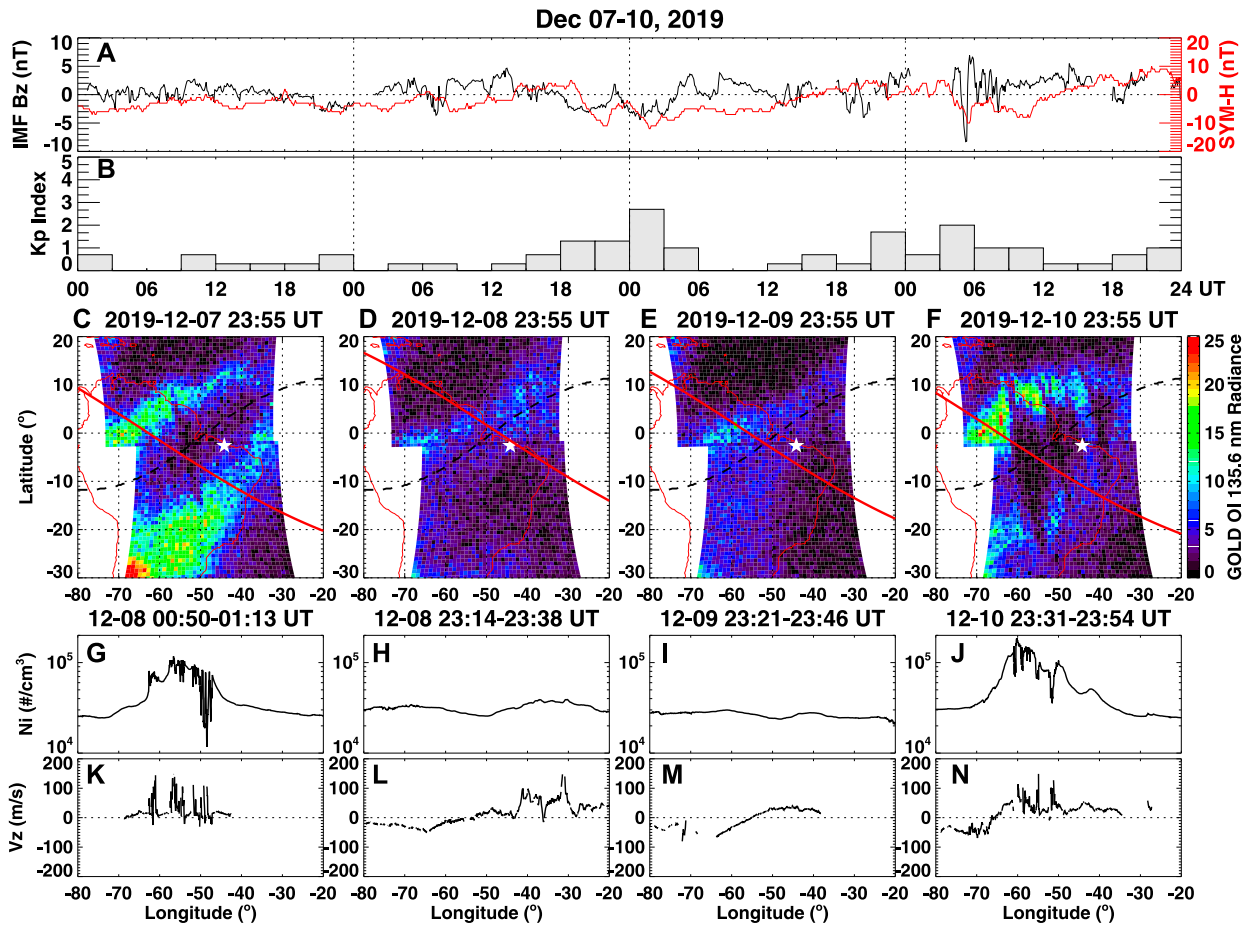

FIGURE 1
(A,B) Interplanetary magnetic field (IMF) Bz, longitudinally symmetric index (SYM-H), and Kp index variations during December 07–10, 2019. **(C–F)** GOLD nighttime ultraviolet images of OI 135.6 nm emission radiance at 23:55 UT on December 07–10, respectively. The Sao Luis ionosonde (white star), overlapping ICON orbit (red line), and the geomagnetic equator (black dashed line) are also marked. **(G–N)** Corresponding longitudinal profiles of ICON IVM plasma density and vertical drift.

latitude ionospheric structures in the Atlantic/American sector, especially the equatorial ionization anomaly (EIA) and EPBs (e.g., Aa et al., 2020a; Eastes et al., 2020; Karan et al., 2020).

ICON is a low-Earth orbit satellite for ionospheric and thermospheric measurements that flies at an altitude of 575 km with an inclination angle of 27°, which is equipped with four instruments: a Michelson interferometer for Global High-Resolution Thermospheric Imaging (MIGHTI) that measures the thermospheric winds and temperatures; an ion velocity meter (IVM) that provides *in-situ* measurements of ionospheric plasma drift velocity and number density; and two ultraviolet imagers (FUV and EUV) that measure airglow emission to derive ionospheric and thermospheric density and composition (Harding et al., 2017; Heelis et al., 2017; Immel et al., 2018). In this study, we will use the IVM ion density/drift and MIGHTI neutral wind data to investigate the possible connection between EPBs and background ionosphere and thermosphere conditions.

Ground-based GNSS TEC data are derived at Massachusetts Institute of Technology's Haystack Observatory using 6000 + worldwide receivers. The gridded vertical TEC data are provided to the community through the Madrigal distributed data system with a spatial resolution 1° (longitude) by 1° (latitude) and a time cadence of 5 min, with the data quality being examined to remove bad data points and outliers (Rideout and Coster, 2006; Vierinen et al., 2016). The sensitivity of the TEC data is a few percent of the TEC unit (1 TEC unit = 10^{16} electrons/m^2), which is sufficiently accurate to represent EPBs. Moreover, we here also use the detrended TEC (dTEC) to examine the wavelike TID features as a proxy of AGWs, which is computed by removing the background trend for all satellite-receiver line-of-sight TEC pairs *via* a Savitzky-Golay low-pass filter (Savitzky and Golay, 1964) algorithm with a 30-min sliding window (Zhang et al., 2017). Besides GNSS TEC, we also use ionosonde measurements from equatorial stations of Sao Luis (2.6°S, 44.2°W) and Fortaleza (3.9°S, 39.4°W) to explore the local irregularity features and/or background ionospheric conditions. In particular, the ionograms are used to check for spread-F echoes, the iso-frequency contours of ionospheric true heights are used to check possible wave activities, and the vertical drift measurements are used to calculate localized Rayleigh-Taylor growth rate. These ionosonde data are automatically derived, which may have some limitations on their accuracy but will not considerably impact the qualitative analysis.

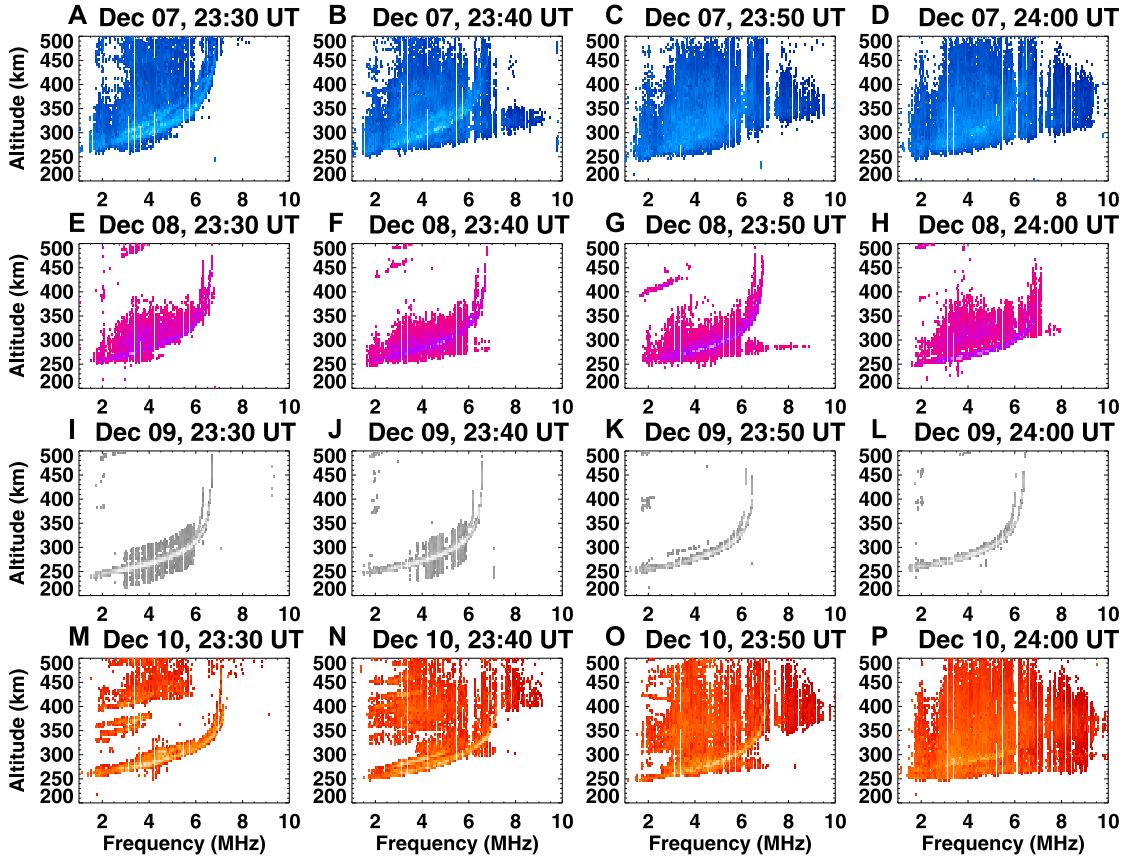

FIGURE 2
(A–P) Sao Luis ionograms during 23:30–24:00 UT on December 07 (blue), 08 (purple), 09 (silver), and 10 (red), 2019, respectively.

3 Results

Figures 1A, B show the temporal variation of interplanetary magnetic field (IMF) Bz, the longitudinally symmetric index (SYM-H), and planetary K-index (Kp) during 07–10 December 2019, respectively. Solar activity was at a very low level during this period with the F10.7 solar radio flux being around 69 SFU (1 SFU = 10^{-22} W/m^2/Hz). The geomagnetic activity was at a quiet condition during this period: the IMF Bz and SYM-H were mainly confined within ±5 and ±10 nT respectively with merely minor fluctuations; most of the Kp indices were ≤2 except for 00–03 UT on December 09 with Kp reaching 3-. This relatively quiet geomagnetic condition suggests that the possibility of significant magnetospheric driving forces causing large ionospheric day-to-day variability is less likely under such a circumstance.

Nevertheless, the low-latitude ionospheric morphology in the American sector, especially the postsunset EPBs activity, exhibited considerable day-to-day variation, even though there was no hint of a geomagnetic storm or substorm onset within a few hours before local dusk. **Figures 1C–F** show the GOLD nighttime ultraviolet images of OI 135.6 nm radiance at 23:55 UT on December 07–10, respectively, overlapping with ICON orbital path (red line) at close to the same time. **Figure 1G–N** show the corresponding longitudinal variation of ICON IVM *in-situ* plasma density and vertical drift measurements. On December 07, we can see from the GOLD image (**Figure 1C**) the signatures of EIA crests as two bright low-latitude zonal bands that were produced by enhanced oxygen ion emission therein. There were also noticeable meridional dark streaks embedded in the equatorial trough and cut through the EIA crests, manifesting typical EPBs structure with low density and reduced emission. The signature of EPBs can also be captured by ICON-IVM *in-situ* ion density measurements (**Figure 1G**) as noticeable plasma bite-outs, which were associated with the strong pre-reversal enhancement (PRE) of large equatorial upward plasma drift of 100 m/s as shown in **Figure 1K**. For the following two nights, however, the EPBs feature was largely diminished in GOLD images around the same UT interval on December 08 (**Figure 1D**) and was almost indiscernible on December 09 (**Figure 1E**). Similarly, the ICON-IVM measurements during these two nights showed relatively low background ion density conditions with no clear plasma bite-outs (**Figures 1H, I**), although the plasma vertical drift still showed some spontaneous large values of 100 m/s on December 08 (**Figure 1L**). In contrast, strong EPBs re-appeared the next evening on December 10 that were simultaneously captured by GOLD image (**Figure 1F**) and ICON-IVM *in-situ* measurements (**Figure 1J**), associated with large upward plasma drift (**Figure 1N**). In conclusion, the coordinated GOLD and ICON measurements collectively showed that there was large day-to-day variability of

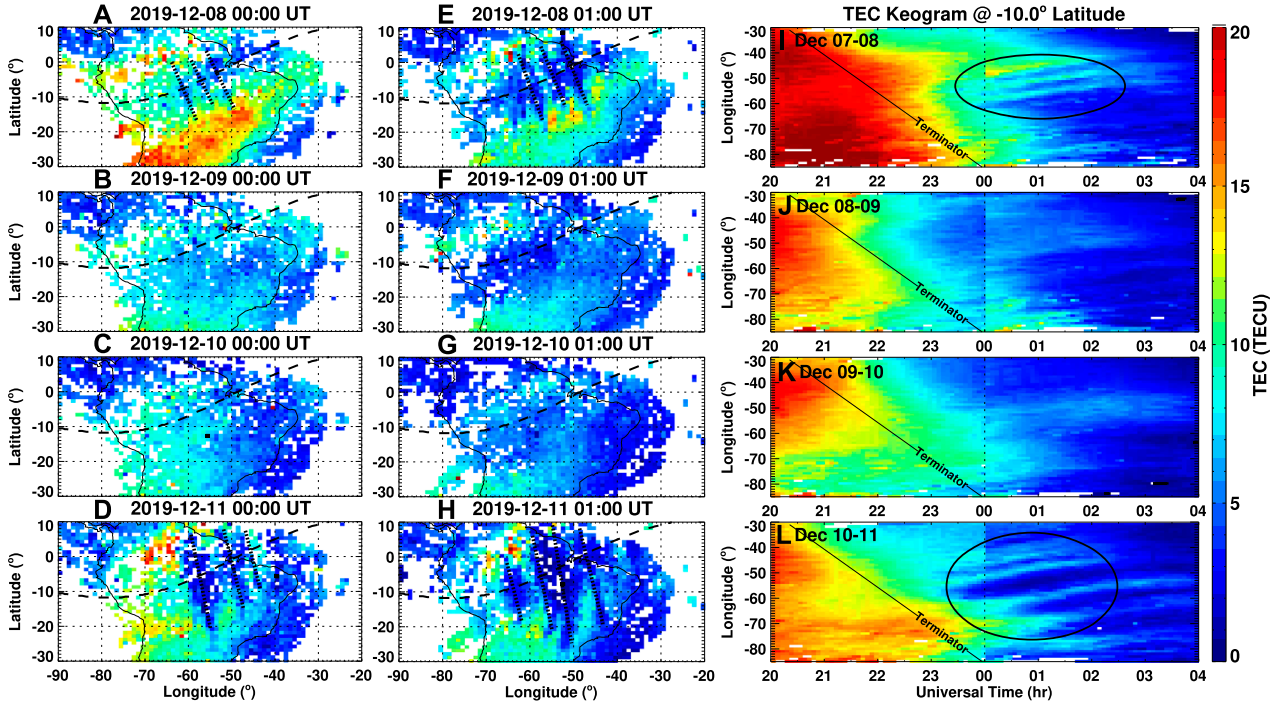

FIGURE 3
(A–H) Gridded TEC maps over the South American area at 00 and 01 UT on 08–11 December 2019, respectively. The geomagnetic equator is marked with a dashed line. The quasi-parallel dotted lines marked strong EPBs. **(I–L)** TEC keogram as a function of time and longitude along −10° latitude during 07–11 December 2019, respectively. The sunset terminator is marked, and ovals mark strong EPBs.

EPB activity with considerable suppression on certain nights but intensification on other nights within consecutive 4 days under geomagnetic quiet conditions.

Moreover, such a large day-to-day variability of EPBs intensity can also be deduced from local ionosonde measurements. **Figure 2** displays a series of ionograms at the equatorial Sao Luis station between 23:30–24:00 UT on 07–10 December 2019, respectively. As can be seen, on December 07 (**Figures 2A–D**), there were strong diffuse echoes of range-type spread-F traces that spread across the whole F-region, which are typical characteristics suggesting the presence of large-scale ionospheric plasma irregularities that developed *via* the R-T instability (Abdu, 2001). At the same UT interval on December 08 (**Figures 2E–H**), the spread-F signatures were still considerable, but the diffuse echoes were less predominant than the previous night and were mainly confined within the bottomside F-region below 350 km virtual heights. Furthermore, on December 09 (**Figure 2I–L**), there were almost no spread-F features around midnight yet merely some sporadic and limited structures. Nevertheless, on December 10 (**Figure 2M–P**), significant spread-F signatures were revived in the same UT interval across the whole F-region, which was much stronger than those from the previous two nights but was comparable to that of December 07. These localized ionogram results are generally in agreement with the above-mentioned GOLD and ICON measurements.

Besides ground-based ionosonde measurements and space-borne GOLD/ICON observations, strong day-to-day variation of EPBs can also be observed in GNSS TEC maps. **Figures 3A–H** show the two-dimensional TEC maps over the South American area at 00:00 and 01:00 UT on 08–11 December 2019, respectively. Considering GOLD has no nighttime measurements after 00:25 UT, we here include the TEC map at a slightly later interval of 01 UT to fill the data gap and illustrate the bubble evolution more clearly. As can be seen, significant EPBs occurred on December 08 (**Figures 3A, E**) as depletion streaks with reduced TEC values that are marked by dashed lines perpendicular to the geomagnetic equator. In contrast, EPBs features were hardly identified on December 09 (**Figures 3B, F**) and 10 (**Figures 3C, G**), yet revived on December 11 (**Figures 3D, H**) at the same UT intervals. Compared with the surrounding area, the amplitude of the TEC depletion within these EPBs was approximately 5–8 TECU. Moreover, to better identify and trace the temporal evolution of EPBs, **Figure 3I–L** display the corresponding TEC keogram as a function of time and longitude along −10° latitude between 20 and 04 UT during 07–11 December. As encircled by the black ovals, pronounced postsunset EPBs occurred on December 07–08 (**Figure 3I**) and 10–11 (**Figure 3L**), manifesting as parallel comb-like depletion streaks that persisted from 23 to 00 UT to at least 03–04 UT. The inter-bubble distances were estimated to be ~400–1000 km, which are consistent with typical GOLD observations (e.g., Aa et al., 2020a; Huba and Liu, 2020; Karan et al., 2020). Nevertheless, the EPB intensity on December 08–09 and 09–10 are much weaker and less organized than the first and last days though there were some vague yet blurred streaks.

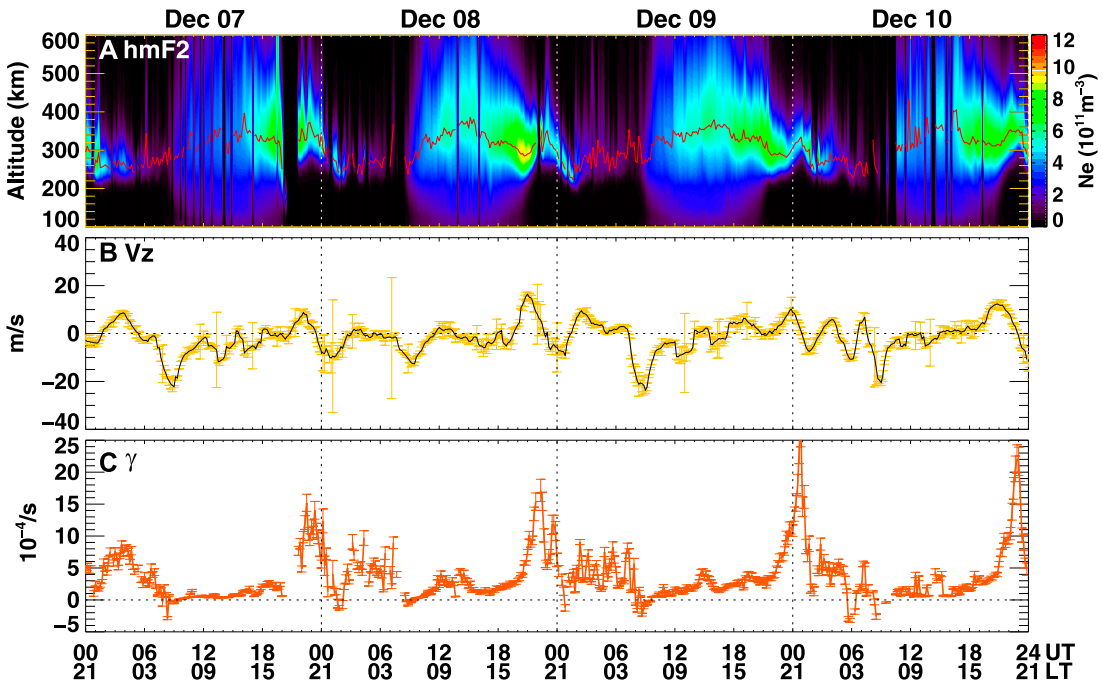

FIGURE 4
Sao Luis ionosonde measurements of **(A)** electron density profiles and F2-layer peak height (hmF2) as well as **(B)** F-layer vertical plasma drift with error bars during December 07–10, 2019. **(C)** Temporal variation of the corresponding linear growth rate of R-T instability.

4 Discussion

4.1 Variation of R-T instability growth rate

To discuss the potential drivers of such large day-to-day variability of EPBs' intensity, we first examine the R-T instability growth rate variation among the above-mentioned time period of December 07–10, 2019. It is known that Eq. **1** and its derivatives have been widely used in numerical simulations to estimate the flux-tube integrated R-T instability growth rate (e.g., Sultan, 1996; Wu, 2015). However, in order to maximize the usage of realistic observations and avoid the disadvantage of lack of measurements along the flux tube, we here adopt Equation 25 in Sultan (1996) to calculate the local R-T instability growth rate at bottomside F-region around the geomagnetic equator:

$$\gamma = \left(\frac{E}{B} - \frac{g}{\nu_{in}}\right)\frac{1}{n_0}\frac{\partial n_0}{\partial z}, \tag{2}$$

where γ is the R-T instability growth rate; E and B are the zonal electric field and geomagnetic field magnitude, respectively; g is the gravitational acceleration; ν_{in} is the ion-neutral collision frequency; n_0 is the background F-region electron density; z is the altitude. This equation has been proved as an effective approximation to estimate the local linear growth rate of R-T instability near the geomagnetic equator, though its value might be slightly larger than those using flux-tube integrated quantities (e.g., Kelley, 1989; Otsuka, 2018; Das et al., 2021). Note that the meridional neutral wind term is not included in this simplified equation, partially because the nearly parallel-to-**B** wind in the magnetic meridional plane does not effectively change the conductivity around the equatorial area due to small dip angles therein. The recombination damping term is also excluded since the recombination damp is suggested to be not quite effective (Huba et al., 1996). Other flux-tube terms, such as the integrated Pedersen conductivity in the F-region and E-region, are less likely subject to significant day-to-day variability and thus will not be discussed in the current study.

We here adopted a similar method as indicated by Das et al. (2021) and Kelley (1989) to calculate these parameters. Specifically, the velocity factor (E/B) is replaced by the vertical plasma drift, that is, given by Doppler drift mode measurements of Sao Luis digisonde; the inverse vertical gradient scale length of electron density, $1/n_0\,(\partial n_0/\partial z)$, is calculated from the bottomside electron density profile of Sao Luis digisonde. The ion-neutral collision frequency ν_{in} is derived from Kelley (1989) as follows:

$$\nu_{in} = 2.6\times10^{-9}\left(n_n + n_i\right)A^{-\frac{1}{2}}, \tag{3}$$

where n_n and n_i refer to neutral and ion density. The variable A denotes the mean neutral molecular mass in atomic mass units. These parameters are calculated using NRLMSISE-00 model (Picone et al., 2002). For more details about the mathematical description, readers may refer to Kelley (1989).

Figures 4A, B show Sao Luis ionosonde measurements of electron density profiles and F2-layer peak height (hmF2) as well as F-layer vertical plasma drift with error bars during December 07–10, 2019. **Figure 4C** displays the corresponding temporal variation of the local linear growth rate of R-T instability derived using Eq. **2** based on those Sao Luis ionosonde measurements. In general, the R-T instability growth rate is larger around nighttime, with peak values typically appearing in the postsunset hours around 19–22 LT (22–01 UT) due to the equatorial PRE effect of the uplifted ionosphere as

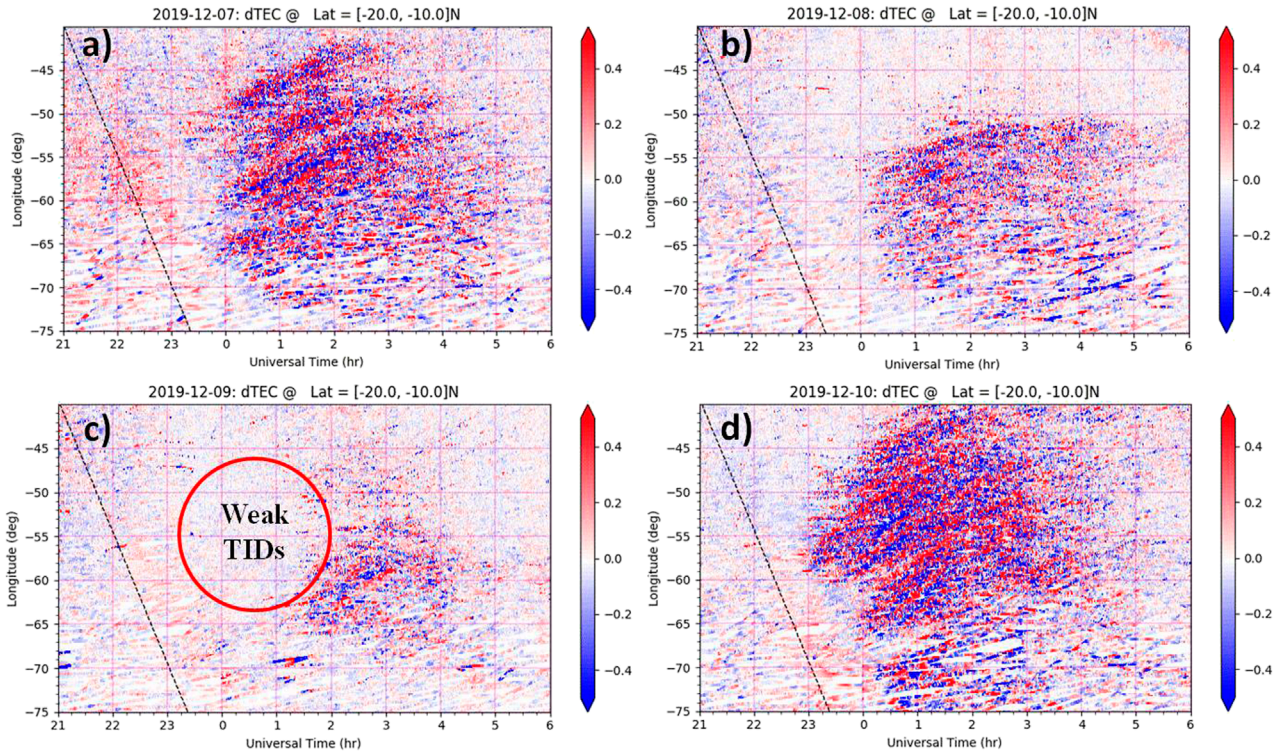

FIGURE 5
(A–D) Detrended TEC keogram as a function of time and longitude along −10 ~-20° latitude during 07–10 December 2019, respectively. The sunset terminator is marked with a dashed line. The red oval marks relatively weak TID intensity in panel c.

well as the large density gradient in the bottomside F-region after local sunset and decaying of E-region, as previously interpreted in the Introduction section. Besides this typical diurnal variation pattern, one important question is whether the R-T instability growth rate also experienced similar day-to-day variability in the postsunset evening hours as that of observed EPBs activity among these days. We here compare the magnitude and timing when γ reached peak value in each evening among these 4 days: which are 15×10^{-4} around 22:30 UT (December 07), 18×10^{-4} around 22:30 UT (December 08), 25×10^{-4} around 00:50 + 1 UT (December 09), and 22×10^{-4} around 22:50 UT (December 10), respectively. As can be seen, the day-to-day variation of the peak magnitude of the R-T instability growth rate does not have a strict one-to-one relationship with observed EPBs intensity. For instance, the postsunset peak intensity of γ in the middle 2 days are comparable or even slightly larger than those of the first and fourth days, yet the EPB activity was much more suppressed in the middle 2 days as shown in **Figures 1–3**. Moreover, the peak value of γ was the smallest on December 07 among those days, while the EPBs intensity on that day is considerably stronger than on December 08 and 09. It is worth noting that, on December 09–10, γ reached its peak value at a later time around 00:50 UT about 2 h later than the other evenings, which might partially explain the inhibited EPBs on that day due to this timing difference. However, it should also be noted that the peak intensity of γ ($\sim 25 \times 10^{-4}$) at this time was the highest in the same UT interval among those days, while the TEC keogram in **Figure 3G** showed that the nighttime EPB activity even after 01 UT on December 10 was still weaker compared with other nights. Therefore, such a complicated day-to-day variability of EPBs can hardly be explained if solely considering the day-to-day variation of R-T instability growth rate. Some other parameters, such as the seeding factor of TID/AGWs, might also play an indispensable role in causing the observed day-to-day variability of EPBs in this event.

4.2 TIDs/AGWs activities

We next discuss the background ionospheric conditions in terms of wave structures to investigate the possible seeding effect due to the presence of AGWs on these days. **Figure 5** shows four detrended TEC keogram as a function of time and longitude along −10 ~−20° latitude around the observed EPBs region during 07–10 December 2019, respectively. During the evening of December 07 (**Figure 5A**) and December 10 (**Figure 5D**), there were noticeable wavelike fluctuations of medium-scale TID features that propagated eastward during 23–05 UT between −70 ~−40° longitudes. These TID structures are sometimes considered a proxy that may represent ionospheric signatures of AGWs. The zonal propagating velocity of TID wavefronts is estimated to be around 80–100 m/s, which is generally consistent with the background EPB drifting speed derived from ultraviolet measurements given by previous studies (e.g., Immel et al., 2003; Park et al., 2007; Karan et al., 2020). Moreover, the wavelength of TIDs was estimated to be around a few hundred kilometers, which is generally smaller than the inter-bubble distances. These TIDs were sometimes embedded in the

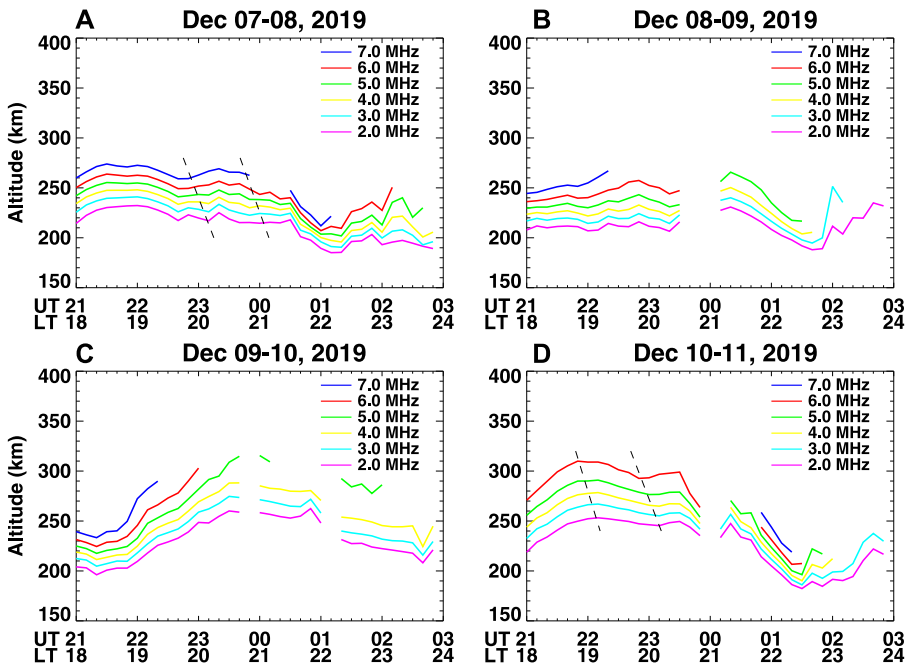

FIGURE 6
(A–D) Temporal variation of F-layer true heights for different frequencies between 2 and 7 MHz at Fortaleza station during 07–11 December 2019, respectively.

bubbles and were much more evenly distributed across latitudes than bubbles. These TIDs represent medium-scale wave structures that are different from the large-scale bubbles themselves but were present concurrently with the bubbles. In contrary to these two nights with strong TIDs, the TID intensities in the same UT interval were weak during the evening on December 08 (**Figure 5B**) and were significantly suppressed on December 09 (**Figure 5C**) as marked by the red oval. This lacking of ionospheric wave structures is in agreement with the observations of inhibited EPBs during the same nights.

To better check the AGW activities, **Figure 6** shows the temporal variation of F-layer true heights at different plasma frequencies (2.0–7.0 MHz) at Fortaleza ionosonde between 21 and 03 UT (18–24 LT) during December 07–10. Here we use Fortaleza as a substitute since there are some data gaps in the Sao Luis results. On December 07 (**Figure 6A**) and December 10 (**Figure 6D**), there were identifiable downward phase propagation trends that were marked with dashed lines suggesting the possible presence of AGWs in the upper atmosphere during these two nights (Abdu et al., 2009), while such a downward phase propagation pattern was not so noticeable on December 08 and 09 (**Figures 6B, C**). This is consistent with those of detrended TEC results. Thus, this coincidence of strong (weak) TID/AGW characteristics together with enhanced (suppressed) EPB activities on the same night collectively illustrate a potential connection between the background wave structures and the development of EPBs. As previously described in the Introduction section, these ionospheric wave structures could not only provide important initial seed perturbations but also large undulation and upwelling of the equatorial F-layer to destabilize the density gradient. Therefore, the stronger (weaker) magnitude the background perturbations have, the less (more) R-T instability growth rate is needed to amplify the fluctuations into the non-linear regime, and the plasma bubbles will be more efficient (inefficient) to be developed (Huang and Kelley, 1996; Retterer and Roddy, 2014). For instance, in the evening of December 09–10, the TID/AGW activity was much weaker than the other nights, and the R-T instability growth rate reached a peak value more than 2 hours later than the other nights. Thus, the combination of these insufficient seeding perturbations and delayed catalyzing factors collectively caused the significant inhibition of EPBs at that night.

Last but not least, we briefly examine the thermospheric neutral wind variation during the selected period of December 07–10, 2019. **Figure 7** shows the ICON-MIGHTI observation tracks and corresponding local time, zonal wind, and meridional wind profiles for consecutive orbits focusing on the American sector between 21 and 24 UT that was slightly prior to the observed EPBs on December 07 (**Figures 7A–F**), December 08 (**Figures 7G–L**), December 09 (**Figure 7M–R**), and December 10 (**Figures 7S–X**), 2019, respectively. Although the zonal and meridional winds showed generally similar longitudinal distribution patterns with comparable amplitudes among these 4 days, there were still some discernible day-to-day differences. In particular, the horizontal winds on December 07 exhibited large wavelike fluctuations of 100 m/s that were associated with a downward phase propagation trend, especially in **Figures 7C, E** as marked by the parallel dotted lines. Such strong neutral wind perturbations with a downward phase propagation trend are considered to be signatures of traveling atmospheric disturbances (TADs) due to the modulation of upward propagating AGWs from the lower atmosphere, though the latitude-longitude variations were also mixed with such altitudinal variations. In comparison, the wind profiles on other days also have some moderate oscillations though not as strong as that on

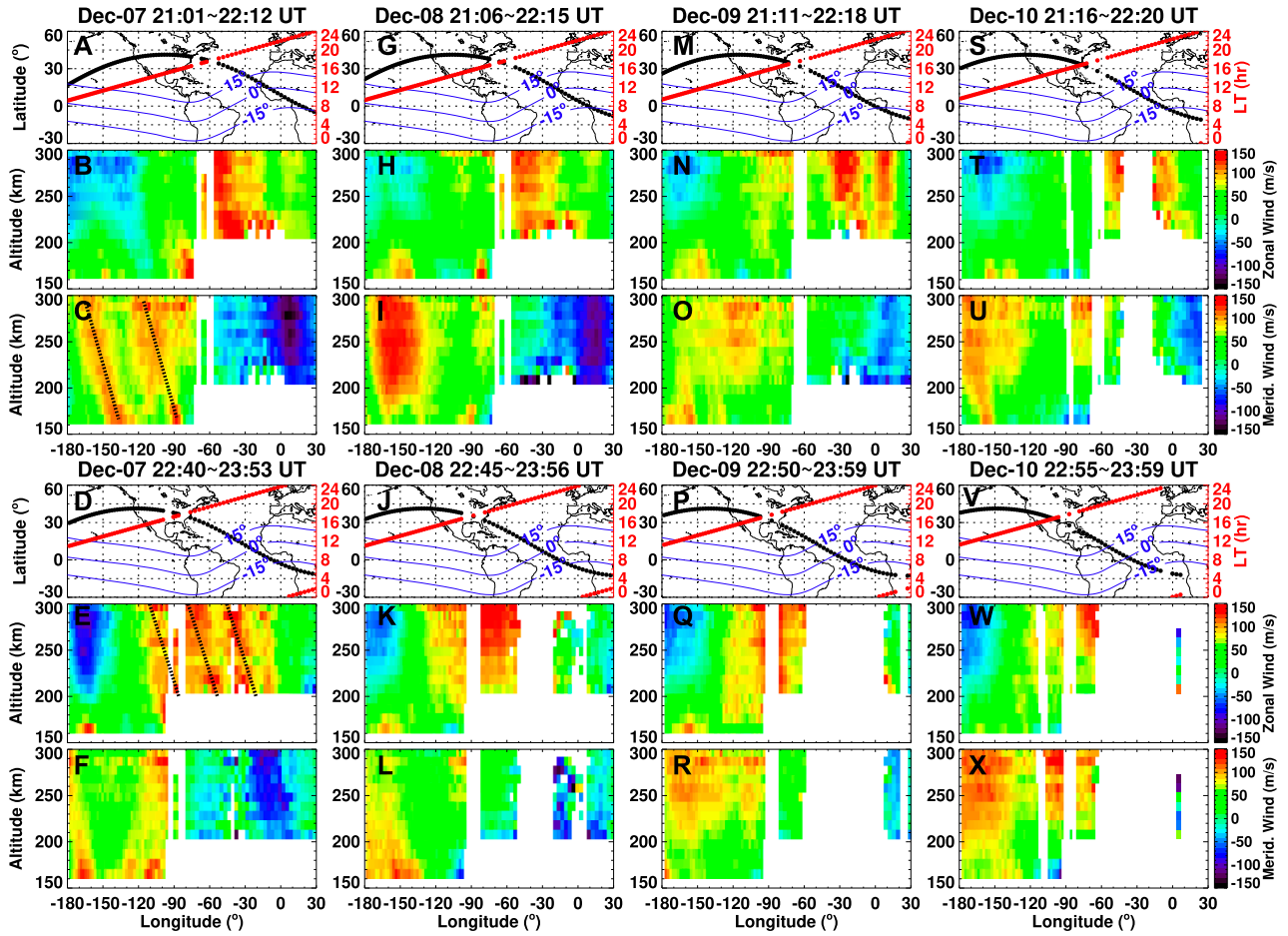

FIGURE 7
ICON MIGHTI observation tracks and corresponding local time, zonal wind (positive eastward), and meridional wind (positive northward) profiles for two consecutive orbits over American sector between 21 and 24 UT on December 07 **(A–F)**, December 08 **(G–L)**, December 09 **(M–R)**, and December 10 **(S–X)**, 2019, respectively. The geomagnetic dip equator and ±15° latitudes are shown by blue lines. The parallel dotted lines in **(C,E)** mark large neutral wind oscillations with a downward phase propagation trend.

December 07. Recall from Figure 4 that the peak value of the linear R-T instability growth rate on December 07 was the smallest for the same postsunset period among those consecutive 4 days, while the postsunset EPB intensity on December 07 was much stronger than the following 2 days as shown in Figures 1–3. This could be possibly related to considerable initial seeding perturbations on December 07 caused by those strong neutral wind fluctuations possibly due to AGWs, which can create polarization electric fields to modulate plasma density *via* E×B drift and/or directly cause plasma perturbation along the geomagnetic field *via* ion-neutral collision (e.g., Tsunoda et al., 2010; Krall et al., 2013; Zhang et al., 2021). Such important seeding perturbations could be a necessary prerequisite to effectively compensate for the modest strength of the R-T instability growth rate and thus facilitate the development of EPBs on December 07, otherwise, it would be a more inefficient process if irregularities were to develop from merely noise-like small background fluctuations even with relatively large R-T instability growth rate (Retterer and Roddy, 2014), as was likely the cases for December 08 and 09. It is worth noting that the observed wind oscillations are not exactly around the equatorial area due to MIGHTI's north-looking remote sensing geometry, plus that there were some nighttime data gaps in MIGHTI. However, it is still reasonable to deduce a similar conclusion from the TID/AGWs results shown by the detrended TEC and ionosonde measurements in Figure 6 and Figure 7. A future theoretical simulation is needed to further quantify the neutral wind contribution, which is beyond the scope of the current study.

5 Summary and conclusion

In this study, we conducted a multi-instrument analysis of the day-to-day variability of EPBs over the American sector and potential drivers under a geomagnetically quiet period on 07–10 December 2019. We coordinately utilized GOLD ultraviolet nighttime disk measurements, ICON IVM *in-situ* plasma and MIGHTI remote sensing wind measurements, ground-based GNSS TEC observations, as well as ionosonde datasets. The main findings and conclusions are as follows:

1) The intensity of postsunset EPBs exhibited a large day-to-day variation in the same UT intervals around 23–03 UT (20–24 LT)

during December 07–10. In particular, the EPBs and spread-F irregularity signatures were quite noticeable on the evening of December 07, yet considerably suppressed on December 08, and almost completely inhibited on December 09, then dramatically revived and enhanced on December 10.

2) The day-to-day variation of the local R-T instability growth rate γ), derived using some actual observations *via* a simple approach, does not have an exact one-to-one relationship with the observed EPBs intensity. Specifically, the peak magnitude and timing of postsunset R-T instability growth rate among those consecutive four nights of December 07–10 was 15×10^{-4}/s at 22:30 UT, 18×10^{-4}/s at 22:30 UT, 25×10^{-4}/s at 00:50 UT, and 22×10^{-4}/s at 22:50 UT, respectively. Compared with other evenings, there was a 2-h delay on December 09 when γ reached its peak value, which might partially explain the inhibited EPBs on that night due to this timing difference.
3) The day-to-day variation of TID/TADs feature has a much better agreement with EPBs' activity: there were relatively strong wavelike perturbations preceded and/or accompanying the considerable EPBs on December 07 and 10, whereas relatively weak wave fluctuations occurred on December 08 and 09 corresponding to EPB inhibition despite of large γ values. These TID/TADs structures are a proxy of atmospheric waves in the upper atmosphere, which played an important seeding role that could effectively compensate for the modest strength of R-T instability growth rate in facilitating the development of EPBs (e.g., December 07). To the contrary, the instability growth would be a more inefficient process if EPBs were to develop from merely small fluctuations of background thermosphere and ionosphere conditions even with a relatively large yet delayed peak value of R-T instability growth rate (e.g., December 09).

Our new results indicate that certain seeding factors due to wave activity in the ionosphere/thermosphere can make an important contribution to EPBs' day-to-day variability during geomagnetically quiet time. A future direction is to conduct a longer-term analysis of EPBs' variation and to analyze the contribution of drivers from above and below.

Data availability statement

The original contributions presented in the study are included in the article/Supplementary Material, further inquiries can be directed to the corresponding author.

Author contributions

EA was responsible for the scientific analysis of the observational results, preparing the manuscript, and organizing team efforts. S-RZ was responsible for differential TEC derivation. AC was responsible for GNSS data management. PE contributed substantially to manuscript development. WR was responsible for software development of GNSS data processing and daily GNSS data processing. All members contributed to science discussion and manuscript development.

Funding

GNSS TEC data are part of the United States NSF Geospace Facility program under a cooperative agreement AGS-1952737 with the Massachusetts Institute of Technology. We acknowledge NSF awards AGS-2033787, AGS-2149698, PHY-2028125, and NSFC41974184, NASA support 80NSSC22K0171, 80NSSC21K1310, 80NSSC21K1775, 80NSSC19K0834, and 80GSFC22CA011, AFOSR MURI Project FA9559-16-1-0364, and ONR Grant N00014-17-1-2186 and N00014-22-1-2284.

Acknowledgments

Data for the TEC processing is provided from the following organizations: The Crustal Dynamics Data Information System (CDDIS), the Scripps Orbit and Permanent Array Center (SOPAC), the Continuously Operating Reference System (CORS), the EUREF Permanent GNSS network (EPN), the University NAVSTAR Consortium (UNAVCO), Institut Geographique National in France (IGN), the Brazilian Network for Continuous Monitoring (RBMC), National Geodetic Survey, Instituto Brasileiro de Geografia e Estat*i*stica, RAMSAC CORS of Instituto Geog*r*afico Nacional de la Rep*u*blica Argentina, Arecibo Observatory, Low-Latitude Ionospheric Sensor Network (LISN), Topcon Positioning Systems, Inc., Canadian High Arctic Ionospheric Network, Centro di Ricerche Sismologiche, Syst*e*me d'Observation du Niveau des Eaux Littorales (SONEL), RENAG: REseau NAtional GPS permanent, GeoNet - the official source of geological hazard information for New Zealand, GNSS Reference Networks, Finnish Meteorological Institute, SWEPOS - Sweden. GNSS TEC data products are provided through the Madrigal distributed data system at (http://cedar.openmadrigal.org/) by MIT Haystack Observatory. The GOLD data can be accessed at (https://gold.cs.ucf.edu/). The ICON data can be accessed at (https://icon.ssl.berkeley.edu/Data. The solar wind and geophysical parameters data are acquired from NASA/GSFC's Space Physics Data Facility's OMNIWeb service (https://cdaweb.gsfc.nasa.gov/) and Kyoto world data center for Geomagnetism (http://wdc.kugi.kyoto-u.ac.jp/). The ionosonde data are provided by the University of Massachusetts Lowell DIDB database of Global Ionospheric Radio Observatory (https://giro.uml.edu/didbase/scaled.php).

Conflict of interest

The authors declare that the research was conducted in the absence of any commercial or financial relationships that could be construed as a potential conflict of interest.

Publisher's note

References

Aa, E., Huang, W., Liu, S., Ridley, A., Zou, S., Shi, L., et al. (2018). Midlatitude plasma bubbles over China and adjacent areas during a magnetic storm on 8 september 2017. *Space Weather* 16, 321–331. doi:10.1002/2017SW001776

Aa, E., Zou, S., Ridley, A., Zhang, S., Coster, A. J., Erickson, P. J., et al. (2019). Merging of storm time midlatitude traveling ionospheric disturbances and equatorial plasma bubbles. *Space Weather* 17, 285–298. doi:10.1029/2018SW002101

Aa, E., Zou, S., Eastes, R., Karan, D. K., Zhang, S.-R., Erickson, P. J., et al. (2020a). Coordinated ground-based and space-based observations of equatorial plasma bubbles. *J. Geophys. Res. Space Phys.* 125, e27569. doi:10.1029/2019JA027569

Aa, E., Zou, S., and Liu, S. (2020b). Statistical analysis of equatorial plasma irregularities retrieved from swarm 2013-2019 observations. *J. Geophys. Res. Space Phys.* 125, e27022. doi:10.1029/2019JA027022

Abdu, M. A., de Medeiros, R. T., and Sobral, J. H. A. (1982). Equatorial spread F instability conditions as determined from ionograms. *Geophys. Res. Lett.* 9, 692–695. doi:10.1029/GL009i006p00692

Abdu, M. A., de Medeiros, R. T., Bittencourt, J. A., and Batista, I. S. (1983). Vertical ionization drift velocities and range type spread F in the evening equatorial ionosphere. *J. Geophys. Res.* 88, 399–402. doi:10.1029/JA088iA01p00399

Abdu, M. A., Alam Kherani, E., Batista, I. S., de Paula, E. R., Fritts, D. C., and Sobral, J. H. A. (2009). Gravity wave initiation of equatorial spread F/plasma bubble irregularities based on observational data from the SpreadFEx campaign. *Ann. Geophys.* 27, 2607–2622. doi:10.5194/angeo-27-2607-2009

Abdu, M. A. (2001). Outstanding problems in the equatorial ionosphere-thermosphere electrodynamics relevant to spread F. *J. Atmos. Solar-Terr. Phys.* 63, 869–884. doi:10.1016/S1364-6826(00)00201-7

Abdu, M. A. (2019). Day-to-day and short-term variabilities in the equatorial plasma bubble/spread F irregularity seeding and development. *Prog. Earth Planet. Sci.* 6, 11. doi:10.1186/s40645-019-0258-1

Alfonsi, L., Cesaroni, C., Spogli, L., Regi, M., Paul, A., Ray, S., et al. (2021). Ionospheric disturbances over the Indian sector during 8 september 2017 geomagnetic storm: Plasma structuring and propagation. *Space Weather* 19, e2020SW002607. doi:10.1029/2020SW002607

Anderson, D. N., Reinisch, B., Valladare, C., Chau, J., and Veliz, O. (2004). Forecasting the occurrence of ionospheric scintillation activity in the equatorial ionosphere on a day-to-day basis. *J. Atmos. Solar-Terr. Phys.* 66, 1567–1572. doi:10.1016/j.jastp.2004.07.010

Basu, S., Kudeki, E., Basu, S., Valladares, C. E., Weber, E. J., Zengingonul, H. P., et al. (1996). Scintillations, plasma drifts, and neutral winds in the equatorial ionosphere after sunset. *J. Geophys. Res.* 101, 26795–26809. doi:10.1029/96JA00760

Booker, H. G., and Wells, H. W. (1938). Scattering of radio waves by the F-region of the ionosphere. *Terr. Magn. Atmos. Electr.* 43, 249. doi:10.1029/TE043i003p00249

Burke, W. J., Gentile, L. C., Huang, C. Y., Valladares, C. E., and Su, S. Y. (2004). Longitudinal variability of equatorial plasma bubbles observed by DMSP and ROCSAT-1. *J. Geophys. Res. Space Phys.* 109, A12301. doi:10.1029/2004JA010583

Carter, B. A., Yizengaw, E., Retterer, J. M., Francis, M., Terkildsen, M., Marshall, R., et al. (2014). An analysis of the quiet time day-to-day variability in the formation of postsunset equatorial plasma bubbles in the Southeast Asian region. *J. Geophys. Res. Space Phys.* 119, 3206–3223. doi:10.1002/2013JA019570

Cherniak, I., and Zakharenkova, I. (2016). First observations of super plasma bubbles in Europe. *Geophys. Res. Lett.* 43, 11,137–11,145. doi:10.1002/2016GL071421

Chou, M.-Y., Pedatella, N. M., Wu, Q., Huba, J. D., Lin, C. C. H., Schreiner, W. S., et al. (2020). Observation and simulation of the development of equatorial plasma bubbles: Post-sunset rise or upwelling growth? *J. Geophys. Res. Space Phys.* 125, e28544. doi:10.1029/2020JA028544

Cohen, R., and Bowles, K. L. (1961). On the nature of equatorial spread F. *J. Geophys. Res.* 66, 1081–1106. doi:10.1029/JZ066i004p01081

Das, S. K., Patra, A. K., Kherani, E. A., Chaitanya, P. P., and Niranjan, K. (2020). Relationship between presunset wave structures and interbubble spacing: The seeding perspective of equatorial plasma bubble. *J. Geophys. Res. Space Phys.* 125, e28122. doi:10.1029/2020JA028122

Das, S. K., Patra, A. K., and Niranjan, K. (2021). On the assessment of day-to-day occurrence of equatorial plasma bubble. *J. Geophys. Res. Space Phys.* 126, e2021JA029129. doi:10.1029/2021JA029129

Eastes, R. W., McClintock, W. E., Burns, A. G., Anderson, D. N., Andersson, L., Codrescu, M., et al. (2017). The global-scale observations of the limb and disk (GOLD) mission. *Space Sci. Rev.* 212, 383–408. doi:10.1007/s11214-017-0392-2

Eastes, R. W., Solomon, S. C., Daniell, R. E., Anderson, D. N., Burns, A. G., England, S. L., et al. (2019). Global-scale observations of the equatorial ionization anomaly. *Geophys. Res. Lett.* 46, 9318–9326. doi:10.1029/2019GL084199

Eastes, R. W., McClintock, W. E., Burns, A. G., Anderson, D. N., Andersson, L., Aryal, S., et al. (2020). Initial observations by the GOLD mission. *J. Geophys. Res. Space Phys.* 125, e27823. doi:10.1029/2020JA027823

Eccles, J. V., St. Maurice, J. P., and Schunk, R. W. (2015). Mechanisms underlying the prereversal enhancement of the vertical plasma drift in the low-latitude ionosphere. *J. Geophys. Res. Space Phys.* 120, 4950–4970. doi:10.1002/2014JA020664

Farley, D. T., Bonelli, E., Fejer, B. G., and Larsen, M. F. (1986). The prereversal enhancement of the zonal electric field in the equatorial ionosphere. *J. Geophys. Res.* 91, 13723–13728. doi:10.1029/JA091iA12p13723

Fejer, B. G., Scherliess, L., and de Paula, E. R. (1999). Effects of the vertical plasma drift velocity on the generation and evolution of equatorial spread F. *J. Geophys. Res.* 104, 19859–19869. doi:10.1029/1999JA900271

Fukao, S., Yokoyama, T., Tayama, T., Yamamoto, M., Maruyama, T., and Saito, S. (2006). Eastward traverse of equatorial plasma plumes observed with the Equatorial Atmosphere Radar in Indonesia. *Ann. Geophys.* 24, 1411–1418. doi:10.5194/angeo-24-1411-2006

Harding, B. J., Makela, J. J., Englert, C. R., Marr, K. D., Harlander, J. M., England, S. L., et al. (2017). The MIGHTI wind retrieval algorithm: Description and verification. *Space Sci. Rev.* 212, 585–600. doi:10.1007/s11214-017-0359-3

Heelis, R. A., Crowley, G., Rodrigues, F., Reynolds, A., Wilder, R., Azeem, I., et al. (2012). The role of zonal winds in the production of a pre-reversal enhancement in the vertical ion drift in the low latitude ionosphere. *J. Geophys. Res. Space Phys.* 117, A08308. doi:10.1029/2012JA017547

Heelis, R. A., Stoneback, R. A., Perdue, M. D., Depew, M. D., Morgan, W. A., Mankey, M. W., et al. (2017). Ion velocity measurements for the ionospheric connections explorer. *Space Sci. Rev.* 212, 615–629. doi:10.1007/s11214-017-0383-3

Heelis, R. A. (2004). Electrodynamics in the low and middle latitude ionosphere: A tutorial. *J. Atmos. Solar-Terr. Phys.* 66, 825–838. doi:10.1016/j.jastp.2004.01.034

Huang, C.-S., and Hairston, M. R. (2015). The postsunset vertical plasma drift and its effects on the generation of equatorial plasma bubbles observed by the C/NOFS satellite. *J. Geophys. Res. Space Phys.* 120, 2263–2275. doi:10.1002/2014JA020735

Huang, C.-S., and Kelley, M. C. (1996). Nonlinear evolution of equatorial spread F. 2. Gravity wave seeding of Rayleigh-Taylor instability. *J. Geophys. Res.* 101, 293–302. doi:10.1029/95JA02210

Huang, C.-S., de La Beaujardiere, O., Roddy, P. A., Hunton, D. E., Ballenthin, J. O., and Hairston, M. R. (2012). Generation and characteristics of equatorial plasma bubbles detected by the C/NOFS satellite near the sunset terminator. *J. Geophys. Res. Space Phys.* 117, A11313. doi:10.1029/2012JA018163

Huba, J. D., and Joyce, G. (2010). Global modeling of equatorial plasma bubbles. *Geophys. Res. Lett.* 37, L17104. doi:10.1029/2010GL044281

Huba, J. D., and Krall, J. (2013). Impact of meridional winds on equatorial spread F: Revisited. *Geophys. Res. Lett.* 40, 1268–1272. doi:10.1002/grl.50292

Huba, J. D., and Liu, H. L. (2020). Global modeling of equatorial spread F with SAMI3/WACCM-X. *Geophys. Res. Lett.* 47, e88258. doi:10.1029/2020GL088258

Huba, J. D., Bernhardt, P. A., Ossakow, S. L., and Zalesak, S. T. (1996). The Rayleigh-Taylor instability is not damped by recombination in the F region. *J. Geophys. Res.* 101, 24553–24556. doi:10.1029/96JA02527

Huba, J. D., Joyce, G., and Krall, J. (2008). Three-dimensional equatorial spread F modeling. *Geophys. Res. Lett.* 35, L10102. doi:10.1029/2008GL033509

Hysell, D. L., and Burcham, J. D. (2002). Long term studies of equatorial spread/F using the JULIA radar at Jicamarca. *J. Atmos. Solar-Terr. Phys.* 64, 1531–1543. doi:10.1016/S1364-6826(02)00091-3

Hysell, D. L. (2000). An overview and synthesis of plasma irregularities in equatorial spread/F. *J. Atmos. Solar-Terr. Phys.* 62, 1037–1056. doi:10.1016/S1364-6826(00)00095-X

Immel, T. J., Mende, S. B., Frey, H. U., Peticolas, L. M., and Sagawa, E. (2003). Determination of low latitude plasma drift speeds from FUV images. *Geophys. Res. Lett.* 30, 1945. doi:10.1029/2003GL017573

Immel, T. J., England, S. L., Mende, S. B., Heelis, R. A., Englert, C. R., Edelstein, J., et al. (2018). The ionospheric connection explorer mission: Mission goals and design. *Space Sci. Rev.* 214, 13. doi:10.1007/s11214-017-0449-2

Jin, H., Zou, S., Chen, G., Yan, C., Zhang, S., and Yang, G. (2018). Formation and evolution of low-latitude F region field-aligned irregularities during the 7-8 september 2017 storm: Hainan coherent scatter phased Array radar and digisonde observations. *Space Weather* 16, 648–659. doi:10.1029/2018SW001865

Karan, D. K., Daniell, R. E., England, S. L., Martinis, C. R., Eastes, R. W., Burns, A. G., et al. (2020). First zonal drift velocity measurement of equatorial plasma bubbles (EPBs) from a geostationary orbit using GOLD data. *J. Geophys. Res. Space Phys.* 125, e28173. doi:10.1029/2020JA028173

Kelley, M. C., Larsen, M. F., Lahoz, C., and McClure, J. P. (1981). Gravity wave initiation of equatorial spread F: A case study. *J. Geophys. Res.* 86, 9087–9100. doi:10.1029/JA086iA11p09087

Kelley, M. C. (1989). "Equatorial plasma instabilities," in *The Earth's ionosphere: Plasma Physics and electrodynamics*. Editor M. C. Kelley (Academic Press), 113–185. doi:10.1016/B978-0-12-404013-7.50009-5

Kil, H., Su, S. Y., Paxton, L. J., Wolven, B. C., Zhang, Y., Morrison, D., et al. (2004). Coincident equatorial bubble detection by TIMED/GUVI and ROCSAT-1. *Geophys. Res. Lett.* 31, L03809. doi:10.1029/2003GL018696

Kil, H., Paxton, L. J., and Oh, S.-J. (2009). Global bubble distribution seen from ROCSAT-1 and its association with the evening prereversal enhancement. *J. Geophys. Res. Space Phys.* 114, A06307. doi:10.1029/2008JA013672

Krall, J., Huba, J. D., Joyce, G., and Zalesak, S. T. (2009). Three-dimensional simulation of equatorial spread-F with meridional wind effects. *Ann. Geophys.* 27, 1821–1830. doi:10.5194/angeo-27-1821-2009

Krall, J., Huba, J. D., and Fritts, D. C. (2013). On the seeding of equatorial spread F by gravity waves. *Geophys. Res. Lett.* 40, 661–664. doi:10.1002/grl.50144

Kudeki, E., Akgiray, A., Milla, M., Chau, J. L., and Hysell, D. L. (2007). Equatorial spread-F initiation: Post-sunset vortex, thermospheric winds, gravity waves. *J. Atmos. Solar-Terr. Phys.* 69, 2416–2427. doi:10.1016/j.jastp.2007.04.012

Makela, J. J., and Kelley, M. C. (2003). Field-aligned 777.4-nm composite airglow images of equatorial plasma depletions. *Geophys. Res. Lett.* 30, 1442. doi:10.1029/2003GL017106

Makela, J. J., Vadas, S. L., Muryanto, R., Duly, T., and Crowley, G. (2010). Periodic spacing between consecutive equatorial plasma bubbles. *Geophys. Res. Lett.* 37, L14103. doi:10.1029/2010GL043968

Martinis, C., Baumgardner, J., Mendillo, M., Wroten, J., Coster, A., and Paxton, L. (2015). The night when the auroral and equatorial ionospheres converged. *J. Geophys. Res. Space Phys.* 120, 8085–8095. doi:10.1002/2015JA021555

Maruyama, T. (1988). A diagnostic model for equatorial spread F. 1. Model description and application to electric field and neutral wind effects. *J. Geophys. Res.* 93, 14611–14622. doi:10.1029/JA093iA12p14611

Mendillo, M., and Baumgardner, J. (1982). Airglow characteristics of equatorial plasma depletions. *J. Geophys. Res.* 87, 7641–7652. doi:10.1029/JA087iA09p07641

Mendillo, M., Meriwether, J., and Biondi, M. (2001). Testing the thermospheric neutral wind suppression mechanism for day-to-day variability of equatorial spread F. *J. Geophys. Res.* 106, 3655–3663. doi:10.1029/2000JA000148

Otsuka, Y., Shiokawa, K., Ogawa, T., and Wilkinson, P. (2002). Geomagnetic conjugate observations of equatorial airglow depletions. *Geophys. Res. Lett.* 29, 43-1–43-4. doi:10.1029/2002GL015347

Otsuka, Y. (2018). Review of the generation mechanisms of post-midnight irregularities in the equatorial and low-latitude ionosphere. *Prog. Earth Planet. Sci.* 5, 57. doi:10.1186/s40645-018-0212-7

Park, S. H., England, S. L., Immel, T. J., Frey, H. U., and Mende, S. B. (2007). A method for determining the drift velocity of plasma depletions in the equatorial ionosphere using far-ultraviolet spacecraft observations. *J. Geophys. Res. Space Phys.* 112, A11314. doi:10.1029/2007JA012327

Picone, J. M., Hedin, A. E., Drob, D. P., and Aikin, A. C. (2002). NRLMSISE-00 empirical model of the atmosphere: Statistical comparisons and scientific issues. *J. Geophys. Res. Space Phys.* 107, SIA 15-21–SIA 15-16. doi:10.1029/2002JA009430

Retterer, J. M., and Roddy, P. (2014). Faith in a seed: On the origins of equatorial plasma bubbles. *Ann. Geophys.* 32, 485–498. doi:10.5194/angeo-32-485-2014

Retterer, J. M., Decker, D. T., Borer, W. S., Daniell, R. E., and Fejer, B. G. (2005). Assimilative modeling of the equatorial ionosphere for scintillation forecasting: Modeling with vertical drifts. *J. Geophys. Res. Space Phys.* 110, A11307. doi:10.1029/2002JA009613

Rideout, W., and Coster, A. (2006). Automated gps processing for global total electron content data. *GPS Solut.* 10, 219–228. doi:10.1007/s10291-006-0029-5

Rodrigues, F. S., Hickey, D. A., Zhan, W., Martinis, C. R., Fejer, B. G., Milla, M. A., et al. (2018). Multi-instrumented observations of the equatorial F-region during june solstice: Large-scale wave structures and spread- F. *Prog. Earth Planet. Sci.* 5, 14. doi:10.1186/s40645-018-0170-0

Röttger, J. (1973). Wave-like structures of large-scale equatorial spread-F irregularities. *J. Atmos. Terr. Phys.* 35, 1195–1206. doi:10.1016/0021-9169(73)90016-0

Saito, S., and Maruyama, T. (2006). Ionospheric height variations observed by ionosondes along magnetic meridian and plasma bubble onsets. *Ann. Geophys.* 24, 2991–2996. doi:10.5194/angeo-24-2991-2006

Saito, S., and Maruyama, T. (2007). Large-scale longitudinal variation in ionospheric height and equatorial spread F occurrences observed by ionosondes. *Geophys. Res. Lett.* 34, L16109. doi:10.1029/2007GL030618

Sarudin, I., Hamid, N. S. A., Abdullah, M., Buhari, S. M., Shiokawa, K., Otsuka, Y., et al. (2021). Influence of zonal wind velocity variation on equatorial plasma bubble occurrences over southeast asia. *J. Geophys. Res. Space Phys.* 126, e28994. doi:10.1029/2020JA028994

Savitzky, A., and Golay, M. J. E. (1964). Smoothing and differentiation of data by simplified least squares procedures. *Anal. Chem.* 36, 1627–1639. doi:10.1021/ac60214a047

Shinagawa, H., Jin, H., Miyoshi, Y., Fujiwara, H., Yokoyama, T., and Otsuka, Y. (2018). Daily and seasonal variations in the linear growth rate of the Rayleigh-Taylor instability in the ionosphere obtained with GAIA. *Prog. Earth Planet. Sci.* 5, 16. doi:10.1186/s40645-018-0175-8

Singh, S., Johnson, F. S., and Power, R. A. (1997). Gravity wave seeding of equatorial plasma bubbles. *J. Geophys. Res.* 102, 7399–7410. doi:10.1029/96JA03998

Smith, J. M., Rodrigues, F. S., Fejer, B. G., and Milla, M. A. (2016). Coherent and incoherent scatter radar study of the climatology and day-to-day variability of mean F region vertical drifts and equatorial spread F. *J. Geophys. Res. Space Phys.* 121, 1466–1482. doi:10.1002/2015JA021934

Stolle, C., Lühr, H., Rother, M., and Balasis, G. (2006). Magnetic signatures of equatorial spread F as observed by the CHAMP satellite. *J. Geophys. Res.* 111, A02304. doi:10.1029/2005JA011184

Su, S. Y., Chao, C. K., and Liu, C. H. (2008). On monthly/seasonal/longitudinal variations of equatorial irregularity occurrences and their relationship with the postsunset vertical drift velocities. *J. Geophys. Res. Space Phys.* 113, A05307. doi:10.1029/2007JA012809

Sultan, P. J. (1996). Linear theory and modeling of the Rayleigh-Taylor instability leading to the occurrence of equatorial spread F. *J. Geophys. Res.* 101, 26875–26891. doi:10.1029/96JA00682

Takahashi, H., Taylor, M. J., Pautet, P. D., Medeiros, A. F., Gobbi, D., Wrasse, C. M., et al. (2009). Simultaneous observation of ionospheric plasma bubbles and mesospheric gravity waves during the SpreadFEx Campaign. *Ann. Geophys.* 27, 1477–1487. doi:10.5194/angeo-27-1477-2009

Takahashi, H., Wrasse, C. M., Otsuka, Y., Ivo, A., Gomes, V., Paulino, I., et al. (2015). Plasma bubble monitoring by TEC map and 630 nm airglow image. *J. Atmos. Solar-Terr. Phys.* 130, 151–158. doi:10.1016/j.jastp.2015.06.003

Takahashi, H., Wrasse, C. M., Figueiredo, C. A. O. B., Barros, D., Abdu, M. A., Otsuka, Y., et al. (2018). Equatorial plasma bubble seeding by MSTIDs in the ionosphere. *Prog. Earth Planet. Sci.* 5, 32. doi:10.1186/s40645-018-0189-2

Taori, A., Patra, A. K., and Joshi, L. M. (2011). Gravity wave seeding of equatorial plasma bubbles: An investigation with simultaneous F region, E region, and middle atmospheric measurements. *J. Geophys. Res. Space Phys.* 116, A05310. doi:10.1029/2010JA016229

Tsunoda, R. T., and White, B. R. (1981). On the generation and growth of equatorial backscatter plumes 1. Wave structure in the Bottomside F layer. *J. Geophys. Res.* 86, 3610–3616. doi:10.1029/JA086iA05p03610

Tsunoda, R. T., Bubenik, D. M., Thampi, S. V., and Yamamoto, M. (2010). On large-scale wave structure and equatorial spread F without a post-sunset rise of the F layer. *Geophys. Res. Lett.* 37, L07105. doi:10.1029/2009GL042357

Tsunoda, R. T., Saito, S., and Nguyen, T. T. (2018). Post-sunset rise of equatorial F layer—Or upwelling growth? *Prog. Earth Planet. Sci.* 5, 22. doi:10.1186/s40645-018-0179-4

Tsunoda, R. T. (2005). On the enigma of day-to-day variability in equatorial spread F. *Geophys. Res. Lett.* 32, L08103. doi:10.1029/2005GL022512

Tsunoda, R. T. (2010). On equatorial spread F: Establishing a seeding hypothesis. *J. Geophys. Res. Space Phys.* 115, A12303. doi:10.1029/2010JA015564

Tsunoda, R. T. (2015). Upwelling: A unit of disturbance in equatorial spread F. *Prog. Earth Planet. Sci.* 2, 9. doi:10.1186/s40645-015-0038-5

Vadas, S. L. (2007). Horizontal and vertical propagation and dissipation of gravity waves in the thermosphere from lower atmospheric and thermospheric sources. *J. Geophys. Res. Space Phys.* 112, A06305. doi:10.1029/2006JA011845

Valladares, C. E., and Chau, J. L. (2012). The low-latitude ionosphere sensor network: Initial results. *Radio Sci.* 47, RS0L17. doi:10.1029/2011RS004978

Vankadara, R. K., Panda, S. K., Amory-Mazaudier, C., Fleury, R., Devananboyina, V. R., Pant, T. K., et al. (2022). Signatures of equatorial plasma bubbles and ionospheric scintillations from magnetometer and GNSS observations in the Indian longitudes during the space weather events of early september 2017. *Remote Sens.* 14, 652. doi:10.3390/rs14030652

Vierinen, J., Coster, A. J., Rideout, W. C., Erickson, P. J., and Norberg, J. (2016). Statistical framework for estimating GNSS bias. *Atmos. Meas. Tech.* 9, 1303–1312. doi:10.5194/amt-9-1303-2016

Whalen, J. A. (2001). The equatorial anomaly: Its quantitative relation to equatorial bubbles, bottomside spread F, and E×B drift velocity during a month at solar maximum. *J. Geophys. Res.* 106, 29125–29132. doi:10.1029/2001JA000089

Woodman, R. F., and La Hoz, C. (1976). Radar observations of F region equatorial irregularities. *J. Geophys. Res.* 81, 5447–5466. doi:10.1029/JA081i031p05447

Wu, Q. (2015). Longitudinal and seasonal variation of the equatorial flux tube integrated Rayleigh-Taylor instability growth rate. *J. Geophys. Res. Space Phys.* 120, 7952–7957. doi:10.1002/2015JA021553

Xiong, C., Stolle, C., Lühr, H., Park, J., Fejer, B. G., and Kervalishvili, G. N. (2016). Scale analysis of equatorial plasma irregularities derived from Swarm constellation. *Earth, Planets Space* 68, 121. doi:10.1186/s40623-016-0502-5

Yamamoto, M., Otsuka, Y., Jin, H., and Miyoshi, Y. (2018). Relationship between day-to-day variability of equatorial plasma bubble activity from GPS scintillation and atmospheric properties from Ground-to-topside model of Atmosphere and Ionosphere for Aeronomy (GAIA) assimilation. *Prog. Earth Planet. Sci.* 5, 26. doi:10.1186/s40645-018-0184-7

Yizengaw, E., and Groves, K. M. (2018). Longitudinal and seasonal variability of equatorial ionospheric irregularities and electrodynamics. *Space Weather* 16, 946–968. doi:10.1029/2018SW001980

Yokoyama, T., Shinagawa, H., and Jin, H. (2014). Nonlinear growth, bifurcation, and pinching of equatorial plasma bubble simulated by three-dimensional high-resolution bubble model. *J. Geophys. Res. Space Phys.* 119, 10,474–10,482. doi:10.1002/2014JA020708

Yokoyama, T., Jin, H., Shinagawa, H., and Liu, H. (2019). Seeding of equatorial plasma bubbles by vertical neutral wind. *Geophys. Res. Lett.* 46, 7088–7095. doi:10.1029/2019GL083629

Yokoyama, T. (2017). A review on the numerical simulation of equatorial plasma bubbles toward scintillation evaluation and forecasting. *Prog. Earth Planet. Sci.* 4, 37. doi:10.1186/s40645-017-0153-6

Zakharenkova, I., Astafyeva, E., and Cherniak, I. (2016). GPS and *in situ* Swarm observations of the equatorial plasma density irregularities in the topside ionosphere. *Earth, Planets Space* 68, 120. doi:10.1186/s40623-016-0490-5

Zhang, S.-R., Erickson, P. J., Goncharenko, L. P., Coster, A. J., Rideout, W., and Vierinen, J. (2017). Ionospheric bow waves and perturbations induced by the 21 august 2017 solar eclipse. *Geophys. Res. Lett.* 44, 12,067–12,073. doi:10.1002/2017GL076054

Zhang, S.-R., Erickson, P. J., Gasque, L. C., Aa, E., Rideout, W., Vierinen, J., et al. (2021). Electrified postsunrise ionospheric perturbations at millstone hill. *Geophys. Res. Lett.* 48, e95151. doi:10.1029/2021GL095151

frontiers | Frontiers in Astronomy and Space Sciences

TYPE Original Research
PUBLISHED 22 March 2023
DOI 10.3389/fspas.2023.1147571

OPEN ACCESS

EDITED BY
Huixin Liu,
Kyushu University, Japan

REVIEWED BY
Andrés Calabia,
University of Alcalá, Spain
Yun Gong,
Wuhan University, China

*CORRESPONDENCE
Astrid Maute,
astrid.maute@colorado.edu

SPECIALTY SECTION
This article was submitted to Space Physics, a section of the journal Frontiers in Astronomy and Space Sciences

RECEIVED 18 January 2023
ACCEPTED 07 March 2023
PUBLISHED 22 March 2023

CITATION
Maute A, Forbes JM, Cullens CY and Immel TJ (2023), Delineating the effect of upward propagating migrating solar tides with the TIEGCM-ICON. *Front. Astron. Space Sci.* 10:1147571. doi: 10.3389/fspas.2023.1147571

Delineating the effect of upward propagating migrating solar tides with the TIEGCM-ICON

Astrid Maute[1]*, Jeffrey M. Forbes[2], Chihoko Y. Cullens[3] and Thomas J. Immel[4]

[1]High Altitude Observatory, National Center for Atmospheric Research, Boulder, CO, United States, [2]Ann and H.J. Smead Aerospace Engineering Sciences, University of Colorado, Boulder, CO, United States, [3]Laboratory for Atmospheric and Space Physics, Boulder, CO, United States, [4]Space Sciences Laboratory at University of California, Berkeley, CA, United States

Introduction: The vertical coupling of the lower and upper atmosphere *via* atmospheric solar tides is very variable and affects the thermosphere and ionosphere system. In this study, we use Ionospheric Connection (ICON) explorer data from 220–270 Day Of Year (DOY), 2020 when large changes in the migrating semidiurnal tide (SW2) and the zonal and diurnal mean (ZM) zonal wind occur within 8 days.

Method: We use the ICON Level4 product, the thermosphere-ionosphere-electrodynamics general circulation model (TIEGCM) driven by tides fitted to ICON observations *via* the Hough Mode Extension (HME) method. The effect of the upward propagating tides is isolated by examining the difference between two TIEGCM simulations with and without tidal HME forcing at the model lower boundary.

Results: The simulations reveals that the solar SW2 changes its latitudinal structure at 250 after DOY 232 from two peaks at mid latitudes to one broad low latitude peak, while at 110 km the two-peak structure persists. The ZM zonal wind at 250 km undergoes a similar dramatic change. These SW2 changes are associated with the prevalence of antisymmetric HMEs after DOY 232. The migrating diurnal, terdiurnal and quaddiurnal tides at 250 km undergo similar variations as SW2. TW3 is strong in the thermosphere and most likely caused by non-linear tidal interaction between DW1 and SW2 above 130 km. Surprisingly, the solar *in situ* forcing of TW3 and SW2 in the upper thermosphere is not nearly as important as their upward propagating tidal component. Associated with the strong dynamical changes, the zonal and diurnal mean NmF2 decreases by approximately 15%–20%, which has a major contribution from the O/N_2 decrease by roughly 10%. These changes are stronger than general seasonal behavior.

Discussion: While studies have reported on the dynamical changes *via* SW2 in the mesosphere-lower thermosphere (MLT) region during the equinox transition period, this study is, to our knowledge, the first to examine the effects of rapid changes in SW2 on the upper thermosphere and ionosphere. The study highlights the potential of using ICON-TIEGCM for scientific studies.

KEYWORDS

migrating solar tides, tide-tide interaction, hough modes, composition, plasma distribution, vertical coupling

1 Introduction

Solar atmospheric tides excited in the lower atmosphere can propagate into the lower thermosphere where they modify among others, the neutral wind circulation, the composition, and the electrodynamics. Some tides can even propagate into the upper thermosphere, directly changing the plasma distribution. The Ionosphere Connection (ICON) explorer (Immel et al., 2018) is designed to study the connection between the lower and upper atmosphere by observing key quantities. The value of the ICON observations are demonstrated in many studies (e.g., Immel et al., 2021; Cullens et al., 2022; England et al., 2022; Harding et al., 2022; Heelis et al., 2022). The ICON mission is augmented by accompanying numerical simulations to enhance the scientific return (e.g., Forbes et al., 2017; Huba et al., 2017; Maute, 2017; Cullens et al., 2020). In this study, we demonstrate the value of these simulations in aiding the interpretation of the ICON observations during the August-September 2020 time period.

Upward propagating solar tides from the lower atmosphere have a rich spectrum due to different generation processes, i. e., absorption of solar radiation by tropospheric water vapor, by stratospheric ozone, by lower thermospheric molecular oxygen, by thermospheric atomic oxygen, and latent heat release in the tropics due to deep convection (e.g., Butler and Small, 1963; Lindzen and Chapman, 1969; Forbes, 1982b; a; Hagan et al., 2007). In addition, depending on tidal characteristics and the mean atmospheric conditions, tides might propagate upward, are modulated, dissipate, and/or interact non-linearly with other tides, planetary waves, and gravity waves (e.g., Holton, 1975; Volland, 1988; Miyahara and Forbes, 1991). In the following, we use the term "upward propagating lower atmospheric tides" for the tidal spectrum close to 97 km.

In this study, our primary focus is on the various harmonics of solar tides with frequencies $n\Omega$ and zonal wavenumbers s = n, denoted [n, s], where $\Omega = 2\pi/24$ h. Here, if n and s are equal and s is positive it implies westward migration with the apparent motion of the Sun to a ground-based observer, and thus are referred to as "migrating" tides. We use the common shorthand notation DW1, SW2, TW3 and QW4 to denote migrating diurnal (D), semidiurnal (S), terdiurnal (T) and quaddiurnal (Q) tides, respectively. We use alternatively [1, 1], [2, 2], [3, 3], and [4, 4] when quantifying primary and secondary waves engaged in non-linear interactions. Stationary planetary waves are denoted by SPWs or [0, s] and the zonal and diurnal mean as ZM = [0, 0]. Eastward propagating tides are denoted by an "E" e.g., SE2 is the eastward propagating semidiurnal tide with zonal wavenumber 2 or [2,-2].

It is now well accepted, based on both, observations and theory, that the interaction between two primary waves $[n_1,s_1]$ and $[n_2,s_2]$ results in two secondary waves (sw) with frequencies and zonal wavenumbers that are the sums and differences of the frequencies and zonal wavenumbers of the primary waves: sw+ = $[n_1+n_2,s_1+s_2]$, sw- = $[n_1-n_2,s_1-s_2]$ (e.g., see Teitelbaum and Vial, 1991). These relationships will be used in the current study to identify the likely origins of some waves.

The current study focuses on the time period August 7 - 26 September 2020 (Day of Year DOY 220–270) when the migrating semidiurnal tide (SW2) and the thermospheric background circulation exhibits large, sudden changes. This period is close to the equinox transition time, therefore we will provide some overview of associated studies in the following, even though in the discussion of our results we do not focus on a connection to the equinox transition.

The equinox transitions in thermosphere and ionosphere (TI) are complex since the TI is influence by processes in different regions, each with their associated seasonal behavior, e.g., lower atmospheric upward propagating tides (e.g., Hagan and Forbes, 2002, 2003; Oberheide et al., 2011a) and corresponding changes in the mean circulation and composition (e.g., Fesen et al., 1991; Fuller-Rowell, 1998), *in situ* processes such as direct solar radiation (e.g., Ward et al., 2021), and coupling to the polar regions (e.g., Millward et al., 1996). Therefore, studies have shown that the equinox transition exhibits variability from year to year and does not necessarily align with the solar equinox (e.g., Pancheva et al., 2009; Burns et al., 2012; Venkateswara Rao et al., 2015).

While seasonal changes occur all the time, recently Conte et al. (2018) reported on a sharp semidiurnal solar tidal (S2) amplitude decrease during the equinox transitions, especially around September, which was observed by three meteor radars in the northern hemisphere and southern hemisphere (Conte et al., 2017). They found that the S2 decrease extends from the mesosphere to the lower thermosphere (approximately 75–100 km) with varying onset DOY (between DOY 265–295) for different years. By employing the Hamburg Model of the Neutral and Ionized Atmosphere (HAMMONIA) model (Schmidt et al., 2006), the authors could attribute the S2 changes mainly to distinct SW2 tidal changes with some contribution from SW1 later in the seasonal transition.

In a follow on study, Pedatella et al. (2021) used the Specified Dynamics Whole Atmosphere Community Climate Model with thermosphere-ionosphere eXtension simulations (SD-WACCMX) to find that during the September transition the antisymmetric Hough modes (2,3) and (2,5) are decreasing in amplitude leading to the decrease in SW2 amplitude. The timing of the lower thermospheric SW2 transition was linked to the seasonal transition in the middle atmosphere. Other studies have also used differences in Hough modes and vertical wavelengths to understand the changes in the SW2 latitudinal variation with altitude (e.g., Azeem et al., 2016; Stober et al., 2021; Forbes and Zhang, 2022). In addition, signals of distinct September transitions are observed in the D-region ionosphere in the propagation of very low frequency (VLF) radio wave signals (Macotela et al., 2021), suggesting an association with the mean temperature variation at 70–80 km and the semidiurnal solar tidal enhancement.

As noted by Pedatella et al. (2021), evolution of the latitude structure of SW2 during the 1–2 months leading up to solar equinox (DOY 266) is complex, and characterized by asymmetries between hemispheres that vary from year to year. While the troposphere and stratosphere excitations of SW2 project mainly onto the first symmetric mode of SW2 during both equinox and solstice conditions (e.g., Forbes and Garrett, 1978), it is the interaction of this mode with the middle atmosphere zonal wind field that plays a strong role in exciting antisymmetric modes through "mode coupling" (Lindzen and Hong, 1974) or "cross coupling" (Walterscheid and Venkateswaran, 1979a; b). Moreover, vertical propagation of the first symmetric mode of SW2 is sensitive to the vertical temperature gradient in the mesosphere (Geller, 1970; Forbes et al., 2022). At lower thermospheric heights, these modes,

all with different vertical and latitudinal structures, achieve their largest amplitudes and constructively and destructively interfere as a function of time to produce the evolution of latitude structures at any given height that comprise the complexity noted above.

Several studies examined the connection between different migrating tidal changes in the mesosphere-lower thermosphere region (MLT) during the September-October season and we mention only a few recent ones in the following. van Caspel et al. (2020) used 16 years of northern hemisphere high latitude Super Dual Auroral Radar Network (SuperDARN) meteor winds finding the largest SW2 amplitudes in early fall of all seasons (peaking around DOY 260) and they attributed the seasonal variation of SW2 mainly to the changes in the background atmospheric conditions (e.g., Hagan et al., 1999). In addition, the authors reported on a pronounced migrating terdiurnal tidal (TW3) peak at DOY 265, which agrees with modeling results by Du and Ward (2010); Conde et al. (2018) reported on terdiurnal tides in meteor radar (40N–70N) with sudden changes starting after DOY 250.

Terdiurnal tides can be generated by the non-linear interaction between diurnal and semidiural tides (e.g., Teitelbaum et al., 1989; Smith, 2000; Younger et al., 2002) and/or diurnal tides with gravity waves (Miyahara and Forbes, 1991), and direct solar forcing. There is still discussion about the importance of these different mechanisms with season and we refer to the literature for more insights. Direct solar forcing was identified as the dominant TW3 driver during all seasons (e.g., Smith and Ortland, 2001; Du and Ward, 2010; Lilienthal et al., 2018). Non-linear interaction between tides and/or gravity waves were found to become more important in January and April (Lilienthal et al., 2018). Akmaev (2001) stated that non-linear interactions play a role especially at equinox between 95 and 100 km. Similarly, Huang et al. (2007); Moudden and Forbes (2013) determined that non-linear tidal interaction of DW1 and SW2 is important in TW3 excitation and is overlaid on the upward propagating part.

In general, the terdiurnal tides in the zonal and meridional wind is small in the MLT region, roughly around 4–6 m/s with peaks around equinox (e.g., Du and Ward, 2010; Liu et al., 2020; Pancheva et al., 2021). This could be a factor why less is known about the terdiurnal tide in the upper thermosphere. Gong and Zhou (2011) reported on the terdiurnal tide in the meridional wind between 90 and 350 km at Arecibo for January 2010, finding amplitude in the F-region smaller than the diurnal tidal amplitudes but larger than the semidiurnal tides. Note that the terdiurnal tide at a location is the superposition of various terdiurnal tides with different zonal wavenumbers and can therefore be an over- or underestimation of TW3 (e.g., Du and Ward, 2010).

The quaddiurnal tide is in general even smaller than the terdiurnal tide in the MLT region and therefore not the focus of many studies. Jacobi et al. (2017) examined meteor radar observations at mid-latitude in Europe, finding that the quaddiurnal tide in the zonal wind is up to 7 m/s around December and approximately 1–2 m/s in August-September with much shorter vertical wavelength in northern hemisphere summer than winter. Model diagnostics indicate that the non-linear tidal interactions contribute to the generation of the quaddiurnal tides (e.g., Smith et al., 2004). However, Geißler et al. (2020) found through numerical experiments that solar forcing is the most important mechanism in generating quaddiurnal tides in the MLT region, and non-linear interactions and gravity waves can be important during September equinox conditions. Not much is known about the quaddiurnal tide in the upper thermosphere.

While the distinct changes in the upward propagating SW2 around September equinox have been examined in the MLT region, to our knowledge, their upper thermospheric effects have not been investigated. In the current paper, we examine a time period with distinct SW2 changes in TIEGCM driven by ICON derived tides and focus on the effect of these changes on the thermosphere, specifically on the migrating tides, mean circulation, composition, and plasma distribution.

The paper is structured as follows. In **Section 2**, we described the ICON data (**Section 2.1**), the Hough Mode extension (HME) method (**Section 2.2**), and the TIEGCM simulation (**Section 2.3**). In addition in **Section 2.4**, we provide some validation of the simulation by comparing to the ICON observations. In **Section 3**, we characterize the effect of the sudden changes on the mean circulation and migrating tidal components (**Section 3.1**). We use HMEs to explain the changes in latitudinal structure of SW2 with time. In **Section 3.2**, we quantify the effect on the mean composition and mean electron density as well. In **Section 4**, we summarize our findings.

2 Method and data

2.1 ICON

The ICON observatory was launched on 11 October 2019 into a 27^o low inclination orbit with an approximate 580 km orbit altitude (Immel et al., 2018). On board of ICON are 4 types of instruments. This study is based on Michelson Interferometer for Global High-Resolution Thermospheric Imaging (MIGHTI) neutral wind and neutral temperature measurements (Englert et al., 2017). The two MIGHTI instruments nominally point northward with a 90^o difference in the horizontal look direction. Therefore, backward-looking MIGHTI-B measures the same volume as the forward-looking MIGHTI-A approximately 7–8 min later. From the common volume line of sight wind measurements in the two look-directions, the neutral wind vector can be derived (Harding et al., 2017; Harding et al., 2021). MIGHTI measures the Doppler shift in the 557.7 nm (green) and 630.0 nm (red) atomic oxygen emissions. During the daytime green and red line observations provide continuous wind measurements between 94 and 300 km altitude. At nighttime the wind can be observed by green line emission between 90 and 109 km and by red line emissions between 210 and 300 km. The wind retrievals were validated by, e.g., Harding et al. (2021); Makela et al. (2021); Dhadly et al. (2021). In addition, MIGHTI measures the O_2 762 nm band emission from which the neutral temperature can be derived in the 94–105 km altitude range (Stevens et al., 2018; Stevens et al., 2022). The neutral temperatures were validated by, e.g.,,Yuan et al. (2021). MIGHTI horizontal winds and temperatures in the 94–102 km region are used in the Hough Mode Extension (HME) method to derived the atmospheric tides (Forbes et al., 2017; Cullens et al., 2020).

2.2 Hough mode extension (HME) tides

An ICON science objective is to study the vertical coupling between the lower and upper atmosphere. This can be done by deriving global tidal specifications from the ICON observations and using these to drive a general circulation model. ICON measures neutral winds between 10S and 40N and covers all longitudes and local times in 41 days in the 94–102 km altitude range (Cullens et al., 2020). To derive atmospheric solar tides, which are global in nature, the Hough Mode Extension (HME) method is used (e.g., Oberheide et al., 2011b; Forbes et al., 2017; Cullens et al., 2020). Specific symmetric and antisymmetric HME for different tides are fitted to the observed tidal winds and temperatures.

A 45 days sliding time window is used to derived the HME tides with a 10 days temporal smoothing window. The daily HME tides include specification of the diurnal tides from DE3 to DW2 and semidiurnal tides from SE3 to SW4. No terdiurnal and quaddiurnal tidal specifications are included in the HME tides. The HME tides at 97 km are used to drive the TIEGCM at its lower boundary by reconstructing the perturbation field based on all HME tidal amplitudes and phases. The level 4 HME data product and HME lower boundary version 2 revision 0 (v02r000) was used in this study.

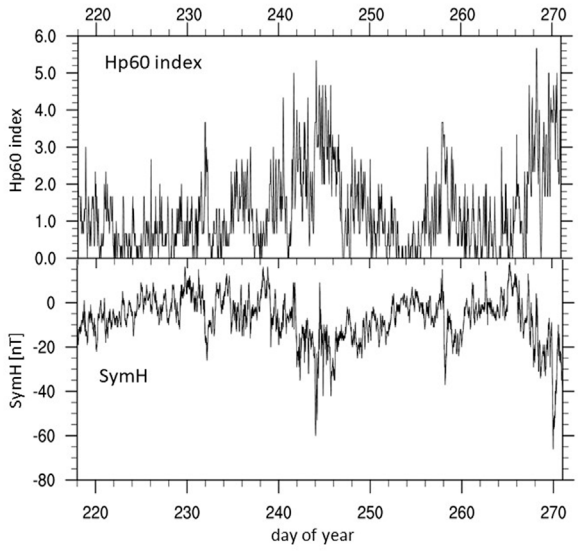

FIGURE 1
Geophysical conditions from August 5 (DOY 218) to September 26 (DOY 270) 2020: Hp60 index (top) and Sym/H [nT] (bottom).

2.3 Thermosphere-ionosphere-electrodynamics GCM simulations

The Thermosphere-Ionosphere-Electrodynamics General Circulation Model (TIEGCM) describes self-consistently the dynamics, energetics, and chemistry in thermosphere and ionosphere with coupled ionospheric electrodynamics (e.g., Richmond, 1995; Qian et al., 2014). The TIEGCM model used for ICON is described by Maute (2017) and is driven at the model's 97 km lower boundary by hourly perturbations constructed from the HME tides. The background, i.e., zonal and diurnal mean, neutral wind, temperature, and geopotential height is based on HWM07 (Drob et al., 2008) and MSISE00 (Drob et al., 2008) to introduce seasonal and latitudinal variations. Details of the background such as using HWM07 *versus* HWM14 are not important for the thermosphere response to upward propagating tides (e.g., Maute, 2017).

In the high-latitude region, magnetosphere-ionosphere coupling is simulated by specifying the ion convection pattern based on Weimer (2005) driven by solar wind data, i.e., interplanetary magnetic field (IMF) B_y, B_z and solar wind velocity and pressure. The auroral precipitation is based on the analytical model by Roble and Ridley (1987) with parametrization by Emery et al. (2012). This standard way of driving TIEGCM has been used to examine geomagnetic storms and quiescent time variation (e.g.,; Qian et al., 2014; Lei et al., 2015; Mannucci et al., 2015). In the high-latitude region, magnetosphere-ionosphere coupling is simulated by specifying the ion convection pattern based on Weimer (2005) driven by solar wind data, i.e., interplanetary magnetic field (IMF) B_y, B_z and solar wind velocity and pressure. The auroral precipitation is based on the analytical model by Roble and Ridley (1987) with parametrization by Emery et al. (2012). This standard way of driving TIEGCM has been used to examine geomagnetic storms and quiescent time variation (e.g.,; Qian et al., 2014; Lei et al., 2015; Mannucci et al., 2015).

The model is run with a 2.5^ox2.5^o geographic longitude and latitude resolution and a quarter scale height vertical resolution. To isolate the effect of the lower atmospheric forcing on the thermosphere-ionosphere (TI) system the ICON mission provides two TIEGCM simulations to the public. One simulation includes the tidal forcing at the TIEGCM lower boundary *via* the HME tides. The other simulation does not include any tidal forcing at the lower boundary. In the following we take advantage of these two simulations to examine the effect of upward propagating tides between August 7 and 26 September 2020 (DOY 220–270). The level 4 TIEGCM data products version 1 revision 0 (v01r000) is used in this study.

2.4 Overview of DOY 220–270 2020 time period

The DOY 220–270 2020 time period is especially interesting because of significant changes in the zonal and diurnal mean state of the upper atmosphere and the migrating tides. The solar radio flux $F_{10.7}$ does not exhibit significant variation ($F_{10.7}$ is between 69 and 76 sfu). The time period included some minor to moderate geomagnetic activity as can be seen in **Figure 1**. The Hp60 (**Figure 1** top), an index similar to Kp but with an hourly cadence and open-ended by allowing values above 9o (Matzka et al., 2022; Yamazaki et al., 2022), has three periods with $Hp60 \geq 5$ around DOY 242, 244 and 268, and in addition a few time periods with $Hp60 \geq 4$– where SymH (**Figure 1** bottom), an hourly index capturing changes in the ring current, has some sudden decreases. However, only the

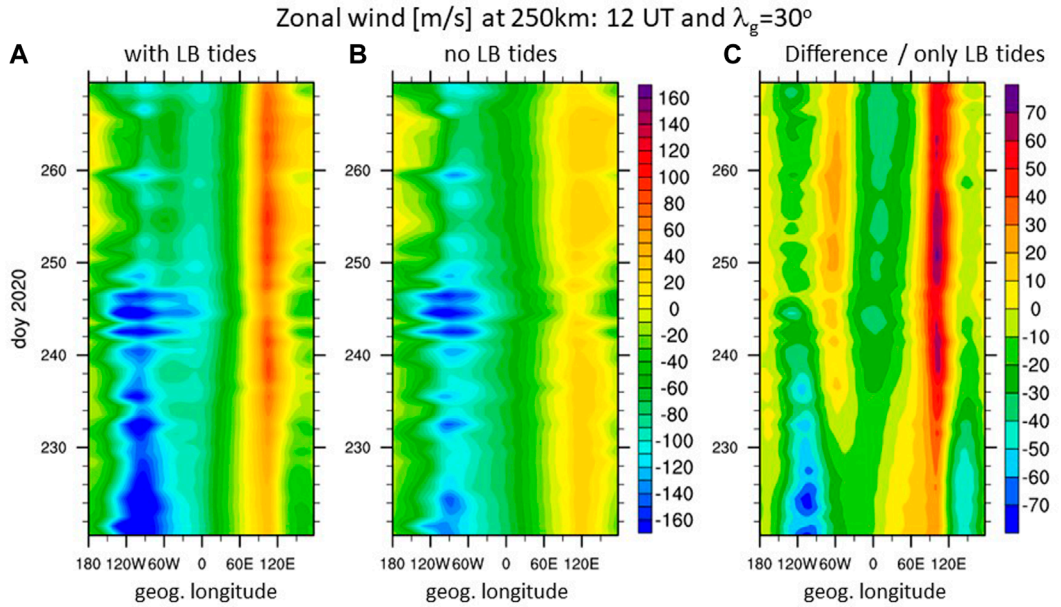

FIGURE 2
Zonal wind [m/s] at 250 km for 12 UT and geographic latitude $\lambda_g = 30^O$ for simulation **(A)** with tides at the lower boundary (LB), **(B)** without tides at the LB, **(C)** differences between **(A)** and **(B)** which isolates the effect of the LB tides.

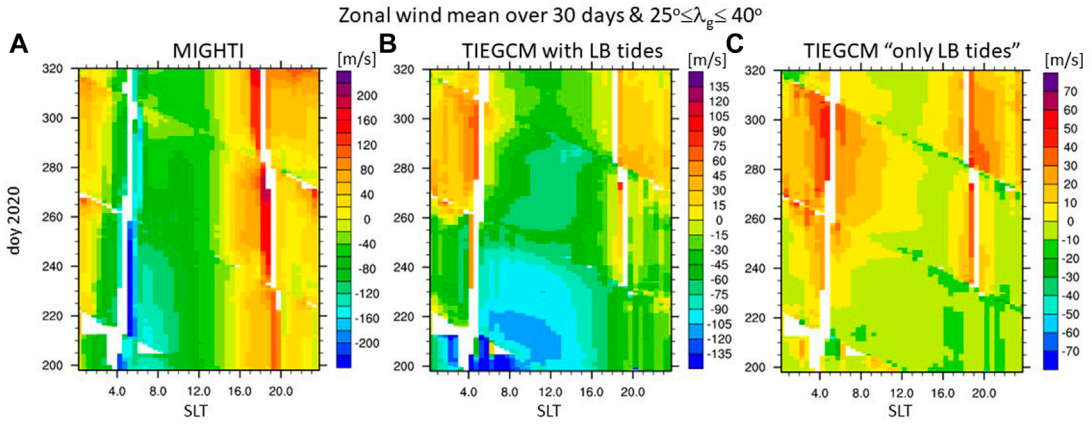

FIGURE 3
Zonal wind [m/s] at 250 km averaged over 30 days and between geographic latitudes λ_g of $25^O \leq \lambda_g \leq 40^O$ **(A)**. MIGHTI zonal wind, **(B)**. TIEGCM with LB tides sampled as MIGHTI winds, **(C)**. TIEGCM only due to LB tides.

time around DOY 244 and 270 has a SymH < -50 nT which is considered a moderate geomagnetic disturbed period.

The effect of the geomagnetic active period is visible in the F-region neutral wind at 250 km illustrated at geographic latitude $\lambda_g = 30^o$ for 12 UT in Figure 2 with the time and longitudinal variation indicated in the y- and *x*-direction, respectively. We label the simulation with tidal forcing at the lower boundary (LB) "with LB tides" (Figure 2A) and the simulation without tides at the LB "no LB tides" (Figure 2B.), the difference between the two simulations is labeled "only LB tides" (Figure 2C). The difference or the "only tides" case removes most of the effect from *in situ* generated tides due to the absorption of solar radiation in the F-region and from the geomagnetic forcing although some minor non-linear effects remain.

The zonal wind clearly shows a diurnal variation with a strong zonal wave number 1 in the case "with LB tides" and "no LB tides". However, in the case "with LB tides" higher order zonal wave numbers develop after approximately DOY 230 within a few days as visible in the longitudinal variation. This rapid transition, happening between approximately DOY 232 and DOY 238, is even more apparent in the "only tides" case in Figure 2C. In the following, we will focus on DOY 220–270 period to investigate how the lower

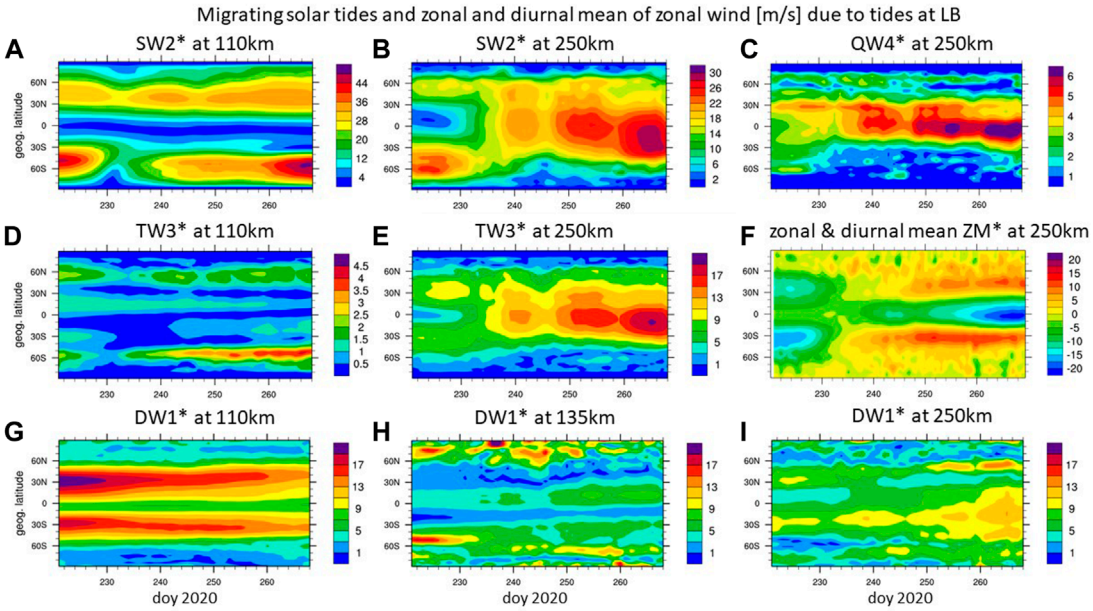

FIGURE 4
Amplitudes of migrating solar tides in zonal wind [m/s] only due to tides at lower boundary (LB) in **(A)**. SW2 at 110 km and **(B)**. SW2 at 250 km, **(C)**. QW4 at 250 km, **(D)**. TW3 at 110 km and **(E)**. TW3 at 250 km, **(G)**. DW1 at 110 km, **(H)**. DW1 at 135 km, and **(I)**. DW1 at 250 km, and **(F)**. zonal and diurnal mean zonal mean wind at 250 km over geographic latitude and day of year (DOY) 2020.

atmospheric tides can facilitate this change. Note that the neutral wind in Figure 2 is depicted at a constant universal time (UT) and therefore the longitudinal axis corresponds to solar local time (SLT).

It is important to examine that the model in general reproduces the observed variation in the zonal wind at 250 km altitude. The ICON observatory samples all local times at each orbit but not for all longitudes and latitudes. We therefore average data using a 30 days sliding window between 25^o to 40^o geographic latitude (λ_g) to determine a longitudinal mean zonal wind over DOY and SLT. The model is sampled at the location of MIGHTI vector winds with the best quality flag. The model and data are processed in the same way. Figure 3 depicts the MIGHTI zonal wind (3a) and the MIGHTI-sampled TIEGCM zonal winds (3b) at 250 km.

The diagonal lines in Figure 3 are an indication that longitudes are not equally sampled in the 30 days window (Cullens et al., 2020). The observations (Figure 3A) experience larger variations than the model (Figure 3B) and therefore, the color scale is adapted. This is not surprising, as first, the model is not perfect and secondly, even a perfect model could not reproduce the observed variations since it is forced by time averaged tidal variations. Even though the zonal wind magnitude is not the same, the variations with local time and over day of year are similar. The model (Figure 3B) exhibits more westward wind in the morning between DOY 200–230, compared to the observations, which becomes less westward with increasing DOY. In the late afternoon the observed zonal wind is eastward with the wind magnitude increasing with DOY, especially in the early evening (approximately 18–20 SLT). The model exhibits a similar variation with the zonal wind getting more eastward with increasing DOY. In general, the simulated zonal wind tends to be more westward than the observed one, but displays similar local time and DOY variations.

We established that the model captures the prevalent local time and DOY variations of the MIGHTI zonal wind. Therefore, we will use the model to isolate the effect of upward propagating tides on the noted wind changes (Figure 2). We examine the difference between the simulation with HME LB tides and without HME LB tides illustrated in Figure 3C. An increase in the semidiurnal component of the zonal wind with increasing DOY is visible in Figure 3C with approximate early morning and evening peaks. Note that signals of non-migrating tides are small since we average over almost all longitudes. In the following, tidal components for the "only LB tides" case will be illustrated and labels by $(\cdot)^*$. We note that we first take the difference between the simulations before determining the tidal components *via* a 2D Fast Fourier transformation (FFT) using a 2 days window.

3 Results

3.1 Dynamical changes

To better understand the illustrated changes in the zonal wind in Figure 2C occurring after approximately DOY 232 we examine the changes in several tidal components in the following. Figure 4A depicts the migrating SW2* at 110 km with a maximum amplitude of roughly 45 m/s at middle latitudes. Figure 4B also shows SW2* but at 250 km, illustrating that between DOY 220 to approximately DOY 230 the latitudinal structure of SW2* at 110 km and 250 km are similar with the distinct middle latitude peaks in each hemisphere.

After approximately DOY 232 the latitudinal structure is evolving differently at 250 km compared to 110 km. At 250 km the SW2* latitudinal structure is changed from the two middle latitude peaks to a single maximum amplitude peak at low latitude (**Figure 4B**).

The migrating quaddiurnal QW4* tide is not included in the HME LB forcing but is present at 250 km in the zonal wind with maximum amplitudes around 6 m/s at low latitudes (**Figure 4C**). The temporal and latitudinal structures of QW4* and SW2* at 250 km are similar. Therefore, we suggest that it is generated by tide-tide interaction of DW1 x TW3 = [1,1] x [3,3] leading to [4,4] + [2,2] = QW4 + SW2. Some smaller contributions might come from SW2 x SW2 = [4,4] + [0,0] = QW4 + ZM. Several studies suggested the generation of quaddiurnal tides through self-interaction of the semidiurnal tide, e.g., in SABER/TIMED temperatures (Liu et al., 2015) and during SSW (Gong et al., 2021) as well as through the diurnal and terdiurnal non-linear interaction as observed in the upper thermosphere at Arecibo during the 2016 SSW (Gong et al., 2018). While QW4 can be excited by the non-linear interaction of SW3 x SW1 = [2,3] x [2,1] leading to [4,4] + [0,2], SW3 and SW1 amplitudes are relatively small in the simulation and this non-linear interaction is therefore excluded from our consideration.

The migrating terdiurnal tide TW3* is shown at 110 km and 250 km in **Figures 4D, E**, respectively. The terdiurnal tides are not included in the HME LB tidal specification. TW3* amplitudes are small at 110 km with a maximum of 4 m/s at middle latitudes, but TW3* amplitude is up to 19 m/s at 250 km with the maximum at very low latitudes. The TW3* at 250 km (**Figure 4E**) emulates very closely the latitudinal and time variation of SW2* (**Figure 4B**). With TW3* amplitudes being approximately 2/3 of SW2* amplitude we suggest that TW3* is generated mainly by DW1 x SW2 = [1,1] x [2,2] leading to [3,3] + [1,1] = TW3 + DW1. DW1 serves here as primary and secondary wave. Note that **Figure 4** depicts the difference between a simulation with and without HME LB tidal forcing and therefore most *in situ* solar heating induced tides in the thermosphere are removed.

DW1* is depicted at 110 km (**Figure 4G**) and at 250 km (**Figure 4I**). At 250 km DW1* has a similar temporal variation equatorward of 30^o geographic latitude as SW2* and TW3* with an amplitude peak around DOY 265, and minor peaks around 255 and 240. The importance of the DW1 x SW2 interaction is well accepted in the literature as an important source of TW3 (see, e.g., Moudden and Forbes, 2013, and references therein), although generally of secondary importance to direct thermal forcing. Ours is the first report of TW3 production in the thermosphere by this mechanism.

DW1* is strongly forced at the lower boundary as evidenced by its 10–18 m/s amplitudes at 110 km in **Figure 4G**. However, DW1 has a short vertical wavelength (≈30 km) and does not penetrate much above 110 km; see for instance, **Figure 4H** which indicates amplitudes of 4–8 m/s at 135 km and low latitudes after DOY 232. We conclude that the DW1* signature in **Figure 4I** is not the result of DW1 propagating upwards from the LB, but rather is excited *in situ* through non-linear interaction as noted above.

Finally, we note the intensification of zonal and diurnal mean (ZM*) zonal winds after DOY 232 at 250 km (**Figure 4F**) leading to wind magnitudes ranging from −20 to 15 m/s around DOY 260. We conclude that these are due to the momentum deposited into the background atmosphere of the intensified migrating tides DW1*, SW2*, TW3*, QW4* after DOY 232 which is supported by the change in latitudinal structure of ZM* after DOY 232 reflecting the strong change in SW2* and TW3* (**Figures 4B, E**). As noted by Angelats i Coll and Forbes (2002), through examination of Eliassen-Palm flux divergences, it is not unexpected to see regions of eastward acceleration (and therefore eastward ZM zonal winds) in connection with dissipation of westward-propagating waves.

In the following, we focus on DOY 265 when the migrating tides exhibit a peak at low latitudes at 250 km (see **Figures 4B, C, E, I**). In **Figure 5** the latitude-height variations of tidal amplitudes in zonal and meridional wind at DOY 265 are depicted. **Figures 5A–C** show the DW1, SW2, and TW3 zonal wind amplitudes only due to *in situ* forcing without any upward propagating LB tides. These diagnostics will be helpful to assess the importance of upward propagating tides in comparison to the *in situ* forced components.

Figure 5A shows that the DW1 zonal wind component of the *in situ* solar EUV-driven circulation is strongest at middle to high latitudes (amplitudes of up to 80 m/s) and at low latitudes (equatorward of ±30° geographic latitude) has amplitudes of 40 m/s between 200 and 300 km. The *in situ* forced SW2 (**Figure 5B**) is very small with values less than 10 m/s over most of the domain. The SW2* amplitude from the upward propagating tides is around 30 m/s (**Figure 5E**) and much larger than the *in situ* driven SW2. SW2* due to upward propagating tides has almost the same magnitude as the *in situ* driven DW1 at low latitudes (**Figure 5A**). Thus, it is expected that SW2* due to upward propagating tides contributes significantly to the thermospheric circulation at these latitudes and altitudes.

Only a few studies (e.g., Forbes and Garrett, 1979; Forbes et al., 2011) investigated the relative importance of *in situ* vs. vertically-propagating semidiurnal tides to the dynamics of the upper thermosphere, finding that the major contribution comes from thermal excitation above 100 km except during solar minimum conditions when contributions from upward propagating semidiurnal tides can be comparable in magnitude. Forbes et al. (2011) fit HMEs to semidiurnal tidal temperatures derived from TIMED/SABER in the lower thermosphere, and compared the HME-extrapolated values with SW2 exosphere temperatures derived from CHAMP and GRACE densities near ~400 km. The comparisons were made during the January-July 2004 (F10.7 ≈ 90-130sfu) and December 2005-July 2006 (F10.7 ≈ 75-100sfu) intervals, and revealed maxima during the Dec-Feb and Apr-Jul months. Interestingly, they concluded that the *in situ* contribution to SW2 dominated over any contribution propagating from below, opposite to the conclusion made above based on TIEGCM driven by HME LB tides. Unfortunately, no results from this study were available during September (i.e., DOY 265), and the present results moreover correspond to deeper solar minimum (F10.7 ≈ 70sfu), precluding any definitive conclusions based on comparisons between the two studies. Therefore, further work remains to be done on this aspect of thermosphere dynamics.

The depiction of TW3 meridional wind amplitude in **Figure 5F** can be contrasted against that in **Figure 5G** as further evidence for *in situ* generation of TW3* due to tide-tide interactions (recall that terdiurnal tides are not included in the LB forcing). Comparison

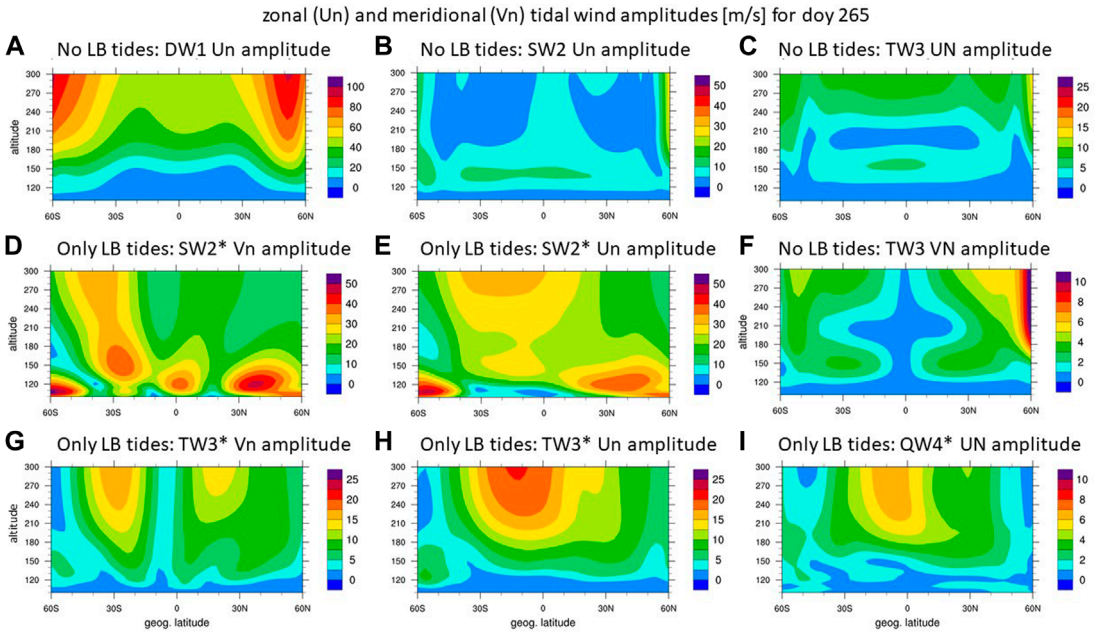

FIGURE 5
Amplitude of migrating solar tides in neutral wind [m/s] at DOY 265 over geographic latitude from the simulation with no LB tides **(A)**. DW1 in zonal wind, **(B)**. SW2 in zonal wind, **(C)**. TW3 in zonal wind, **(F)**. TW3 in meridional wind; and only due to tides at the LB **(D)**. SW2 in meridional wind, **(E)**. SW2 in zonal wind, **(G)**. TW3 in meridional wind, **(H)**. TW3 in zonal wind, **(I)**. QW4 in zonal wind.

between **Figures 5H, C** supports the same conclusion for the zonal wind component of TW3. We want to point out that the "no LB tides" depictions of tides (**Figures 5A–C, F**) are not based on simulation differences and therefore can show tidal signatures at high latitude induced by the offset of the aurora region with respect to the geographic coordinate system.

Surprisingly, maximum zonal wind amplitudes for TW3* (**Figure 5H**) are approaching those of SW2* (**Figure 5E**) at low latitudes and are approximately half of the *in situ* generated DW1 (**Figure 5A**). Noting the meridional wind amplitudes of order 10–20 m/s for both SW2* (**Figure 5D**) and TW3* (**Figure 5G**) around ±20–30° latitude, from which we conclude that their combined effects on field-align plasma transport may be significant.

Finally, QW4* is plotted in **Figure 5I**, indicating amplitudes of order 8 m/s. While significantly smaller than its SW2* and TW3* counterparts in **Figures 5E, H**, respectively, it is nevertheless noteworthy in terms of its obvious origins of tide-tide non-linear interactions.

The evolution of SW2* structures as evident in the presented TIEGCM-ICON simulation (e.g., **Figure 4B**) is one reason why this time period is so interesting. In the presented case, we wish to consider the height evolution of the latitude structures as well and connecting the latitude vs. DOY evolutions of SW2* U at 110 km and 250 km (**Figures 4A, B**, respectively). The HMEs are useful in providing that interpretation. We use the tidal fitting to a minimum number of HMEs to capture the simulated SW2 structure. The resulting SW2 zonal wind amplitude illustrated in **Figures 6C, D** represents the upward propagating tidal component. The height vs. latitude structures of SW2* U at DOY 224 and DOY 265 (**Figures 6A, B**) will be interpreted with the help of HMEs (**Figures 4A, B**). The corresponding illustration to **Figure 6** for SW2* meridional wind at DOY 224 and DOY 265 is given in **Supplementary Figure S1**.

In general, it was determined that the height vs. latitude structures of tides are well represented by the superimposed latitude-height structures of combined HME1, HME2, HME3, and HME4 (Cullens et al., 2020; Forbes et al., 2022). Therefore, reconstructions based on various combinations of HMEs can be performed, and those that assumed the greatest role in accounting for the simulated TIEGCM-ICON structures can be identified. It is important to note that these HMEs (1–4) have vertical wavelengths (λ_z) entering the thermosphere of ≳300 km, ~85 km, ~57 km, ~40 km, respectively, and that the longer the λ_z the more effectively that HME penetrates to, say, 250 km.

It was found that for DOY 224, the dominant HME was the first antisymmetric HME2 (**Supplementary Figure S2B**), which accounts for the double-maxima in latitude occurring at both 110 km and 250 km for zonal wind U in **Figure 6A**. Unequal peaks between hemispheres at both heights are accounted for by interference with the symmetric mode HME3 and HME1 and/or HME4. Adding HME4 does not seem to make it agree better with TIEGCM results and the reconstruction using the combination of HME1, HME2, and HME3 for the zonal wind captures the salient latitude-height variations in the TIEGCM-ICON SW2* **Figures 6A, C**).

For the period after about DOY 240 at 250 km, all HMEs play a role as can be seen in the reconstruction in **Figure 6D** and the HME amplitudes in **Supplementary Figures S2I, J, M, N**. For zonal wind U, HME3 reinforces HME1 in the equatorial region above approximately 150 km, and nearly cancels HME1 at higher latitudes

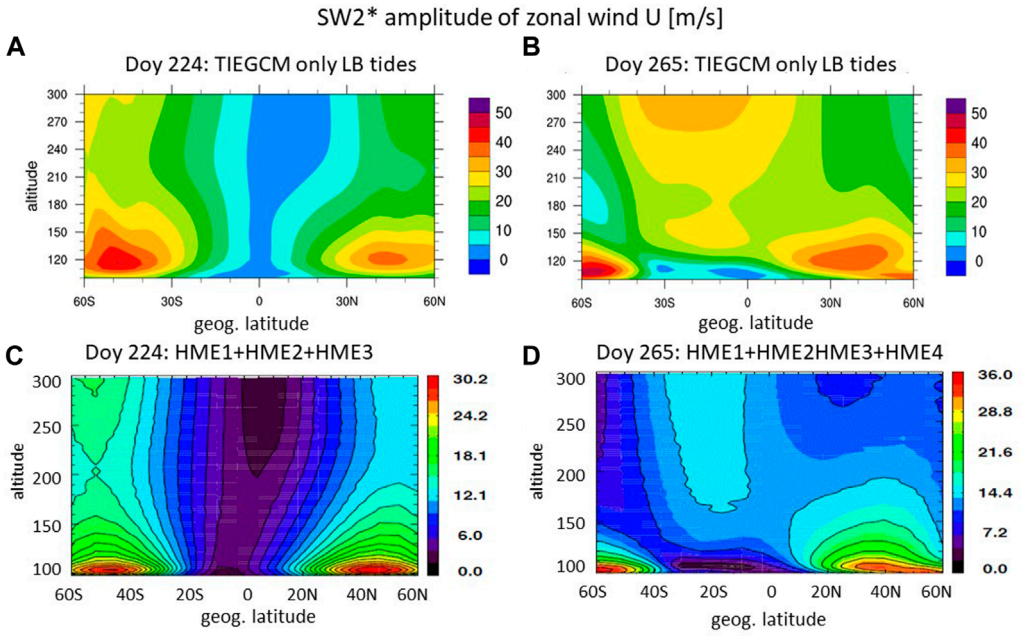

FIGURE 6
Amplitude of semidiurnal migrating tides for zonal wind [m/s] for DOY 224 [left panels **(A, C)**] and DOY 265 [right panels **(B, D)**] based on TIEGCM only due to LB tides [(top panels **(A, B)**] and HME fitting with the least HMEs: 3 modes for DOY 224 (c.) and 4 modes for DOY 265 **(D)**.

above 150 km, resulting in a more restricted latitude extent of the total response. Below 150 km the behavior of the combined HME1 and HME3 is reversed with an almost cancellation in the equatorial region and two maxima at high latitudes. HME2 and HME4 both contribute to the pronounced asymmetries at 250 km and 110 km (**Supplementary Figure S2**). All of the HMEs play a non-negligible role at 110 km and 250 km. The stark difference in the importance of the HME modes at DOY 224 with a dominant asymmetric HME2 *versus* DOY 265 with HME1 to HME4 all playing a role has probably its origin the middle atmosphere where antisymmetric modes can be excited as discussed in the introduction.

3.2 Compositional and electron density changes

In the following, we examine the effect of significant dynamical changes during this period on the mean ionosphere-thermosphere state, specifically the NmF2 and composition *via* O/N_2. First, we evaluate the simulated NmF2, which we do by comparing to FORMOSAT-7/COSMIC-2 (COSMIC-2) observations (Schreiner et al., 2020). COSMIC-2 was launched in June 2019 and consists of 6 satellites in low 24^o inclination orbits with GNSS-radio occultation payload providing more than 4,000 high-quality electron density profiles per day. We are using RO Level 2 data product "ionPrf" which contains the ionospheric electron density profiles validated by Cherniak et al. (2021).

We use the maximum electron density (Ne) in the "ionPrf" data files if the associated altitude is at least 200 km, which eliminates instances of capturing sporadic E occurrence. In the following, we use the maximum Ne as a measure of NmF2, which is a reasonable approximation since the major part of the vertical extent of the F-region is sampled. The maximum Ne observations between 11 SLT to 18 SLT are binned by DOY and by 2.5^o in quasi dipole latitude. **Figure 7A** illustrates the median of the maximum Ne in each bin. Note that the median is chosen to reduce the effect of outliers, however in our case using the average of the maximum Ne of each bin leads to very similar variations. Since the COSMIC-2 constellation was not spread evenly during this early mission phase, there is a longitudinal bias with respect to quasi-dipole latitude in the data (see **Supplementary Figure S4**). The negative quasi-dipole latitudes are preferably sampled in the African-Asian sector where the magnetic equator is in the northern hemisphere and therefore, the orbit dips to lower quasi-dipole latitudes than in the Pacific-American sector. However, this longitudinal bias does not explain the larger median Ne values in the northern than southern EIA crest (**Figure 7A**.) since even when restricting the geographic longitudes to the African-Asian sector a north-south differences in median Ne magnitude remains. We conclude that the north-south asymmetry in the EIA is not an artifact of the data sampling and processing.

The TIEGCM simulation with HME LB tides is binned like the observations with the difference of using NmF2 and all available longitudes (**Figure 7B**). In the model the southern part of the EIA is larger than the northern part, which is opposite to the observations (**Figure 7A**). The study period starts just 40 days after solstice and therefore the influence of northern hemisphere summer conditions are reflected in the observations with larger northern than southern EIA, but the difference reverses around October (e.g., Burns et al., 2012). The TIEGCM can in general reproduce the hemispheric difference in the EIA strength (e.g., Maute, 2017). However, in

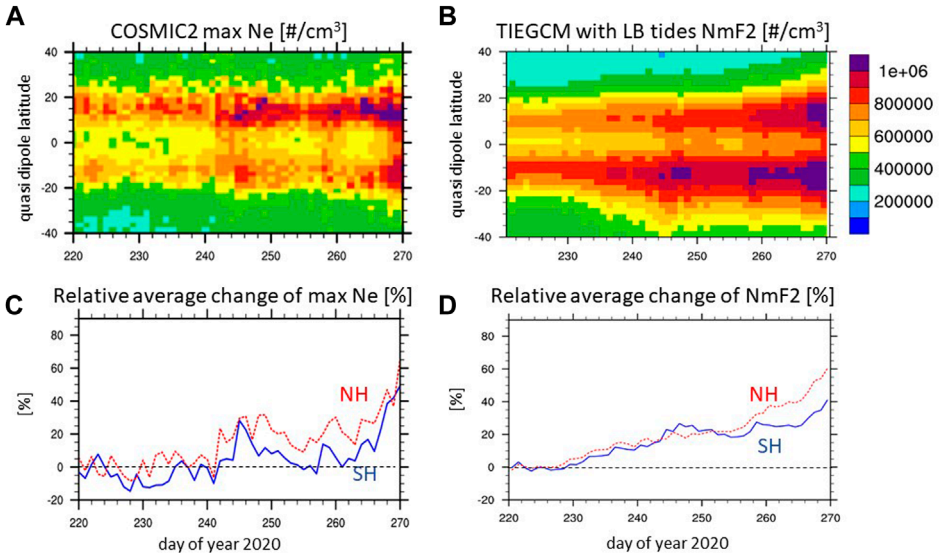

FIGURE 7
Top panels **(A)**. Median of maximum electron density from COSMIC2 RO (equivalent to NmF2) and **(B)** average of NmF2 from TIEGCM with LB tides [$1/cm^3$] for binned values (bin size 1 day and 2.5^o quasi dipole latitude); bottom panels: relative change of quasi dipole latitudinal average between $5^o \leq |\lambda_{qd}| \leq 20^o$ of **(C)** maximum electron density from COSMIC and **(D)** NmF2 from TIEGCM with respect to average latitudinal variation between DOY 220–225.

the current case the model lacks representing the hemispheric difference. This apparent model bias needs further examination which is beyond the scope of the current study.

Both observations and model exhibit an increase in NmF2 with DOY. To compare the temporal variation, we average the NmF2 over $5^o \leq |\lambda_{qd}| \leq 20^o$ with quasi dipole latitude λ_{qd} in both hemispheres and reference to the 5days-average of DOY 220–224 to remove the baseline bias. Figures 7C, D depict the relative change of NmF2 for the observations and simulation, respectively, with an increase after DOY 240 in the observations and after approximately DOY 235 in the simulation. The temporal variation of simulated average NmF2 in the northern EIA crest compares better with the observations than in the southern hemisphere crest. In the southern hemisphere, the observed relative changes of maximum Ne are smaller than in the simulation. We should note that signals of geomagnetic activity are visible around DOY 244, DOY 258, and DOY 268 in the observation and the model (Figures 7A, B). Overall, the simulation can reproduce the salient temporal variation of observed NmF2 and therefore, it will be used to examine the contribution of the LB tides to this temporal variation.

Figure 8A illustrates the zonal and diurnal mean change in NmF2 due to LB tides with respect to the simulation without LB tides. We note that the simulation without LB tides includes the effect of geomagnetic forcing while the "only LB tides" case does not, and therefore there are slight decreases in the percent changes during the geomagnetic active times (Figure 8A). The overall changes are negative and increase significantly with time, especially after DOY 235. At low latitudes a decrease of approximately 15%–20% compared to the beginning of the period can be attributed to the effect of LB tides. To provide more details of the relative changes in NmF2 (Figure 8A), we illustrated the increase in NmF2 over the time period with respect to DOY 220 for the simulation with and without LB tides (Supplementary Figures S5A, B, respectively). The magnitude of the temporal changes in NmF2 after approximately DOY 235 are different between the two simulations with a strong increase in NmF2 occurring in the simulation without LB tides while the simulation with LB tides exhibits a very modest increase, which leads to the negative change in NmF2 in the "only LB tide" case (Figure 8A).

Part of the decrease in NmF2 is related to compositional changes which can be approximated by O/N_2 at 300 km. Figure 8B illustrates the relative change of the zonal and diurnal mean O/N_2 for the "only LB tides" case with respect to the "no LB tide" case. The mean O/N_2 is decreasing by approximately 10% compared to the beginning of the time period. Supplementary Figure S5 illustrates that the zonal and diurnal mean O/N_2 at 300 km is decreasing in the simulation with LB tides, especially after DOY 235 (Supplementary Figure S5C), but the low latitude maximum O/N_2 is almost constant with time in the simulation without LB tides (Supplementary Figure S5D). The similar timing of the O/N_2 changes and of the migrating tides and background wind (Figure 4) in the simulation with LB tides strongly suggest that the dynamical and compositional changes are connected.

These results indicate that the decrease in O/N_2 due to LB tides partly compensate for the seasonal increase in NmF2 (Figure 8B) and therefore leads to a smaller increase in NmF2 with DOY in the simulation with LB tides compared to without LB tides (Supplementary Figures S5A, B, respectively). The relative change of the mean NmF2 in the "only LB tides" case has a strong correlation to the relative change of the mean O/N_2 at 300 km (Figure 8C). The difference in the NmF2 latitudinal variation in Supplementary Figures S5A, B suggests that there are additional contributions from the low latitude ExB drift and the meridional

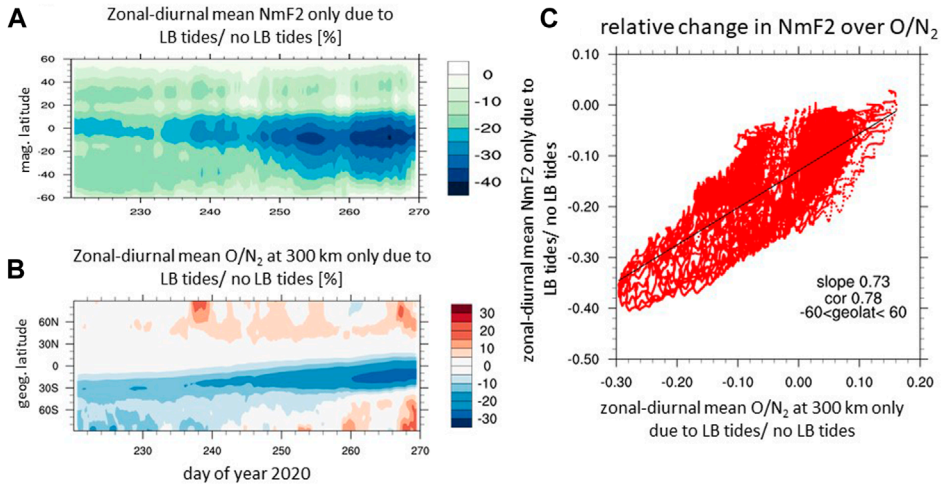

FIGURE 8
Time evolution of the relative change in the zonal and diurnal mean **(A)**. NmF2 over quasi dipole latitude and **(B)** O/N_2 ratio at 300 km over geographic latitude due to lower atmospheric tidal forcing with respect to no tidal forcing; **(C)** correlation between relative NmF2 change and O/N_2 equatorward of $|\lambda_m| \leq 60^o$ and $|\lambda_g| \leq 60^o$, respectively for the time window.

wind leading to EIA differences, such as the EIA position at higher magnetic latitude and with less hemispheric difference in the simulation with LB tides than without. However, the simulation suggests that the main contribution to the temporal changes in NmF2 and O/N_2 are due to the dynamical changes associated with the LB forcing since no strong temporal variation in the EIA location and hemispheric difference was identified. Note that the daytime NmF2 dominates the diurnal mean NmF2.

4 Summary

This study focuses on the DOY 220–270, 2020 time period which exhibits significant temporal and spatial changes in the migrating solar tides as captured by the TIEGCM-ICON driven by the observationally based ICON-HME tides. The ICON mission provides TIEGCM simulations forced at its 97 km lower boundary with and without HME tides. This set of simulations enables us to quantify the effect of upward propagating tides, specifically the impact of the significant temporal and spatial tidal changes, on the lower and upper thermosphere and the ionosphere.

While strong SW2 changes were observed and simulated before and associated with the equinox transitions (e.g., Conde et al., 2018; Pedatella et al., 2021), these studies focused on the mesosphere and lower thermosphere. To our knowledge the current study is the first report of the effects of the strong sudden changes in SW2 on the upper thermosphere and ionosphere. Equinox transitions in the thermosphere are complex since they are influenced by the combined effect of transition characteristics in different altitude regions. During the DOY 220–270, 2020 study period the large tidal changes start 34 days before September equinox (DOY 266). We do not speculate about potential connection to equinox transition, but rather focus on the dynamical changes and its associated effect on composition and plasma distribution. We summarize our main findings.

- The latitudinal structure of SW2 amplitude in zonal wind at 250 km is changing quickly within approximately 8 days after DOY 232 from mid-latitudes peaks in either hemisphere to one broad low latitude peak. The change in SW2 latitudinal structure is associated with the increasing importance of antisymmetric HMEs after DOY 240 when HME1, HME2, HME3, HME4, corresponding to (2,2), (2,3), (2,4), (2,5), respectively, are of comparable size, while before DOY 232 HME1, HME2, HME3, corresponding to (2,2), (2,3), and (2,4), are important with HME2 (2,3) having the largest amplitude.

Studies showed that mean zonal wind condition changes in the middle atmosphere influence the propagation of different Hough Modes (e.g., Hagan et al., 1992; Xu et al., 2010). Therefore, the significant changes in the prevalence of different Hough Mode components during the study period is indicative of changes in the middle atmosphere. Due to the vertical coupling of the middle to upper atmosphere, the strong upper thermospheric tidal changes occur within approximately 8 days.

The simulation indicates that the upward propagating SW2 is more important that the *in situ* forced SW2 in the upper thermosphere during the study period. Previous results by Forbes et al. (2011) for solar medium conditions and December to July season demonstrated than the *in situ* forced SW2 dominates over the propagating SW2 component. Further studies are necessary to understand this difference.

- The latitudinal structure of migrating tides during this time periods is strongly modified at 250 km compared to 110 km. The temporal and latitudinal variation of SW2 is imprinted on the migrating tides, DW1, TW3, and QW4. In the simulations, the terdiurnal and quaddiurnal tides are generated internally since only diurnal and semidiurnal tides are included in the lower boundary forcing.

QW4 is the smallest of the migrating tides and might be generated by non-linear interaction between DW1xTW3 as well as some contribution might come from SW2xSW2. TW3 amplitudes at 250 km are large, approximately 2/3 of SW2. The simulation indicates it is generated by the non-linear interaction between DW1xSW2 in the upper thermosphere. While this non-linear interaction is well documented in the lower thermosphere, to our knowledge, its importance for the upper thermosphere was not noted before. Since both SW2 and TW3 in the meridional wind are strong at 250 km, it is conceivable that they play an important role for field-aligend plasma drift.

- Associated with the changes in SW2 and the other migrating tides, the background winds are significantly changed within approximately 8 days, suggesting that dissipating migrating tides deposited their momentum into the background atmosphere. Angelats i Coll and Forbes (2002) found that dissipation of westward propagating tides can create eastward accelerations of mean zonal wind at some latitudes.

These dynamical changes influence the composition and the plasma distribution. The simulation results indicate that during the time period a 15%–20% change in the zonal and diurnal mean NmF2 is associated with the strong tidal and background changes during this time period. The mean change in NmF2 is strongly aligned with the modification of roughly 10% in the composition as approximated by O/N_2 during this time period.

To set the compositional and plasma density changes during DOY 220–270, 2020 period in perspective, we compare with some previous studies. Jones Jr. et al. (2014) used the TIEGCM forced with and without Climatological Tidal Model of Thermosphere (CTMT) (Oberheide et al., 2011a) to delineate the effect of upward propagating tides on the TI system. They find a 20% decrease in NmF2 and 4% decrease in $[O]/[N_2]$ due to the inclusion of tides with respect to the simulation without tides in August-September but no strong change within days or even 40 days. Similarly, Maute (2017) using the TIEGCM driven by daily varying LB tides smoothed by a 27 days running mean of the Thermosphere-Ionosphere-Mesosphere-Electrodynamic GCM (TIMEGCM) did not see the strong changes in the SW2 reported in this study. This highlights that the change we report here is much stronger than expected from seasonal and climatological behavior.

The study period clearly demonstrates the effect of strong and sudden tidal and mean circulation changes on the upper thermosphere and ionosphere. However, the study has uncertainties due to the limited data coverage. While ICON provides unique observations to study the vertical coupling effects on the thermosphere and ionosphere, atmospheric tides described by HME are based on 10S-40N observations within an up to 41 days window. More frequent sampling of all latitudes, local times, and longitudes are crucial to capture higher order symmetric and antisymmetric HME modes without ambiguity and with higher temporal cadence. Future missions like DYNAMIC (National Research Council, Solar and space physics: a science for a technological society, 2013) will provide tidal specification on a shorter time scale and therefore can provide new insight into their temporal and spatial variations.

Data availability statement

The solar wind parameters are available from the NASA/GSFC's Space Physics Data Facility's OMNIWeb service at https://omniweb.gsfc.nasa.gov/ow min.html. The Hp60 index (Matzka et al., 2022) is available at Geoforschungszentrum Potsdam (GFZ), Germany via https://kp.gfz-potsdam.de/en/hp30-hp60/data. COSMIC Level 2 "ionPrf" product is provided by COSMIC Data Analysis and Archive Center (CDAAC) available via https://doi.org/10.5065/t353-c093. We used the "ionPrf" files of ionospheric electron density profiles. The ICON mission data is available at Goddard Space Flight Center Space Physics Data Facility (SPDF) https://cdaweb.gsfc.nasa.gov/ and at the Space Science Laboratary (SSL) ftp server ftp://icon576science.ssl.berkeley.edu/pub. The ICON-MIGHTI neutral wind vectors Level 2.1 V05 data can be found at SSL ftp server under Level2/MIGHTI/2020/DOY/ZIP/ICON L2-1 MIGHTI 2020 MM-DD v05r000.ZIP). The ICON-HME product Level4 V02 can be found at SSL ftp server under Level4/HME/2020/ZIP/ICON L4-1 HME 2020-MM-DD v02r004.ZIP. The TIEGCM-ICON simulations Level 4 V01 are available at ftp://icon-science.ssl.berkeley.edu/pub with HME LB forcing at Level4/TIEGCM/2020/ZIP/ICON L4-3 TIEGCM 2020 MM-DD v01r000.ZIP and without HME LB forcing Level4/TIEGCM-NOHME/2020/ZIP/ICON L4-3 TIEGCM-NOHME 2020 MM584 DD v01r000.ZIP.

Author contributions

AM conducted the analysis. CC and JF conducted the HME analysis. AM and JF drafted the manuscript. AM, JF, CC, TI worked on the interpretation of the analysis.

Funding

AM is supported by ICON NASA grant 80NSSC21K1990. JF and CC were supported by the ICON mission through NASA Explorers Program contracts NNG12FA45C and NNG12FA42I. We would like to acknowledge high-performance computing support from Cheyenne (doi:10.5065/D6RX99HX) provided by NCAR's Computational and Information Systems Laboratory, sponsored by the National Science Foundation. This material is based upon work supported by the National Center for Atmospheric Research, which is a major facility sponsored by the National Science Foundation under Cooperative Agreement No. 1852977.

Acknowledgments

AM would like to thank Dr. N. Pedatella for comments on an earlier draft.

Conflict of interest

The authors declare that the research was conducted in the absence of any commercial or financial relationships that could be construed as a potential conflict of interest.

Publisher's note

All claims expressed in this article are solely those of the authors and do not necessarily represent those of their affiliated organizations, or those of the publisher, the editors and the reviewers. Any product that may be evaluated in this article, or claim that may be made by its manufacturer, is not guaranteed or endorsed by the publisher.

Supplementary material

The Supplementary Material for this article can be found online at: https://www.frontiersin.org/articles/10.3389/fspas.2023.1147571/full#supplementary-material

References

Akmaev, R. A. (2001). Seasonal variations of the terdiurnal tide in the mesosphere and lower thermosphere: A model study. *Geophys. Res. Lett.* 28, 3817–3820. doi:10.1029/2001GL013002

Angelats i Coll, M., and Forbes, J. M. (2002). Nonlinear interactions in the upper atmosphere: The s = 1 and s = 3 nonmigrating semidiurnal tides. *J. Geophys. Res.* 107, SIA 3-1–SIA 3-15. doi:10.1029/2001JA900179

Azeem, I., Walterscheid, R. L., Crowley, G., Bishop, R. L., and Christensen, A. B. (2016). Observations of the migrating semidiurnal and quaddiurnal tides from the RAIDS/NIRS instrument. *J. Geophys. Res. Space Phys.* 121, 4626–4637. doi:10.1002/2015JA022240

Burns, A. G., Solomon, S. C., Wang, W., Qian, L., Zhang, Y., and Paxton, L. J. (2012). Daytime climatology of ionospheric $N_m F_2$ and $h_m F_2$ from COSMIC data. *J. Geophys. Res. Space Phys.* 117. doi:10.1029/2012ja017529

Butler, S., and Small, K. (1963). The excitation of atmospheric oscillations. *Proc. R. Soc. Lond. Ser. A. Math. Phys. Sci.* 274, 91–121.

Cherniak, I., Zakharenkova, I., Braun, J., Wu, Q., Pedatella, N., Schreiner, W., et al. (2021). Accuracy assessment of the quiet-time ionospheric F2 peak parameters as derived from COSMIC-2 multi-GNSS radio occultation measurements. *J. Space Weather Space Clim.* 11, 18. doi:10.1051/swsc/2020080

Conde, M. G., Bristow, W. A., Hampton, D. L., and Elliott, J. (2018). Multiinstrument studies of thermospheric weather above Alaska. *J. Geophys. Res. Space Phys.* 123, 9836–9861. doi:10.1029/2018JA025806

Conte, J. F., Chau, J. L., Laskar, F. I., Stober, G., Schmidt, H., and Brown, P. (2018). Semidiurnal solar tide differences between fall and spring transition times in the northern hemisphere. *Ann. Geophys.* 36, 999–1008. doi:10.5194/angeo-36-999-2018

Conte, J. F., Chau, J. L., Stober, G., Pedatella, N., Maute, A., Hoffmann, P., et al. (2017). Climatology of semidiurnal lunar and solar tides at middle and high latitudes: Interhemispheric comparison. *J. Geophys. Res. Space Phys.* 122, 7750–7760. doi:10.1002/2017JA024396

Cullens, C., Immel, T. J., Triplett, C. C., Yen-Jung, W., England, S. L., Forbes, J. M., et al. (2020). Sensitivity study for ICON tidal analysis. *Prog. Earth Planet. Sci.* 7, 18. doi:10.1186/s40645-020-00330-6

Cullens, C. Y., England, S. L., Immel, T. J., Maute, A., Harding, B. J., Triplett, C. C., et al. (2022). Seasonal variations of medium-scale waves observed by icon-mighti. *Geophys. Res. Lett.* 49, e2022GL099383. doi:10.1029/2022gl099383

Dhadly, M. S., Englert, C. R., Drob, D. P., Emmert, J. T., Niciejewski, R., and Zawdie, K. A. (2021). Comparison of ICON/MIGHTI and TIMED/TIDI neutral wind measurements in the lower thermosphere. *J. Geophys. Res. Space Phys.* 126, e2021JA029904. doi:10.1029/2021ja029904

Drob, D. P., Emmert, J. T., Crowley, G., Picone, J. M., Shepherd, G. G., Skinner, W., et al. (2008). An empirical model of the earth's horizontal wind fields: HWM07. *J. Geophys. Res. Space Phys.* 113. doi:10.1029/2008ja013668

Du, J., and Ward, W. (2010). Terdiurnal tide in the extended canadian middle atmospheric model (CMAM. *J. Geophys. Res. Atmos.* 115. doi:10.1029/2010jd014479

Emery, B., Roble, R., Ridley, E., Richmond, A., Knipp, D., Crowley, G., et al. (2012). *Parameterization of the ion convection and the auroral oval in the NCAR thermospheric general circulation models*. Tech. rep. Boulder CO, USA: National Center for Atmospheric Research. doi:10.5065/D6N29TXZ

England, S. L., Englert, C. R., Harding, B. J., Triplett, C. C., Marr, K., Harlander, J. M., et al. (2022). Vertical shears of horizontal winds in the lower thermosphere observed by ICON. *Geophys. Res. Lett.* 49, e2022GL098337. doi:10.1029/2022gl098337

Englert, C. R., Harlander, J. M., Brown, C. M., Marr, K. D., Miller, I. J., Stump, J. E., et al. (2017). Michelson interferometer for global high-resolution thermospheric imaging (MIGHTI): Instrument design and calibration. *Space Sci. Rev.* 212, 553–584. doi:10.1007/s11214-017-0358-4

Fesen, C. G., Roble, R. G., and Ridley, E. C. (1991). Thermospheric tides at equinox: Simulations with coupled composition and auroral forcings: 2. Semidiurnal component. *J. Geophys. Res. Space Phys.* 96, 3663–3677. doi:10.1029/90JA02189

Forbes, J. M. (1982a). Atmospheric tide: 2. The solar and lunar semidiurnal components. *J. Geophys. Res.* 87, 5241–5252. doi:10.1029/JA087iA07p05241

Forbes, J. M. (1982b). Atmospheric tides: 1. Model description and results for the solar diurnal component. *J. Geophys. Res.* 87, 5222–5240. doi:10.1029/JA087iA07p05222

Forbes, J. M., and Garrett, H. B. (1978). Seasonal-latitudinal structure of the diurnal thermospheric tide. *J. Atmos. Sci.* 35, 148–159. doi:10.1175/1520-0469(1978)035<0148:slsotd>2.0.co;2

Forbes, J. M., and Garrett, H. B. (1979). The solar cycle variability of diurnal and semidiurnal thermospheric temperatures. *J. Geophys. Res. Space Phys.* 84, 1947–1949. doi:10.1029/ja084ia05p01947

Forbes, J. M., Oberheide, J., Zhang, X., Cullens, C., Englert, C. R., Harding, B. J., et al. (2022). Vertical coupling by solar semidiurnal tides in the thermosphere from ICON/MIGHTI measurements. *J. Geophys. Res. Space Phys.* 127, e2022JA030288. doi:10.1029/2022ja030288

Forbes, J. M., Zhang, X., Bruinsma, S., and Oberheide, J. (2011). Sun-synchronous thermal tides in exosphere temperature from CHAMP and GRACE accelerometer measurements. *J. Geophys. Res. Space Phys.* 116. doi:10.1029/2011JA016855

Forbes, J. M., Zhang, X., Hagan, M. E., England, S. L., Liu, G., and Gasperini, F. (2017). On the specification of upward-propagating tides for ICON science investigations. *Space Sci. Rev.* 212, 697–713. doi:10.1007/s11214-017-0401-5

Forbes, J. M., and Zhang, X. (2022). Hough mode extensions (HMEs) and solar tide behavior in the dissipative thermosphere. *J. Geophys. Res. Space Phys.* 127, e2022JA030962. doi:10.1029/2022JA030962

Fuller-Rowell, T. J. (1998). The "thermospheric spoon": A mechanism for the semiannual density variation. *J. Geophys. Res. Space Phys.* 103, 3951–3956. doi:10.1029/97JA03335

Geißler, C., Jacobi, C., and Lilienthal, F. (2020). Forcing mechanisms of the migrating quarterdiurnal tide. *Ann. Geophys.* 38, 527–544. doi:10.5194/angeo-38-527-2020

Geller, M. A. (1970). An investigation of the lunar semidiurnal tide in the atmosphere. *J. Atmos. Sci.* 27, 202–218. doi:10.1175/1520-0469(1970)027<0202:aiotls>2.0.co;2

Gong, Y., Ma, Z., Lv, X., Zhang, S., Zhou, Q., Aponte, N., et al. (2018). A study on the quarterdiurnal tide in the thermosphere at Arecibo during the February 2016 Sudden Stratospheric Warming event. *Geophys. Res. Lett.* 45 (13), 149. doi:10.1029/2018GL080422

Gong, Y., Xue, J., Ma, Z., Zhang, S., Zhou, Q., Huang, C., et al. (2021). Strong quarterdiurnal tides in the mesosphere and lower thermosphere during the 2019 Arctic Sudden Stratospheric Warming over mohe, China. *J. Geophys. Res. Space Phys.* 126, e2020JA029066. doi:10.1029/2020ja029066

Gong, Y., and Zhou, Q. (2011). Incoherent scatter radar study of the terdiurnal tide in the E- and F-region heights at Arecibo. *Geophys. Res. Lett.* 38. doi:10.1029/2011GL048318

Hagan, M. E., Burrage, M. D., Forbes, J. M., Hackney, J., Randel, W. J., and Zhang, X. (1999). GSWM-98: Results for migrating solar tides. *J. Geophys. Res.* 104, 6813–6827. doi:10.1029/1998JA900125

Hagan, M. E., and Forbes, J. M. (2002). Migrating and nonmigrating diurnal tides in the middle and upper atmosphere excited by tropospheric latent heat release. *J. Geophys. Res. Atmos.* 107. ACL 6–1–ACL 6–15. doi:10.1029/2001JD001236

Hagan, M. E., Maute, A., Roble, R. G., Richmond, A. D., Immel, T. J., and England, S. L. (2007). Connections between deep tropical clouds and the Earth's ionosphere. *Geophys. Res. Lett.* 34, L20109. doi:10.1029/2007GL030142

Hagan, M., and Forbes, J. (2003). Migrating and nonmigrating semidiurnal tides in the upper atmosphere excited by tropospheric latent heat release. *J. Geophys. Res.* 108, 10–1029. doi:10.1029/2002ja009466

Hagan, M., Vial, F., and Forbes, J. (1992). Variability in the upward propagating semidiurnal tide due to effects of qbo in the lower atmosphere. *J. Atmos. Terr. Phys.* 54, 1465–1474. doi:10.1016/0021-9169(92)90153-c

Harding, B. J., Chau, J. L., He, M., Englert, C. R., Harlander, J. M., Marr, K. D., et al. (2021). Validation of ICON-MIGHTI thermospheric wind observations: 2. Green-Line comparisons to specular meteor radars. *J. Geophys. Res. Space Phys.* 126, e2020JA028947. doi:10.1029/2020ja028947

Harding, B. J., Makela, J. J., Englert, C. R., Marr, K. D., Harlander, J. M., England, S. L., et al. (2017). The MIGHTI wind retrieval algorithm: Description and verification. *Space Sci. Rev.* 212, 585–600. doi:10.1007/s11214-017-0359-3

Harding, B. J., Wu, Y.-J. J., Alken, P., Yamazaki, Y., Triplett, C. C., Immel, T. J., et al. (2022). Impacts of the january 2022 Tonga volcanic eruption on the ionospheric dynamo: ICON-MIGHTI and swarm observations of extreme neutral winds and currents. *Geophys. Res. Lett.* 49, e2022GL098577. doi:10.1029/2022gl098577

Heelis, R. A., Chen, Y.-J., Depew, M. D., Harding, B. J., Immel, T. J., Wu, Y.-J., et al. (2022). Topside plasma flows in the equatorial ionosphere and their relationships to F-Region winds near 250 km. *J. Geophys. Res. Space Phys.* 127, e2022JA030415. doi:10.1029/2022ja030415

Holton, J. (1975). "The dynamic meteorology of the stratosphere and mesosphere," in *Meteorological monograph 15* (United States: American Meteorological Society).

Huang, C. M., Zhang, S. D., and Yi, F. (2007). A numerical study on amplitude characteristics of the terdiurnal tide excited by nonlinear interaction between the diurnal and semidiurnal tides. *Earth, planets space* 59, 183–191. doi:10.1186/bf03353094

Huba, J., Maute, A., and Crowley, G. (2017). Sami3_ICON: Model of the ionosphere/plasmasphere system. *Space Sci. Rev.* 212, 731–742. doi:10.1007/s11214-017-0415-z

Immel, T. J., England, S., Mende, S., Heelis, R., Englert, C., Edelstein, J., et al. (2018). The ionospheric connection explorer mission: Mission goals and design. *Space Sci. Rev.* 214, 13. doi:10.1007/s11214-017-0449-2

Immel, T. J., Harding, B. J., Heelis, R. A., Maute, A., Forbes, J. M., England, S. L., et al. (2021). Regulation of ionospheric plasma velocities by thermospheric winds. *Nat. Geosci.* 14, 893–898. doi:10.1038/s41561-021-00848-4

Jacobi, C., Krug, A., and Merzlyakov, E. (2017). Radar observations of the quarterdiurnal tide at midlatitudes: Seasonal and long-term variations. *J. Atmos. Solar-Terrestrial Phys.* 163, 70–77. doi:10.1016/j.jastp.2017.05.014

Jones, M., Jr., Forbes, J. M., Hagan, M. E., and Maute, A. (2014). Impacts of vertically propagating tides on the mean state of the ionosphere-thermosphere system. *J. Geophys. Res. Space Phys.* 119, 2197–2213. doi:10.1002/2013JA019744

Lei, J., Zhu, Q., Wang, W., Burns, A. G., Zhao, B., Luan, X., et al. (2015). Response of the topside and bottomside ionosphere at low and middle latitudes to the October 2003 superstorms. *J. Geophys. Res. Space Phys.* 120, 6974–6986. doi:10.1002/2015JA021310

Lilienthal, F., Jacobi, C., and Geißler, C. (2018). Forcing mechanisms of the terdiurnal tide. *Atmos. Chem. Phys.* 18, 15725–15742. doi:10.5194/acp-18-15725-2018

Lindzen, R. S., and Chapman, S. (1969). Atmospheric tides. *Space Sci. Rev.* 10, 3–188. doi:10.1007/bf00171584

Lindzen, R. S., and Hong, S.-s. (1974). Effects of mean winds and horizontal temperature gradients on solar and lunar semidiurnal tides in the atmosphere. *J. Atmos. Sci.* 31, 1421–1446. doi:10.1175/1520-0469(1974)031<1421:eomwah>2.0.co;2

Liu, G., Janches, D., Lieberman, R. S., Moffat-Griffin, T., Fritts, D. C., and Mitchell, N. J. (2020). Coordinated observations of 8- and 6-hr tides in the mesosphere and lower thermosphere by three meteor radars near 60°s latitude. *Geophys. Res. Lett.* 47, e2019GL086629. doi:10.1029/2019gl086629

Liu, M., Xu, J., Yue, J., and Jiang, G. (2015). Global structure and seasonal variations of the migrating 6-h tide observed by SABER/TIMED. *Sci. China Earth Sci.* 58, 1216–1227. doi:10.1007/s11430-014-5046-6

Macotela, E. L., Clilverd, M., Renkwitz, T., Chau, J., Manninen, J., and Banyś, D. (2021). Spring-Fall asymmetry in VLF amplitudes recorded in the North Atlantic region: The Fall-effect. *Geophys. Res. Lett.* 48, e2021GL094581. doi:10.1029/2021GL094581

Makela, J. J., Baughman, M., Navarro, L. A., Harding, B. J., Englert, C. R., Harlander, J. M., et al. (2021). Validation of ICON-MIGHTI thermospheric wind observations: 1. Nighttime red-line ground-based fabry-perot interferometers. *J. Geophys. Res. Space Phys.* 126, e2020JA028726. doi:10.1029/2020ja028726

Mannucci, A. J., Verkhoglyadova, O. P., Tsurutani, B. T., Meng, X., Pi, X., Wang, C., et al. (2015). Medium-range thermosphere-ionosphere storm forecasts. *Space* 13, 125–129. doi:10.1002/2014SW001125

Matzka, J., Bronkalla, O., Kervalishvili, G., Rauberg, J., and Yamazaki, Y. (2022). Geomagnetic hpo index. *GFZ Data Serv.* 2022. doi:10.5880/Hpo.000

Maute, A. (2017). Thermosphere-ionosphere-electrodynamics general circulation model for the ionospheric connection explorer: TIEGCM-ICON. *Space Sci. Rev.* 212, 523–551. doi:10.1007/s11214-017-0330-3

Millward, G. H., Moffett, R. J., Quegan, S., Fuller-Rowell, T. J., and Moffett, R. J. (1996). Ionospheric F-2 layer seasonal and semiannual variations. *J. Geophys. Res. Space Phys.* 101, 5149–5156. doi:10.1029/95JA03343

Miyahara, S., and Forbes, J. M. (1991). Interactions between gravity waves and the diurnal tide in the mesosphere and lower thermosphere. *J. Meteorological Soc. Jpn. Ser. II* 69, 523–531. doi:10.2151/jmsj1965.69.5_523

Moudden, Y., and Forbes, J. M. (2013). A decade-long climatology of terdiurnal tides using TIMED/SABER observations. *J. Geophys. Res. Space Phys.* 118, 4534–4550. doi:10.1002/jgra.50273

Oberheide, J., Forbes, J. M., Zhang, X., and Bruinsma, S. L. (2011a). Climatology of upward propagating diurnal and semidiurnal tides in the thermosphere. *J. Geophys. Res.* 116. doi:10.1029/2011JA016784

Oberheide, J., Forbes, J. M., Zhang, X., and Bruinsma, S. L. (2011b). Wave-driven variability in the ionosphere-thermosphere-mesosphere system from TIMED observations: What contributes to the "wave 4. *J. Geophys. Res.* 116. doi:10.1029/2010JA015911

Pancheva, D., Mukhtarov, P., and Andonov, B. (2009). Nonmigrating tidal activity related to the sudden stratospheric warming in the Arctic winter of 2003-2004. *Ann. Geophys.* 27, 975–987. doi:10.5194/angeo-27-975-2009

Pancheva, D., Mukhtarov, P., Hall, C., Smith, A., and Tsutsumi, M. (2021). Climatology of the short-period (8-h and 6-h) tides observed by meteor radars at Tromsø and svalbard. *J. Atmos. Solar-Terrestrial Phys.* 212, 105513. doi:10.1016/j.jastp.2020.105513

Pedatella, N. M., Liu, H.-L., Conte, J. F., Chau, J. L., Hall, C., Jacobi, C., et al. (2021). Migrating semidiurnal tide during the September equinox transition in the Northern Hemisphere. *J. Geophys. Res. Atmos.* 126. doi:10.1029/2020JD033822

Qian, L., Burns, A. G., Emery, B. A., Foster, B., Lu, G., Maute, A., et al. (2014). The NCAR TIE-GCM: A community model of the coupled thermosphere/ionosphere system. *Model. Ionosphere-Thermosphere Syst. Geophys. Monogr. Ser* 201, 73–83.

Richmond, A. (1995). Ionospheric electrodynamics using magnetic apex coordinates. *J. Geomagnetism Geoelectr.* 47, 191–212. doi:10.5636/jgg.47.191

Roble, R., and Ridley, E. (1987). *An auroral model for the NCAR thermospheric general circulation model (TGCM)*. United States: Annales Geophysicae 5A, 369–382.

Schmidt, H., Brasseur, G., Charron, M., Manzini, E., Giorgetta, M., Diehl, T., et al. (2006). The HAMMONIA chemistry climate model: Sensitivity of the mesopause region to the 11-year solar cycle and CO2 doubling. *J. Clim.* 19, 3903–3931. doi:10.1175/jcli3829.1

Schreiner, W., Weiss, J., Anthes, R., Braun, J., Chu, V., Fong, J., et al. (2020). COSMIC-2 radio occultation constellation: First results. *Geophys. Res. Lett.* 47, e2019GL086841. doi:10.1029/2019GL086841

Smith, A. K., Pancheva, D. V., and Mitchell, N. J. (2004). Observations and modeling of the 6-hour tide in the upper mesosphere. *J. Geophys. Res. Atmos.* 109, D10105. doi:10.1029/2003JD004421

Smith, A. K. (2000). Structure of the terdiurnal tide at 95 km. *Geophys. Res. Lett.* 27, 177–180. doi:10.1029/1999GL010843

Smith, A., and Ortland, D. (2001). Modeling and analysis of the structure and generation of the terdiurnal tide. *J. Atmos. Sci.* 58, 3116–3134. doi:10.1175/1520-0469(2001)0583116:MAAOTS2.0.CO;2

Stevens, M., Englert, C., Harlander, J., Marr, K., Harding, B., Triplett, C., et al. (2022). Temperatures in the upper mesosphere and lower thermosphere from o2 atmospheric band emission observed by icon/mighti. *Space Sci. Rev.* 218, 67–32. doi:10.1007/s11214-022-00935-x

Stevens, M. H., Englert, C. R., Harlander, J. M., England, S. L., Marr, K. D., Brown, C. M., et al. (2018). Retrieval of lower thermospheric temperatures from O2 A band emission: The MIGHTI experiment on ICON. *Space Sci. Rev.* 214, 4–9. doi:10.1007/s11214-017-0434-9

Stober, G., Kuchar, A., Pokhotelov, D., Liu, H., Liu, H.-L., Schmidt, H., et al. (2021). Interhemispheric differences of mesosphere–lower thermosphere winds and tides investigated from three whole-atmosphere models and meteor radar observations. *Atmos. Chem. Phys.* 21, 13855–13902. doi:10.5194/acp-21-13855-2021

Teitelbaum, H., Vial, F., Manson, A., Giraldez, R., and Massebeuf, M. (1989). Non-linear interaction between the diurnal and semidiurnal tides: Terdiurnal and diurnal secondary waves. *J. Atmos. Terr. Phys.* 51, 627–634. doi:10.1016/0021-9169(89)90061-5

Teitelbaum, H., and Vial, F. (1991). On tidal variability induced by nonlinear interaction with planetary waves. *J. Geophys. Res. Space Phys.* 96, 14169–14178. doi:10.1029/91JA01019

van Caspel, W. E., Espy, P. J., Hibbins, R. E., and McCormack, J. P. (2020). Migrating tide climatologies measured by a high-latitude array of SuperDARN HF radars. *Ann. Geophys.* 38, 1257–1265. doi:10.5194/angeo-38-1257-2020

Venkateswara Rao, N., Espy, P. J., Hibbins, R. E., Fritts, D. C., and Kavanagh, A. J. (2015). Observational evidence of the influence of Antarctic stratospheric ozone variability on middle atmosphere dynamics. *Geophys. Res. Lett.* 42, 7853–7859. doi:10.1002/2015GL065432

Volland, H. (1988). *Atmospheric tidal and planetary waves*. Berlin, Germany: Springer Science and Business Media.

Walterscheid, R., and Venkateswaran, S. (1979a). Influence of mean zonal motion and meridional temperature gradients on the solar semidiurnal atmospheric tide: A spectral study. Part I: Theory. *J. Atmos. Sci.* 36, 1623–1635. doi:10.1175/1520-0469(1979)036<1623:iomzma>2.0.co;2

Walterscheid, R., and Venkateswaran, S. (1979b). Influence of mean zonal motion and meridional temperature gradients on the solar semidiurnal atmospheric tide: A spectral study. Part II: Numerical results. *J. Atmos. Sci.* 36, 1636–1662. doi:10.1175/1520-0469(1979)036¡1636:IOMZMA¿2.0.CO;2

Ward, W., Seppälä, A., Yiğit, E., Nakamura, T., Stolle, C., Laštovička, J., et al. (2021). Role of the sun and the middle atmosphere/thermosphere/ionosphere in climate (rosmic): A retrospective and prospective view. *Prog. Earth Planet. Sci.* 8, 47–38. doi:10.1186/s40645-021-00433-8

Weimer, D. R. (2005). Improved ionospheric electrodynamic models and application to calculating Joule heating rates. *J. Geophys. Res.* 110, A05306. doi:10.1029/2004JA010884

Xu, J., Smith, A. K., Jiang, G., and Yuan, W. (2010). Seasonal variation of the hough modes of the diurnal component of ozone heating evaluated from aura microwave limb sounder observations. *J. Geophys. Res. Atmos.* 115, D10110. doi:10.1029/2009JD013179

Yamazaki, Y., Matzka, J., Stolle, C., Kervalishvili, G., Rauberg, J., Bronkalla, O., et al. (2022). Geomagnetic activity index hpo. *Geophys. Res. Lett.* 49, e2022GL098860. doi:10.1029/2022gl098860

Younger, P. T., Pancheva, D., Middleton, H. R., and Mitchell, N. J. (2002). The 8-hour tide in the arctic mesosphere and lower thermosphere. *J. Geophys. Res. Space Phys.* 107, SIA 2-1–SIA 2-11. doi:10.1029/2001JA005086

Yuan, T., Stevens, M. H., Englert, C. R., and Immel, T. J. (2021). Temperature tides across the mid-latitude summer turbopause measured by a sodium lidar and mighti/icon. *J. Geophys. Res. Atmos.* 126, e2021JD035321. doi:10.1029/2021jd035321

frontiers | Frontiers in Astronomy and Space Sciences

TYPE Original Research
PUBLISHED 24 April 2023
DOI 10.3389/fspas.2023.1092850

OPEN ACCESS

EDITED BY
Joseph Huba,
Syntek Technologies, United States

REVIEWED BY
Shun-Rong Zhang,
Haystack Observatory, United States
Bapan Paul,
Vivekananda B.Ed and D.El.Ed College, India

*CORRESPONDENCE
K. A. Berényi,
berenyi.kitti@epss.hu

RECEIVED 08 November 2022
ACCEPTED 11 April 2023
PUBLISHED 24 April 2023

CITATION
Berényi KA, Heilig B, Urbář J, Kouba D, Kis Á and Barta V (2023), Comprehensive analysis of the ionospheric response to the largest geomagnetic storms from solar cycle 24 over Europe.
Front. Astron. Space Sci. 10:1092850.
doi: 10.3389/fspas.2023.1092850

Comprehensive analysis of the ionospheric response to the largest geomagnetic storms from solar cycle 24 over Europe

K. A. Berényi[1,2,3]*, B. Heilig[3,4], J. Urbář[5], D. Kouba[5], Á. Kis[3] and V. Barta[3]

[1]ELKH-ELTE Space Research Group, Budapest, Hungary, [2]Doctoral School of Environmental Sciences, ELTE Eötvös Loránd University, Budapest, Hungary, [3]Institute of Earth Physics and Space Science, Sopron, Hungary, [4]Space Research Group, Eötvös Loránd University, Budapest, Hungary, [5]Institute of Atmospheric Physics CAS, Prague, Czechia

A multi-instrumental analysis of the meridional ionospheric response is presented over Europe during the two largest ICME-driven geomagnetic storms of solar cycle #24 maximum. Data from 5 European digisonde stations, ground-based Global Navigation Satellite System, Total Electron Content (GNSS TEC), the ratio of the TEC difference (rTEC), as well as Swarm and Thermosphere, Ionosphere, Mesosphere, Energetics and Dynamics (TIMED) satellite observations have been used for the investigation of selected intervals (11–17 November, 2012, and 16–25 March, 2015). The storm evolution is monitored by digisonde foF2 critical frequency (related to the maximum electron density of F2-layer) and GNSS TEC data. Moreover, Global Ultraviolet Imager (GUVI) measurements from the TIMED satellite are used to investigate the changes in the thermospheric O/N_2 ratio. Our main focus was on the main phase of the geomagnetic storms, when during the nighttime hours extremely depleted plasma was detected. The extreme depletion is observed in foF2, TEC and rTEC, which is found to be directly connected to the equatorward motion of the midlatitude ionospheric trough (MIT) on the nightside. We demonstrate a method (beside the existing ones) which allows the monitoring of the storm-time evolution of the disturbances (e.g., MIT, SAPS, SED) in the thermosphere-ionosphere-plasmasphere system by the combined analysis of the worldwide digisonde system data (with the drift measurements and the ionospheric layer parameters with 5–15 min cadence), with rTEC and GNSS TEC data, and with the satellite data like Swarm, TIMED/GUVI.

KEYWORDS

geomagnetic storms, space weather, ionosphere, ionospheric storm, midlatitude ionospheric trough, GNSS TEC, ionosphere-plasmasphere coupling, Swarm observations

1 Introduction

The physical processes of the Earth's plasma environment responsible for the perturbations of the system and the exact mechanisms of action of solar events affecting the near-Earth space have been of interest to researchers for decades. The most remarkable disturbing solar activity events are interplanetary coronal mass ejections (ICMEs) and high-speed solar wind streams (HSSWS)/corotating interaction regions (CIRs). When they collide with the Earth's magnetic field, they trigger geomagnetic storms. The two types of geomagnetic storms have different time courses and result in different magnitudes of

perturbations. Besides there are several processes that have to be taken into consideration during the examination of the mid- and low latitude ionosphere, as follows: photo-production, chemical loss, and transport by thermal expansion, neutral winds, waves, tides and electric fields of internal and external origin (Mendillo and Narvaez, 2009). In addition, several other influencing factors must be taken into consideration, such as: geomagnetic storm size, local time (LT) of the sudden storm commencement (SSC), time of the day, season, geomagnetic latitude and longitude (Immel and Mannucci, 2013; Mendillo and Narvaez, 2010; Mendillo and Narvaez, 2009).

Within the Earth's plasma environment (ionosphere, plasmasphere, outer magnetosphere), all regions are closely related to each other. In the presence of an external forcing (e.g., ICME or CIR/HSSWS), perturbations can be observed in each plasma layer. The F-layer of the ionosphere has the highest electron density, so electron density changes are the most pronounced there. The electric fields generated during geomagnetically disturbed periods (e.g., prompt penetration of magnetospheric convection electric field-PPEF and disturbance dynamo electric field-DDEF) map along geomagnetic field lines through all these regions and can interact with all of them (see e.g., Nava et al., 2016). The Earth's plasma environment is a very complex, tightly coupled system, and the effects cannot be studied and explained in their entirety if we do not consider them as part of the system.

Geomagnetic storms generate so-called ionospheric storms, which have similar evolution and phases to those of geomagnetic storms, but with a faster procession. Ionospheric storms have already been studied using several types of observations of the F2-layer: ionosonde data of the maximum electron density (NmF2); measurements of the total electron content; incoherent scatter radar measurements of electron and ion densities, temperatures and plasma dynamics; satellite measurements of ionospheric/thermospheric parameters along their orbits (see e.g., Kane and Makarevich, 2010). Comprehensive reviews of storm effects in NmF2 and TEC have been given by Prölss (1995) and Mendillo (2006), for incoherent scatter radar results by Buonsanto (1999), and for *in-situ* satellite data by Prölss and Zahn (1974).

In early studies, two different phases of ionospheric storms were distinguished: positive ionospheric storm phase, when the electron density is increased, and negative ionospheric storm phase, when the electron density is decreased with respect to its expected value. Earlier studies during the past few decades have already found clear and unambiguous patterns in the ionosphere during geomagnetic storms, see for example, the great reviews of Sato (1957), Matsushita (1959), Prölss (1995), Danilov (2013) (for ionosonde data) and Mendillo (2006) (for TEC data).

The various perturbations in the midlatitude ionosphere during geomagnetic storms can be linked to various processes detailed below. For case studies of ionospheric storm effects, it is necessary to determine the key drivers of the actual events.

(1) During geomagnetic storms, the Joule dissipation of currents and the absorption of precipitating particles in the auroral region of the lower thermosphere (100–140 km) are the cause of the so called auroral heating of the thermosphere (Prölss, 1995; Danilov, 2013). The location of both the precipitation boundary and the auroral currents depends on the geomagnetic activity. For intense storms, it could be found below L = 2.5 (Mendillo and Narvaez, 2009). There are two major consequences of high-latitude heating: composition changes (specifically, decrease in the O/N_2 ratio) and the intensification of equatorward winds that can carry the composition change toward lower latitudes (Buonsanto, 1999). Both processes contribute to the formation of long-duration negative storm phases. The electron density near the F2-layer maximum is, approximately, directly proportional to the O/N_2 ratio (Rishbeth and Barron, 1960; Pirog, 2006). This means, if other conditions are unchanged (constant pressure), we should detect depletion in electron density (negative phase) in all regions where O/N_2 ratio has been decreased at F2-layer heights (Danilov, 2013). Under geomagnetic storm conditions this so-called compositional disturbance zone at F2-layer heights reaches lower latitudes because of the intensified heating induced equatorward meridional winds. Negative phase is most common in the summer hemisphere (both day and night) due to the seasonal variation of the background thermospheric wind circulation, but during intense geomagnetic storms it can be detected even in winter months. It favors the postmidnight and morning sectors, because then the background and the storm-induced circulation coincide and add up and therefore can reach much lower latitudes (Prölss, 1995; Buonsanto, 1999; Danilov, 2013). This equatorward expansion of the negative phase has about 50–300 m/s velocity (Danilov and Belik, 1991). Besides the O/N_2 ratio depletion, the increased temperature of the heated thermospheric gas itself is an important factor in forming a negative storm phase in the ionosphere (Mikhailov and Foster, 1997). The increase in temperature leads to an increase in the recombination coefficient causing a further decrease in electron density (see Mikhailov et al., 1995). Previous studies concluded that at high and middle latitudes this negative phase type occurs more often, and has much more dangerous effect on HF propagation (Danilov, 2013).

Long-duration positive ionospheric storm phase can be generated by the enhanced storm-induced equatorward meridional winds because they cause the downwelling of the neutral atomic oxygen and the uplifting of the F-layer along the magnetic field lines due to wind induced vertical ExB drift (Prölss, 1995; Danilov, 2013). A similar drift can also be caused by an increase in E-fields of other origin (e.g., from the magnetosphere) (Danilov, 2013). As the loss-rate decreases with altitude, the density increases.

(2) The ionospheric F- region plasma is the base of the plasmasphere (Mendillo et al., 1974), i.e., the plasmasphere is filled from the dayside ionosphere and empties into the nightside F-region through diffusion along the geomagnetic field lines. Under quiet conditions the midlatitude region maps into the plasmasphere corotating with the Earth. During storms the footprint of the plasmapause (PP) often moves to midlatitudes, especially after sunset (Mendillo and Narvaez, 2009) as the plasmapause moves inward due to the increased geomagnetic activity, while the plasmasphere can still remain conjugated with the midlatitude ionosphere during

daytime hours. Thus, from local noon to dusk the dynamical plasmaspheric processes may contribute to daytime positive-phase ionospheric storms (Lanzerotti et al., 1975), which is followed after sunset by a sharp transition to a depleted state beyond the footprint of the plasmapause (Mendillo et al., 1974). After sunset, both the above discussed dynamics and chemistry cause the onset of a negative phase.

(3) During intense geomagnetic storm events, mainly in the main phase, at night, a drastic "peeling off" of the magnetospheric plasma can be seen, and the ionospheric projection of the PP can penetrate into the midlatitude region also on the dayside. In such a case, an all-day negative phase storm is expected. Based on earlier studies like Heilig et al. (2022), it is stated that the ionospheric footprint of the PP is tightly coupled to the minimum of the midlatitude (main) ionospheric trough (MIT). The poleward edge of the MIT in the evening sector has been observed to coincide with the equatorward boundary of the soft electron precipitation, and the precipitation has therefore been proposed as a major source of electrons building up the poleward wall of the MIT in the evening sector (Turunen and Liszka, 1972; Rodger et al., 1986; Voiculescu et al., 2010). During the night the ionospheric F-layer on the equatorward side of the plasmapause is maintained by the plasmasphere, but not on the global convection dominated poleward side (Schunk and Banks, 1975). Consequently, an MIT minimum could be bounded by a plasmasphere-maintained and the precipitation-maintained ionosphere. The minimum could be sharpened by storm-time developed subauroral polarization streams (SAPS) due to SAPS E-field, and by plasma heating (frictional heating by the drifting plasma) and its consequences (Rodger et al., 1992; Horváth and Lovell, 2016), and by enhancing recombination due to molecular composition changes by neutral winds or diffusion from the aurora oval = composition disturbance zone (1) (Schunk and Banks, 1975).

MIT is a longitudinally elongated and latitudinally restricted region of depleted plasma in the ionosphere (He et al., 2011). Its typical latitudinal extent (width) is 5°–10° (Voiculescu et al., 2010), 10°–15° (Liu and Xiong, 2020), but it can be as wide as 20°. MIT is typically found somewhere between 55° and 75° geographic latitude depending on the geomagnetic activity and MLT (e.g., Whalen, 1989; Werner and Prölss, 1997; Voiculescu et al., 2006; Deminov and Shubin, 2018; Karpachev et al., 2019; Aa et al., 2020; Liu and Xiong, 2020). However, as we will show, in severely disturbed cases it can move even further equatorward. MIT typically occurs in the dark hemisphere, thus, it is most regularly observed during winter months and equinoxes, while in summer, it is mainly restricted to the midnight sector (Rodger et al., 1992; Voiculescu et al., 2006).

Over the years, the general behavior of the ionosphere during storms has become well studied. However, each space weather event and the involved processes are unique, and in many cases the magnitude of the effects cannot yet be predicted. Consequently, case studies of extraordinary/high magnitude events are still important as they can deepen/refine our understanding of the extent of change that can be expected in the individual layers of the Earth's plasma in response to a geomagnetic storm. Furthermore, multi-instrumental comprehensive analysis of the thermosphere-ionosphere-plasmasphere coupling processes during individual geomagnetic storms are rare in the literature. Most studies are based on one or two types of observational data, however the effects cannot be studied separately since the Earth's plasma environment is a very complex, multiplied coupled system.

In this study our aim is to determine the exact connections between the thermosphere-ionosphere-plasmasphere system during two intense ICME-caused geomagnetic storm events. We analyzed the effects through a meridional chain of digisondes (foF2, h'F2 and drift data) across Europe (Northern Hemisphere) complemented by GNSS TEC, Swarm satellite observations of the topside electron density, electron temperature and PP location data, as well as O/N_2 ratio observations from TIMED satellite. Another aim is to identify the processes responsible for the extreme decrease during the night in the main phase of the geomagnetic storm. The rest of the paper is organized as follows. First, the utilized data and the applied methods are introduced. In Section 3 the observations are presented, followed by the discussion in Section 4. Finally, main conclusions are summarized in Section 5.

2 Data and method

In the present study our main focus is on the analysis of the effects in the ionospheric F2-layer during two intense ($Dst_{min} > -100$ nT) ICME related geomagnetic storms. The storms considered are from the winter/equinox of 2012 and 2015 (the maximum of #24 solar cycle), respectively, with the following characteristics: 11–17/11/2012 ($Dst_{min} = -108$ nT, $Kp_{max} = 6.33$) and 16–25/03/2015 ($Dst_{min} = -223$ nT, $Kp_{max} = 7.67$).

For the investigation, intervals covering all the pre-storm (24 h before the SSC), initial, main and recovery phase were selected. We used the geomagnetic Dst-index to identify the storm phases. A sudden sharp increase in the data is observed when an SSC occurs, this is followed by a major decrease in the data (main phase), and then a slower recovery lasting for several days. The magnitude of the storm itself is given by the minimum value of Dst. The AE-index (auroral electrojet index - mainly characterizing the polar region) increases as the substorm activity intensifies.

We analyzed individual events to see in detail the processes and to determine the key drivers of the geomagnetic storm generated ionospheric perturbations. Using the meridional station chain, the latitudinal evolution of the effects can be followed. With the digisonde drift measurements the directions of the associated plasma drifts can be determined. Using also satellite data, the thermospheric (with TIMED, GUVI measurements) and plasmaspheric (with Swarm, Langmuir probe measurements) processes can be linked to the perturbations observed in the ionosphere. The measurements and data utilized are listed below:

2.1 Solar and geomagnetic indices

During case studies we typically identify and characterize the storm events considering the magnitude of geomagnetic indices such as Kp, Dst and AE. The Kp index represents the geomagnetic activity of the midlatitudal regions, and it has logarithmic scale.

TABLE 1 In this table, we can see information about the used 5 digisonde stations. For the geomagnetic coordinates, International Geomagnetic Reference Field (IGRF-13)-model (for year 2015) based calculator was used.

	Name of the station	Station ID	Geomagnetic latitude (deg)	Geomagnetic longitude (deg)	Geographic latitude (deg)	Geographic longitude (deg)
High mid-latitude	Juliusruh	JR055	53.95° N	99.48°E	54.6° N	13.4° E
Middle latitude	Pruhonice	PQ052	49.32° N	98.61° E	50° N	14.6° E
	Sopron	SO148	46.67° N	99.75° E	47.63° N	16.72° E
Low mid-latitude	Rome	RO041	41.7° N	93.76° E	41.8° N	12.5° E
	Athens	AT138	36.17° N	103.33° E	38° N	23.5° E

The Dst index shows the intensity of the ring current and as we mentioned above are generally used to separate the geomagnetic storm's phases case to case. The AE index describe the evolution of the auroral electrojets, so it inform us about the processes at high latitudes.

2.2 Ionosonde data

A meridional ionosonde station chain across Europe was selected to represent the latitudinal changes. The following 5 stations were chosen for the analysis (from North to South): Juliusruh (JR), Pruhonice (PQ), Sopron (SO), Rome (RO), and Athens (AT). In Table 1, information on the ionosonde stations is given. LT = UT +1. Most of the stations are operating with a DPS-4D type of ionosonde, a digisonde. Only SO is an exception where a VISRC-2 type ionosonde operated until 2018, when the same DPS-4D type digisonde was installed also here (Bór et al., 2020). Old ionosonde/digisonde data has typically 30/15 min resolution, respectively, however, in some cases (like at Athens station) data are available at 5-min cadence.

During this investigation, two ionospheric parameters of the F2-layer were examined, namely, foF2, h'F2. The foF2 parameter represent the F2 layer critical frequency associated with the maximum plasma (electron) density of the F2 layer, while the h'F2 parameter reflects the changes in the virtual height of the layer. All digisonde data were manually checked and corrected with SAO Explorer. Besides, modern digital ionosondes provide also routine ionospheric drift measurements in addition to classical vertical ionospheric sounding (for more see the Supplementary Data section and Kouba et al., 2008; Kouba and Koucka Knizova, 2012; Kouba and Koucka Knizova, 2016). The ionospheric drift data for the selected storms of this study were manually processed for the PQ station. Nowadays, tens of digisondes worldwide measure ionospheric drifts routinely and store their data in Global Ionosphere Radio Observatory (GIRO).

Reference values were needed to determine the magnitude of the storm-time deviations from the nominal state. For this, we chose the 3 closest geomagnetically quiet days (QDs) preceding the storms investigated (8, 9, 10 November 2012 and 10, 13, 14 March 2015, respecti721vely) based on the International Q-days (QD) list, and averaged them. These reference values appear as green lines in Figure 3; Figure 4; Figure 5; Figure 6.

2.3 TEC data

GNSS TEC IONEX (IONosphere Map EXchange) maps data (http://ftp.aiub.unibe.ch/ionex/draft/ionex11.pdf) International GPS Service for Geodynamics (IGSG) with 2-hourly cadence were used to determine vertical TEC (vTEC) development in areas surrounding the respective digisondes, each map area of size 2.5 (latitude) x 5 (longitude) degrees.

For comparison, the National Institute of Information and Communications Technology (NICT) Ratio of the TEC difference (rTEC) global maps constructed using the RINEX files obtained from thousands of GNSS receivers all over the world were applied for the European region with a grid of 0.5 × 0.5° and smoothed with a 5 × 5 boxcar. The rTEC value was defined as the difference between the observed TEC and the monthly average quiet TEC value (mean of 10 geomagnetically quietest days), normalized by the average TEC.

2.4 TIMED satellite, global ultraviolet imager (GUVI) O/N_2 measurements

The TIMED satellite has been operating at 625 km altitude since December of 2001 and focuses its measurements to the appr. 60–180 km altitude range (neutral thermosphere and ionosphere) below the satellite (Christensen et al., 2003). TIMED is orbiting on a circular polar orbit with an inclination of 74.1° corresponding to 97.8 min period, which means that a global map of the measurements can be derived from 14.9 daily orbits.

GUVI measurements provide dayside O/N_2 composition (note that this is a column integrated value for an altitude range) and temperature profile of the Mesosphere and Lower Thermosphere/Ionosphere (MLTI) region, as well as the auroral energy inputs (Christensen et al., 2003; Crowley et al., 2006; http://guvitimed.jhuapl.edu/home_background).

2.5 Swarm satellite measurements

The three Swarm satellites were launched into a polar low-Earth orbit (LEO) in November 2013. The altitude of Swarm A

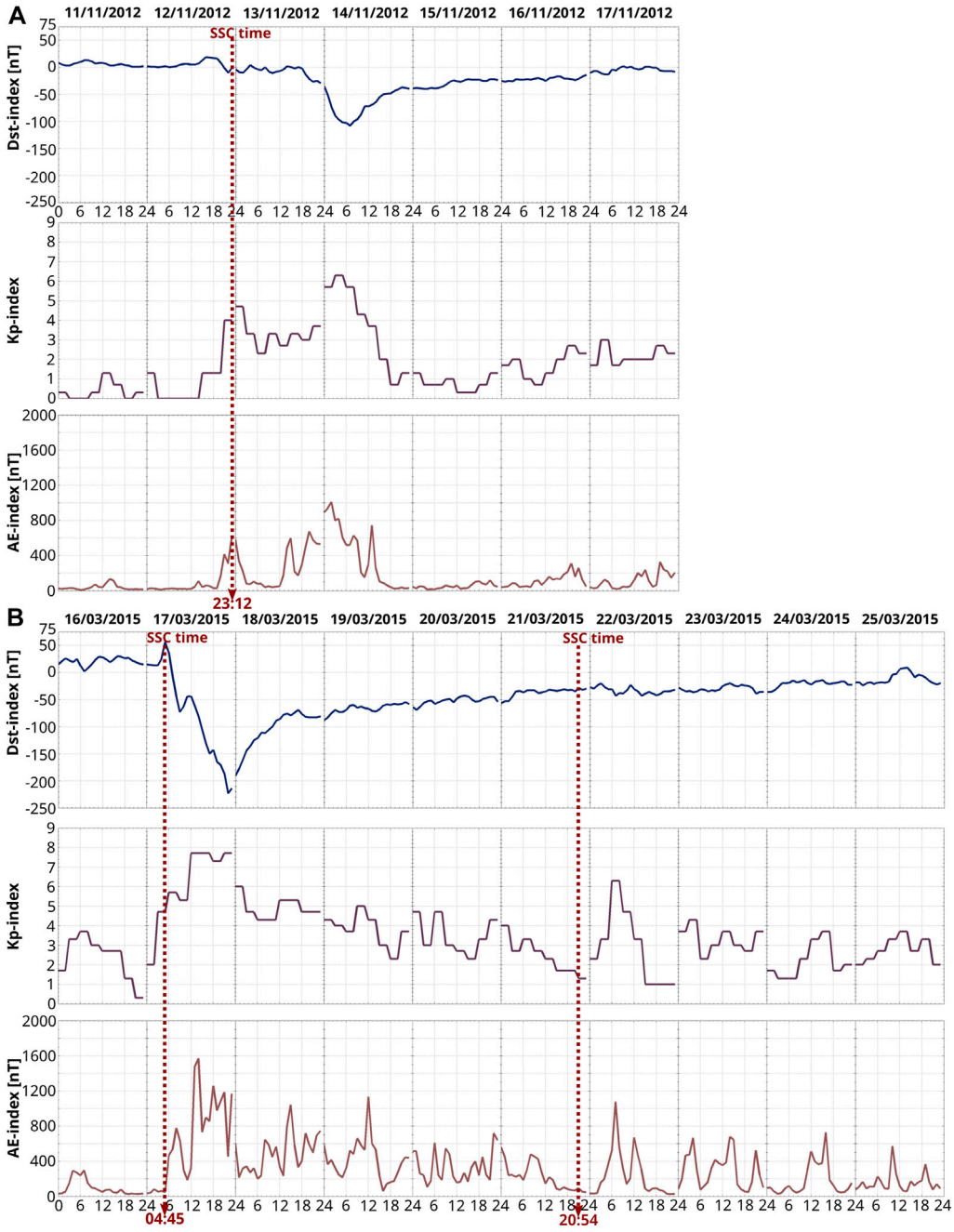

FIGURE 1
The geomagnetic Dst, Kp and AE indices are plotted for the 2012 November storm **(A)**, and for the 2015 March storm **(B)**. In the upper diagrams the daily variation of the Dst index is presented, in the middle panel the Kp index, while in the bottom the daily variation of the AE index is shown. The UT of the SSC was at 23:12 for the 2012 storm marked with a red dotted line. In the 2015 storm, the first storm commenced at UT 04:45, while the second SSC was at 20:54 (red dotted lines).

and C (flying side-by-side with ca. 1.5° longitudinal difference) was around 460 km in March 2015, while Swarm B was operating at around 520 km altitude, with a 91 min orbiting period. Swarm satellites provide *in-situ* measurements of the electron density and temperature observed by Langmuir probes, as well as the location of the MIT from which the footprint of the nightside plasmapause can be derived.

3 Observations

In our previous article (Berényi et al., 2018), the characteristics of the 2012 November and 2015 March storm were described in detail, the course of the storms was investigated in several aspects using data from the Sopron ionosonde station. In this article, we discuss the meridional evolution and characteristics of the two

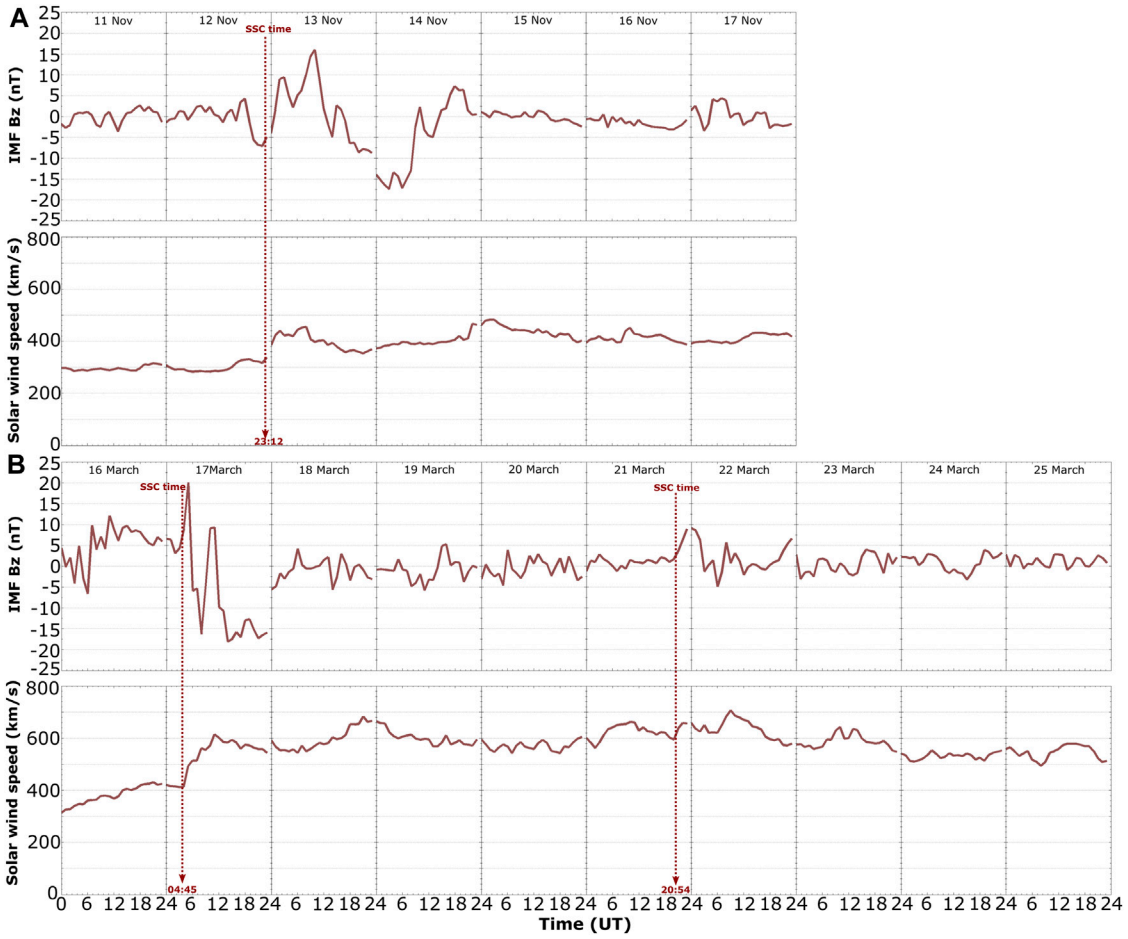

FIGURE 2
The interplanetary magnetic field (IMF) Bz component and the solar wind speed data can be seen for the two investigated storm intervals. **(A)** Is for the 2012 November, **(B)** is for the 2015 March storm. The SSC times are with red dotted lines (Supplementary Figure S1 is the same, except that it is with 1-min resolution).

investigated storms using several types of measurements, detailed in Section 2.

According to the ACE satellite data, in the case of storm from 2012 November, the geomagnetic disturbance started with two ICMEs shock arrivals at 22:16 UT on 12 November (source: SWPC PRF 1942, 19 November, 2012; https://izw1.caltech.edu/ACE/ASC/DATA/level3/icmetable2.htm). The storm started with a Sudden Storm Commencement (SSC) at 23:12 UT (00:12 LT) on 12 November On Figure 2A the evolution of the interplanetary magnetic field (IMF) Bz component and the solar wind (SW) speed data are plotted (1-min resolution is on Supplementary Figure S1A). During the SSC time, short southward turning of the Bz appeared which 1 h later turned northward and lasted until ca. 13 h. In the meanwhile the SW speed from 300 km/s after the SSC went up to 420 km/s and it oscillated around this value through the whole storm interval. Early on 14 November the storm reached its maximum magnitude (major storm), which was caused by a prolonged period of negative Bz (Figure 2A) from 8 h to 18 h, attributed to a combination of lingering ICME effects and a solar sector boundary crossing that occurred at approximately 02:45 UT. Right after that a negative polarity coronal hole associated high speed solar wind stream (HSSWS) arrived. The main phase of the geomagnetic storm started on 14 November (Dst_{min} = −108 nT, Kp_{max} = 6.33), this can be distinctly seen in Figure 1A in the evolution of the geomagnetic Dst, Kp and AE indices.

The 2015 March geomagnetic storm started with an SSC at 04:45 UT (05:45 LT) on 17 March, around equinox. The magnitude of this storm was (on day 17 March): Dst_{min} = −234 nT, Kp_{max} = 7.67 (see also Figure 1B). More information about this ICME generated geomagnetic storm can be found in the article of Wu et al. (2016). On Figure 2B the IMF Bz and SW speed values were displayed (1-min resolution is on Supplementary Figure S1B). The most significant episodes: right after the SSC the northward Bz turned southward around 7 UT, this followed by a northward turning around 10, then from noon until midnight a prolonged southward Bz can be observed. The SW speed values increased from an initial 400 km/s to 600 km/s around noon on17 March, and peaked at 700 km/s on the night of 18 March. On the days after the ICME the Earth was inside the flow of HSSWS (Nava et al., 2016). A subsequent geomagnetic

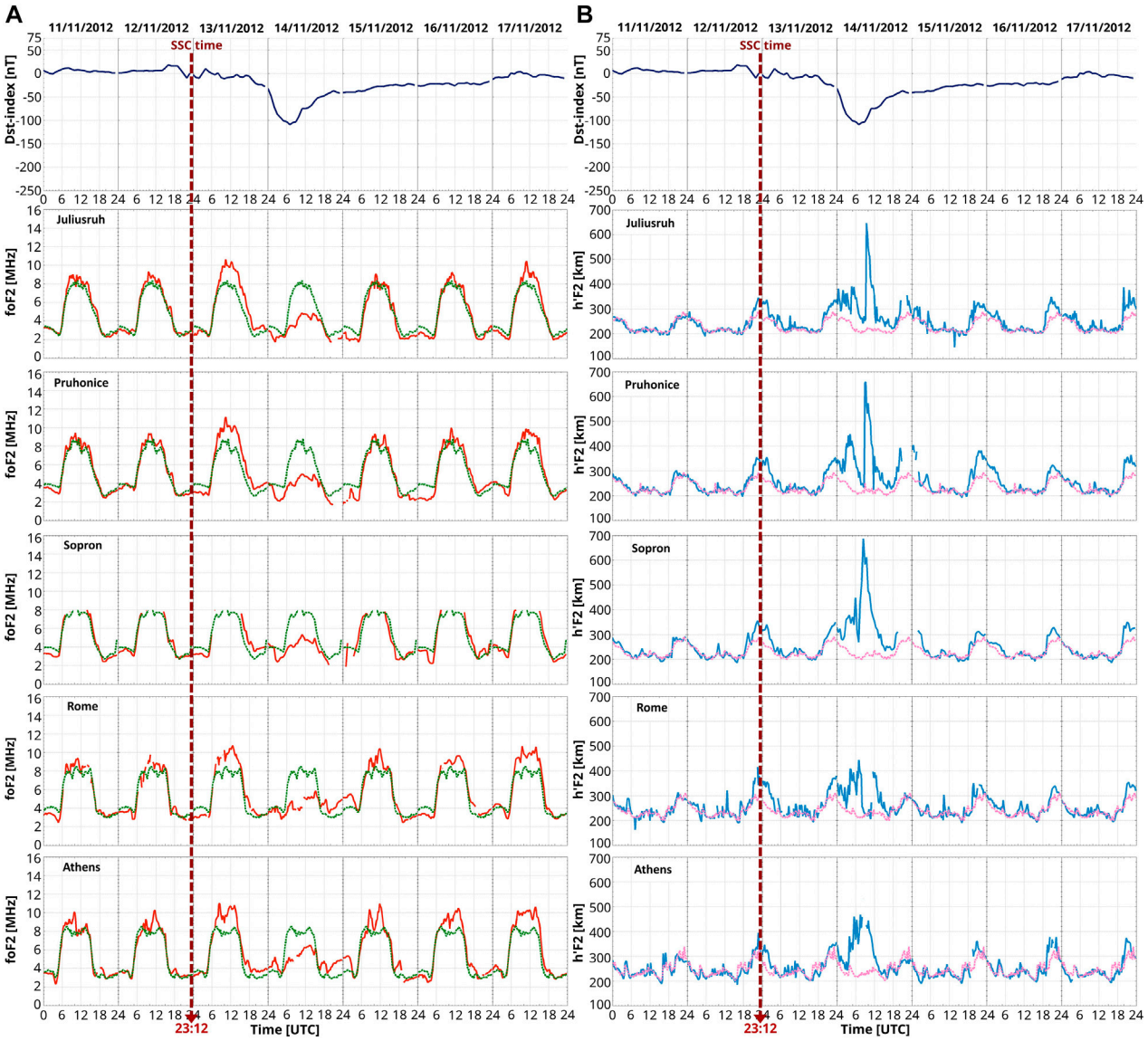

FIGURE 3
On the upper diagrams the Dst-index values and on the lower diagrams the storm-time foF2 (with red line, A)) and h'F2 (with light blue line, B)) with the reference foF2, h'F2 values of selected 3 quiet days [with dotted green **(A)** and pink line **(B)**] are portrayed for storm 2012 over the meridional station chain.

disturbance which is connected to a HSSWS (see Figure 1B) started at 20:54 UT on 21 March, which does not appear in the value of the Dst index, but is clearly visible in the Kp and AE index (see Figure 1B) (Nava et al., 2016). Several articles have been published in recent years about this storm, also known as St. Patrick's Day storm, which is the largest storm of the solar cycle 24 (e.g., Astafyeva et al., 2015; Cherniak and Zakharenkova, 2015; Zhang J.J. et al., 2015; Zhang S.R. et al., 2015; Li et al., 2016; Wu et al., 2016; Nayak et al., 2016; Nava et al., 2016; Kalita et al., 2016; Tulasi et al., 2016; Hairston et al., 2016; Jin et al., 2017; Polekh et al., 2017; Zhang S.R. et al., 2017a; Zhang S.R. et al., 2017b and references therein; Berényi et al., 2018; Huang et al., 2018; Habarulema et al., 2018; Kumar and Kumar, 2019; Ratovsky et al., 2019; Lu et al., 2020).

3.1 Digisonde data over Europe

The main results presented in the following were derived from ionosonde and digisonde measurements across a meridional station chain introduced in Section 2. In this section, the evolution of the ionospheric foF2, h'F2 is shown. Using data of European ionosonde stations for comparison, our primary goal is to check whether the ionosonde recorded effects at Sopron station (Berényi et al., 2018) were local or regional/global. Furthermore, we would like to illustrate how an ionospheric storm develops from North to South, along a geomagnetic meridian. Through this demonstration, the turning point of the ionospheric phase development can be determined (see Buonsanto, 1999; Kane, 2005). In a general case, over the auroral region a negative

ionospheric storm phase can be observed, while over lower latitudes (closer to the equator) this turns into a positive phase (the exact latitude of the phase reversal depends e.g., on the season, LT, the strength of the geomagnetic storm, meridional winds, etc.). First, we present ionosonde observations for the extended 2012 and 2015 storm periods.

3.1.1 Geomagnetic storm 11-17/11/2012

The first phenomenon known from previous studies, which can appear in foF2 even 24 h before the SSC during the daytime hours, is called the pre-storm enhancement (Kane, 2005; Burešová and Laštovička, 2007; Danilov, 2013). This can be also observed in all the 5 digisonde stations, though it is not very well pronounced (see Figure 3). On the contrary, during the night on 11/12 November all station data show negative phase, except for AT where no change can be detected.

On the right panel of Figure 3, the virtual height of the F2-layer (h'F2) is presented, not any significant daytime change at any station can be seen on 12 November, however a quite significant increase can be observed during the night starting at 21:00 UT, just before the SSC.

Right after the SSC at 23:12 UT, an increase in electron density (foF2 parameter) can be seen during that night and then during the day on 13 November at all stations. This is the main phase of the ionospheric storm, but the geomagnetic storm main phase starts only later on the following day. At the beginning of the following night, still positive phase at all stations can be seen, but around midnight it turns negative at JR, PQ and SO. Besides, a significant increase in h'F2 appears already around 20:00 UT which lasts even throughout the next day (14 November).

During the daytime hours in the main phase of the geomagnetic storm (14 November) a negative ionospheric storm phase was observed at all stations. In the meantime, the F2 layer was extremely uplifted, up to 680 km at stations SO, PQ and JR (Figure 3, right panel). In this case, we observe a negative ionospheric storm phase during a relatively weak (i.e., closer to moderate) geomagnetic storm. This event can be considered as an atypical storm, since the main phase of the geomagnetic storm is delayed by 1 day. In a regular storm, the main phase typically starts with a significant positive or negative ionospheric storm phase within a few hours after the SSC.

Note. during this storm the ionosonde at Sopron provided observations only up to 8 MHz, but the negative ionospheric response during the main phase of the geomagnetic storm clearly shows up.

This storm can be identified as a Regular Positive Phase (RPP) storm type following the nomenclature introduced by Mendillo and Narvaez (2010) according to the meridional evolution of foF2. Their classification is based on the local time of the SSC, which was in this case around midnight (00:12 LT) on 13 November The significant increase of foF2 (electron density) lasted from around 10–11:00 to 20:00 LT at all stations, and this positive phase was followed by a negative phase on 14 November.

In Figure 3 during the main phase of the geomagnetic storm at night hours (18:00–02:30 UT), a negative ionospheric storm phase can be observed at the SO, PQ and JR stations. The electron density decreased below the detectability level (disappeared from the ionograms) at these stations. Along with this electron density drop, the virtual height of the F2-layer increased up to 400 km (from the 250–280 km QD value) before the observed fade-out (see Figures 1, 3, as well as the Supplementary Table S1). On the contrary, at RO and AT stations, a significant increase of the foF2 parameter (electron density) with respect to the reference days could be seen during the night. Furthermore, the h'F2 was not as increased at RO and AT during this period as at the other stations. In Supplementary Table S1 the exact time and duration of the fade-outs, the start time of the decrease/increase and the minimum/maximum values are tabulated (the foF2 value in MHz).

From 15 November, during the early recovery phase, a so-called early recovery phase enhancement effect was detected in foF2 at stations AT, RO, SO and PQ (see Figure 3). This effect with increased electron density around noon lasts 3-day long, most significantly at Rome and Athens station, but observable at the other stations, too (see Figure 3). On the other hand, during the nighttime hours of 15 November a negative phase appears at all stations, while on 16 November only JR and PQ are negative, SO does not show any clear trend, and RO and AT are positive.

During the recovery phase, no deviation from the reference quiet time h'F2 was seen during daytime, however there was a quite significant increase during the night, first of all at the PQ station, but less pronounced also at SO and JR.

3.1.2 Geomagnetic storm 16-25/03/2015

The evolution of the 2015 March geomagnetic storm started on day 17th. The local time of the SSC was at 05:45 on 17 March (these are marked with a red dotted line in Figure 4). After the SSC, during the main phase of the ionospheric and geomagnetic storm, a positive phase of the ionospheric storm started at all stations. These kinds of storms are called Regular Positive Phase (RPP) storms because in the main phase of the storm, the electron density (foF2) increases, with no delay (Mendillo and Narvaez, 2010). At the same time, there is also a significant increase in height of F2-layer (h'F2) during daylight hours at all stations, but much less pronounced at RO and AT (see the right panel of Figure 4).

The most significant increase in the virtual height of the F2-layer occurred from around 20:00 UT (21 LT) on 17 March. The highest peak of the h'F2 parameter was observed at Pruhonice at 587.6 km at 22:45 UT. This main phase pattern in h'F2 parameter lasts until 21 March, and appears significant at SO, PQ and JR stations (see Figure 4).

Besides, during the evening/night on 17/18 March, a sharp decrease in the electron density was observed, the start of the negative phase began at noon at JR and it occurred later and later with decreasing latitude. The depletion was the most pronounced at PQ, SO and RO (see Figure 4 and Supplementary Table S2). The electron density decreased below the detectability level (disappeared from the ionograms) for a short period at RO and SO station. In Supplementary Table S2 the exact time and duration of the fade-outs, the start time of the negative phase and the time of the observed minimum value are tabulated. Along with this electron density drop, the virtual height of the F2-layer increased up to 483 km (from the 250–280 km QD value) before the fade-out at Sopron (see Figure 4).

Depletions in the foF2 parameter value (negative phase) compared to the main phase value can be observed on the next

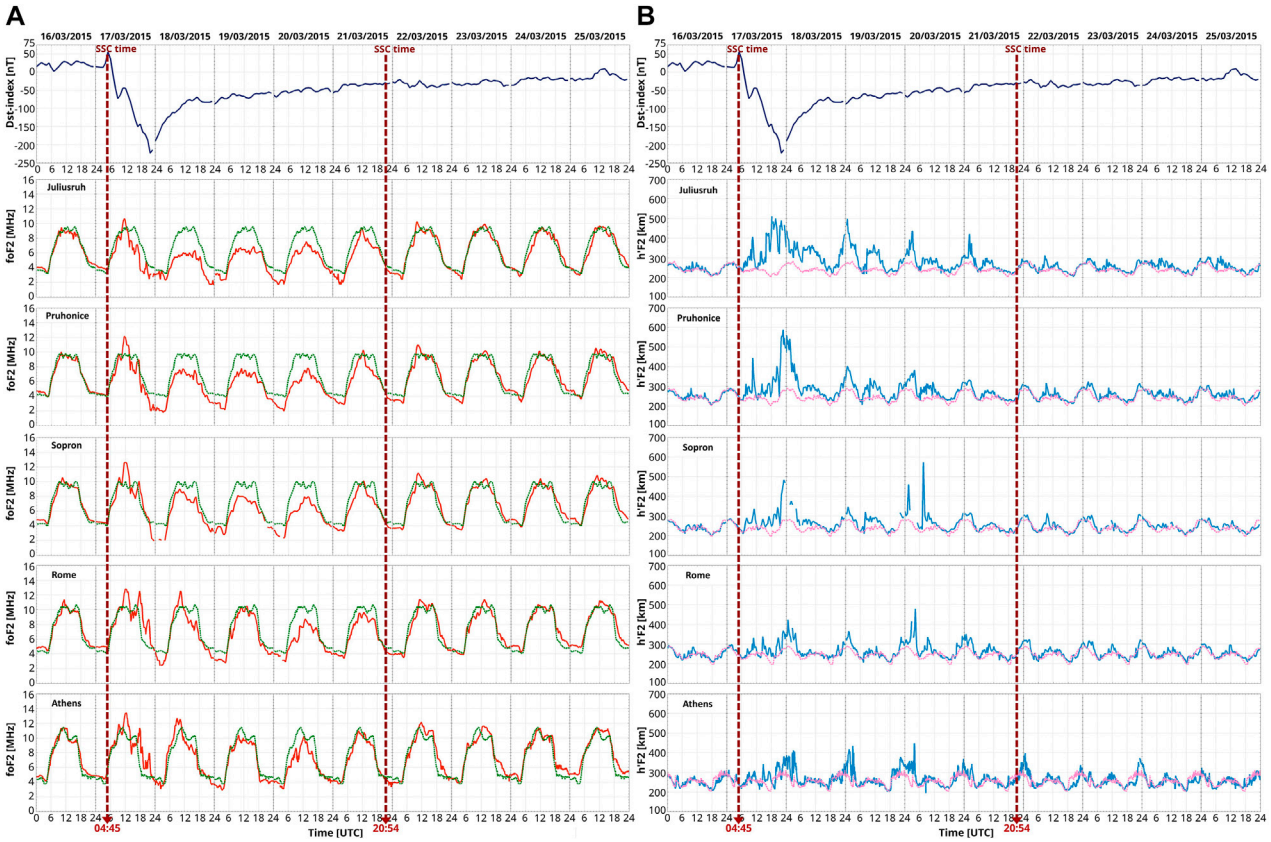

FIGURE 4
In the upper diagrams the Dst index values and in the other diagrams **(A)** the storm-time foF2 (red line) and **(B)** the storm-time h'F2 (light blue line) and the corresponding reference foF2 and h'F2 values (green **(A)** and pink **(B)**, respectively) are portrayed for the 2015 storm along the meridional chain.

days (during the early recovery phase) at SO, PQ and JR stations (middle - and high midlatitude), during both days and nights. Even at AT and RO, for a short period positive phase occurred around 9 UT, then it is turned into a significant negative phase around 11 UT. At RO and AT stations (low mid-latitude) the depletion became really significant (see Figure 4) only on 20 March. It can be stated that in the early recovery phase the low mid-latitude and the high mid-latitude regions behave differently.

A subsequent geomagnetic disturbance, associated with a HSSWS (see Figures 1, 4) started at 20:54 UT on 21 March, occurred during the recovery phase of the first storm and generated a positive ionospheric storm. Decreased electron density during the daytime and nighttime of 21th can be observed at all stations, but most significantly at RO. In the h'F2 parameter just a slight increase can be seen right after the SSC during the night, mostly at AT and RO stations. Meanwhile on 22 March no change was observed at JR, and only a slight increase in foF2 at PQ, SO, RO, AT. During the night the storm turns negative at all stations, except for RO and AT, where no change was observed.

During the remaining days in the recovery phase: on 23 March no changes at JR and PQ were detected, but a slight increase in foF2 at SO, RO, AT can be seen around noon. During the night just JR showed no changes, the others were positive. On 24 March no changes were observed in foF2 at all stations during the day, but at night just JR did not show changes, the other stations had positive phase. On 25 March the situation was the same as on day 23. The h'F2 parameter did not show any deviation from the QD curve during these days.

3.2 GNSS TEC data

To provide a wider context for the ionosonde observations, changes in the total electron content (TEC) data was compared with the foF2 values measured by the ionosondes. TEC data are presented similarly to Figures 3, 4 for a better comparison. The TEC represents the total electron content as an integrated value between the receiver on the ground and the GNSS satellite (MEO orbit, at around 20,000 km altitude), therefore it contains not just the whole ionosphere, but also most of the plasmasphere (Hofmann-Wellenhof and Lichtenegger, 2001).

In Figure 5 the TEC values (red) along with their corresponding references (green) for the 2012 November storm are plotted. Before the SSC time, on 11 and 12 November a small positive deviation can be seen during the day at all stations, while during the night on 11 November no significant deviation was observed. On the following night (12 November) a slight negative phase appeared at RO, SO and PQ. On 13 November, the day after the SSC, very impressive positive ionospheric storm phase developed at all stations during both day and night. In the main phase of the geomagnetic

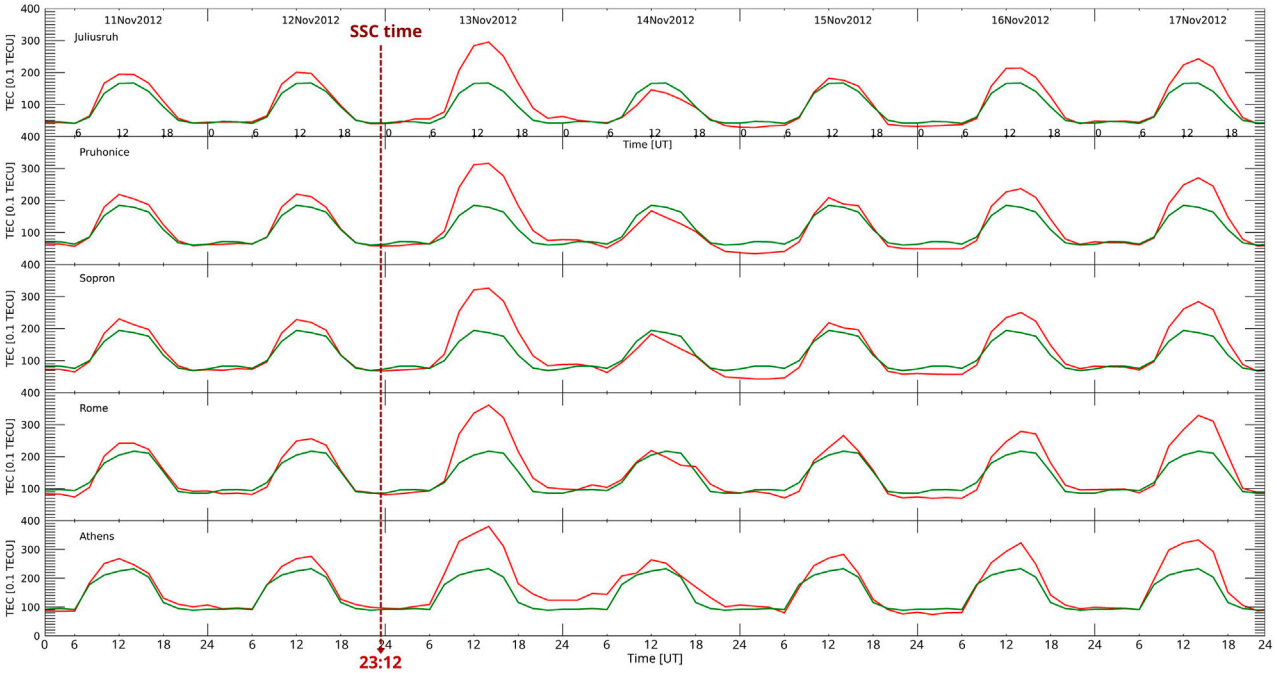

FIGURE 5
The meridional evolution of the storm-time GNSS TEC (with red line) with the reference TEC derived from selected 3 quiet days (with green line) are portrayed for storm 2012. SSC time is marked with a red dashed line.

storm (14 November) all stations turned negative except for RO, where there until 12 UT the TEC variation followed the mean variation. Later a slight decrease started and lasted until 18 UT. Also AT behaved differently, because here a TEC enhancement took place during the whole day. In the recovery phase (15–17 November) during the day positive phase was detected. On the contrary, during the nighttime hours on 15 November negative phase, and on 16 November no change was observed at all stations.

In Figure 6 the 2015 March storm can be seen in the TEC data. On the pre-storm day and night (16 March) no deviation from the reference values can be seen at any stations. In the main phase of the storm (17 March) significant positive phase is detected during the day at all stations, but during the night the storm phase is turned negative at all stations, except at JR where first a positive phase and then after midnight no deviation can be seen. During the early recovery phase between 18 and 20 March, a negative effect in TEC is detected during both day and night at all stations. Interestingly at RO and AT on 18 March between around 06–12 UT the TEC is increased with respect to the QD value, then rapidly decreases and stays decreased during the following 3 days. On 21 March the same effect was repeated during the day, but at night JR station showed no deviation, while all the other station data was negative. On 22 March (the day after the 2nd SSC) a positive ionospheric storm phase appeared in TEC during the day at all stations, but during the nighttime hours there was no effect. Between 23 and 25 March a slight positive phase can be seen during the day and night at all stations, except at JR where there is no effect during the night of 23 March.

The more specific connections are explained in the Discussion Section 4 below.

3.2.1 rTEC maps of the storms

In Figure 7 the Ratio of the TEC difference (rTEC) maps are shown for (geomagnetic) main phase of the two storms during the nighttime hours (18–04:00 UT). These maps show the relative deviation of TEC from its QD value (10 quietest days of the month). These rTEC maps clearly present the evolution of the nighttime negative phase along the examined stations in Europe.

In the case of the 2012 storm as shown in Figure 7A, the reduced electron density region moves from higher to lower latitudes, reaching its minimum latitude around midnight near the Athens-Rome line. Meanwhile, it is also nicely seen that the low-midlatitude Athens-Rome region remains in a positive phase throughout the night. In the 00:00 and 02:00 UT maps the depleted electron density zone is nicely drawn out in blue, and it can be seen that JR, PQ, SO stations are all located within it.

For the 2015 storm, a very strong positive phase (red color in Figure 7B) is visible at 18 UT on 17 March spreading in a NW-SE direction, its boundary shows up in yellow along the line connecting the Black See and North-France (see Figure 7B). SO, PQ to the North is green, indicating that there is no deviation from the expected value, while JR is in negative phase. Interestingly, there is a narrow but strong positive-phase region at high latitudes (over Scandinavia). As we move into the night, at 22:00 UT the negative phase moves towards the equator and the positive phase region also decreases in strength in the Athens-Rome line. At 00:00, the depleted plasma has gone even lower, and this is when both Rome and Athens go into negative phase at night, so the low mid-latitude region is also under the influence of this negative storm effect, which lasts until 04:00 UT.

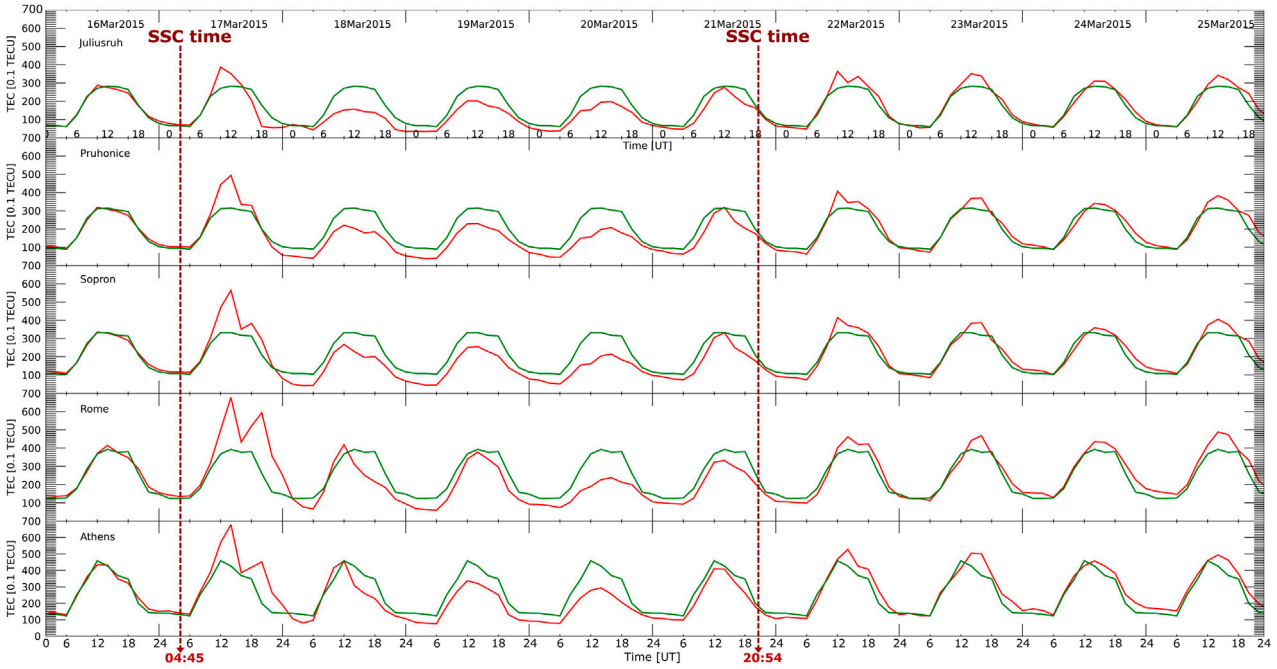

FIGURE 6
The meridional evolution of the storm-time GNSS TEC (with red line) with the reference TEC of selected 3 quiet days (with green line) are portrayed for storm 2015. SSC time is marked with red dashed line.

3.3 GUVI measurements

The TIMED satellite GUVI measurements were used to examine the variation of the daytime thermospheric O/N_2 composition during the evolution of the considered ionospheric storms. In Figures 8, 9 the three QDs as a reference are shown (Figure 8A; Figure 9A) and also 3 days from the storm (Figure 8B; Figure 9B) to present the main features. The whole storm intervals are plotted in Supplementary Figure S2 and Supplementary Figure S3 (note that time runs from right to left).

For the 2012 November storm the GUVI data presented in Figure 8 do not show any deviation in the O/N_2 ratio from the QD level over the examined stations during the daytime hours in the pre-storm phase (12 November). On 13 November (the day after the SSC) around noon (in LT) a slight increase in the O/N_2 (yellow) can be seen over Europe. In the main phase (when the Dst minimum value occurred), on 14 November around 12 LT, a significant decrease (blue) in the GUVI measured O/N_2 ratio can be observed all over Europe. On 15 November there is no deviation (green), but on 16 and 17 November a slight increase appears in GUVI data marked with yellow (see Supplementary Figure S2).

St. Patrick's Day storm 2015 (Figure 9): during the pre-storm phase was on 16 March, the O/N_2 ratio shows a decrease (blue) in the subauroral region, e.g., over JR station. After the SSC, during the main phase of the geomagnetic and ionospheric storm, on 17 March in the daytime GUVI data do not show any significant departure from the reference values.

On the contrary, during the following day, on 18 March, a quite deep depletion was observed in the O/N_2 ratio at JR, PQ and SO, but most significantly over the JR station. This effect also happens on the two following days just the same way, with one difference. On 20 March a slight depletion (light blue) showed up also at RO and AT stations (see Supplementary Figure S3). On 21 March, when the second SSC happened, another slight decrease follows in the GUVI data over JR, PQ, SO. During the next day, on 22 March, right over the JR station a slight decrease can be observed. On 23–25 March SO, PQ and JR stations are in the slightly depleted O/N_2 region (light blue) during the day.

3.4 Swarm satellite measurements

While ground ionosondes are good at monitoring the temporal variation of ionospheric parameters at fixed locations, LEO observations can provide pole-to-pole latitudinal profiles of the considered parameters recorded during around 45 min. The location of the plasmapause (PP), more precisely the location of ionospheric phenomena conjugated with PP, such as the MIT can also be monitored by LEO satellites (e.g., Heilig and Lühr, 2013; 2018; Heilig et al., 2022). Swarm observations are only available for the 2015 storm event. Figure 10 shows the change in the topside electron density (top panel) for three orbits of Swarm B, each separated by 9.5 h (in UT). All measurements were taken at around 21 h MLT but along different meridians. Thus this plot represents primarily the temporal evolution of the topside electron density at 21 h MLT, but the profiles are also influenced by longitudinal effects.

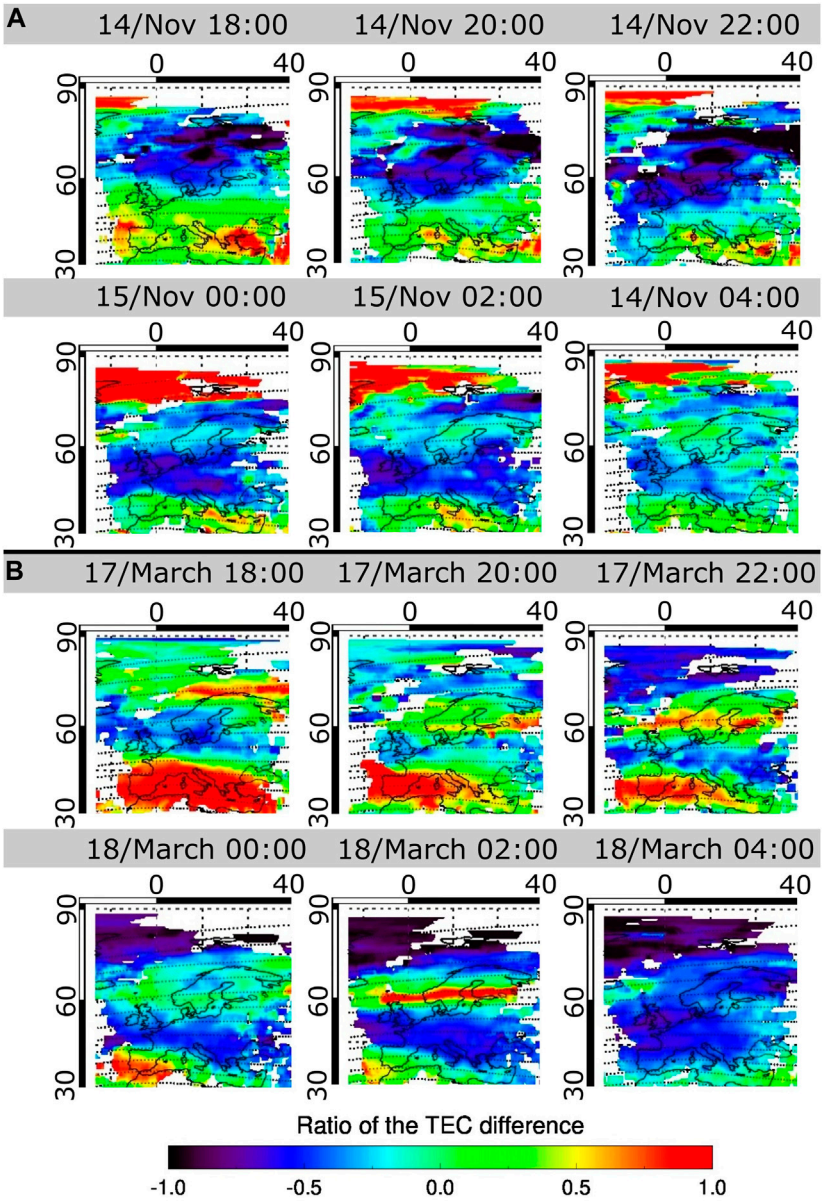

FIGURE 7
The rTEC values are plotted for the nighttime hours (18:00–04:00 UT) on 14 November, 2012 **(A)**, and on 17 March, 2015 **(B)**.

A deepening density minima (marked by vertical dashed lines on the Northern Hemisphere) can be observed in both hemispheres, moving progressively equatorward as the geomagnetic storm main phase develops. These are the minima of the MIT that is typically well observed in the nighttime ionosphere during equinoxes. Poleward of MIT, the erosion by the increased ExB drift continued along the whole day, while at lower latitudes at the altitude of Swarm B (505–525 km) a general increase was observed. The presented profiles were all taken following the SSC (04:45 UT). The latest profile corresponds to the time of the maximum of the plasmasphere erosion (most equatorward MIT).

Sharp MIT minima are accompanied by an enhanced electron temperature (bottom panel). This is a well-known feature of sub-auroral dynamics and appears mainly as a result of frictional heating by the intense westward drift that in turn are driven by an intense substorm (precipitation) associated poleward electric field (e.g., Heilig et al., 2022).

MIT minimum in this MLT sector is tightly coupled to the footprint of the plasmapause (Heilig et al., 2022). Thus the equatorward movement of MIT reflects the shrinking of the plasmasphere due to the increased magnetospheric convection and intensified substorm-related sub-auroral electric field (see also in Supplementary Figure S4).

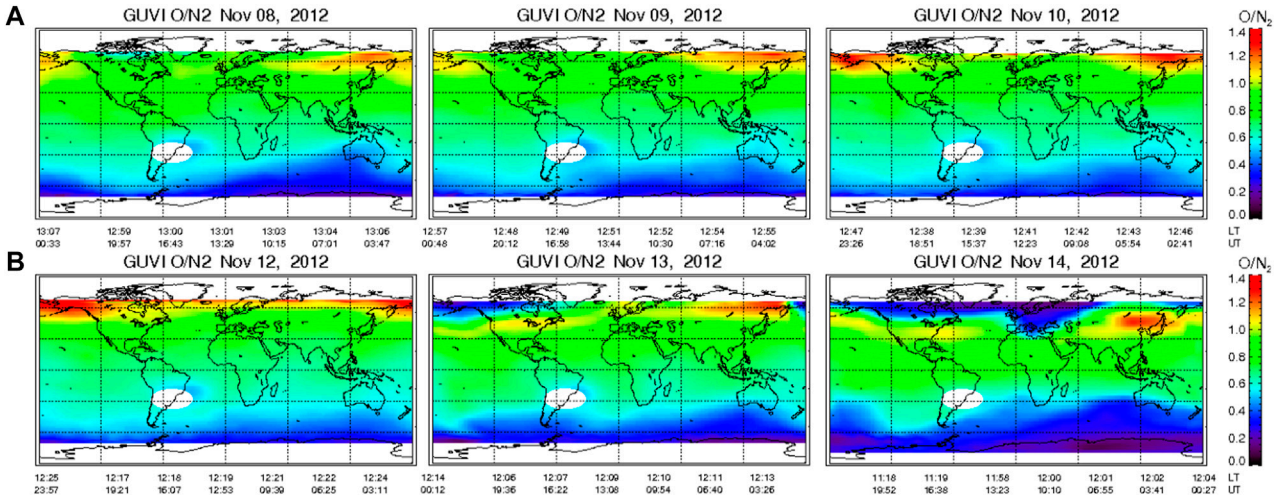

FIGURE 8
The GUVI measured O/N_2 ratio for the 2012 November storm. In the upper plot **(A)** reference data for 3 quiet days are shown; in the lower plots **(B)** data of 3 selected days from the storm interval are presented, namely, the day of SSC (12 November), the main phase of the ionospheric storm (13 November), and the main phase of the geomagnetic storm (14 November) (Note: a plot of GUVI data for the whole storm can be found in Supplementary Figure S1).

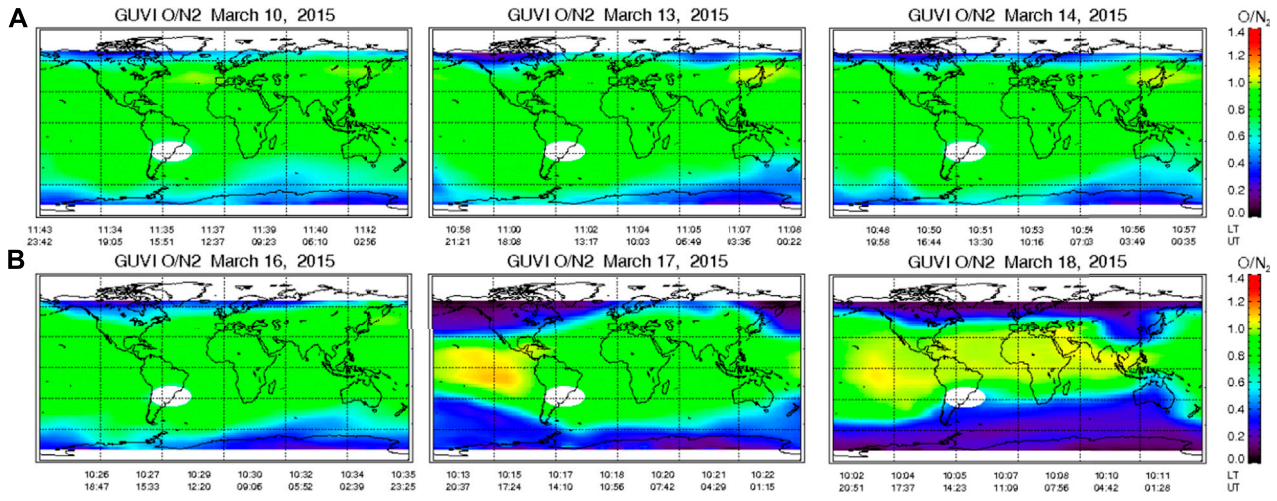

FIGURE 9
The GUVI measured O/N_2 ratio for the 2015 March storm. In the upper plot **(A)** reference data for 3 quiet days are shown; in the lower plots **(B)** data of 3 selected days from the storm interval are presented, namely, the day of pre-storm phase (16 March), the main phase of the ionospheric and geomagnetic storm (17 March), and 1 day from the recovery phase (18 March) (Note: a plot of GUVI data for the whole storm can be found in Supplementary Figure S2).

The time evolution of the MIT minimum position based on Swarm *in-situ* observations made on the Northern Hemisphere is presented in Figure 11. The two colors depict observations of Swarm B and C satellites. Right after the SSC, MIT started to shift equatorward. This decrease lasted the whole day, and by the end of the day MIT approached 45° magnetic latitude. The lowest latitude of the MIT position actually observed (by Swarm B) was 46.3°. This observation took place on 18 March at 00:15 UT (21.9 h MLT) at −43.2° longitude.

As shown in the lower panel, the MLT difference between Swarm B (red) and C (blue) observations was fairly stable, around 1.5 h on the average. The MIT position is well-known to have a strong MLT dependence (e.g., Heilig et al., 2022). The MIT latitude decreases during afternoon and also during nighttime until 4–6 h MLT. Here this dependence is reflected in the latitude difference between Swarm B and C observations, Swarm B observations are consequently equatorward of Swarm C observations by 2.3° on the average.

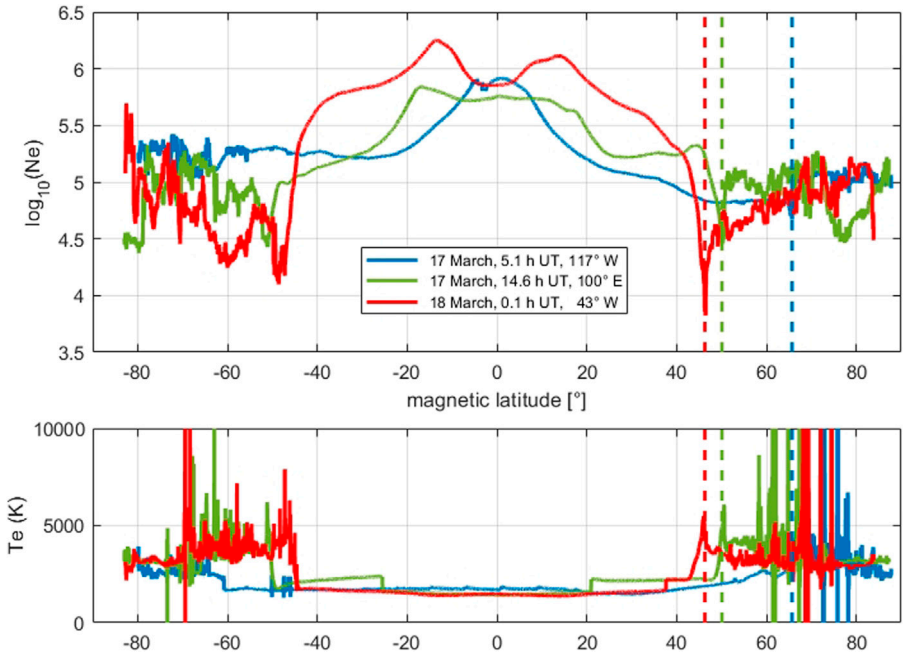

FIGURE 10
Meridional profiles of the topside electron density (top panel) and electron temperature (bottom panel) observed by Swarm B on 17 and 18 March, 2015. Vertical dashed lines indicate the location of MIT on the Northern hemisphere.

At the time of the minimum observation, MLT at Sopron was 0.72 h. Estimating from the MLT difference between Sopron and Swarm B (1.1 h) and the rate of decrease (2.3°/1.5 h = 1.53°/h), the MIT minimum at 0.72 h MLT was located around 45.6°. The formula (their Equation 4) of Deminov and Shubin (2018) for the MLT dependence yields a somewhat higher MIT latitude (45.9°). However, these values are already lower than the latitude of Pruhonice and very close to that of Sopron.

The MIT position is also known to depend on the geographic longitude (e.g., Heilig et al., 2022). In the American sector MIT appears a few degrees higher than in the European or Asian sector. The Equation 5 of Deminov and Shubin (2018) estimates this difference to 0.98°, while according to the statistical results of Karpachev et al. (2019), this difference could easily be 2°–3°. Using these adjustments the MIT at Sopron could have moved down as low as to magnetic latitude 44.6°, maybe even below 42°.

The width of the most equatorward MIT was 3.6° as observed by Swarm B. This width is shared between the equatorward wall (1.9°) and the poleward wall (1.7°). This means that on 17 March during the night MIT (but at least its equatorward wall) should have reached the Sopron station. Thus, the Sopron ionosonde observed the depleted plasma associated with the MIT structure. It is also clear that the MIT could not approach Athens, located at 36.1° magnetic latitude.

3.5 Digisonde drift measurements

Digisonde drift measurements from Pruhonice station were analyzed manually in order to determine the true horizontal and vertical motion of the F-layer during the two storm intervals. For the detailed analysis method of the manual correction see the Supplementary section. Now we are going to detail the phenomena found in the manual drift data for each storm separately.

The first significant manifestations of the 2012 November storm event can be seen on the drifts in the night from 13 to 14 November (Figure 12A). On 13 November around 20:30 UT a pronounced episode of westward drift begins. Roughly until 14 November 10:00 UT we observe dominantly horizontal westward drifts. The speed of the observed drifts is significantly higher than the horizontal speeds observed under quiet conditions (<100 m/s, according to Kouba and Koucka Knizova, 2012). The detected maximum speeds exceed even 350 m/s.

The quality of the skymap is very good and corresponds to the assumption of one drift velocity vector in the area above the station. Estimated vectors are determined reliably.

On 14 November around 00:00 UT, a significantly increased value of the vertical drift velocity component (to the tens of m/s) and its very rapid changes is added to the above-described effect. The drift measurement cadence was 15 min. The dramatic changes are visible in every consequent measurement, it is obvious that the period of the vertical drift velocity variation is significantly smaller than 15 min and cannot be studied (described) in more detail due to the limitations of the drift measurements.

During the day-time on 14 November both described manifestations practically disappeared. The value of the vertical velocity component no longer fluctuates quickly, and the value of the horizontal (westward) component drops to small values. Here it is necessary to note that the quality of measured skymaps during the

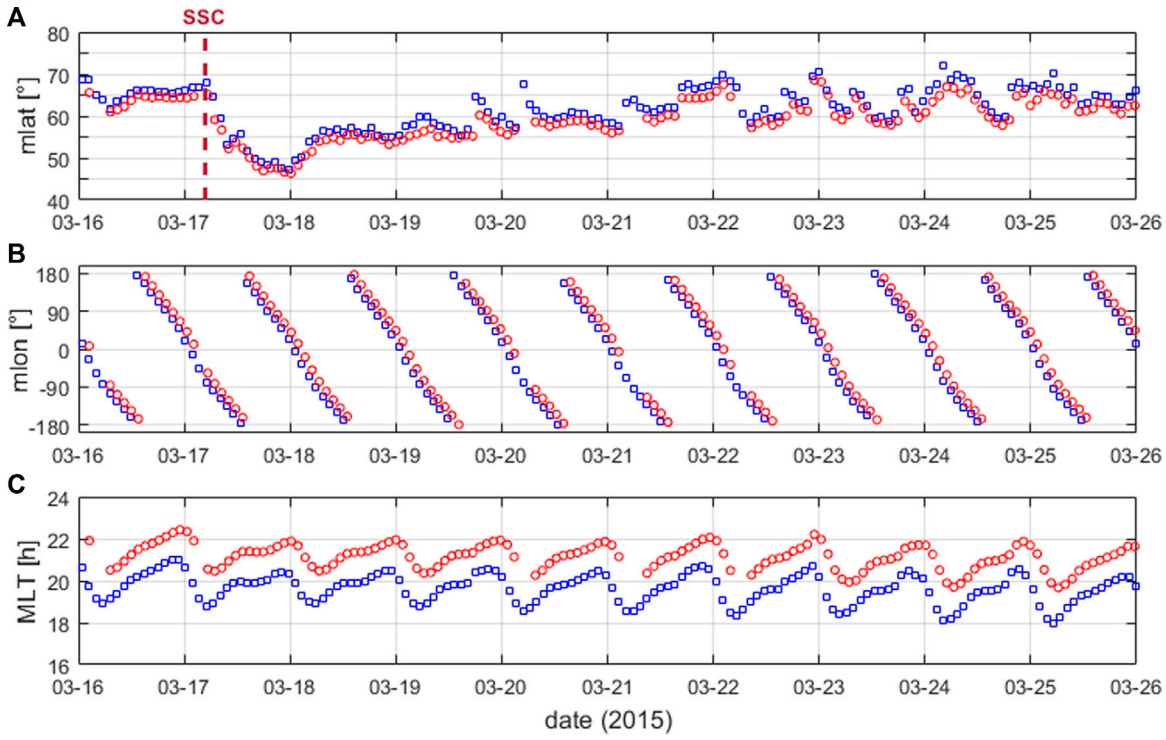

FIGURE 11
Evolution of the MIT minimum position (quasi dipole magnetic latitude) on the course of the 2015 event **(A)**; magnetic longitude **(B)** and MLT **(C)** of the *in-situ* Swarm observations. Red and blue colors depict Swarm B and C observations, respectively.

day-time is significantly lower than during the night-time. Therefore, information about the value of westward drift should be taken with a large margin. In most cases, the daytime skymap quality is not sufficient to determine the horizontal drift components with good reliability.

The second significant episode is observed during the night of 14/15 November This episode has similar characteristics, again between approx. 21:00 UT and 03:00 UT there is increased activity of the vertical component – larger values and rapid variations. In the horizontal components, a significant increase in the westward component can be seen again in the time interval between 23:00 – 08:00 UT. In this episode, the maximal measured values of the westward component exceed 250 m/s. It can be seen that the observed manifestations in the case of the second episode are smaller than in the case of the first.

In the drift measurements of 2015 March storm (Figure 12B), the first significant manifestations of the storm are observed on 17 March around 20:00 UT. The measurements show very quick variations of all observed parameters. The variations are significantly faster than the cadence of measurements and therefore the fluctuation period cannot be resolved. The value of the vertical drift velocity component exceeds the extreme values of +/- 50 m/s.

Unfortunately, in this phase of the storm, the actual extreme ionospheric situation (the values of foF2 and h'F2) does not allow successful realization of drift measurement in most cases. Between 22:00 UT and 01:00 UT successful measurements are rare.

During day-time 18 March no significant manifestations of the storm are observed in the drift measurements.

The next episode is coming at night 18/19 March. Rapid changes occur in the vertical component between 23:00 UT and 06:00 UT, and the amplitude of the vertical drift is significantly greater than values under normal conditions. In the horizontal component, we observe a pronounced westward peak between about 18:00 UT and 06:00 UT. The maximum detected values significantly exceed 200 m/s.

The last significant episode is observed the following night. On 20 March at around 00:00 – 04:00 UT the features described for the previous episode are repeated. It is interesting that this episode is significantly shorter than the previous one (roughly half) but the manifestations are more pronounced (on both the westward and the vertical components).

Drift activity affected by the storm is apparently observable also the following night (21 March, approx. 00:00 – 05:00 UT) on the westward component. The maximum detected velocity value is close to 200 m/s. In this case, however, the insufficient number of high-quality measurements does not allow proving a clear connection to the storm.

4 Discussion

In this section, we attempt to define the cause-effect relationships in order to gain a more detailed understanding of the response of the terrestrial ionosphere-plasmasphere system to geomagnetic storms. Our main focus was on the main phase of the geomagnetic storm, when during the night extremely depleted

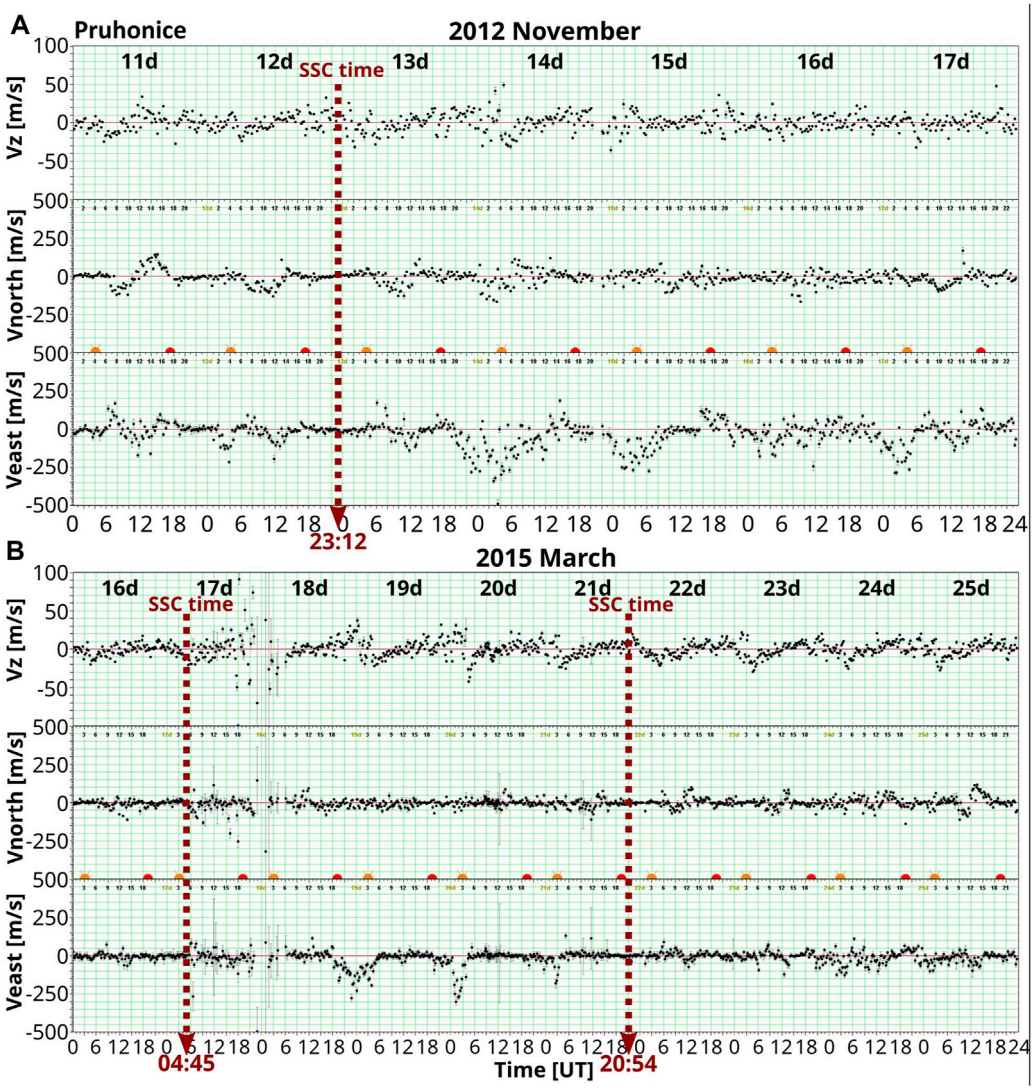

FIGURE 12
The manually corrected digisonde drift measurement of F-region for the 2012 November **(A)** and 2015 March **(B)** storm at Pruhonice station.

plasma was detected. Case studies are still important to shed light on deeper relationships that cannot be easily extracted from multi-event-based statistical investigations.

4.1 Pre-storm phase

In the pre-storm phase of the 2012 storm (11–12 November - Dst_{min} = 0 nT; Kp_{max} = 1,33; AE_{max} = 134 nT) foF2 and TEC show a slight positive deviation at all stations, while by the 2015 storm (16 March - Dst_{min} = 0 nT; Kp_{max} = 3,77; AE_{max} = 300 nT) no deviation from the reference value is detected. However, the O/N_2 data for this storm shows a decrease in the subauroral region already in this phase (16 March). Earlier studies (e.g., Kane, 1973a; Araujo-Pradere and Fuller-Rowell, 2002; Kane, 2005; Burešová and Laštovička, 2007) found a pre-storm feature (positive effect) in foF2 24 h before the SSC, however other authors doubt its presence (Mikhailov and Perrone, 2009). Burešová and Laštovička (2007) examined 65 strong geomagnetic storms from the period of 1995–2005 and found that about 20%–25% of the storms had a significantly strong pre-storm effect. Similarly to the finding of Liu et al. (2008), we found a slight pre-storm enhancement in both TEC and foF2 in the 2012 storm case. Other authors suggested that this effect could be related to some different channel of penetration of the energy from the interplanetary environment and magnetosphere to the ionosphere (Danilov and Belik, 1991; 1992; Blagoveshchensky and Kalishin, 2009), but this needs verification.

4.2 The main phase of ionospheric and geomagnetic storm

On the day right after the SSC (on 13 November 2012 - Dst_{min} = −29nT; Kp_{max} = 4,77; AE_{max} = 674 nT and on

17 March, 2015 - Dst_{min} = −234nT; Kp_{max} = 7,7; AE_{max} = 1570 nT) we observed a positive ionospheric storm phase at all station in both foF2 and TEC in both storms. This behavior is consistent with the average winter ionospheric response (in foF2 and TEC) to geomagnetic storms observed in previous studies (e.g., Matsuhita, 1959; Prölss, 1995; Buonsanto, 1999; Mendillo, 2006; Danilov, 2013). Astafyeva et al. (2015) examined the St. Patrick's Day storm's main phase (17–18 March) globally with multi-instrument measurements (e.g., Swarm VTEC, GUVI, GNSS TEC), and they found that the daytime positive phase during the day of 17 March at lower latitudes was due to increased O/N_2 ratio. This finding was also investigated and supported by Nayak et al. (2016); Kalita et al. (2016). The AE-index mostly exceeded 500 nT and increased often up to 1,500 nT during the day, which indicates the possibility of intense Joule heating of the thermosphere, which can cause positive storm phase by two ways: 1) the uplift of the layer through enhanced meridional winds, and then lift the ionization to greater heights (Prölss and Zahn, 1974). 2) the downwelling of atomic [O] causing the increase of O/N_2 ratio (see also in Introduction). Nava et al. (2016); Polekh et al. (2017) found also that the positive ionospheric effects at middle and low latitudes are related to different inputs of energy (as we see in AE-index; Figure 1B), and as they described the high latitude heating of the thermosphere travelled toward the equator with the velocity of 460 m/s during 17 March (along 120°E, see Polekh et al., 2017). Besides, Zhang S.R. et al. (2017a) found PPEF signatures on dayside over American sector, appearing as poleward/upward ion drift, and the observations showed meridional wind equatorward surges during also daytime hours. The upward ion drift could also contribute to the daytime positive phase (Zhang S.R. et al., 2017a). The diurnal evolution of the positive phase was different, dual peak can be seen at all stations. The first peak was at noon with maximum half hour delay, the second was around 18 h (UT). The second peak was observed (station-hour): JR-17 h, PQ and SO-17:30, RO and AT-18 h (UT). This could connected to the propagation of storm-induced electric field from north to south (e.g., PPEFs). After Kumar and Kumar (2022), eastward/westward PPEFs are associated with the southward/northward IMF Bz. The southward turnings of the IMF Bz component (induce eastward PPEF) can cause electron density increase during the daytime hours (Kumar and Kumar, 2022). There were two significant southward Bz episodes: around 8 and 14 (UT) during this time, which could support the above detailed assumption, but this needs verification.

For the 2012 November storm, the GUVI data show a slight increase in the O/N_2 over Europe on 13 November around LT noon (Figure 8), which could contribute to the positive phase in foF2 (Figure 3). There was a second peak (after the SSC) in AE-index with ~600 nT, which here indicates also the Joule-heating of the thermosphere. The generated processes here also could contribute to the positive phase similarly to 2015 storm by two ways. Unfortunately, there is no digisonde drift episode, which could strengthen the presence of uplifting of the layer or the enhanced equatorward meridional winds. This assumption needs verification also with Horizontal Wind Model 2007 (HWM07, Huang et al., 2018). Kumar and Kumar (2022) found that the PPEFs were contributors in the electron density increase during the day of 13 November, 2012. Interestingly, this day is the main phase of the ionospheric storm, and normally it develops on the course of the main phase of the geomagnetic storm, but by the 2012 storm, the geomagnetic storm's main phase was delayed by 1 day.

In the main phase of the geomagnetic storm in 2012 (14 November) during the daytime extremely depleted electron density was observed in foF2 at all stations. A similar decrease was observed also in TEC at all stations but with lower magnitude, except for AT and RO where it turned into negative only after 12 UT (see Figures 3, 5). Kane (2005) also found a deep decrease in electron density over the surrounding stations at midlatitude during the main phase of a similar storm (Dst_{min} = −589 nT). He also found that the magnitude of the Dst is not proportional to the magnitude of the negative effect in the ionosphere at middle and high-latitude. Pirog et al. (2006) strengthened it, where the analyzed geographic latitude range was similar to our case. The decrease of foF2 during the main phase of a geomagnetic storm is a known response of the ionosphere in winter, but usually during intense storms (Dst_{min}<= −100 nT) can reach lower latitudes (Danilov, 2013). According to the GUVI measurements around 12 LT a significant decrease of O/N_2 ratio was observed over Europe by GUVI (marked by blue in Figure 8). Generally, the main cause of a negative ionospheric storm is related to the depletion in the O/N_2 ratio, which is generated by the storm-time Joule-heating of the auroral thermospheric neutral gas leading to the formation of composition disturbance zone (with decreased O/N_2 rate) this zone is transported by the enhanced thermospheric meridional winds (TADs) equatorward (Seaton, 1956; Prölss and von Zahn, 1974; Mikhailov et al., 1989; Mikhailov et al., 1995; Prölss et al., 1995; Bunonsanto, 1999; Astafyeva et al., 2015). The third peak in AE-index with 1,000 nT happened at ~01:00 UT. This energy input could generate also Joule-heating of the thermosphere and this strengthen the possibility of our hypothesis. This is strengthening our earlier assumption that the main reason for the negative phase is due to the decreased O/N_2 ratio transported to lower latitudes (up to Sopron station) by meridional neutral winds (Berényi et al., 2018).

4.3 Deep electron density depletion during the night of 14 November and 17 March

Significantly eroded ionospheric plasma was detected during the nighttime hours in the main phase of the geomagnetic storms (from 18:00 UT on 14 November 2012 and from 20:43 on 17 March 2015) with short duration fade-out of the layers in the ionograms at some stations (detailed in section 3.1). The foF2 and TEC data show a clear negative phase at JR, PQ and SO stations in the 2012 November storm. On the contrary, a strong positive phase mainly in foF2 but slightly also in TEC at AT and RO stations was detected during the whole night of 14 November The rTEC maps of storm 2012 (Figure 7A) show the variation during the nighttime hours (18–4: 00 UT) on 14 November These rTEC maps show clearly how the reduced electron density region moves from the higher latitudes equatorward, reaching its minimum latitude around midnight along the Athens-Rome line. Between 00:00 and 02:00 UT, the depleted electron density region is very nicely drawn out, and it can be seen that JR, PQ and SO stations are fully located within it. In the meantime, the low-midlatitude Athens-Rome region remains in the positive phase throughout the night. Based on our observations and the findings of previous studies like Yizengaw et al. (2005), we can assume, that this nighttime positive phase at AT and RO region, is

caused by plasmasphere-ionosphere coupling due to the enhanced downward ExB drift (leading to a maintaining effect by the plasmasphere), which in the meantime led to a strong erosion of the plasmasphere. For the 2012 storm the drift measurements from PQ during that night shows the presence of a strong westward motion of F-layer plasma (v ~ 350 m/s) indicating the presence of the ionospheric trough (MIT) (see also Heilig et al., 2022). Thus we can conclude based on foF2 and drift data that the equatorward motion of the MIT region (so the PP footprint) was the main cause of the detected sharp electron density decrease in foF2, GNSS TEC and rTEC data during the night of the geomagnetic storm main phase at SO, PQ and JR stations. Another contributor was possibly also the depleted O/N_2 ratio, GUVI measurements show significant depletion above Europe during daytime, which could corotate with Earth (by westward winds) into the night sector, causing long-lasting negative phase (see Figure 8).

During the 2015 St. Patrick's Day storm both foF2 and TEC decreased at all stations during the night. In the rTEC maps, a very strong positive phase is visible at 18 UT on 17 March at lower latitudes, its boundary located along the line connecting the Black See and N-France (shown by yellow in Figure 7B). SO, PQ are in the green area, indicating that there is no deviation from the quiet level, as confirmed by the foF2 value (Figure 4). At the same time, JR is in negative phase, the foF2 shows significantly decreased electron density. It should be noted that the start time of the negative phase in TEC (and rTEC) was delayed by 3 h comparing it with the foF2 parameter at the same location. Based on the Swarm data (Figure 11) the MIT has already reached that latitude and it moved further to lower latitudes later, so it possibly caused the negative effect at JR. Previous studies indicated that the afternoon appearance of MIT may be linked to a plasmaspheric plume (see Heilig et al., 2022). According to the observed rTEC values, as we move into the night at 22:00 UT (note that in reality most possibly this happened ~01:00 UT based on the aforementioned 3 h delay in rTEC), the zone with depleted electron density moves towards the equator, and even the positive phase region has been pushed back in the Athens-Rome line. By 00:00, the depleted zone moved even lower, at this time both Rome and Athens go into negative phase based on the foF2 data, indicating that the low mid-latitude region is also under the influence of MIT. The location of the MIT reached the 44.6° magnetic latitude (or maybe even below 42°) at 0.72 h MLT based on Swarm electron density and temperature measurements (Figures 10, 11) and the method described in Heilig et al. (2022). This sharp MIT minima was also accompanied by increased electron temperature with more than 5000 K (Figure 10), which was also observed by Liu et al. (2016), Zhang S.R. et al. (2015, Zhang S.R. et al. (2017a) during 16–19:30 UT on 17 March, which was presumably caused by strong frictional heating due to large plasma drifts. The equatorward motion of the minima of MIT is indicating that the plasmasphere was shrinking (see also Supplementary Figure S4), and the stations (JR, PQ, SO) went outside the plasmasphere where the ionosphere was not filled any more from the plasmasphere leading to extremely decreased electron density (detailed in Section 2). The severely depleted ionosphere was conjugated to the depleted outer magnetosphere (plasma trough) (see also Heilig et al., 2022). The F-layer drift measurement (at PQ) detected an intense ~500 m/s speed westward drift from appr. 20–02:00 UT (see Figure 12B) which is associated with the MIT formation mechanism. The effect of MIT lasts until 04:00 UT. Our findings are in good agreement with the results of previous articles like Nayak et al. (2016), who examined the equatorward motion of the MIT in the American sector (reached up to 40° N latitude) and Huang et al. (2018) also observed obvious westward disturbances in the zonal wind over central China (Asia, 38.7°N, 111.6°E). From 22:00 -02:00 UT strong westward neutral wind appeared, and at 03:00 UT a poleward wind surge of ~100 m/s appeared due to the poleward Coriolis force arising from the significant westward wind amplitudes (see Zhang S.R. et al., 2015; Tulasi et al., 2016; Huang et al., 2018). These were found to be driven by strong SAPS westward ion drift of >500 m/s peaking in the MIT and were accompanied by > 50 m/s upward ion drift in the E– and F-layers during SAPS periods at 22:43 UT at subauroral and midlatitudes (Zhang S.R. et al., 2015; Zhang S.R. et al., 2017a). But at lower latitudes poleward winds might not be driven by SAPS, most probably these wind changes are associated with travelling atmospheric disturbances (TADs) originated from the disturbance source region in the southern hemisphere (Huang et al., 2018).

After the observation of Zhang S.R. et al. (2017a) the SED plume over America (Millstone Hill) 20–24 UT can be linked to the positive phase over Southern Europe (AT and RO) from 18–22 UT: the westward winds could bring the plasma from Europe to North America leading to the detected SED plume over there (see Figure 4; Figure 7B) within a few hours, however, PPEF may also play some role in its formation (Liu et al., 2016). Investigation of Liu et al. (2016) and model results of Lu et al. (2020) confirm this possibility. Interestingly, a strong positive-phase region appeared at high latitudes (over Scandinavia), which can represent the poleward boundary of the MIT. The data show positive deviation, partly because the electron density was quite low in that region during QDs, while during the subsequent storm a quite significant increase took place in association with the equatorward movement of the MIT.

To speak about the lower latitudes, previous studies found the cumulative effect of enhanced meridional wind and changes in the electric fields, during night of the main phase at the 30–40°N zone. At low latitudes (like RO and AT) the detected variations in the ionosphere were governed by the superposition of disturbed electric fields (DDEFs), and the PPEF, which triggered the drop of foF2 in the evening on 17 March and the morning on 18 March (see Astafyeva et al., 2016; Jin et al., 2017; Polekh et al., 2017). For the St. Patrick's Day storm, the ionospheric effects of PPEF to low latitudes and the ionospheric disturbance dynamo (DDEF) were examined and discussed by several other papers: Le Huy and Amory-Mazauider, (2008); Lu et al. (2012); Abdu et al. (2013); Nava et al. (2016); Nayak et al. (2016); Ramsingh et al. (2015); Ram et al. (2016); Kalita et al. (2016). This could contribute to the nighttime electron density decrease at lower latitudes (AT, RO).

4.4 Recovery phase

During the recovery phase (on 15–17 November 2012 - Dst_{min} = −40;-27;-13nT; Kp_{max} = 1,33; 2,77; 3; AE_{max} = 119; 310; 328 nT and 18–20 March 2015 - Dst_{min} = −200;-99;-81 nT; Kp_{max} = 6; 5;4,77; AE_{max} = 1,043; 1,134; 611 nT) all station's TEC and foF2 data showed a positive phase in the 2012 storm case, while

they showed a significant negative phase in the 2015 St. Patrick storm case. Yizengaw et al. (2005) examined a geomagnetic storm from 31 March, 2001 (Dst_{min} = −380 nT) and found also an extended, long-lasting negative phase during the recovery phase. The reason for the long-lasting negative phase during storm 2015 can be the great extension of composition disturbance zone to low latitudes as suggested by Danilov (2013 and references therein). These statements are also confirmed by our analysis of GUVI data. On 18 March, 2015, a quite deep depletion was observed in O/N_2 ratio over Juliusruh (Figure 9) accompanied by foF2 decrease (Figure 4). The effect also re-occurs on 19 March, moreover the foF2 parameter data show a slight depletion also at PQ, SO and RO on 20 March. Nava et al. (2016), Huang et al. (2018) and Chernigovskaya et al. (2021) also found this depletion in electron density (18–20 March). They found that, during the recovery phase the important role in dynamics of the midlatitude ionosphere may belong to the wave-like thermospheric disturbances of molecular gas, propagating westward for several days causing electron density decrease along the trajectories of propagation. Besides, after the investigation of Kumar and Kumar (2019) another contributor to formation of the negative phase can be related to DDEFs. As for the 2012 storm, a negative phase changed to a positive one, which is believed to be caused by travelling atmospheric disturbances (TADs) (Danilov, 2013). These are generally brought by the same storm-time equatorward meridional wind discussed above, and have velocity of about 440 m/s (Mansilla, 2003). These processes uplift the layer to greater altitude, where the loss rate is lower, beside there is downwelling in atomic [O], resulting in an increase in electron density. On 16–17 November a slightly increased O/N_2 was observed by GUVI (marked with yellow in Figure 8), which could contribute to the daytime positive effect in foF2 around 10–15 UT at all investigated stations (Figure 3; see also article of Illes-Almar et al., 1987; Pirog et al., 2006).

The 2015 storm was followed by a second SSC by an HSSWS happened on 21 March at night. During that day, a negative phase was detected at all stations in both TEC and foF2 but not any disturbance was observed in GUVI data. One day later (Dst_{min} = −56 nT; Kp_{max} = 6.33; AE_{max} = 1078 nT) a slight positive phase was present both in TEC and in foF2 at all stations. During the remaining days in the recovery phase, foF2 data do not show significant departure from the QD values, while in TEC a slightly positive effect was recorded. The possible reason for the late recovery phase behavior may be linked to the fact that the examined European stations were then inside the plasmasphere during the daytime. Thus the effect of the composition change could have been suppressed by other factors. Another possible reason could be that the HSSWS caused electron density increase during the first 2 days. Nava et al. (2016) found that the HSSWS event is added some energy into the magnetosphere, extending the lifetime of the recovery phase.

We detail the observed diversities between foF2 and TEC during the daytime and nighttime of the two storms in the Supplementary section. The differences between the behavior of the foF2 parameter and TEC can be linked to the fact that TEC includes the plasma not only from the topside ionosphere (from above the height of foF2 parameter - hmF2) but also from plasmasphere. It is generally accepted that about 2/3 of the integrated TEC comes from the region above hmF2 (Mendillo, 2006). Due to this fact TEC is the best for portraying, assessing and understanding the overall behavior of the near-Earth thermal plasma (ionosphere and plasmasphere) (Mendillo, 2006). It has to be mentioned here that TEC plots used for this study (on Figures 5, 6) are based on a TEC grid map (not from individual GNSS stations). The plotted values are taken at a grid point (closest to each ionosonde station) of these TEC maps, so it is a smoothed interpolated value that can also be a reason for that it is less sensitive than the foF2 measured at individual stations.

In future studies, we found important to compare these results with some existing models/simulations in order to analyze and test the aforementioned processes: with NRL ionosphere/plasmasphere model SAMI3 (Huba et al., 2017), the thermosphere-ionosphere-electrodynamic general circulation model (TIEGCM, see the article of Lu et al., 2020), Horizontal Wind Model 2007 (HWM07, Huang et al., 2018), Global Self-consistent Model of the Thermosphere, Ionosphere, and Protonosphere (GSM TIP, Ratovsky et al., 2019) and also with the simulations of Fuller-Rowell et al. (1994) and Forbes and Roble et al. (1990). It is important mainly for the 2012 storm case where we do not have Swarm satellite measurement, and Fabry–Perot interferometer neutral wind observations to confirm our assumptions about the possible ionospheric effect drivers.

5 Conclusion

During the evolution of two ICME-related geomagnetic storms, we investigated the extent of disturbances in the ionosphere. Our supreme aim was to find connections between geomagnetic storm induced processes in the ionosphere and to determine the evolution of the effects over Europe through a meridional chain of digisondes. We used various measurements (GNSS TEC, GUVI, Swarm, digisonde drift data) to find the possible cause of the detected features. The results of this study are summarized below:

[1] On 13 November 2012: the thermospheric composition changes and PPEFs contributed to the evolution of the daytime positive phase at all stations. Drift measurements from Pruhonice indicate the presence of the ionospheric trough (MIT) between 20:30–10:00 UT, reflected in the westward motion of the F-layer plasma with a velocity of 350 m/s, which was the main cause of the depletion in foF2 during the postmidnight sector at JR, PQ and SO.

[2] On 17 March 2015, a daytime positive ionospheric storm developed at all stations except at JR. We can conclude that the negative phase at JR is a consequence of the equatorward motion of the MIT during the daytime. By GUVI data we assume that the composition change possibly had no effect. We assume that the possible cause of the positive phase was mainly connected to the Joule-heating of the auroral thermosphere, which lifted up the plasma through enhanced equatorward winds to altitudes where chemical loss rate of ions are slow. Besides, after previous studies, one of the cause was most possibly the PPEFs. The observed virtual height variation and the vertical drift data along with previous studies also confirms the uplifting scenario.

[3] On 14 November 2012: in foF2 data the negative phase is extremely significant at all stations from 6 UT till the afternoon hours. Based on the GUVI data, this effect is related to a very strong decrease in O/N_2 ratio during the day.
[4] During the night of the 14 November, 2012 we found that the presence of the midlatitude ionospheric trough (MIT) was the primary reason for the formation of the negative phase at JR, PQ, SO stations. The rTEC maps and the drift measurements at PQ also confirms the presence of a nighttime trough. In addition, based on the GUVI data the daytime compositional disturbance zone seems to extend equatorward during the night, contributing to a more pronounced electron density drop.
[5] The location of MIT minima (coincides with the ionospheric footprint of the PP) is likely reached the latitude of Sopron at night of 14 November according to the data. On the contrary AT and RO remained inside the plasmasphere, appearing as increase in foF2. It is in line with previous studies.
[6] Swarm data together with the digisonde drift measurements support our hypothesis that the extreme decrease in foF2 and TEC at night of 17 March is related to the equatorward motion of the MIT along with the intense SAPS westward ion drift, as MIT went down to 44.6° (or even below 42°) geomagnetic latitude at 0.72 h MLT. This condition resulted in an even pronounced electron density drop in the ionosphere above SO and PQ. The decreased O/N_2 ratio also contributed to the depletion effect.
[7] After the observation of previous studies, the SED plume over America (at subauroral latitudes) between 20 and 24 UT on 17 March can be linked to the positive phase (SED) from 18–22 UT in foF2 and rTEC over Southern Europe (RO and AT): the westward winds could bring the plasma from Europe to North America leading to the detected SED plume over there.
[8] By the 2012 storm" recovery phase, the variation from the daytime positive to negative phase in foF2 and TEC is probably due to the change in the neutral composition.
[9] The foF2 and TEC data are similar in their main patterns during the two investigated geomagnetic storms.
[10] The combined analysis of Swarm, rTEC, drift and foF2 measurements give another method beside the existing ones of previous researchers to monitor the evolution and movement of the ionospheric features like MIT (the ionospheric footprint of the plasmapause), SED and SAPS. This can deepen our understanding of the processes during different geomagnetic storms, and could be use in the future in space weather prediction models.
[11] In future studies, we found important to compare these results with some existing models/simulations in order to analyze and test the aforementioned processes.

Data availability statement

The datasets presented in this study can be found in online repositories. The names of the repository/repositories and accession number(s) can be found below (accessed on 09 March 2023): The IMF Bz and SW data and also Dst-, Kp-, and AE-index are from OMNIWEB (http://omniweb.gsfc.nasa.gov/form/dx1.html) with a resolution of 1 h and 1 min, as well as from WDC Kyoto (https://wdc.kugi.kyoto-u.ac.jp/dst_final/index.html). International Q-days (QD) list (https://wdc.kugi.kyoto-u.ac.jp/qddays/), geomagnetic coordinate calculator (https://wdc.kugi.kyoto-u.ac.jp/igrf/gggm/index.html), GIRO scaled digisonde parameters (https://giro.uml.edu/didbase/scaled.php) and for drift data (https://giro.uml.edu/driftbase/), GUVI data available at http://guvitimed.jhuapl.edu/data_fetch_l3_on2_gif, Swarm satellite constellation, Langmuir Probe data are available at: (https://earth.esa.int/eogateway/missions/swarm/product-data-handbook/preliminary-level-1b-plasma-dataset).

Author contributions

KB was the main organizer and writer of this article, and responsible for the manual correction of all ionosonde data used for the analysis. VB contributed to the structure of the research, the basic concept, checked the workflow and improved the manuscript. BH performed the analysis of Swarm satellite data, added figures. JU selected and plotted the GNSS TEC data. DK manually corrected the digisonde drift measurements and wrote the description for it. ÁK supported the first author with ideas and fundings. All members contributed substantially to science discussion and manuscript development.

Funding

This article is supported by the NKM55/2018 MTA mobility tender. Global GNSS-TEC data processing has been supported by JSPS KAKENHI Grant Number 16H06286. The contribution of VB was supported by OTKA, Hungarian Scientific Research Fund (grant no. PD 141967) of the National Research, Development and Innovation Office and by Bolyai Fellowship (GD, no. BO/00461/21). Furthermore, her work was supported by the GINOP-2.3.2-15-2016-00003 project.

Acknowledgments

We thank the data centers (OMNIWEB and WDC for Geomagnetism, Kyoto) and the Széchenyi István Geophysical Observatory at Nagycenk, Hungary, Athens (AT138), Rome (RO041), Pruhonice (PQ052) and Juliusruh (JR055) station for supplying high quality ionosonde and digisonde data for the research. The GUVI instrument was designed and built by The Aerospace Corporation and The Johns Hopkins University. The Principal Investigator is Dr. Andrew B. Christensen and the Chief Scientist and co-PI is Dr. Larry J. Paxton. GNSS RINEX files for the GNSS-TEC processing are provided from many organizations listed by the webpage (http://stdb2.isee.nagoya-u.ac.jp/GPS/GPS-TEC/gnss_provider_list.html). Also we are grateful for the reviewers for their valuable advices, which improved our article. The GUVI data used here are provided through support from the NASA MO&DA program.

Conflict of interest

The authors declare that the research was conducted in the absence of any commercial or financial relationships that could be construed as a potential conflict of interest.

Publisher's note

All claims expressed in this article are solely those of the authors and do not necessarily represent those of their affiliated organizations, or those of the publisher, the editors and the reviewers. Any product that may be evaluated in this article, or claim that may be made by its manufacturer, is not guaranteed or endorsed by the publisher.

Supplementary material

The Supplementary Material for this article can be found online at: https://www.frontiersin.org/articles/10.3389/fspas.2023.1092850/full#supplementary-material

References

Aa, E., Zou, S., Erickson, P. J., Zhang, S.-R., and Liu, S. (2020). Statistical analysis of the main ionospheric trough using Swarm *in situ* measurements. *J. Geophys. Res. Space Phys.* 125, e2019JA027583. doi:10.1029/2019JA027583

Abdu, M. A., Souza, J. R., Batista, I. S., Fejer, B. G., and Sobral, J. H. A. (2013). Sporadic E layer development and disruption at low latitudes by prompt penetration electric fields during magnetic storms. *J. Geophys. Res. Space Phys.* 118, 2639–2647. doi:10.1002/jgra.50271

Araujo-Pradere, E. A., and Fuller-Rowell, T. J. (2002). Storm: An empirical storm-time ionospheric correction model, 2. Validation. *Radio Sci.* 37 (5), 4-1–4-14. doi:10.1029/2002RS002620

Astafyeva, E., Zakharenkova, I., and Alken, P. (2016). Prompt penetration electric fields and the extreme topside ionospheric response to the June 22–23, 2015 geomagnetic storm as seen by the Swarm constellation. *Earth Planet Sp.* 68, 152. doi:10.1186/s40623-016-0526-x

Astafyeva, E., Zakharenkova, I., and Förster, M. (2015). Ionospheric response to the 2015 St. Patrick's day storm: A global multi-instrumental overview. *J. Geophys. Res. Space Phys.* 120, 9023–9037. doi:10.1002/2015JA021629

Berényi, K. A., Barta, V., and Kis, V. (2018). Midlatitude ionospheric F2-layer response to eruptive solar events-caused geomagnetic disturbances over Hungary during the maximum of the solar cycle 24: A case study. *Adv. Space Res.* 61, 1230–1243. doi:10.1016/j.asr.2017.12.021

Blagoveshchensky, D. V., and Kalishin, A. S. (2009). Increase in the critical frequency of the ionospheric F region prior to the substorm expansion phase. *Geomagn. Aeron.* 49, 200–209. doi:10.1134/S0016793209020091

Bór, J., Sátori, G., Barta, V., Szabóné-André, K., Szendroi, J., Wesztergom, V., et al. (2020). Measurements of atmospheric electricity in the Széchenyi István geophysical observatory, Hungary. *Hist. Geo-and Space Sci.* 11 (1), 53–70. doi:10.5194/hgss-11-53-2020

Buonsanto, M. J. (1999). Ionospheric storms – a review. *Space Sci. Rev.* 88, 563–601. doi:10.1023/a:1005107532631

Burešová, D., and Laštovička, J. (2007). Pre-storm enhancements of foF2 above Europe. *Adv. Space Res.* 39, 1298–1303. doi:10.1016/j.asr.2007.03.003

Cherniak, I., and Zakharenkova, I. (2015). Dependence of the high-latitude plasma irregularities on the auroral activity indices: A case study of 17 March 2015 geomagnetic storm. *Earth Planet Sp.* 67, 151. doi:10.1186/s40623-015-0316-x

Chernigovskaya, M. A., Shpynev, B. G., Yasyukevich, A. S., Khabituev, D. S., Ratovsky, K. G., Belinskaya, A. Yu., et al. (2021). Longitudinal variations of geomagnetic and ionospheric parameters in the Northern Hemisphere during magnetic storms according to multi-instrument observations. *Adv. Space Res.* 67, 762–776. doi:10.1016/j.asr.2020.10.028

Christensen, A. B., Paxton, L. J., Avery, S., Craven, J., Crowley, G., Humm, D. C., et al. (2003). Initial observations with the global ultraviolet imager (GUVI) in the NASA TIMED satellite mission. *J. Geophys. Res.* 108, 1451. doi:10.1029/2003JA009918,A12

Crowley, G., Hackert, C. L., Meier, R. R., Strickland, D. J., Paxton, L. J., Pi, X., et al. (2006). Global thermosphere-ionosphere response to onset of 20 November 2003 magnetic storm. *J. Geophys. Res.* 111, A10S18. doi:10.1029/2005JA011518

Danilov, A. D., and Belik, L. D., (1991). Thermosphere-ionosphere inter-action in a period of ionospheric storms, *Geomagn. andAeronomy*, 31, 157–167.

Danilov, A. D., and Belik, L. D. (1992). Thermospheric composition and the positive phase of an ionospheric storm. *Adv. Space Res.* 12 (10), 257–260. ISSN 0273-1177. doi:10.1016/0273-1177(92)90475-D

Danilov, A. D. (2013). Ionospheric F-region response to geomagnetic disturbances. *Adv. Space Res.* 52, 343–366. doi:10.1016/j.asr.2013.04.019

Deminov, M. G., and Shubin, V. N. (2018). Empirical model of the location of the main ionospheric trough. *Geomagn. Aeron.* 58, 348–355. doi:10.1134/S0016793218030064

Forbes, J. M., and Roble, R. G. (1990). Thermosphere-ionosphere coupling: An experiment in interactive modeling. *J. Geophys. Res.* 95 (A1), 201. doi:10.1029/JA095iA01p00201

Fuller-Rowell, T. J., Codrescu, M. V., Moffett, R. J., and Quegan, S. (1994). Response of the thermosphere and ionosphere to geomagnetic storms. *J. Geophys. Res.* 99 (A3), 3893–3914. doi:10.1029/93JA02015

Habarulema, J. B., Yizengaw, E., Katamzi-Joseph, Z. T., Moldwin, M. B., and Buchert, S. (2018). Storm time global observations of large-scale TIDs from ground-based and *in situ* satellite measurements. *J. Geophys. Res. Space Phys.* 123, 711–724. doi:10.1002/2017JA024510

Hairston, M., Coley, W. R., and Stoneback, R. (2016). Responses in the polar and equatorial ionosphere to the March 2015 St. Patrick Day storm. *J. Geophys. Res. Space Phys.* 121, 11,213–11,234. doi:10.1002/2016JA023165

He, M., Liu, L., Wan, W., and Zhao, B. (2011). A study on the nighttime midlatitude ionospheric trough. *J. Geophys. Res. Space Phys.* 116, 5315. doi:10.1029/2010ja016252

Heilig, B., and Lühr, H. (2013). New plasmapause model derived from CHAMP field-aligned current signatures. *Ann. Geophys.* 31, 529–539. doi:10.5194/angeo-31-529-2013

Heilig, B., and Lühr, H. (2018). Quantifying the relationship between the plasmapause and the inner boundary of small-scale field-aligned currents, as deduced from Swarm observations. *Ann. Geophys.* 36, 595–607. doi:10.5194/angeo-36-595-2018

Heilig, B., Stolle, C., Kervalishvili, G., Rauberg, J., Miyoshi, Y., Tsuchiya, F., et al. (2022). Relation of the plasmapause to the midlatitude ionospheric trough, the sub-auroral temperature enhancement and the distribution of small-scale field aligned currents as observed in the magnetosphere by THEMIS, RBSP, and arase, and in the topside ionosphere by Swarm. *J. Geophys. Res. Space Phys.* 127, e2021JA029646. doi:10.1029/2021ja029646

Hofmann-Wellenhof, B., and Lichtenegger, H. (2001). "Global positioning system," in *Theory and practice* (Australia: Flinders University).

Horváth, I., and Lovell, B. C. (2016). Structured subauroral polarization streams and related auroral undulations occurring on the storm day of 21 January 2005. *J. Geophys. Res. Space Phys.* 121, 1680–1695. doi:10.1002/2015JA022057

Huang, C., Xu, J-Y., Zhang, X-X., Liu, D., Yuan, W., and Jiang, G-Y. (2018). Mid-latitude thermospheric wind changes during the St. Patrick's Day storm of 2015 observed by two Fabry-Perot interferometers in China. *Adv. Space Res.* 61 (7), 1873–1879. doi:10.1016/j.asr.2017.10.013

Huba, J. D., Sazykin, S., and Coster, A. (2017). Sami3-RCM simulation of the 17 March 2015 geomagnetic storm. *J. Geophys. Res. Space Phys.* 122, 1246–1257. doi:10.1002/2016JA023341

Illes-Almar, E., Almar, I., Bencze, P., and Horváth, A. (1987). Investigation of the thermosphere-ionosphere interaction by means of the neutral post-storm effect. *Adv. Space Res.* 7, 53–57. doi:10.1016/0273-1177(87)90189-x

Immel, T. J., and Mannucci, A. J. (2013). Ionospheric redistribution during geomagnetic storms. *J. Geophys. Res. Space Physics* 118, 7928–7939. doi:10.1002/2013JA018919

Jin, S., Jin, R., and Kutoglu, H. (2017). Positive and negative ionospheric responses to the March 2015 geomagnetic storm from BDS observations. *J. Geod.* 91, 613–626. doi:10.1007/s00190-016-0988-4

Kalita, B. R., Hazarika, R., Kakoti, G., Bhuyan, P. K., Chakrabarty, D., Seemala, G. K., et al. (2016). Conjugate hemisphere ionospheric response to the St. Patrick's Day storms of 2013 and 2015in the 100°E longitude sector. *J. Geohys. Res. Space Phys.* 121, 11364–11390. doi:10.1002/2016JA023119

Kane, R. P. (2005). Ionospheric <i>fo</i>F2 anomalies during some intense geomagnetic storms. *Ann. Geophys.* 23, 2487–2499. doi:10.5194/angeo-23-2487-2005

Kane, R. P. (1973a). Storm-time variations of F2. *Ann. Geophys.* 29, 25–42.

Kane, T. A., and Makarevich, R. A. (2010). HF radar observations of the F region ionospheric plasma response to Storm Sudden Commencements. *J. Geophys. Res. Space Phys.* 115, 1–13. doi:10.1029/2009ja014974

Karpachev, A. T., Klimenko, M. V., and Klimenko, V. V. (2019). Longitudinal variations of the ionospheric trough position. *Adv. Space Res.* 63, 950–966. doi:10.1016/j.asr.2018.09.038

Kouba, D., Boška, J., Galkin, I. A., Santolík, O., and šauli, P. (2008). Ionospheric drift measurements: Skymap points selection. *Radio Sci.* 43 (01), 1–11. doi:10.1029/2007RS003633

Kouba, D., and Koucká Knížová, P. (2012). Analysis of digisonde drift measurements quality. *J. Atmos. Solar-Terrestrial Phys.* 90-91, 212–221. doi:10.1016/j.jastp.2012.05.006

Kouba, D., and Koucká Knížová, P. (2016). Ionospheric vertical drift response at a mid-latitude station. *Adv. Space Res.* 58 (1), 108–116. doi:10.1016/j.asr.2016.04.018

Kumar, E. A., and Kumar, S. (2022). Geomagnetic storm effect on F2-region ionosphere during 2012 at low- and mid-latitude-latitude stations in the southern hemisphere. *Atmosphere* 13, 480. doi:10.3390/atmos13030480

Kumar, S., and Kumar, V. V. (2019). Ionospheric response to the St. Patrick's Day space weather events in March 2012, 2013, and 2015 at southern low and middle latitudes. *J. Geophys. Res. Space Phys.* 124, 584–602. doi:10.1029/2018JA025674

Lanzerotti, L. J., Cogger, L. L., and Mendillo, M. (1975). Latitude dependence of ionosphere total electron content: Observations during sudden commencement storms. *J. Geophys. Res.* 80 (10), 1287–1306. doi:10.1029/JA080i010p01287

Le Huy, M., and Amory-Mazaudier, C. (2008). Planetary magnetic signature of the storm wind disturbance dynamo currents:Ddyn. *J. Geophys.Res.* 113, A02312. doi:10.1029/2007JA012686

Li, W., Ma, Q., Thorne, R. M., Bortnik, J., Zhang, X., Li, J., et al. (2016). Radiation belt electron acceleration during the 17 March 2015 geomagnetic storm: Observations and simulations. *J. Geophys. Res. Space Phys.* 121, 5520–5536. doi:10.1002/2016JA022400

Liu, J., Wang, W., Burns, A., Yue, X., Zhang, S., Zhang, Y., et al. (2016). Profiles of ionospheric storm-enhanced density during the 17 March 2015 great storm. *J. Geophys. Res. Space Phys.* 121, 727–744. doi:10.1002/2015JA021832

Liu, L., Wan, W., Zhang, M.-L., Zhao, B., and Ning, B. (2008). Prestorm enhancements in NmF2 and total electron content at low latitudes. *J. Geophys. Res.* 113, A02311. doi:10.1029/2007JA012832

Liu, Y., and Xiong, C. (2020). Morphology evolution of the midlatitude ionospheric trough in nighttime under geomagnetic quiet conditions. *J. Geophys. Res. Space Phys.* 125, e2019JA027361. doi:10.1029/2019JA027361

Lu, G., Goncharenko, L., Nicolls, M. J., Maute, A., Coster, A., and Paxton, L. J. (2012). Ionospheric and thermospheric variations associated with prompt penetration electric fields. *J. Geophys. Res.* 117, A08312. doi:10.1029/2012JA017769

Lu, G., Zakharenkova, I., Cherniak, I., and Dang, T. (2020). Large-scale ionospheric disturbances during the 17 March 2015 storm: A model-data comparative study. *J. Geophys. Res. Space Phys.* 125, e2019JA027726. doi:10.1029/2019JA027726

Mansilla, G. A. (2003). Disturbances at F2-region heights of equatorial anomaly during geomagnetic storms. *J. Atmos. Solar-Terrestrial Phys.* 65 (9), 987–995. ISSN 1364-6826. doi:10.1016/S1364-6826(03)00119-6

Matsushita, S. (1959). A study of the morphology of ionospheric storms. *J. Geophys. Res.* 64, 305–321. doi:10.1029/jz064i003p00305

Mendillo, M., Klobuchar, J. A., and Hajeb-Hosseinieh, H. (1974). Ionospheric disturbances: Evidence for the contraction of the plasmasphere during severe geomagnetic storms. *Planet. Space Sci.* 22, 223–236. doi:10.1016/0032-0633(74)90026-9

Mendillo, M., and Narvaez, C. (2010). Ionospheric storms at geophysically-equivalent sites - Part 2: Local time storm patterns for sub-auroral ionospheres. *Ann. Geophys.* 28, 1449–1462. doi:10.5194/angeo-28-1449-2010

Mendillo, M., and Narvaez, C. (2009). Ionospheric storms at geophysically-equivalent sites – Part 1: Storm-time patterns for sub-auroral ionospheres. *Ann. Geophys* 27, 1679–1694. doi:10.5194/angeo-27-1679-2009

Mendillo, M. (2006). Storms in the ionosphere: Patterns and processes for total electron content. *Rev. Geophys.* 44, RG4001–47. doi:10.1029/2005rg000193

Mikhailov, A. V., and Forster, M. (1997). Day-to-day thermosphere parameter variation as deduced from Millstone Hill incoherent scatter radar observations during March 16–22, 1990 magnetic storm period. *Ann. Geophys.* 15, 1429–1438.

Mikhailov, A. V., and Perrone, L. (2009). Pre-storm NmF2 enhancements at middle latitudes: Delusion or reality? *Ann. Geophys* 27, 1321–1330. doi:10.5194/angeo-27-1321-2009

Mikhailov, A. V., Skoblin, M. G., and Forster, M. (1995). Daytime F2-layer positive storm effect at middle and lower latitudes. *Ann. Geophys.* 13, 532–540. doi:10.1007/s00585-995-0532-y

Mikhailov, A. V., Terekhin, Yu.L., and Mikhailov, V. V. (1989). Does the F2 layerfollow the constant pressure level? *Geomag. Aeron.* 29, 906–908.

Nava, B., Rodríguez-Zuluaga, J., Alazo-Cuartas, K., Kashcheyev, A., Migoya-Orué, Y., Radicella, S. M., et al. (2016). Middle- and low-latitude ionosphere response to 2015 St. Patrick's Day geomagnetic storm. *J. Geophys. Res. Space Phys.* 121, 3421–3438. doi:10.1002/2015ja022299

Nayak, C., Tsai, L.-C., Su, S.-Y., Galkin, I. A., Tan, A. T. K., Nofri, E., et al. (2016). Peculiar features of the low-latitude and midlatitude ionospheric response to the St. Patrick's Day geomagnetic storm of 17 March 2015. *J. Geophys. Res. Space Phys.* 121, 7941–7960. doi:10.1002/2016JA022489

Pirog, O. M., Polekh, N. M., Tashchilin, A. V., Romanova, E. B., and Zherebtsov, G. A. (2006). Response of ionosphere to the great geomagnetic storm of September 1998: Observation and modeling. *Adv. Space Res.* 37 (5), 1081–1087. doi:10.1016/j.asr.2006.02.005

Polekh, N., Zolotukhina, N., Kurkin, V., Zherebtsov, G., Shi, J., Wang, G., et al. (2017). Dynamics of ionospheric disturbances during the 17–19 March 2015 geomagnetic storm over East Asia. *Adv. Space Res.* 60 (11), 2464–2476. doi:10.1016/j.asr.2017.09.030

Prölss, G. W. (1995). "Ionospheric F-region storms," in *Handbook of atmospheric electrodynamics*. Editor H. Volland (Boca Raton, Fla: CRC Press).

Prölss, G. W., and Zahn, U. (1974). Esro 4 Gas Analyzer results 2. Direct measurements of changes in the neutral composition during an ionospheric storm. *J. Geophys. Res.* 79, 2535–2539. doi:10.1029/ja079i016p02535

Ram, S. T., Yokoyama, T., Otsuka, Y., Shiokawa, K., Sripathi, S., Veenadhari, B., et al. (2016). Duskside enhancement of equatorialzonal electric field response to convection electric fields during the St.Patrick's Day storm on 17 March 2015. *J. Geophys. Res. Space Phys.* 121, 538–548. doi:10.1002/2015ja021932

Ramsingh, T., Sripathi, S., Sreekumar, S., Banola, S., Emperumal, K., Tiwari, P., et al. (2015). Low-latitude ionosphere response tosuper geomagnetic storm of 17/18 March 2015: Results from a chain ofground-based observations over Indian sector. *J. Geophys. Res. SpacePhys.* 120, 10864–10882. doi:10.1002/2015JA021509

Ratovsky, K. G., Klimenko, M. V., Vasilyev, R. V., and Klimenko, V. V. (2019). "Upper atmosphere wind pattern during St. Patrick's day geomagnetic storm: Fabry-perot interferometer measurements and modeling," in 2019 PhotonIcs & Electromagnetics Research Symposium - Spring (PIERS-Spring), Italy, 17-20 June 2019.

Rishbeth, H., and Barron, D. W. (1960). Equilibrium electron distributions in the ionospheric F2-layer. *J. Atmos. Terr. Phys.* 18, 234–252. doi:10.1016/0021-9169(60)90095-7

Rodger, A. S., Brace, L. H., Hoegy, W. R., and Winningham, J. D. (1986). The poleward edge of the mid-latitude trough—its formation, orientation and dynamics. *J. Atmos. Terr. Phys.* 48, 715–728. doi:10.1016/0021-9169(86)90021-8

Rodger, A. S., Moffett, R. J., and Quegan, S. (1992). The role of ion drift in the formation of ionisation troughs in the mid- and high-latitude ionosphere—A review. *J. Atmos. Terr. Phys.* 54, 1–30. doi:10.1016/0021-9169(92)90082-v

Sato, T. (1957). Disturbances in the ionosphericF2 region asso-ciated with geomagnetic storms II. Middle latitudes. *J. Geomagn. Geoelectr.* 9, 1–22. doi:10.5636/jgg.9.1

Schunk, R. W., and Banks, P. M. (1975). Auroral N2 vibrational excitation and the electron density trough. *Geophys. Res. Lett.* 2, 239–242. doi:10.1029/gl002i006p00239

Seaton, M. J. (1956). A possible explanation of the drop in F-region criticaldensities accompanying major ionospheric storms. *J. Atmos. Terr.Phys.* 8, 122–124. doi:10.1016/0021-9169(56)90102-7

Tulasi, R. S., Yokoyama, T., Otsuka, Y., Shiokawa, K., Sripathi, S., Veenadhari, B., et al. (2016). Duskside enhance-ment of equatorial zonal electric field response to convection electricfields during the St. Patrick's Day storm on 17 March 2015. *J.Geophys. Res. Space Phys.* 121, 538–548. doi:10.1002/2015JA021932

Turunen, T., and Liszka, L. (1972). Comparison of simultaneous satellite measurements of auroral particle precipitation with bottomside ionosonde measurements of the electron density in the F-region. *J. Atmos. Terr. Phys.* 34, 365–372. doi:10.1016/0021-9169(72)90039-6

Voiculescu, M., Nygrn, T., Aikio, A., and Kuula, R. (2010). An olden but golden EISCAT observation of a quiet-time ionospheric trough. *J. Geophys. Res. Space Phys.* 115, 10315. doi:10.1029/2010JA015557

Voiculescu, M., Virtanen, I., and Nygrén, T. (2006). The F-region trough: Seasonal morphology and relation to interplanetary magnetic field. *Ann. Geophys.* 24, 173–185. doi:10.5194/angeo-24-173-2006

Werner, S., and Prölss, G. W. (1997). The position of the ionospheric trough as a function of local time and magnetic activity. *Adv. Space Res.* 20, 1717–1722. doi:10.1016/S0273-1177(97)00578-4

Whalen, J. A. (1989). The daytime F layer trough and its relation to ionospheric-magnetospheric convection. *J. Geophys. Res.* 94 (A12), 17169–17184. doi:10.1029/JA094iA12p17169

Wu, C. C., Liou, K., Lepping, R. P., Hutting, L., Plunkett, S., Howard, R. A., et al. (2016). The first super geomagnetic storm of solar cycle 24: "The St. Patrick's day event (17 March 2015)". *Earth Planet Sp.* 68, 151. doi:10.1186/s40623-016-0525-y

Yizengaw, E., Wei, H., Moldwin, M. B., Galvan, D., Mandrake, L., Mannucci, A., et al. (2005). The correlation between mid-latitude trough and the plasmapause. *Geophys. Res. Lett.* 32, L10102. doi:10.1029/2005GL022954

Zhang, J. J., Wang, C., Sun, T. R., Liu, C. M., and Wang, K. R. (2015). GIC due to storm sudden commencement in low-latitude high-voltage power network in China: Observation and simulation. *Space weather.* 13, 643–655. doi:10.1002/2015SW001263

Zhang, S. R., Erickson, P. J., Foster, J. C., Holt, J. M., Coster, A. J., Makela, J. J., et al. (2015). Thermospheric pole-ward wind surge at midlatitudes during great storm intervals. *Geophys.Res. Lett.* 42, 5132–5140. doi:10.1002/2015gl064836

Zhang, S. R., Erickson, P. J., Zhang, Y., Wang, W., Huang, C., Coster, A. J., et al. (2017a). Observations of ion-neutral coupling associated with strong electrodynamic disturbances during the 2015 St. Patrick's Day storm. *J. Geophys. Res. Space Phys.* 122, 1314–1337. doi:10.1002/2016JA023307

Zhang, S. R., Zhang, Y., Wang, W., and Verkhoglyadova, O. P. (2017b). Geospace system responses to the St. Patrick's Day storms in 2013 and 2015. *J. Geophys. Res. Space Phys.* 122, 6901–6906. doi:10.1002/2017JA024232

frontiers | Frontiers in Astronomy and Space Sciences

TYPE Original Research
PUBLISHED 15 May 2023
DOI 10.3389/fspas.2023.1198739

OPEN ACCESS

EDITED BY
Yongliang Zhang,
Johns Hopkins University, United States

REVIEWED BY
Hyosub Kil,
Johns Hopkins University, United States
Ercha Aa,
Massachusetts Institute of Technology, United States

*CORRESPONDENCE
Huixin Liu,
liu.huixin.295@m.kyushu-u.ac.jp

RECEIVED 02 April 2023
ACCEPTED 03 May 2023
PUBLISHED 15 May 2023

CITATION
Liu H, Otsuka Y, Hozumi K and Yu T (2023), Day-to-day variability of the equatorial ionosphere in Asian sector during August–October 2019.
Front. Astron. Space Sci. 10:1198739.
doi: 10.3389/fspas.2023.1198739

Day-to-day variability of the equatorial ionosphere in Asian sector during August–October 2019

Huixin Liu[1]*, Yuichi Otsuka[2], Kornyanat Hozumi[3] and Tao Yu[4]

[1]Department of Earth and Planetary Science, Kyushu University, Fukuoka, Japan, [2]Institute of Sun-Earth Environment, Nagoya University, Nagoya, Japan, [3]National Institute of Information and Communications Technology, Tokyo, Japan, [4]Institute of Geophysics and Geomatics, China University of Geosciences, Wuhun, China

This brief report examines the ground-based total electron content (TEC) in Asian sector during August–October 2019, covering the period of a stratosphere sudden warming (SSW) occurred in Antarctica. The analysis reveals pronounced ionospheric day-to-day variability with distinct periodicities. The most dominant and long-lasting periodicities are quasi-10 days and quasi 14-day during September and October, while a quasi 6-day also present in September. The 10-day and 6-day TEC oscillations were attributed by previous studies solely to the Antarctic SSW while assuming negligible geomagnetic effects. By comparing co-located ground mesospheric wind observations, along with the interplanetary electric field (IEF) and geomagnetic activity (Kp index), we demonstrate that the quasi 14-day oscillation is mainly driven by low-level geomagnetic activities, while quasi-6 days oscillation is driven by mesospheric wind changes during the SSW. The 10-day oscillation, on the other hand, is driven by both IEF and mesospheric wind in September, but by IEF in October. These results demonstrate that low-level geomagnetic activities traditionally classified as "quiet conditions" can induce significant day-to-day oscillations in TEC, and their impacts should not be ignored when studying meteorological (e.g., SSWs) impacts on the ionosphere.

KEYWORDS

SSW, day-to-day variability, ionosphere perturbation, atmosphere-ionosphere coupling, atmosphere tides

1 Introduction

Equatorial ionosphere is known to be sensitive to both solar/geomagnetic activities such as solar flares and geomagnetic storms, and meteorological conditions such as stratosphere sudden warming (SSW) (see reviews by Liu et al, 2021; Gonchalenko et al, 2021, and references therein). Geomagnetic activities have been generally thought to affect the ionosphere when the Kp index is above 3. However, Cai et al (2021) recently showed that minor geomagnetic activity below 2 can have significant effects on the ionosphere 24 total electron content (TEC). Siddiqui et al (2021) also demonstrated, using numerical simulation, that TEC variabilities during the January 2019 stratosphere sudden warming (SSW) were dominantly caused by geomagnetic activities with low Kp (mostly below 3), rather than by the lower atmosphere forcing during the SSW. These results thus call proper treatment of the impact of "quiet" geomagnetic activities with Kp below 3 when discussing meteorological impacts on the ionosphere.

The 2019 SSW occurred in the Antarctica has attracted intensive scientific attention due to its rareness (17 years after previous SSW in 2002, compared to Arctic SSWs that occur every year or every other year in recently years). Its impacts on the ionosphere have been studied, which revealed significant quasi-6 and-10 days oscillations in the equatorial TEC (e.g., Goncharenko et al, 2020; Lin et al, 2020; Yamazaki et al, 2020; Wang et al, 2021). The oscillations were all attributed to the occurrence of the SSW in these studies, with geomagnetic forcing being neglected. The Kp index in September 2019 did experience significant periodic variations, with 47% of its values above 2, and 23% above 3 (see Figure 4B). In light of the high ionospheric sensitivity to low geomagnetic activities (Cai et al, 2021; Siddiqui et al, 2021), it is natural to ask whether the varying geomagnetic forcing contributed to the ionospheric multi-day oscillations during the 2019 SSW? To answer this question, we examine the day-to-day variability of the ground-based TEC during August–October 2019, and their connection to the geomagnetic forcing and SSW forcing.

2 Data

To examine the day-to-day variation in the ionosphere and mesosphere, we make use of ground observations co-located in southeast Asia between 90E–115E as shown in Figure 1. For the ionosphere, we use GPS-TEC observations in the crest regions of the equatorial ionization anomaly (EIA) at Bako (6.5S 107E geographic, 15.9S geomagnetic) and Juri (24.5N 92.1E geographic, 15.2N geomagnetic) (Otsuka et al, 2002). The equatorial electrojet (EEJ) near dip equator are obtained at Phuket (8.1N 98.3E geographic, 1S geomagnetic) from the difference between the horizontal magnetic field component at Phuket and Kototabang (0.2S, 100.3E geographic, 9.5S geomagnetic), which is a classical method given by Rusch and Richmond (1973). For the mesosphere, we use wind observations from the meteor radar at SanYa (18.0N, 110.0E geographic) that cover altitudes of 70–110 km. Diurnal and semidiurnal tides are derived from these wind measurements.

Compared to satellite observations used in previous studies(e.g., Yamazaki et al, 2020), these ground observations offer full 24 h local time coverage each day and thus afford us to examine TEC and mesospheric wind in terms of tidal components, which makes more physical sense as tides are the direct agents for atmosphere-ionosphere coupling. Hourly data for TEC, EEJ and mesospheric wind are used in the following analysis during August 1– 30 October 2019 (DoY 213–303), which covers the Antarctic SSW event (onset at DoY 237). The variability of the geomagnetic forcing are examined using the Kp index and the interplanetary electric field (IEF).

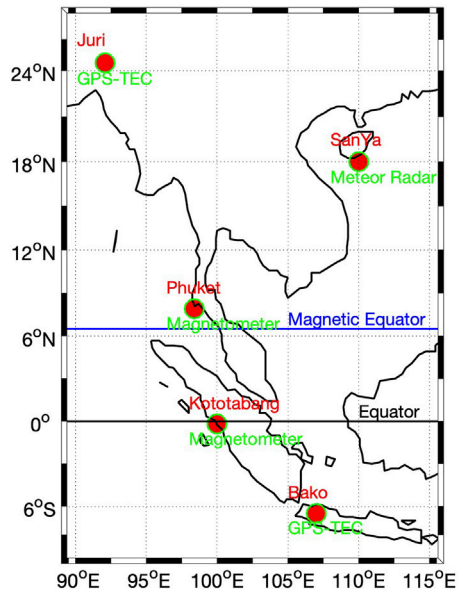

FIGURE 1
Locations of ground stations used in this study.

3 Results

3.1 Day-to-day variability in the ionosphere TEC

Figures 2A,B show TEC observed in the EIA northern and southern crests during DoY 213–303 2019. The stratosphere temperature at 90S at 10 hPa (from MERRA-2) is overlaid as the thick line to indicate the temporal development of the Antarctic SSW. The corresponding wavelet spectra of TEC are shown in 2c and 2d, revealing significant diurnal and semidiurnal components in both hemispheres. We extract these components using least-square fitting method with a window length of 3 days and the results are shown in Figures 3E,F. The magnitude of the diurnal component ranges between 5 and 15 TECU, about 3 times of that of the semidiurnal component. Both components exhibit the seasonal increasing trend from August towards October.

Riding on the seasonal trend are apparent day-to-day oscillations. As revealed in their wavelet spectra (Figures 2G–J), a prominent and persistent quasi 10-day periodicity occurs during DoY 243–293 in both hemispheres. A quasi 14-day oscillation enhances during DoY 243–303, best seen in Figures 2H,I. Furthermore, a quasi-6 days oscillation is evident in the northern crest during DoY 253–273, but is very weak in the southern crest. The weaker 6-day amplitude in the southern EIA crest was also noticed in the Antarctica SSW in year 2002 (Mo and Zhang, 2020), and was likely related to meridional wind that can cause hemispheric asymmetry in TEC.

3.2 Day-to-day variability in mesospheric winds

The diurnal and semidiurnal tidal components are extracted from the meteor wind observations at SanYa and displayed in Figures 3A,C for the zonal wind, in Figures 3B,D for the meridional wind. The meridional wind generally has twice as large tidal amplitudes as that of the zonal wind, reaching over 80 m/s for the diurnal and 60 m/s for the semidiurnal components. Significant day-to-day variation are evident in the tidal amplitudes, persisting throughout most altitudes.

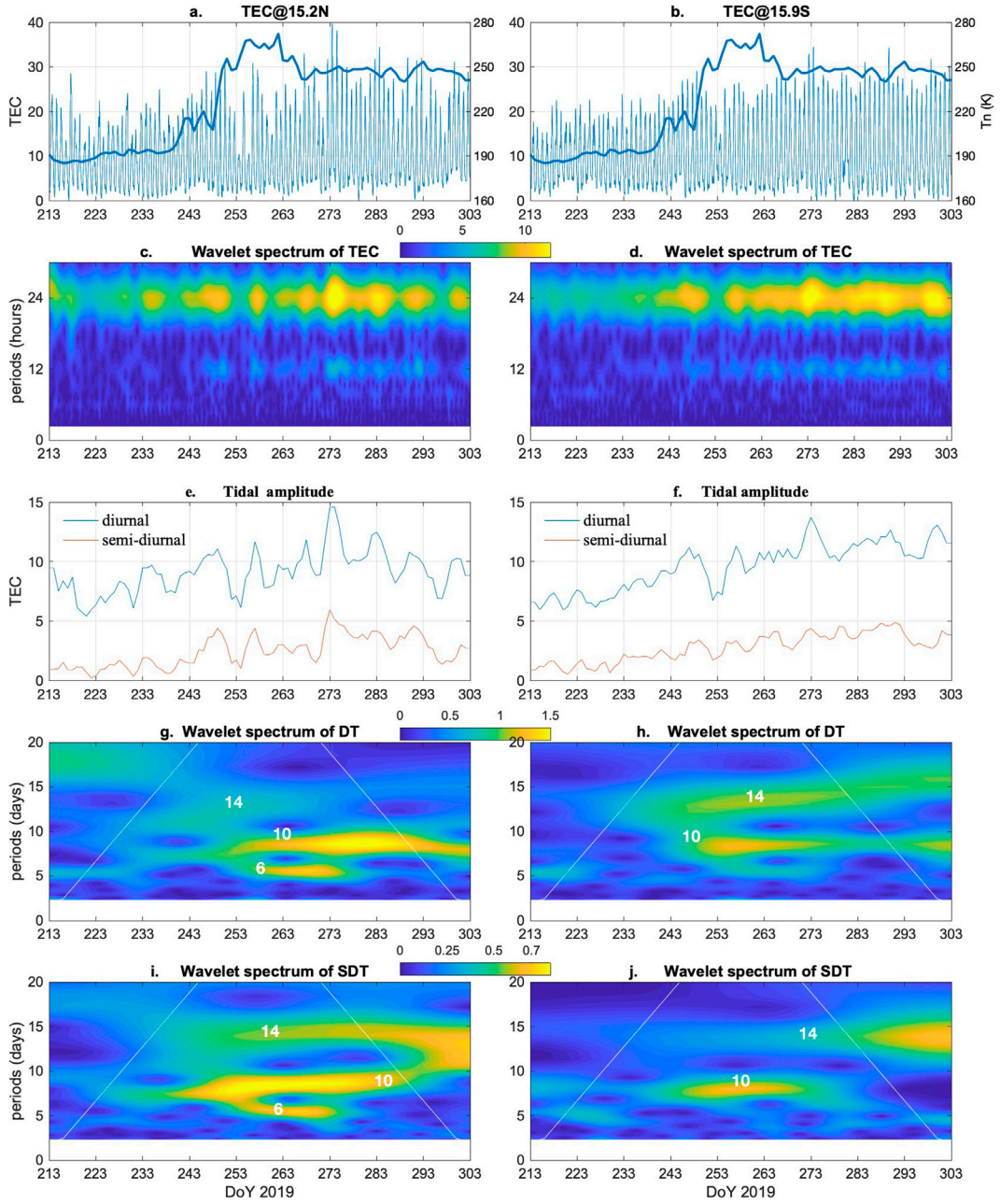

FIGURE 2
TEC in EIA crests and the day-to-day variability in its tidal components during DoY 213–303. (August 1—October 30), 2019. Row 1: TEC along with the stratosphere temperature at 90S at 10 hPa (thick line). Row 2: corresponding wavelet spectrum of TEC, revealing the diurnal and semidiurnal components. Row 3: amplitudes of the diurnal and semidiurnal tidal amplitudes extracted from TEC. Row 4: Wavelet spectrum of the diurnal (DT) and semidiurnal tidal components (SDT) in row 3, revealing dominant periods for the multi-day oscillations.

To quantitatively examine the periodicities and their temporal evolution, the wavelet spectrum of the tidal amplitudes averaged over 85–96 km are obtained. As shown in Figures 3E–H, a quasi 6-day periodicity occur in all tidal components, being more pronounced in the zonal wind with peaks around DoY 233 and 263 (see 3e, 3g). A quasi 10-day periodicity is prominent in the meridional wind, peaking around DoY 243 and 278 (3f). Satellite observations also showed the quasi 10-day oscillation mainly present in the meridional wind (Wang et al, 2021).

These 6- and 10-day periodicities in tides observed in tropical regions resemble those of planetary waves (PW) found in the mesosphere wind that are caused by the Antarctic SSW in 2019, such as the quasi 6-day (Yamazaki et al, 2020) and quasi 10-day waves (He et al, 2020; Wang et al, 2021), thus imply PW modulation of tides via tide-PW interaction during the SSW.

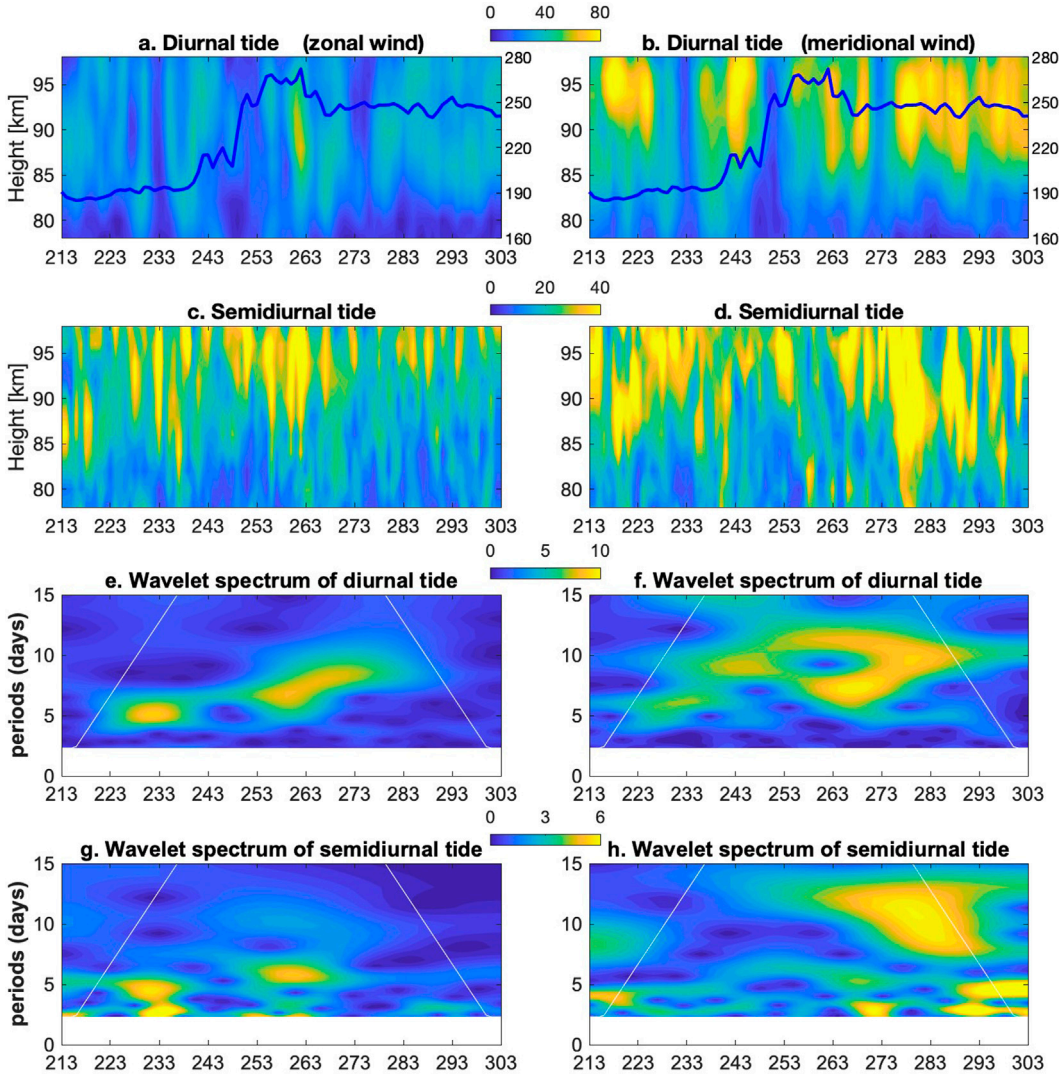

FIGURE 3
Tides in mesosphere winds (in unit of m/s) observed at SanYa during August 1—30 October 2019, with the left column for zonal wind and the right for meridional wind. Row 1: diurnal tide with the stratosphere temperature at 90S at 10 hPa is overlaid (thick line). Row 2: semidiurnal tide; third row: wavelet spectrum of diurnal tides averaged over 85–95 km; fourth row: wavelet spectrum of semidiurnal tides averaged over 85–95 km.

3.3 Day-to-day variabilities in EEJ and geomagnetic activities

Tides propagating from the lower atmosphere are known to affect the ionospheric electric field via the wind dynamo, which directly drives the equatorial eletrojet (EEJ) around 110 km altitude. Previous studies have shown EEJ being highly sensitive to the occurrence of SSWs (e.g., Liu et al, 2011). Here we use the EEJ as an indicator for SSW to examine whether or not the 6-day and 10-day oscillations in mesospheric wind were transmitted to the ionosphere. At the same time, we examine the solar and geomagnetic forcing that could also affect the equatorial TEC.

The EEJ and its wavelet spectrum are presented in Figures 4A,D, respectively. The spectrum reveals prominent quasi 6-day periodicity between DoY 253—283, and quasi 10-day periodicity between DoY 243—263. Periodicities around 2–3 days are discernible between DoY 253–293.

The Kp index and interplanetary electric field (IEF) are used to represent the geomagnetic forcing. As shown in Figures 4B,C, both experience periodic strengthening around DoY 218, 243, 273, 298, which is a manifestation of the well-known quasi 27-day solar rotation. At shorter period, the wavelet spectrums reveal significant quasi 6-day and quasi 14-day oscillation in the Kp index (Figure 4E), with the former enhancing strongly around DoY 213 and 243, and the later persisting throughout DoY 233—283. In contrast, the IEF exhibits a persistent quasi 10-day signal during DoY 243—303. The absence of the quasi-10 days signal in Kp index demonstrate that IEF and Kp may represent different physical processes and both should be considered when examining geomagnetic activity effects on the ionosphere.

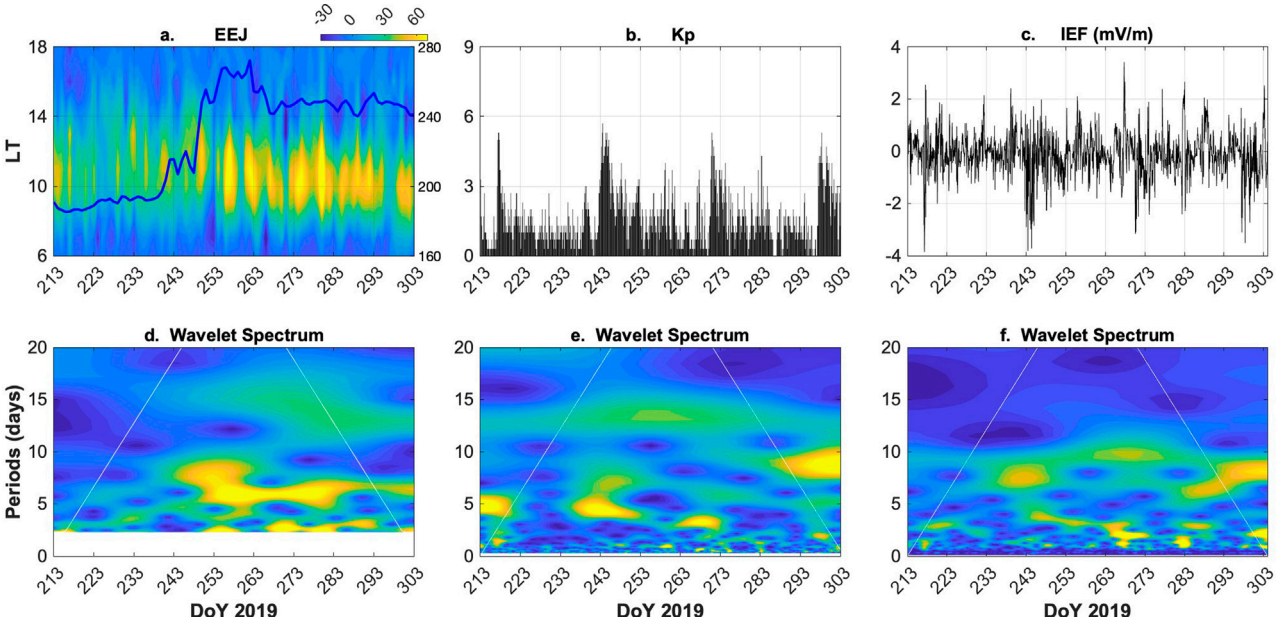

FIGURE 4
Top row: the equatorial electrojet (EEJ), Kp index, and the interplanetary electric field (IEF) during August 1—30 October 2019. Bottom row: the corresponding wavelet spectrum of top row. Note that panel Figure 4D is the wavelet spectrum of EEJ averaged over 10–14 LT.

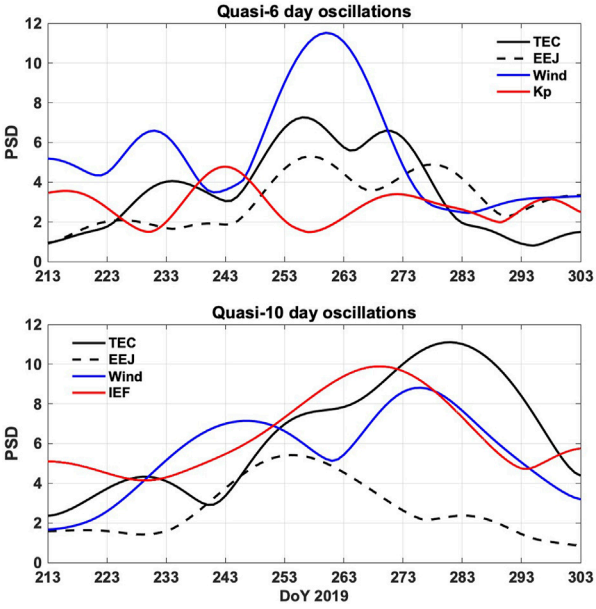

FIGURE 5
Upper: quasi-6 days oscillations in semidiurnal component of TEC at 15N, semidiurnal component of mesospheric zonal wind, EEJ and Kp index. Lower: quasi-10 days oscillations in diurnal component of TEC at 15N, diurnal component of mesospheric meridional wind, EEJ and IEF. Note that the PSDs are scaled arbitrarily to fit all parameters into one panel for easy comparison of their temporal variations but not for their absolute values.

We note that solar radiation represented by the F10.7 index during the corresponding period varied between 64 and 75 solar flux unit, but with no periodic oscillations of 6-day, 10-day, or 14-day (see supplement Figure). Therefore, the solar radiation cannot be the cause for TEC oscillations discussed in this study.

4 Discussions and Conclusion

The above analysis revealed prominent day-to-day variations of tides derived from ground-based TEC observations in Asian sector with major periodicities of ~14 and ~10 days in September–October, and ~6 days in September 2019. To explore their potential drivers, we examined periodic variability in mesosphere tides as forcing from below, in Kp index and IEF as forcing from above. In the following, we attempt attributions for these three periodicities.

First, the ~14-day periodicity in TEC is most likely driven by geomagnetic activity forcing represented by the Kp index. This attribution is straightforward as neither the mesospheric wind nor the IEF exhibited pronounced quasi 14-day signal. The timing of the enhanced signal in Kp during DoY 233–283 (see Figure 4E) also corresponds well with that in the TEC (see, e.g., Figure 2I). This Kp signal is likely a sub-harmonic of the ~27-day solar rotation.

Next, we examine the ~6- and ~10-day periodicities. These periodicities occurred in both the mesospheric tides and the Kp index (6-day) or IEF (10-day). To better elucidate their relation to TEC oscillations, we extract the quasi 6- and 10-day signals in these

parameters and compare their temporal evolution. The result is shown in Figure 5.

As shown in the upper panel, the enhancement of ~6-day oscillations in TEC between DOY 253–273 generally coincides with that in the EEJ and mesospheric wind. On the other hand, the ~6-day oscillation in the Kp index is rather weak during the same interval, thus making its contribution less likely. Consequently the ~6-day periodicity in TEC can be reasonably attributed to the mesospheric wind perturbations due to the SSW. Since the atmosphere-ionosphere coupling processes are largely dominated by tidal-driven electrodynamics, our tidal analysis strengthens the argument of the SSW origin of the ~6-day periodicity of TEC in previously reported studies (e.g., Lin et al, 2020; Yamazaki et al, 2020) (which did not examine the tides). The co-location of TEC and mesosphere wind measurements in the same longitude sector in our study demonstrate their close connection at regional scales.

The lower panel of Figure 5 shows the quasi 10-day oscillations in TEC, EEJ, wind and IEF. The prominent 10-day oscillation in TEC starts growing around DoY 243 and peaks around DoY 283. The ~10-day signal in IEF is strong during DoY 233–293, with its peak around DoY 273. The mesosphere wind also has a strong 10-day signal with peaks around DoY 243 and DoY 278. On the other hand, the EEJ only peaks around DoY 253, which is quite different from that of TEC. Since mesospheric wind affects the ionosphere TEC mainly via the wind dynamo that also affects the EEJ, the missing 10-day signal in EEJ after DoY 273 may suggest that the ~10-day signal in the mesosphere was not transmitted into the ionosphere wind dynamo in this longitudinal sector (we have no immediate explanation at the moment). Consequently, it seems reasonable to attribute the 10-day TEC signal before DoY 273 to Both the SSW-induced mesospheric wind perturbation and the IEF, but to IEF alone after DoY 273. Significant geomagnetic impacts on the TEC in September 2019 was also reported by Aa et al (2021). Wang et al (2021) attributed the TEC 10-day oscillation before DoY 270 totally to lower atmosphere forcing by the SSW, but did not consider geomagnetic forcing from above.

The mechanism of IEF affecting equatorial TECs could be via thermosphere wind perturbations driven by Joule heating and/or prompt penetration electric field (PPEF) (e.g., Anghel et al, 2007), though detailed processes warrant further study and is out of the scope of current work. For our current case, both processes may have contributed before DoY 273, while PPEF was probably missing afterwards as implied by the missing 10-day signal in EEJ after DoY 273. In any case, to quantify the relative contribution from geomagnetic activity forcing and lower atmosphere forcing, one would need to carry out numerical experiments similar to that done in Hagan et al (2015); Pedatella (2016); Siddiqui et al (2021). However, we note that to capture impacts of low geomagnetic activities on the ionosphere requires models to have both good representation of PPEF and high model sensitivity to low-level geomagnetic forcing. Both features are missing in currently available whole atmosphere models like WACCM-X, WAM and GAIA (Jin et al, 2011; Fang et al, 2018; Liu et al, 2018). The MAGE model that self-consistently couples the solar wind—magnetosphere-ionosphere-thermosphere may provide a more accurate representation of the PPEF in the near future (Pham et al, 2022).

Data availability statement

Publicly available datasets were analyzed in this study. This data can be found here: https://archive.iii.kyushu-u.ac.jp/public/ZX3QQA1Je4CAd04B84OAS-ll9UPxeM6CH42KnaRHsl9n.

Author contributions

HL initiated this study, analyzed the data and wrote up the manuscript. YO, KH, and TY provided the TEC, EEJ, and meteor wind data, respectively. All authors contributed to the interpretation of the results.

Funding

This work is supported by the JSPS KAKENHI grants 18H01270, 17KK0095, and JRPs-LEAD with DFG (JPJSJPR 20181602). KH was partially supported by the JSPS KAKENHI Grant Number 20H00197.

Acknowledgments

We thank M. Kogure for helping with part of data processing.

Conflict of interest

The authors declare that the research was conducted in the absence of any commercial or financial relationships that could be construed as a potential conflict of interest.

Publisher's note

References

Aa, E., Zhang, S.-R., Erickson, P. J., Coster, A. J., Goncharenko, L. P., Varney, R. H., et al. (2021). Salient midlatitude ionosphere-thermosphere disturbances associated with SAPS during a minor but geo-effective storm at deep solar minimum. *J. Geophys. Res. (Space Phys.* 126, e29509. doi:10.1029/2021JA029509

Anghel, A., Anderson, D., Maruyama, N., Chau, J., Yumoto, K., Bhattacharyya, A., et al. (2007). Interplanetary electric fields and their relationship to low-latitude electric fields under disturbed conditions. *J. Atmos. Solar-Terrestrial Phys.* 69, 1147–1159. doi:10.1016/j.jastp.2006.08.018

Cai, X., Burns, A. G., Wang, W., Qian, L., Solomon, S. C., Eastes, R. W., et al. (2021). Variations in thermosphere composition and ionosphere total electron content under geomagnetically quiet conditions at solar minimum. *Geophys. Res. Lett.* 48. doi:10.1029/2021gl093300

Fang, T.-W., Fuller-Rowell, T., Yudin, V., Matsuo, T., and Viereck, R. (2018). Quantifying the sources of ionosphere day-to-day variability. *J. Geophys. Res. (Space Phys.* 123, 9682–9696. doi:10.1029/2018JA025525

Gonchalenko, L., Harvey, L., Liu, H., and Pedatella, N. (2021). "Sudden stratospheric warming impacts on the ionosphere-thermosphere system: A review of recent progress," in *Space Physics and aeronomy collection volume 3: Ionosphere dynamics and applications, geophysical monograph 260*. Editors C. Huang and G. Lu (Washington, United States: American Geophysical Union).

Goncharenko, L. P., Harvey, V. L., Greer, K. R., Zhang, S. R., and Coster, A. J. (2020). Longitudinally dependent low-latitude ionospheric disturbances linked to the antarctic sudden stratospheric warming of september 2019. *J. Geophys. Res. (Space Phys.* 125, e28199. doi:10.1029/2020JA028199

Hagan, M. E., Hausler, K., Lu, G., Forbes, J. M., and Zhang, X. (2015). Upper thermospheric responses to forcing from above and below during 1-10 April 2010: Results from an ensemble of numerical simulations. *J. Geophys. Res. (Space Phys.* 120, 3160–3174. doi:10.1002/2014JA020706

He, M., Chau, J. L., Forbes, J. M., Thorsen, D., Li, G., Siddiqui, T. A., et al. (2020). Quasi-10-Day wave and semidiurnal tide nonlinear interactions during the southern hemispheric SSW 2019 observed in the northern hemispheric mesosphere. *Geophys. Res. Lett.* 47, e91453. doi:10.1029/2020GL091453

Jin, H., Miyoshi, Y., Fujiwara, H., Shinagawa, H., Terada, K., Terada, N., et al. (2011). Vertical connection from the tropospheric activities to the ionospheric longitudinal structure simulated by a new Earth's whole atmosphere-ionosphere coupled model. *J. Geophys. Res. (Space Phys.* 116, A01316. doi:10.1029/2010JA015925

Lin, J. T., Lin, C. H., Rajesh, P. K., Yue, J., Lin, C. Y., and Matsuo, T. (2020). Local-time and vertical characteristics of quasi-6-day oscillation in the ionosphere during the 2019 antarctic sudden stratospheric warming. *Geophys. Res. Lett.* 47, e90345. doi:10.1029/2020GL090345

Liu, H.-L., Bardeen, C. G., Foster, B. T., Lauritzen, P., Liu, J., Lu, G., et al. (2018). Development and validation of the whole atmosphere community climate model with thermosphere and ionosphere extension (WACCM-X 2.0). *J. Adv. Model. Earth Syst.* 10, 381–402. doi:10.1002/2017MS001232

Liu, H., Yamamoto, M., Tulasi Ram, S., Tsugawa, T., Otsuka, Y., Stolle, C., et al. (2011). Equatorial electrodynamics and neutral background in the Asian sector during the 2009 stratospheric sudden warming. *J. Geophys. Res. (Space Phys.* 116, A08308. doi:10.1029/2011JA016607

Liu, H., Yamazaki, Y., and Lei, J. (2021). "Day-to-day variability of the thermosphere and ionosphere," in *Space Physics and aeronomy collection volume 4: Upper atmosphere dynamics and energetics,Geophysical monograph 261*. Editors W. Wang and Y. Zhang (Washington, United States: American Geophysical Union).

Mo, X. H., and Zhang, D. H. (2020). Six-day periodic variation in equatorial ionization anomaly region. *J. Geophys. Res. (Space Phys.* 125, e28225. doi:10.1029/2020JA028225

Otsuka, Y., Ogawa, T., Saito, A., Tsugawa, T., Fukao, S., and Miyazaki, S. (2002). A new technique for mapping of total electron content using GPS network in Japan. *Earth, Planets Space* 54, 63–70. doi:10.1186/bf03352422

Pedatella, N. M. (2016). Impact of the lower atmosphere on the ionosphere response to a geomagnetic superstorm. *Geophys. Res. Lett.* 43, 9383–9389. doi:10.1002/2016GL070592

Pham, K. H., Zhang, B., Sorathia, K., Dang, T., Wang, W., Merkin, V., et al. (2022). Thermospheric density perturbations produced by traveling atmospheric disturbances during August 2005 storm. *J. Geophys. Res. (Space Phys.* 127. doi:10.1029/2021JA030071

Rusch, C. M., and Richmond, A. D. (1973). The relationship between the structure of the equatorial anomaly and the strength of the equatorial electrojet. *J. Atmos. Solar-Terrestrial Phys.* 35, 1171–1180. doi:10.1016/0021-9169(73)90013-5

Siddiqui, T. A., Yamazaki, Y., Stolle, C., Maute, A., Lastoviõcka, J., Edemskiy, I. K., et al. (2021). õ understanding the total electron content variability over europe during 2009 and 2019 SSWs. *J. Geophys. Res. (Space Phys.* 126, e28751. doi:10.1029/2020JA028751

Wang, J. C., Palo, S. E., Forbes, J. M., Marino, J., Moffat-Griffin, T., and Mitchell, N. J. (2021). Unusual quasi 10-day planetary wave activity and the ionospheric response during the 2019 southern hemisphere sudden stratospheric warming. *J. Geophys. Res. (Space Phys.* 126, e29286. doi:10.1029/2021JA029286

Yamazaki, Y., Matthias, V., Miyoshi, Y., Stolle, C., Siddiqui, T., Kervalishvili, G., et al. (2020). September 2019 antarctic sudden stratospheric warming: Quasi-6-Day wave burst and ionospheric effects. *Geophys. Res. Lett.* 47, e86577. doi:10.1029/2019GL086577

frontiers | Frontiers in Astronomy and Space Sciences

TYPE Original Research
PUBLISHED 25 May 2023
DOI 10.3389/fspas.2023.1193268

OPEN ACCESS

EDITED BY
Veronika Barta,
Institute of Earth Physics and Space Science (EPSS, ELKH), Hungary

REVIEWED BY
Zbysek Mosna,
Institute of Atmospheric Physics (ASCR), Czechia
Zhonghua Xu,
Virginia Tech, United States

*CORRESPONDENCE
L. C. A. Resende,
laysa.resende@inpe.br
laysa.resende@gmail.com

RECEIVED 24 March 2023
ACCEPTED 15 May 2023
PUBLISHED 25 May 2023

CITATION
Resende LCA, Zhu Y, Denardini CM, Chagas RAJ, Da Silva LA, Andrioli VF, Figueiredo CAO, Marchezi JP, Chen SS, Moro J, Silva RP, Li H, Wang C and Liu Z (2023), Analysis of the different physical mechanisms in the atypical sporadic E (Es) layer occurrence over a low latitude region in the Brazilian sector.
Front. Astron. Space Sci. 10:1193268.
doi: 10.3389/fspas.2023.1193268

Analysis of the different physical mechanisms in the atypical sporadic E (Es) layer occurrence over a low latitude region in the Brazilian sector

L. C. A. Resende[1,2]*, Y. Zhu[1,3], C. M. Denardini[2], R. A. J. Chagas[2], L. A. Da Silva[1,2], V. F. Andrioli[1,2], C. A. O. Figueiredo[2], J. P. Marchezi[4], S. S. Chen[2], J. Moro[1,5], R. P. Silva[2], H. Li[1], C. Wang[1] and Z. Liu[1]

[1]State Key Laboratory of Space Weather, NSSC/CAS, Beijing, China, [2]National Institute for Space Research—INPE, São José dos Campos, Brazil, [3]University of Chinese Academy of Sciences, Beijing, China, [4]Institute for the Study of Earth, Oceans, \& Space, University of New Hampshire, Durham, NH, United States, [5]Southern Space Coordination—COESU/INPE, Santa Maria, Brazil

We present a study about the atypical and spreading Sporadic E-layers (Es) observed in Digisonde data. We analyzed a set of days around space weather events from 2016 to 2018 over Cachoeira Paulista (CXP, 22.41°S, 45°W, dip ~35°), a low-latitude Brazilian station. The inhomogeneous Es layer is associated with the auroral-type Es layer (Es_a) occurrence in this region due to the presence of South American Magnetic Anomaly (SAMA). However, we also observe that the spreading Es layers occurred days before the magnetic storms or quiet times. Also, this specific type of Es layer has some different characteristics concerning the Es_a layer. We used data from the imager, satellite, and meteor radar to understand the dynamic processes acting in this Es layer formation. Our results lead us to believe that other mechanisms affect the Es layer development. We show evidence that the instabilities added to the wind shear mechanism can cause the atypical Es layers, such as Kelvin-Helmholtz instability (KHI). Finally, an important discovery of this work is that the spreading Es layer, mainly during quiet times, is not necessarily due to the particle precipitation due to the SAMA. We found that the wind shear can be turbulent, influencing the Es layer development. Lastly, our analysis better understood the Es layer behavior during quiet and disturbed times.

KEYWORDS

sporadic E layer, ionosphere, plasma instability, gravity waves, particle precipitation, South American magnetic anomaly

Highlights

- Digisonde data is used to study the spreading of Sporadic E-layers (Es) over Cachoeira Paulista, a low-latitude Brazilian station.
- The inhomogeneous Es layer also occurred days before the magnetic storms or quiet times, not associated with the particle precipitation due to the SAMA.
- The results show evidence that the instabilities added to the wind shear mechanism can cause the atypical Es layers, such as Kelvin-Helmholtz instability (KHI).

1 Introduction

Sporadic E layers (Es) are electron density increments located at 100–150 km in the ionosphere, composed mainly of metallic ions, such as Fe^+, Mg^+, Na^+, K^+, and Si^+ (Whitehead, 1961; Kopp, 1997; Mathews, 1998). They are classified into different types associated with lowercase letters, allowing us to distinguish the physical mechanism action in these Es layer development. The main mechanism refers to the vertical wind shear process (Haldoupis, 2011), occurring mainly at low and middle latitudes, in which the types "c" (cusp), "h" (high), and "l (low)/f" (flat) are found in Digisonde data (ionograms). At equatorial latitudes, it is observed the "q" (equatorial) type that happens due to the Equatorial Electrojet Current (EEJ) plasma instabilities, in specific the Gradient Drift instability (Type II irregularities) driven by the vertical polarization electric field. The other two Es layer categories are "a", associated with particle precipitation, and "s", due to the gravity waves. All details about these types can be found in Resende et al., (2013).

Atypical spreading and multiple Es layers can occur in low and middle latitudes ionograms. This Es layer behavior can be associated with other physical mechanism formations, such as disturbed electric fields. Resende et al., (2020) and Resende et al., (2021) detected anomalous Es layers over the Brazilian sector, Boa Vista (2.8°N, 60.7°W, dip ~18o) and São Luís (2.3°S, 44.2°W, dip ~8°), in which the disturbed electric fields during magnetic storms modified the Es layer structure in these regions. In fact, the electric field due to the disturbance dynamo effect (DDEF) caused the Es layer intensification over Boa Vista. Over São Luís, a transition station from equatorial to low latitude, there was an EEJ extension, causing instabilities during the magnetic storms.

The disturbed electric fields do not act at latitudes far from the geographic/magnetic equator (Resende et al., 2021). However, sometimes it is possible to observe a strong and spreading Es layer over the Brazilian sector. A geomagnetic anomaly known as South American Magnetic Anomaly (SAMA) is present in the low/midlatitude region of Brazil and it is characterized by a weak geomagnetic field intensity. Thus, these atypical Es layers are generally related to the particle precipitation mechanism due to the SAMA presence. Specifically, in some stations, as in Santa Maria (29.7°S, 53.8°W, dip ~ -37°) and Cachoeira Paulista (22.7°S, 45°W, dip ~35°), the auroral or Es_a layer occurred during geomagnetically disturbed times (Da Silva et al., 2022; Moro et al., 2022).

Kumar et al., (2009) studied the E-region field-aligned irregularities, named FAIs, at low latitudes using measurements of radar and ionosonde. The authors analyzed the relationship between the FAIs occurrence and Es layer frequency parameters. Although they did not conclude ultimately, the neutral winds play an important role in generating FAIs at low latitudes, forming atypical (spreading) Es layers in ionograms. Yan et al., (2021) recently showed a statistical characteristic of irregularities around 100 km at low-latitude stations over Chinese sites. Their work used the Hainan COherent Scatter Phased Array Radar (HCOPAR) and frequency parameters of the Es layer driven by Digisonde. Their results suggested that these irregularities occurred due to the Kelvin-Helmholtz instability (KHI) during the daytime. On the other hand, gradient drift instability in the low photoionization background creates unstable Es layers during the nighttime.

The electric field plays a small role in the Es layer development at middle and low latitudes, as mentioned in Whitehead (1961), Dagar et al., (1977), and Haldoupis (2011), being the wind shear is the main responsible to Es layer formation. Thus, the electric field effect can be neglected (Resende et al., 2017). Thus, it is a challenge to analyze the spreading and strength of Es layers during quiet periods over the Brazilian sector. Indeed, as the electric fields and the particle precipitation can be discarded in the Es layer formation during the quiet magnetic time over Cachoeira Paulista, the instability occurrence can be the answer in such cases. In middle latitudes, radar data show that unstable Es layers appear due to KHI (Ecklund et al., 1981; Chen et al., 2020; Yan et al., 2021). Their occurrence is associated with the gravity wave presence or winds with large amplitudes, causing complex structures at 100–110 km (Matsushita and Reddy, 1967). This instability can be seen in ionograms through the spreading in the Es layer (Resende et al., 2022).

Considering the above discussion, this work analyses the physical mechanism of these atypical Es layer formations on quiet and disturbed days, providing novel insights about their open questions on this subject. First, we analyzed a set of days around 5 magnetic storms at a low latitude station, Cachoeira Paulista (CXP). We performed an in-depth analysis of Es layer types and frequency parameters using Digisonde data. Afterward, we investigated the hiss waves inside the plasmasphere to discard the particle precipitation mechanism in the Es layer development. Finally, we include a study about the turbulence in the winds and the gravity wave occurrences. Thus, this analysis allowed us to discuss the physical phenomena, mainly during quiet periods, which is not much addressed in the literature, as shown in the following sections.

2 Data set and methodology

We used the data obtained from the Digisonde over CXP to analyze the Es layer behavior. Digisonde is a high-frequency radar that transmits waves from 1 to 30 MHz with a frequency step on 0.05 MHz for CXP and 10 or 15 min of time resolution (Reinisch et al., 2004). In this work, we used the fbEs (blanketing frequency), which refers to the frequency point in the upper ionospheric layer where the Es layer blocks the transmitted electromagnetic signal. We also used the ftEs (top frequency) characterized by the maximum frequency that the Es layer reached.

We process both frequencies (fbEs and ftEs) manually because there are differences between the automatic and real ionospheric profiles at low latitudes. Furthermore, we classified the Es layer types to see what the physical mechanism is acting along the day. As mentioned before, this classification is given in lowercase letters as "c" (cusp), "h" (high), and "l (low)/f" (flat) due to the winds, "s" (slant) refers to the gravity waves presence, "q" (equatorial) due to Gradient Drift instability, and "a" (auroral) due to the particle precipitation. More details about these types seen in ionograms are found in Conceição-Santos et al., 2019.

Our analysis is completed using the magnetic field power spectral density from the Electric and Magnetic Field Instrument Suite and Integrated Science (EMFISIS) onboard Van Allen Probe A

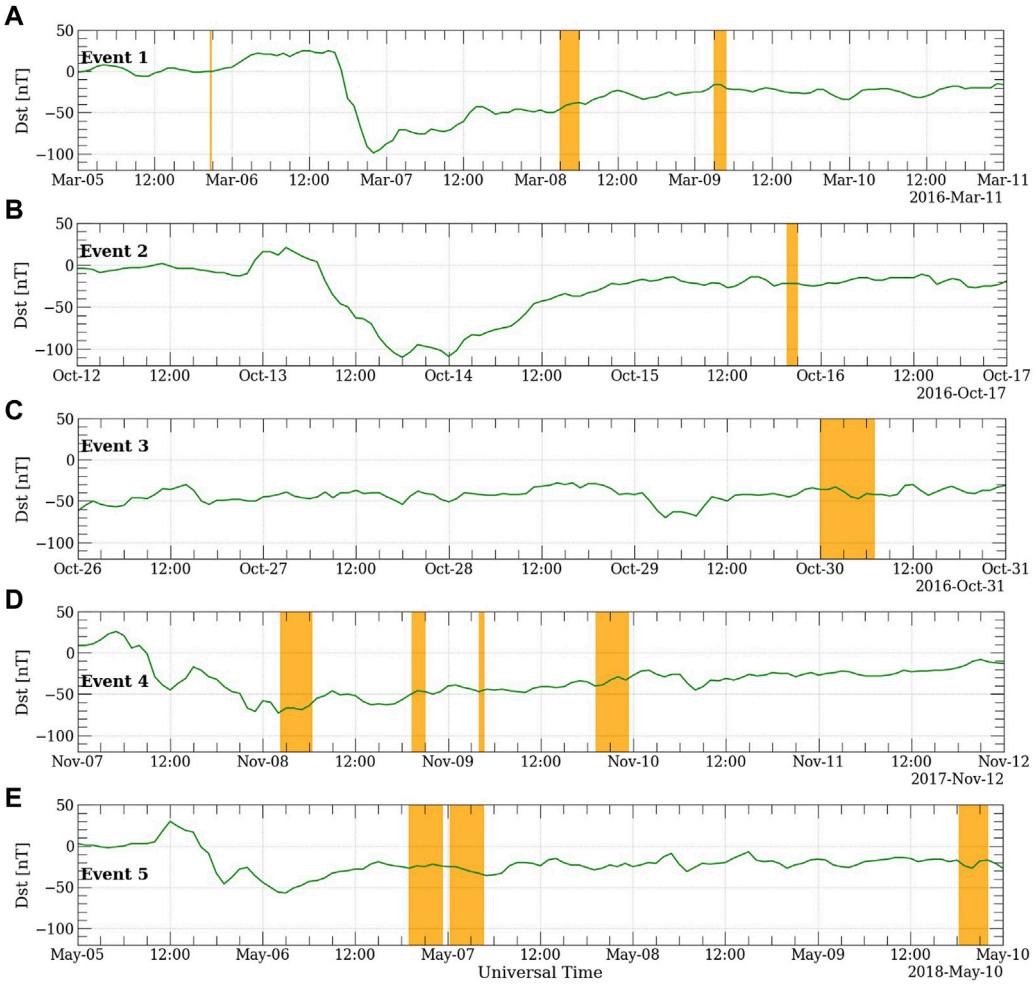

FIGURE 1
The Dst index for the events **(A)** March 05–10, 2016, **(B)** October 12–17, 2016, **(C)** March 26–31, 2016, **(D)** November 07–12, 2017, and **(E)** May 05–10, 2018, over CXP.

and B (Kletzing et al., 2013; Mauk et al., 2012). We used this instrument to detect the hiss waves inside the plasmasphere. Our purpose is to verify the low-energy electron precipitation (from 0.5 keV to tens of keV) through the pitch angle scattering mechanism driven by hiss waves (Da Silva et al., 2022). We concentrate only on the Van Allen Probes' data when the satellites are at the perigee.

We also used the winds from 80 to 100 km acquired from the All-Sky Interferometric Meteor Radar (SKiYMET) installed at CXP. This type of radar emits RF pulses at 35.24 MHz and receives the echoes on five receiver antennas. This radar has a 2 km and 1 h height and time resolution, respectively. The echoes are separated in height/time bins, providing the total, meridional, and zonal components of the horizontal winds. The radar system description is found in Hocking and Thayaparan (1997); Hocking et al., (2001). Lastly, the all-sky airglow imager in the OH band (720–910 nm, 86 km) or OI (557.7 nm, emission altitude 96 km) is used to confirm the gravity wave occurrences over CXP. This equipment consists of a charge-coupled device (CCD) camera, an interference filter, and a fish-eye lens. The camera uses a fast all-sky telecentric lens system that enables high signal-to-noise ratio images of the wave structure. More details are found in Medeiros et al., (2004).

3 Results and discussions

3.1 Interplanetary medium conditions of the studied events

We chose 5 events where the atypical and spreading Es layer were identified over CXP between 2016 and 2018. These events occurred around the geomagnetic storm periods but not necessarily on disturbed days. Figure 1 shows the Disturbance storm time (Dst) variation for the following periods analyzed in this work: (a) March 05–10, 2016, (b) October 12–17, 2016, (c) March 26–31, 2016, (d) November 07–12, 2017, and (e) May 05–10, 2018. Except for the event on May 2018 (panel e), caused by high-solar wind speed stream (HSS), the other events were caused by coronal mass ejection (CME).

TABLE 1 List of the characteristics of selected events from 2016 to 2018 used in this analysis over CXP. We have the magnetic storm's day, the Dst minimum, the day of the atypical Es layer occurrence, the hour of their occurrence and the condition of the period.

Magnetic storm	Minimum Dst (nT)	Day of Es layer occurrence	Hour of occurrence	Condition
06 March 2016	−98	05 March 2016	2040–2050	Quiet
		08 March 2016	0300–0600	Quiet
		09 March 2016	0300–0450	Quiet
October 13, 2016	−104	15 October 2016	1940–2100	Quiet
29 October 2016	−64	30 October 2016	0000–0700	Disturbed
07 November 2017	−71	08 November 2017	0220–0620	Disturbed
		08 November 2017	1920–2100	Disturbed
		09 November 2017	0400–0440	Disturbed
		09 November 2017	1910–2320	Quiet
06 May 2018	−56	06 May 2018	1900–2320	Quiet
		07 May 2018	0020–0440	Quiet
		08 May 2018	1820–2200	Quiet

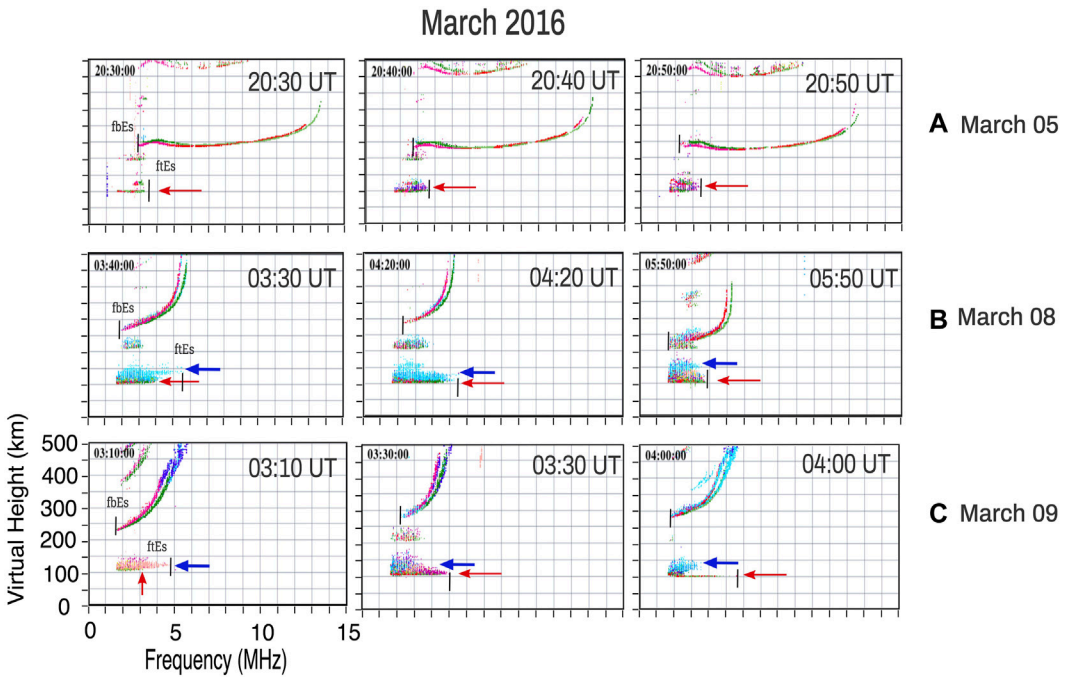

FIGURE 2
Ionograms at CXP **(A)** from 2030 UT to 2050 UT on 05 March, 2016, **(B)** collected at hours 0330 UT, 0420 UT, and 0550 UT on 08 March 2016, **(C)** collected at hours 0310 UT, 0330 UT, and 0400 UT on 09 March 2016.

It is well-known that during magnetic storms, disturbed electric fields can influence the ionosphere through the Prompt Penetration Electric Field (PPEF) (Forbes et al., 1995) or by the Disturbance Dynamo Electric Field (DDEF) (Blanc and Richmond, 1980). However, as shown by Resende et al., (2021), these disturbed electric fields are not capable of causing some influence in the Es layer over CXP. Thus, in this work, we only want to show that the days of the atypical Es layer presence are around the magnetic storm, occurring on both quiet and disturbed days. For this reason, we do not present other interplanetary medium parameters.

Table 1 shows the day of geomagnetic storm onset, the level of the magnetic storm represented by the minimum value reached by the Dst index, the day of the atypical Es layer occurrence, the hour (in universal time), and the condition of the period (quiet or

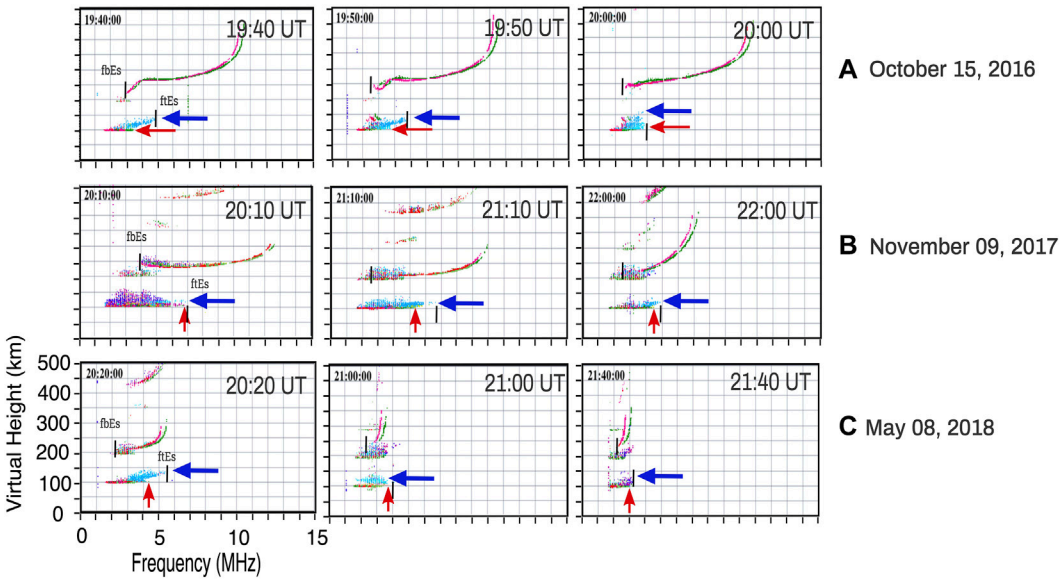

FIGURE 3
Some selected ionograms at CXP for **(A)** 1940 UT, 1950 UT, and 2000 UT on 15 October 2016, **(B)** 2010 UT, 2110 UT, and 2200 UT on 09 November 2017, **(C)** 2020 UT, 2100 UT, and 2140 UT on 08 May 2018.

disturbed). The Dst threshold used to classify whether the period is quiet or disturbed is −30 nT. Thus, the days with Dst lower than −30 nT are assumed to be disturbed in this study. Here, it is possible to clearly see that the Es layer spreading also occurred in quiet periods. In most cases, the atypical Es layer appears during the recovery magnetic storm phase, which is intriguing since the other Es layer physical formation mechanics also acted in this period. We discuss this behavior later on.

3.2 The anomalous Es layers occurrence over CXP

The significant modifications in the Es layer electron density distribution occurred in the periods shown in Table 1. Figure 2 shows some ionograms for (a) March 05, (b) March 08, and (c) March 09. The fbEs and the ftEs are shown in vertical black lines. We observe a spread Es layer (red and blue arrows) in all ionograms. The main characteristic here is the low values of the fbEs, which means that the Es layer did not block the F region significantly.

We believe that the wind shear mechanism is acting in all the Es layer development shown in Figure 2 (represented by red arrows). The background and second reflection trace in ionograms consolidates this statement. On March 05, 2016, an Es layer of the "c" type developed around 115 km beyond the spreading Es layer at 2050 UT. On March 08 and 09, 2016, we noticed a slant Es layer (blue arrow), more expressive at 0330 UT on March 08 and 0400 UT on March 09. This specific type, called "s", is associated with the gravity waves presence (Cohen et al., 1962).

Another important point is that these events occurred in periods considered quiet times, although March 08 and 09, 2016, are in the recovery magnetic storm phase. In fact, this spread Es layer can be attributed to the Es_a (auroral) layer during the recovery magnetic storm phase. As discussed by Da Silva et al., (2022) and Moro et al., (2022), the particle precipitation mechanism can develop the Es_a layer over the Brazilian sector due to the SAMA presence. The Es_a layer signatures are expected during the recovery magnetic storm phase over Santa Maria and Cachoeira Paulista, which is discussed in the following section.

The same spreading Es layer behavior occurred in the other events. Figure 3 presents some selected ionograms on (a) 15 October 2016, (b) 09 November 2017, and (c) May 08, 2018. In these ionograms, the fbEs also have low values (fbEs $\leq$ 3 MHz). The ftEs was lower than 7 MHz. The Es_s presence is also observed over CXP (red arrow).

The other case in which the Es layer over CXP suffered a significant modification was on 30 October 2016. Figure 4 shows the ionogram sequences of these Es layers over CXP between 0330 UT and 0610 UT intervals. We notice that the Es_s is present between 0430 UT and 0450 UT. Also, the ftEs reached values around 7 MHz at 0410 UT. In this specific ionogram, it is plausible that competition is occurring between the Es layer formation mechanisms, such as wind shear, particle precipitation, and instabilities. The following section shows the particle precipitation's role in these events.

3.3 Particle precipitation analysis

The reason that intrigues us about these events is that the spread Es layer has two different characteristics to the auroral trace, such as: (1) the spread occurrence during quiet periods (Dst larger than −30 nT) and (2) the inclination of the trace in some cases, showing the gravity waves presence. Thus, one important step of this work is to discard the particle precipitation mechanism. In this context, we examined the AE index and particle dynamics in the inner radiation belt.

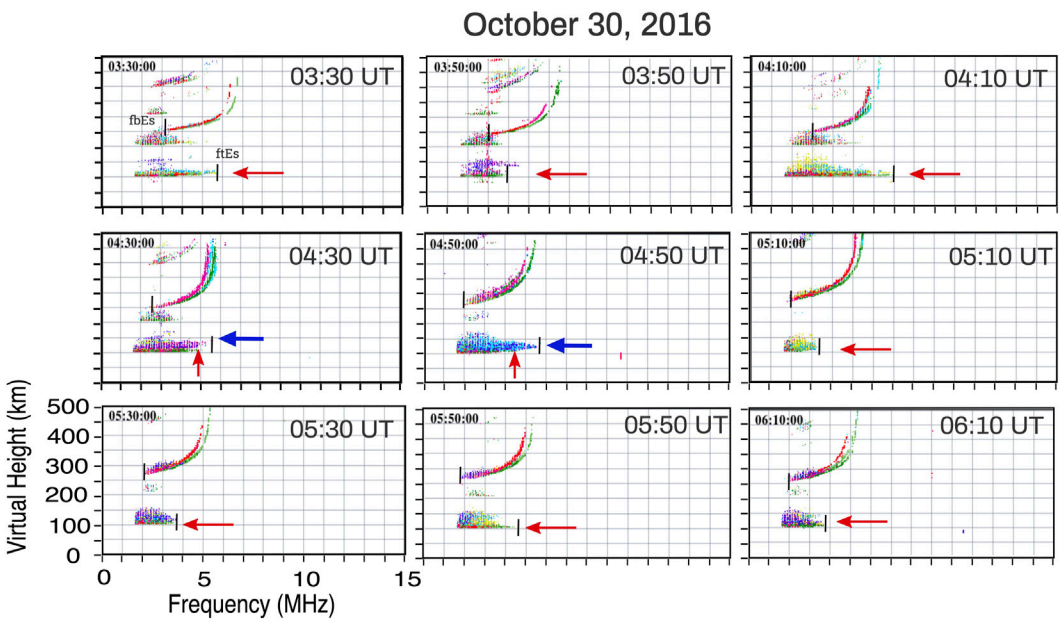

FIGURE 4
Ionograms at CXP from 0330 UT to 06100 UT for each 20 min on 30 October 2016.

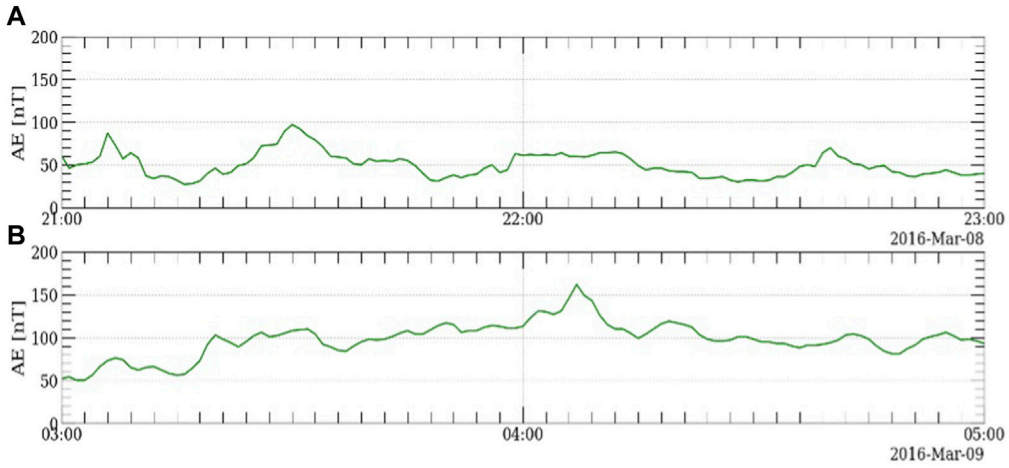

FIGURE 5
AE index on 08 March 2016, between 2100 UT and 2300 UT upper-**(A)** and between 0300 UT and 0500 UT bottom-**(B)** on 09 March 2016.

Figure 5 shows the AE index on 08 March 2016, between 2100 UT and 2300 UT (upper -a) and between 0300 UT and 0500 UT (bottom -b) on 09 March 2016, as used as an example. In general, the AE index shows low values in these hours, not reaching 150 nT most of the time. A short period (after 04:00 UT) that the AE was more extensive than 150 nT. This means that the entry of particles into the polar ionosphere and, consequently, their transport toward the low/equatorial ionosphere is not visible in this period. Thus, particle precipitation is an unlikely mechanism in these Es layer development. In other cases of Table 1, the AE is following the same pattern with low values, except on 30 October 2016.

To confirm that these spreading Es layer does not correlate with the particle precipitation, we show Figure 6. In this figure, the Power Spectral Density (PSD) of the magnetic field (Bw) is presented during the short times on March 05, 2016 (panel a), 08 March 2018 (panel b), and March 09 (panel c). We concentrate on the period that the spreading Es layer was observed. Red, yellow, black, and blue lines represent 0.9 fce, 0.5 fce, 0.1 fce, and total electron density, respectively. The purpose is to detect the hiss waves close to the perigee (at the inner radiation belt), that are responsible for causing the particle precipitation into the atmosphere over the SAMA region. This figure shows that the PSD of the hiss waves is

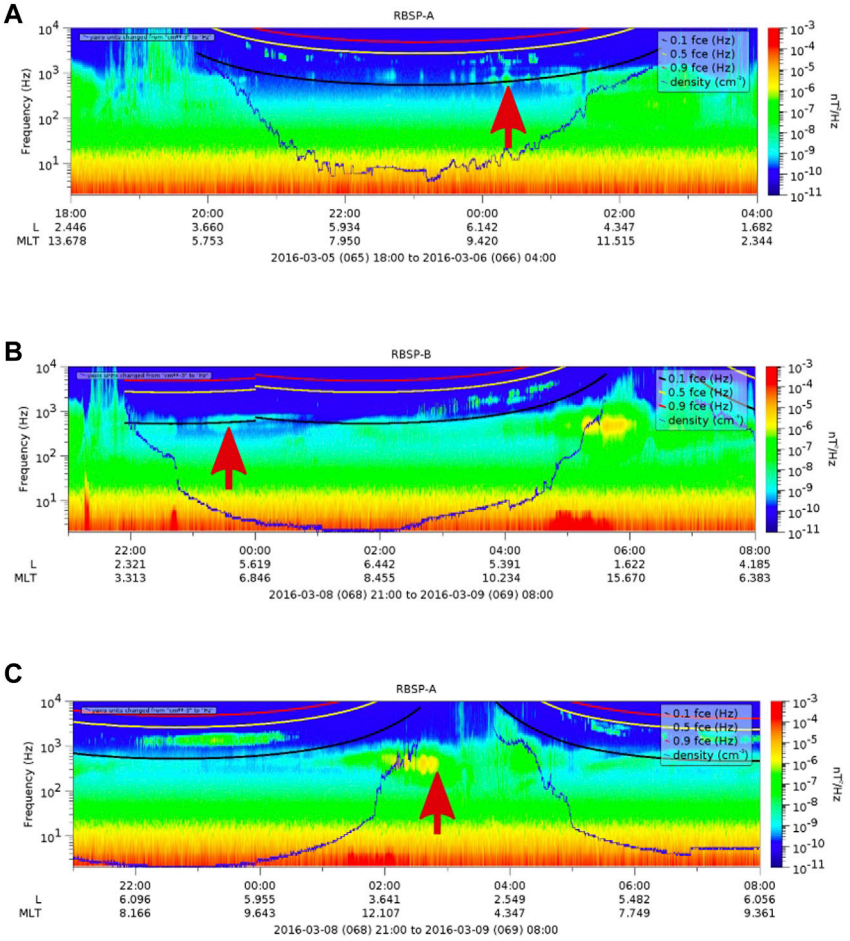

FIGURE 6
Power spectral density of the magnetic field from EMFISIS instrument onboard Van Allen Probes on March 05, 2016 **(A)**, 08 March 2018 **(B)**, and March 09 **(C)**.

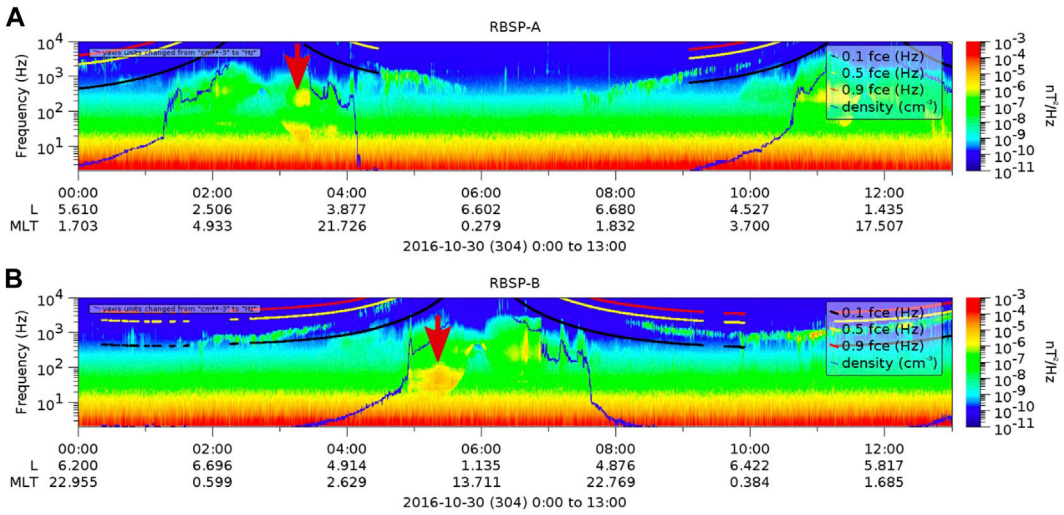

FIGURE 7
Power spectral density of the magnetic field from EMFISIS instrument onboard Van Allen Probe **(A)** and **(B)** on 30 October 2016.

considerably low ($\leq 10^{-7}$ nT^2/Hz-red arrows) during these three quiet periods. The literature (Da Silva et al., 2022; Moro et al., 2022) shows that the power spectral density of the hiss waves able to cause the low-energy electron precipitation (tens of keV) over the SAMA region is $\geq 10^{-5}$ nT^2/Hz. Therefore, the low PSD of the hiss waves during these quiet periods ($<10^{-7}$ nT^2/Hz) may not be efficient in causing the low-energy electron precipitation (from 0.5 keV to tens of keV) over the SAMA region. The other cases also presented low values in PSD of the hiss waves ($\leq 10^{-7}$ nT^2/Hz) (not shown here).

The exception occurred on 30 October 2016, in which it is possible to observe that the hiss wave PSD (~10^{-4} nT^2/Hz) (Figure 7) is similar to the results discussed by Da Silva et al., (2022). This value is enough to allow low-energy electron precipitation (from 0.5 keV to tens of keV) caused by hiss waves over the SAMA region. In this case, the AE reached values higher than 500 nT. Here, we intend to show that the plasmaspheric hiss waves inside the inner radiation belt reached significant values, and the particle precipitation in the SAMA region can occur in this event.

Therefore, we proposed here that the spreading Es layer can occur due to other physical mechanisms than particle precipitation due to the SAMA in most cases. Evidence of low values of the power spectral density of the hiss waves and AE index confirms this statement. Additionally, although the event on 30 October 2016, can have particle precipitation influence, we notice the gravity wave presence (Es_s occurrence). Thus, we believe that there are competing physics mechanisms in the Es layer formation in this event.

3.4 The possible instability action in the Es layer development

One of the possibilities of these spreading Es layer occurrences is the instability formation that can affect the wind shear. In other words, the Es layer may be formed initially by wind shear, and the environment becomes unstable due to gravity waves, creating inhomogeneous layers in ionograms. In this context, the Kelvin-Helmholtz instability (KHI) stands out as one of the most classical instabilities in fluid mechanics. These instability billows are triggered by unstable winds or gravity waves (Yan et al., 2021).

Another instability that can occur is Gradient Drift instability (GDI), which has an initial condition, the polarization electric field produced by a Hall current, and the density gradient in the same vertical direction (Rastogi 1972). The GDI is common in equatorial regions, where the Electrojet Equatorial Current (EEJ) presence creates favorable circumstances for their occurrence. Resende et al., (2016) showed the effect of this irregularity in the Es layer over the Brazilian sector. In their results, the authors mentioned that this instability depends on the strong electric field, which is found in the EEJ. Thus, the GDI is responsible for the equatorial Es layer (Es_q) in stations near the magnetic equator.

Although some authors have studied this type of instability at mid-latitudes [see Rosado-Román et al., 2004 and references therein], the GDI effect occurs around sunset because the electric field is stronger (around 3 mV/m). However, the layers associated with this irregularity were only observed in data from radar and rockets and did not last long. Resende et al., (2021) mention that the electric field does not influence the Es layer behavior over Cachoeira Paulista. For this reason, we believe that the most probable mechanism that acted in the atypical Es layer is the KHI.

The first evidence of the instabilities in the ionospheric plasma is the low values of the fbEs, meaning that the upper region above the Es layer has not been blocked. Table 2 shows the difference between the ftEs and fbEs (ftEs-fbEs) during the spreading Es layer occurrence. We present the maximum and minimum differences within the period studied.

In general, the differences between the frequency parameters show that the winds have a secondary role in the Es layer development in most cases. The low values of the ftEs-fbEs mean that the upper region is blocked. On the other hands, the high values of these differences mean that the Es layers have not blocked the upper layer. Thus, the wind shear that is the main mechanism to form denser layers could be stronger in such hours. The Es layer can be also formed by other mechanisms such as instabilities, particle precipitation, and gravity waves. However, the Es layers formed by these other mechanisms do not absorb the digosonde signal, from upper ionosphere layers, as those denser layers formed by wind shear. This is an indication that irregularities can be present. The minimum values of the ftEs-fbEs observed in our events analyzed here were higher than 1, except on 30 October 2018. Therefore, our results showed an indication that the unstable Es layer in the ionograms profile over CXP can be due to the instabilities since the particle precipitation seems to have influenced only the event on 30 October 2018.

The instability due to the winds or gravity waves is the most probable cause of this unusual Es layer behavior. We used the SKiYMET data for zonal and meridional winds to analyze if the winds were unstable. The wind measurements were interpolated to obtain a sample interval of 1 min. Afterward, we obtained the energy spectrum E(k) through Fourier transformation. Hence, we verified whether the result follows the −5/3 Kolmogorov spectrum prediction for turbulent flows. If this behavior happens, the winds are considered turbulent. All the details about the Kolmogorov technique are given by Calif et al., (2016).

Figure 8 shows the previous analysis results using the SKiYMET data for the zonal (right) and meridional (left) wind components on March 05–06, 2016, and October 29–30, 2016 (blue line). We choose the height of 99 km, which is the typical altitude of the Es layer occurrence. We also compared the results to the −5/3 Kolmogorov spectrum, plotted in orange in these graphs. The wind speed sampling step is 1 h due to the limitations of the technique and equipment used to obtain the data. We interpolated the values using a cubic spline to 1 min to.

1. Use the existing, validated FFT algorithms available;
2. Fill minor gaps in the data; and
3. Slightly smooth the output due to the signal characteristics.

Although this procedure can change the spectrum in higher frequencies, we analyzed only the frequencies up to $10^{(-3.5)}$ Hz. This region corresponds to periods of roughly 1 h, which matches the equipment sampling rate. Hence, the interpolation used in this work does not significantly modify the spectrum in the region we are interested in.

The wind components spectra demonstrate an unstable behavior for the frequencies between 10^{-5} and 10^{-4} on March

TABLE 2 Maximum and minimum differences of the *ft*Es and *fb*Es parameters of the period shown in Table 1.

Day of occurrence	Hour of occurrence	Maximum/Minimum ftEs-fbEs (MHz)
05 March 2016	2040–2050	2.49/1.14
08 March 2016	2150–2220	4.37/1.23
09 March 2016	0300–0450	3.29/1.18
15 October 2016	1940–2100	2.26/1.02
30 October 2016	0000–0700	4.26/0.82
08 November 2017	0220–0620	4.25/1.07
08 November 2017	1920–2100	4.47/1.49
09 November 2017	0400–0440	2.67/1.34
09 November 2017	1910–2320	3.25/1.05
06 May 2018	1900–2320	3.75/1.08
07 May 2018	0020–0440	5.00/1.10
08 May 2018	1820–2200	3.98/1.16

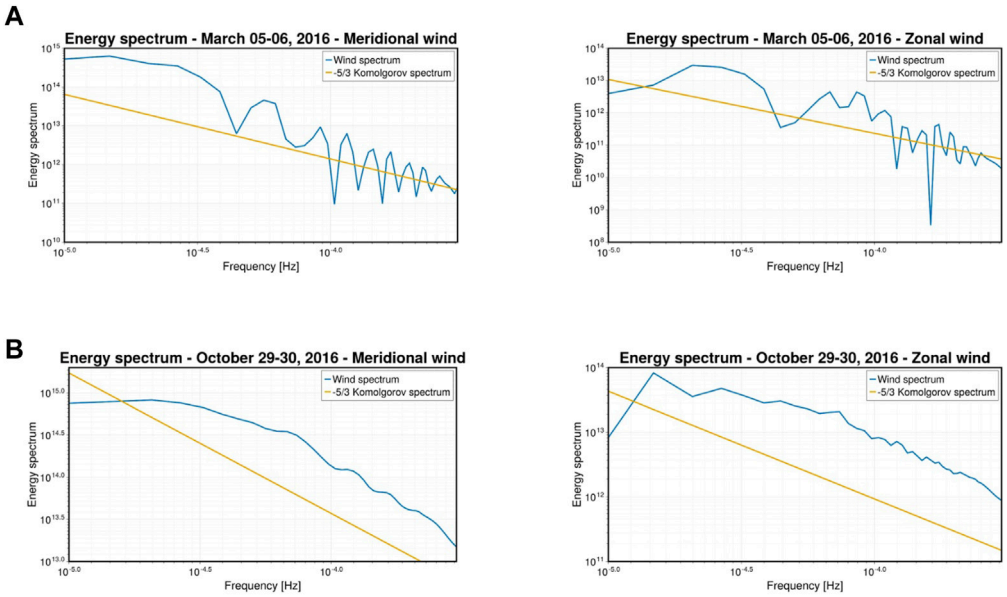

FIGURE 8
The Fourier power spectral densities of the SKiYMET data for the meridional (upper) and zonal (below) components on March 05–06, 2016 **(A)**, and October 29–30, 2016 **(B)**, in the blue line. The −5/3 Kolmogorov spectrum given in the orange line in these graphs.

05–06, 2016, as seen in Figure 8. Notice that this result was found close to the −5/3 Kolmogorov value. This fact means that the wind is turbulent at this height during this period. However, in the specific case of October 29–30, 2016, the components of the winds are not oscillating, and the power spectral density is not so close to the −5/3 Kolmogorov value. In other words, the wind does not appear to be turbulent.

This analysis provides clear evidence that the spreading Es layer over a low latitude station can occur due to the instabilities. The most probable is the KHI, which is driven by shear flow and is common in the atmosphere (Ecklund et al., 1981; Chen et al., 2020). Using simulations, Wu et al., (2022) analyzed the KHI in the middle and low Es layers. The simulations presented multiple striation structures in the Es layer. The authors found that the polarization electric field is induced in the horizontal structure of the sporadic E (Es) layer, and it is an initial condition to grow up the KHI or GDI.

The KHI mechanism in the Es layer development, mainly in the low latitude regions, has not been widely studied yet. Bernhardt

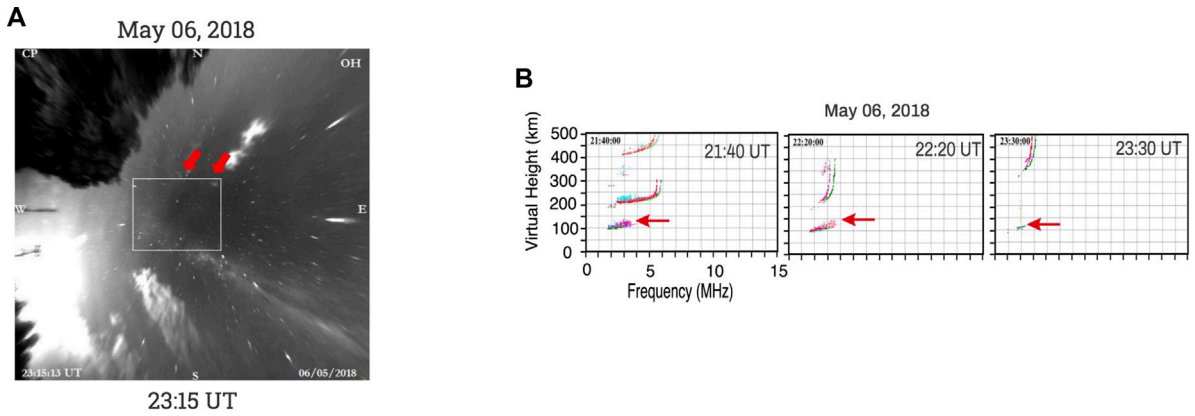

FIGURE 9
The OH images showing the gravity waves presence at 2315 UT on 06 May 2018 **(A)**, and the Es_s layer in ionograms **(B)** in the nighttime period on 06 May 2018.

(2002) studied the KHI effect driven by wind shear to explain the unstable structures in the Es layer. They used coupled models of the irregularities generated by sheared neutral winds and KHI billows in the Es layer between 100–120 km. The simulations indicated that the KHI could significantly impact the sporadic-E layer structures. Additionally, Bernhardt (2002) concluded that a complex evolution of the Es layer from the KHI and other improvements in the model is necessary to answer the real instability role in developing these unstable Es layers.

Liu et al., (2022) analyze the Es layer behavior using the Digisonde data applying a technique called frequency domain interferometry (FDI) over Wuhan, China (114°E, 30°N). The FDI allowed them to observe the inhomogeneous Es layer occurrence in such station. The complex structure of the Es layer found by the authors can be associated with instability or gravity wave modulation. One plausible explanation is the KHI presence in the Es layer formation that is caused by the strong shear of the neutral background wind.

Several authors mentioned that gravity waves could trigger the instabilities besides the winds. Unfortunately, the airglow images are restricted to clear skies. Therefore, among the analyzed events, only one presents good images. Figure 9 shows the OH images on 06 May 2018, at 2315 UT (panel a). The white square with red arrows means the gravity waves presence. In fact, we observed the clear gravity wave propagation for the entire night on May 06 and 07, 2018. Panel b of Figure 9 shows the Es_s layer presence in ionograms during the nighttime when we observe the gravity waves in imager data.

The Es_s is associated with the gravity wave mechanism, and it is characterized by a trace that grows continuously in frequency and emerges from another type of Es trace, as shown in red arrows. This specific Es layer type is not common in the Brazilian sector, as shown in Conceição-Santos et al., (2019) and Moro et al., (2022). We notice that the Es_s layer was observed in some hours for all events mentioned in Table 1. Thus, there is a possibility that the gravity waves may have a precursor to the growth of instability.

Therefore, an important discovery of this work is that the spreading Es layer, mainly during quiet times, is not necessarily due to the particle precipitation due to the SAMA presence. We found that the wind shear can be turbulent, influencing the Es layer development. Lastly, further research is necessary to affirm what is the exact instability that acts on the Es layer formation.

4 Conclusion

We study the atypical and spreading Es layer over CXP in days before, during, and after the magnetic storms from 2016 to 2018. We analyzed the Digisonde data, imager, satellite, and meteor radar to understand the dynamic formation processes of these inhomogeneous Es layers.

The significant modifications in the Es layer electron density distribution were observed in ionograms on days before and after the magnetic storm. The main characteristic is the low values of the fbEs, which means that the Es layer does not block the F region significantly. In fact, the high difference between the ftEs and fbEs (ftEs-fbEs) during the spreading Es layer occurrence indicated that the irregularities could be present.

The inhomogeneous Es layer is associated with the Es_a layer over CXP due to SAMA. However, we also observe that the spreading Es layers occurred in days before the magnetic storms or quiet times. We examined the AE index and particle dynamics in the inner radiation belt to discard the particle precipitation mechanism. Our results showed a low power spectral density of the hiss waves in these events ($<10^{-7}$ nT^2/Hz), inefficiently causing electron precipitation over the SAMA region.

The exception was on 30 October 2016. In this case, the spreading Es layer occurred in hours when AE was higher than 500 nT. Also, the power spectral density of the hiss waves was ~10^{-4} nT^2/Hz, similar to the previous studies about the Es_a layer formation. Therefore, this value is enough to cause low-energy electron precipitation (from 0.5 keV to tens of keV) by hiss waves over the SAMA region.

One of the possibilities of these spreading Es layer occurrences is the instability formation that can affect the wind shear. In other words, the Es layer may be formed initially by wind shear, and the environment

becomes unstable due to the electric field or gravity waves, creating inhomogeneous layers in ionograms. We used the SKiYMET data for zonal and meridional winds to analyze if the winds were unstable. The temporal resolution of these wind data is 1 h. As no other wind data is available, a linear interpolation was performed every minute to visualize whether the wind could have turbulence. The analysis is not so impaired as we only use measurements between 80 and 100 km.

Using these winds data, we compute energy spectrum E(k) to verify the turbulence in the winds. In fact, we analyzed whether the power spectral densities are close to the −5/3 Kolmogorov spectrum. In almost all events, the wind components spectra were close to the −5/3 Kolmogorov value. This fact means that the wind is turbulent. However, in the specific case of 30 October 2016, the wind energy spectrum components were not oscillating, and the power spectral density is not so close to the −5/3 Kolmogorov value.

The spreading Es layer observed in our data has an inclined trace in some hours, the Es_s layer. This Es layer type is associated with the gravity wave mechanism. Several authors mentioned that gravity waves could trigger the instabilities besides the winds. The OH emission in airglow images shows a gravity wave propagation on May 06 and 07, 2018. At the same hours, we observe the Es_s layer presence in ionograms. Thus, the presence of gravity waves may have been a trigger for the instability occurrence.

Finally, an important discovery of this work is that the spreading Es layer, mainly during quiet times, is not necessarily formed by the particle precipitation due to the SAMA. We found that the wind shear can be turbulent, influencing the Es layer development and contributing significantly to our understanding of the different mechanism actions in the atypical Es layer. However, further research is necessary to conclude precisely what instability caused these inhomogeneous Es layers over CXP.

Data availability statement

The datasets presented in this study can be found in online repositories. The names of the repository/repositories and accession number(s) can be found below: http://www2.inpe.br/climaespacial/portal/en/.

Author contributions

LR, YZ, CD, and LD contributed to the conception and design of the study. LR, VA, LD, and CF organized the database. JM and SC analyzed the interplanetary medium conditions and magnetospheric conditions. LR, JM, RS, SC, CW, HL, ZL, and CF interpreted the ionospheric data. RC help in the mathematical tools. LR, LD, and JM analyzed the Atmospheric ionization over SAMA. LR wrote the first draft of the manuscript. All authors contributed to the article and approved the submitted version.

Funding

This research was also supported by the National Natural Science Foundation of China (42074201 and 41674145), by the International Partnership Program of Chinese Academy of Sciences (grants 183311KYSB20200003 and 183311KYSB20200017).

Acknowledgments

LR would like to thank the China-Brazil Joint Laboratory for Space Weather (CBJLSW), National Space Science Center (NSSC), Chinese Academy of Sciences (CAS) for supporting her postdoctoral. CD thanks CNPq/MCTI, grant 03121/2014-9. SC and RS thanks CNPq/MCTI (grants 303643/2017-0 and 300849/2023-0). VA, LD, and JM would like to thank the CBJLSW/NSSC/CAS for supporting their postdoctoral. SC thanks CAPES/MEC (grant 88887.362982/2019-00). The authors thank the OMNIWEB for providing AE and Dst parameters used in the classification of the days. The Digisonde data from Cachoeira Paulista, imager data, and wind data can be downloaded upon registration at the Embrace webpage from INPE Space Weather Program in the following link: http://www2.inpe.br/climaespacial/portal/en/.

Conflict of interest

The authors declare that the research was conducted in the absence of any commercial or financial relationships that could be construed as a potential conflict of interest.

Publisher's note

References

Bernhardt, P. A. (2002). The modulation of sporadic-E layers by Kelvin–Helmholtz billows in the neutral atmosphere. *J. Atmos. Solar-Terrestrial Phys.* 64 (12-14), 1487–1504. doi:10.1016/S1364-6826(02)00086-X

Blanc, M., and Richmond, A. D. (1980). The ionospheric disturbance dynamo. *J. Geophys. Res. Space Phys.* 85 (4), 1669–1686. doi:10.1029/JA085iA04p01669

Calif, R., Schmitt, F., and Medina, O. (2016). "−5/3 Kolmogorov turbulent behavior and intermittent sustainable energies," in *Sustainable energy - technological issues, applications and case studies* (London, UK: Intechopen). doi:10.5772/106341

Chen, G., Wang, Z., Jin, H., Yan, C., Zhang, S., Feng, J., et al. (2020). A case study of the daytime intense radar backscatter and strong ionospheric scintillation related to the low-latitude E-region irregularities. *J. Geophys. Res. Space Phys.* 125, e2019JA027532. doi:10.1029/2019JA027532

Cohen, R., Calvert, W., and Bowles, K. L. (1962). On the nature of equatorial slant sporadic*E. J. Geophys. Res. Space Phys.* 67, 965–972. doi:10.1029/JZ067i003p00965

Conceiçãõ-Santos, F., Muella, M. T. A. H., Resende, L. C. A., Fagundes, P. R., Andrioli, V. F., Batista, P. P., et al.(2019). Occurrence and modeling examination of sporadic-E

layers in the region of the south America (atlantic) magnetic anomaly. *J. Geophys. Res. Space Phys.* 124 (11), 9676–9694. doi:10.1029/2018JA026397

Da Silva, L. A., Shi, J., Resende, L. C. A., Agapitov, O. V., AlvesBatistaArras, L. R. I. S. C., Vieira, L. E., et al. (2022). High-energy electron flux enhancement pattern in the outer radiation belt in response to the alfvénic fluctuations within high-speed solar wind stream: A statistical analysis. *J. Geophys. Research-Space Phys.* 126. doi:10.1029/2021ja029363

Dagar, R., Verma, P., Napgal, O. P., and Setty, C. S. G. K. (1977). The relative effects of the electric fields and neutral winds on the formation of the equatorial sporadic layers. *Ann. Geophys.* 33 (3), 333–340.

Ecklund, W. L., Carter, D. A., and Balsley, B. B. (1981). Gradient drift irregularities in mid-latitude sporadic*E*. *J. Geophys. Res. Space Phys.* 88 (2), 858–862. doi:10.1029/JA086iA02p00858

Forbes, J. M., Roble, R. G., and Marcos, F. A. (1995). Equatorial penetration of magnetic disturbance effects in the thermosphere and ionosphere. *J. Atmos. Terr. Phys.* 57 (10), 1085–1093. doi:10.1016/0021-9169(94)00124-7

Haldoupis, C. (2011). A tutorial review on sporadic E layers. *IAGA Book Ser.* 29 (2), 381–394. doi:10.1007/978-94-007-0326-1_29

Hocking, W. K., Fuller, B., and Vandepeer, B. (2001). Real-time determination of meteorrelated parameters utilizing modern digital technology. *J. Atmos. Terr. Phys.* 63 (2-3), 155–169. doi:10.1016/S1364-6826(00)00138-3

Hocking, W. K., and Thayaparan, T. (1997). Simultaneous and colocated observation of winds and tides by MF and meteor radars over London, Canada (43°N, 81°W), during 1994-1996. *Radio Sci.* 32, 833–865. doi:10.1029/96RS03467

Kletzing, C. A., Kurth, W. S., Acuna, M., MacDowall, R. J., Torbert, R. B., Averkamp, T., et al.(2013). The electric and magnetic field instrument suite and integrated science (EMFISIS) on RBSP. *Space Sci. Rev.* 179 (1–4), 127–181. doi:10.1007/s11214-013-9993-6

Kopp, E. (1997). On the abundance of metal ions in the lower ionosphere. *J. Geophys. Res. Space Phys.* 102, 9667–9674. doi:10.1029/97ja00384

Kumar, D. V. P., Patra, A. K., Kwark, Y. S., Kim, K. H., and Yellaiah, G. (2009). Low latitude E-region irregularities studied using Gadanki radar, ionosonde and *in situ* measured electron density. *Astrophysics Space Sci.* 323, 225–233. doi:10.1007/s10509-009-0066-y

Liu, T., Yang, G., Zhou, C., Jiang, C., Xu, W., Ni, B., et al. (2022). Improved ionosonde monitoring of the sporadic E layer using the frequency domain interferometry technique. *Remote Sens.* 14, 1915. doi:10.3390/rs14081915

Mathews, J. D. (1998). Sporadic E: Current views and recent progress. *J. Atmos. Terr. Phys.* 60, 413–435. doi:10.1016/S1364-6826(97)00043-6

Matsushita, S., and Reddy, C. A. (1967). A study of blanketing sporadic E at middle latitudes. *J. Geophys. Res. Space Phys.* 72 (11), 2903–2916. doi:10.1029/JZ072i011p02903

Mauk, B. H., Fox, N. J., Kanekal, S. G., Kessel, R. L., Sibeck, D. G., and Ukhorskiy, A. (2012). Science objectives and rationale for the radiation belt storm probes mission. *Space Sci. Rev.* 179, 3–27. doi:10.1007/s11214-012-9908-y

Medeiros, A. F., Buriti, R. A., Machado, E. A., Takahashi, H., Batista, P. P., Gobbi, D., et al. (2004). Comparison of gravity wave activity observed by airglow imaging at two different latitudes in Brazil. *J. Atmos. Solar-Terrestrial Phys.* 66 (6-9), 647–654. doi:10.1016/j.jastp.2004.01.016

Moro, J., Xu, J., Denardini, C. M., Resende, L. C. A., Da Silva, L. A., Chen, S. S., et al. (2022). Different sporadic-E (Es) layer types development during the august 2018 geomagnetic storm: Evidence of auroral type (Esa) over the SAMA region. *J. Geophys. Res. Space Phys.* 127, e2021JA029701. doi:10.1029/2021JA029701

Rastogi, R. G. (1972). Equatorial sporadic E and plasma instabilities. *Nature* 237, 73–75. doi:10.1038/physci237073b0

Reinisch, B. W., Galkin, I. A., Khmyrov, G. M., Kozlov, A., and Kitrosser, D. (2004). Automated collection and dissemination of ionospheric data from the Digisonde network. *Adv. Radio Sci.* 2, 241–247. doi:10.5194/ars-2-241-2004

Resende, L. C. A., Batista, I. S., Denardini, C. M., Batista, P. P., Carrasco, A. J., Andrioli, V. F., et al. (2017). Simulations of blanketing sporadic E-layer over the Brazilian sector driven by tidal winds. *J. Atmos. Solar-Terrestrial Phys.* 154, 104–114. doi:10.1016/j.jastp.2016.12.012

Resende, L. C. A., Batista, I. S., Denardini, C. M., Carrasco, A. J., Andrioli, V. F., Moro, J., et al. (2016). Competition between winds and electric fields in the formation of blanketing sporadic E layers at equatorial regions. *Earth Planets Space* 68, 201. doi:10.1186/s40623-016-0577-z

Resende, L. C. A., Denardini, C. M., and Batista, I. S. (2013). Abnormal *fb*Es enhancements in equatorial Es layers during magnetic storms of solar cycle 23. *J. Atmos. Solar-Terrestrial Phys.* 102, 228–234. doi:10.1016/j.jastp.2013.05.020

Resende, L. C. A., J Shi, J. K., Denardini, C. M., Batista, I. S., Picanço, G. A., Moro, J., et al. (2021). The impact of the disturbed electric field in the sporadic E (Es) layer development over Brazilian region. *J. Geophys. Res. Space Phys.* 126, e2020JA028598. doi:10.1029/2020JA028598

Resende, L. C. A., Zhu, Y., Denardini, C. M., Moro, J., Arras, C., Chagas, R. A. J., et al.(2022). Worldwide study of the Sporadic E (Es) layer development during a space weather event. *J. Atmos. Solar-Terrestrial Phys.* 241, 105966. doi:10.1016/j.jastp.2022.105966

Resende, L. C. A., Shi, J. K., Denardini, C. M., Batista, I. S., Nogueira, P. A. B., Arras, C., Andrioli, V. F., Moro, J., et al. (2020). The influence of disturbance dynamo electric field in the formation of strong sporadic E-layers over Boa Vista, a low latitude station in American Sector. *J. Geophys. Res. Space Phys.* 108 (5), 1176. doi:10.1029/2019JA027519

Rosado-Román, J. M., Swartz, W. E., and Farley, D. T. (2004). Plasma instabilities observed in the E region over Arecibo and a proposed nonlocal theory. *J. Atmos. Solar-Terrestrial Phys.* 66 (17), 1593–1602. doi:10.1016/j.jastp.2004.07.005

Whitehead, J. (1961). The formation of the sporadic-E layer in the temperate zones. *J. Atmos. Terr. Phys.* 20 (1), 49–58. doi:10.1016/0021-9169(61)90097-6

Wu, J., Zhou, C., Wang, G., Liu, Y., Jiang, C., and Zhao, Z. (2022). Simulation of Es layer modulated by nonlinear Kelvin–Helmholtz instability. *J. Geophys. Res. Space Phys.* 127, e2021JA030065. doi:10.1029/2021JA030065

Yan, C., Chen, G., Wang, Z., Zhang, M., Zhang, S., Li, Y., et al. (2021). Statistical characteristics of the low-latitude E-region irregularities observed by the HCOPAR in south China. *J. Geophys. Res. Space Phys.* 126, e2021JA029972. doi:10.1029/2021JA029972

frontiers | Frontiers in Astronomy and Space Sciences

TYPE Original Research
PUBLISHED 05 June 2023
DOI 10.3389/fspas.2023.1113706

OPEN ACCESS

EDITED BY
Huixin Liu,
Kyushu University, Japan

REVIEWED BY
Sai Gowtam Valluri,
University of Alaska Fairbanks, United States
Stavros Dimitrakoudis,
National and Kapodistrian University of Athens, Greece

*CORRESPONDENCE
Dmytro Kotov,
dmitrykotoff@gmail.com

RECEIVED 01 December 2022
ACCEPTED 23 May 2023
PUBLISHED 05 June 2023

CITATION
Kotov D, Richards PG, Reznychenko M, Bogomaz O, Truhlík V, Nossal S, Mierkiewicz E, Zhivolup T, Domnin I, Miyoshi Y, Tsuchiya F, Kumamoto A, Kasahara Y, Kitahara M, Nakamura S, Matsuoka A, Shinohara I and Hairston M (2023), Interhemispheric ionosphere-plasmasphere system shows a high sensitivity to the exospheric neutral hydrogen density: a caution of the global reference atmospheric model hydrogen density.
Front. Astron. Space Sci. 10:1113706.
doi: 10.3389/fspas.2023.1113706

Interhemispheric ionosphere-plasmasphere system shows a high sensitivity to the exospheric neutral hydrogen density: a caution of the global reference atmospheric model hydrogen density

Dmytro Kotov[1]*, Phil G. Richards[2], Maryna Reznychenko[1], Oleksandr Bogomaz[1,3], Vladimír Truhlík[4], Susan Nossal[5], Edwin Mierkiewicz[6], Taras Zhivolup[1], Igor Domnin[1], Yoshizumi Miyoshi[7], Fuminori Tsuchiya[8], Atsushi Kumamoto[8], Yoshiya Kasahara[9], Masahiro Kitahara[8], Satoko Nakamura[10], Ayako Matsuoka[11], Iku Shinohara[12] and Marc Hairston[13]

[1]Institute of Ionosphere, Kharkiv, Ukraine, [2]Department of Computer Science, University of Alabama in Huntsville, Huntsville, AL, United States, [3]State Institution National Antarctic Scientific Center of the Ministry of Education and Science of Ukraine, Kharkiv, Kyiv, Ukraine, [4]Institute of Atmospheric Physics of the Czech Academy of Sciences, Prague, Czechia, [5]Physics Department, University of Wisconsin-Madison, Madison, WI, United States, [6]Department of Physical Sciences, Embry-Riddle Aeronautical University, Daytona Beach, FL, United States, [7]Institute for Space-Earth Environmental Research, Nagoya University, Nagoya, Japan, [8]Planetary Plasma and Atmospheric Research Center, Graduate School of Science, Tohoku University, Sendai, Japan, [9]Graduate School of Natural Science and Technology, Kanazawa University, Kanazawa, Japan, [10]Institute for Space-Earth Environmental Research, Nagoya University, Nagoya, Japan, [11]Data Analysis Center for Geomagnetism and Space Magnetism, Graduate School of Science, Kyoto University, Kyoto, Japan, [12]Institute of Space and Astronautical Science, Japan Aerospace Exploration Agency, Sagamihara, Japan, [13]William B. Hanson Center for Space Sciences, The University of Texas at Dallas, Richardson, TX, United States

This study explores the impact of the exosphere hydrogen (H) density on the ionosphere-plasmasphere system using a model whose key inputs are constrained by ionosphere observations at both ends of the magnetic field line with an L-value of 1.75 in the American longitudinal sector during a period with low solar and magnetic activities. This study is the first to be validated by ground-based and satellite data in the plasmasphere and both hemispheres. The main finding is that the entire ionosphere-plasmasphere system is very sensitive to the neutral hydrogen density in the lower exosphere. It was found that an increase in the H density by a factor of 2.75 from the commonly accepted values was necessary to bring the simulated plasma density into satisfactory agreement with Arase satellite measurements in the plasmasphere and also with DMSP satellite measurements in the topside ionospheres of the northern and southern hemispheres. A factor of 2.75 increase in the H density increases the simulated plasma density in the afternoon plasmasphere up to ~80% and in the nighttime topside ionosphere up to ~100%. These results indicate prominently that using the commonly accepted empirical model of the

H density causes unacceptable errors in the simulated plasma density of the near-Earth plasma shells. We alert the space science community of this problem.

KEYWORDS

plasmasphere, ionosphere, exosphere, hydrogen, interhemispheric coupling, multiinstrumental observations, observation-based simulation, NRLMSISE-00 hydrogen density

1 Introduction

The plasmasphere is comprised of shells of cold plasma that are confined by the Earth's magnetic field. The plasmasphere plays an important role in clearing the near-Earth space of dangerous high-energy particles of the Van Allen radiation belts through the generation of hiss waves in the plasmasphere (e.g., Kanekal and Miyoshi, 2021). Recent studies show that the hiss power directly depends on the cold plasma density (Malaspina et al., 2018). Also, the transport of plasma plumes consisting of low-energy plasmasphere particles to the magnetopause acts to reduce magnetic reconnection, thereby helping to decrease the storm intensity (Borovsky et al., 2013). Thus, appropriate simulation of the plasmasphere density is critical for success in creating global physical models capable of simulating complex coupled effects of solar-terrestrial interaction and space weather phenomena.

The plasmasphere must be investigated with its coupling to the ionospheres of both hemispheres, which are the sources (during the daytime) and sinks (during the nighttime) of the plasmasphere content. It is well-known that this content is mostly H^+, originating in the $H+O^+$ resonant charge exchange reaction at altitudes where the ionospheric O^+ density becomes low enough to allow H^+ to flow into the plasmasphere (Richards and Torr, 1985). This is the topside ionosphere region between about 500 and 1000 km altitude, which overlaps with the lower part of the hydrogen exosphere. Thus, the plasmasphere H^+ density is inextricably linked to the H density in the lower exosphere.

Our motivation to explore the impact of the H density in the lower exosphere on the plasmasphere is all the more understandable given that the H density values are still a subject of intensive discussion. Several studies with a variety of techniques have found significantly different values of H density for similar conditions. Using the H density provided by the widely used NRLMSISE-00 model (Picone et al., 2002) as a reference, the H density multiplication factors estimates range from 1/3 (Waldrop and Paxton, 2013) to two (Nossal et al., 2012; Kotov et al., 2018; 2019; Wan et al., 2022), and even up to a three (Kotov et al., 2015; Kotov et al., 2016). The new NRLMSIS 2.0 atm model (Emmert et al., 2021) has H densities identical to those of NRLMSISE-00, so this study uses the NRLMSISE-00 model.

Previously, this H density uncertainty motivated a study with 'Sami3 is A Model of the Ionosphere' (SAMI3) physical plasma model to explore how different values of the H density influence processes in near-Earth space during and after extreme space weather events (Krall et al., 2018). Their model parameter studies of plasmasphere refilling rates at L = 4.0 and L = 5.2 essentially re-verified the dependence of the refilling rate on the topside H density that was determined by Richards and Torr (1985) both analytically and computationally. The parameter study of Krall et al. (2018) differs from the current study in that they did not validate their results with observations in either the plasmasphere or the ionosphere. When modeling the ionosphere-plasmasphere system with parameter studies, it is important to ensure that the results are consistent with observations, as uncertainties in the state of the ionosphere can affect the validity of the plasmasphere simulations and complicate conclusions on the net impact of the H density on the ionosphere-plasmasphere system.

The Field Line Interhemispheric Plasma (FLIP) physical model ensures the validity of the calculated plasma parameters by using certain key ionospheric observations as constraints. FLIP model comparisons with the plasmaspheric density data from the Arase satellite by Kotov et al. (2018) revealed that reproducing the Arase plasmasphere density in December 2017 required doubling the NRLMSISE-00 H density. However, that study only had ionosphere data in the Northern hemisphere available to constrain and validate the model.

This current study advances our knowledge by simulating the impact of the lower exosphere H density on the entire ionosphere-plasmasphere system from the Northern hemisphere through the plasmasphere to the conjugate ionosphere in the Southern hemisphere. These simulations accurately estimate the lower exosphere H density by finding the best fit to the Arase observations in the plasmasphere and the DMSP satellites' topside observations in both hemispheres.

2 Methods and tools

2.1 The method and justification of the place and time for the study

The method involves finding the best fit for the ionosphere and plasmasphere data by systematically varying the NRLMSISE-00 H density in the FLIP model while it is constrained by key ionosphere data. The multiplier to the NRLMSISE-00 H density that gives the best model fit to the coincident observations in the plasmasphere and topside ionospheres of the Northern and Southern hemispheres produces an estimate of the actual neutral hydrogen density in the lower exosphere. The sensitivity of the ionosphere-plasmasphere system to the lower exosphere H density is explored by comparison of the best-fit results with the results obtained using the standard NRLMSISE-00 H density.

This study is for a flux tube with an L-value of ~1.75 in the American longitudinal sector from 27 April to 1 May 2017. The solar activity was low with both the daily and averaged $F_{10.7}$ index being 77–78 during all considered dates. This flux tube, region, and time for the study were chosen to satisfy the following criteria, 1)

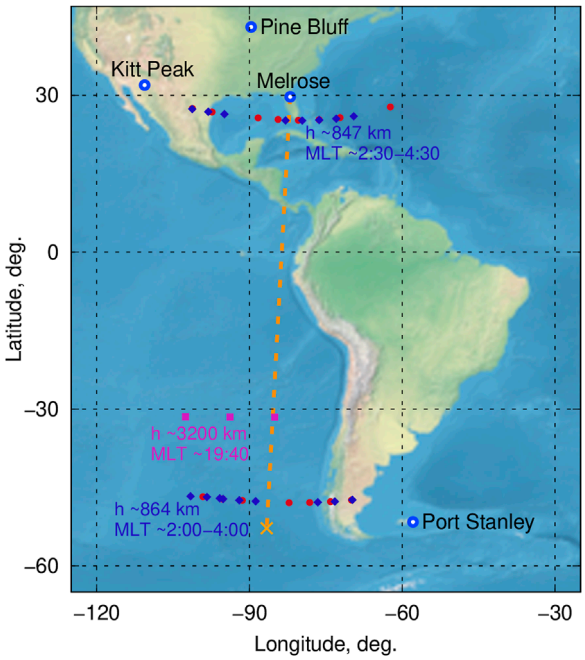

FIGURE 1
Projection of the plasma tube with L-value 1.75 for which the simulations were conducted (orange dashed line) and spatial and time location of satellites plasma data which are sensitive to neutral hydrogen density in the lower exosphere. Data were collected at L = 1.75 during 27 April—1 May 2017. Red circles and blue diamonds show DMSP F15 and F16 satellite data respectively. Pink squares denote Arase satellite data. Digisondes which data were used to constrain the FLIP model in the simulations are located at Melrose and Port Stanley. In Pine Bluff and Kitt Peak, the WHAM Balmer-α observatories were operated within the 23rd solar cycle.

the flux tube should be located in the inner plasmasphere where it is not significantly affected by transverse plasma transport under quiet magnetic conditions, 2) quiet magnetic conditions so that the flux tube has not recently been depleted, 3) the tube should be large enough to adequately represent refilling of the ionosphere-plasmasphere system, 4) the availability of high-quality F2-layer peak height data from the nearby digisondes in both hemispheres, 5) the availability of coincident satellite data for altitudes and local times when the satellite plasma density data is expected to be sensitive to the H density in the lower exosphere.

In addition to satisfying the above criteria, the selected longitudinal sector is located to the west of South America and thus avoids possible contamination of the results from the South Atlantic magnetic anomaly.

There is an earlier extensive historical database obtained by independent optical techniques in the same region. The ground-based optical Pine Bluff Observatory (43.08°N, 89.67°W) and Kitt Peak Observatory (31.96°N, 111.60°W) were located close to the latitude and longitude corresponding to the starting point of our flux tube (see **Figure 1**).

2.2 FLIP model

The FLIP model is a one-dimensional physical model of the entire coupled ionosphere-plasmasphere system. The model calculates the electron and ion densities and temperatures along magnetic field lines from ~100 km altitude in the Northern hemisphere through the plasmasphere to ~100 km in the Southern hemisphere (Richards et al., 2010). The FLIP model magnetic field was recently updated to use the latest IGRF-13 model. The model uses 3-h Kp indices and F10.7 indices for the periods of simulations to specify neutral composition with the NRLMSISE-00 model. A description of the analysis techniques to be employed here is provided by Kotov et al. (2015). The FLIP capabilities employed for this study were 1) adjust the equivalent neutral wind velocity automatically (Richards, 1991) to reproduce the observed variation of the F2-layer peak height (h_mF_2) from the digisondes, 2) modify the plasmasphere heating to match the satellite temperature observations in the topside ionosphere, and 3) adjust the H density by multiplying the NRLMSISE-00 values to match all the plasma density measurements. Note that there are a number of possible heat sources in the plasmasphere that can affect the model temperatures and that are difficult to quantify. These sources include the ring current, plasma waves, and trapping of photoelectrons as they transit the plasmasphere. Since all the heat is ultimately lost to the ionosphere in both conjugate hemispheres as heat flux, the topside electron temperature constitutes an accurate proxy for the plasmasphere heating.

2.3 Digisondes

The diurnal variations of h_mF_2 for constraining the model are deduced from digisonde ionograms. In the Northern hemisphere, the data were obtained at Melrose (29.71°N, 278.00°E), which served as the coordinates for the starting point of the magnetic field line for the simulations. In the Southern hemisphere, the data were obtained at Port Stanley (51.60°S, 302.1°E), which is the closest digisonde to the conjugate point of Melrose (52.80°S, 273.37°E), see **Figure 1**. The ionogram traces were checked manually to provide the best accuracy of the h_mF_2 estimation before the inversion (Huang and Reinisch, 1996).

2.4 Arase satellite

The data from the Arase satellite Plasma Wave Experiment (PWE)/Onboard Frequency Analyzer (OFA) and High-Frequency Analyzer (HFA) instruments onboard allows the determination of the ambient plasma density along the satellite orbit from the frequency of the upper hybrid resonance emissions observed by OFA and HFA and the local cyclotron frequency measured by the magnetometer (Miyoshi et al., 2018a; Kasahara et al., 2018; Kumamoto et al., 2018; Matsuoka et al., 2018). The Arase electron density data were collected every other day in the local afternoon near 3,200-km altitude in the American sector close to the longitude of the simulated plasma tube (see **Figure 1**). At 3,200 km altitude, the electron density is almost equal to the H^+ density since this altitude is significantly above the upper transition height for moderate solar activity conditions at mid- and low latitudes (e.g., Truhlik et al., 2004). This means that the Arase electron density is sensitive to the H density in the dayside lower exosphere.

2.5 DMSP satellites

Data from all four operating satellites of the Defense Meteorological Satellite Program (F15—F18) were used in this study. The satellites have near-circular orbits that cross the model L-shell at altitudes of ~847 km in the Northern hemisphere and of ~864 km in the Southern hemisphere.

Electron temperature data in the topside ionosphere from the electron probe of the DMSP satellites (Rich, 1994) were used to adjust the FLIP model plasmasphere heating rate to match the DMSP observed electron temperature. The DMSP topside ionosphere ion temperature data from retarding potential analyzer were used for validation of the simulated ion temperature.

The DMSP total ion density data in the topside ionosphere from the scintillation meter (Rich, 1994) were used to validate the FLIP model diurnal variations of the topside electron density. The ion density data that are collected by the F15 and F16 satellites every night between local midnight and sunrise (see **Figure 1**) are valuable because H^+ is dominant near the DMSP orbits at night and they are supplied from the plasmasphere, making this DMSP data sensitive to the neutral H density in the dayside lower exosphere.

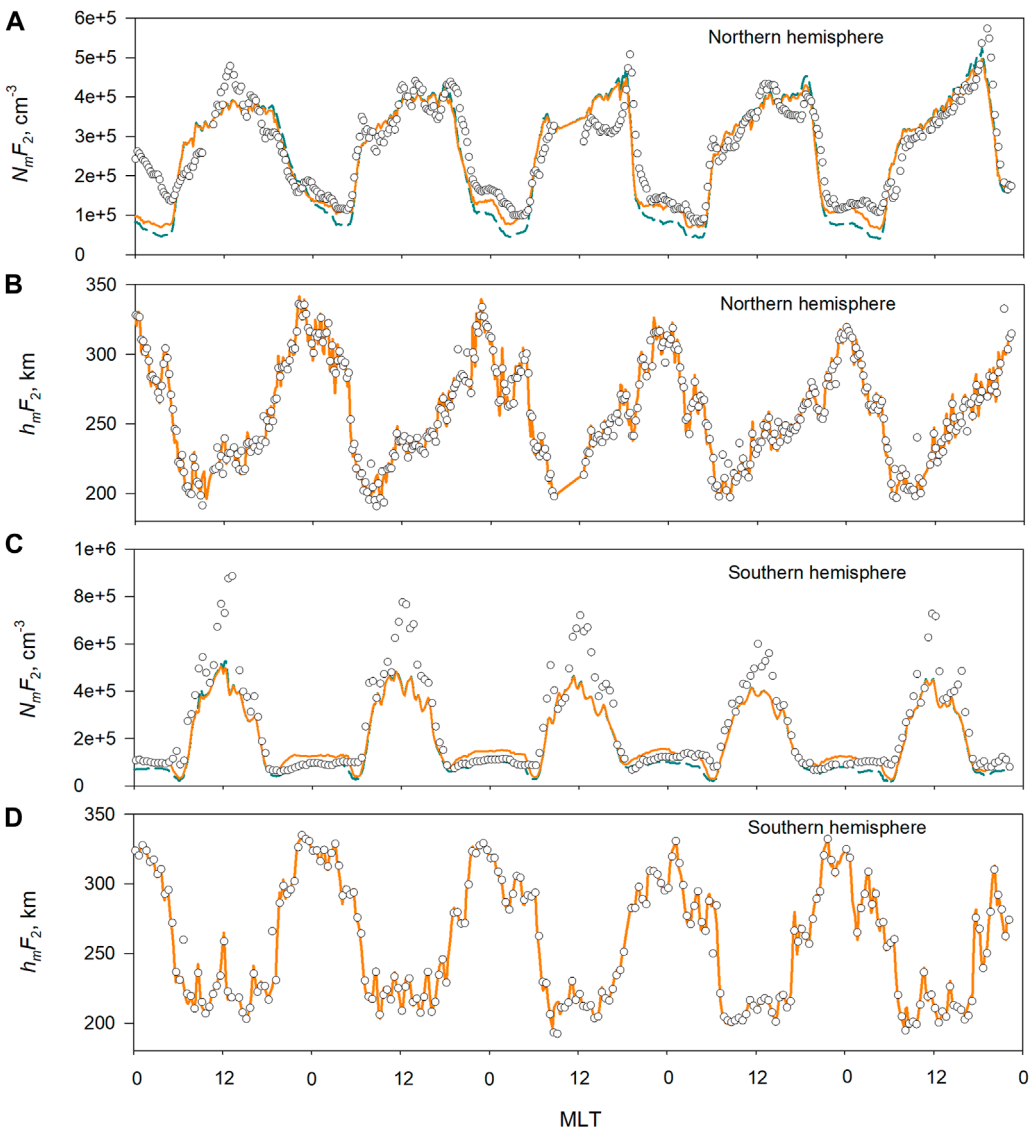

FIGURE 2
Diurnal variations of the F2-layer peak density N_mF_2 **(A,C)** and height h_mF_2 **(B,D)** at the ends of the L = 1.75 flux tube during 27 April—1 May 2017. The open circles show the digisonde data at Melrose (two top panels) and Port Stanley (two bottom panels). The solid orange line shows the FLIP model simulations using the NRLMSIS H density multiplied by a factor of 2.75, dashed dark blue line on the N_mF_2 panels show the simulations using the NRLMSIS H density. The model was constrained to follow the observed h_mF_2 variations in both hemispheres.

3 Results

The FLIP model's ability to follow the observed h_mF_2 very closely by adjusting the neutral wind as it steps in time was used at both ends of the ionosphere-plasmasphere system (Figure 2).

The first step was to run tests to find the model settings to provide near-optimal agreement between the simulated plasma parameters and observations along the entire flux tube. Specifically, the model should match, 1) the observed DMSP plasma densities in the topside ionosphere of both hemispheres and the high altitude Arase plasmasphere densities, and 2) the DMSP electron and ion temperatures in the topside ionosphere of both hemispheres. It is important to note that, because local heating and cooling are insignificant in the topside ionosphere, the topside electron temperature is directly related to the electron heat flux from the plasmasphere, which in turn is determined by the amount of heat deposited within the plasmasphere.

One complication in this process is that the model topside temperatures are not independent of the plasmasphere electron density because the plasmasphere heating by photoelectrons is proportional to the electron density. Thus, adjusting the H density to increase the plasmasphere density will increase heat flow to the topside ionosphere, which affects the topside temperature and density. An iterative process is necessary to ensure that the model parameters controlling the neutral H density and plasmasphere heat sources are consistent.

To control the heating of the plasmasphere, the model has two parameters, 1) the fraction of photoelectrons trapped in the

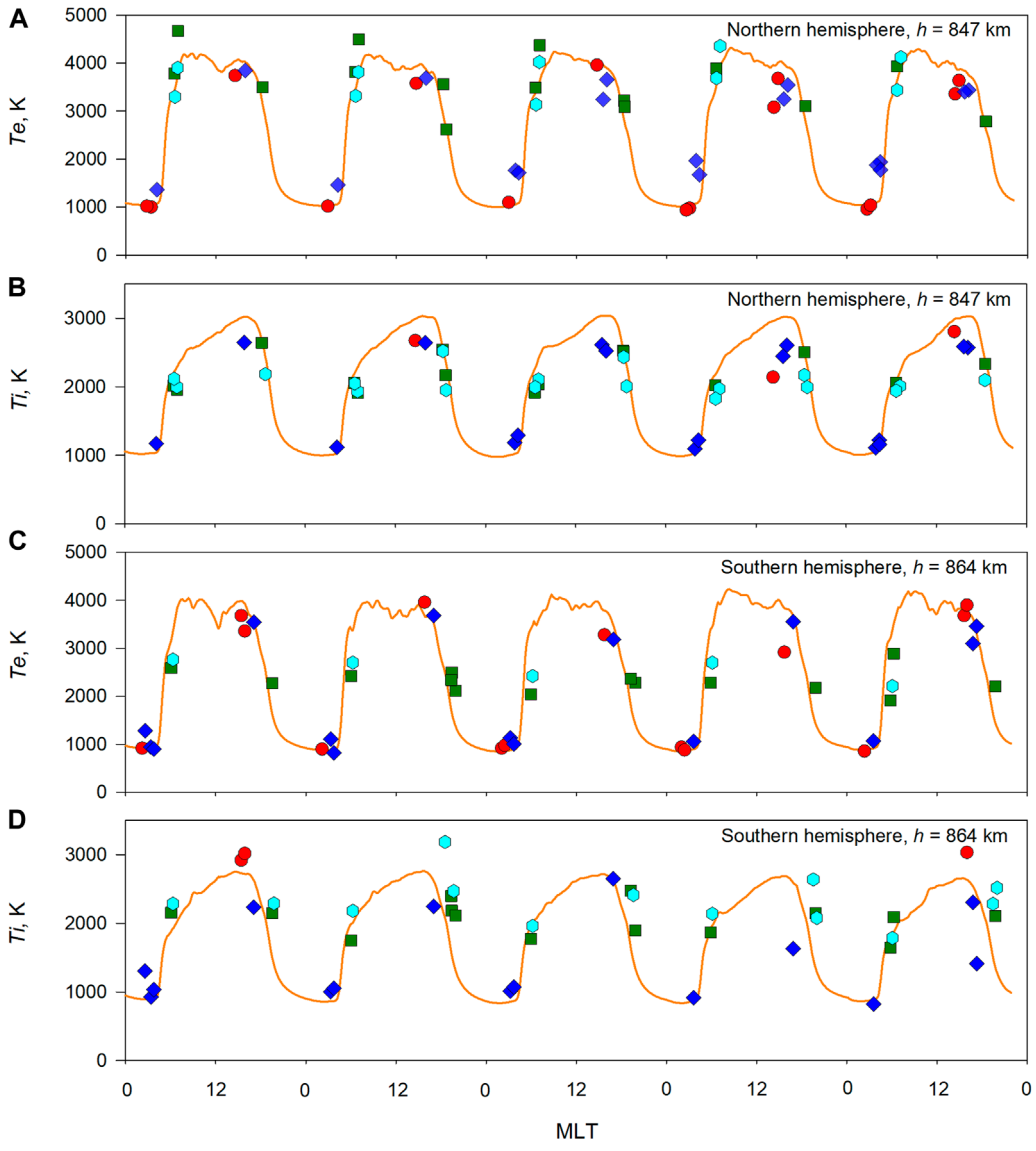

FIGURE 3
Diurnal variations of the topside ionosphere electron T_e **(A,C)** and ion T_i **(B,D)** temperatures at both ends of the L = 1.75 plasma flux tube during 27 April—1 May 2017. The symbols show DMSP data: F15 (red circles), F16 (blue diamonds), F17 (dark green squares), and F18 (cyan hexagons). The solid orange line shows the FLIP model simulations using the NRLMSIS H density multiplied by a factor of 2.75.

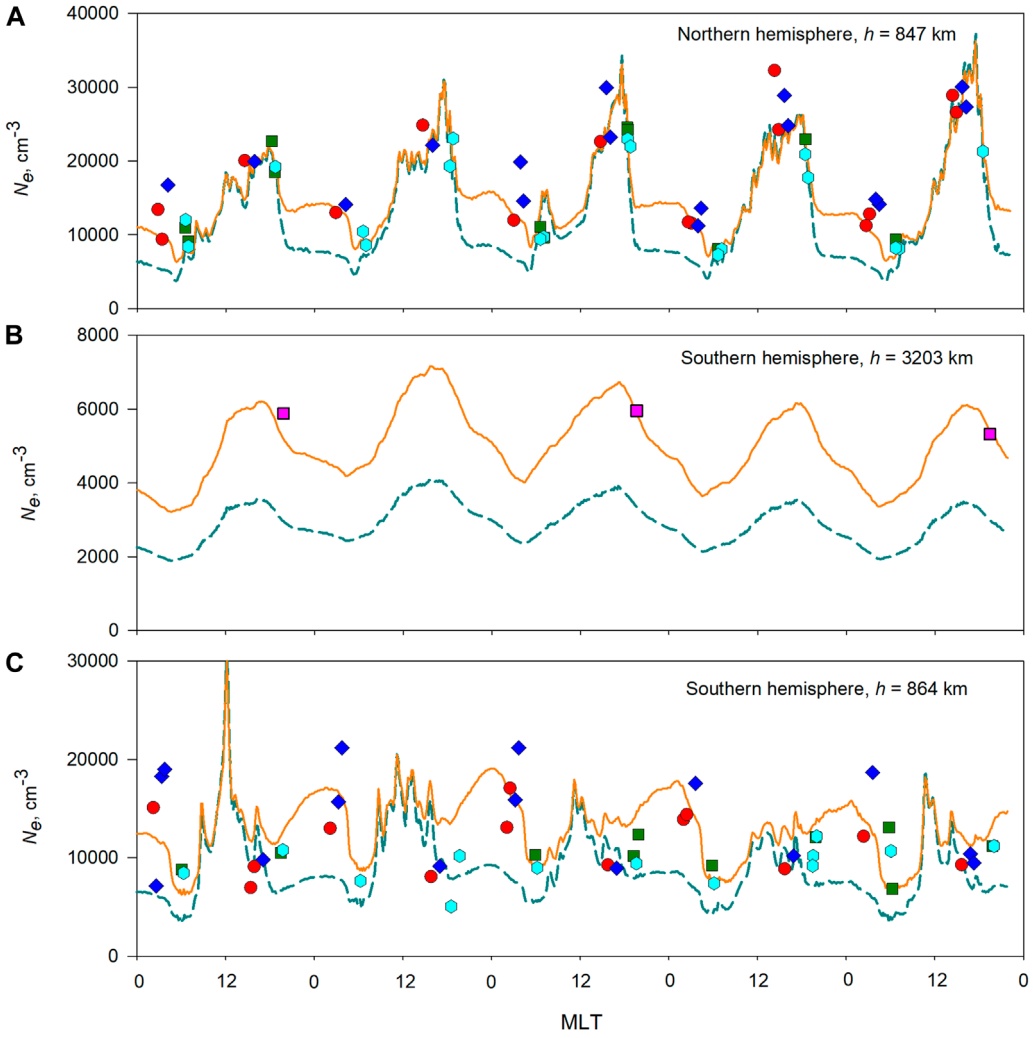

FIGURE 4
Diurnal variations of the plasma density in the topside ionosphere at northern **(A)** and southern **(C)** ends and in the high-altitude plasmaspheric part **(B)** of the L = 1.75 flux tube during 27 April—1 May 2017. The dashed dark blue line shows the simulation using the standard NRLMSIS H density while the solid orange line is for the NRLMSIS H density multiplied by a factor of 2.75. In the top and bottom panels, the symbols show DMSP data: F15 (red circles), F16 (blue diamonds), F17 (dark green squares), and F18 (cyan hexagons). Pink squares on the middle panel denote the Arase satellite data.

plasmasphere and depositing all their heat there. This is only operative when the photoelectrons transit the plasmasphere, 2) the plasmasphere heating rate, which can be adjusted artificially to match the observed topside electron temperature both day and night. This parameter is meant to account for possible unknown heat sources, such as the ring current. It is most useful at night when there are no photoelectrons because both conjugate ionospheres are in darkness.

The best agreement with the observations was reached with the multiplier of 2.75 for the NRLMSISE-00 H density. Because the H density has a large scale height, a simple altitude-independent multiplier is adequate. Figure 3 shows that the model produces the observed topside T_e variations in both hemispheres. Figure 3 also demonstrates that the calculated topside ion temperatures are in a good agreement with the observations. Figure 4 shows that matching the topside temperatures and using a multiplier of 2.75 for the NRLMSISE-00 H density produces a good match to all the satellite plasma density observations.

With regard to the F2-layer peak density N_mF_2, the model/data agreement is excellent in the Northern hemisphere (Figure 2) while the difference in the Southern hemisphere reaches ~60% for some days near noon. A possible reason for the difference could be the separation between the Port Stanley digisonde and the Melrose conjugate point (see Figure 1) for which the simulation was made. However, a simulation made for the actual coordinates of Port Stanley has the same behavior. It is possible that the ~60% underestimation of the midday N_mF_2 by the FLIP model in the Southern hemisphere indicates that the midday O to N_2 density ratio is too low in the NRLMSISE-00 model. Another capability of the FLIP model was used to test this. It can reproduce the measured N_mF_2 by modifying the neutral temperature in the NRLMSISE-00 model to change the O to N_2 density ratio self-consistently. This simulation (not shown) found that good model/data agreement was

reached for N_mF_2 with midday neutral temperatures a moderate ~60–70 K lower than that of the NRLMSISE-00 model. This N_mF_2 algorithm was not used for the results presented here because the N_mF_2 variation at the southern end of the flux tube may be different from Port Stanley and because these model/data differences have only a small effect on our key results in the plasmasphere and topside ionosphere. The topside ionosphere and plasmasphere densities deviate from the main results up to ~10% and ~5%, respectively.

To determine the sensitivity of the ionosphere-plasmasphere system to the H density, an additional simulation was made with the standard NRLMSISE-00 H density with the model adjusting the plasmasphere heating rate to maintain the model-data temperature agreement in the topside ionospheres. **Figure 4** demonstrates that decreasing the H density by a factor of 2.75 reduces the simulated nighttime plasma density in the topside ionospheres of both hemispheres by up to ~50% and the simulated afternoon plasmasphere density by up to ~45%.

The decrease by a factor of 2.75 in the H density also causes up to a ~35% decrease in the simulated N_mF_2 at night in both hemispheres (**Figure 2**). In the Northern hemisphere, this worsens the agreement with the observations. In the Southern hemisphere, the model/data agreement improves for some hours but worsens at other times.

4 Discussion

This study examines the impact of the neutral hydrogen density in the lower exosphere on the ionosphere-plasmasphere system as a whole. Let us consider how the current results compare with previous studies.

This study complements and expands on the Kotov et al. (2018) study, which employed similar analysis techniques in the European sector at L ~2.1 from 2016 to 2018. Although there were only observational data for the Northern hemisphere in that study, a similar sensitivity to the H density was shown for the topside ionosphere in all the seasons and for the plasmasphere near the winter solstice. In addition to being in a different longitude sector, this current study is different in being during a transition from spring to summer.

The current results verify that the ionosphere-plasmasphere system's sensitivity to the lower exosphere H density is strong. Increasing the H density from the standard NRLMSISE-00 model by a factor of 2.75 enhances the ionosphere-plasmasphere H^+ fluxes by a factor of ~2.0–2.5 (**Figure 5**), and that increases the plasma density in the afternoon plasmasphere by up to ~80% and in the nighttime topside ionosphere up to ~100%. These sensitivity estimates for the H^+ fluxes and plasma densities are close to those found by Kotov et al. (2015), Kotov et al., 2016, and Kotov et al. (2018) that were obtained for different seasons in the European sector.

It is difficult to compare our results with the results obtained by Krall et al. (2018) with the SAMI3 model. The reason is that the SAMI3 was not constrained by ionospheric observations (h_mF_2 and topside T_e), and their simulation results were not compared with measurements of the plasma density in the plasmasphere and topside ionosphere. Also, Krall et al. averaged their results over all longitudes while we consider one flux tube. This may be one of the reasons for the much smaller sensitivity of the steady-state plasmasphere of Krall et al. to strong changes in the H density (see **Figure 2** of their paper). One other reason for FLIP/SAMI3 differences could be that Krall et al. simulated for somewhat higher L-shells (L = 4.0 and L = 5.2). On the other hand, our observation-based simulations with the FLIP model for L = 4.0 (not shown) indicate just as high a sensitivity of the plasmasphere to the H density as for L = 1.75. At the same time, there is a reasonable agreement between the plasmasphere refilling rates seen from our simulation at L = 4.0 and those of Krall et al. (2018).

An examination of the variation of the O^+/H^+ transition height lends additional support for the 2.75 multiplication factor for the daytime NRLMSISE-00 H density. **Figure 6** shows that the transition height is quite sensitive to the H density during the day but almost insensitive during the night. This nighttime feature is understandable because, when the solar activity is low, the downward nighttime H^+ flux is responsible not only for the H^+ density in the topside ionosphere but for the O^+ density as well. Much of the O^+ in the nighttime topside ionosphere is from the H^+ that is supplied by the downward H^+ flux. Thus, more H^+ leads to more O^+. As a result, the nighttime O^+/H^+ transition height shows only a small dependence on the H^+ flux which changes significantly with the H density (**Figure 5**). Earlier results for the European sector showed similar behavior (Kotov et al., 2015).

During the day, the H^+ flux is upward and removes H^+ from the topside ionosphere. The H^+ is produced from the O^+ and the amount is directly proportional to the H density. On the contrary, the amount of O^+ is determined mostly by ionization processes in the atmosphere followed by upward diffusion to the topside ionosphere. There is a small decrease in the O^+ density with an increase in the H density through the O^++H reaction. However, this effect is much smaller than the loss of H^+ due to the upward flux. As a result, there is an increasing difference between the H^+ and O^+ densities with the increase in the daytime H density, which leads to the high sensitivity of the daytime O^+/H^+ transition height to the H density.

The FLIP model transition height behavior is supported by the empirical climatological TBT-15 model of topside ion composition. The TBT-15 model is included in the International Reference Ionosphere (IRI-2020) model (Truhlik et al., 2015; Bilitza et al., 2022). It was constructed from an extensive database of independent satellite observations. The TBT-15 model daytime O^+/H transition height is closer to our simulations with the multiplier 2.75 to the NRLMSISE-00 H density.

The estimated 2.75 multiplier to the NRLMSISE-00 H density agrees reasonably with the multiplier of ~2 implied by extensive optical observations of Balmer-α emission conducted during the 23rd solar cycle by the Wisconsin H-alpha Mapper (WHAM) Fabry-Perot located at the Pine Bluff Observatory (43.08°N, 89.67°W) in Wisconsin (Gallant et al., 2019) and Kitt Peak Observatory (31.96°N, 111.60°W) in Arizona (Nossal et al., 2012). The latitudes and longitudes of both observatories are close to the coordinates of the starting point of the flux tube we simulate (see **Figure 1**). Note that while our technique estimates the dayside H density in the lower exosphere, WHAM estimates the H density for the dusk and dawn periods in the same region. Thus, the techniques complement each other very well, and using both techniques jointly at the same region would certainly provide more opportunities for the lower exosphere H density investigation.

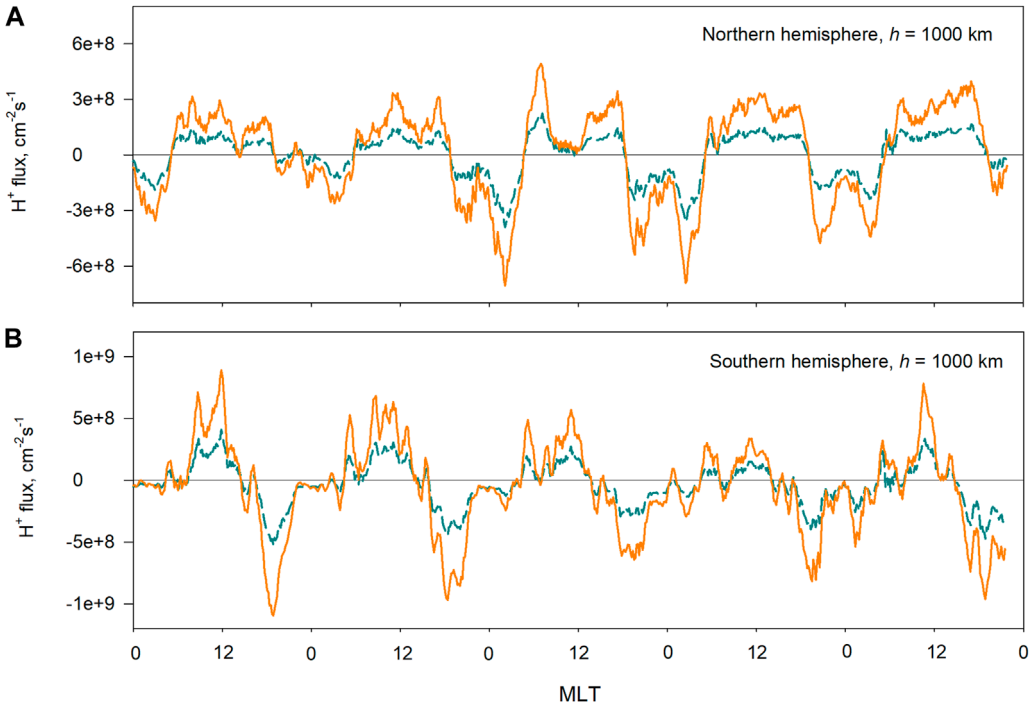

FIGURE 5
Diurnal variations of the ionosphere-plasmasphere H^+ flux at 1000 km altitude at the northern **(A)** and southern **(B)** ends of the L = 1.75 flux tube during 27 April—1 May 2017. The dashed dark blue line shows the simulation with the standard NRLMSIS density while the solid orange line is for the NRLMSIS H density multiplied by a factor of 2.75. The plots are running average of the simulated fluxes over 45 min intervals.

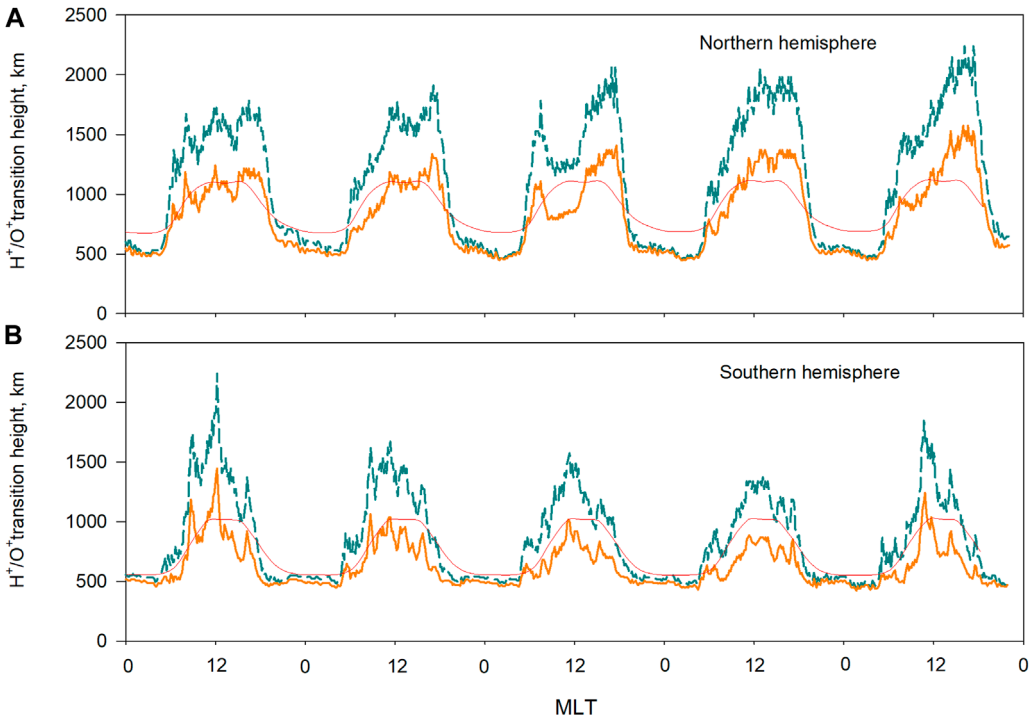

FIGURE 6
Diurnal variation of the H^+/O^+ transition height at the northern **(A)** and southern **(B)** ends of the L = 1.75 flux tube during 27 April—1 May 2017. The dashed dark blue line shows the simulation with the standard NRLMSIS density while the solid orange line is for the NRLMSIS H density multiplied by a factor of 2.75. The thin red solid line shows the variation calculated using empirical TBT-2015 model of ion composition of climatological International Reference Ionosphere model (IRI-2020 version).

The multiplier 2.75 found here is also in excellent agreement with values obtained in numerous previous investigations performed for low/low-to-medium solar activity and magnetically quiet conditions in the European sector (Kotov et al., 2015; Kotov et al., 2016; Kotov et al., 2018; Kotov et al., 2019) and Asian sector (Panasenko et al., 2021). These previous studies show the multiplier to the NRLMSIS H density ranging from 2.0 to 3.0 for low/medium and extremely low solar activity, respectively. Recent work of Wan et al. (2022) employing GUVI Layman-α observations for the 2002–2007 period, which covers the same solar activity conditions, also shows a multiplier of ~2.

Based on the accumulation of evidence, we recommend that ionosphere modelers increase the neutral H density from the NRLMSISE-00 model by a factor of 2 for low-to-medium solar activity and magnetically quiet conditions so that the simulated plasma densities in the ionosphere and plasmasphere can reproduce the plasma observations with acceptable accuracy.

5 Conclusion

The main conclusions from the results of this observation-based study of the entire ionosphere-plasmasphere system performed for the period with low solar and magnetic activities are the following.

1) The entire ionosphere-plasmasphere system is highly sensitive to the neutral hydrogen density in the lower exosphere. Increasing the H density by a factor of 2.75 from the standard NRLMSISE-00 values increases the simulated plasma density in the afternoon plasmasphere up to ~80% and in the nighttime topside ionosphere up to ~100%, bringing the simulated densities into agreement with the Arase and DMSP satellite observations. The last point indicates that using the NRLMSISE-00 H density causes unacceptable errors in the simulated plasma density of the near-Earth plasma shells. We alert the space science community of this problem.
2) The high sensitivity obtained for the American longitudinal sector for L = 1.75 agrees well with the high sensitivity seen in the simulations in the European sector at L = 2.1 (Kotov et al., 2015; Kotov et al., 2016; Kotov et al., 2018).
3) The estimated multiplier 2.75 to the NRLMSISE-00 H density is consistent with values obtained in the numerous previous investigations conducted for low-to-medium solar activity and magnetically quiet conditions with different techniques in the American sector (Nossal et al., 2012; Gallant et al., 2019), European sector (Kotov et al., 2015; Kotov et al., 2016; Kotov et al., 2018; Kotov et al., 2019), and Asian sector (Panasenko et al., 2021) and around the globe (Wan et al., 2022). These determinations that use independent techniques for different conditions bolster the need to reexamine the H density in the NRLMSISE-00 model at least for periods with low solar and magnetic activities.

Data availability statement

The raw data supporting the conclusion of this article will be made available by the authors, without undue reservation.

Author contributions

DK proposed concept of the study, participated in conducting simulations with FLIP model and interpretation of the results and wrote the first draft of the manuscript. PR consulted on the simulations by FLIP model, participated in the interpretation of the results, and contributed to writing the manuscript. MR and OB processed and analyzed satellite data. VT contributed to satellite data analyzes. SN and EM consulted on the features of optical data discussed in the manuscript. TZ and ID processed the digisondes data. YM, FT, AK, YK, MK, SN, AM, and IS were responsible to analysis of Arase satellite data. MH consulted on the DMSP satellites data. All authors contributed to the article and approved the submitted version.

Funding

DK and MR were supported by the National Academy of Sciences of Ukraine (project 0122U000187 “Investigation of variations in the ion composition of the topside ionosphere during the weak maximum of the 25th solar cycle”). OB was supported by the State Institution National Antarctic Scientific Center of the Ministry of Education and Science of Ukraine (project 0121U112420 “Investigation of machine learning applicability for detection of traveling ionospheric disturbances”). VT was supported, in part, by grant LTAUSA17100 of the Ministry of Education, Youth and Sports of the Czechia. SN is supported by National Science Foundation grant #AGS-2050072. EM is supported by National Science Foundation grant AGS-2050077. YM is supported by JSPS 20H01959.

Acknowledgments

DK, MR, OB, TZ, and ID are grateful to every Ukrainian soldier, volunteer, medic, personnel of emergency and municipal services, and to all the Ukrainians whose fearless resistances to genocidal war of Russia allow Ukrainian scientists to do their usual peaceful job. VT also fully supports this statement.

Conflict of interest

The authors declare that the research was conducted in the absence of any commercial or financial relationships that could be construed as a potential conflict of interest.

Publisher’s note

References

Bilitza, D., Pezzopane, M., Truhlik, V., Altadill, D., Reinisch, B. W., and Pignalberi, A. (2022). The international reference ionosphere model: A review and description of an ionospheric benchmark. *Rev. Geophys.* 60, e2022RG000792. doi:10.1029/2022RG000792

Borovsky, J. E., Denton, M. H., Denton, R. E., Jordanova, V. K., and Krall, J. (2013). Estimating the effects of ionospheric plasma on solar wind/magnetosphere coupling via mass loading of dayside reconnection: Ion-plasma-sheet oxygen, plasmaspheric drainage plumes, and the plasma cloak. *J. Geophys. Res. Space Phys.* 118, 5695–5719. doi:10.1002/jgra.50527

Emmert, J. T., Drob, D. P., Picone, J. M., Siskind, D. E., Jones, M., Jr., Mlynczak, M. G., et al. (2021). Nrlmsis 2.0: A whole-atmosphere empirical model of temperature and neutral species densities. *Earth Space Sci.* 8 (3), e2020EA001321. doi:10.1029/2020EA001321

Gallant, M. A., Mierkiewicz, E. J., Nossal, S. M., Qian, L., Burns, A. G., Zacharias, A. R., et al. (2019). Signatures of thermospheric-exospheric coupling of hydrogen in observed seasonal trends of H α intensity. *J. Geophys. Res. Space Phys.* 124 (6), 4525–4538. doi:10.1029/2018JA026426

Huang, X., and Reinisch, B. W. (1996). Vertical electron density profiles from the digisonde network. *Adv. Space Res.* 18 (6), 121–129. doi:10.1016/0273-1177(95)00912-4

Kanekal, S., and Miyoshi, Y. (2021). Dynamics of the terrestrial radiation belts: A review of recent results during the VarSITI (variability of the sun and its terrestrial impact) era, 2014–2018. *Prog. Earth Planet. Sci.* 8, 35. doi:10.1186/s40645-021-00413-y

Kasahara, Y., Kasaba, Y., Kojima, H., Yagitani, S., Ishisaka, K., Kumamoto, A., et al. (2018). The plasma wave experiment (PWE) on board the Arase (ERG) satellite. *Earth, Planets Space* 70 (1), 86. doi:10.1186/s40623-018-0842-4

Kotov, D. V., Richards, P. G., Bogomaz, O. V., Chernogor, L. F., Truhlík, V., Emelyanov, L. Y., et al. (2016). The importance of neutral hydrogen for the maintenance of the midlatitude winter nighttime ionosphere: Evidence from IS observations at Kharkiv, Ukraine, and field line interhemispheric plasma model simulations. *J. Geophys. Res. Space Phys.* 121, 7013–7025. doi:10.1002/2016JA022442

Kotov, D. V., Richards, P. G., Truhlík, V., Bogomaz, O. V., Shulha, M. O., Maruyama, N., et al. (2018). Coincident observations by the Kharkiv IS radar and ionosonde, DMSP and Arase (ERG) satellites, and FLIP model simulations: Implications for the NRLMSISE-00 hydrogen density, plasmasphere, and ionosphere. *Geophys. Res. Lett.* 45, 8062–8071. doi:10.1029/2018GL079206

Kotov, D. V., Richards, P. G., Truhlík, V., Maruyama, N., Fedrizzi, M., Shulha, M. O., et al. (2019). Weak magnetic storms can modulate ionosphere-plasmasphere interaction significantly: Mechanisms and manifestations at mid-latitudes. *J. Geophys. Res. Space Phys.* 124, 9665–9675. doi:10.1029/2019JA027076

Kotov, D. V., Truhlík, V., Richards, P. G., Stankov, S., Bogomaz, O. V., Chernogor, L. F., et al. (2015). Night-time light ion transition height behaviour over the Kharkiv (50°N, 36°E) IS radar during the equinoxes of 2006–2010. *J. Atmos. Sol. Terr. Phys.* 132, 1–12. doi:10.1016/j.jastp.2015.06.004

Krall, J., Glocer, A., Fok, M.-C., Nossal, S. M., and Huba, J. D. (2018). The unknown hydrogen exosphere: Space weather implications. *Space weather.* 16, 205–215. doi:10.1002/2017SW001780

Kumamoto, A., Tsuchiya, F., Kasahara, Y., Kasaba, Y., Kojima, H., Yagitani, S., et al. (2018). High frequency analyzer (HFA) of plasma wave experiment (PWE) onboard the Arase spacecraft. *Earth, Planets Space* 70 (1), 82. doi:10.1186/s40623-018-0854-0

Malaspina, D. M., Ripoll, J.-F., Chu, X., Hospodarsky, G., and Wygant, J. (2018). Variation in plasmaspheric hiss wave power with plasma density. *Geophys. Res. Lett.* 45, 9417–9426. doi:10.1029/2018GL078564

Matsuoka, A., Teramoto, M., Nomura, R., Nose, M., Fujimoto, A., Tanaka, Y., et al. (2018). The ARASE (ERG) magnetic field investigation. *Earth, Planets Space* 70 (1), 43. doi:10.1186/s40623-018-0800-1

Miyoshi, Y., Hori, T., Shoji, M., Teramoto, M., Chang, T-F., Segawa, T., et al. (2018b). The ERG science center. *Earth, Planets, Space* 70, 96. doi:10.1186/s40623-018-0867-8

Miyoshi, Y., Shinohara, I., Takashima, T., Asamura, K., Higashio, N., Mitani, S., et al. (2018a). Geospace exploration project ERG. *Earth, Planets Space* 70 (1), 101. doi:10.1186/s40623-018-0862-0

Nossal, S. M., Mierkiewicz, E. J., and Roesler, F. L. (2012). Observed and modeled solar cycle variation in geocoronal hydrogen using NRLMSISE-00 thermosphere conditions and the Bishop analytic exosphere model. *J. Geophys. Res.* 117, A03311. doi:10.1029/2011JA017074

Panasenko, S. V., Kotov, D. V., Otsuka, Y., Yamamoto, M., Hashiguchi, H., Richards, P. G., et al. (2021). Coupled investigations of ionosphere variations over European and Japanese regions: Observations, comparative analysis, and validation of models and facilities. *Prog. Earth Planet Sci.* 8, 45. doi:10.1186/s40645-021-00441-8

Picone, J. M., Hedin, A. E., Drob, D. P., and Aikin, A. C. (2002). NRLMSISE-00 empirical model of the atmosphere: Statistical comparisons and scientific issues. *J. Geophys. Res.* 107 (A12), 15-21–15-16. doi:10.1029/2002JA009430

Rich, F. J. (1994). Users guide for the topside ionospheric plasma monitor (SSIES, SSIES-2, and SSIES-3) on spacecraft of the Defense Meteorological Satellite Program. volume 1: Technical description. (Technical report PL-TR-94-2187). Phillips Laboratory. Available at https://satdat.ngdc.noaa.gov/dmsp/docs/Rich%20-%201994%20-%20Users%20Guide%20SSIES-1%20SSIES-2%20SSIES-3%20-%20PL-TR-94-2187.pdf.

Richards, P. G. (1991). An improved algorithm for determining neutral winds from the height of the F_2 peak electron density. *J. Geophys. Res.* 96 (A10), 17839–17846. doi:10.1029/91JA01467

Richards, P. G., Bilitza, D., and Voglozin, D. (2010). Ion density calculator (idc): A new efficient model of ionospheric ion densities. *Radio Sci.* 45, RS5007. doi:10.1029/2009RS004332

Richards, P. G., and Torr, D. G. (1985). Seasonal, diurnal, and solar cyclical variations of the limiting H^+ flux in the Earth's topside ionosphere. *J. Geophys. Res.* 90 (A6), 5261–5268. doi:10.1029/JA090iA06p05261

Truhlik, V., Bilitza, D., and Třísková, L. (2015). Towards better description of solar activity variation in the International Reference Ionosphere topside ion composition model. *Adv. Space Res.* 55 (8), 2099–2105. doi:10.1016/j.asr.2014.07.033

Truhlik, V., Triskova, L., and Smilauer, J. (2004). New advances in empirical modelling of ion composition in the outer ionosphere. *Adv. Space Res.* 33 (6), 844–849. doi:10.1016/j.asr.2003.06.006

Waldrop, L., and Paxton, L. J. (2013). Lyman α airglow emission: Implications for atomic hydrogen geocorona variability with solar cycle. *J. Geophys. Res. Space Phys.* 118, 5874–5890. doi:10.1002/jgra.50496

Wan, C., Qin, J., and Paxton, L. J. (2022). Solar cycle, seasonal, and dawn-to dusk variations of the hydrogen in the upper thermosphere. *J. Geophys. Res. Space Phys.* 127, e2022JA030504. doi:10.1029/2022JA030504

frontiers | Frontiers in Astronomy and Space Sciences

TYPE Original Research
PUBLISHED 14 June 2023
DOI 10.3389/fspas.2023.1197832

OPEN ACCESS

EDITED BY
Olga V. Khabarova,
Tel Aviv University, Israel

REVIEWED BY
Albino Carbognani,
National Institute of Astrophysics (INAF), Italy
Adam Popowicz,
Silesian University of Technology, Poland

*CORRESPONDENCE
Cs. Szárnya,
szarnya.csilla@epss.hu

RECEIVED 31 March 2023
ACCEPTED 19 May 2023
PUBLISHED 14 June 2023

CITATION
Szárnya C, Chum J, Podolská K, Kouba D, Koucká Knížová P, Mošna Z and Barta V (2023), Multi-instrumental detection of a fireball during Leonids of 2019. *Front. Astron. Space Sci.* 10:1197832. doi: 10.3389/fspas.2023.1197832

Multi-instrumental detection of a fireball during Leonids of 2019

Cs. Szárnya[1,2]*, J. Chum[3], K. Podolská[3], D. Kouba[3], P. Koucká Knížová[3], Z. Mošna[3] and V. Barta[1]

[1]Institute of Earth Physics and Space Science (ELKH EPSS), Sopron, Hungary, [2]Doctoral School of Earth Sciences, ELTE Eötvös Loránd University, Budapest, Hungary, [3]Department of Ionosphere and Aeronomy, Institute of Atmospheric Physics, Czech Academy of Sciences, Prague, Czechia

During the 2019 Leonid meteor shower, the European Fireball Network recorded a bright fireball (meteor code: EN171119_041459) at 04:15:0.2 (UT) on 17 November 2019. The fireball appeared at coordinates 49.95°N 15.56°E at the height of 134.46 km, and disappeared at coordinates 50.23°N 15.26°E and at the height of 71.81 km. The ionization effect caused by the fireball appeared in the digisonde's campaign measurements taken with a 2 ionogram/min time resolution at Průhonice station (50.00°N, 14.60°E). The trace appeared on the ionograms as a faint sporadic E-like layer, and the maximum ionization reached the upper limit of the measurement, 17 MHz. The trace persisted for 20 min on the ionograms, first appearing at 04:15:40 (UT) and finally disappearing at 04:35:40 (UT). The virtual height of the trace according to the ionograms appeared between 114 and 142 km, first it descended and then it ascended. Drift measurements were also taken with the digisonde every minute. Between 04:19:20 and 04:35:20 (UT), between altitudes of 122–142 km, 1-5 reflections were recorded on most SkyMaps. In addition, the Continuous Doppler Sounding developed by the Institute of Atmospheric Physics CAS also recorded the ionization signature of the fireball between 04:18 and 04:30 (UT) on 2 of the 3 sounding paths operating at 4.65 MHz. This is the first evidence that the plasma trail of a documented fireball can be detected by a DPS-4D digisonde (not only on ionograms, but also by drift measurements) and by the Continuous Doppler Sounding system.

KEYWORDS

european fireball network, digital autonomous fireball observatory (DAFO), GIRO network, digisonde, drift measurements, continuous Doppler sounding, sporadic E, leonid fireball

1 Introduction

The Leonid meteor swarm is one of the best-known meteor falls, associated with the comet 55P/Temple-Tuttle (Yeomans et al., 1996). It occurs between 6 November and 30 November and usually peaks on 17 November. The Leonids are a fast-moving swarm that reaches and enters the Earth's atmosphere at an average geocentric speed of 71 km/s (Beech, 1998) and have an average size of 10 mm (Höffner et al., 1999). Leonid meteors which are visible to the naked eye have an average mass of 0.5 g and can usually generate an average brightness of −1.5 apparent magnitude (Hawkes, 2007).

A meteoric fireball or bolide, as defined by the International Astronomical Union (IAU) in 2017, is a meteor with a brightness greater than −4 absolute visual magnitude. The difference between a fireball and a bolide is that the bolide is the special fireball that explodes in a terminal flash and often visual fragmentation can be observed. On average

every thousandth meteor entering the Earth's atmosphere is a fireball. Above −17 absolute visual magnitude these bodies are called superbolides (Ceplecha et al., 1999; Di Martino and Cellino, 2004).

When meteors enter the Earth's atmosphere, the vast majority of them burn up due to the friction and compression, and spread their material over an altitude of 70–110 km (Kozlovsky et al., 2020). Spectral analyses show that in the case of the Leonids, the meteors' material is composed of atomic O and N, as well as Mg, Fe, Na and Ca, which are ionized at high temperatures (Borovička et al., 1999).

This meteoric dust and metallic material deposited in the lower atmosphere can form thin layers of ionization by vertical ion convergence. That trapping mechanism is created by the combined effect of the vertical shear of the zonal winds, the meridional winds and the Lorentz force controlling the movement of ions due to the local magnetic field. This ion convergence creates the phenomenon known as the sporadic E layer (Whitehead, 1961; Axford, 1963; Haldoupis, 2011). At middle latitudes this is the accepted theory of formation of sporadic E layers so far and is usually referred to as the wind shear theory.

The most commonly used meteor detection methods are optical observations (Koten et al., 2019) and meteor radars (Fukao and Hamazu, 2014; Chen et al., 2020), but during major meteor falls, echo traces were often observed on ionograms, which were classified into separate categories (Ellyett and Goldsbrough, 1976). However, this classification led to controversy, which was finally resolved by Maruyama et al. (2003). In the study, these echo traces are attributed to Fresnel scattering by increased plasma density in the meteor's trail supported by extensive analysis and visual observations.

In summary, this means that it is possible to detect meteors with ionosondes (Kereszturi et al., 2021) because of the ionization they cause. These traces have a generally short lifetime and usually have an ionization (maximum frequency on the ionograms) exceeding that of regular sporadic E layers (in the Maruyama et al. (2003) the traces accepted as meteors are those above 5 MHz), and also different in height (Maruyama et al., 2003). They often show a distinct direction on ionograms made by Digisonde DPS-4D type of ionosonde (usually referred as digisonde), unlike the vertical reflection of the regular sporadic E layers.

The first observation of the ionization effect of a fireball event was on 28 January 1976 (Rajaram and Chandra, 1991). The Dhajala fireball passed close to Ahmedabad ionosonde station (23.2°N, 72.30°E) at 20:40 (IST–India Standard Time, UTC+5:30 h). The trace persisted for 1 h and showed an ionization of 3.4 MHz. Also mentioned in the article is that the trace breaks up into 2–3 distinct layers at altitudes of 120–140 km, separated by 6 km.

During the 2001 Leonid meteor shower on 17 November 2001, a trace appeared over Kokubunji/Tokyo (35.71°N, 139.49°E) that persisted for nearly 40 min (20:25 UTC first appearance, 21:00 UTC last appearance, Maruyama et al., 2003) and reached a top frequency of nearly 30 MHz, while its height steadily decreased over time. In the article it was called a long-duration meteor event (LDME). In 2002, during the Perseids, on 11 August at 01:50 (JST–Japanese Standard Time, UTC+9 h), another so called LDME appeared over Yamagawa (31.20° N, 130.62° E) at an apparent height of 120 km (Maruyama et al., 2008), with a top frequency of 27 MHz. It disappeared permanently at 02:47 (JST). However, its height-changes were different from the 2001 Leonids event–first decreasing and then increasing in apparent height.

On 4 December 2020 at 13:30 (UTC), a fireball was detected by several different instruments (including two cameras and an ionosonde) over northern Sweden, which has been named the Pajala fireball and is believed to have originated from the Northern Taurids. On the ionogram (captured by Sodankylä Geophysical Observatory, 67.36°N, 26.63°E), the trace appears at 13:31:07 (UTC) and persists for about 30 min as a sporadic E-like pattern that reached its maximum measurement frequency of 16 MHz at the time of its appearance and the frequency did not drop below 10 MHz until about 10 min after the trace appeared (Vierinen et al., 2022). And finally, on 17 January 2009, a fireball named Maribo was detected over Juliusruh, captured by a meteor radar operating at 32.5 MHz (Schult et al., 2015).

Due to the 2019 Leonids meteor shower, 2 ionograms/minute digisonde campaign measurements took place in both Průhonice and Sopron stations on 16, 17 and 18 November, starting after sunset and ending before sunrise. During the campaign measurement, on 17 November 2019 at 04:15:40, a trace was recorded by the digisonde of Průhonice (50.00°N, 14.60°E) that persisted for 20 min and showed high ionization levels. Based on previous studies, it was assumed that this was the trace of a fireball or a bolide. It being a fireball was confirmed by the Department of Interplanetary Matter of Astronomical Institute of Czech Academy of Sciences.

The group of Meteor physics at Department of Interplanetary Matter of Astronomical Institute of Czech Academy of Sciences observes meteors and performs theoretical interpretations of the observations. The Czech Fireball Network belongs to the European Fireball Network. The main instrument on every Czech station is the Digital Autonomous Fireball Observatory (Spurný et al., 2017; Borovička et al., 2019). The observational data are used to study physical processes during the penetration of meteoroids into Earth's atmosphere, including radiation and ionization. The meteorite's fall was observed in detail by Czech Fireball Network sensitive fireball cameras. The basic observational system is the European Fireball Network (Borovička et al., 2022).

The main purpose of this article is to describe and study the fireball which appeared near Prague, as detected by the Czech Fireball Network's fireball cameras, the digisonde of Průhonice and the Continuous Doppler Sounding system. Measurements from the digisonde of Sopron were used as a reference. The secondary purpose of this article is to assess the potential of the digisonde in these kind of studies. Meteor radars usually operate at frequencies between 30 and 40 MHz, while the digisonde measures between 1 and 17 MHz. Can this be used for meteor detection? European digisonde stations measure with a time resolution of 5, 10 or 15 min. The most commonly used 5-min time resolution may be suitable for statistical studies, but is it possible to detect more meteors with high cadence campaign measurements? Can it be used to determine the geographic directions of meteorite trails? Do the Skymaps derived from the drift measurements of the digisonde show traces of meteors? These questions have never been studied, yet.

In this paper, we will first discuss the data collection methods, possibly the settings of these instruments, summarize the observations, and then compare it with a regional phenomenon before the discussion and the conclusions.

2 Methods and data

2.1 Astronomic detection methods

The main instrument on every Czech station belongs to the European Fireball Network is the Digital Autonomous Fireball Observatory (Spurný et al., 2017; Borovička et al., 2019). There are cameras providing very accurate fireball recordings. These observations are only made at night and also during the darker parts of dusk and dawn.

The highest meteors can be captured by the all-sky camera at a height of 199 km. Special behavior of fireballs can be observed from an initial height above 130 km (Koten et al., 2006; **Table 1**.)

As mentioned in Spurný et al. (2000) when these meteors reach an altitude of about 130 km, their shape quickly changes to a typically drop-like form. Leonid meteor showers are typified by production meteors with a higher beginning height. The high-altitude fireballs were observed during several observations of the Leonids Multiinstrument Aircraft Campaign (MAC) in the years 1998–2001. **Table 1** shows the number of observed Leonid fireballs in this period by individual height, by (Koten et al., 2006).

The observation of radio reflections from meteor trails is not rare. There is no reliable data available for the mesospheric conditions for the observed period. Therefore, in this case it is rather difficult to infer a distortion of the ionized meteor trail. This is precisely why it is very useful to track these reflections multi-instrumentally.

2.2 Digisonde (ionogram and SkyMap)

Using vertical sounding, the ionosphere reflects electromagnetic waves at a particular height at which the plasma frequency corresponds to the transmitted signal. The plasma frequency is proportional to the electron density (Eq. **(1)**.) (Davies, 1990). An ionosonde emits electromagnetic pulses and measures time of flight of the reflected electromagnetic waves. The stratification, electron content and virtual height of the ionospheric layers can be scanned when the frequency of the sounding signal reaches the plasma frequency.

Typically, frequencies between 1 and 20 MHz are used by the ionosondes, which allows the observation of the E and F layers. A given layer will reflect the electromagnetic signals back till the critical plasma frequency of that layer (Eq. **(1)**). The critical frequency is the frequency at which the sounding frequency reaches the maximum plasma frequency within the layer–here, depending on the sentiment, it can be considered that the energy of the electromagnetic wave is absorbed or that the wave's travel time becomes infinite. Signals above this frequency are reflected from a layer with higher electron density situated above that or pass through the ionosphere without reflection.

The equation for the plasma frequency is

$$\omega_{pe} = \sqrt{\frac{n_e e^2}{m^* \varepsilon_0}} \tag{1}$$

where ω_{pe} is the electron plasma frequency (Hz), n_e is electron density (number of electrons/m^3), e is the electron charge ($1.609 \cdot 10^{-19}$ C), m^* is effective mass of the electron ($9.11 \cdot 10^{-31}$ kg) and ε_0 is the vacuum permittivity ($8.85 \cdot 10^{-12}$ F/m).

The result of such a measurement is the ionogram–on which the height-frequency values are plotted, and from which electron density profiles can be constructed. It should be noted that the height of the reflection derived directly from measurement corresponds to the situation when the electromagnetic wave travels through vacuum without any delay caused by local conditions. In case of the E and Es layer, the delay in time of flight is small and usually neglected, higher within the F layer the profile inversion is necessary.

A Digisonde DPS-4D station is installed at Průhonice (50.00°N, 14.60°E) and at Sopron (47.63°N, 16.72°E) (**Figure 1**.) and has been providing measurements since January 2004 in Průhonice and since June 2018 in Sopron as a part of the GIRO Network (Reinisch and Galkin, 2011). This type of ionosonde is able to sound not only vertically but also obliquely, which is made possible by the four additional receiver antennas surrounding the central vertical transmitter antenna (Reinisch, 1996; Reinisch et al., 2005; Reinisch et al., 2008). This arrangement allows the direction determination based on the phase-difference of the reflected signals observed at the different receiver antennas. After collecting and processing the raw data, the ionogram is produced, where the direction of the signals is indicated by the color code.

The DPS-4D digisonde can also be used to perform drift measurements, which are usually timed after the measurements required for the ionogram, because the automatically scaled ionograms can provide the necessary parameters for the setup of the drift measurement (e.g., critical frequency for the E (foE) or F (foF2) layer). If the medium is moving, a Doppler-effect will occur in the signal propagation. The estimation of the drift velocity vector is made possible by determining the location of reflection points in the ionosphere (enabled by the antenna layout) and the Doppler frequency shift. The digisonde allows for automatically processed, real-time drift measurements. The final product of the measurements is three velocity vector components: vertical (v_z), north (v_n), and east (v_e) directions. These are represented graphically in color-coded east-west and north-south planes by the so-called SkyMap.

2.3 Continuous Doppler Sounding

The Continuous Doppler Sounding (CDS) system was developed by the Institute of Atmospheric Physics CAS to study short time-scale ionospheric fluctuations (Laštovička and Chum, 2017; Chum et al., 2018; Kouba and Chum, 2018; Chum et al., 2021). The CDS instrument is suitable for fast identification of the wave-like phenomena within the ionosphere. It works on the principle of the electromagnetic wave reflection from the plasma with corresponding plasma frequency. For instance, up and down motion of the reflecting layer due to the atmospheric gravity waves causes Doppler-changes in the reflected signal. However, it does not provide data from which electron-density profiles can be derived and should be therefore completed by independent measurement.

It is worth noting that Doppler-shifts may not only be caused by the movement of the layer from which the radio waves reflect, but also, for example, by density changes caused by pressure waves

TABLE 1 Initial altitudes and numbers of meteor fireballs with an initial high-altitude above 130 km in the period of years 1999–2001, (Koten et al., 2006). The Leonid meteor swarm reaches its maximum number of meteors about every 33 years, often referred to as an "outbreak". The last one was in 2002, but 2001 also produced high numbers as shown in the table (Molau et al., 2002).

	Number of cases	130–150 km	150–160 km	>160 km
Leonids, 1998	18	5	4	9
Leonids, 1999	11	10	0	1
Leonids, 2000	17	15	0	2
Leonids, 2001	102	101	0	1

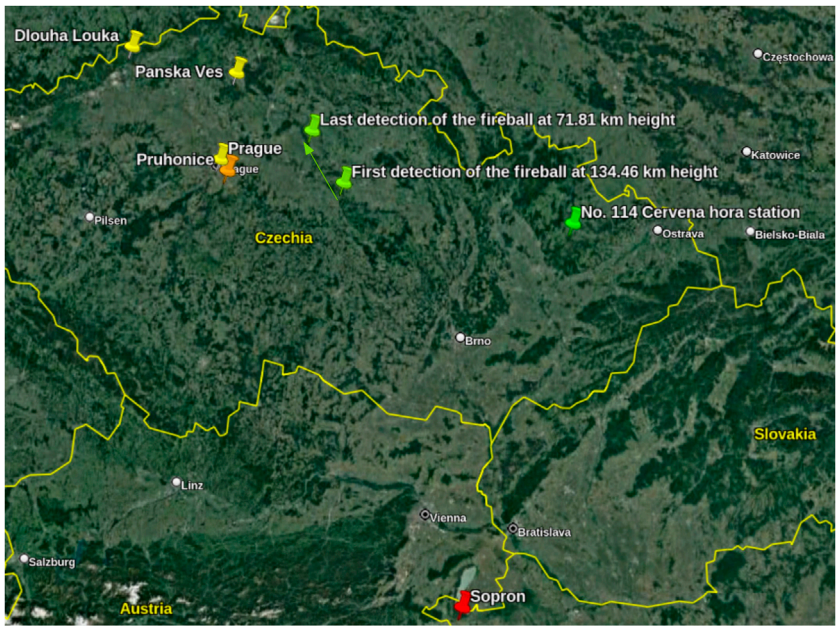

FIGURE 1
The locations of measurements, instruments and stations. The first and last detections of the fireball are marked lime green and an arrow showing projection of the recorded luminous trajectory of the fireball onto the Earth's surface. The No. 114 Červená hora station which registered the fireball is marked bright green. The digisondes (Průhonice, Sopron) are marked orange and red respectively. The CDS transmitters (Průhonice, Panská Ves, Dlouhá Louka) and the CDS receiver (Prague) are marked with yellow. Since the digisonde and the CDS transmitter are located in Průhonice, the station is marked with orange.

(long-period infrasound) or solar flares (Chum et al., 2016; Chum et al., 2018).

The system consists of transmitters distributed across the western half of the Czech Republic and a receiver set up in Prague (Figure 1). Currently, the operation is on frequencies 3.59, 4.65 and 7.0 MHz. One transmitter is located directly next to the digisonde and is separated from the receiver by 7 km (Kouba and Chum, 2018).

3 Observations and results

3.1 Astronomic observations

A bright fireball was recorded by the European Fireball Network on 17 November 2019 after 04:15:0.2 UT (±0.10 s). The meteor code of this Leonid fireball is EN171119_041459 (Figure 2).

The geographic coordinates of the captured starting point of the fireball are 49.957°N, 15.563°E, at 134.46 km height, and ending 50.237°N, 15.267°E, at 71.81 km height. Linear length of the trajectory was 73.44 km, velocity at the average trajectory point 71.18 km/s, and terminal velocity (at height 72.7 km) 70.49 km/s (Table 2). Geocentric right ascension was 153.60°, geocentric declination 21.80°, and maximum at Solar longitude 235.4°. Closest distance was 185.8 km to station No. 114 Červená hora (49.777°N, 17.542°E) with maximal convergence angle 71.7°.

Maximum apparent magnitude of the observed fireball was −15.96 (at height 83.0 km), radiated energy $5.58 \cdot 10^8$ J, and maximum brightness point was at 50.186° N and 15.321° E, at 83.03 km height. The initial photometric mass of this meteor was primarily determined to be 1.448 kg (P. Spurný, priv. comm.).

Observation was carried out using 5 cameras from closest distance 185.8 km at the station No. 114 Červená hora (Figures 1, 2). The fireball was observed by the cameras of the European Fireball

FIGURE 2
Optical image of the trail left by the fireball detected at 04:15:0.2 on 17 November 2019. The picture was taken at Červená hora station by the Czech Fireball Network betweeen 04:15:10 - 04:15:45 UT, the exposition time was 35 s.

TABLE 2 A summary of the localization of the Leonid bolide above the Czech Republic, data were provided by P. Spurný (priv. comm.).

Meteor code	EN171119_041459
Time of arrival	2019.11.17.04:15:0.2 UT (±0.10 s)
Duration	1 s
Coordinates of appearance	49.957° N, 15.563° E, 134.46 km (height)
Coordinates of disappearance	50.237° N, 15.267° E, 71.81 km (height)

Network (Borovička et al., 2022) and the data were provided by P. Spurný (priv. comm.).

3.2 Ionogram and SkyMap

During the passage of the 2019 Leonid meteor swarm, on 16, 17, and 18 November, joint 1-min temporal resolution campaign measurements were launched in both Průhonice and Sopron digisonde stations (**Figure 1**) between 16:30:00 (UT) in the afternoon and 06:30:00 (UT) in the morning. 2 ionograms were taken every minute. The measurement was performed between 1.5 and 17 MHz. Furthermore, high resolution SkyMap (1/min) measurements at ~ 2,500 kHz were also performed during the above-mentioned periods.

3.2.1 Ionograms

The first trace of the fireball appears on the ionogram taken at Průhonice station at 04:15:40 (UT) on 17 November 2019. The ionogram in front of it, taken at 04:15:00 (UT), shows no meteor traces. This agrees well with astronomical observations (**Figure 2**; **Table 2**).

The trace on the ionogram at 04:16:00 resembles the pattern of a sporadic E layer (**Figure 3**) similar to those described in other studies (Maruyama et al., 2003; Maruyama et al., 2008; Schult et al., 2015; Kereszturi et al., 2021; Vierinen et al., 2022). However, the trace differs in almost all respects from the regular sporadic E layer's behavior (see **Section 3.4**), it was detected as a very thin layer up to high frequency range. For the months of November and December of 2019, analysis of ionograms from both Průhonice and Sopron stations shows that the median of the sporadic E frequency is 2.55 MHz for Průhonice station and 2.49 MHz for Sopron station, while the median of the height is 107.6 km for Průhonice station and 102.3 km for Sopron station. These data are based on 10406 ionograms processed for Průhonice station, with 20.2% sporadic E occurrence rate. For Sopron station, 14069 ionograms were processed, with 19.1% sporadic E occurrence rate.

The maximum reflection frequency of the ionization caused by the 17 November 2019 Leonid fireball reached 17 MHz already at its first appearance on the ionograms (**Table 3**). It is very likely that the frequency is saturated at 17 MHz and the actual value of top frequency can be much higher. The ionization rate did not go below 10 MHz until 04:26:00 (**Table 3**). The last ionogram on which the fireball's effect can still be clearly identified was taken at 04:35:40 (UT).

The height of the fireball's trace (**Figure 3**.) started at 129.3 km virtual height at 04:15:40 (**Table 3**). On the next ionogram, the trace is already split into three distinct and separeted "layers", and this remains the case in all the following ionograms. The trace reached a maximum of 5 distinct "layers". The height of these layers according to the ionogram readings (**Table 3**.) first decreased, then increased slowly but steadily over time–the lowest is at 114.9 km virtual height, while the highest before the decay of the fireball's trace is at 142.6 km virtual height. The rise in the height of the fireball's trace is a phenomenon that has not only been observed elsewhere (Maruyama et al., 2008), but is also reproduced by numerical modeling (Zinn and Drummond, 2005; Zinn and Drummond, 2007). However, these height changes observed on the ionograms should not be interpreted as clear vertical motion only, especially that the CDS measurements indicate the presence of wind shear. The movements are probably the results of the digisonde's setup with 3D motions of fireball's trace, since the measurement is based on the time-of-flight of the sounding electromagnetic waves so the exact height changes cannot be determined based on that.

Meanwhile, the ionograms of Sopron station did not show any similar effect–there is no regular sporadic E layer on the ionograms (**Figure 3**). Both stations were taking measurements synchronously allowing for oblique measurement. With high probability, we also ruled out the presence of sporadic E layer in half of the distance between the stations as it would be observed on oblique ionograms.

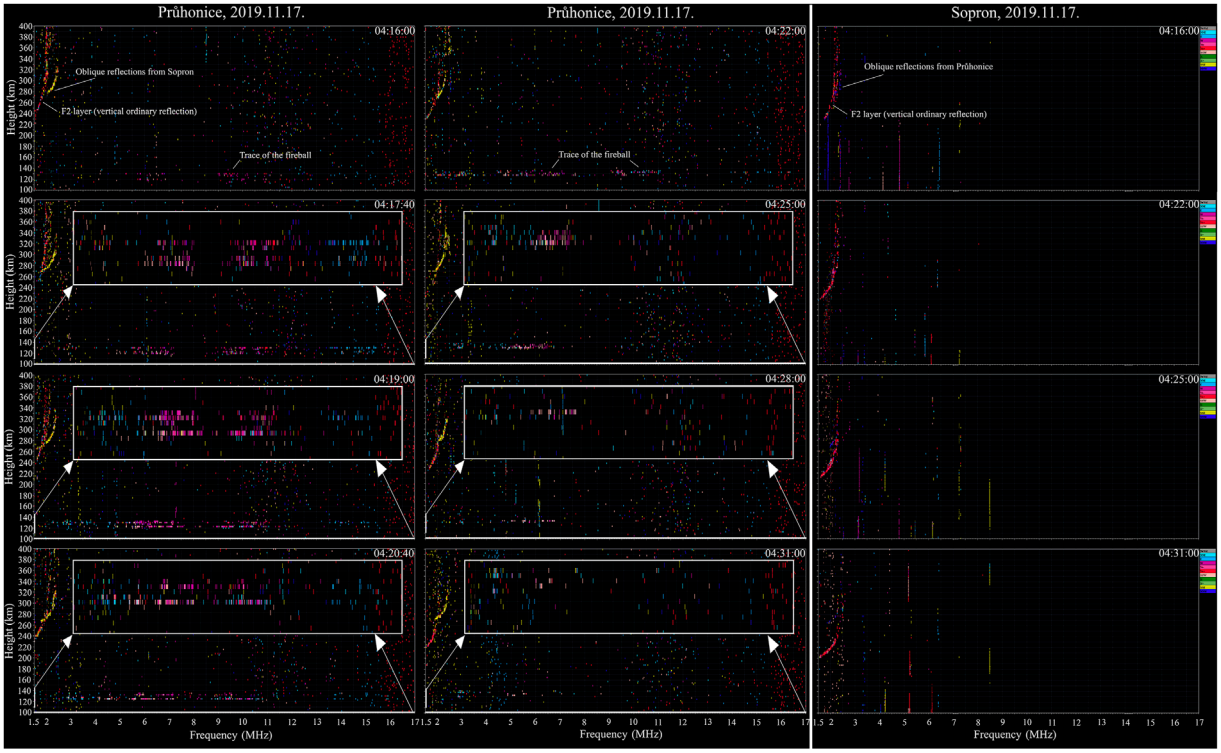

FIGURE 3
Selected ionograms from Průhonice and Sopron stations, between 1.5 and 17 MHz, at virtual heights between 100 and 400 km and at time between 04:16 - 04:31 (UT), taken at 6 dB MPA threshold. For a white background picture about the ionograms of Průhonice please see **Supplementary Figure S1** and for pictures made at 4 dB MPA threshold please see **Supplementary Figure S2**. The ionograms from Průhonice station (left and middle column, left column between 04:16 - 04:21, middle column between 04:22 - 04:31) show the trace of the fireball-induced ionization and its evolution over time. The white rectangle shows the 110–145 km and 1.5–17 MHz zoomed-in part of the ionograms. In contrast, the ionograms of Sopron station used as reference do not show any similar phenomena, not even regular sporadic E, indicating the localisation of plasma trace related to the fireball in the near region of Průhonice station.

Therefore we deduced that the trace detected at Průhonice station is a local plasma structure restricted to a limited area close to Průhonice DPS-4D (**Figure 1**). Indeed, the location of the meteor trace corresponds to the sounding cone of the Průhonice's digisonde, while it is out of the cone of Sopron's digisonde.

It may also be worth noting that for the most often used 6 dB data presentation threshold (defined as a noise level based on the most probable amplitude (MPA)), it appears as if reflections are disappearing in bursts by frequency. However, this is not a real physical phenomenon, but is due to a filtering in the processing software and/or in the raw data save settings after the digisonde measurement (Reinisch et al., 2008; Reinisch, 2009). When the threshold is set to 4 dB or lower, these reflections can be found (**Figure 4**).

Another known measurement feature is the phase jump. Although the antenna layout allows the direction of the reflections to be determined, it is possible that due to phase ambiguity of the signal the direction of the arriving signal is misinterpreted and rotated by 180°. The ionization cloud caused by the fireball shows E, NNE, W and SSW oblique reflections (**Figures 3**, **4**), but the W and SSW directions only occur at well-defined frequency ranges (usually between 5–13 MHz) and, given the fireball's detection and the drift measurements, there is a strong possibility that the W and SSW directions were in reality probably E and NNE directions (Reinisch et al., 2008; Reinisch, 2009).

The ionograms were also scaled manually between 03:45:00 and 04:45:00 (UT) for both Průhonice and Sopron stations, in order to see if the fireball had any local effect on the heights of the ionospheric layers because bolides and superbolides are capable of generating traveling ionospheric disturbance-like phenomena (Chernogor, 2015). Based on the ionograms, there was only the F2 layer at this time of that day beside the thin sporadic E layer caused by the fireball at Průhonice station. It is worth noting that the limited quality of the ionograms (because of the 1 min cadence) and the presence of a strong spread F activity (Wang et al., 2018) made the manual evaluation difficult and subject to bias.

According to the height analysis (see **Supplementary Figure S3**), there was a spike in the F2 layer's virtual height at 04:13:40 (UT) at Sopron station and at 04:14:40 (UT) at Průhonice station. Relatively close to the appearance of the fireball's trace–which happened at 04:15:0.2 (UT) according to the astronomical observations (**Figure 2**; **Table 2**) and 04:15:40 (UT) according to the ionograms–it would be easy to attribute this phenomenon as the fireball's effect,

10.3389/fspas.2023.1197832

TABLE 3 The maximum frequencies reached by the fireball's trace, according to the height of the layer, and their evolution over time. These were taken by manual reading at 4 dB MPA threshold if there were distinct reflections at 6 dB threshold of the given height. The readings are highly subjective and are included here for illustrative purposes only.

Time (UT, h:mm:ss)	Virtual height (km)											
	114.9	117	119.9	123	125.1	127.3	130.3	133.3	135.2	137.7	139.6	142.6
4:15:40							17					
4:16:00	15.9		16.2			11.2	12.6					
4:16:40	13.73		17			16.22	16.22					
4:17:00	11		16.8			15.43	15.43					
4:17:40	8.6	8.6	16.56	15.34		16.5	16.83					
4:18:00		7.17	14.58	16.2		15.5	16.8					
4:18:40		7.1	11.6	16.68		6.8	17	11.98				
4:19:00			9.4	15.3		7.3	16.3	15.1				
4:19:40				11.7	16.8		15.9	15.6				
4:20:00				10.7	16.4		14.9	15.2				
4:20:40					16.3	9.3		14.4				
4:21:00					16.73	14.46	17	12.37				
4:21:40					11.17	14.78	11.9	16.2	13.5			
4:22:00					7.1	13.98	15	16.37	14.6			
4:22:40					6.5	10.8	12.6	15.3	14.1			
4:23:00						11.2	11.6	15.1	12.8			
4:23:40						7.58	11.36	13.73	16.2			
4:24:00						7.19	10.6	12.26	13.8			
4:24:40						7.19	9.4	11.9	10.18			
4:25:00						7.15	7.8	11.33	6.9			
4:25:40						6.58	7.54	11.12	3.7	3.6		
4:26:00						6.69	7.6		7.2	3.34	2.97	
4:26:40							7.2	7.15				
4:27:00						5.4	6.95		7.16	3.5	3.23	
4:27:40							6.86	6.9				
4:28:00							6.74	6.84				
4:28:40							5.94	6.46				
4:29:00							5.76	6.64		7.04		
4:29:40							4.62	5.83				
4:30:00						5.45	5.41		5.83	6.58	6.03	
4:30:40							5.66	7.17	6.86	6.89	7.1	
4:31:00							4.5	5.99	6.77	5.38	7.3	
4:31:40							4.28	5.76	6.89	4.92	4.66	
4:32:00							3.05		6.39	4.66	4.8	5.28
4:32:40								3.55	5.64	3.82	5.7	6.5
4:33:00								3.18	4.94	3.46	3.53	6.2
4:33:40												
4:34:00								3.1	4.9	3.36	3.2	3.9
4:34:40			Above 15 MHz							3.4	3.6	5.2
4:35:00			Above 10 MHz							3.2		
4:35:40												2.95
	Maximum frequency (MHz)											

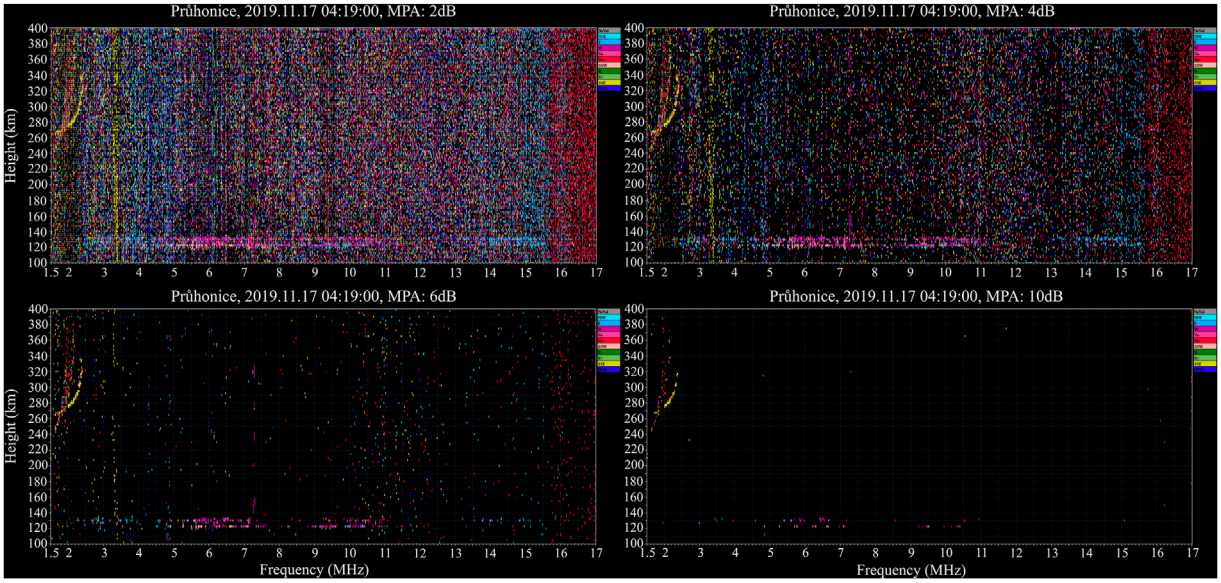

FIGURE 4
The effect of the most probable amplitude threshold settings. The lower the threshold (2 dB or 4 dB, upper row) the noisier the ionogram, but also more details of the fireball's effect can be seen. The higher the threshold (6 dB–the default setting used for processing–or 10 dB, lower row), the lower the noise, but the more detail is lost from the fireball's effect.

but the ionograms of Sopron station also showed this spike in height almost a minute earlier than Průhonice station. This suggested that this sudden increase in height was probably a regional, disturbance-like phenomenon since it was unlikely that a fireball with a linear trajectory length of 73.44 km and a duration of 1 s could have taken a perceivable effect at Sopron station almost 2 min before the event itself. This means that, presumably, the fireball had no effect on the height of the F2 layer, which is not surprising given that it is a fireball and not a bolide or superbolide.

3.2.2 SkyMaps

During the campaign measurements, drift measurements were also taken every minute. The measurement settings were chosen based on the automatic scaling of the ionograms. Between 04:19:20 (UT) and 04:35:20 (UT)—with the exception of 04:21:20, 04:27:40 and 04:34:20 (UT) SkyMaps –,1 to 5 reflection points were displayed on each SkyMap (**Figure 5**). These are not sufficient to determine a plasma drift velocity, but can serve to estimate the height of the reflection points which varies between 122 and 140 km, suggesting that they are reflected from the fireball's trace (**Table 3**). Before 04:19:20 and after 04:35:20 the SkyMaps are completely empty for a long time. Presence of only a few reflection points on the SkyMaps indicate that in general the ionosphere is nicely stratified with only a small and very localized distortions of reflection planes due to the fireball's passage and follow-up processes of sporadic E layer formation.

Based on the drift measurements, the approximate location of the sporadic E layer-like ionization cloud caused by the fireball can be determined and it agrees well with the trajectory estimated by the astronomical observations (**Figure 1**). Furthermore, it is consistent with what can be seen in the spectrograms of the Continuous Doppler Sounding, where the trace appears on the Panská Ves-Prague and the Průhonice-Prague sounding paths, but not on the Dlouhá Louka-Prague path (see **Section 3.3**).

3.3 CDS

Continuous Doppler Sounding measurements were taken at 4.65 MHz and were plotted on the Doppler-shift spectrogram for the time period of 04:00-05:00 UT on 17 November in **Figure 6**. The fireball trace appeared as a diffuse blip on 2 of the 3 sounding paths from about 04:18 UT to 04:30 UT, which roughly coincides with the observations on the ionograms (**Table 3**). The fact that it appeared on only 2 sounding lines (on the Průhonice-Prague and Panská-Ves-Prague lines, but not on the Dlouhá Louka-Prague line) may also suggest that this is a relatively small-scale localized phenomenon (**Figure 1**).

In addition to the relatively broad and diffuse spectrum (blip) observed on these two sounding tracks, two peaks in the spectral densities can be seen. One in the vicinity of zero Doppler shift (indicated by the ground wave–horizontal line in the Doppler-shift spectrogram) and the other with a negative Doppler-shift; the negative Doppler-shift decreases with time (absolute Doppler shift increases). This means that there are two subregions with different radial velocities relative to the midpoints between transmitters and receiver from which radio waves predominantly reflect, which might indicate a wind shear in the region of reflection (meteoric trail). The subregion with the negative Doppler shifts moves away. Interestingly, the signal strength of the subregion corresponding to the approximately zero Doppler-shifts increases just before the signal disappears, probably due to some dynamic changes in the electron densities.

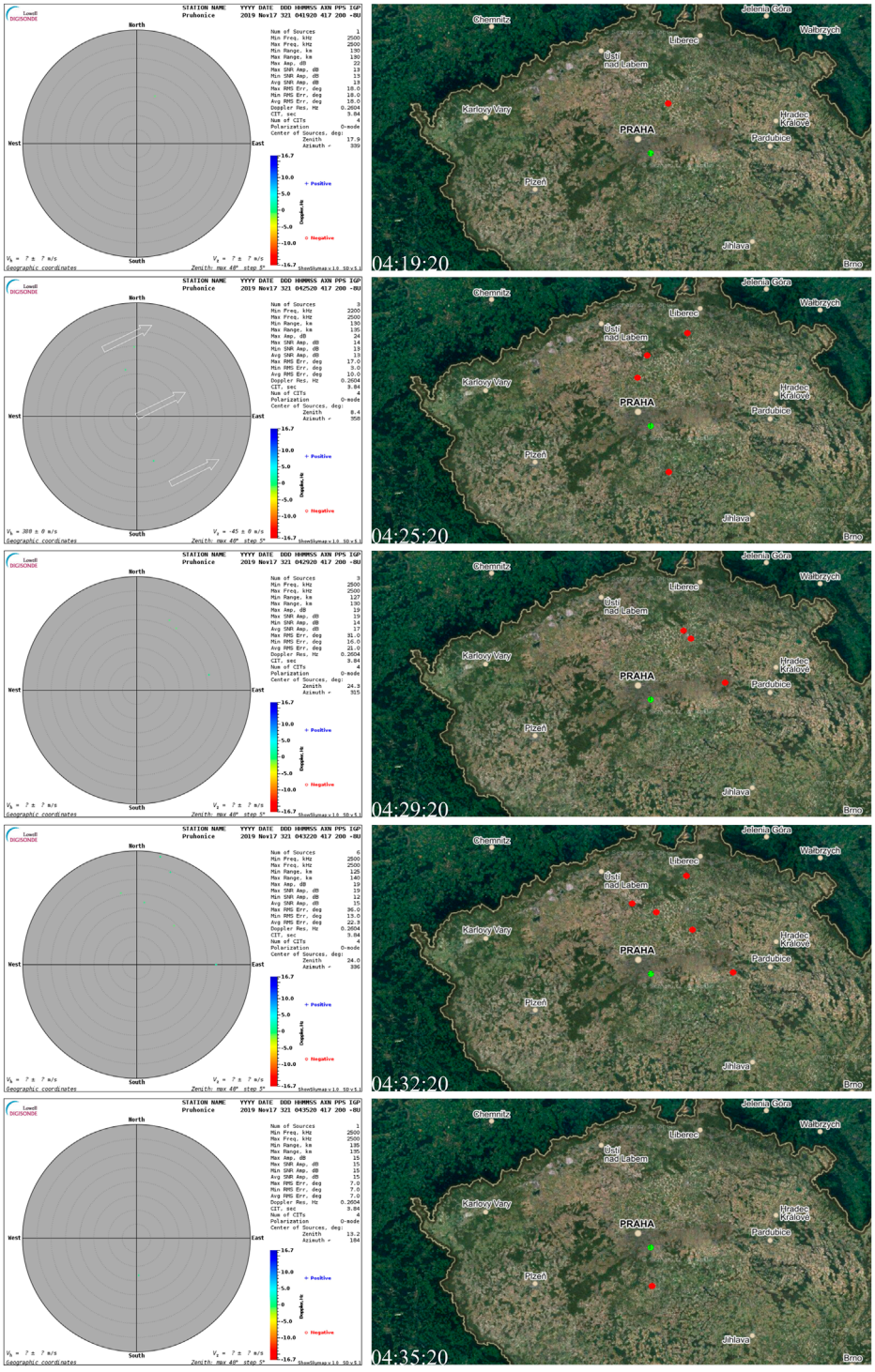

FIGURE 5
Selected SkyMaps, displaying the drift measurement (left column), the geographical location of the reflection (right column). Průhonice station is marked with a green dot. The reflections detected by the digisonde are marked with red dots. Since the measurements were not enough to reliably determine a drift velocity, the red dots of the right column are only representative and do not indicate any physical quantity.

This event is very different from how a descending sporadic E usually appears on spectrograms (see **Section 3.4.2**). It should be noted here that sporadic E layer is rather a summer phenomenon, however it could be observed through the year as there are many physical processes contributing to the layer formation (Whitehead, 1961; Whitehead, 1989; Mathews, 1998; Haldoupis, 2012; Arras and Wickert, 2018 among others).

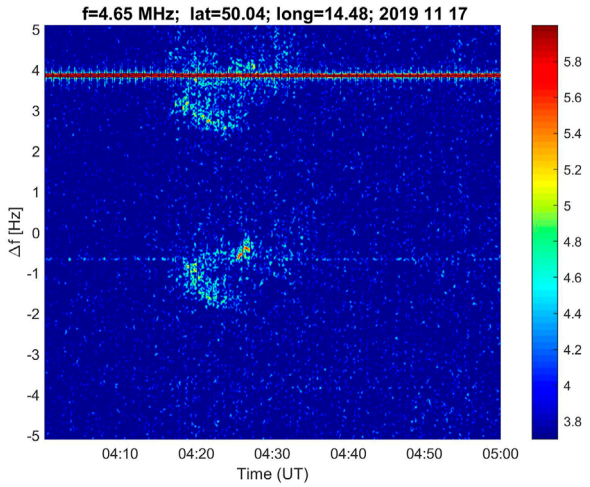

FIGURE 6
Doppler shift spectrogram taken on 17 November 2019 between 4:00 and 5:00 a.m. The fireball's trace is visible between 4:18 and 4:30 on 2 of the 3 paths (**Figure 1**).

3.4 Comparison with a strong sporadic E

It may be useful to compare these traces left by the fireball with cases when a sporadic E layer is present at the ionograms and also in the Doppler-shift spectrogram. For comparison, we have taken a case from 1 January 2020, showing a southward drifting sporadic E with relatively high ionization level (~8 MHz critical frequency (foEs) in certain times) which is also nicely visible in the CDS measurements.

The geomagnetic conditions show a quiet day (based on the OmniWeb: Kp ~ 1, Dst ~ −5 nT, see **Supplementary Figure S4**) and according to the satellite data the tropospheric conditions were calm, too (see **Supplementary Figure S5**). The ionograms (**Figure 7**.) and the Continuous Doppler Sounding (**Figure 8**.) show a clear difference compared to the previously shown fireball-induced changes. Unfortunately, the drift measurements were primed to observed motions at the F2 layer at both stations and could not be used here (see **Supplementary Figure S6**).

3.4.1 Ionograms during a strong sporadic E activity

Průhonice station made an ionogram every 15 min at this time, while Sopron station made one every 5 min. The measurements of the two stations were asynchronous at this time, with the ionograms of Sopron station being taken 10 s later than the ionograms of Průhonice station.

A strong, patchy sporadic E layer was detected at both stations during the evening hours (16:00 - 18:30 UT) on 01.01.2020. **Figure 7** displays the temporal evolution of this regional sporadic E layer, with strong ionization and spread. Both stations show northward reflections at the beginning and southward reflections before the disappearance of the sporadic E layer, which may suggest a southward direction of plasma motion. Despite the proximity of the stations, the temporal behavior is different, with sporadic E appearing and disappearing earlier in Sopron than in Průhonice.

Some features are also worth noting. The critical frequency of sporadic E layer (foEs) over Sopron station almost reaches 8 MHz at 17:00:10 (UT). The ionograms show a second reflection at 17:15:10 (UT) and at 17:45:10 (UT) a third reflection, too. For Sopron station, between 17:05:10 and 17:55:10 (UT) the F2 layer is completely blanketed.

Similar features can be observed for Průhonice station, although the effects are somewhat weaker and the durations are not the same. The maximum critical frequency (foEs) of 5.83 MHz is reached at 17:15:00 and the sporadic E layer on this ionogram produces a third reflection. The F2 layer is also completely blanketed but only on this ionogram. On the 17:45:00 ionogram there is still some blanketing, but at 18:00:00 the sporadic E layer has disappeared in the ordinary component, but is still detectable in the extraordinary component, unlike in Sopron station.

All of this is in sharp contrast to what can be seen with the fireball's effect–despite the much higher ionization (reaching 17 MHz), there is no second reflection and no blanketing (**Figure 3**), also, the effect was local and not regional since nothing can be seen on the ionograms of Sopron.

3.4.2 CDS measurement during a strong sporadic E activity

There is a sequence of two sporadic E layers seen as oblique spread structures in the Doppler shift spectrogram recorded between 16:00 and 18:00 UT (**Figure 8**). Sporadic E was moving at velocity of approximately 100–110 m/s in a roughly south-westerly direction (azimuth approximately 210°–220°), which can be inferred from the time lags between occurrences of the structure along the various sounding paths (transmitter-receiver pairs). The trace of a distinct regional inhomogeneous sporadic E layer usually appears as such a massive signal (oblique spread structure), in contrast to the faint, diffuse and dispersed signal of the fireball (**Figure 6**).

4 Discussion

Compared to ionospheric scales, the effect of the fireball was highly localized. This can be observed in the fact that while the Průhonice station ionograms showed a clear trace, the measurements of Sopron station showed no reflection originating from the Es region. It has been shown that the sporadic E layers are driven by modulation of large-scale tidal waves by planetary waves (Pancheva et al., 2003; Haldoupis et al., 2006; Šauli and Bourdillon, 2008; Mošna et al., 2015) which means that the presence of sporadic E layers at two close locations as Průhonice and Sopron is typically driven by the same forcing and therefore highly correlated. Furthermore, in the case of Continuous Doppler Sounding, which measures 3 sounding paths at 4.65 MHz, the effect was only visible on 2 of the 3 paths, Panská Ves-Prague and Průhonice-Prague, but not on the Dlouhá Louka-Prague path. This can also be seen in the drift measurements of Průhonice station because there is an average of 1–3 reflections per SkyMap from 122 to 142 km height over the duration of the event, and although these points are scattered, they still fall within a well-defined area, which is consistent with what is observed in Continuous Doppler Sounding and are within reasonable distance from the original trajectory of the fireball.

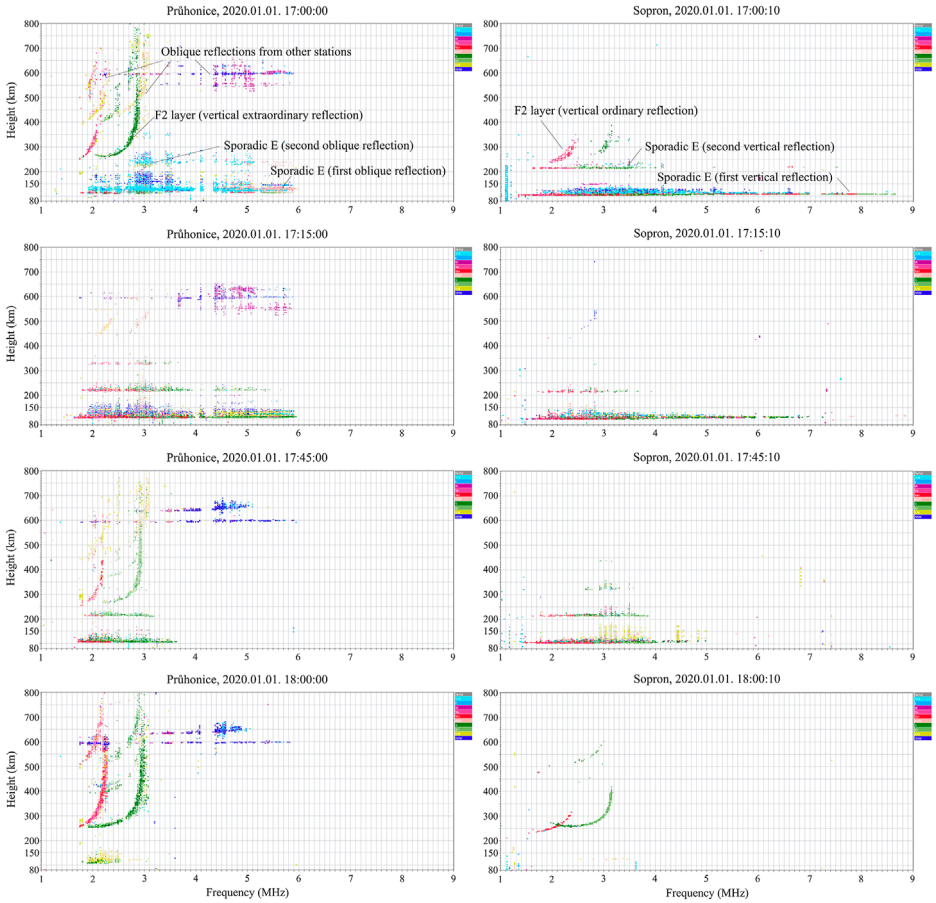

FIGURE 7
Ionograms recorded at 17:00, 17:15, 17:45 and 18:00 (UT) at Průhonice (left column) and at Sopron (right column) stations. They show the temporal evolution of a strong, regional sporadic E layer.

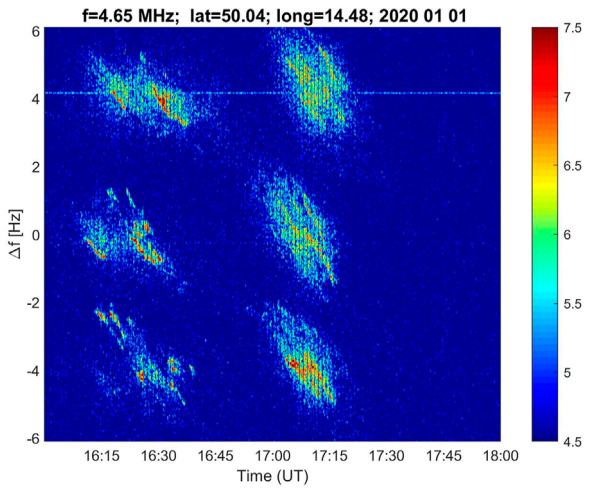

FIGURE 8
A regional sporadic E layer drifting toward south on 4.65 MHz Doppler-shift spectrogram made on 1 January 2020.

The movement of the fireball's ionization trace was within expectations. The manual readings of the heights (**Table 3**) showed that the height of the layer decreased immediately after its appearance, and then increased shortly afterwards. This is consistent with what was described by Maruyama et al. (2008) and reproduced by numerical modeling in Zinn and Drummond 2005 and Zinn and Drummond 2007. But these motions observed on the ionograms should not be interpreted as clear vertical motion, especially that the CDS measurements indicate the presence of wind shear. The movements were probably the results of the digisonde's setup with 3D motions of fireball's trace.

Regarding the layers or stratification of the trace (it has broken up into 3–5 distinct layers, usually separated by 3–6 km) a similar behavior has been observed before in the case of the Dhajala fireball (3 layer, separated by 6 km, Rajaram and Chandra, 1991).

The lifetime of the ionized layer was 12 min according to the Continuous Doppler Sounding measurements and 20 min according to the digisonde measurements. This was slightly below what has been observed so far. Maruyama et al. (2003) and Maruyama et al. (2008) reported lifetimes of 40 min although the

exact origin of their phenomena is unclear. Vierinen et al. (2022) reported a lifetime of 30 min for the Pajala fireball. The Dhajala fireball's trace lasted for an hour (Rajaram and Chandra, 1991). The lifetime of the observed faint sporadic E layer probably depends on parameters of the particular observed fireballs like mass (Dhajala fireball was estimated to be above 10 kg, the Pajala fireball's dynamic mass was estimated between 0.6 and 1.7 kg, the fireball of this study had a photometric mass of 1.45 kg), velocity, local atmospheric and ionospheric conditions including the wind conditions, geomagnetic location, and lower atmosphere situation due to coupling within the neutral and ionized atmosphere.

Discussing the extent of ionization is somewhat complicated by the fact that the upper limit of the digisonde measurement was 17 MHz. In several cases, the ionograms clearly showed that saturation occurs at this frequency, i.e., the maximum was above this value. This situation was similar to that observed for the Pajala fireball, where the measurement limit was 16 MHz. Since Schult et al. (2015) detected a fireball at 32.5 MHz with meteor radar; the ionosonde measurements of Maruyama et al. (2003) reached a top frequency of 30 MHz and Maruyama et al. (2008) reached 27 MHz, it is in agreement with our assumption that the top frequency of the fireball exceeded 17 MHz. In addition, the phenomenon observed for the Pajala fireball, where the top frequency dropped below 10 MHz only after 10 min, was also produced by this fireball.

The trace caused by a fireball (which resembles a faint sporadic E) compared to a strong sporadic E shows substantial differences. For this purpose, a case was chosen when both the geomagnetic and tropospheric conditions were quiescent. The sporadic E layer of 1 January 2020 was a southward moving (based on CDS measurements), probably tilted layer, showing a strong spread and ionization reaching 6–8 MHz on the ionograms. The explanation of the large spread feature is unknown since it happened during tropospherically and geomagnetically quiet conditions. The important characteristics of the fireball induced sporadic E layer was its thickness. Sporadic E layers are often observed as electromagnetically thick layers reflecting almost all the sounding signals, while the structures observed in connection with meteor occurrence we observe thin and localized structures. In comparison it may worth noting that, unlike the behavior of this stronger sporadic E layer, no second reflection or blanketing occurred with the trace of the fireball was observed, suggesting that despite the high plasma frequency of the trace its ionization was not strong enough to cause blanketing for the upper layers and/or the trace occurred only in a very small area near the ionosonde.

Manual scaling was used to investigate whether the fireball had any effect on the height of the F2 region. For the Průhonice station, there was an increase in the height of the F2 layer at 04:14:40 (UT), followed by a rapid decrease in height. The same features can be observed in the data of Sopron station used as a reference, but the peak occured at 04:13:40 (UT). While the timing of these spikes were highly convenient, especially considering the trajectory of the fireball, is most likely not the result of the fireball, but rather of a regional small-scale traveling ionospheric disturbance (TID) or some similar atmospheric phenomenon. Since the investigated phenomena was classified as a fireball, and not as a bolide or superbolide, this is within expectations.

It may be of interest to note that the fireball effect is first detected by the CDS measurements at 04:18 (UT), while the drift measurements detected it at 04:19:20 (UT), i.e. 3 and 4 min after the fireball's appearance. Furthermore, although the drift measurements were detecting it until the disappearance of the trace at 04:35:40 (UT), the diffuse blip on CDS measurements disappeared 5 min earlier, as early as 04:30. Since the ionosonde measurements show that there was still ionization above 4.65 MHz after 04:30, but the ionosonde covers a larger area, it is conceivable that there was not enough of the trace left in the sounding paths for the CDS to detect it.

Unfortunately, there was no reliable high-altitude wind data. The impact of the wind seems to appear on the optical observation of the fireball itself (**Figure 2**). The fact that the trace on the ionograms splits into 3 distinct layers immediately after its first appearance like the Dhajala-fireball, and that this number goes up to 5 over time (**Figure 3**), and that the trace also occurs between altitudes 114.9 and 142.6 km (**Table 3**) during its 20 min lifetime, suggests that there was some kind of wind activity above altitude 100 km and that possibly some wind shear has occurred. Another clue to this might be the spatial distribution of the trajectory marked in **Figure 1** and the incoming reflections on the SkyMaps shown in **Figure 5**, which shows a good correlation, but the points reflected from the ionosphere are coming from a wider area, which could be due to wind effects. Further evidence of this may be the strong frequency spread F activity on the ionograms, a known nighttime phenomenon which has roots in the atmospheric conditions (Wang et al., 2018).

5 Conclusion

A bright fireball was recorded between 49.957°N, 15.563°E, at 136.46 km height and 50.237°N 15.267°E at 71.81 km height on 17 November 2019 04:15:0.2 (UT). Once in the atmosphere, the fireball caused strong ionization. Due to its proximity to the Průhonice digisonde station and the Continuous Doppler Sounding network developed by the Institute of Atmospheric Physics CAS, the event allowed for observation of the ionospheric effects.

It was the first evidence, to our knowledge, that a digisonde (DPS-4D type) detected a documented fireball. A major advantage of the digisonde over other "classical" ionosondes is its ability to determine direction. Furthermore, this is the first time that drift measurements made by the digisonde have shown reflections attributable to the fireball's effect. In the ionograms recorded by the digisonde, the trace of the fireball appeared as a faint sporadic E layer. The ionization reached 17 MHz which was the measurement's limit, the trace was split into several layers, the height of which moved downwards and then upwards. This cannot be assessed as a purely vertical movement due to the lack of wind data and was probably the result of complex 3D movements which is also indicated by the CDS measurement. There were also synchronized measurements at Sopron station. In these ionograms there was no trace of sporadic E activity (neither vertical nor oblique), suggesting that the observed effect at Průhonice station was a local one.

It was the first time that Continuous Doppler Sounding had detected a trace of a fireball. It appeared as a relatively broad and diffuse spectrum (blip) observed on 2 of the 3 sounding paths, indicating a relative localization. The measurements displayed

two subregions with different radial velocities relative to the midpoints between transmitters and receiver from which radio waves predominantly reflect, which might indicate a wind shear in the region of reflection.

Since many properties observed in this paper (height changes, stratification, high top frequency, duration, *etc.*) are scattered but have been reported in previous literatures (Rajaram and Chandra, 1991; Maruyama et al., 2003; Maruyama et al., 2008; Schult et al., 2015; Vierinen et al., 2022), we compared this with the behavior of a strong sporadic E layer. Clear differences were observed between the fireball's trace and the "average" sporadic E layer (e.g., blanketing, secondary reflections).

As for the digisonde itself and its capabilities, this example illustrates that this instrument can be used to detect bodies of meteoric origin. The range of sizes over which it operates will need to be further investigated. These measurements can be carried out regardless of the time of day and metrological conditions, however, the measurements are limited to a roughly 100 km radius of the digisonde. A trace of a fireball can be expected to persist for 20–60 min, based on the evidence so far. The most commonly used 5 min time resolution measurements may be suitable for detecting such an object, but for detecting smaller bodies it may be more appropriate to use a higher time resolution. The digisonde direction determination may contain an error of 180°. It is necessary to take this into account and the development of this feature would be desirable in the future. The drift measurements and Skymaps clearly showed reflections associated with the fireball. In this case, complex 3D movements and the extent of the affected area can be inferred.

Detection of meteors by means of high sampling rate digisonde measurement represents useful complementary observation techniques. This well documented example for the plasma trace detection of a fireball by digisonde measurements can open the door for further investigations of ionospheric impacts of individual meteors.

Data availability statement

The SAOExplorer (used for manual scaling) is available at https://ulcar.uml.edu/SAO-X/SAO-X.html NASA/GSFC's OMNI data set through OMNIWeb https://omniweb.gsfc.nasa.gov/ The astronomical data is the property of Czech Fireball Network and cannot be distributed freely. The Doppler data in the form of spectrograms are available at http://datacenter.ufa.cas.cz/ under the link to Spectrogram archive. The datasets of digisonde measurements (ionograms, SkyMaps) presented in this study can be found in online repositories. The names of the repository/repositories and accession number(s) can be found below: Global Ionospheric Radio Observatory http://giro.uml.edu The SAT24 meteorological satellite pictures are available at: https://www.sat24.com/history.aspx further inquiries can be directed to the corresponding author.

Author contributions

VB was conceptual author of the digisonde campaign measurements leading to this article and helped with extensive knowledge regarding various ionospheric phenomena. CsSz found the fireball's trace on the ionograms, pre-wrote the manuscript, analyzed the movements of the trace and scaled ionograms by hand. JCh found the trace of the fireball in the CDS, analyzed the CDS measurements and chose the sporadic E used for the comparison, also helped with extensive knowledge regarding various ionospheric phenomena. PKk helped with finding and linking the separate data (astronomical, ionospheric) on which the article is based on, helped with the height contour analysis and helped with extensive knowledge regarding various ionospheric phenomena. ZM analyzed the general behavior of the sporadic E in 2019 November and December (manually processing 20000+ ionograms) and helped with extensive knowledge regarding various ionospheric phenomena. KP prepared, analyzed and calculated everything related to astronomical data. DK analyzed the drift measurements and made the plots about the geographical representation of the reflections. All authors contributed to the article and approved the submitted version.

Funding

The work was supported also by the GINOP-2.3.2-15-2016-00003 (titled "Kozmikus hatások és kockázatok") Hungarian national project. This work was made possible by the "Multiinstrumental investigation of the midlatitude ionospheric variability" bilateral project of the Czech Academy of Sciences and Hungarian Academy of Sciences (MTA-19-03 and NKM 2018-28). The support under the grant GA21-03295S by the Czech Science Foundation is acknowledged. The contribution of VB was partially supported by Bolyai Fellowship (GD, no. BO/00461/21).

Acknowledgments

This fireball was observed by the cameras of the European Fireball Network (Borovička et al., 2022) and the data were provided by P. Spurný (priv. comm.). We also thank Czech Fireball Network, especially J. Borovička and P. Spurný for very kindly providing the data.

Conflict of interest

The authors declare that the research was conducted in the absence of any commercial or financial relationships that could be construed as a potential conflict of interest.

Publisher's note

All claims expressed in this article are solely those of the authors and do not necessarily represent those of

their affiliated organizations, or those of the publisher, the editors and the reviewers. Any product that may be evaluated in this article, or claim that may be made by its manufacturer, is not guaranteed or endorsed by the publisher.

Supplementary material

The Supplementary Material for this article can be found online at: https://www.frontiersin.org/articles/10.3389/fspas.2023.1197832/full#supplementary-material

References

Arras, C., and Wickert, J. (2018). Estimation of ionospheric sporadic E intensities from GPS radio occultation measurements. *J. Atmos. Sol. Terr. Phys.* 171, 60–63. doi:10.1016/j.jastp.2017.08.006

Axford, W. I. (1963). The formation and vertical movement of dense ionized layers in the ionosphere due to neutral wind shears. *J. Geophys Res.* 68, 769–779. doi:10.1029/JZ068i003p00769

Beech, M. (1998). Large-body meteoroids in the Leonid stream. *Astron J.* 116, 499–502. doi:10.1086/300435

Borovička, J., Spurný, P., and Shrbený, L. (2019). "New spectroscopic program of the European fireball network," in *International meteor conference, pezinok-modra, Slovakia*. Editors R. Rudawska, J. Rendtel, C. Powell, R. Lunsford, and C. Verbeeck (Knofel), 28–32.

Borovička, J., Spurný, P., Shrbený, L., Štork, R., Kotková, L., Fuchs, J., et al. (2022). Data on 824 fireballs observed by the digital cameras of the European Fireball Network in 2017–2018. *Astron Astrophys.* 667, A157. doi:10.1051/0004-6361/202244184

Borovička, J., Štork, R., and Bocek, J. (1999). First results from video spectroscopy of 1998 Leonid meteors. *Meteorit. Planet Sci.* 34, 987–994. doi:10.1111/j.1945-5100.1999.tb01418.x

Ceplecha, Z., Spalding, E. R., Jacobs, C., Revelle, D. O., Tagliaferri, E., and Brown, P. (1999). "Superbolides," in *Meteroids 1998*. Editors W. J. Baggaley, and V. Porubcan, 37.

Chen, J. S., Wang, C. Y., Su, C. L., and Chu, Y.-H. (2020). Meteor observations using radar imaging techniques and norm-constrained Capon method. *Planet Space Sci.* 184, 104884. doi:10.1016/j.pss.2020.104884

Chernogor, L. F. (2015). Ionospheric effects of the Chelyabinsk meteoroid. *Geomagnetism Aeronomy* 55, 353–368. doi:10.1134/S0016793215030044

Chum, J., Liu, J. Y., Laštovička, J., Fišer, J., Mošna, Z., Baše, J., et al. (2016). Ionospheric signatures of the April 25, 2015 Nepal earthquake and the relative role of compression and advection for Doppler sounding of infrasound in the ionosphere. *Earth, Planets Space* 68, 24. doi:10.1186/s40623-016-0401-9

Chum, J., Podolská, K., Rusz, J., Baše, J., and Tedoradze, N. (2021). Statistical investigation of gravity wave characteristics in the ionosphere. *Earth, Planets Space* 73, 60. doi:10.1186/s40623-021-01379-3

Chum, J., Urbář, J., Laštovička, J., Cabrera, M. A., Liu, J.-Y., Bonomi, F. A. M., et al. (2018). Continuous Doppler sounding of the ionosphere during solar flares. *Earth, Planets Space* 70, 198. doi:10.1186/s40623-018-0976-4

Davies, K. (1990). *Ionospheric radio*. IEE Electromagnetic Wave Series.

Di Martino, M., and Cellino, A. (2004). "Physical properties of comets and asteroids inferred from fireball observations," in *Mitigation of hazardous comets and asteroids*, 156.

Ellyett, C. D., and Goldsbrough, P. F. (1976). Relationship of meteors to sporadic E, 1. A sorting of facts. *J. Geophys Res.* 81, 6131–6134. doi:10.1029/JA081i034p06131

Fukao, S., and Hamazu, K. (2014). "Observations by atmospheric radar," in *Radar for meteorological and atmospheric observations* (Tokyo: Springer Japan), 435–485. doi:10.1007/978-4-431-54334-3_12

Haldoupis, C. (2011). "A tutorial review on sporadic E layers," in *Aeronomy of the Earth's atmosphere and ionosphere* (Dordrecht: Springer Netherlands), 381–394. doi:10.1007/978-94-007-0326-1_29

Haldoupis, C., Meek, C., Christakis, N., Pancheva, D., and Bourdillon, A. (2006). Ionogram height–time–intensity observations of descending sporadic E layers at mid-latitude. *J. Atmos. Sol. Terr. Phys.* 68, 539–557. doi:10.1016/j.jastp.2005.03.020

Haldoupis, C. (2012). Midlatitude sporadic E. A typical paradigm of atmosphere-ionosphere coupling. *Space Sci. Rev.* 168, 441–461. doi:10.1007/s11214-011-9786-8

Hawkes, R. L. (2007). Peter jenniskens, meteor showers and their parent comets. *Earth Moon Planets* 101, 93–95. doi:10.1007/s11038-007-9145-7

Höffner, J., von Zahn, U., McNeil, W. J., and Murad, E. (1999). The 1996 Leonid shower as studied with a potassium lidar: Observations and inferred meteoroid sizes. *J. Geophys Res. Space Phys.* 104, 2633–2643. doi:10.1029/1998JA900063

Kereszturi, Á., Barta, V., Bondár, I., Czanik, C., Igaz, A., Mónus, P., et al. (2021). Review of synergic meteor observations: Linking the results from cameras, ionosondes, infrasound and seismic detectors. *Mon. Not. R. Astron Soc.* 506, 3629–3640. doi:10.1093/mnras/stab1918

Koten, P., Rendtel, J., Shrbený, L., Gural, P., Borovička, J., and Kozak, P. (2019). "Meteors and meteor showers as observed by optical techniques," in *Meteoroids: Sources of meteors on Earth and beyond*. Editors G. O. Ryabova, D. J. Asher, and M. J. Campbell-Brown, 90.

Koten, P., Spurný, P., Borovička, J., Evans, S., Elliott, A., Betlem, H., et al. (2006). The beginning heights and light curves of high-altitude meteors. *Meteorit. Planet Sci.* 41, 1305–1320. doi:10.1111/j.1945-5100.2006.tb00523.x

Kouba, D., and Chum, J. (2018). Ground-based measurements of ionospheric dynamics. *J. Space Weather Space Clim.* 8, A29. doi:10.1051/swsc/2018018

Kozlovsky, A., Lukianova, R., and Lester, M. (2020). Occurrence and altitude of the long-lived nonspecular meteor trails during meteor showers at high latitudes. *J. Geophys Res. Space Phys.* 125. doi:10.1029/2019JA027746

Laštovička, J., and Chum, J. (2017). A review of results of the international ionospheric Doppler sounder network. *Adv. Space Res.* 60, 1629–1643. doi:10.1016/j.asr.2017.01.032

Maruyama, T., Kato, H., and Nakamura, M. (2003). Ionospheric effects of the Leonid meteor shower in November 2001 as observed by rapid run ionosondes. *J. Geophys Res.* 108 (1), 4–13. doi:10.1029/2003JA009831

Maruyama, T., Kato, H., and Nakamura, M. (2008). Meteor-induced transient sporadic E as inferred from rapid-run ionosonde observations at midlatitudes. *J. Geophys Res. Space Phys.* 113. n/a-n/a. doi:10.1029/2008JA013362

Mathews, J. D. (1998). Sporadic E: Current views and recent progress. *J. Atmos. Sol. Terr. Phys.* 60, 413–435. doi:10.1016/S1364-6826(97)00043-6

Molau, S., Gural, P. S., and Okamura, O. (2002). Comparison of the "American" and the "Asian" 2001 Leonid meteor storm. *WGN, J. Int. Meteor Organ.* 30, 3–21.

Mošna, Z., Knížová, P. K., and Potužníková, K. (2015). Coherent structures in the Es layer and neutral middle atmosphere. *J. Atmos. Sol. Terr. Phys.* 136, 155–162. doi:10.1016/j.jastp.2015.06.007

Pancheva, D., Haldoupis, C., Meek, C. E., Manson, A. H., and Mitchell, N. J. (2003). Evidence of a role for modulated atmospheric tides in the dependence of sporadic *E* layers on planetary waves. *J. Geophys Res. Space Phys.* 108. doi:10.1029/2002JA009788

Rajaram, G., and Chandra, H. (1991). Sporadic E ionization associated with meteor events. *Proc. Indian Acad. Sciences-Earth Planet. Sci.* 100, 255–265. doi:10.1007/bf02895986

Reinisch, B. W. (2009). *Digisonde 4D technical manual*. Version 1.0.

Reinisch, B. W., and Galkin, I. A. (2011). Global ionospheric radio observatory (GIRO). *Earth, Planets Space* 63, 377–381. doi:10.5047/eps.2011.03.001

Reinisch, B. W., Galkin, I. A., Khmyrov, G. M., Kozlov, A. V., Lisysyan, I. A., Bibl, K., et al. (2008). Advancing digisonde technology: The DPS4. In. *Radio Sound. Plasma Phys. AIP Conf. Proc.* 974, 127–143.

Reinisch, B. W., Huang, X., Galkin, I. A., Paznukhov, V., and Kozlov, A. (2005). Recent advances in real-time analysis of ionograms and ionospheric drift measurements with digisondes. *J. Atmos. Sol. Terr. Phys.* 67, 1054–1062. doi:10.1016/j.jastp.2005.01.009

Reinisch, B. W. (1996). *Modern ionospheric science*. Germany): EGS Katlenburg-Lindau, 440–458.

Šauli, P., and Bourdillon, A. (2008). Height and critical frequency variations of the sporadic-E layer at midlatitudes. *J. Atmos. Sol. Terr. Phys.* 70, 1904–1910. doi:10.1016/j.jastp.2008.03.016

Schult, C., Stober, G., Keuer, D., and Singer, W. (2015). Radar observations of the Maribo fireball over Juliusruh: Revised trajectory and meteoroid mass estimation. *Mon. Not. R. Astron Soc.* 450, 1460–1464. doi:10.1093/mnras/stv614

Spurný, P., Betlem, H., Jobse, K., Koten, P., and Levenvan't, J. (2000). New type of radiation of bright Leonid meteors above 130 km. *Meteorit. Planet Sci.* 35, 1109–1115. doi:10.1111/j.1945-5100.2000.tb01497.x

Spurný, P., Borovička, J., Mucke, H., and Svoreň, J. (2017). Discovery of a new branch of the Taurid meteoroid stream as a real source of potentially hazardous bodies. *Astron Astrophys.* 605, A68. doi:10.1051/0004-6361/201730787

Vierinen, J., Aslaksen, T., Chau, J. L., Gritsevich, M., Gustavsson, B., Kastinen, D., et al. (2022). Multi-instrument observations of the Pajala fireball: Origin,

characteristics, and atmospheric implications. *Front. Astronomy Space Sci.* 9. doi:10.3389/fspas.2022.1027750

Wang, N., Guo, L., Zhao, Z., Ding, Z., and Lin, L. (2018). Spread-F occurrences and relationships with foF2 and h′F at low- and mid-latitudes in China. *Earth, Planets Space* 70, 59. doi:10.1186/s40623-018-0821-9

Whitehead, J. D. (1989). Recent work on mid-latitude and equatorial sporadic-E. *J. Atmos. Terr. Phys.* 51, 401–424. doi:10.1016/0021-9169(89)90122-0

Whitehead, J. D. (1961). The formation of the sporadic-E layer in the temperate zones. *J. Atmos. Terr. Phys.* 20, 49–58. doi:10.1016/0021-9169(61)90097-6

Yeomans, D. K., Yau, K. K., and Weissman, P. R. (1996). The impending appearance of comet tempel–tuttle and the Leonid meteors. *Icarus* 124, 407–413. doi:10.1006/icar.1996.0218

Zinn, J., and Drummond, J. (2007). Formation of parallel meteor trail pairs as associated with their buoyant rise. *Adv. Space Res.* 39, 555–561. doi:10.1016/j.asr.2006.12.007

Zinn, J., and Drummond, J. (2005). Observations of persistent Leonid meteor trails: 4. Buoyant rise/vortex formation as mechanism for creation of parallel meteor train pairs. *J. Geophys Res. Space Phys.* 110. doi:10.1029/2004JA010575

frontiers | Frontiers in Astronomy and Space Sciences

TYPE Original Research
PUBLISHED 23 June 2023
DOI 10.3389/fspas.2023.1197157

OPEN ACCESS

EDITED BY
Jorge Luis Chau,
Leibniz Institute of Atmospheric Physics (LG), Germany

REVIEWED BY
Savely M. Grach,
Lobachevsky State University of Nizhny Novgorod, Russia
Federico Gasperini,
Orion Space Solutions LLC, United States

*CORRESPONDENCE
Petra Koucká Knížová,
pkn@ufa.cas.cz

RECEIVED 30 March 2023
ACCEPTED 05 June 2023
PUBLISHED 23 June 2023

CITATION
Koucká Knížová P, Potužníková K, Podolská K, Hannawald P, Mošna Z, Kouba D, Chum J, Wüst S, Bittner M and Kerum J (2023), Multi-instrumental observation of mesoscale tropospheric systems in July 2021 with a potential impact on ionospheric variability in midlatitudes.
Front. Astron. Space Sci. 10:1197157.
doi: 10.3389/fspas.2023.1197157

Multi-instrumental observation of mesoscale tropospheric systems in July 2021 with a potential impact on ionospheric variability in midlatitudes

Petra Koucká Knížová [1]*, Kateřina Potužníková[2], Kateřina Podolská [1], Patrick Hannawald[3], Zbyšek Mošna[1], Daniel Kouba[1], Jaroslav Chum[1], Sabine Wüst [3], Michael Bittner[3] and Jacek Kerum[2]

[1]Department of Ionosphere and Aeronomy, Institute of Atmospheric Physics, Czech Academy of Sciences, Prague, Czechia, [2]Department of Meteorology, Institute of Atmospheric Physics, Czech Academy of Sciences, Prague, Czechia, [3]German Aerospace Center, German Remote Sensing Data Center, Weßling, Germany

The ionosphere as a part of Earth's atmosphere supports a wide range of oscillations, of which acoustic–gravity waves (AGWs) form an important part. AGWs distribute energy and momentum from the source region over large distances. A significant portion of AGWs originates in the lower atmosphere and propagates through the atmosphere up to the ionospheric heights where, due to the coupling between neutral and ionized particles, it could be detected as wavelike disturbances of the plasma. Primarily, the ionospheric behavior is driven by solar and geomagnetic activity, while the influence from neutral and below-laying regions of the atmosphere most of the time forms a substantially smaller part of the observed variability. However, it could significantly alter ionospheric behavior. Our study is limited to a time span of rather low solar and geomagnetic activity in order to highlight neutral atmosphere influence. In this study, we focus on two tropospheric situations above Europe that may lead to AGW generation, which propagate up to the F-layer where they potentially induce variability that we observe within ionospheric plasma parameters.

KEYWORDS

gravity wave activity, short-term variability, troposphere, cyclone, atmospheric coupling, mesosphere, ionosphere

1 Introduction

The ionosphere is a part of the atmosphere that significantly influences the propagation of electromagnetic signals due to the presence of ionized particles (recently, for instance, in Radicella and Migoya-Orué, 2021). The state of the ionosphere is predominantly driven by the (quasi) periodic as well as irregular solar activity (e.g., Borries et al., 2015; Bederman et al., 2018) and geomagnetic activity (e.g., Prölls, 1995; Buonsanto, 1999, among others). The importance of a neutral atmosphere influence on the ionosphere as high as the F2 layer ionosphere was pointed out in the 1970s. Increasing interest of the ionosphere scientific community in this topic is well observed in the last two decades of the 20th century.

In past years, it has been widely accepted that the ionosphere is affected by pronounced phenomena originating within the neutral atmosphere as close as to the Earth's surface in the troposphere and stratosphere, i.e., in the regions located below the mesosphere and lower thermosphere (MLT) region (see for instance Laštovička, 2006; Kazimirovski and Kokourov, 1991; Koucká Knížová et al., 2021). Medveděv and Gavrilov (1995) numerically simulated the tropospheric meso- and macro-scale source evolution and consequent propagation up to the thermospheric heights. Most of the wave energy propagates quasi-horizontally, and part of the energy is transported into the upper atmosphere by internal gravity waves, which can create regions of wave disturbances in the mesosphere/lower thermosphere. Their study also involved real meteorological geopotential data. They identified the following effective meteorological sources: a center of cyclones, a center of anticyclones, a curvature of jet streams, a saddle point between a cyclone and an anticyclone, and an outlying area of vortices.

A large statistical study was performed by Forbes et al. (2000) who analyzed the impact of "meteorological influences" defined as non-periodic dynamical effects originating in the lower atmosphere on the F2 region using data from more than 100 ionosondes during the period 1967–1989. They showed that the ionospheric variability of meteorological origin is approximately ±25%–35% at periods of a few hours to 1–2 days and approximately ±15%–20% at periods of approximately 2–30 days compared to the mean of ionospheric variability, at all latitudes. However, Rishbeth and Mendillo (2001) suggested that the contribution of solar/geomagnetic activity and lower-atmosphere forcing to day-to-day ionosphere variability should be equally considered. Pedatella and Liu (2018) demonstrated that omitting lower-atmosphere variability leads to uncertainty in the ionosphere response to a geomagnetic storm that is typically ~20%–40% but can be as large as 100% regionally.

As mentioned previously, the ionosphere represents the transition zone from the space environment (plasma) to the neutral atmosphere being coupled both from above into the fully ionized Earth's magnetosphere and from below into the neutral atmosphere. The behavior of the environment above and below significantly differs being determined by electromagnetic forcing and collisions, respectively. Ionospheric plasma is only a weakly ionized medium. With increasing height, the neutral particle concentration decreases, while due to ionization processes, the concentration of charged particles increases, reaching its maximum within the F2 layer, where the maximum electron concentration is usually located. The ionization degree here reaches values of up to approximately 0.01, and the charged particles are directly influenced by the neutral particles. With increasing height, collisions are less important and plasma motion is more determined by the electromagnetic forcing. Neutral and charged particles are strongly coupled. Their interactions lead to mass, momentum, and energy transfers.

On longer time scales, the effects of large circulation structures within variability of ionospheric parameters were reported. In particular, Chang et al. (2018) reported the dependence of the S4 scintillation index in the E-region midlatitudes on variation of the El Nino–Southern Oscillation (ENSO) in the troposphere. ENSO signatures can be transmitted to Es formation mechanisms, potentially through the modulation of vertically propagating atmospheric tides that alter lower thermospheric wind shears. A substantial response within the ionospheric plasma parameters was identified during sudden stratospheric warmings (SSWs) (see for instance Mošna et al., 2021; Korenkov et al., 2012; Siddiqui et al., 2021). In the coupling during SSWs, planetary-scale waves, particularly semi-diurnal solar and lunar tides, play a key role in altering atmospheric circulation (Pancheva et al., 2008; Pedatella and Forbes, 2010).

It has been shown that severe tropospheric events such as cyclones (Guha et al., 2016; Koucká Knížová et al., 2020; Zakharov and Sigachev, 2022), hurricanes (Bauer, 1958; Li et al., 2017), typhoons (Xiao et al., 2007; Chum et al., 2018), thunderstorms (Blanc et al., 2014; Lay, 2018; Rahmani et al., 2020), synoptic-scale frontal systems (Boška and Šauli, 2001; Šauli and Boška, 2001), storms (Borchevkina et al., 2020; Borchevkina et al., 2020), and tornadoes (Hung et al., 1979) influence the ionosphere. Acoustic–gravity waves (AGWs) and their propagation to the ionosphere play an important role in vertical coupling (Kazimirovsky and Kokourov, 1991; Bishop et al., 2006 and references therein) as the amplitudes of AGWs increase significantly in the thermosphere and the waves dissipate in the thermospheric viscous fluid (Vadas et al., 2015), resulting in a change in the momentum (acceleration) and internal energy of the substantial part of the ionosphere.

The stratosphere also affects the state of the ionosphere. An increasing number of reports indicate that SSWs affect the mesosphere–thermosphere–ionosphere region mainly in the equatorial and low latitudes (Chau et al., 2012; Yiğit and Medvedev, 2015) but, as recently demonstrated, also in middle latitudes (Goncharenko and Zhang, 2008; Goncharenko et al., 2018; Siddiqui et al., 2021).

Within a previous study, 13 years of routine radiosonde data from Prague (50.008°N, 14.448°E) with temporal highly resolved temperature, pressure, and wind measurements were analyzed with respect to gravity wave activity in the lower stratosphere (Kramer et al., 2016). The data indicated that the maxima of gravity wave activity and vertical flux of horizontal momentum often appear together with minima in surface pressure. Kramer et al., 2015 reported about gravity waves which were excited above Mallorca (39.647°N, 2.689°E) during the passage of a cold front and which obviously managed—at least partly—to propagate up to the mesopause region.

Figure 1 shows one of our early detection/identification of AGW signatures on ionogram records using the now replaced ionosonde IPS 42 KEL Aerospace. It operated in the Průhonice Observatory till the beginning of 2004. An irregularity is well observed on the course of virtual reflection height at a fixed frequency as derived from raw ionograms. On the course of radiowave virtual reflection height, there occurred strong spread-F echo on 12 October. The echo registered at fixed frequency = 3 MHz arrived from a virtual height range of approximately 250 km–500 km, and the spread situation took place for a short period between 09 and 10 UTC.

Ionosondes and/or Digisondes regularly transmit electromagnetic waves vertically upward and register reflected waves. From the wave time of flight, they calculate the virtual height of the plasma with a concentration corresponding to the sounding frequency. The virtual height corresponds to a simplified

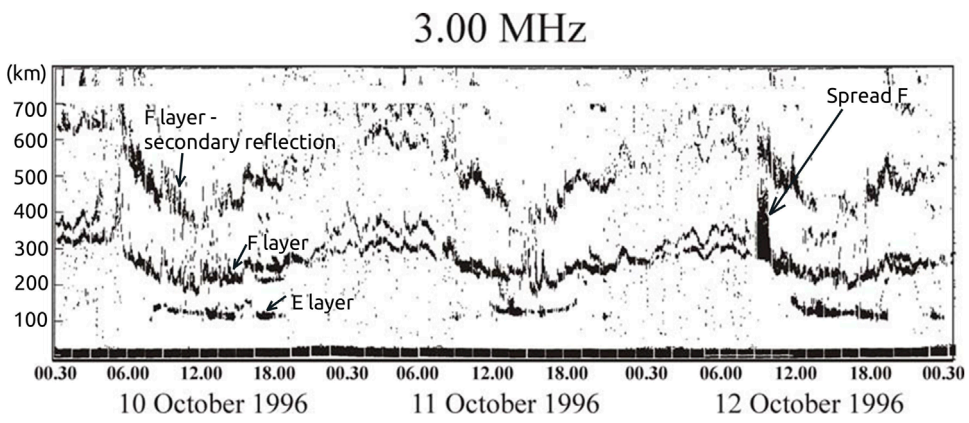

FIGURE 1
Observation of the passage of a cold front system on 12 October 1996 by Ionosonde IPS 42 KEL Aerospace in the Průhonice Observatory. This visualization shows the virtual height of vertical echo reflection at a fixed frequency of 3 MHz. The instrument did not distinguish between ordinary and extraordinary waves. A strong spread in the F-region is clearly seen as reflection in the interval 250 km–500 km visible on 12 October between 09 and 10 a.m. The geomagnetic activity was low to moderate.

situation in which an electromagnetic wave travels through vacuum up to the reflection point. This value is slightly higher than the true height because the signal's speed propagating in plasma is lower than the speed of light in the vacuum. The graph showing the dependence of the virtual height on the sounding frequency is called an ionogram, and it represents the standard output of the ionosondes and digisondes. The h(f) characteristics depend on particular ionospheric conditions. In an ideal situation, the reflection occurs on the perfect plane. In a real situation, the reflection surface is usually undulated. It leads to the presence of a significant amount of off-vertical echoes. On the ionograms, one can observe deviations from ideal planar and stationary situations such as the spread of the echo signal, cusp stratification, and split double echo. The classification of ionogram scaling and interpretation can be found, for instance, in the manual of ionogram scaling (Wakai et al., 1987) or the URSI manual (UAG-23A, 1978). Off-vertical echo ionograms must be manually checked (Kouba and Koucká Knížová, 2011).

A particular type of the radiowave reflection represents the spread-F echo in range (height), frequency, or mixed form on ionograms. In such cases, the receiver registers several reflections from a range of heights and frequencies rather than one vertical reflection. It means that the reflection plane of constant concentration is not an ideal plane but rather undulated and/or contains density irregularities. Spread-F-type reflection ionograms are often recorded during episodes of high geomagnetic activity in association with traveling ionospheric disturbances (TIDs). Bowman et al. (1987) proposed that a deformed ionosphere by the passage of TIDs was the main factor for spread F during daytime ionograms at midlatitudes; Jiang et al. (2016) reported the presence of TIDs before the occurrence of daytime spread F and suggested that downward vertical neutral winds excited by traveling atmospheric disturbances/atmospheric gravity waves might play a significant role in forming daytime spread F during geomagnetic storms; Jonah et al. (2018) reported the presence of both equatorward propagating large-scale TIDs connected with enhanced auroral activity owing to geomagnetic storm conditions and poleward propagating medium-scale TIDs likely induced by local atmospheric gravity wave sources originating from convection activities in the lower atmosphere during geomagnetic storm events in May 2017; Xiao et al. (2012) observed daytime ionospheric irregularities by HF Doppler sounding and suggested that a typhoon was a source of daytime spread F at midlatitude; Koucká Knížová et al. (2020) reported a spread-F echo situation associated with frontal cyclones of sub-synoptic scales that were very quickly moving over Central Europe. Further observations of spread-F ionograms in association with AGWs were also reported (Bowman, 1981; 1988; 1990; Dyson et al., 1995; Bencze and Bakki, 2002; Xiao et al., 2009; Pezzopane et al., 2011; Yu et al., 2016).

Usually, large-scale TIDs (LSTIDs) observed during episodes of increased geomagnetic activity and medium-scale TIDs (MSTIDs) were reported in connection with vertical coupling within the atmosphere. Upward propagation of AGWs depends on the state of the entire atmosphere from the troposphere up to the ionosphere. Fritts and Vadas (2008) identified three key influence parameters on GW survival and penetration to high altitudes. These major factors are refraction accompanying Doppler shifting by strong mean winds in the MLT and thermosphere, GW evanescence and reflection at turning levels, and viscous dissipation. The model study indicates changes in GW ability to reach high altitudes depending on solar forcing.

Wavelike structures in the midlatitude nightglow have been previously studied before satellite imagery. Taylor and Hapgood (1988) observed concentric gravity waves for a period of 10–20 min in the mesospheric nightglow (horizontal wavelength of the airglow structures was 26 km). They identified an isolated midlatitude summer thunderstorm (with a horizontal radius of 10 km) over the European continent as a possible source. A theoretical explanation for the source of oscillations in the form of penetrating convection in the growth phase of storms was proposed by Pierce and Coroniti (1966). Recently, the source of waves in the upper troposphere and stratosphere can be easily traced from satellite images (Yue et al., 2014).

Many past and recent satellite and radar measurements in the midlatitude region have focused on the interaction of gravity waves generated by different sources in the troposphere and their propagation upward into the ionosphere. Pavelin and Whiteway (2002) presented the case of radar observations of turbulence in the tropopause region generated by the interaction between an inertial gravity wave over the jet stream and a smaller-scale mountain wave. Bertin et al. (1978), based on geosatellite measurements, discussed the origin of a medium-scale gravity wave (for a period of less than 45 min) that was probably produced by the interaction of wind shear in the jet stream region and penetrative convective systems. Fritts and Alexander (2003) summarized the results of theoretical, numerical, and observational studies dealing with the sources and characteristics of gravity waves in the middle atmosphere (at altitudes between 10 and 100 km). This concludes that there is a need to extend both numerical studies and more detailed observations to quantify wave discontinuities caused by different sources, propagation conditions, etc., as discontinuities have a major impact on wave effects at higher altitudes, including instability processes, wave–wave interactions and mean flow, and secondary wave emission.

2 Motivation

Our study aimed to show tropospheric situations that may lead to observable Earth's atmosphere variability up to the heights of the F2 layer ionosphere. In this study, we focus on rather recent tropospheric cases. Due to coincidental occurrences of disturbances within mesosphere and ionosphere datasets, without solar–geomagnetic energetic impulses, we assume that we observe variability induced by AGWs launched by tropospheric systems.

We chose two particular synoptic situations that fall into periods of stable solar conditions and rather low (low-to-moderate) geomagnetic activity. The low geomagnetic activity was chosen in order to highlight the effects of meteorological influence as much as possible as it is practically unfeasible to untangle and isolate the effects. During our time of interest, the geomagnetic activity is rather low (Kp_{mean} = 1.26 and Kp_{median} = 1; maximum value Kp = 4+ only once during the analyzed period). Solar activity characterized by solar flux F10.7 is stable with values $F10.7_{mean}$ = 81.06 and $F10.7_{median}$ = 77.65. Selected tropospheric situations differ in their nature. The first case of 13/14 July 2021 represents disturbances caused by convective upward motions in the squall line ahead of a cold front with heavy rainfall (Bernd cyclone). The second case occurred on 29 July 2021, and it was a polar front jet stream in the upper troposphere enhanced by orography with an atypical location of the jet stream.

Figure 2 shows the geomagnetic situation from 1 July to 15 August 2021 according to the finalized Kp-index and Ap-index (data from GFZ German Research Centre for Geosciences). Geomagnetic activity was low to moderate during all the studied periods. The activity shortly increases twice, reaching the values 4+ and 4–. On 14 July, for a few hours after 16 UT, the Kp index exceeded value 3. On 28 July, only two recorded Kp values reached 4-. The rest of the time recorded values remain below value 3. Therefore, we consider the analyzed time as rather geomagnetically quiet.

Our experimental datasets involved in this study cover the troposphere, mesosphere, and ionosphere. Tropospheric data consist of standard surface and radiosonde meteorological measurements, together with weather radar, as well as surface and upper-air weather maps. The datasets are completed by upper mesospheric/lower thermospheric airglow measurements taken by the FAIM2 (Fast Airglow IMager2) instrument operated by the German Aerospace Center at the Panská Ves Observatory (50.527°N, 14.568°E). Ionosphere datasets consist of vertical sounding data from Digisonde DPS-4D operating in the Průhonice Observatory, together with oblique sounding at fixed frequency continuous Doppler sounding (CDS) with the receiver located in Prague.

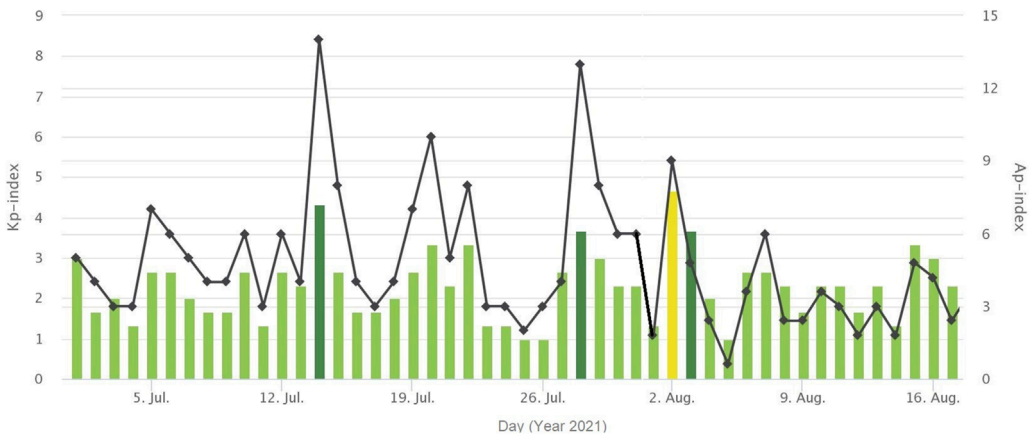

FIGURE 2
Geomagnetic situation from 1 July–15 August 2021. Geomagnetic activity is low to moderate during all the studied periods. The activity shortly increases twice reaching the values 4– and 4+. On 14 July, Kp increased for a few hours after 16:00 UTC exceeding value 3. On 28 July, only two recorded Kp values reached 4–. The rest of the time, the recorded values remain below value 3 according to the finalized Kp-index of GFZ Potsdam. The black line and points mark the daily value of the Ap-index (data from the GFZ German Research Centre for Geosciences).

3 Data

3.1 Tropospheric data

Meteorological datasets include standard weather measurements of temperature, pressure, and wind operated by the Institute of Atmospheric Physics, Czech Academy of Sciences (geographic coordinates 50.041°N, 14.477°E). For the description of the troposphere situation and development, we use surface pressure maps provided by WetterKontor at https://www.wetterkontor.de/de/wetterlage.asp, last access: 24 January 2023, and archived weather charts offered at http://wetter3.de and https://www.firenzemeteo.it/, last access: 24 January 2023, produced from data based on the US Global Forecast System (GFS) model and the model of the German Weather Service ICON. We also use the atmospheric vertical sounding radiometer data available at https://weather.uwyo.edu/upperair/sounding.html.

3.2 Mesospheric data

In particular, OH nightglow with a mean emission altitude of approximately 86 km is well-suited to investigate the dynamics in the upper mesosphere and lower thermosphere region (see Wüst et al., 2023 and references given therein). The OH nightglow layer has its strongest emission in the short-wave infrared range at approximately 1.5–1.6 μm [rotational–vibrational transitions OH(3-1) and OH(4-2)]. Such ground-based observations of the OH nightglow layer are affected by clouds, and the best results are achieved at cloud-free nights. For the thermal convection event, clear-sky imager data are analyzed during the nights of 12–13 (5 h of good data quality), 14–15 (1.9 h of good data quality), and 15–16 (6.2 h of good data quality) July. No data are available for the nights of 13–14. For the event on 29 July, we analyzed the data of the nights of 28–29 (4.5 h of good data quality), 29–30 (5.4 h of good data quality), and 30–31 (2 h of good data quality) July.

The short-wave infrared camera FAIM2 observes the nightglow emission in the spectral range from 0.9 to 1.65 μm, taking one image every second during each night from sunset to sunrise. Due to the comparatively intense OH emissions, OH(3-1) and OH(4-2) are mainly observed using the camera; the strong O_2 emission at 1.26 μm decays relatively faster and is then weaker than the OH emission about 30 min after sunset (Hannawald et al., 2016). As previously mentioned, the camera is located at the observatory Panská Ves with the field of view (FOV) oriented to the south between the observatory and Prague. It has a size of approximately 27° times 33°, which corresponds to an area of approximately 47 km times 56 km at an altitude of 86 km and a spatial resolution of 180 m. The images are analyzed using a 2D-FFT in order to derive spatiotemporal wave parameters (Hannawald et al., 2019). However, the analyzed wave structures are, of course, limited to the FOV size (i.e., a maximum horizontal wavelength of approximately 47 km).

The images are analyzed using a 2D-FFT in order to derive spatiotemporal wave parameters. While the 2D-FFT analysis provides information about the horizontal wave parameters like horizontal wavelength and horizontal angle of propagation (with a 180° ambiguity), the temporal wave parameters are derived by investigating these horizontal wave parameters for consecutive images. A wave event is defined as the occurrence of the same horizontal wavelength and angle of propagation (denoted as a "wave signature") connected in time. Connected in time means that the wave signature is present in consecutive images (small time gaps are allowed). For each group of wave signatures connected in time, the change in the phase information (calculated by the 2D-FFT) with time is investigated to derive, e.g., the unambiguous direction of propagation and the phase speed (see Hannawald et al., 2019 for a more detailed description of the analysis).

3.3 Ionospheric data

Continuous Doppler sounding is an effective continuous method for monitoring the state of the ionosphere (Kouba and Chum, 2018). It can detect ionospheric fluctuations of periods ~10 s and longer. The system is most suitable for studying waves of periods from ~20 s to ~100 min. The electromagnetic wave of fixed frequency is reflected from the ionosphere and detected in the receiver. In our study, we use a system that comprises three transmitters and one receiver. CDS measurement does not allow the determination of reflection height of the sounding signal. It is further determined from a nearby ionosonde. The best Doppler shift results are usually obtained when the reflection is obtained from the F2 layer (~180–300 km). If the reflection is from altitudes lower than ~150 km (E-layer), the Doppler shift is usually very small and often difficult to analyze. In addition, during summer days, if the D-layer is well-developed, the sounding radio signal might experience a strong attenuation (very weak signal is received) around noon. The specific frequencies of the individual transmitters are shifted by 4 Hz so that the signals of all transmitters could be displayed in one common Doppler shift spectrogram. Signals from the transmitter located in Panská Ves (50.528°N, 14.567°E) and received in Prague (50.041°N, 14.477°E) are used in this study. Further technical details can be found at https://www.ufa.cas.cz/DATA/files/oia/Doppler_des_365.pdf and in works by Chum and Podolská (2018), Chum et al. (2021), and Laštovička and Chum (2017). The system works for larger periods as well, but the ionosonde might be more advantageous since it provides information from the whole range of altitudes.

Digisonde for vertical ionospheric sounding operates on a similar principle. It transmits electromagnetic signals usually in a frequency range of 1–20 MHz and measures the time of flight of the reflected signal. In a regular sounding regime, it works typically with 15 min of repetition time. After the ionogram measurement, the system automatically searches for critical frequency and performs a restricted range drift measurement below the F2 layer critical frequency. Our Digisonde has a double-crossed delta transmitting antenna and four cross-loop receiving antennas. The configuration of the antenna field, together with coded signal and high number of transmitting signal repetitions, allows to identify parameters of the reflected wave. Afterward, the ionograms and drift data are manually checked and scaled for further processing (Kouba and Koucká Knížová, 2011; Kouba and Koucká Knížová, 2012; Kouba and Koucká Knížová, 2016). Ionograms and drift measurements are automatically sent into the world database GIRO (https://giro.uml.edu/). Digisonde data used in this study are measured

at the Průhonice Observatory (geographic coordinates 49.990°N, 14.539°E).

4 Observation

4.1 Tropospheric observation

First of all, it is important to mention that determining events such as atmospheric front transitions and convective storm development requires a great deal of experience and largely manual analysis of meteorological conditions both at synoptic and sub-synoptic scales. Not only does the stability of the air mass but also the overall dynamics of the troposphere play a role in determining the development of storms. An essential condition for the formation of severe convection is sufficient moisture in the lower levels of the troposphere and the upper-level divergent air flux (Kašpar et al., 2009). Surface measurements of meteorological conditions before and after the passage of the front are used to determine the passage of atmospheric fronts, especially significant changes in temperature and pressure tendencies, wind shifts, atmospheric precipitation, and wind gusts. Another criterion is the strong horizontal temperature gradient at the 850 hPa geopotential level. In our analyses, we use the pseudo-equivalent potential temperature field, which synthetically represents both temperature and humidity characteristics at the lower part of the troposphere. Narrow transformation zones with a strong gradient of pseudo-equivalent potential temperature at 850 hPa locate the positions of fronts on the surface pressure field (Kašpar, 2003). Another criterion for assessing the dynamics of the troposphere is the density and curvature of isohypse of 500 hPa geopotential height. The 500-hPa maps show the main flow regime of the troposphere. In synoptic meteorology, a 500-hPa map is used to determine the speed and direction of synoptic patterns and thus middle latitude atmospheric dynamics at an altitude of approximately 5.5 km. The small distance between isobars at 500 hPa represents an area of strong pressure gradient and strong wind speed. We also use a pressure level of 300 hPa or usually 200 hPa in summer, located near the tropopause at an altitude of approximately 9 or 12 km, to assess tropospheric flow dynamics. This level is used to determine the location and character of the polar front (zonal/meridional) and the associated jet stream. The jet stream can, under certain conditions, intensify severe

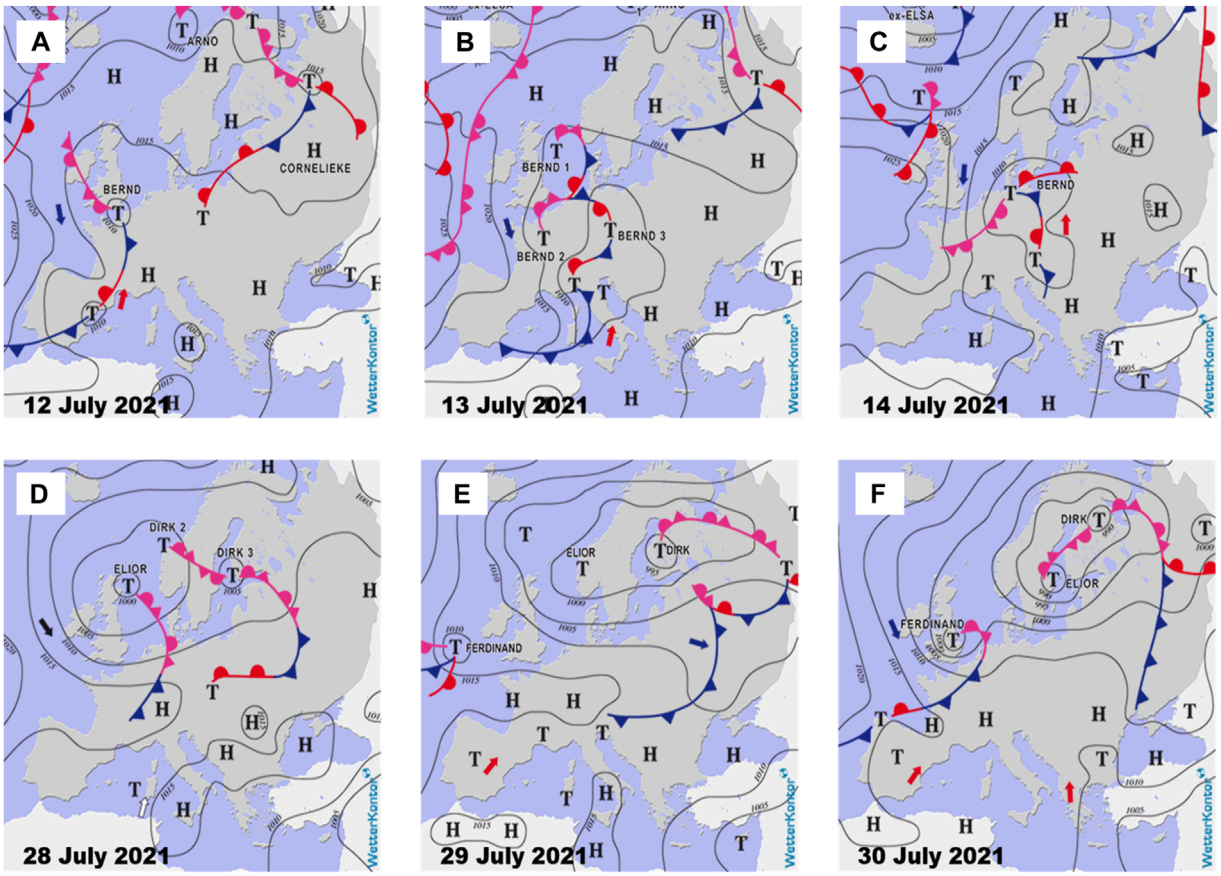

FIGURE 3
Surface pressure maps provided by WetterKontor, from https://www.wetterkontor.de/wetterlage.asp. Surface pressure is plotted with solid lines with 5-hPa steps. Atmospheric fronts (red curved lines with red semicircles that point in the direction of the warm front, blue curved lines with blue triangles that point in the direction of the cold front, and purple lines with alternating triangles and semicircles pointing in the direction in which the occluded front moves) and the locations of the centers of high- (H) and low (T)-pressure systems are also presented. Upper panels **(A–C)** show the evolution of Cyclone Bernd, and bottom panels **(D–F)** show an atypical jet stream situation.

weather associated with a cold front. However, even a strong jet stream alone, without the accompanying effects of thunderstorms or sustained precipitation, can cause gravity waves to propagate into the ionosphere.

In this paper, we show two cases—a thermal convective event on 13 and 14 July 2021, associated with thunderstorms and convective precipitation occurring along boundaries of weather cold fronts, and an orographically driven convective event on 29 July 2021 in the jet stream region.

4.1.1 Thermal convection event of 13–14 July 2021 (Bernd cyclone)

The synoptic analysis given in Figures 3A–C shows that a relatively cold air mass from the Atlantic Ocean spreads over Western Europe. During this period, most of Eastern and Central Europe and the Mediterranean were affected by the southwesterly flow regime. (In meteorology, the direction given for the wind flow refers to the direction from which it comes.) Consequently, cold fronts formed at the surface over Central Europe on 12 July 2021. During the next 24 h, Central Europe was still under the influence of surface to upper-tropospheric flow of warm air originating from the Africa continent, supplemented by moisture from the Mediterranean. (The origin of the air mass mixed with dust from the Sahara is also evidenced by numerous observations of the yellowish color of the sky and clouds over the Czech Republic on 12 and 13 July.) The persistent advection of thermally unstable tropical air mass caused both the waving of atmospheric fronts associated with cyclones and the regeneration of cyclones over Central Europe. Subsequently, organized thunderstorms (squall lines) occurred in warm sectors ahead of cold fronts. On 13 July, thunderstorms were recorded in Germany and also in the Czech Republic, associated with widespread manifestations such as strong wind gusts, torrential rainfall, very frequent lightning activity, and large temperature fluctuations. On June 14, a cold front characterized by more persistent precipitation passed over Central Europe.

Figure 4 shows the average 10-min measurement recorded at the Institute of Atmospheric Physics (IAP) surface weather station. The records show the passage of three cold fronts within 48 h. The first most significant cold front passage occurred on 13 July at 19:00 UTC. It was characterized by a dramatic shift in wind and temperature, as well as heavy rain associated with thunderstorm activity. The temperature decreased by 7°C in 1 hour. At the same time, the pressure rose sharply by 6 hPa. The wind shifted from a southeasterly to westerly direction, and a wind gust of 8 ms^{-1} occurred. Subsequent fluctuations in pressure and wind speed (between 19:00 and 22:00 UTC on 13 July) indicate the existence of a storm activity on the cold front. (The sudden drop in temperature and pressure is due to a "downburst"—that is, a downward flow of cold air and precipitation at the front of a dissipating storm phase. A downburst brings cold air from the upper troposphere to the surface.) The second clear evidence of a storm event illustrated by both pressure fluctuations and precipitation in the morning hours on 14 July was related to

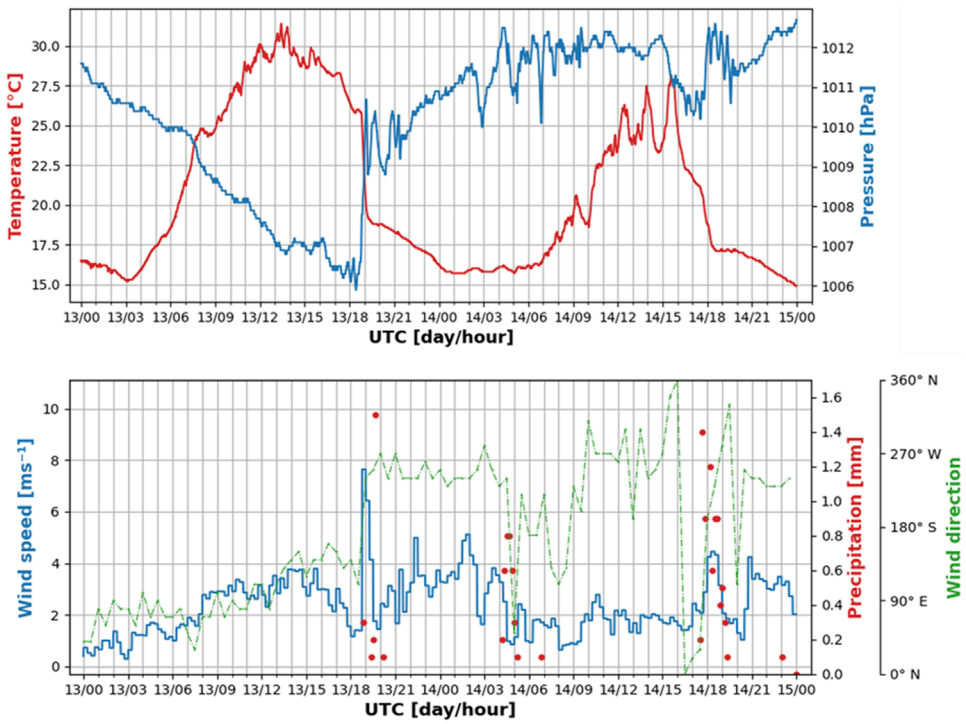

FIGURE 4
Meteorological data recorded at the IAP ground weather station on 13–14 July. The upper panel shows the course of atmospheric pressure and air temperature, and the bottom panel represents wind speed, wind direction, and precipitation (red circles). Sudden changes in atmospheric parameters indicate the passage of the frontal system above the measurement site. Atmospheric pressure, air temperature, and precipitation are measured at 2 m, while wind speed and direction are measured 10 m above the surface.

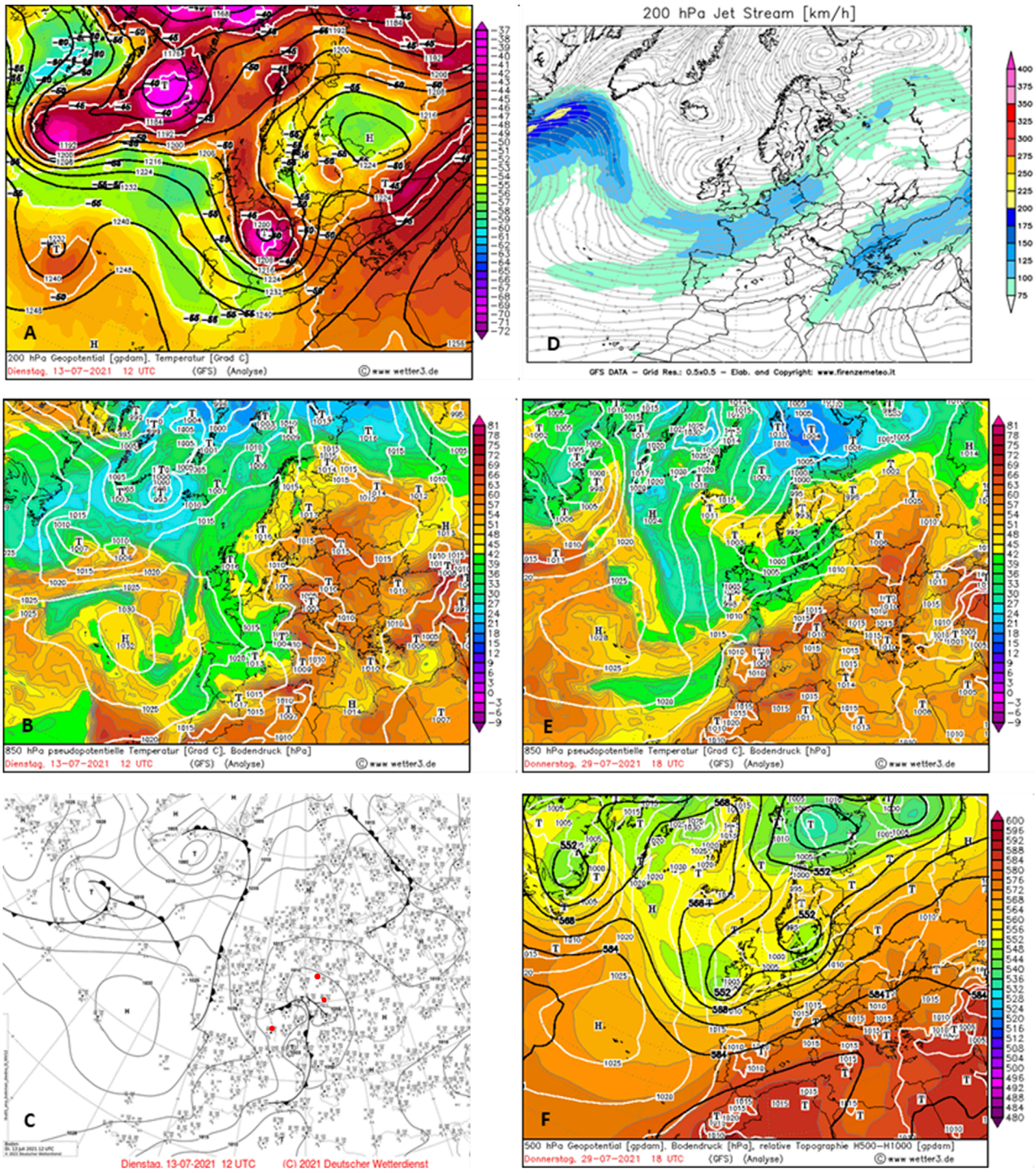

FIGURE 5
Panels in the left column refer to thermal convection on 13–14 July, and panels in the right column refer to orographically driven convection on 29 July. The analyses are valid for 13 July 2021 at 12:00 UTC and 29 July 2021 at 18:00 UTC, respectively. Panel **(A)** shows the geopotential height of the 200 hPa level (black contours, decameter) and temperature at a 200 hPa pressure level (color scale and white contours). Panels **(B, E)** show pseudo-equivalent potential temperature at the 850 hPa pressure level (color scale) and sea-level pressure (white contours). Panel **(C)** shows sea-level pressure with analysis of fronts and air pressure systems, where the letter H/T describes the high/low air pressure centers. The red points indicate the location of Berlin, Prague, and Paris. Panel **(D)** shows jet stream (color scale) and wind speed and direction (gray contours with arrows) at the geopotential height of the 200 hPa level. Panel **(F)** shows geopotential height of the 500 hPa level (black contours, decameter), sea-level pressure (white contours), and relative topography between 500 and 1,000 hPa (color scale)—represents the vertical distance between the 1,000 hPa (surface) and 500 hPa (middle troposphere, approximately 5.5 km) levels and varies with temperature and moisture (it is a function of the average virtual temperature). Thus, the color scale regions are directly related to the mean temperature and moisture of the middle troposphere (orange/red values indicate tropical air mass, and yellow/green indicate polar air mass).

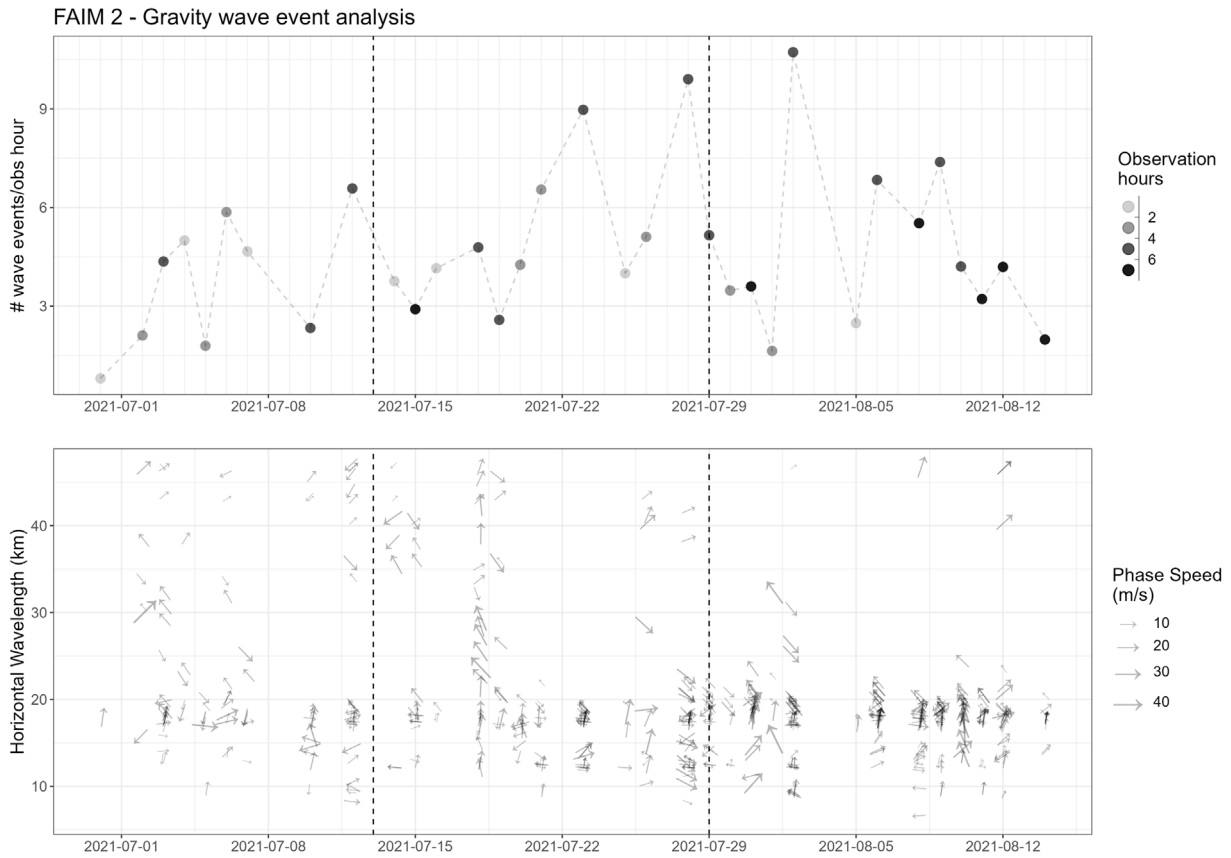

FIGURE 6
Result of the 2D-FFT image series analysis of FAIM2 data for the interval from the beginning of July to mid-August. The upper panel shows the number of the identified GW events per observation hour. The number of observation hours is given by color scaling for better comprehension. Naturally, values derived from more observation hours per night are more representative. The bottom panel shows the horizontal wavelength up to the field-of-view of the derived wave events. The arrow length provides information about the observed phase speeds, and the direction of the arrows shows the cardinal direction of the horizontal wave propagation. The two dashed lines mark the times of the investigated case studies.

the passage of a cold front at 4:00 UTC. The third cold front passed on 14 July at 17:00 UTC and was manifested by a local drop in atmospheric pressure, a sharp decrease in temperature of 5° per hour, and relatively more persistent stratiform precipitation.

On the surface air map, we can see two cyclones with a central pressure of 1,010 hPa located over southeastern France and the Czech Republic (Figure 5C). The position of the waving cold front on the surface pressure field corresponds to the zone with the strongest gradient of pseudo-equivalent potential temperature, *θep* (Figure 5B). The center of the cyclone over the Czech Republic is also an area of local maximum θep, i.e., an area with extremely high temperature and humidity in the middle troposphere. High θep values at 850 hPa indicate a mid-troposphere instability. In the Czech Republic, θep values above 60°C at 850 hPa are rarely reached (only on a few summer days per year), while values above 70°C are very rare, reflecting the presence of very warm and humid tropical air. In the warm sector of the cyclone, a squall line (quasi-linear convective storm system) formed ahead of the cold front, indicated by the twig-shaped line on the surface pressure field map. The upper level weather chart of 200 hPa at an altitude of approximately 12.2 km (Figure 5A) shows that the center of the massive cyclone over France is located almost in the same place as on the surface (Figure 5C). The exit (northeastern) part of this cyclone extends into an upper-level divergence zone located over the Czech Republic. Divergence in the upper troposphere helps deepen the cyclone and associated convection in the lower and middle troposphere. Both convection, which occurs throughout the vertical extent of the troposphere, and very unstable hot and humid air are the ingredients for the explosive development of storm systems.

4.1.2 Jet stream by orography on 29 July 2021

Weather in Central Europe is influenced by dominant frontal cyclones over Scandinavia and the British Isles (Figures 3D–F). On 29 July, a weak ridge of high pressure from the west in the lower part of the troposphere spread into Central Europe. The ridge was formed by the passive flow of relatively cold Atlantic air into areas of intense thermal convection; hence, pressure gradients near the surface became generally weak. The middle and upper troposphere, however, was associated with a well-marked thermal boundary that formed the so-called polar front. This was formed along the southern flank of the dominant cyclones and divided Europe into a cold north and a hot south (as is shown in the upper air charts in Figures 5E, F).

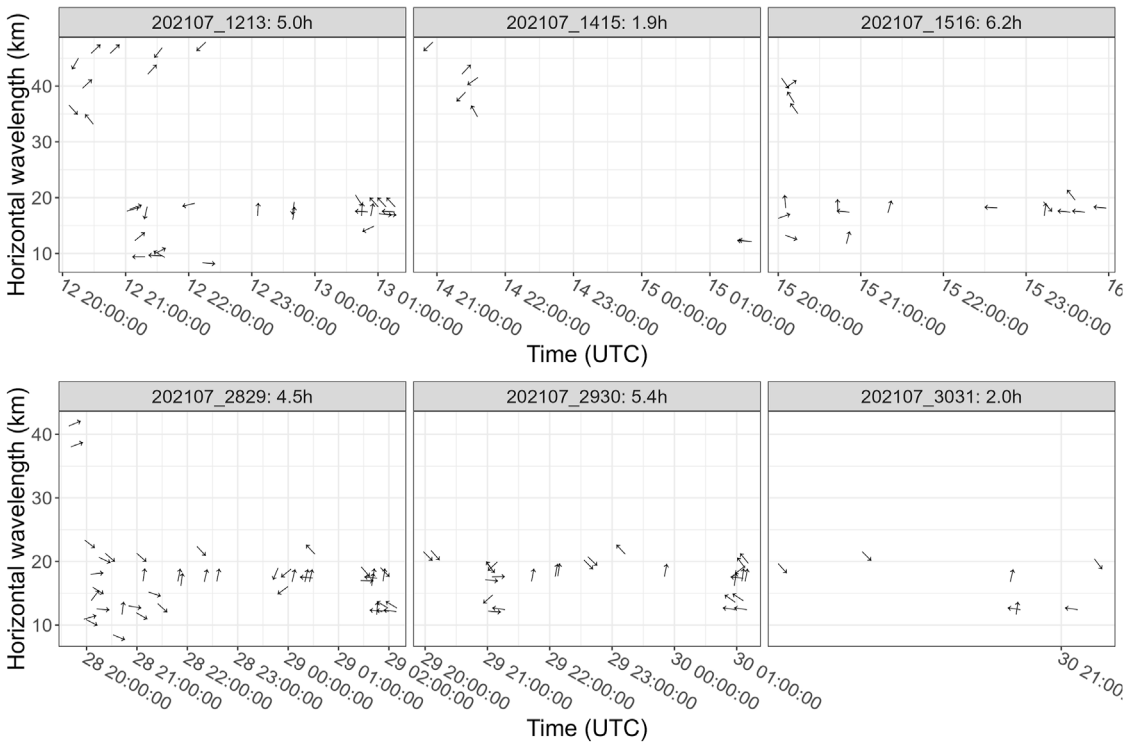

FIGURE 7
Result of the 2D-FFT image series analysis of FAIM2 data. Each arrow shows the gravity wave parameters of a wave event. The arrows show the cardinal directions of horizontal wave propagation (top oriented = north; right oriented = east). The investigated nights and the respective number of observation hours available for analysis are written in the facet titles. The top row is related to the first case study about the thermal convection event, while the second row is related to the second case study.

It should be noted that this polar front was located at an unusually low latitude (in midlatitudes, the polar front tends to occur in spring or autumn).

It is evident from both the upper pressure field maps (Figures 5D, F) and ground pressure isobars (white lines in Figure 5F) that the flow pattern in the troposphere is vertically very homogeneous. The plot of the pseudo-equivalent potential temperature at 850 hPa (Figure 5E) clearly shows the location of a strong polar front in the lower troposphere, separating the cool marine air in the north and northwest of Europe (green color shades) from the moist and very warm tropical air in the rest of Europe (orange and red color shades). The upper air chart of 500 hPa depicts the main flow regime in the mid-troposphere. The relatively small spacing between isohypses at 500 hPa (black lines in Figure 5F) indicates strong horizontal wind speeds in the polar front region.

Figure 5D shows both the wind and position of a jet stream several hundred kilometers wide in horizontal and vertical directions reaching wind speeds of over 125 km/h at 200 hPa. The jet stream usually appears at the location of a narrow transition zone (front) between two air masses with very different temperatures. The axis of the jet stream (the area of maximum wind speed) is near the tropopause. In the summer, the jet stream axis is usually at 200 hPa (approximately 12 km), while in the winter, it is usually at 300 hPa (approximately 9 km) due to the lower temperatures of air mass and hence its higher density and lower tropospheric thickness. In our particular case, however, the axis of the jet stream is already at approximately 9.3 km above the ground where it reaches a speed of up to 175 km/h over Germany (not shown here). This is significant for the unusually low temperature of the polar air mass for the summer season. We chose the image of the jet stream at 200 hPa because there is a clearly visible area of increased speed over the Ore Mountains in the Czech–German border region. Wind field isotachs show that the wind in the high troposphere was flowing from the southwest along the Ore Mountains. Furthermore, a moderate southwesterly wind (with a speed of approximately 15 km/h) was moving just above the ground. As the wind direction was at an angle of less than 30° to the mountain ridge, no transverse bands of mountain waves were generated as the wind passed around the mountain massif. Moreover, the Ore Mountains are not a monolithic ridge, but there are numerous mountains that pass through the Ore Mountains. In them, the so-called gap wind flowed, where cold air penetrated over the warmer air on the leeward side of the ridge, becoming thermodynamically unstable. Thus, an area of turbulent convective flow was formed over the mountain ridge due to orographic convergence at the surface. Although the humidity was not sufficient to form cumulus clouds and precipitation, increased convection contributed to locally increased wind shear in the evening on 29 July. The wind shear in the jet stream region, enhanced by the aforementioned orographic

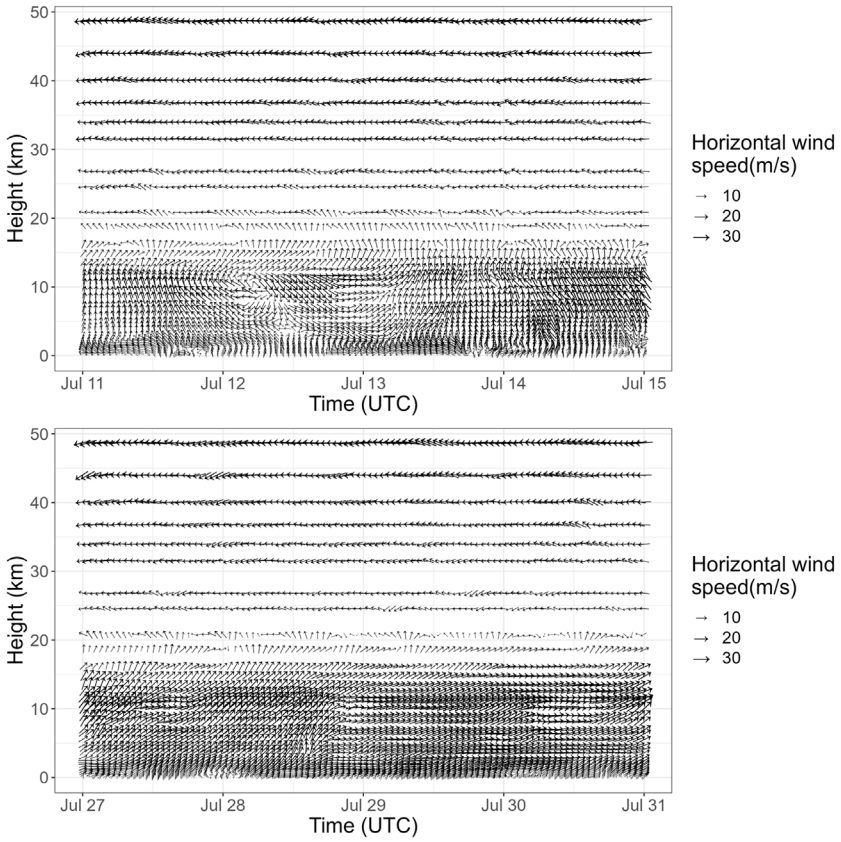

FIGURE 8
Horizontal wind in the troposphere and stratosphere from ERA5 reanalysis data. The orientation of the arrows shows the cardinal directions (top oriented = northward; right oriented = eastward). The top plot is for the first case study, and the bottom plot is for the second case study. Data source: Copernicus Climate Change Service (C3S) (2017). ERA5: Fifth generation of ECMWF atmospheric reanalysis of the global climate. Technical report: Copernicus Climate Change Service Climate Data Store (CDS).

effects, likely led to the fluctuations that were observed in the ionosphere.

4.2 Mesospheric observations

Figure 6 shows the gravity wave activity measured as the number of wave events per observation hour. This metric does not consider the amplitude or duration of the waves but provides some indication about how many different wave signatures (horizontal wavelength and propagation direction) are observed in the mesosphere. The temporal course of this wave activity is characterized by a steady increase until around the beginning of August, only to then decrease again. Superimposed on this steady increase is a modulation of wave activity with a period in the range of approximately 4–6 days. These are typical periods of planetary waves. Planetary waves can interact with gravity waves in various ways due to generation or filtering (see, e.g., Smith, 1996). A more detailed investigation of this possible relation is beyond the scope of this issue. It can be seen that approximately 1 day before the investigated case studies, the gravity wave activity reaches a local maximum. This is larger for the second case study. As mentioned previously, there are also other local maxima of gravity wave activity, e.g., on 23 July and 2 August. These are not analyzed further as this is beyond the scope of this paper, but comparisons with ERA5 data similar to those performed for the case studies (refer to the following paragraphs) show either wind shear between different height levels or sudden changes in the horizontal wind direction in the troposphere shortly before or around these maxima (not shown here).

Gravity waves generated in the troposphere might be well excited prior to the arrival of the decreased surface pressure front at the Panska Ves Observatory. As they require some time to propagate upward to the mesopause region, which might take up to 24 h, the data are analyzed before, during, and after the events [typical vertical velocities of gravity waves are of the order of 1–3 m/s, see, e.g., Mitchell and Howells (1998)].

Figure 7 shows the wave events for the investigated time periods. The upper row of panels is related to the thermal convection event on 13–14 July 2021. Here, it is remarkable that a majority of waves is observed at the night from 12 to 13th before the cold front reached the Czech Republic (while for the night of 13–14 July, no airglow observations are available due to heavy cloud cover). The waves with larger horizontal wavelengths (30–50 km) propagate to northeast and southwest and are observed at the beginning of the night and continued with smaller-scale waves in different directions. In addition, on 14–15 July, the observed larger-scale waves have an

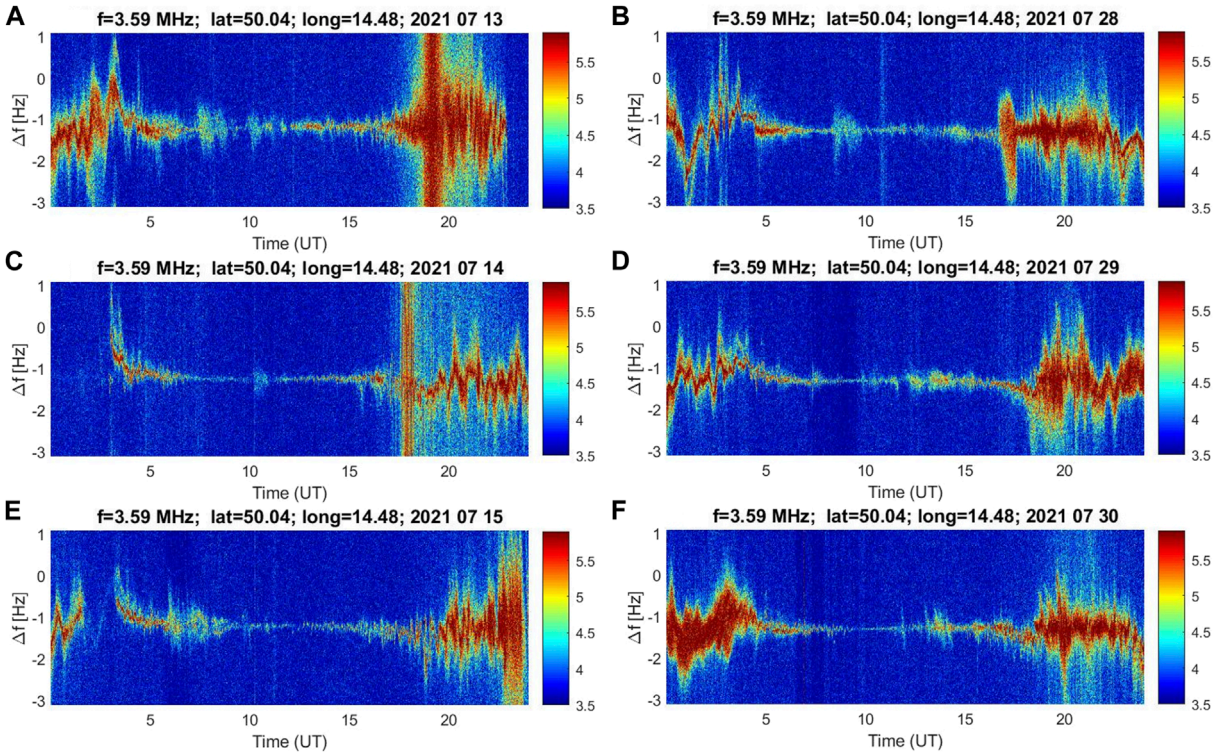

FIGURE 9
CDS spectrograms recorded on several consequent days around the events of interest. Left panels **(A,C,E)** show measurements during the passage of Bernd cyclone (13–15 July, 2021) while right panels **(B,D,F)** show the corresponding observation during an orographically driven jet stream situation (28–30 July, 2021). Remarkable noise bands across the whole spectrum are observed in coincidence with frontal passage on 13 and 14 July, which are caused by lightning that occurred near the Doppler receiver. In both cases a relatively broad spectrum associated with the Spread F situation in the ionosphere is registered.

orientation to northeast and southwest and one wave event to the NW direction. This behavior changes during 15–16 July to northwest and southeast and one event to the northeast. A majority of the smaller-scale waves propagates to the northwest and west direction for this night.

Interpreting the propagation directions regarding sources of the gravity waves is difficult. It is well-known that gravity waves are strongly influenced by the environment through which they propagate (e.g., Fritts et al., 2006; Wüst et al., 2017). In particular, one has to consider the effect of wind filtering, i.e., when the wind is in the same direction as the wave propagates, the wave might get filtered depending on its phase speed. On the other hand, wave breaking might itself lead to secondary gravity waves, and wind shear can generate gravity waves as well. In July 2021, the stratospheric wind, which is the most likely reason for wind filtering of waves coming from the troposphere, is westward (see Figure 8, Copernicus Climate Change Service (2017)), and thus we do not expect to see westward propagating (primary) waves which are generated in the troposphere except for very fast waves.

So, if generated by the cold front and thunderstorms on 12 July over Germany, the observed larger-scale waves propagating in the northeast direction should have been able to pass through the atmosphere up to the upper mesosphere and lower thermosphere region and possibly even higher. The source of the observed southwestward propagating gravity waves cannot be in the troposphere. However, due to a 180° shift, there might be some coincidence with the northeast propagating waves. Even though having carefully checked the results of the Fourier transform analysis and the aggregation to wave events as well as the image data, it might be an analysis issue, leading to a 180° ambiguity. However, there could also be a physical reason for the 180° shift such as wave reflection.

The observed smaller-scale wavelike structures might be instability features of larger-scale waves when they dissipate (i.e., "ripples") or smaller-scale gravity waves. This cannot be determined by the observations performed here. The tropospheric and lower-stratospheric winds (ERA5 reanalysis horizontal wind data, see Figure 8 top panel) show different orientations of wind shears at the investigated location. We assume that these wind features could lead to small-scale gravity waves in different propagation directions.

At first glance, the gravity waves in the northwest and west directions on 15 July fit well the interpretation that the cold front is emitting those waves which are in the east of the observation site at this time. However, this contradicts the effect of wind filtering. If these waves were generated in the troposphere, they were very likely to be filtered in the stratospheric westward winds. However, the stratospheric winds are relatively weak with only about 20–30 m/s. Another possibility could be that while waves in eastward directions

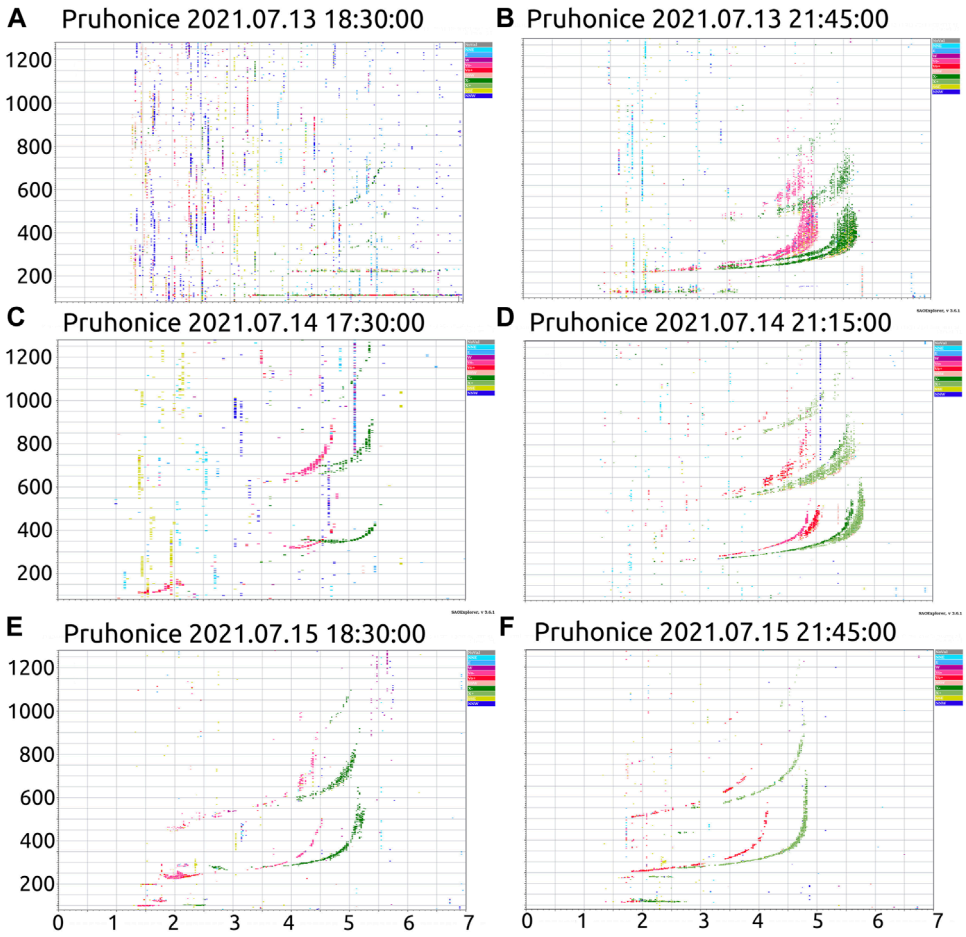

FIGURE 10
Digisonde ionograms in standard representation (horizontal axis shows frequency of the received signal in MHz, while the vertical axis shows height of reflection in km). Vertical ordinary (Vo+ and Vo–) and vertical extraordinary (X+, X–) reflections are denoted in red and green, respectively. Oblique reflections are denoted in blue, magenta, yellow, and pink depending on the direction of reflection. During Bernd cyclone passage above the measurement site, the ionograms recorded by Digisonde are very noisy with strong attenuation of vertical signals **(A)** and with plenty of off-vertical echo and strong spread-F echo **(B)**. The ionogram **(C)** is recorded during the passage of the frontal system on 14 July and displays similar features as the preceding frontal passage on 13 July. The ionogram **(D)** shows that the spread-F echo occurs again, and this example represents a typical ionogram of the night. The spread-F echo is recorded on most ionograms from time intervals (19:00 UTC on 13 July till 5:00 UTC on 14 July and 18:00 UTC on 14 July till 6:00 UTC on 15 July over the ionospheric station Průhonice). The ionograms **(E, F)** from time comparable to **(A–D)** show a normal ionosphere stratification situation with almost only vertical echo.

are emitted by the passed cold front on 15 July, they might emit secondary gravity waves when partially dissipating.

The bottom panel of Figure 7 shows the wave events related to the second investigated event on 29 July. Except for 28 July, no larger-scale waves (within the imager field-of-view of 46 km) are observed; only smaller-scale waves are observed in the range of 10–20 km horizontal wavelength. The number of detected events is the highest in the night from 28 to 29 July with 45 events compared to the 28 events in the night following it and seven events the night after that (but with only two observation hours compared to 4.5 h and 5.4 h). The predominant wave propagation directions are northward and southeastward as well as northwestward during the night from 29 to 30 July.

One might assume a gravity wave source in the south of the observation site and also one in the north on 28 July (or maybe on 27, assuming slowly upward propagating gravity waves), which could be related to the nearby cold polar front in the north and the warm air in the south as mentioned previously. Interestingly, mainly smaller-scale gravity waves are observed in the upper-mesosphere and lower-thermosphere OH airglow emission.

4.3 Ionospheric observation

4.3.1 Continuous Doppler sounding

Figure 9 shows CDS spectrograms recorded on several consequent days around the events of interest. Spectrogram records reveal substantial differences between the two analyzed cases. Figures 9A, C, E show the Doppler shift spectrograms recorded at 3.59 MHz on the sounding path Panská Ves—Prague from 13 to 15 July 2021. The signal received at night is characterized by a relatively broad spectrum associated with spread F. In addition, two

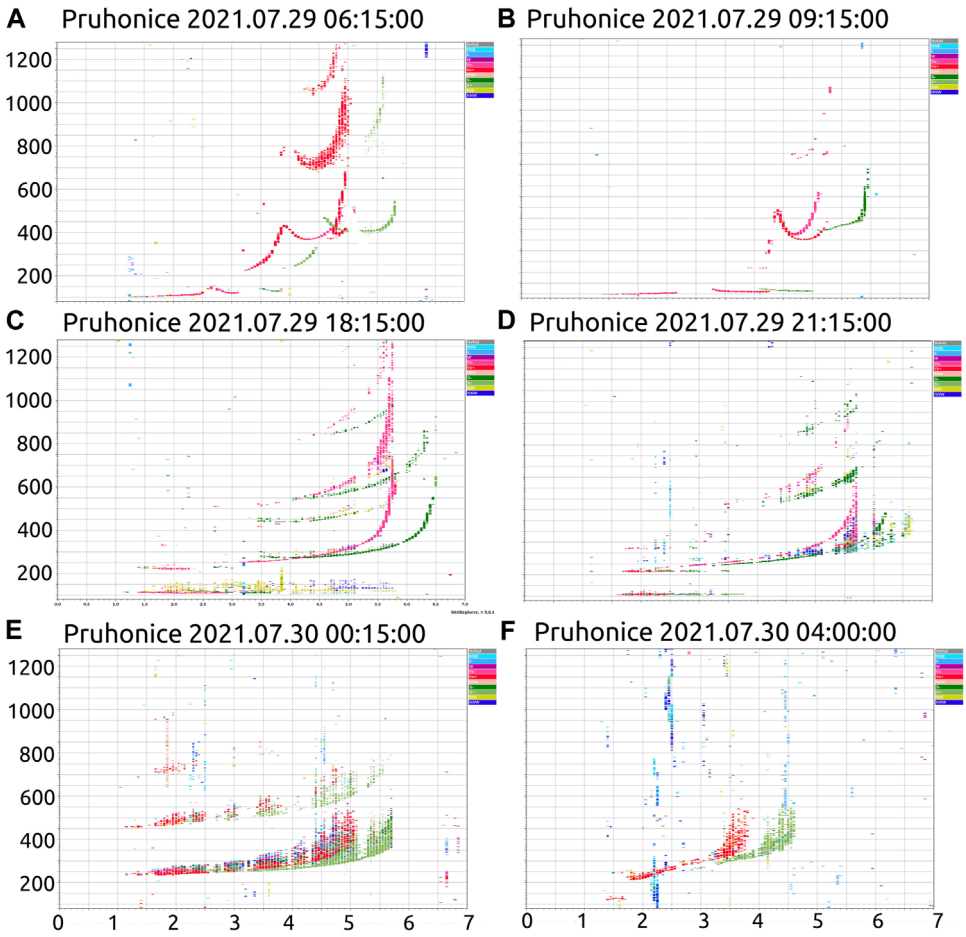

FIGURE 11
Digisonde ionograms as in Figure 10. During the jet stream event, many irregularities were well observed on ionograms. The ionograms **(A**, **B)** represent the situation when a cusp occurs on the profile. On the ionograms, there are split echo from the F2 layer. Panels **(C, D)** show rather good-quality ionograms with well-developed vertical reflections, together with some off-vertical echo. The sporadic E-layer is present on both ionograms. Panels **(E, F)** represent the spread-F echo that remains till the morning of the following day.

remarkable noise bands across the whole spectrum are observed at approximately 19:00 UTC on 13 July and approximately 18:00 UTC on 14 July. These noise bands consist of many individual vertical lines in the spectrograms and are caused by lightning that occurred near the Doppler receiver. Lightning activity and electrically charged thunderclouds were also observed by the electric field mill located in Panska Ves. The sharp/sudden increase in noise within CDS spectra in time coinciding with the fast moving midlatitude frontal cyclone was reported by Koucká Knížová et al. (2020).

The spectrum broadening of signals associated with spread F is also clearly visible on the spectrograms recorded during jet stream meteorological event from 28 to 30 July, as shown in Figures 9B, D, F. The broadening is the largest in the night during 29–30 July 2021; it is well-pronounced until approximately 04:00 UTC on 30 July. It should be noted in this regard that it is generally believed that acoustic–gravity waves propagating from below may act as a seeding mechanism for the development of spread F (Booker, 1979; Huang et al., 1994; Nicolls and Kelley, 2005).

4.3.2 Digisonde

Panels in Figure 10 show raw ionograms recorded during 3 days, from 13 to 15 July 2021. During the Bernd cyclone passage above the measurement site on 13 July, the ionograms (A) and (B) recorded by DPS-4D are very noisy with plenty of off-vertical echoes. The vertical signal of both ordinary and extraordinary modes is attenuated, especially on ionogram (A). Ionogram (B) represents the situation with the spread-F echo that is recorded on most ionograms of this day. On the middle part, the left ionogram (C) is recorded during the passage of the frontal system on 14 July and displays similar features as ionograms from the previous event. On the right ionogram (D), spread-F echo occurs again and represents a typical ionogram of the night. The spread-F conditions exist during geomagnetically disturbed situations. However, under geomagnetic forcing, the F2 traces are usually deformed, and significant changes in shape (e.g., cups) of the F traces are observed. Contrary to this, the ionograms (A–D) do not differ at first sight from the quiet ionograms by means of shape of the reflection. Therefore, the main deviation from the quiet-time ionograms is the presence of spread-F reflections.

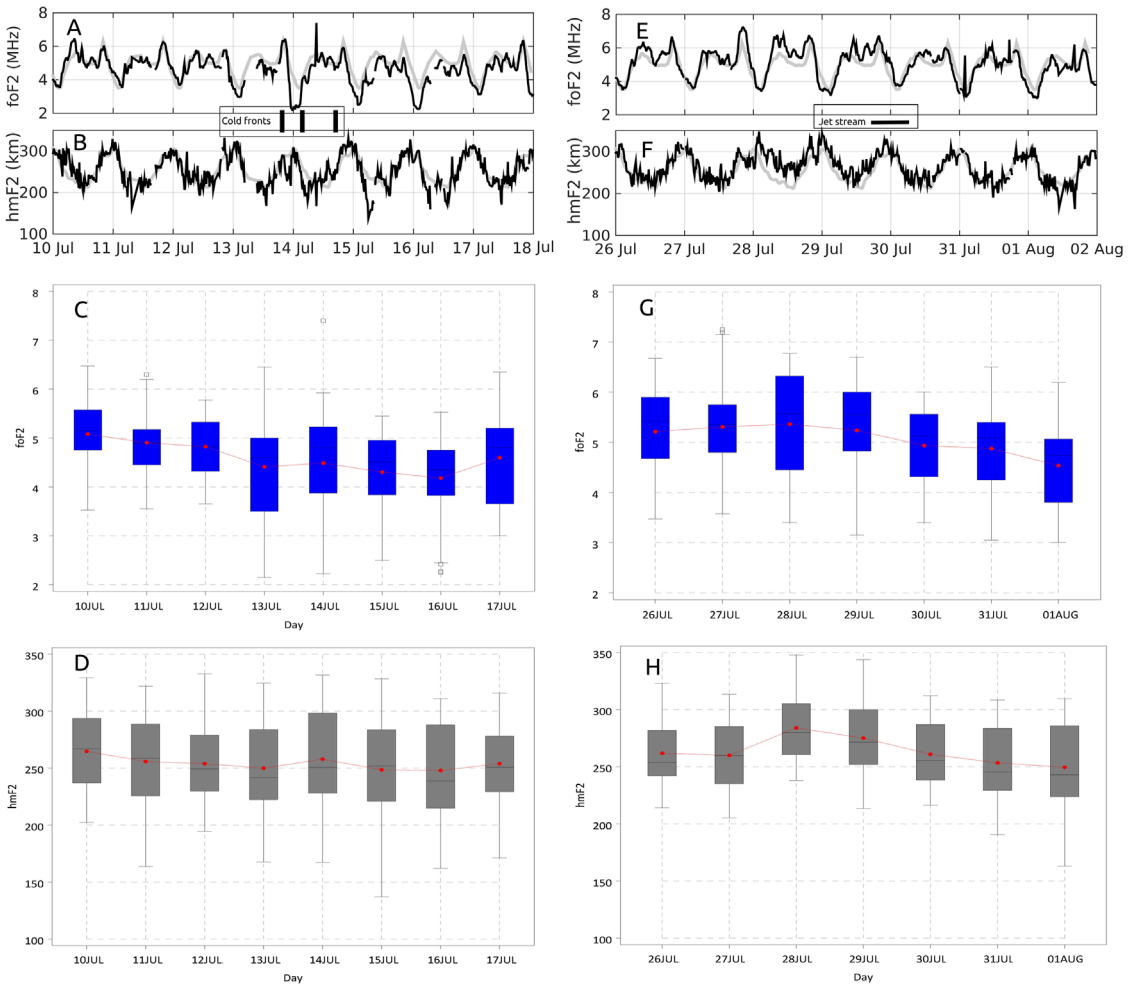

FIGURE 12
Bernd cyclone situation **(A–D)** and jet stream situation **(E–H)**. Vertical lines in **(A, B)** denote individual passages of cold fronts, and the horizontal line in **(E, F)** denotes the period of the jet stream situation. Panels **(A, E)** show critical frequencies foF2 (black) with median values (gray). Panels **(B, F)** show peak heights of the F2 region hmF2 with median values. Both time intervals are described using boxplot graphs **(C, D)** for a convective situation and **(G, H)** for a jet stream situation. Comparison with monthly median values of foF2 shows that the days 10–13 July match the median values well. A significant decrease in night values of foF2 occurred shortly after the Bernd **(A)** passage. During daytime, only a slight decrease in noon values of foF2 compared to preceding days can be identified. Critical frequency foF2 during noon hours stayed at lower values for the following 3 days compared to median values and the days prior to the Bernd passage. No significant changes in hmF2 could be well seen **(B)**. Boxplots **(C, D)** and **(G, H)** are organized in groups by days. Box and whisker plots display the mean (dot signs), median (horizontal lines in boxes), quartiles (color boxes), outliers (rings), and minimum and maximum observations (whiskers) for data groups. Rather stronger oscillation/variability could be identified on the course of foF2 on 29 July **(E)** compared to the preceding and following days; however, the general course of the day corresponds roughly to the monthly medians of foF2. A significant increase in hmF2 beginning on 28 July can be observed till 29 July.

As we will show further, changes in foF2 and hmF2 parameters compared to quiet time were observed. Two bottom ionograms from 15 July (E) and (F) show normal ionosphere stratification with almost only vertical echoes, implying that the ionosphere returned to a normal state. As mentioned previously, the spread-F ionograms indicate irregular stratification of the ionosphere. According to our experience (for instance, Koucká Knížová et al., 2021), the presence of atmospheric gravity waves leads to observation of spread-F situations even during periods of rather low geomagnetic activity.

Ionograms given in Figure 11 are related to the jet stream event. They show a large variety of echo types with plenty of irregularities. The first ionogram (A) represents a situation when a cusp occurs on the profile (the cusp can be observed between 4.8 and 5.2 MHz). On the following ionogram (B), echo from the F2 layer splits into two. Then, ionograms (C) and (D) show irregular stratification at heights of the F1 layer which seems to be split into two sublayers. The further two ionograms (E) and (F) show good quality with well-developed vertical reflections, together with some off-vertical echoes. Such a large variability of ionogram records indicates a rather non-stable situation within the ionosphere that is probably disturbed by the presence of propagating atmospheric waves. In addition to spread-F echo ionograms, the cusp occurrence on the profile also points to the propagating atmospheric gravity waves.

Figure 12 shows the daily course of critical frequency foF2 (on panels A and E) and hmF2 (on panels B and F) measured for 7

consecutive days. Left panels A–D refer to the Bernd event, and right panels E–H show the jet stream situation. During 11 and 12 July the foF2 shows regular course, it means the increase of foF2 during daytime due to direct solar ionization and decrease of foF2 with decreasing amount of solar radiation to night values, when due to recombination processes only low ionization remains at F2 layer. The asymmetry in the maximum of foF2, which is shifted toward afternoon hours rather than to the time of minimum zenith angle at noon (time of maximum ionization), is well-documented phenomena attributed to recombination processes (see, for instance, Davies, 1990). A rather interesting feature on 13 July is a sharp decrease in foF2 after 18:00 UTC with respect to preceding days. In general, the foF2 stays a bit lower for the following 3 days and starts to rise again on 18 July. Correspondingly, the height hmF2 slightly decreases for a few days. It indicates that the whole profile of electron concentration is moved downward and remains there for several days. It is important to point out that during all studied days of convective events, the height of the layer maximum (Figure 12B) is lower than during the following orographically driven convective situation in the jet stream zone (Figure 12F). In addition to that, on the course of hmF2, less variability could be observed during the later event showing, at first glance, a much more regular course. However, a small decrease in the whole profile can be observed beginning on 29 July. On the course of foF2, as shown in Figure 12E, one can notice a decrease in the critical frequency foF2 during days 30 and 31 July for daytime. The difference in night time values can be observed between 29/30 July compared to 31 July/01 August and 01/02 August; however, a slight decrease in night foF2 is also observed compared to the nights of 25/26–29/30 July.

The boxplot procedure indicates a significant departure of the foF2 and hmF2 diurnal course from normal behavior. Figures 12C, D, G, H show statistical boxplots of foF2 and hmF2. Plots are organized in groups by days. Box and whisker plots display the mean (dot signs), median (horizontal lines in boxes), quartiles (color boxes), outliers (rings), and minimum and maximum

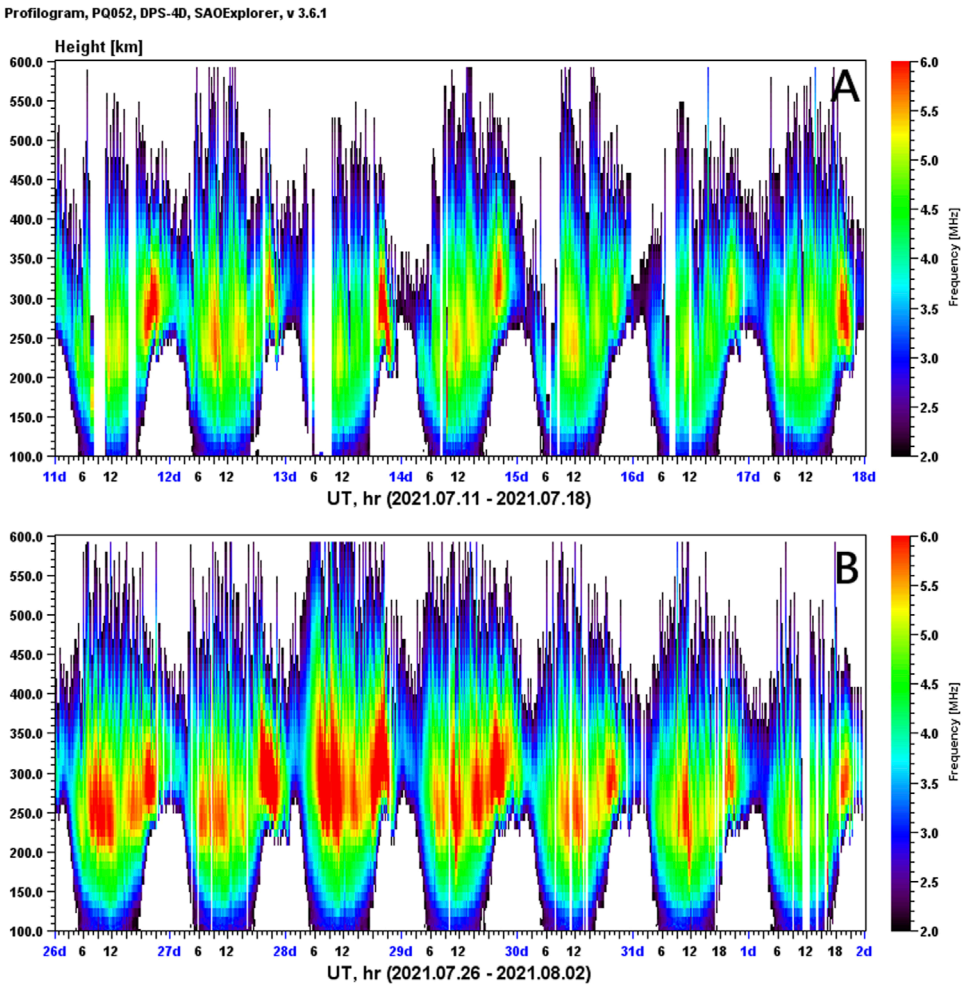

FIGURE 13
Profilograms obtained from full electron concentration profiles (ionograms are manually scaled, and the NHPC inversion method within the SAO explorer is applied) for a Bernd event **(A)** and jet stream **(B)**. Profilograms indicate that ionization within the whole F-layer ionosphere is higher during the jet stream event on 29 July **(B)** than ionization around mid-July **(A)**. In both cases, oscillations in the gravity wave domain are well observed during the entire studied time span.

observations (whiskers) for data groups. Figure 12C shows a substantial change in the foF2 distribution. The mean value remains lower than the median value till the end of the analyzed term. Figure 12D shows a difference in the mean and median values for the entire observation time; the largest difference is visible on 13 and 14 July. Furthermore, plots in Figures 12G, H show the same analyses for the orographically driven convection in the jet stream zone event. Contrary to the thermal convection event, mean and median values differ consistently for the entire monitored time. The median value stays higher than the mean value of foF2, while the median value remains smaller than the mean value of hmF2. However, the largest difference in the case of foF2 is observed on 29 July, while for hmF2, the difference starts to increase on 30 July. The deformation of the diurnal courses of the main ionospheric parameters in both analyzed cases is probably linked to the increase in AGW activity within ionospheric heights with the origin in tropospheric situations. Wavelet transform analysis applied on foF2 and hmF2 reveals an increase in power on oscillation periods 30 min and 1–3 h and approximately 3 h on 13/14 July and on periods 3–4 h on 29 July. Oscillations are better pronounced within foF2.

Profilograms in Figure 13 show the variation in profiles during several consequent days around the studied events. Gaps are caused by the presence of a sporadic E-layer which partially or fully prevents the sounding signal from reaching upper laying layers. However, scaling of the main parameters, foF2 and hmF2, could still be possible when the blanketing frequency is lower than the critical

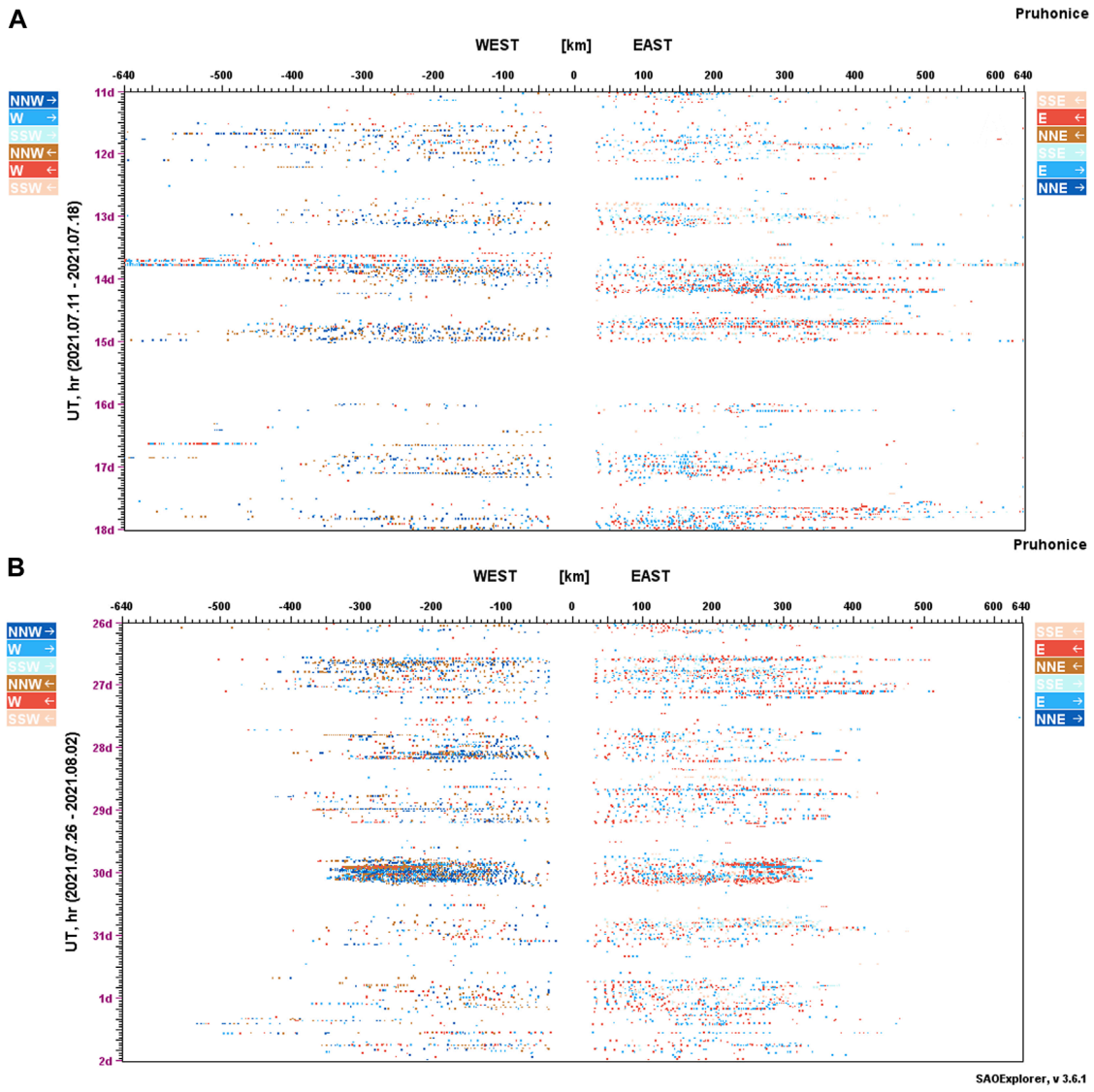

FIGURE 14
On both directograms, the increase in amplitudes is visible for the analyzed events; however, it was more pronounced on 29 July **(B)**. During the day, there is very low activity, as usual, visible till evening hours. Panel **(A)** shows two episodes of increased activity on 13 and 14 July in coincidence with the passage of the storm systems of the Bernd cyclone. Panel **(B)** indicates strong plasma motion on 29 July. The registered off-vertical signal is stronger than that on the preceding and following days. It shows strong plasma motion in north north west–south south east direction. The direction of plasma motion rapidly changes to the opposite direction, which indicates dislocation of the reflection planes by upward-propagating gravity waves.

frequency of the F-layer. Accuracy of the electron density profile scaling or main parameters foF2 and hmF2 is affected by the spread-F echo or cusps present on the profile.

On both panels of Figure 13, the Bernd cyclone on panel (A) and jet stream event (B), there are visible wavelike oscillations of the entire profile in the period range of gravity waves with periods of approximately 3 h observed in a regular increase and decrease in the detected plasma frequency. The estimation is qualitative due to limitations in profile scaling. The ionization level observed during the observation time of the Bernd cyclone passage event is lower during the entire monitoring period of the orographically driven convection in the jet stream zone. In agreement with foF2 courses given in Figure 12, the ionization decreases in the entire profile after the Bernd cyclone passage (Figure 13A) and jet stream event (Figure 13B).

On both directogram plots (Figure 14), the increase in echo amplitudes is well-visible for both analyzed cases. During the quiet daytime period, there is very low activity visible on the directograms till the evening hours. Figure 14A shows two episodes of increased activity on 13 and 14 July in coincidence with the passage of the storm systems of the Bernd cyclone. The DPS 4D antenna system registers variable signals and detects the quickly changing direction of the plasma motion. On the night of 13/14 July, the detected plasma flow and shears appeared first in east-west (EW) direction and were later observed in the north northwest–south southeast (NNW–SSE) direction. On 14/15 July, in the night, the plasma flow and shears were detected almost only in the NNW–SSE direction. Figure 14B shows strong plasma motion on 29 July. The registered signal is substantially stronger than that on the preceding and following days. It shows strong plasma motion in the NNW–SSE direction. The direction of plasma motion rapidly changes into the opposite direction.

The increased Doppler echo can indicate both increase in the plasma flow in the horizontal direction and substantial changes in the undulation of reflection planes. The direction of the registered plasma flow quickly changes to the opposite direction, which confirms that the reflection planes are probably disrupted by the propagation of atmospheric waves with both horizontal and vertical components.

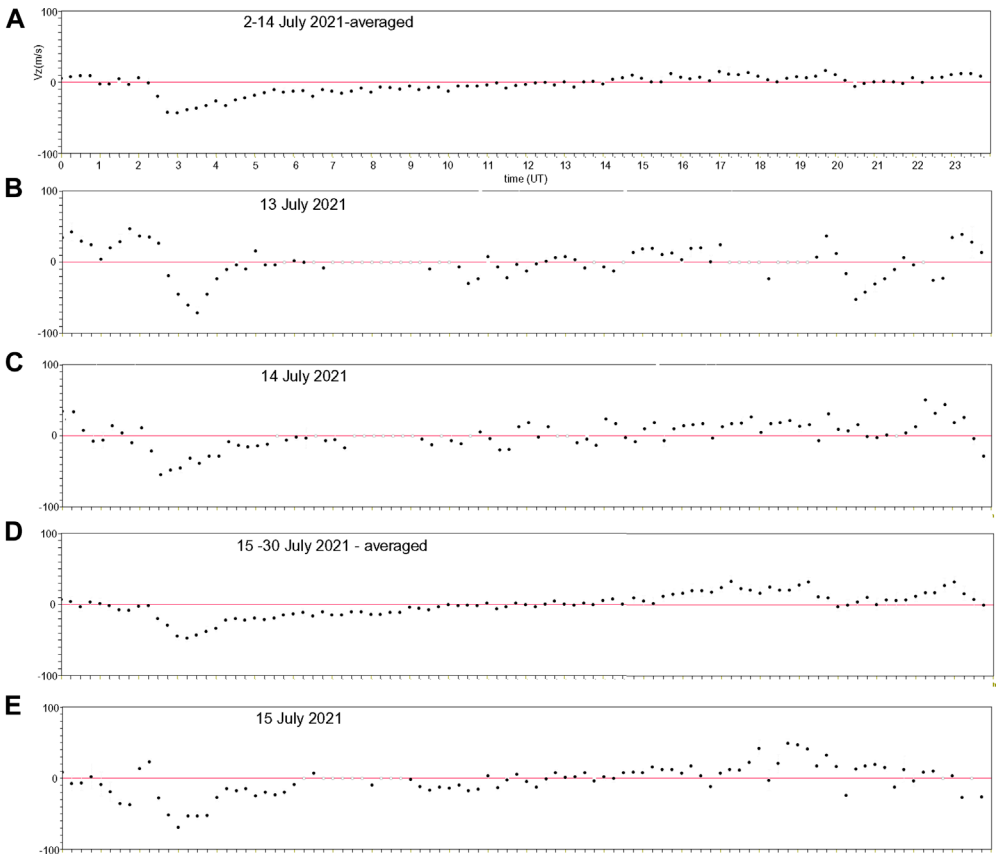

FIGURE 15
Occurrence of sporadic E does not allow the determination of plasma drift velocity during whole days of interest. On 13 July **(B)** shortly after the frontal passage, strong opposite plasma flow was detected. It was followed by a less pronounced morning downward peak on 14 July compared to the averaged values of the reference time span **(A)**. On 14 July **(C)** after the second frontal passage, higher values of plasma were observed than those in the reference diurnal course. On the course of the vertical component of plasma drift, rather high variability during the whole day can be observed **(E)**. In the morning hours, a short episode of opposite plasma motion appears. The morning downward peak is less pronounced compared to the reference time span. During evening hours, larger values of the drift are recorded with respect to the reference course. During evening hours, the vertical component significantly changes the direction. Drift course data are compared to averaged values for the reference time span of 5 days preceding the event **(D)**.

As mentioned previously, the occurrence of sporadic E does not allow the determination of all ionospheric plasma properties for all ionograms, and the plasma drift velocity cannot be computed for whole days of interest. However, qualitative interpretation of the vertical plasma drift component (Figure 15) is still possible. Drift data recorded during days of events are compared to averaged values obtained for 5 days preceding the event. On 13 July, shortly after the frontal passage, strong opposite plasma flow was detected (Figure 15B) with respect to the reference day (Figure 15A). It is followed by a less pronounced morning downward peak on 14 July (Figure 15C) compared to the reference behavior. On 14 July, after the second frontal passage, plasma flows in the same direction as on the reference day. Somewhat higher values of plasma were observed compared to the reference diurnal course.

On the course of the vertical component of plasma drift, (Figure 15E) rather high variability during the whole day can be seen apparently. In the morning hours, a short episode of opposite plasma motion appears. The morning downward peak is less pronounced than the reference diurnal course (Figure 15D). In evening hours, larger values of the drift are recorded with respect to the reference course. In addition to that, the vertical component significantly changes the direction in the afternoon hours and mainly during evening hours.

5 Conclusion

We analyzed two tropospheric mesoscale situations caused by exceptional synoptic-scale circulation conditions enhanced by the influence of the local convective environment. The first situation represents changes induced by convective upward motions in the squall line ahead of a cold front with heavy rainfall on 13–14 July 2021 (Bernd cyclone). The second situation describes induced effects of the polar front jet stream in the upper troposphere enhanced by orography with an atypical location of the jet stream on 29 July 2021. These two selected tropospheric situations evolved during rather low and stable solar and geomagnetic conditions ($F10.7_{mean}$ = 81.06 and $F10.7_{median}$ = 77.65; Kp_{mean} = 1.26 and Kp_{median} = 1). Therefore, we expect that the observed perturbations within ionospheric plasma are of neutral atmosphere origin. Geomagnetic activity increased only for two short episodes classified as moderate. Using meteorological, mesosphere, stratosphere, and ionosphere data, we identified tropospheric disturbances and further detected and analyzed possible induced effects through the atmosphere up to the ionospheric F2 region. Due to the coincidental occurrence of the observed variability within the mesosphere and ionosphere, we attribute the resulting ionospheric disturbances to the neutral lower-atmosphere forcing rising from the discussed tropospheric situations.

We identified substantial changes in the behavior of particular atmospheric parameters in time coherence with observed meteorological situations. Our main observational findings are summarized as follows:

1. Spread-F echo occurs after the frontal passage on CDS spectra and DPS 4D ionograms.
2. Spread-F echo develops in connection with orographically enhanced jet stream on CDS spectra and DPS 4D ionograms.
3. Irregularities (cusps, layer splitting, and spread F) occur on ionograms related to orographically enhanced jet stream.
4. Distortion of diurnal foF2 and hmF2 distributions is observed during both analyzed events.
5. Wavelike oscillation in the GW mode develops in ionospheric parameters, in particular, on profilograms.
6. Increase in the detected amplitude of horizontal plasma flow is registered during event days.
7. Qualitative changes in the vertical plasma drift during the studied days are recorded with respect to the reference time.
8. Increase in GW activity in the mesosphere is detected before and around the analyzed events. Stronger activity is observed in connection with orographically enhanced jet stream, likely due to cloud coverage.
9. A majority of waves observed in the mesosphere occur during the night before the cold front reaches the observational point.
10. Identified GW structures in the mesosphere propagate into a wide range of directions, and no prevailing direction can be identified.
11. Large-scale and small-scale GW structures are observed in the mesosphere during Cyclone Bernd.
12. Only small-scale GW structures are registered in the mesosphere in relation to the jet stream situation.

As mentioned previously, the study involves selected events observed during the time of low solar activity and low-to-moderate geomagnetic activity; hence, we consider it correct to attribute most of the observed ionospheric variability to the sources within the lower-lying neutral atmosphere. In our cases, we assume that the waving frontal boundary (Cyclone Bernd) and boundary of air masses with a sharp temperature gradient (polar front jet stream situation) may act as an effective source of the gravity waves that propagate as high as the F2 ionospheric region. Certainly, due to the presence of winds, part of the launched gravity wave spectra may be filtered out without reaching the ionosphere. However, part of the observed gravity wave activity may be caused by the secondary waves due to primary wave breaking.

Our study suggests that the observed larger-scale gravity waves, seen within mesospheric and ionospheric data, can be generated by the movement of the frontal system of the continental scale. Large-scale GW structures are completely missing in the mesospheric observations in the case of a polar jet stream event. In both analyzed cases, we observe small-scale GW structures within mesosphere airglow data.

Our investigation shows the possible link between the source meteorological systems that effectively launch the atmospheric waves that propagate upward through the mesosphere up to ionospheric heights where they influence the general state of neutral atmosphere and also due to coupling ionospheric plasma. The observed mesospheric and ionospheric response to the initial meteorological situations shows some differences. Airglow measurement seems to be sensitive to GW detection that very likely

originates from an atypically located jet stream and intensive frontal systems.

The observed departures from the regular ionospheric behavior account for the fact that the forcing from the lower-lying atmospheric regions should not be neglected and may form an important part of the observed variability and a substantial part of the day-to-day variability under stable solar forcing. The CDS spectrograms seem to be an effective and instant tool for the detection of AGW-induced disturbances in the ionosphere associated with moving frontal systems.

For additional requirements for specific article types and further information please refer to "Article types" on every Frontiers journal page.

Data availability statement

The datasets presented in this study can be found in online repositories. The names of the repository/repositories and accession number(s) can be found at: Geomagnetic Data Center: https://www.gfz-potsdam.de/en/; Meteodata: https://www.wetterkontor.de/de/wetterlage.asp#erlaeuterungen, https://www1.wetter3.de/Archiv/https://www.firenzemeteo.it/maps/mappe-previsioni-meteo-gfs.php,https://weather.uwyo.edu/upperair/sounding.html, https://www.ufa.cas.cz/en/stanice-praha-sporilov-2/; Ionosphere: https://www.ufa.cas.cz/DATA/files/oia/Doppler_des_365.pdf, http://datacenter.ufa.cas.cz/, http://giro.uml.edu; Mesosphere: FAIM2 data are stored in the World Data Center for Remote Sensing the Atmosphere (WDC-RSAT). Data available on request. Copernicus Climate Change Service (C3S) (2017). ERA5: Fifth generation of ECMWF atmospheric reanalysis of the global climate. Technical report, Copernicus Climate Change Service Climate Data Store (CDS). For the scaling of raw ionogram Software SAO Explorer: https://ulcar.uml.edu/SAO-X/SAO-X.html.

Author contributions

PK analyzed Digisonde data, performed analyses, provided interpretation, prepared the review part, and wrote the first draft of the paper. KP analyzed tropospheric flow dynamics and classified meteorological situations and wrote the meteorological part of the manuscript. KP analyzed Digisonde data and performed statistical analyses. JC operated CDS, analyzed data, and provided interpretation. ZM analyzed Digisonde data and provided interpretation. DK operated Digisonde, prepared campaigns, analyzed Digisonde data (drifts), and provided interpretation. The analysis methods for the FAIM data (mesospheric part of the manuscript) were developed by PH supported by SW and MB within the project VoCaS-Alp. PH analyzed the FAIM data for this manuscript. Together with SW and MB, he interpreted them and wrote the corresponding part of the manuscript. JK substantially contributed to the synoptic evaluation and interpretations of meteorological events. All authors contributed to the article and approved the submitted version.

Funding

Part of the data collection and analyses of the IAP team was performed under the support of H2020-INFRAIA-2018-2020 PITHIA-NRF (Grant Agreement Number: 101007599) and Project HORIZON-CL4-2022-SPACE-01101081835 T-FORS. Work of KPod was partly supported under the grant GA21-03295S by the Czech Science Foundation, and work of JC was supported by the Mobility Project of the Academy of Sciences CONICET-22-02. The analysis methods for FAIM data were developed within the project VoCaS-ALP which received funding from the Bavarian State Ministry of the Environment and Consumer Protection under Grant No. TKP01KPB-70581. Both teams acknowledge the HR Project Development of Research and Development Capacities at the Institute of Atmospheric Physics CAS (Project Reg. No. CZ.02.2.69/0.0/0.0/18_054/0014500).

Acknowledgments

The authors would like to thank Josef Boška, who passed away before completing the manuscript, for his advice and suggestions.

Conflict of interest

The authors declare that the research was conducted in the absence of any commercial or financial relationships that could be construed as a potential conflict of interest.

Publisher's note

References

Bauer, S. (1958). An apparent ionospheric response to the passage of hurricanes. *J. Geophys. Res.* 63, 265–269. doi:10.1029/JZ063i001p00265

Bencze, P., and Bakki, P. (2002). On the origin of mid-latitude spread-F. *Acta Geod. geoph. hung.* 37, 409–417. doi:10.1556/AGeod.37.2002.4.4

Berdermann, J., Kriegel, M., Banyś, D., Heymann, F., Hoque, M. M., Wilken, V., et al. (2018). Ionospheric response to the X9. 3 flare on 6 September 2017 and its implication for navigation services over Europe. *Space weather.* 16 (10), 1604–1615. doi:10.1029/2018SW001933

Bertin, F., Testud, J., Kersley, L., and Rees, P. R. (1978). The meteorological jet stream as a source of medium scale gravity waves in the thermosphere: An experimental study. *J. Atmos. Terr. Phys.* 40, 1161–1183. doi:10.1016/0021-9169(78)90067-3

Bishop, R. L., Aponte, N., Earle, G. D., Sulzer, M., Larsen, M. F., and Peng, G. S. (2006). Arecibo observations of ionospheric perturbations associated with the passage of tropical storm Odette. *J. Geophys. Res.* 111, A11320. doi:10.1029/2006JA011668

Blanc, E., Farges, T., Le Pichon, A., and Heinrich, P. (2014). Ten year observations of gravity waves from thunderstorms in Western Africa. *J. Geophys. Res. Atmos.* 119, 6409–6418. doi:10.1002/2013JD020499

Booker, H. G. (1979). The role of acoustic gravity waves in the generation of spread-F and ionospheric scintillation. *J. Atmos. Terr. Phys.* 41, 501–515. doi:10.1016/0021-9169(79)90074-6

Borchevkina, O., Karpov, I., and Karpov, M. (2020). Meteorological storm influence on the ionosphere parameters. *Atmosphere* 11, 1017. doi:10.3390/atmos11091017

Borries, C., Berdermann, J., Jakowski, N., and Wilken, V. (2015). Ionospheric storms—a challenge for empirical forecast of the total electron content. *J. Geophys. Res. Space Phys.* 120 (4), 3175–3186. doi:10.1002/2015JA020988

Boška, J., and Šauli, P. (2001). Observations of gravity waves of meteorological origin in the F-Region ionosphere. *Phys. Chem. Earth Part C.* 26 (6), 425–428. doi:10.1016/S1464-1917(01)00024-1

Bowman, G. G. (1990). A review of some recent work on mid-latitude spread-F occurrence as detected by ionosondes. *J. Geomag. Geoelectr.* 42, 109–138. doi:10.5636/jgg.42.109

Bowman, G. G., Dunne, G. S., and Hainsworth, D. W. (1987). Mid-latitude spread-F occurrence during daylight hours. *J. Atmos. Terr. Phys.* 49, 165–176. doi:10.1016/0021-9169(87)90051-1

Bowman, G. G. (1988). Small-scale stratifications associated with daytime travelling ionospheric disturbances in mid-latitude regions. *Ann. Geophys.* 6, 187–194.

Bowman, G. G. (1981). The nature of ionospheric spread-F irregularities in mid-latitude regions. *J. Atmos. Terr. Phys.* 43, 65–79. doi:10.1016/0021-9169(81)90010-6

Buonsanto, M. J. (1999). Ionospheric storms—A review. *Space Sci. Rev.* 88, 563–601. doi:10.1023/A:1005107532631

Chang, L. C., Chiu, P. Y., Salinas, C. C. J. H., Chen, S. P., Duann, Y., Liu, J. Y., et al. (2018). On the relationship between E region scintillation and ENSO observed by FORMOSAT-3/COSMIC. *J. Geophys. Res. Space. Phys.* 123, 4053–4065. doi:10.1029/2018JA025299

Chau, J. L., Goncharenko, L. P., Fejer, B. G., and Liu, H. L. (2012). Equatorial and low latitude ionospheric effects during sudden stratospheric warming events. *Space Sci. Rev.* 168, 385–417. doi:10.1007/s11214-011-9797-5

Chum, J., Liu, J.-Y., Podolská, K., and Šindelářová, T. (2018). Infrasound in the ionosphere from earthquakes and typhoons. *J. Atmos. Sol. Terr. Phys.* 171, 72–82. doi:10.1016/j.jastp.2017.07.022

Chum, J., and Podolská, K. (2018). 3D analysis of GW propagation in the ionosphere. *Geophys. Res. Lett.* 45(21), 11,562–11,571. doi:10.1029/2018GL079695

Chum, J., Podolská, K., Rusz, J., Baše, J., and Tedoradze, N. (2021). Statistical investigation of gravity wave characteristics in the ionosphere. *Earth Planets Space* 73, 60. doi:10.1186/s40623-021-01379-3

Davies, K. (1990). *Ionospheric radio*. London: Peter Peregrinus Ltd. doi:10.1049/PBEW031E

Dyson, P. L., Johnston, D. L., and Scali, J. L. (1995). Observations of gravity waves associated with mid-latitude spread-F. *Adv. Space Res.* 16, 113–116. doi:10.1016/0273-1177(95)00179-I

Forbes, J. M., Palo, S. E., and Zhang, X. (2000). Variability of the ionosphere. *J. Atmos. Sol. Terr. Phys.* 62 (8), 685–693. doi:10.1016/S1364-6826(00)00029-8

Fritts, D. C., and Alexander, M. J. (2003). Gravity wave dynamics and effects in the middle atmosphere. *Rev. Geophys.* 41 (1), 1003. doi:10.1029/2001RG000106

Fritts, D. C., and Vadas, S. (2008). Gravity wave penetration into the thermosphere: Sensitivity to solar cycle variations and mean winds. *Ann. Geophys.* 26, 3841–3861. doi:10.5194/angeo-26-3841-2008

Fritts, D. C., Vadas, S. L., Wan, K., and Werne, J. A. (2006). Mean and variable forcing of the middle atmosphere by gravity waves. *J. Atmos. Sol. Terr. Phys.* 68, 247–265. doi:10.1016/j.jastp.2005.04.010

Goncharenko, L. P., Coster, A. J., Zhang, S. R., Erickson, P. J., Benkovitch, L., Aponte, N., et al. (2018). Deep ionospheric hole created by sudden stratospheric warming in the nighttime ionosphere. *J. Geophys. Res. Space Phys.* 123, 7621–7633. doi:10.1029/2018JA025541

Goncharenko, L., and Zhang, S.-R. (2008). Ionospheric signatures of sudden stratospheric warming: Ion temperature at middle latitude. *Geophys. Res. Lett.* 35, L21103. doi:10.1029/2008GL035684

Guha, A., Paul, B., Chakraborty, M., and De, B. K. (2016). Tropical cyclone effects on the equatorial ionosphere: First result from the Indian sector. *J. Geophys.Res. Space Phys.* 121, 5764–5777. doi:10.1002/2016JA022363

Hannawald, P., Schmidt, C., Sedlak, R., Wüst, S., and Bittner, M. (2019). Seasonal and intra-diurnal variability of small-scale gravity waves in OH airglow at two Alpine stations. *Atmos. Meas. Tech.* 12, 457–469. doi:10.5194/amt-12-457-2019

Hannawald, P., Schmidt, C., Wüst, S., and Bittner, M. (2016). A fast SWIR imager for observations of transient features in OH airglow. *Atmos. Meas. Tech.* 9, 1461–1472. doi:10.5194/amt-9-1461-2016

Huang, Ch.-S., Miller, C. A., and Kelley, M. C. (1994). Basic properties and gravity wave initiation of the midlatitude F region instability. *Radio. Sci.* 29 (1), 395–405. doi:10.1029/93RS01669

Hung, R. J., Phan, T., and Smith, R. E. (1979). Coupling of ionosphere and troposphere during the occurrence of isolated tornadoes on November 20, 1973. *J. Geophys. Res.* 84, 1261–1268. doi:10.1029/JA084iA04p01261

Jiang, C., Yang, G., Liu, J., Yokoyama, T., Komolmis, T., Song, H., et al. (2016). Ionosonde observations of daytime spread F at low latitudes. *J. Geophys. Res. Space Phys.* 121, 12,093–12,103. doi:10.1002/2016JA023123

Jonah, O. F., Coster, A., Zhang, S., Goncharenko, L., Erickson, P. J., de Paula, E. R., et al. (2018). TID observations and source analysis during the 2017 memorial day weekend geomagnetic storm over north America. *J. Geophys. Res. Space Phys.* 123, 8749–8765. doi:10.1029/2018JA025367

Kašpar, M., Müller, M., Kakos, V., Řezáčová, D., and Sokol, Z. (2009). Severe storm in bavaria, the Czech republic and Poland on 12–13 july 1984: A statistic- and model-based analysis. *Atmos. Res.* 93, 99–110. doi:10.1016/j.atmosres.2008.10.004

Kašpar, M. (2003). Objective frontal analysis techniques applied to the extreme/non-extreme precipitation events. *Stud. Geophys. Geod.* 47, 639–640. doi:10.1023/A:1024771820322

Kazimirovsky, E. S., and Kokourov, V. D. (1991). The tropospheric and stratospheric effects in the ionosphere. *J. Geomagn. Geoelec.* 43, 551–562. doi:10.5636/jgg.43.Supplement1_551

Korenkov, Y. N., Klimenko, V. V., Klimenko, M. V., Bessarab, F. S., Korenkova, N. A., Ratovsky, K. G., et al. (2012). The global thermospheric and ionospheric response to the 2008 minor sudden stratospheric warming event. *J. Geophys. Res.* 117, A10309. doi:10.1029/2012JA018018

Kouba, D., and Chum, J. (2018). Ground-based measurements of ionospheric dynamics. *J. Space Weather Space Clim.* 8, A29. doi:10.1051/swsc/2018018

Kouba, D., and Koucká Knížová, P. (2012). Analysis of digisonde drift measurements quality. *J. Atmos. Sol. Terr. Phys. 90–* 91, 212–221. doi:10.1016/j.jastp.2012.05.006

Kouba, D., and Koucka Knizova, P. (2011). "Influence of non-vertical echos to ionogram scaling," in *WDS'11 proceedings of contributed papers: Part II - physics of plasmas and ionized media*. Editors J. Šafránková, and J. Pavlů (Prague: MATFYZPRESS), 67–72.

Kouba, D., and Koucká Knížová, P. (2016). Ionospheric vertical drift response at a mid-latitude station. *Adv. Space Res.* 58, 108–116. doi:10.1016/j.asr.2016.04.018

Koucká Knížová, P., Laštovička, J., Kouba, D., Mošna, Z., Podolská, K., Potužníková, K., et al. (2021). Ionosphere influenced from lower-lying atmospheric regions. *Front. Astro. Space Sci.* 8, 1–29. doi:10.3389/fspas.2021.651445

Koucká Knížová, P., Podolská, K., Potužníková, K., Kouba, D., Mošna, Z., Boška, J., et al. (2020). Evidence of vertical coupling: Meteorological storm fabienne on 23 september 2018 and its related effects observed up to the ionosphere. *Ann. Geophys.* 38, 73–93. doi:10.5194/angeo-38-73-2020

Kramer, R., Wüst, S., and Bittner, M. (2016). Investigation of gravity wave activity based on operational radiosonde data from 13 years (1997-2009): Climatology and possible induced variability. *J. Atmos. Sol. Terr. Phys.* 140, 23–33. doi:10.1016/j.jastp.2016.01.014

Kramer, R., Wüst, S., Schmidt, C., and Bittner, M. (2015). Gravity wave characteristics in the middle atmosphere during the CESAR campaign at Palma de Mallorca in 2011/2012: Impact of extratropical cyclones and cold fronts. *J. Atmos. Sol. Terr. Phys.* 128, 8–23. doi:10.1016/j.jastp.2015.03.001

Laštovička, J., and Chum, J. (2017). A review of results of the international ionosphericDoppler sounder network. *Adv. Space Res.* 60 (8), 1629–1643. doi:10.1016/j.asr.2017.01.032

Laštovička, J. (2006). Forcing of the ionosphere by waves from below. *J. Atmos. Sol. Terr. Phys.* 68, 479–497. doi:10.1016/j.jastp.2005.01.018

Lay, E. H. (2018). Ionospheric irregularities and acoustic/gravity wave activity above low-latitude thunderstorms. *Geophys. Res. Lett.* 45, 90–97. doi:10.1002/2017GL076058

Li, W., Yue, J., Yang, Y., Li, Z., Guo, J., Pan, Y., et al. (2017). Analysis of ionospheric disturbances associated with powerful cyclones in East Asia and North America. *J. Atmos. Sol-Terr. Phys.* 161, 43–54. doi:10.1016/j.jastp.2017.06.012

Medvedev, A. S., and Gavrilov, N. M. (1995). The nonlinear mechanism of gravity wave generation by meteorological motions in the atmosphere. *J. Atmos. Sol. Terr. Phys.* 57 (11), 1221–1231. doi:10.1016/0021-9169(95)00008-p

Mitchell, N. J., and Howells, V. St. C. (1998). Vertical velocities associated with gravity waves measured in the mesosphere and lower thermosphere with the EISCAT VHF radar. *Ann. Geophys.* 16, 1367–1379. doi:10.1007/s00585-998-1367-0

Mošna, Z., Edemskiy, I., Laštovička, J., Kozubek, M., Koucká Knížová, P., Kouba, D., et al. (2021). Observation of the ionosphere in middle latitudes during 2009, 2018 and 2018/2019 sudden stratospheric warming events. *Atmosphere* 12 (5), 602. doi:10.3390/atmos12050602

Nicolls, M. J., and Kelley, M. C. (2005). Strong evidence for gravity wave seeding of an ionospheric plasma instability. *Geophys. Res. Lett.* 32, L05108. doi:10.1029/2004GL020737

Pancheva, D., Mukhtarov, P., Mitchell, N. J., Merzlyakov, E., Smith, A. K., Andonov, B., et al. (2008). Planetary waves in coupling the stratosphere and mesosphere during the major stratospheric warming in 2003/2004. *J. Geophys. Res.* 113, D12105. doi:10.1029/2007JD009011

Pavelin, E., and Whiteway, J. A. (2002). Gravity wave interactions around the jet stream. *Geophys. Res. Lett.* 29 (21), 21–24. doi:10.1029/2002GL015783

Pedatella, N. M., and Forbes, J. M. (2010). Evidence for stratosphere sudden warming-ionosphere coupling due to vertically propagating tides. *Geophys. Res. Lett.* 37, L11104. doi:10.1029/2010GL043560

Pedatella, N. M., and Liu, H.-L. (2018). The influence of internal atmospheric variability on the ionosphere response to a geomagnetic storm. *Geophys. Res. Lett.* 45, 4578–4585. doi:10.1029/2018GL077867

Pezzopane, M., Fagundes, P. R., Ciraolo, L., Correia, E., Cabrera, M. A., and Ezquer, R. G. (2011). Unusual nighttime impulsive foF2 enhancement below the southern anomaly crest under geomagnetically quiet conditions. *J. Geophys. Res. Space Phys.* 116, A12314. doi:10.1029/2011JA016593

Pierce, A. D., and Coroniti, S. C. (1966). A mechanism for the generation of acoustic–gravity waves during thunderstorm formation. *Nature* 210, 1209–1210. doi:10.1038/2101209a0

Prölss, G. W. (1995). "Ionospheric F-region storms," in *Handbook of atmospheric electrodynamics*. Editor H. Volland (Boca Raton, FL: CRC Press), Vol. II, 195–248.

Radicella, S. M., and Migoya-Orué, Y. O. (2021). "GNSS-derived data for the study of the ionosphere," in *GPS and GNSS technology in Geosciences*. Editors G. Petropoulos, and P. Srivastava (Elsevier), 221–239.

Rahmani, Y., Alizadeh, M. M., Schuh, H., Wickert, J., and Tsai, L. C. (2020). Probing vertical coupling effects of thunderstorms on lower ionosphere using GNSS data. *Adv. Space Res.* 66 (8), 1967–1976. doi:10.1016/j.asr.2020.07.018

Rishbeth, H., and Mendillo, M. (2001). Patterns of F2-layer variability. *J. Atmos. Sol. Terr. Phys.* 63, 1661–1680. doi:10.1016/S1364-6826(01)00036-0

Šauli, P., and Boška, J. (2001). Tropospheric events and possible related gravity wave activity effects on the ionosphere. *J. Atm. Sol. Terr. Phys.* 63, 945–950. doi:10.1016/S1364-6826(00)00205-4

Siddiqui, T. A., Yamazaki, Y., Stolle, C., Maute, A., Laštovička, J., Edemskiy, I. K., et al. (2021). Understanding the total electron content variability over Europe during 2009 and 2019 SSWs. *J. Geophys. Res. Space Phys.* 126, e2020JA028751. doi:10.1029/2020JA028751

Smith, A. (1996). Longitudinal variations in mesospheric winds: Evidence for gravity wave filtering by planetary waves. *J. Atmos. Sci.* 53 (8), 1156–1173. doi:10.1175/1520-0469(1996)053<1156:lvimwe>2.0.co;2

Taylor, M. J., and Hapgood, M. A. (1988). Identification of a thunderstorm as a source of short period gravity waves in the upper atmospheric nightglow emissions. *Planet. Space Sci.* 36 (10), 975–985. doi:10.1016/0032-0633(88)90035-9

Vadas, S. L., Makela, J. J., Nicolls, M. J., and Milliff, R. F. (2015). Excitation of gravity waves by ocean surface wave packets: Upward propagation and reconstruction of the thermospheric gravity wave field. *J. Geophys. Res. Space Phys.* 120 (11), 9748–9780. doi:10.1002/2015JA021430

Wakai, N., Ohyama, H., and Koizumi, T. (1987). "Ministry of posts and telecommunications," in *Manual of ionogram scaling* (Tokyo: Radio Research Laboratory). 3rd Version.

Wüst, S., Bittner, M., Espy, P. J., French, W. J. R., and Mulligan, F. J. (2023). Hydroxyl airglow observations for investigating atmospheric dynamics: Results and challenges. *Atmos. Chem. Phys.* 23, 1599–1618. doi:10.5194/acp-23-1599-2023

Wüst, S., Bittner, M., Yee, J-H., Mlynczak, M. G., and Russell, J. M. (2017). Variability of the Brunt–Väisälä frequency at the OH* layer height. *Atmos. Meas. Tech.* 10, 4895–4903. doi:10.5194/amt-10-4895-2017

Xiao, S. G., Xiao, Z., Shi, J. K., Zhang, D. H., Feng, X. S., Hao, Y. Q., et al. (2009). Observational facts in revealing a close relation between acoustic-gravity waves and midlatitude spread F. *J. Geophys. Res. Space Phys.* 114, A01303. doi:10.1029/2008JA013747

Xiao, S., Shi, J., Zhang, D., Hao, Y., and Huang, W. (2012). Observational study of daytime ionospheric irregularities associated with typhoon. *Sci. China Technol. Sci.* 55, 1302–1304. doi:10.1007/s11431-012-4816-7

Xiao, Z., Xiao, S., Hao, Y., and Zhang, D. (2007). Morphological features of ionospheric response to typhoon. *J. Geophys. Res.* 112, A04304. doi:10.1029/2006JA011671

Yiğit, E., and Medvedev, A. S. (2015). Internal wave coupling processes in Earth's atmosphere. *Adv. Space Res.* 55 (4), 983–1003. doi:10.1016/j.asr.2014.11.020

Yu, S., Xiao, Z., Aa, E., Hao, Y., and Zhang, D. (2016). Observational investigation of the possible correlation between medium-scale TIDs and mid-latitude spread F. *Adv. Space Res.* 58, 349–357. doi:10.1016/j.asr.2016.05.002

Yue, J., Miller, S. D., Hoffmann, L., and StrakaIII, W. C. (2014). Stratospheric and mesospheric concentric gravity waves over tropical cyclone Mahasen: Joint AIRS and VIIRS satellite observations. *J. Atmos. Sol-Terr. Phys.* 119, 83–90. doi:10.1016/j.jastp.2014.07.003

Zakharov, V. I., and Sigachev, P. K. (2022). Ionospheric disturbances from tropical cyclones. *Adv. Space Res.* 69 (1), 132–141. doi:10.1016/j.asr.2021.09.025

frontiers | Frontiers in Astronomy and Space Sciences

TYPE Original Research
PUBLISHED 06 July 2023
DOI 10.3389/fspas.2023.1201625

OPEN ACCESS

EDITED BY
Libo Liu,
Institute of Geology and Geophysics (CAS), China

REVIEWED BY
Bo Xiong,
North China Electric Power University, China
Jing Liu,
Shandong University, China

*CORRESPONDENCE
Attila Buzás,
buzas.attila@epss.hu

RECEIVED 06 April 2023
ACCEPTED 16 June 2023
PUBLISHED 06 July 2023

CITATION
Buzás A, Kouba D, Mielich J, Burešová D, Mošna Z, Koucká Knížová P and Barta V (2023), Investigating the effect of large solar flares on the ionosphere based on novel Digisonde data comparing three different methods.
Front. Astron. Space Sci. 10:1201625.
doi: 10.3389/fspas.2023.1201625

Investigating the effect of large solar flares on the ionosphere based on novel Digisonde data comparing three different methods

Attila Buzás[1,2,3]*, Daniel Kouba[4], Jens Mielich[5], Dalia Burešová[4], Zbyšek Mošna[4], Petra Koucká Knížová[4] and Veronika Barta[1]

[1]Institute of Earth Physics and Space Science (EPSS), Sopron, Hungary, [2]Doctoral School of Earth Sciences, Eötvös Loránd University, Budapest, Hungary, [3]ELKH-ELTE Space Research Group, Budapest, Hungary, [4]Department of Ionosphere and Aeronomy, Institute of Atmospheric Physics, Czech Academy of Sciences, Prague, Czechia, [5]Leibniz-Institute of Atmospheric Physics, Rostock, Germany

Increased solar radiation during solar flare events can cause additional ionization and enhanced absorption of the electromagnetic (EM) waves in the ionosphere leading to partial or even total radio fade-outs. In this study, the ionospheric response to large solar flares has been investigated using the ionosonde data from Juliusruh (54.63° N, 13.37° E), Průhonice (49.98° N, 14.55° E) and San Vito (40.6° N, 17.8° E) Digisonde (DPS-4D) stations. We studied the effect of 13 intense (>C4.8) solar flares that occurred between 06:00 and 16:30 (UT, daytime LT = UT+1 h) from 04 to 10 September 2017 using three different methods. A novel method based on the amplitude data of the measured EM waves is used to calculate and investigate the relative absorption changes (compared to quiet period) occurring during the flares. The amplitude data are compared with the variation of the *fmin* parameter (*fmin*, the minimum measured frequency, it is considered as a qualitative proxy for the "non-deviative" radio wave absorption). Furthermore, the signal-to-noise ratio (SNR) measured by the Digisondes was used as well to quantify and characterize the fade-out events and the ionospheric absorption. In order to compare the three different methods, residuals have been defined for all parameters, which provide the percentage changes compared to the selected reference periods. Total and partial radio fade-outs, increased values (+0.4%–318%) of the *fmin* parameter, and +20%–1400% amplitude changes (measured at 2.5 and 4 MHz) were experienced during and after the investigated flares. Generally, the observed changes depended on the intensity, solar zenith angle and duration of the flare events. Although the three different methods have their own advantages/disadvantages and their limitations, the combination of them seems to be an efficient approach to monitor the ionospheric response to solar flares.

KEYWORDS

space weather, solar flare, ionosphere, ionospheric absorption, ionosonde data, HF radio wave absorption, signal-to-noise ratio (SNR), radio fade-out

1 Introduction

The ionosphere is a region of Earth's atmosphere partially ionized mostly by the Sun. While the hard X-rays (<1 nm) of solar radiation penetrate deeper parts of the ionosphere, to the so-called D-region (60–90 km height), the soft X-ray (1–10 nm) and extreme UV flux (5–102.6 nm) reach higher layers (E-region 90–150 km and F-region above approximately 150 km) and cause ionization there (Rishbeth and Garriot, 1969; Zolesi and Cander, 2014). Solar energetic protons ionize the lower ionosphere (60–100 km) mainly in the polar regions.

The ionosphere influences propagation of electromagnetic (EM) waves depending on their frequency affecting the radio and satellite communication and navigation. The attenuation of EM waves propagating through the ionosphere is most significant in the high-frequency (HF) range (3–30 MHz), particularly important for radio wave communication (George and Bradley, 1973). The ionospheric absorption depends on the collisions between electrons and neutral molecules, thus on the collision frequency which strongly changes with altitude (Ratcliffe, 1972). The collision frequency is highest in the D-region (2×10^6 s^{-1}), therefore the radio waves below 10 MHz predominantly attenuate there (Zolesi and Cander, 2014). Like the electron density of the ionosphere (Bilitza et al., 2017) the ionospheric absorption also shows regular daily (maximum around local noon), seasonal (higher at summer, and a secondary maximum at winter) and solar cycle (increasing with higher solar activity) variation (Higashimura et al., 1969a; Higashimura et al., 1969b). Besides these phenomena, transient changes mainly related to solar activity can also occur in the ionosphere.

Solar flares are giant bursts taking place in the active regions on the Sun. During flares, huge amounts of EM energy are emitted at a broad range of wavelengths for a short period (~30 min to ~1 h) (Tsurutani et al., 2009). Solar flares are classified as large (X, >10^{-4} W/m^2), medium-size (M, ~10^{-5}–10^{-4} W/m^2) and small (C, ~10^{-6}–10^{-5} W/m^2) based on the released flux in 0.1–0.8 nm X-rays as measured on the GOES spacecraft. Furthermore, a finer logarithmic scale is also applied ranging from 0 to 9 within the above written classes. During flare events the enhanced radiation causes extra ionization and increased attenuation of the EM waves, leading to so-called short-wave fade-outs which last for tens of minutes or even hours (Rishbeth and Garriot, 1969; Davies, 1990; Tsurutani et al., 2009; Barta et al., 2019; Tao et al., 2020; Barta et al., 2022). Solar flares are also accompanied by energetic particles (protons and electrons from tens of keV to hundreds of MeV) propagating along the magnetic field lines, reaching the Earth at the polar region and causing further ionization and enhanced absorption there (Rishbeth and Garriot, 1969; Tsurutani et al., 2009). The so-called Polar Cap Absorptions following Solar Proton Events can last for even several days (Rose and Ziauddin, 1962). Moreover, recent studies (Liu et al., 2021a; Liu et al., 2021b) demonstrated that solar flare effects are not limited to the ionosphere where radiation energy is absorbed but they extend throughout the geospace via electrodynamic coupling: it causes changes in the dayside solar wind–magnetosphere interaction, causing less Joule heating of the upper atmosphere, leading to the reconfiguration of magnetosphere convection and changes in dayside and nightside auroral precipitation.

The abovementioned shortages and blackouts in radio communication can cause problems especially in commercial and military aircraft operations and affect the navigation systems. Therefore, detecting, modeling, and monitoring the ionospheric changes caused by solar flares became more important from day to day (Handzo et al., 2014; Barta et al., 2019). The theory of ionospheric absorption has been detailed by, e.g., Davies (1990), Sauer and Wilkinson (2008) and Scotto and Settimi (2014). The Absorption Prediction model (D-Region Absorption Prediction, D-RAP2, https://www.swpc.noaa.gov/products/d-region-absorption-predictions-d-rap) developed by the Space Weather Prediction Center (SWPC) is widely used to review the state of the ionospheric absorption globally.

The most common devices to determine the ionospheric absorption are the so-called riometers (Relative Ionospheric Opacity meter) which analyze the cosmic radio noise measured at certain frequencies (usually at the 20–50 MHz range) (Little, 1954). However, these instruments are generally installed at high geographic latitudes (>60°), thus, they mainly measure the ionospheric absorption variation caused by the energetic particle precipitations (Stauning, 1996).

Another method is to use the minimum reflection frequency, *fmin* parameter, recorded on the ionograms, which is the rough measure of the "non-deviative" radio wave absorption (Rishbeth and Gariot, 1969; Davies, 1990) and can be used as an index during high absorption changes. The "*fmin* method" was used to study the ionospheric absorption variation generated by geomagnetic storms (Oksman et al., 1981), by planetary waves (Schmitter, 2011) or by other sources (Kokourov et al., 2006) in the last decades. The absorption changes in the different continents caused by X-ray ionization due to solar flares were also investigated using the *fmin* method (e.g., Sharma et al., 2010; Sripathi et al., 2013; Nogueira et al., 2015; Denardini et al., 2016; Barta et al., 2019; Tao et al., 2020). The observed changes varied between 4 and 8 MHz (more than 100%) at the time of the X-class flares and 1–4 MHz (50%–150%) at the time of the M-class flares comparing to the reference quiet days at the lower-midlatitude, low-latitude and equatorial stations. The relative changes of the ionospheric absorption measured by the *fmin* method depended on the X-ray radiation intensity, but it also showed a solar zenith angle dependence (Barta et al., 2019; 2022). The disadvantage of this method is that the absolute absorption variation cannot be quantitatively determined because the *fmin* parameter also depends on the radar characteristics and the background radio-noise level.

Since nowadays data from many ionosonde stations are available from all over the globe (e.g., GIRO - Global Ionosphere Radio Observatory, https://giro.uml.edu/, Reinisch and Galkin, 2011), it can be worthwhile to develop a novel technique to determine the ionospheric absorption from the different properties of the reflected EM waves measured by the ionosondes. The signal-to-noise ratio (SNR) of radio waves obtained from ionograms during flares and comparing it with values derived from reference days was used by Curto et al. (2018) to study the impact of solar flares on ionospheric absorption. This SNR method has been improved by de Paula et al. (2022). They determined three constraints that a solar flare must accomplish to cause detectable

disturbances by the proposed method, taking into account the geoeffective hard X-ray irradiance, geoeffective hard X-ray radiant exposure and the solar altitude.

The main purpose of this study is to demonstrate a novel method calculating the ionospheric absorption from amplitude data measured by Digisondes (particularly DPS-4D ionosondes) and investigate its effectiveness during flare events. The shown method is based on the work of Sales (2011). The absorption changes determined by the "amplitude method" are compared with the *fmin* parameter and the signal-to-noise ratio measured by the same Digisondes during the same flare events. Following this introduction (Section 1—*Introduction*), the used data and the details of the three methods are described in Section 2 (*Data and methods*). The results coming from the different methods are detailed in Section 3 (*Results*) after which they are compared with each other and with published results from the literature in Section 4 (*Discussion*). Ultimately, the summary of the work and the concluding remarks are given in Section 5 (*Conclusion*).

2 Data and methods

Thirteen flare events have been selected for investigation that occurred between 04 and 10 September 2017, one of the most active periods of Solar Cycle 24 (e.g., Berdermann et al., 2018; Yasyukevich et al., 2018; Mosna et al., 2020, among others). The following criteria were applied during the selection of the flares: the Sun had to be above the horizon, therefore, the solar zenith angle (SZA) <90°; the X-ray class of the flare >C8 because we aimed to study the effectiveness of the presented methods during more intense solar flares. The most important properties of the selected flare events are displayed in Table 1.

Data measured at three different European Digisonde stations were used for the analysis since the solar zenith angle of the Sun at the time of the flare is very important regarding the ionospheric response. The selected stations (Juliusruh: 54.63° N, 13.37° E; Průhonice: 49.98° N, 14.55° E and San Vito: 40.6° N, 17.8° E; Figure 1) are located at similar longitude, however, their latitude is different. Juliusruh (JR) and San Vito (VT) stations operated with 5 min and 15 min time resolution, respectively. The sampling rates were 2 and 15 min at Průhonice (PQ) during the investigated periods. Since the time resolutions were different at the three stations, we were also able to investigate the importance of the sampling rate in regard to the detection of the ionospheric absorption changes. We investigated the variation of the *fmin* parameter, what is a rough measure of the "non-deviative" radio wave absorption. Furthermore, the critical frequencies of the F2 layer (*foF2*) and the sporadic E layer (*foEs*) have also been analyzed because they should also be taken into account during the study of the ionospheric absorption.

In Figure 2 we summarize the solar and geomagnetic activity during 04–10 September 2017. One can see that the investigated period is very complex. The X-class solar flares occurring on 06 September were followed by intense geomagnetic storms on 07 and 08 September as it can be seen in the *Kp* and *Dst* indices. The impact of the energetic particles is also significant as it is shown by the increased proton and electron flux and by the *AE* index. This study focuses on the ionospheric absorption changes which are mainly caused by the solar flares. Nevertheless, it is important to keep in mind the other solar and geomagnetic activities taking place parallelly for the interpretation of the results. The data from the GOES 13 and 15 satellites used to investigate the X-ray, solar proton and electron flux and the geomagnetic indices were available at the OmniWeb database (https://omniweb.gsfc.nasa.gov/ and https://omniweb.gsfc.nasa.gov/form/omni_min_def.html).

2.1 Amplitude method (Sales-absorption method)

Amplitude data of the reflected echoes recorded by the Digisondes were used to calculate the relative ionospheric absorption of EM waves according to the method proposed by G. Sales (Sales, 2011). This method (amplitude method or Sales-absorption method) is based on the Friis transmission formula (Friis, 1946). The Friis transmission equation is used in telecommunications engineering, and gives the power received by one antenna under idealized conditions given another antenna some distance away transmitting a known amount of power. The formula was derived in 1945 by Danish-American radio engineer Harald T. Friis. The decadic logarithmic form of the equation is as shown below (**Eq. 1**):

$$10\lg(L) = 10\lg(P_t G_t G_r) + 20\lg\left(\frac{\lambda}{4\pi 2h}\right) - 10\lg\left(P_r\right) \qquad (1)$$

where L is the loss term including, among other factors, the absorption (in W units); P_t is the power of the transmitted signal (in W units); G_t is the gain of the transmitter (unitless); G_r is the gain of the receiver (unitless); λ is the wavelength of the signal (in m units); h is the height of the reflection (in m units); and P_r is the power of the receiver (in W units). The term on the left side and the three terms on the right side are measured in dB. The known terms are λ, h, and P_r which are recorded by the Digisondes. Please note that further in the text and on the figures we denote $10\lg(L)$ simply as L and $10\lg(P_t G_t G_r)$ simply as $P_t G_t G_r$.

In order to determine the loss term (L), the $P_t G_t G_r$ product must be derived first using the Friis formula (**Eq. 1**). This is done in the case of every investigated station, and it is called the calibration of the Digisonde system. We selected nighttime (18–03 UT which is 19–04 LT (CET) in the winter and 20–05 LT (CEST) in the summer, i.e., between 27 March 2017 and 30 October 2017) data from quiet time periods (X-ray flux<1E-6 W/m^2) and assumed that the loss term (L) was negligible during those periods. Data from 173 quiet days in 2017 and 2018 were selected in total (Supplementary Table SA1 in the Supplementary Material). The calibration was performed in seven frequency ranges (2.5, 3, 3.5, 4, 4.5, 5, and 5.5 MHz ± 200 kHz, respectively). To minimize the effect of sporadic E-layer, only time periods when the critical frequency of the sporadic E-layer (*foEs*) was below 2.3 MHz, the lowest investigated frequency were retained. Please note that the *foEs* parameter was taken from automatically scaled data by the SAO-X (https://ulcar.uml.edu/SAO-X/SAO-X.html) software with a C-score> = 60 (C-score is

TABLE 1 Most important properties of the selected solar flares. The times are in UT. Source of the data is the Hinode flare catalog: https://hinode.isee.nagoya-u.ac.jp/flare_catalogue/.

Date	Start time	Peak time	End time	Duration (min)	Active region location	X-ray class
04 September 2017	11:54	12:22	14:00	126	S07W08	C8.3
04 September 2017	15:11	15:30	15:33	22	S06W13	M1.5
05 September 2017	4:33	4:53	5:07	34	S11W18	M3.2
05 September 2017	6:33	6:40	6:43	10	S82E08	M3.8
06 September 2017	8:57	9:10	9:17	20	S08W32	X2.2
06 September 2017	11:53	12:02	12:10	17	S09W34	X9.3
07 September 2017	9:35	9:54	11:28	113	S08W47	M1.4
07 September 2017	10:11	10:15	10:18	7	S07W46	M7.3
07 September 2017	14:20	14:36	14:55	35	S11W49	X1.3
08 September 2017	7:40	7:49	7:58	18	S10W57	M8.1
08 September 2017	15:09	15:47	16:04	55	S08W68	M2.9
09 September 2017	10:50	11:04	11:42	52	S14W74	M3.7
10 September 2017	15:35	16:06	16:31	56	S08W88	X8.2

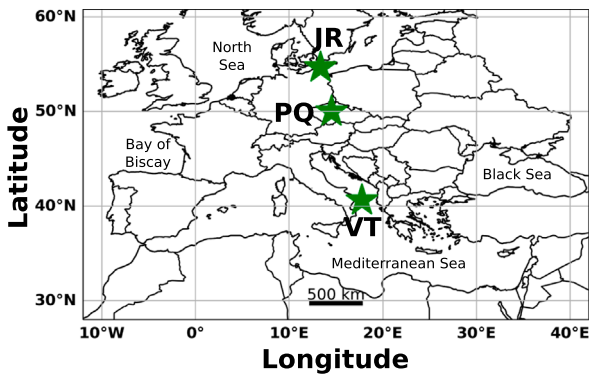

FIGURE 1
Location of the investigated DPS4D ionosonde stations in Europe. JR, Juliusruh; PQ, Průhonice; VT, San Vito.

a measure of the goodness of the automatic evaluation of the ionogram). Moreover, in certain periods at certain frequencies the number of data points at a given sounding can be very low because the echoes might not originate from an actual layer of the ionosphere but basically be generated by noise. Therefore, only soundings with more than 100 data points in each frequency range were retained during the calibration (Supplementary Figure SA1 in Supplementary Material). Only vertical echoes with ordinary polarization were selected, reflected from a height between 80 and 400 km (in order to avoid the second and third reflection of the F-layer). All the selected time periods and selection criteria used for the calibration are summarized in Supplementary Table SA1 in the Supplementary Material.

When assuming that the loss term is negligible, the $P_tG_tG_r$ product (or calibration function), which is characteristic for every Digisonde system depending on the actual technical settings of the measuring system, can be calculated from the Friis formula (Figure 3, **Eq. 2**).

$$10\lg(P_tG_tG_r) = 20\lg\left(\frac{4\pi 2h}{\lambda}\right) + 10\lg(P_r) \quad (2)$$

The values of the $P_tG_tG_r$ product lie in the interval of 150–170 dB at all three stations for the selected frequencies but the shapes of the curves generally differ from station to station (Figures 3A, C, E). The number of data points is the largest in the case of JR station as this station had a sampling rate of 5 min compared to the 15 min sampling rate of PQ and VT stations (Figures 3B, D, F). Moreover, at higher frequencies, i.e., above 3.5 MHz, the number of data points is considerably smaller. This is because the selected calibration periods are quiet, nighttime periods when reflections at higher frequencies occur less frequently which limits the usage of the Sales-absorption method.

After the calibration was performed, the Friis equation can be solved for the loss term which includes the ionospheric absorption relative to the quiet nighttime period (**Eq. 1**). The loss was determined at the abovementioned frequencies (2.5, 3, 3.5, 4, 4.5, 5, and 5.5 MHz ± 200 kHz, respectively) using some of the abovementioned selection criteria (vertical, ordinary echoes; foEs < 2.3 MHz; height of the reflection between 80 and 450 km) for the disturbed time period (04–10 September 2017).

Please note that in the case of PQ station the sampling rate was set from 15 to 2 min during the time period of 08 September 2017 08:40 UT–09 September 2017 21:00 UT which could possibly change (decrease) the sensitivity of the ionosonde due to shorter time of individual measurement. However, according to our analysis, this does not have any effect on the calculated absorption values as they do not display any step-like change around the time of the transitions of the 15–2 min and the 2–15 min periods (Supplementary Figure SA2 in Supplementary Material).

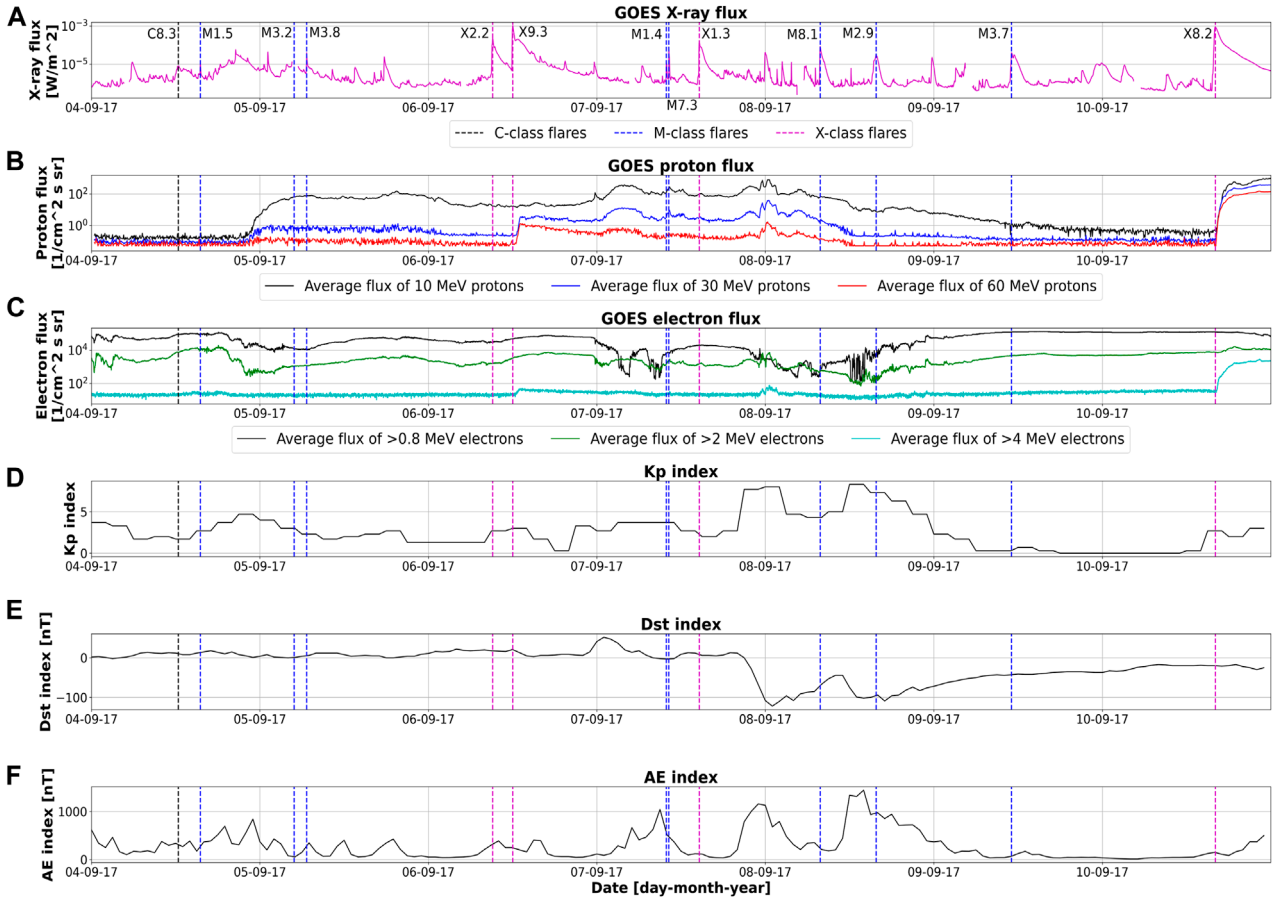

FIGURE 2
Summary of the solar and geomagnetic parameters for the investigated period. The class of the investigated flares are plotted on panel **(A)**. The black, blue and magenta dashed lines indicate C-, M- and X-class flares, respectively. The proton and electron fluxes measured in different energy ranges by the GOES spacecrafts are plotted on panels **(B,C)**, respectively. The variation of *Kp*, *Dst* and *AE* indices are displayed on panels **(D–F)**, respectively.

To evaluate the effect of solar flares on the ionosphere as seen in the absorption data, we determined the quiet diurnal variation of the absorption by calculating the loss term for the calibration period including not only nighttime data but data from all the day. Then we took the mean of the quiet diurnal variation in a time window of ±1 h around the peak time of the investigated flare (abs_{flare}). The absorption after the flare (abs_{flare}) was characterized by the maximum value of the absorption from a time window of the first valid measurement after the peak time of the flare (i.e., after fade-out if there is such) plus 1 h. The impact of the solar flare as seen in the absorption data was quantified by the equation below (**Eq. 3**):

$$\Delta abs = \frac{abs_{flare} - abs_{quiet}}{abs_{quiet}} \times 100[\%] \quad (3)$$

2.2 *fmin* method

The time series of the *fmin* parameter from the ionograms measured during the selected flare events have been analyzed. Since the *fmin* can depend on the radio-noise level and the radar characteristics, data recorded by three DPS-4D Digisondes were used to minimize the instrumental errors. To compare the observed changes measured by the different methods the residuals (relative changes in percentage compared to the reference days) have been defined using the following equation (**Eq. 4**):

$$\Delta fmin = \frac{fmin_{flare} - fmin_{quiet}}{fmin_{quiet}} \times 100[\%] \quad (4)$$

This formula was used in Barta et al. (2022) to investigate the *fmin* variation during flares. It is regularly used to analyze *foF2* parameter changes during geomagnetic storms in the literature (e.g., Buresova et al., 2014; Berényi et al., 2018). We used the same periods (X-ray < 1E-6) as for the Digisonde calibration as reference to the better comparison of the results coming from the two different methods (i.e., the amplitude and the *fmin* methods). It is worth mentioning that the value of the *fmin* parameter can also depend on the time resolution of the measurement at a certain station. The *fmin* parameter can be measured at lower frequencies (<2 MHz) during the standard 15 min settings because of the longer integration time than during high cadence campaigns, e.g., 2 min time resolution at

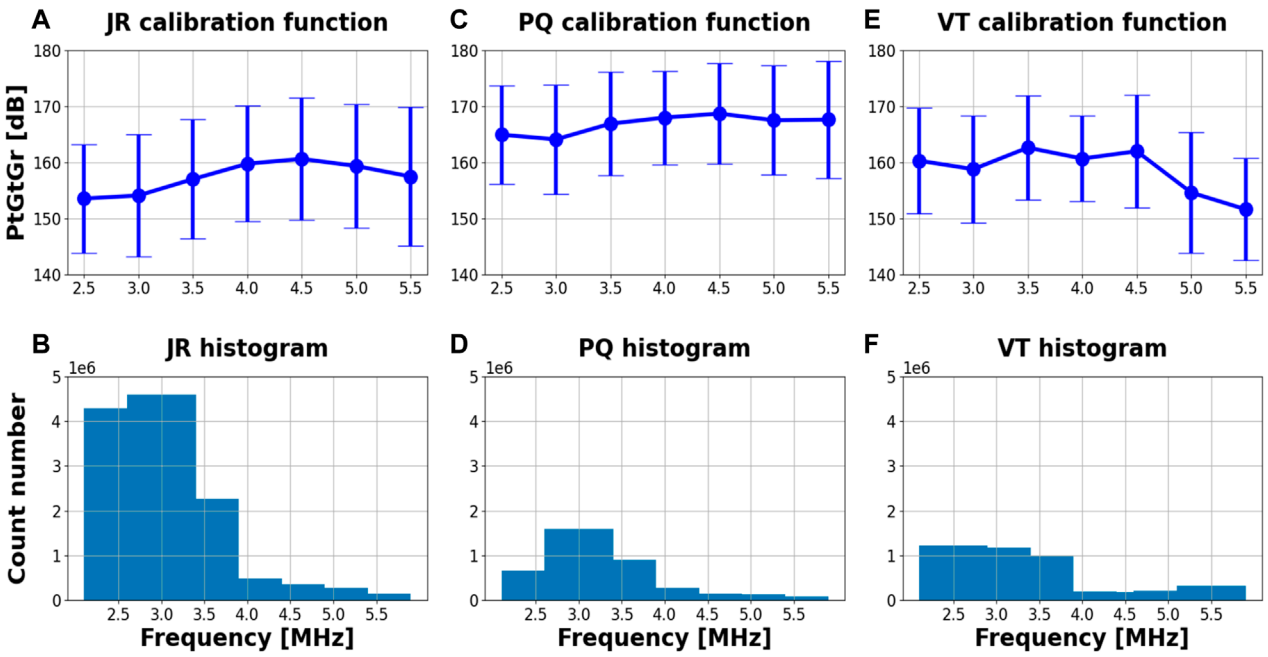

FIGURE 3
Calibration of the Digisonde systems at Juliusruh, Pruhonice, and San Vito (JR, PQ, and VT). Panels **(A,C,E)** show the PtGtGr product (calibration function) for the different stations, whereas the error bars represent two times the standard deviation of the data. The count number of the data used in the calibration in the different frequency ranges at the different stations are shown on panels **(B,D,F)**.

PQ station in some time periods in our case. During these campaign periods the ionograms started at 2, or 2.2 MHz at PQ, thus the traces (*fmin* parameter) was not detectable below these frequencies. Nevertheless, we focus on the impact of the solar flares in this study, when the *fmin* parameter is usually enhanced (e.g., Barta et al., 2019; 2022).

We also investigated the measured *foEs* and *foF2* parameters since their changes can indirectly affect the observed ionospheric absorption, especially in the case of the amplitude method. The ionograms used for our investigation were derived from the GIRO database and were processed and manually evaluated for the investigated period by the SAO-X program using the default 6 dB settings for MPA (most probable amplitude).

2.3 Signal-to-noise ratio

Modern Digisondes record data from which the signal-to-noise ratio (SNR) of the received signals can be derived. The SNR proved to be an efficient diagnostic tool for studying the effect of solar flares on the ionosphere and can visualize the absorption caused by the flares quite expressively (de Paula et al., 2022).

In the present study, we calculated the SNR from the amplitude data of the received echoes by using the following formula (**Eq. 5**):

$$SNR = Amp - MPA \tag{5}$$

Where Amp is the amplitude of the received signal in dB units and MPA is the so-called most probable amplitude which marks the amplitude threshold below the noise level recorded in dB units as well. Only vertical echoes with ordinary polarization were used in calculating the SNR without any constraints on the frequency or height.

To compare the disturbed period to a reference, we took the mean of five quiet days (X-ray < 1E-6) relatively close to the investigated time period (04–10 September 2017): 07, 16, 26 August 2017 and 16, 21 September 2017; and constructed a synthetic day from it. In the case of each flare, we selected data starting from the peak time of the flare until 1 h after the peak time of the flare. When the effect of the consecutive flare overlapped with the effect of the previous one, the end time of the selection window in the case of the first flare was the start time of the second flare. The percentage ratio of SNR values below 10 dB (including missing, i.e., Nan, values as well) and all the SNR values was calculated both in the case of the disturbed and in the case of the quiet time periods in the abovementioned time windows in the case of each flare (**Eq. 6**). The ratio calculated in the disturbed period in comparison to the one derived from the quiet period data is intended to show the impact of the solar flares.

$$SNR\,ratio = \frac{SNR_{below10dB}}{SNR_{all}} \times 100[\%] \tag{6}$$

3 Results

3.1 Amplitude method and *fmin*

3.1.1 Amplitude and ionosonde parameters variation during the whole investigated period

First, we show the amplitude and the ionospheric parameter changes for the whole investigated period (Figures 4, 5). The X-ray and proton flux changes measured by the GOES 13 and 15 satellites are seen in Figure 4 and Figure 5 panels (A) and (B). The peak time of the investigated flares are indicated by magenta dashed lines for X-class, blue dashed lines for M-class and black dashed line for the C8-class flare, respectively. Many intense flares occurred between 04 and 10 September. We only evaluated the events when the Sun was above the horizon at all the investigated stations. The absorption variation measured at 2.5 MHz at JR, PQ and VT stations are seen in Figures 4C–E, respectively. While the ionospheric parameters manually evaluated from the measured ionograms at the three stations are seen in Figures 4F–H. We show here the *fmin* parameter, as an indicator for the non-deviative radio wave absorption, and the *foEs* and *foF2* parameters which also can indirectly affect the measured amplitude values. The total radio fade-outs caused by the flares are determined based on the *fmin* parameter and are indicated by gray shaded areas. One can see that most of the X-class flares and some M-class flares lead to total blackout and the duration of the blackout decreases with the solar zenith angle.

Impact of the X-class flares can be clearly seen at 2.5 MHz at all stations. The changes can be easily tracked especially at JR because of the 5 min time resolution, and at PQ in the periods with 2 min time resolution. The X-class flares caused total radio fade-outs with longer duration and significantly increased values of the *fmin* at the lower midlatitude stations, especially at VT, thus the caused effect is more pronounced in the *fmin* parameter than in the amplitude data itself which is well observed for example on 10 September. One can see enhanced values of the amplitude data following the M-class flares, too. Comparing the data from the three stations during the same flares the *fmin* parameter shows a solar zenith angle dependence: the smaller the zenith angle of the station at the peak time of the flare the larger the *fmin* values. However, the latitude dependence of the amplitude data at 2.5 MHz is not evident especially during the more intense flares because they cause partial or total blackouts which can last for hours at the 2.5 MHz frequency band. The ionospheric response to the C8.3 class flare (peak time at 12:22 UT on 04 September) is also detectable both in the amplitude and in the *fmin* parameters at all three stations. The measured loss is larger at PQ than at JR, therefore it seems to show a latitude dependence. However, the *fmin* value increased above 5 MHz at VT at the peak time, which can explain that the amplitude change is not as large as measured at PQ. We can not exclude the effect of the energetic particles on the ionospheric absorption, especially at JR station which is located in the sub-auroral region. One can see a good example for that in the night of 08 September (around midnight) when there is an enhancement in proton flux (Figure 4B) and in parallel increased amplitude values at 2.5 MHz at JR (Figure 4C). Some enhanced values also appear at PQ at the same time (Figure 4D), but the impact is negligible at VT (Figure 4E) located at lower latitude. This variation of the absorption can not be tracked by the *fmin* parameter, which indicates that the amplitude method is more sensitive for the small changes. We will analyze the details focusing on some events in the following section.

Figure 5 shows the same parameters for the whole period as Figure 4 except that on panels (C), (D) and (E) one can see the absorption variation measured at 4 MHZ at the three stations (at JR, PQ and VT, respectively). The results are similar to the 2.5 MHz case. The amplitude measured at 4 MHz is enhanced at all stations after most of the X-class flares. The enhancement is especially pronounced after the X2.2 and X9.3 flares occurred on 06 September. The ionospheric changes connected to some X-class and the M-class flares are mostly detectable at JR station. It can be explained by the increased values of the *fmin* (>4 MHz) after those flares at PQ and particularly at VT, which means that there was no detectable amplitude data at 4 MHz at the peak time of the flares at these stations. Another interesting difference is what one can see between Figure 4 and Figure 5 is the effect caused by the C8.3 flare on 04 September. At 2.5 MHz the impact was detectable at all three stations, and it was the largest at PQ while at 4 MHz the caused effect is clearly seen only at VT. The impact caused by the energetic protons at JR during nighttime is even more pronounced at 4 MHz than in the previous case. Noticeably increased values are detected around midnight and in the early morning hours (01–03 UT) at 4 MHz at JR (Figure 5C) which is in good agreement with the periods of enhanced proton flux (Figure 5B). No similar effects were detected at 4 MHz at the other two stations during the same time intervals.

The increased values of the absorption (and data gap) detected at JR and PQ especially at 4 MHz during nighttime on 09 and 10 September are also worth mentioning. The reason for that can be the extremely low values of the *foF2* parameter measured at those stations in the nighttime on 09 and 10 September (Figures 5F, G). Consequently, as the 4 MHz frequency was not reflected, no valuable amplitude data were obtained. The impact of chosen individual flare events will be analyzed in detail in the following sections.

3.1.2 Amplitude and ionosonde parameters variation during one day

Figures 6, 7 demonstrate the variations of X-ray flux, proton flux, ionospheric absorption at 2.5 MHz (Figure 6) and at 4 MHz (Figure 7), and the ionospheric parameters at all three studied stations on 07 September, respectively. Two M-class flares (M1.4 and M7.3, peak times at 09:54 and at 10:15 UT, respectively) and an X1.3-class flare (peak time at 14:36 UT) occurred during the daytime, thus it is a good example to compare the impact of the flares on the different ionospheric parameters at the three stations. The duration of the two M-class flares is quite short, while the X-class flare took longer time as can be seen in the X-ray flux variation on Figure 6A, Figure 7A. The impact of the two M-class flares can be clearly seen on the *fmin* variation and on the amplitude changes measured at 4 MHz at JR. The caused effect is not so well tracked at the other two stations, there was a short radio blackout at PQ at the peak time of the M7.3 flare, while the *fmin* increased to ~7 MHz at VT at the same time. However, the impact of the two flares cannot be separated from each other at PQ and at VT. This case indicates that the time resolution of the ionosonde data is very important in studying the ionospheric response to solar flares. The 5 min resolution at JR provided enough information to track the effect of the M1.4 and M7.3 flares despite the

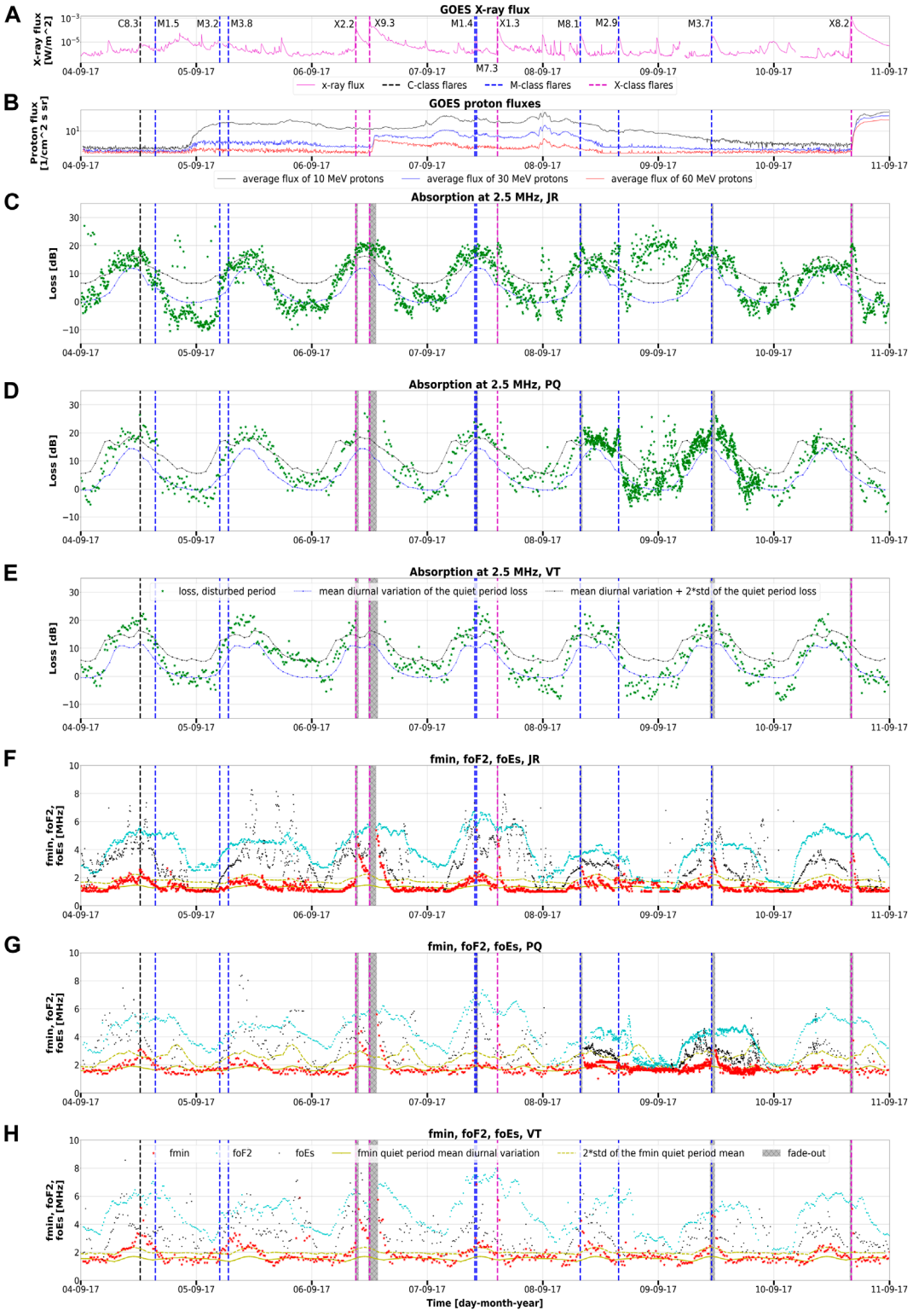

FIGURE 4
Overview of the investigated time period. Variation of X-ray flux **(A)**, proton flux **(B)**, ionospheric absorption at 2.5 MHz **(C–E)**, *fmin* (red dots), *foF2* (cyan dots) and *foEs* (black dots) parameters **(F–H)** at all three studied stations. The gray shaded areas denote the time periods of total absorption at a given frequency. The class of the investigated flares are plotted on panel **(A)**. The black, blue and magenta dashed lines indicate C-, M- and X-class flares, respectively.

10.3389/fspas.2023.1201625

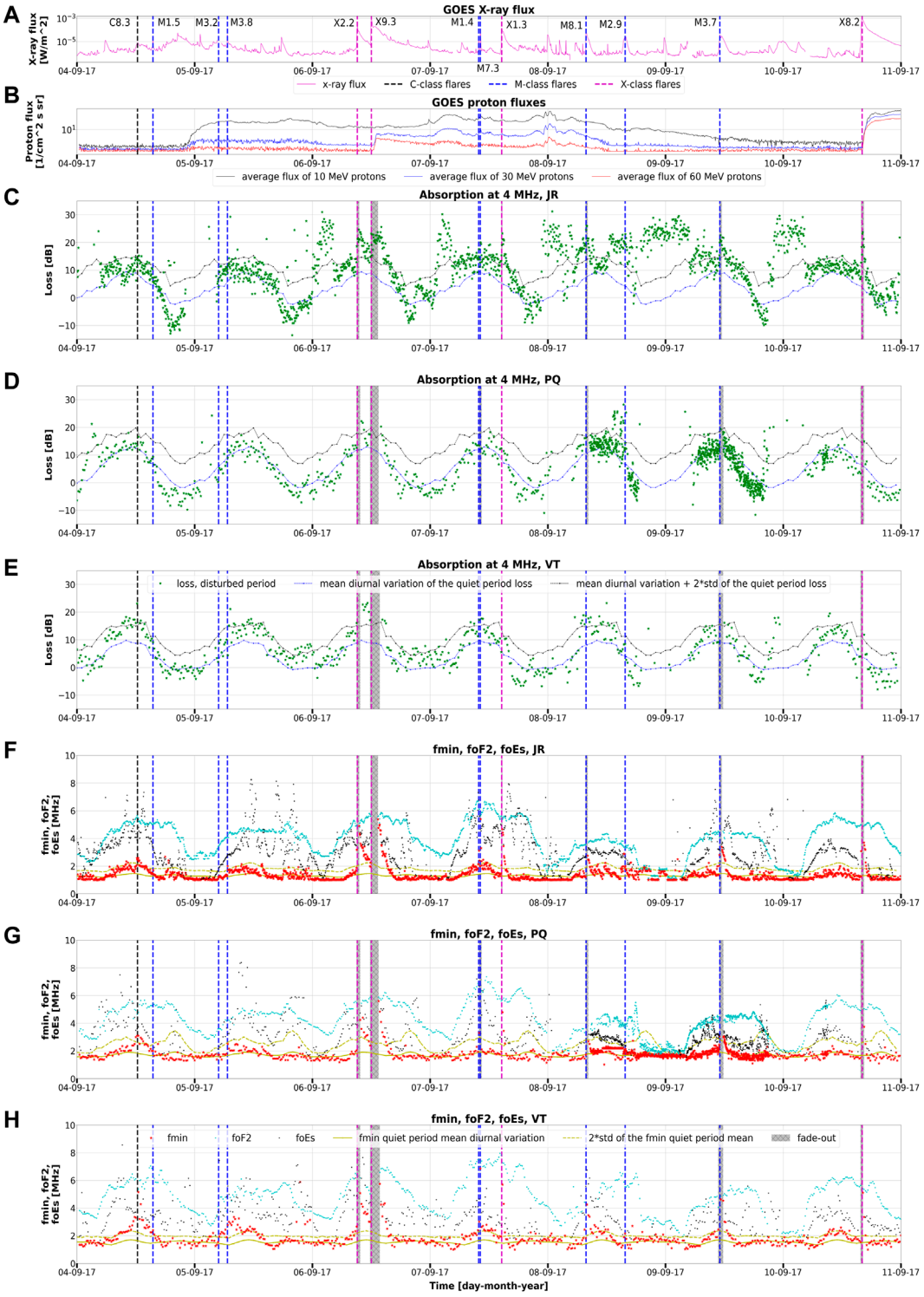

FIGURE 5
Overview of the investigated time period. Variation of X-ray flux **(A)**, proton flux **(B)**, ionospheric absorption at 4 MHz **(C–E)**, *fmin* (red dots), *foF2* (cyan dots) and *foEs* (black dots) parameters **(F–H)** at all three studied stations. The gray shaded areas denote the time periods of total absorption at a given frequency. The class of the investigated flares are plotted on panel **(A)**. The black, blue and magenta dashed lines indicate C-, M- and X-class flares, respectively.

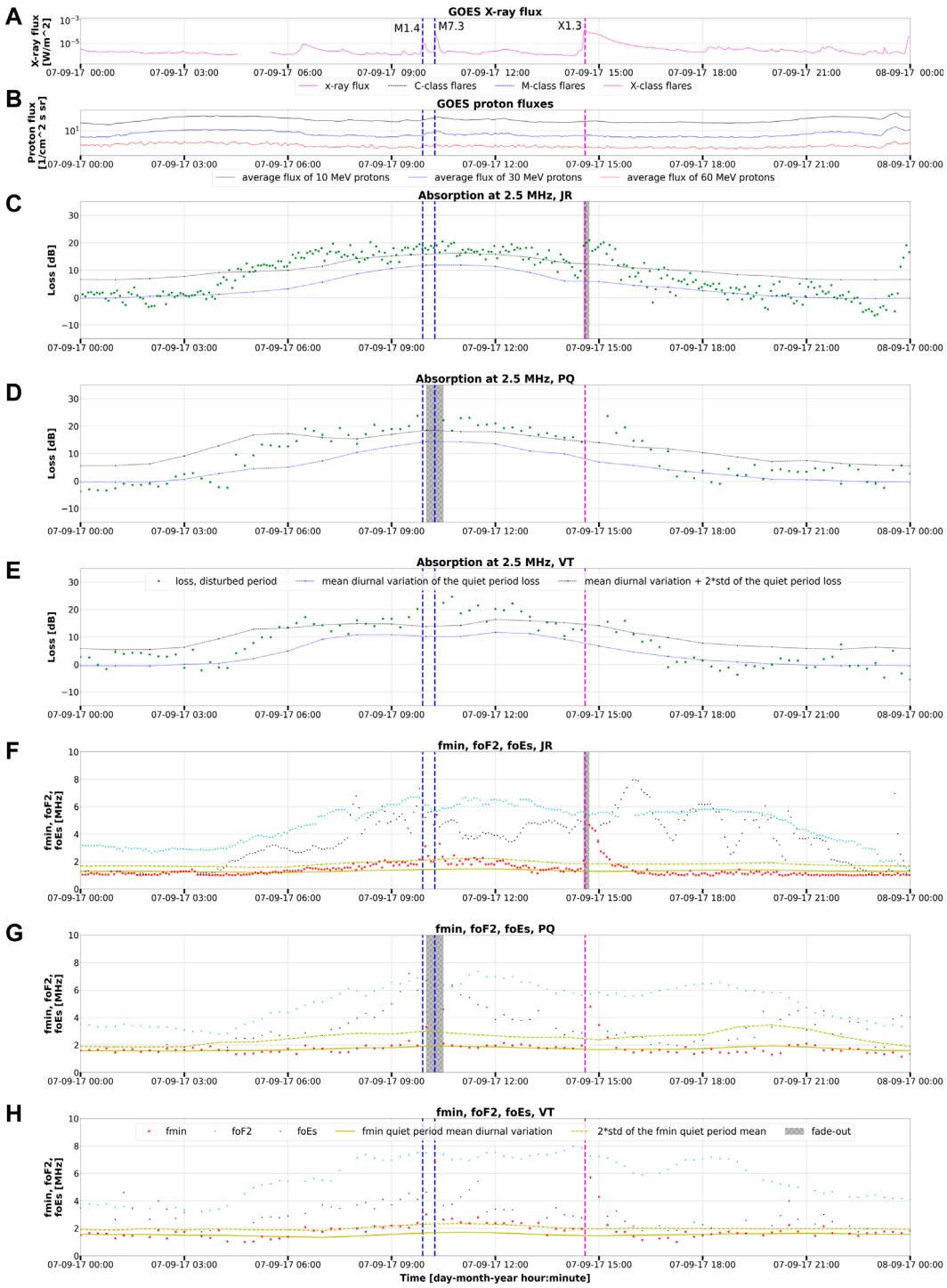

FIGURE 6
Variations of X-ray flux **(A)**, proton flux **(B)**, ionospheric absorption at 2.5 MHz **(C–E)**, *fmin*, *foF2* and *foEs* parameters **(F–H)** at all three studied stations on 07-09-2017. The time on the horizontal axes is in UT. The class of the investigated flares are plotted on panel **(A)**. The blue and magenta dashed lines indicate M- and X-class flares, respectively.

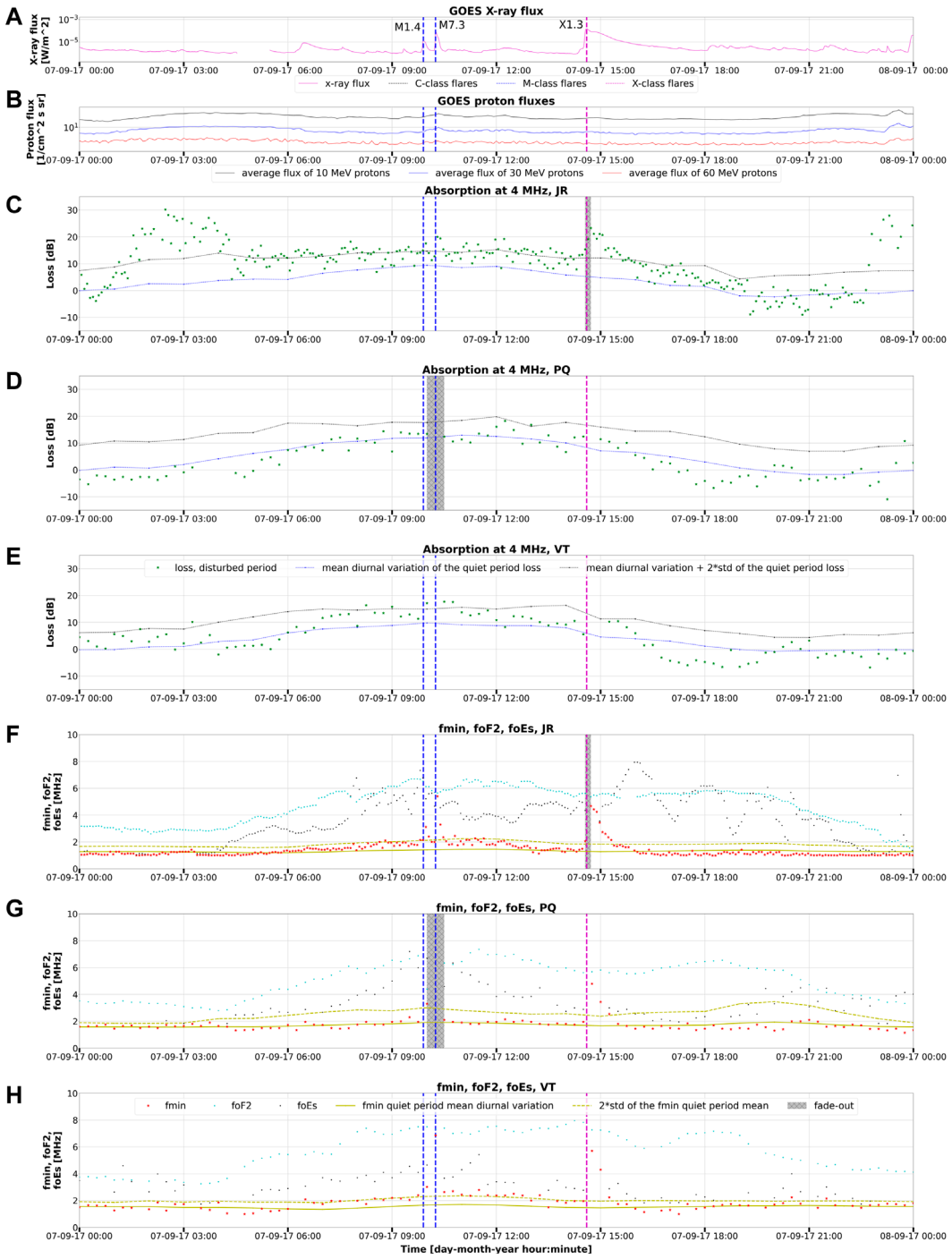

FIGURE 7
Variations of X-ray flux **(A)**, proton flux **(B)**, ionospheric absorption at 4 MHz **(C–E)**, *fmin*, *foF2* and *foEs* parameters **(F–H)** at all three studied stations on 07-09-2017. The time on the horizontal axes is in UT. The class of the investigated flares are plotted on panel **(A)**. The blue and magenta dashed lines indicate M- and X-class flares, respectively.

fact that the peak time of the second flare is only 20 min after the first one and the solar zenith angle was the largest at JR. In contrast, the data measured at every 15 min was not enough to detect the impact of these two flares separately at the other two stations because of the short lifetime of the events. The effect of the X1.3 flare is more apparent at all stations, mainly in the *fmin* at VT station, and in the amplitude at 2.5 MHz at JR and PQ. At 4 MHz, the change is only noticeable at JR (Figure 7C), but it can be explained by the high *fmin* parameter (>4 MHz) at the other two stations after the solar flare.

Two M-class flares occurred on 08 September, one in the morning hours (M8.1, peak time at 07:49 UT) and an M2.9 flare in the afternoon (peak time at 15:47 UT). The observed changes are seen on Figures 8, 9. Interestingly, the M8.1 flare caused total radio fade-out at JR and PQ, but not at VT. The *fmin* parameter was enhanced at all stations after this flare. One can see increased values of the amplitude at 2.5 MHz at JR and PQ (Figures 8C, D), while at VT there is a longer time without amplitude data at 2.5 MHz (Figure 8E) because the *fmin* was above this value here (Figure 8H). In contrast, the caused effect at 4 MHz loss is clearly detectable only at JR (Figure 9C), it is hard to recognize at the other two stations (Figures 9D, E).

The effect of the M2.9 (15:47 UT) flare is clearly seen in the amplitude data measured at 2.5 MHz at all stations (Figures 8C–E), but it is not that pronounced in the detected *fmin* parameters (Figures 8F–H). The caused impact can be tracked very well at PQ (Figure 8D) which station provided the data with 2 min time resolution during this period. This also strengthens that higher time resolution is very important to follow the changes generated by the solar flares. The caused impact is not that evident at the 4 MHz amplitude data measured at the different stations (Figures 9C–E), although it can be explained by the low values of the *foF2* parameter as its value was below 4 MHz at JR and PQ stations during this period.

The panels (D) on Figures 8, 9 show data from a high-rate ionogram campaign for PQ station (ionogram measurement every 2 min). Due to the duration of the ionogram measurement, the sounding frequency range had to be limited during this campaign. In the case of "full" ionograms measured every 15 min, the sounding starts at 1 MHz, but added ionogram soundings start at a higher frequency. From the beginning of the campaign (08:40 UT) until about 11 UT, the starting frequency was 2 MHz, between 11 and 14:30 UT it was 2.2 MHz, later again 2 MHz. Because the trace of the ionogram in these cases often starts at the first sounding frequency, so the *fmin* parameter must be lower than this frequency. These points are marked with less distinct symbols on the graph.

3.1.3 Amplitude and *fmin* parameter variation during the X2.2 flare on 06 September

The other way to demonstrate the results of the amplitude method is to investigate the loss detected at different frequencies at certain measurement times before and after the flare events. Here, we show the ionospheric response to the X2.2 flare on 06 September (Figure 10). The flare started at 08:57 UT and reached its peak at 09:10 UT as we can see in the GOES X-ray flux in the upper plots. Figures 10A–C show the data for JR, PQ and VT stations, respectively. The measured values of the *fmin* parameter at the different stations are seen in the second row, indicating the first, second, etc. measurements before and after the flare with red diamonds (the time of the record is also shown on the X-ray flux plots indicated by red diamonds too). The X2.2 solar flare caused total radio fade-out at all stations, its duration was 30 min at JR and 45 min at PQ and VT. The Digisonde operated with 5 min time resolution at JR and 15 min time resolution at PQ and VT. The *fmin* parameter was ~2 MHz at JR at 08:58 UT (second measurement before the flare), enhanced to ~3.2 MHz at 09:03 UT (first measurement before the flare) and returned with even higher values after the fade-out (4.9 MHz at 09:33 UT, 4.3 MHz at 09:38 UT and 4.2 MHz at 09:43 UT, first, second and third measurement after flare, respectively, Figure 10A). In the subplots showing the loss the blue stars (line) indicate the mean amplitude measured at different frequencies at the same time (from 08:57 UT to 09:48 UT from upper to lower at JR) during the reference periods, while the black stars (line) indicate the mean plus two times its standard deviation (SD). Generally, there are no increased amplitude values at JR at 08:57 UT (second measurement before flare), only the loss at 2.5 MHz and 4.5 MHz is at the values of the 2SD (2 standard deviation). However, the loss is increased (~20 dB) above the 2SD threshold at almost every frequency at 09:03 UT (first measurement before flare). We detected even more increased amplitude values (25 dB) at JR after the fadeout (at 09:33 UT, 09:38 UT and 09:43 UT first, second and third measurement after flare, respectively). The measured values reached the threshold even ~40 min after the peak time of the flare. The same plots for PQ station can be seen in Figure 10B. The *fmin* is ~2 MHz at the second (08:45 UT) and first (09:00 UT) measurements before the peak time of the flare. Its values increased and stayed around 4 MHz at the first (09:45 UT), second (10:00 UT) and third (10:15 UT) measurement after the flare. The amplitude data are above the 2SD threshold only at lower frequencies (2.5 and 3 MHz) before the peak of the flare. There is only one data (point) at 4.5 MHz at 09:45 UT (first measurement after the flare) because of the partial fade-out. Increased amplitudes were observed at 3.5 and 4 MHz at 10:00 UT and 10:15 UT (second and third measurement after flare, still no record at 2.5 and 3 MHz). We still detected enhanced loss at 3.0–4.5 MHz at 10:30 UT, 80 min after the peak time of the flare. The observed effect is even more pronounced at VT (Figure 10C). The *fmin* parameter is 2.3 MHz at 08:45 UT and 2.7 MHz at 09:00 UT (second and first measurement before the peak time of the flare). After the 45 min long total radio fade-out the *fmin* returns with 5.1 MHz at 09:45 UT (first measurement after flare) and it changes to 4.3, 4.1, and 3.6 MHz at 10:00 UT, 10:15 UT and 10:30 UT (second, third and fourth measurement after flare respectively). The decreasing trend of the *fmin* seems to agree well with the GOES X-ray flux variation in the upper plot. We observed increased amplitude values at 2.5–4.5 MHz frequency range even before the peak of the flare (at 09:00 UT). The partial fade-out is very remarkable in the amplitude data display, too. No reflections were detected in the first and second measurement after the flare (09:45 UT and 10:00 UT) in the 2.5–4 MHz band. Furthermore, the partial fade-out (no data in the lower frequency range: 2.5–3 MHz) took place until the start of the next flare (11:53 UT). The detected loss values were above the threshold at every frequency, with especially increased values at 10:00 UT and 10:15 UT (second and third measurement after flare).

3.2 Signal-to-noise ratio analysis

The impact of the solar flares can be investigated also using the signal to noise ratio (SNR) measured by the Digisondes (Curto et al., 2018; de Paula et al., 2022). Here we demonstrate the SNR observed on 06 September 2017 when two large flares occurred (X2.2, peak time: 09:10 UR and X9.3, peak time: 12:02 UT) comparing it to a mean reference day derived from five individual days (07, 16, 26

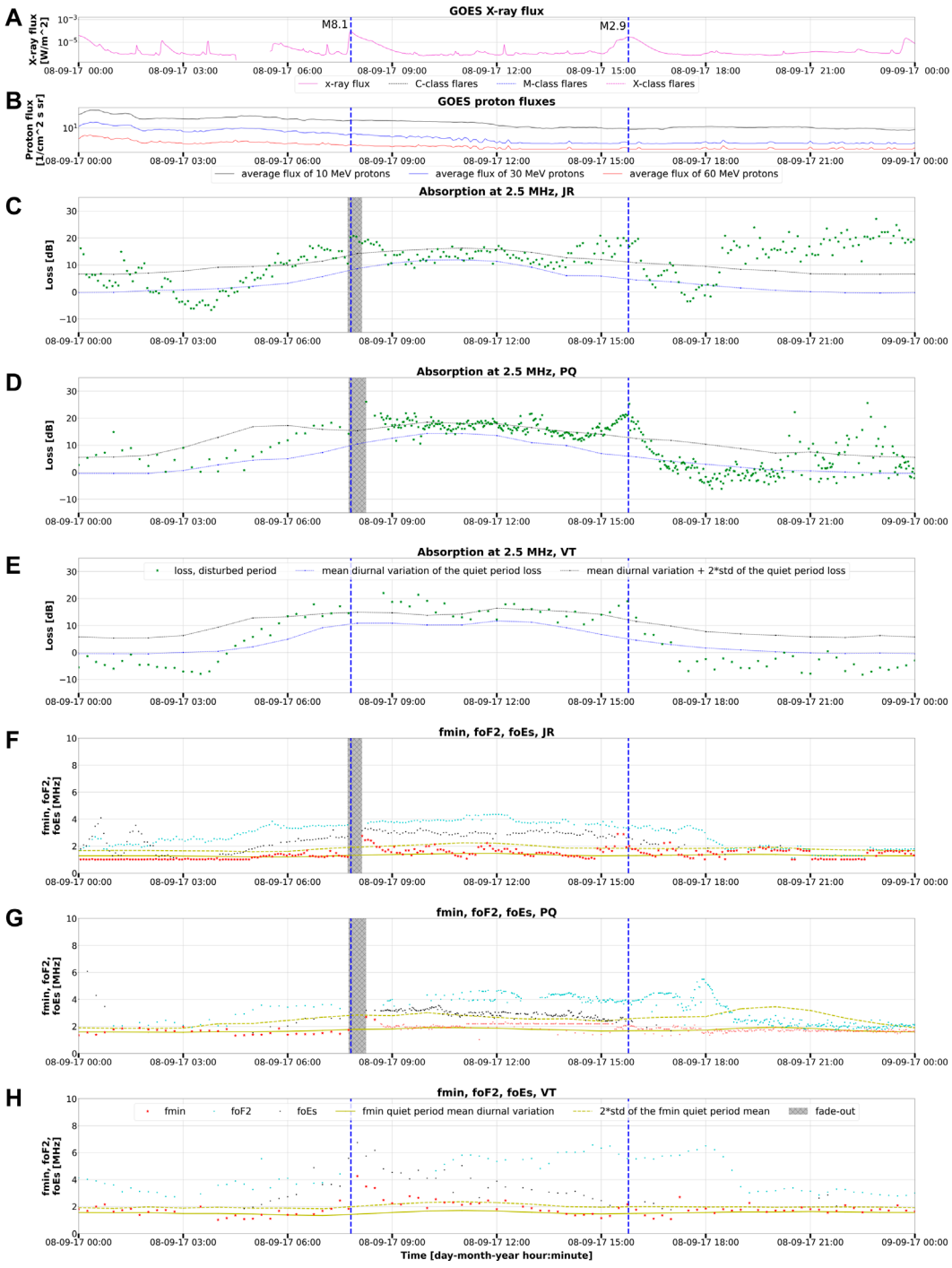

FIGURE 8
Variations of X-ray flux **(A)**, proton flux **(B)**, ionospheric absorption at 2.5 MHz **(C–E)**, *fmin*, *foF2* and *foEs* parameters **(F–H)** at all three studied stations on 08-09-2017. The time on the horizontal axes is in UT. The class of the investigated flares are plotted on panel **(A)**. The blue dashed lines indicate M-class flares.

August 2017 and 16, 21 September 2017; Figure 11). We used the same reference period for the three stations. Looking through the plots of reference days one can see that the diurnal variation of the SNR is a bit different at the three stations. The larger *fmin* values around noon were detected at VT, the highest observed frequencies (*foF2*) reached the highest values also at VT (above 8 MHz from 06:00 to 24:00 UT), above 7 MHz at JR (between 06:00 and 24:00 UT) and only 6–7 MHz at PQ. The total radio fade-outs caused by the two large solar flares are very well pronounced in the SNR tables of the three stations with the large empty territories after their time of occurrence (indicated by magenta lines). The restricted frequencies are also seen as white horizontal lines especially at VT.

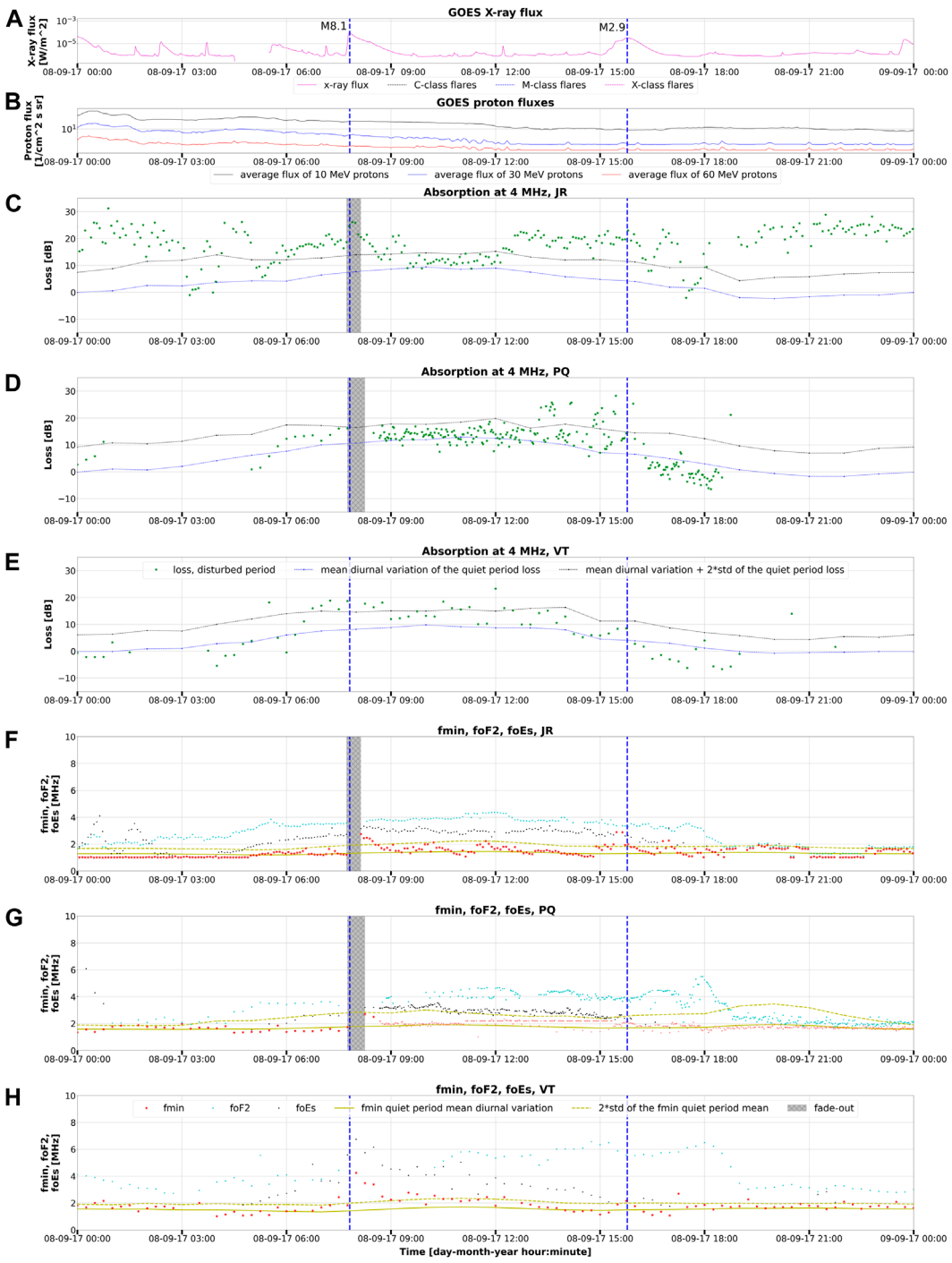

FIGURE 9
Variations of X-ray flux **(A)**, proton flux **(B)**, ionospheric absorption at 4 MHz **(C–E)**, *fmin*, *foF2* and *foEs* parameters **(F–H)** at all three studied stations on 08-09-2017. The time on the horizontal axes is in UT. The class of the investigated flares are plotted on panel **(A)**. The blue dashed lines indicate M-class flares.

4 Discussion

This study demonstrates a novel method to calculate the ionospheric absorption from amplitude data measured by the Digisondes. The amplitude method was introduced by Sales (2011), but it has not been applied to investigate the impact of multiple solar flares and it has not been compared with other methods to measure the ionospheric absorption, yet. One of the main objectives of this study is to fill this gap, namely, to study the solar flare effects on the ionospheric absorption by the amplitude method and to compare it with the *fmin* parameter and the signal-to-noise ratio measured by the same Digisonde during the same events. We

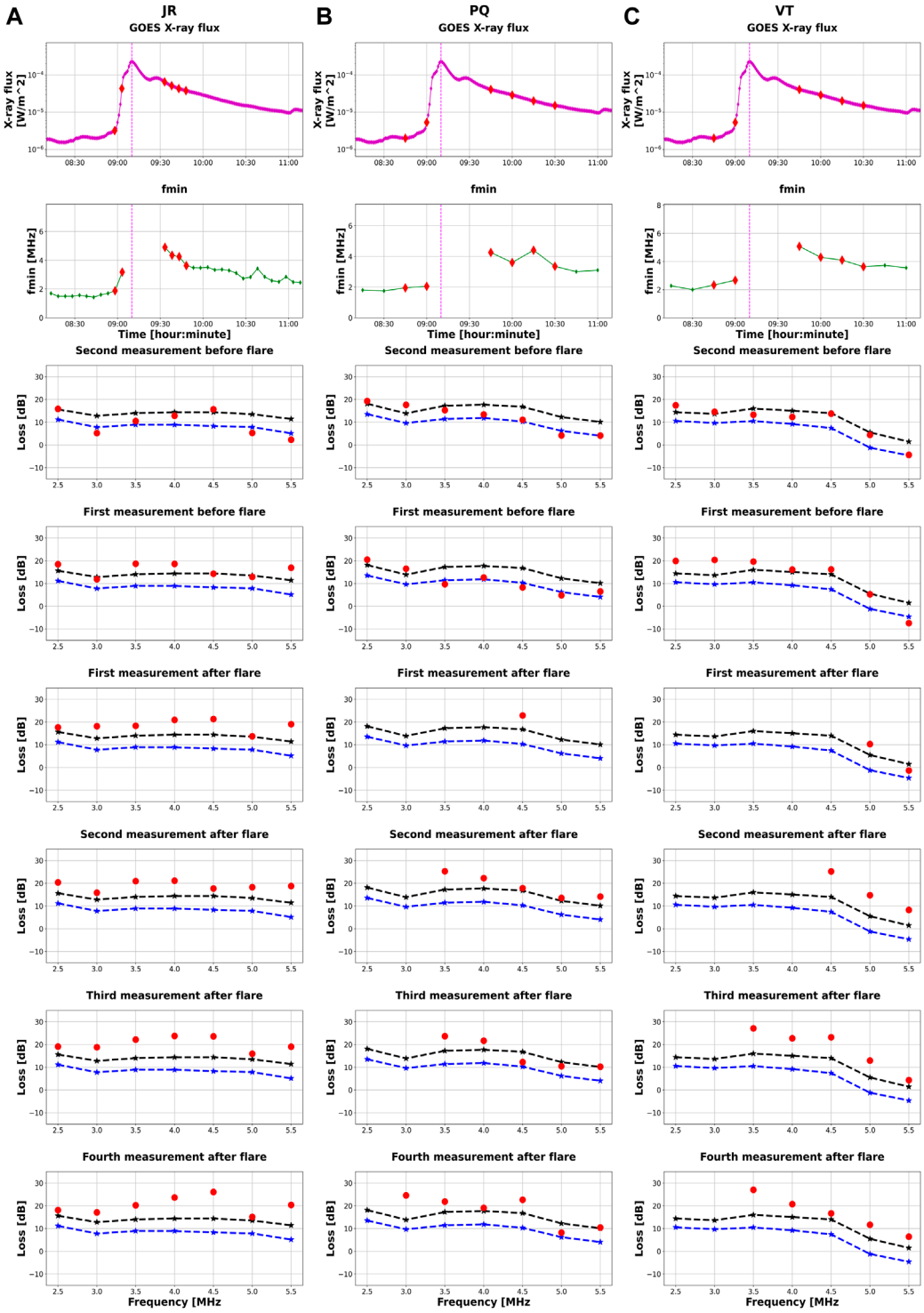

FIGURE 10
The effect of the X2.2 flare on 06 September 2017 in the *fmin* and absorption data at JR **(A)**, PQ **(B)** and VT **(C)** stations at all the investigated frequencies. The first measurement after the investigated flare (and the fade-out if there was any) was performed at 09:33:16 (in UT, at JR station with a sampling rate of 5 min) and at 09:45:00 UT (PQ, VT with a sampling rate of 15 min). The times on the plots in the upper two rows are in UT. The blue and black lines and the red dots denote the quiet period mean of the absorption, the quiet period mean plus 2 times the standard deviation of the absorption and the actual values of the absorption, respectively. Red diamonds on the panels in the upper two rows denote the second and first measurements before the flare and the first, second, third and fourth measurements after the flare. The magenta dashed lines on the upper two rows indicate the time of the flare.

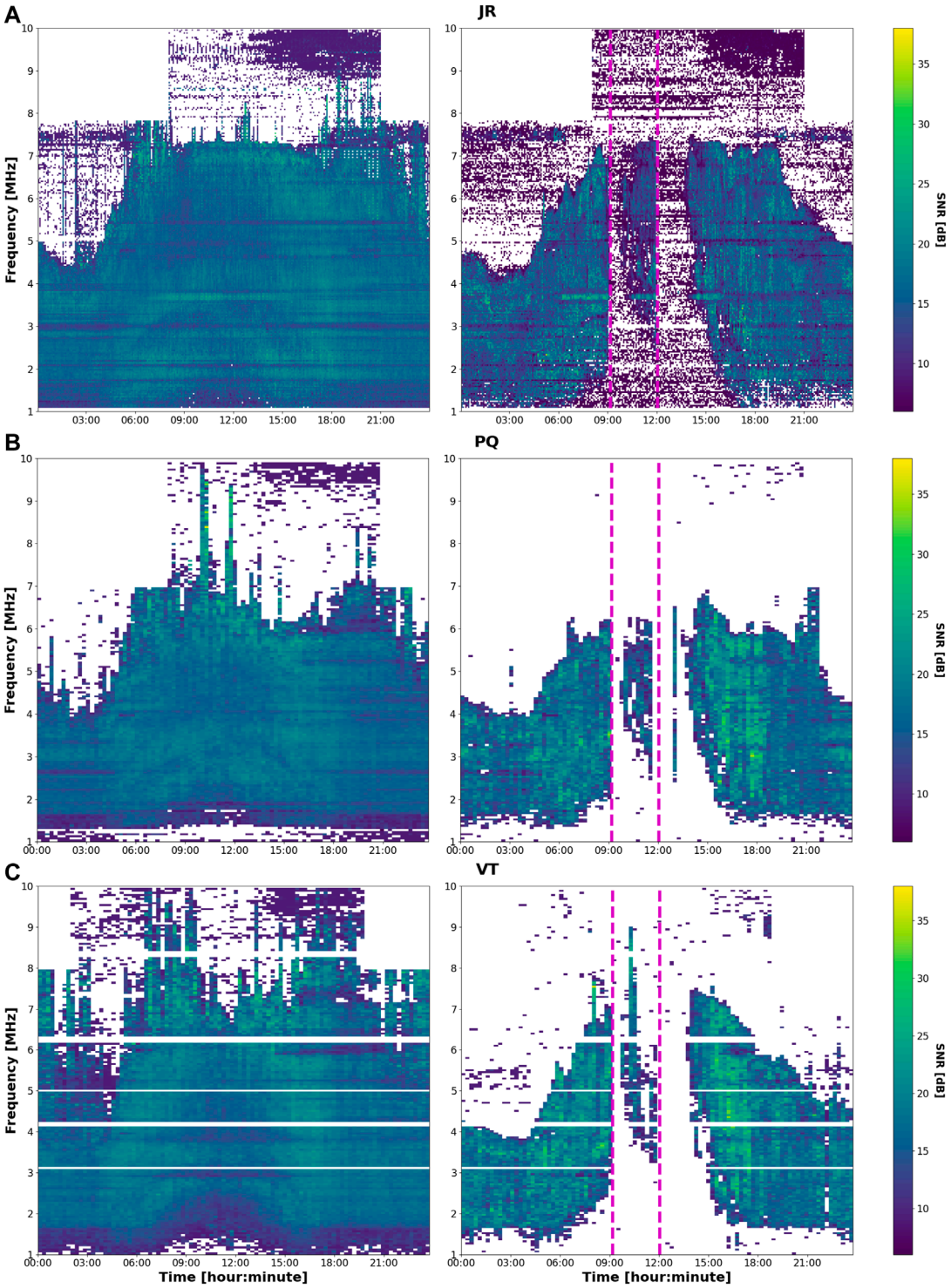

FIGURE 11
Demonstration of the SNR method. On the left, mean SNR taken from five quiet days (07, 16, 26 August 2017 and 16, 21 September 2017) are plotted, whereas on the right data from the disturbed period (06 September 2017) are displayed showing the effect of two X-class flares (vertical dashed magenta lines). The time on the horizontal axes is in UT. Panels **(A–C)** show the data for JR, PQ and VT stations, respectively.

selected thirteen intense solar flares (>C8) from the very active period of 04 and 10 September 2017 for investigation. In order to compare the three methods used for the analysis of the ionospheric absorption variation, residuals have been defined for all parameters, which provide the percentage changes compared to the selected reference periods. The exact determination of the residuals and the used reference periods are detailed in the Data and methods section (Section 2). The changes detected by different methods at JR, PQ and VT stations are shown in Tables 2–4, respectively. In order to help the careful comparison of the impact of the different flares we also added the following columns to Tables 2–4: "Time of first measurement after flare" and "X-ray flux at the time of the first measurement after flare." Because of the total radio fade-out we do not have observed values at the peak time of the larger flares, thus, the first observation happens at a later time, when the X-ray flux is decreased compared to the peak time. If one would like to compare the recorded values and ionospheric changes, it is better to take into account the X-ray flux at the exact time of the observation, than only the class of the flare itself.

The percentage change measured at the three stations after the flares was between +68% to +1430%, −50% to +565% and +0.4% to +318% in the case of the absorption method at 2.5, at 4 MHz and in the case of the *fmin* method, respectively. The ratio of small (<10 dB) and missing values in the case of the SNR method was between 1% and 100% (the maximum value is 100% in this case). The residuals with the largest fluctuations were produced by the absorption method, even indicating a reduction after the flare (−50% in the case of the M2.9 flare with peak time at 15:47 UT on 09 September at 4 MHz at VT). The largest enhancement in the absorption values at 2.5 MHz was after the M3.2 flare (peak time at 4:53 UT) on 05 September at all three stations. However, at 4 MHz the situation is more complex, as the largest increase in the absorption at this frequency was after the X8.2 flare (peak time at 16:06 UT) on 10 September, the M2.9 flare (peak time at 15:47 UT) on 08 September and the M3.2 flare (peak time at 4:53 UT) on 05 September at JR, PQ and VT stations, respectively. Nonetheless, it is important to note that the longest duration of fade-out happened after the largest, X9.3 flare (peak time at 12:02 UT) on 06 September in the case of all three stations and the percentage residuals can not be calculated in the case of fade-out as there are no data present to calculate the absorption. The largest enhancement in the *fmin* values was caused by the X9.3 flare on 06 September in the cases of JR and PQ stations but it happened after the M7.3 flare (peak time at 10:15 UT) on the 07 September in the case of VT station. The duration of the fade-out may have impacted the percentage residuals in the case of the *fmin* data as well. The ratio of missing and small values of the SNR reached its maximum value (100%) after the X9.3 class flare on 06 September in the cases of JR and PQ and it reached 100% after three flares [the two X-class flares on 06 September and the M3.7 flare (peak time at 11:04 UT) on 10 September] at VT station.

The amplitude changes measured at 2.5 MHz can be mainly related to the enhanced absorption occurring in the D-layer, since the signals are reflected generally from the E-layer at 90–130 km height (or from the Es-layer) at this frequency range during daytime. The observed changes at 2.5 MHz varied between 68% and 740% at JR, 75% and 363% at PQ and 76% and 1430% at VT, respectively. Basically, the ground-based VLF measurements are commonly used to monitor the changes of the D-layer after solar flares (e.g., Šulić and Srećković, 2014; Srećković et al., 2021; Kolarski et al., 2023). The electron density profile (Ne) can be determined by the measured amplitude and phase changes using a trial-and-error method where Ne is modified until the LWPC (Long Wave Propagation Capability model, available online: https://github.com/space-physics/LWPC) computed parameters (Šulić et al., 2016) are agreed with the detected ones (Srećković et al., 2021). The latter study also analyzed the impact of the M3.7 flare (peak time at 11:04 UT on 09 September) and they found that the electron density increased at reference height h = 74 km from 2.2×10^8 m^{-3} to 6.7×10^{10} m^{-3}, thus about with two orders of magnitude. We observed 67% (at JR), 85% (at PQ) and 103% (at VT) changes at 2.5 MHz after the same flare, thus the magnitude of the detected changes by the absorption method does not agree with the calculated Ne changes from the VLF data. Although it is important to mention that the M3.7 class flare caused total radio fade-out (30–48 min) at all stations, therefore there was no measured data at the peak time of the flare. According to the results of Kolarski et al. (2023) the electron density (at midlatitude) increased by almost three and about 3.5 orders of magnitude at 74 km after the X2.2 and X9.3 flares on 06 September, respectively. This is a very large value compared to the changes (77%–116%) detected at 2.5 MHz at the ionosonde stations after the same flare. However, these large flares caused long-lasting total radio blackouts at all stations, thus we had detected signals only 30–120 min after the peak time. Nevertheless, the computed Ne changes are ~100% at 74 km after C4.8–C5.1 class flares (Srećković et al., 2021; Barta et al., 2022) which agree with the changes (68%–102%) observed at 2.5 MHz after the C8.3 flare on 04 September, when there was no total radio blackout.

The amplitude changes measured at 4 MHz indicate also the changes of the absorption in the E-region beside the D-layer. We detected 82%–565% (at JR), 18%–222% (at PQ) and 66%–273% (at VT) changes at this frequency range during and after the investigated flare events. The most intense (X9.3) investigated flare caused 96%–174% changes at 4 MHz at the different stations. The impact of the same flare on the ionosphere was investigated also by Incoherent Scatter Radar measurements. Liu et al. (2022) showed that electron density in the E-region (mainly below 150 km) increased by ~$7{\cdot}10^{10}$ m^{-3} over Millstone Hill (42.6°N), a midlatitude/sub-auroral station in the American sector. Furthermore, Liu et al. (2021b) used EISCAT (European Incoherent SCATter) radar data and found that the induced electron density and temperature changes in the E-region are very well pronounced even at high latitudes (69°–72°N). Chen et al. (2021) used numerical modeling to investigate the effect of the X9.3 (06 September) and X8.2 (10 September) flares on the ionosphere and found that at the flare peak, not only the electron and temperature increased but also the E-region conductivity which causes further electrodynamic responses. Barta et al. (2022) found a 0.5–0.7 MHz enhancement of the *foE* parameter (critical frequency of E-region) compared to the reference days at PQ and VT stations after an M6 flare. Furthermore, Sharma et al. (2010) detected increased values (by 0.5 MHz) of the *foE* at Ahmedabad (India) low latitude station after the flare occurred on 12 May 1997. In terms of electron density of the E-region peak it means a ~30% enhancement, which is smaller than the observed changes at 4 MHz (as seen above). Consequently, the absorption variations within the

TABLE 2 Overview of the effect of the flares on the ionosphere as seen by all three studied methods at JR station. For the calculation method of change in absorption please refer to Section 2.1, for the change in *fmin* Section 2.2, and for the SNR ratios Section 2.3. All the times in the table are listed in UT.

JR									
Flares (peak time and class)	SZA	Time of first measurement after flare	X-ray flux at the time of the first measurement after flare	Change in absorption at 2.5 MHz	Change in absorption at 4 MHz	Change in *fmin*	Duration of total fade-out	SNR ratio, disturbed period (%)	SNR ratio, quiet period (%)
09.04.17 12:22 C8.3	50.03°	09.04.17 12:23	8.1e-6 Wm^{-2}	+68%	+82%	+73%	—	11	0
09.04.17 15:30 M1.5	70.62°	09.04.17 15:33	8.3e-6 Wm^{-2}	+103%	+53%	+31%	—	1	0
09.05.17 4:53 M3.2	86.07°	09.05.17 4:53	NaN	+740%	+233%	+0.4%	—	43	11
09.05.17 6:40 M3.8	70.91°	09.05.17 6:43	1.8e-5 Wm^{-2}	+326%	+492%	+65%	—	37	0
09.06.17 9:10 X2.2	53.53°	09.06.17 9:33	6.5e-5 Wm^{-2}	+102%	+188%	+258%	30 min	94	0
09.06.17 12:02 X9.3	49.07°	09.06.17 13:23	1.3e-4 Wm^{-2}	+92%	+174%	+275%	90 min	100	0
09.07.17 9:54 M1.4	50.72°	09.07.17 9:58	8e-6 Wm^{-2}	+97%	+134%	+128%	—	28	0
09.07.17 10:15 M7.3	49.71°	09.07.17 10:18	3.6e-5 Wm^{-2}	+79%	+127%	+283%	—	32	0
09.07.17 14:36 X1.3	64.47°	09.07.17 14:43	8.5e-5 Wm^{-2}	+197%	+287%	+252%	10 min	47	0
09.08.17 7:49 M8.1	62.67°	09.08.17 8:08	2.3e-5 Wm^{-2}	+256%	+329%	+119%	25 min	82	0
09.08.17 15:47 M2.9	74.42°	09.08.17 15:48	3e-5 Wm^{-2}	+262%	+378%	+55%	—	77	0
09.09.17 11:04 M3.7	49.46°	09.09.17 11:28	3e-5 Wm^{-2}	+67%	+152%	+135%	30 min	86	0
09.10.17 16:06 X8.2	77.83°	09.10.17 16:28	4.7e-4 Wm^{-2}	+335%	+565%	+185%	35 min	61	0

TABLE 3 Overview of the effect of the flares on the ionosphere as seen by all three studied methods at PQ station. For the calculation method of change in absorption please refer to Section 2.1, for the change in *fmin* Section 2.2, and for the SNR ratios Section 2.3. All the times in the table are listed in UT.

PQ									
Flares (peak time and class)	SZA	Time of first measurement after flare	X-ray flux at the time of the first measurement after flare	Change in absorption at 2.5 MHz	Change in absorption at 4 MHz	Change in *fmin*	Duration of total fade-out	SNR ratio, disturbed period (%)	SNR ratio, quiet period (%)
09.04.17 12:22 C8.3	46.2°	09.04.17 12:30	7e-6 Wm^{-2}	+75%	+35%	+68%	—	9	0
09.04.17 15:30 M1.5	70.15°	09.04.17 15:30	1.5e-5 Wm^{-2}	+171%	+18%	+18%	—	4	0
09.05.17 4:53 M3.2	85.86°	09.05.17 5:00	NaN	+363%	+154%	+9%	—	36	0
09.05.17 6:40 M3.8	68.97°	09.05.17 6:45	1.3e-5 Wm^{-2}	+241%	+68%	+53%	—	30	0
09.06.17 9:10 X2.2	49.38°	09.06.17 9:45	4.1e-5 Wm^{-2}	+116%	+95%	+132%	45 min	80	0
09.06.17 12:02 X9.3	45.59°	09.06.17 13:30	1.1e-4 Wm^{-2}	+86%	+65%	+203%	105 min	100	0
09.07.17 9:54 M1.4	46.16°	09.07.17 10:00	4.1e-6 Wm^{-2}	+85%	+17%	+80%	—	25	0
09.07.17 10:15 M7.3	45.04°	09.07.17 10:30	1.6e-6 Wm^{-2}	+68%	+11%	+12%	30 min	23	0
09.07.17 14:36 X1.3	63.01°	09.07.17 14:45	8e-5 Wm^{-2}	+156%	+20%	+179%	—	38	0
09.08.17 7:49 M8.1	59.59°	09.08.17 8:15	1.7e-5 Wm^{-2}	+243%	+82%	+59%	30 min	80	0
09.08.17 15:47 M2.9	74.19°	09.08.17 15:48	3e-5 Wm^{-2}	+237%	+222%	+27%	—	37	0
09.09.17 11:04 M3.7	44.83°	09.09.17 11:48	1.6e-5 Wm^{-2}	+85%	+56%	+59%	48 min	98	0
09.10.17 16:06 X8.2	77.89°	09.10.17 16:30	4.3e-4 Wm^{-2}	+303%	+142%	+124%	45 min	45	0

TABLE 4 Overview of the effect of the flares on the ionosphere as seen by all three studied methods at VT station. For the calculation method of change in absorption please refer to Section 2.1, for the change in *fmin* Section 2.2, and for the SNR ratios Section 2.3. All the times in the table are listed in UT.

VT									
Flares (peak time and class)	SZA	Time of first measurement after flare	X-ray flux at the time of the first measurement after flare	Change in absorption at 2.5 MHz	Change in absorption at 4 MHz	Change in *fmin*	Duration of total fade-out	SNR ratio, disturbed period (%)	SNR ratio, quiet period (%)
09.04.17 12:22 C8.3	39.62°	09.04.17 12:30	7e-6 Wm^{-2}	+102%	+91%	+213%	—	56	6
09.04.17 15:30 M1.5	70.72°	09.04.17 15:30	1.5e-5 Wm^{-2}	+89%	+66%	+62%	—	7	6
09.05.17 4:53 M3.2	84.43°	09.05.17 5:00	NaN	+1430%	+309%	+33%	—	12	6
09.05.17 6:40 M3.8	64.4°	09.05.17 6:45	1.3e-5 Wm^{-2}	+269%	+273%	+100%	—	17	6
09.06.17 9:10 X2.2	40.58°	09.06.17 9:45	4.1e-5 Wm^{-2}	+83%	+161%	+227%	45 min	100	6
09.06.17 12:02 X9.3	38.2°	09.06.17 13:45	8.7e-5 Wm^{-2}	+77%	+96%	+249%	120 min	100	6
09.07.17 9:54 M1.4	36.63°	09.07.17 10:00	4.1e-6 Wm^{-2}	+132%	+98%	+95%	—	41	6
09.07.17 10:15 M7.3	35.4°	09.07.17 10:15	8e-5 Wm^{-2}	+136%	+92%	+318%	—	40	6
09.07.17 14:36 X1.3	61.67°	09.07.17 14:45	8e-5 Wm^{-2}	+76%	+47%	+280%	—	49	6
09.08.17 7:49 M8.1	52.86°	09.08.17 8:00	3.4e-5 Wm^{-2}	+166%	+150%	+208%	—	75	6
09.08.17 15:47 M2.9	75.14°	09.08.17 16:00	1.9e-5 Wm^{-2}	+91%	−50%	+20%	—	70	6
09.09.17 11:04 M3.7	35.67°	09.09.17 11:15	2.3e-5 Wm^{-2}	+103%	+76%	+176%	30 min	100	6
09.10.17 16:06 X8.2	79.34°	09.10.17 16:15	7.3e-4 Wm^{-2}	+172%	+213%	+243%	30 min	54	6

D- and E-layer seem to be larger than the electron density changes of the E-region itself.

The *fmin* parameter variation was between 0.4% and 283% at JR, 9% and 203% at PQ and 33% and 318% at VT during and after the investigated flare events. These detected *fmin* changes are in good agreement with the values measured at other European stations (Barta et al., 2019; 2022), in India (Sharma et al., 2010; Sripathi et al., 2013), in Japan (Tao et al., 2020) and in South America (Nogueira et al., 2015; Denardini et al., 2016) during and after M- and X-class flares. The observed changes depended on the intensity of the flare similarly to the results of Tao et al. (2020) and Barta et al. (2019). However, the solar zenith angle of the observation site also plays an important role, which agrees with the conclusion of Barta et al. (2019). These results are in good agreement with Mahajan et al. (2010) and Hazarika et al. (2016) who investigated the variation of total electron content (TEC: Total Electron Content) during intense solar flares and found a good correlation between the enhancement in TEC and increase in EUV flux, however, the local time of occurrence of the flares may also play an important role.

However, the neutral atmospheric circulation also can play a role in the local ionospheric anomalies observed at the different stations. E.g., at VT we observe an increase of *fmin* and similar change in absorption during the C8.3 (12:22 UT on 04. September) and X9.3 (12:02 UT on 06 September) flares, while at both PQ (50°N) and JR (54.6°N) we see higher attenuation during the X-class flare as expected. The neutral atmosphere above VT is influenced by different circulation patterns than the atmosphere above PQ and JR due to the location of Alpine massif and this fact can contribute to the different ionospheric responses. Regarding the model study of Pedatella and Liu (2018), a neutral atmosphere may significantly influence the behaviour of the ionosphere (variability leads to an uncertainty of typically 20%–40%, with localized regions exceeding 100%).

Based on our results, the *foF2* parameter measured during the investigated period is sensitive to the geomagnetic storm. A negative ionospheric storm can be clearly seen on the *foF2* variation during the main phase of the geomagnetic storm on 08 September (see D_{st} variation in Figure 2E) and the following night especially at JR, what is a sub-auroral station (please see Figures 4F, G). The decreased electron density appears also at PQ but it is not so pronounced at VT (please see Figures 4F–H). In parallel, if we look through the variation of the *fmin* parameter we can not recognise any changes of the diurnal pattern in connection with the geomagnetic storm, only the increased values at the time of the flare events are clear. It agrees well with the findings of previous studies, e.g., Barta et al., 2022, that the *fmin* parameter is sensitive to the changes caused by the solar flares, while the *foF2* parameter can show the variation caused by the dynamical changes in the thermosphere–ionosphere (F-region) system during geomagnetic storms.

The three different methods have their own advantages/disadvantages and their limitations. A common limitation of all the methods is that generally they can not be used during and right after the most intense solar flares (>M5) because there are no

measured data due to the generated total radio fade-out. The most intense X-class solar flares can produce clearly detectable changes in the Total Electron Content (TEC) derived from GNSS data (see e.g., Liu et al., 2004; Carrano et al., 2009; Zhang et al., 2011; Hernández-Pajares et al., 2012; Xiong et al., 2014). The advantage of the TEC data is that the GNSS measurements are not affected by the total radio fade-out. On the other hand, the impact of the less intense solar flares (<M5 class) is not that pronounced in TEC changes. Moreover, the effect of the flares can not be recognized during the presence of a strong geomagnetic storm (see Barta et al., 2022), because the TEC variation is more sensitive to the dynamical changes of the thermosphere–ionosphere (F-region) changes during geomagnetic storms. The described methods can be used as three different approaches to analyze the impact of the solar flares on the ionosphere and they can be beneficial despite their limitations.

The limitation of the amplitude method is that it can not be used at higher frequencies (>3.5 MHz) during the early morning hours and evening (and all of the night) when the value of the *foF2* drops below 3 MHz, because there is no reflection from the F-trace in these periods. This problem was particularly striking at the data measured at 4 MHz on the nights of the 08 and 09 September (see Figures 5C, D) during the investigated period. The *foF2* parameter decreased to ~2 MHz at JR and PQ (Figures 5F, G) indicating a negative ionospheric storm probably due to the geomagnetic storm ($Kp = 8.3$, Figure 2D, $Dst \sim -100$ nT; Figure 2E). This problem can be solved if in the analysis we also take into account the oblique traces during synchronized measurements with other ionosonde stations. Similar analyses on oblique sounding paths over longer distances could overcome this limitation. This can be a next step for future work. Moreover, when the *fmin* value is increased (>4–5 MHz) after the more intense solar flares (>M3 class) there are no detected amplitude data at the lower frequency band (2.5–3.5 MHz) because of the partial radio fade-outs which means a further limitation of the absorption method (see the results detailed in Section 3.1 and, e.g., Figures 6, 8, 10). Furthermore, it is difficult to determine which frequency is the best at the different stations to monitor the impact caused by the flares because the detected amplitude data at the different frequencies are highly variable based on the results (see e.g., Figure 10). Further limitation of the amplitude method is that it is difficult to estimate the magnitude of the caused effect based on that. Generally, very low amplitude values are detected in the early morning and evening hours. Therefore, the relative (percentage) change in absorption caused by the flare is large during these periods [see e.g., the impact of M3.2 flare occurred at 4:53 UT on 05 September, 740% changes at 2.5 MHz at JR (Table 2) and 1430% at VT (Table 4.)]. In contrast, around noon, when absorption is higher by default, the percentage change due to an intense flare is not as high. This is well demonstrated in the changes, e.g., after the X9.3 flare (peak time at 12:02 UT) on 06 September: 92% at 2.5 MHz at JR, 86% at PQ and only 77% at VT. This issue should be considered when evaluating the percentage result describing the ionospheric response. In summary, the method is well applicable in the lower frequency band during daytime (08–15 UT) after the less intense M-class flares (M1–M3) which do not cause total radio blackouts and very enhanced values of the *fmin* parameter.

The disadvantage of the *fmin* method is that the *fmin* parameter can depend on the background radio noise level, the radar characteristics and the other settings of the measurement, e.g., on the integration time (applying longer integration time (in standard 15 min mode) leading to lower *fmin* values, while lower integration time (used during campaign measurements, like the 2 min at PQ) resulting in higher *fmin* values). Consequently, the *fmin* method can be used only as a rough measure/indicator for the ionospheric absorption changes. It can be applied to investigate the relative changes: to compare the *fmin* parameter measured by the same system (preferably by the same settings) during flares and reference quiet days (e.g., Barta et al., 2019; 2022). On the other hand, the measurement of the *fmin* parameter is not limited by other ionospheric parameters (*foF2, foEs*) like in the above detailed case of the amplitude method. If there is a detected change in *fmin* value, it can be used as a rough measure of the ionospheric absorption during day and night.

The disadvantage of the SNR method is the saturation. The estimation of the caused effect is based on the ratio between the number of small values (<10 dB) and all the measured values at the investigated frequency ranges within 1 hour after the peak time of the flare (see Section 2.3). This gives an upper limit for the detected effect, because if all the observed values are zero or negligible during the one-hour period (total radio fade-out) it means 100%. Therefore, this limits the comparison of the effects caused by the most intense solar flares. The saturation issue of the SNR method can be solved by using a longer time period before and after the peak time of the flare for comparison. However, the applied time period should be selected carefully, because the larger solar flares (with longer duration) and their impact can overlap with each other. The effect of the geomagnetic storm can be seen on the SNR tables at all three investigated stations (please, see Supplementary Figures SA3A–C in the Supplementary Material). We can see a clear daily pattern at all stations on 04 September (left column on the Supplementary Figure SA3). Stronger signals in a wider frequency range (from approximately 2 to 6–7 MHz) during daytime (06:00–18:00 UT) and weaker signals in a smaller frequency range (1.5–4 MHz at VT, PQ, and 1–3 MHz at JR) in the evening and early morning hours. However, on 8 September the geomagnetic storm causes a negative ionospheric storm (decreased electron density) thus the maximum frequency became 5 MHz during daytime and can decrease below 2 MHz during the evening hours (it is especially pronounced at JR) which changes the daily pattern in the SNR table at the three stations (see Supplementary Figures SA3A–C in the Supplementary Material). Furthermore, the strength of the signal seems to be reduced on 8 September compared to the SNR measured on 04 September. Therefore, the geomagnetic activity should be taken into account when one would like to apply this method. Nevertheless, based on the present results (Tables 2–4) it seems an appropriate index to demonstrate the geoeffectiveness of a solar flare. The calculated changes (in %) depend on the intensity (class of the flare) and they seem to also show a solar zenith angle dependence. Furthermore, this method does not have limits like the amplitude method. Therefore, this method appears to be suitable to study the ionospheric absorption changes during solar flares, but it needs further investigation.

In the future, we plan to focus on the impact caused by the energetic particles (protons and electrons) accompanied by solar flares on the ionospheric absorption. They can have an important role in the sub-auroral region, like JR station. Another

step for future work can be to involve oblique traces recorded during synchronized measurements between two ionosondes into the analysis to overcome the issue related to the low *foF2* values during morning/late afternoon hours. Furthermore, we would like to compare the absorption changes calculated from different EM properties measured by the Digisondes (used in this paper) with other instruments which measure the ionospheric absorption, e.g., with the so-called A1 method (Bischoff and Taubenheim, 1967), or with riometer data. It will be also important to compare our results with the D-RAP model, commonly used to follow the changes in the ionospheric absorption globally. Moreover, we plan to study the geoeffectiveness of the investigated solar flares, namely how the changes (measured by the different methods) depend on the different properties of the flares, e.g., on solar zenith angle, on central meridian distance, or on the duration of the flare.

5 Conclusion

The present study demonstrates a novel method to determine the ionospheric absorption changes from amplitude data measured by European Digisondes (DPS-4D). The method has been applied to study the solar flare effects on the ionospheric absorption. The detected changes have been compared with the *fmin* parameter and the signal-to-noise ratio measured by the same Digisondes during the same events. Thirteen intense solar flares (>C8) have been selected for the investigation from the very active period of 04 and 10 September 2017. The solar zenith angle of the observation sites (to be <90°) was also considered during the selection. In order to compare the three methods used for the analysis of the ionospheric absorption variation, residuals have been defined for all parameters, which provide the percentage changes compared to the selected reference periods. The most important conclusions of the study are the followings:

- The amplitude changes measured at 2.5 MHz—which can be mainly related to the enhanced absorption occurring in the D-layer—varied between 68% and 1430% at the three European stations, Juliusruh, Průhonice and San Vito. The amplitude changes measured at 4 MHz—which indicate also the absorption variation in the E-region beside the D-layer—were between 18% and 565% at the three stations, thus a bit smaller than in the previous case. It agrees with the assumption that larger variations occurred in the D-layer after the solar flares than in the E-region.
- There are two main limitations of the amplitude method: 1) it can not be used at higher frequencies (>3.5 MHz) during the early morning hours and evening when the value of the *foF2* drops below 3 MHz; 2) there are no detected amplitude data at the lower frequency band (2.5–3.5 MHz) after the more intense solar flares (>M3 class) because of the partial radio fade-outs (*fmin* is increased above 4 MHz). Based on the results the method is well applicable in the lower frequency band during daytime (08–15 UT) after the less intense M-class flares (M1–M3) which do not cause total radio blackouts and very enhanced values of the *fmin* parameter. In future, we suggest utilization of oblique sounding as it allows for analysis of higher frequencies of the reflected signal.
- The variation of the *fmin* parameter was between 0.4% and 318% at the three stations during and after the investigated flare events. These detected fmin changes agree with the values measured in Europe and in other continents during and after M- and X-class flares based on the literature. The disadvantage of the *fmin* method is that the *fmin* parameter can depend on the background radio-noise level, the radar characteristics and the other settings of the measurement, e.g., on the integration time. However, it can be applied to investigate the relative changes (compare the *fmin* parameter measured during flares and reference quiet days) and it is not affected by other ionospheric parameters (*foF2*, *foEs*) like the amplitude method.
- The absorption changes detected by the SNR method were between 1% and 100% after the investigated flares. The caused effects are calculated by the ratio between the number of small values (<10 dB, also including missing values) and all the measured values at the investigated frequency ranges within 1 h after the peak time of the flare. Consequently, there is an upper limit (100%) for the detected effect. However, this method does not have other limitations like the amplitude method. Therefore, based on the present results this method appears to be suitable to study the geoeffectiveness of the solar flares on ionospheric absorption.

In summary, the combination of these three methods seems to be an efficient approach to monitor the ionospheric response to solar flares.

Data availability statement

Publicly available datasets were analyzed in this study. This data can be found here: The datasets presented in this study can be found in online repositories. The names of the repository/repositories and access number(s) are the following: Global Ionospheric Radio Observatory http://giro.uml.edu; NASA/GSFC's OMNI data set through OMNIWeb https://omniweb.gsfc.nasa.gov/; GOES 11 and 12 data, National Oceanic and Atmospheric Administration https://satdat.ngdc.noaa.gov/sem/goes/data/avg/; Hinode flare catalog https://hinode.isee.nagoya-u.ac.jp/flare_catalogue/; SAO-X software https://ulcar.uml.edu/SAO-X/SAO-X.html.

Author contributions

AB and VB conducted the scientific analysis of the data, produced the figures, and wrote the main part of the text. JM was responsible for the data from Juliusruh. DK, DB, ZM, and PK were responsible for the data from Pruhonice. All authors contributed to the article and approved the submitted version.

Funding

This work was supported by OTKA, Hungarian Scientific Research Fund (Grant No. PD 141967) of the National Research,

Development and Innovation Office. The contribution of VB was also supported by Bolyai Fellowship (GD, No. BO/00461/21) and by the GINOP-2.3.2-15-2016-00003 project. The authors appreciate support of the bilateral project of the Czech Academy of Sciences and Hungarian Academy of Sciences, title: Multiinstrumental investigation of the midlatitude ionospheric variability (n. MTA-19-03 and NKM 2018-28) in facilitating scientific communication. The work of the Czech team was also supported by the HORIZON 2020 PITHIA-NRF project (Grant Agreement No. 101007599).

Acknowledgments

The authors wish to express their gratitude to the late Gary Sales who made a substantial contribution in developing the absorption method used in this study and to Prof. Bodo Reinisch who attracted our attention to this method. The authors wish to thank the OMNIWeb data center for providing web access to the solar data of the Geostationary Operational Environmental Satellites (GOES) satellites.

Conflict of interest

The authors declare that the research was conducted in the absence of any commercial or financial relationships that could be construed as a potential conflict of interest.

Publisher's note

All claims expressed in this article are solely those of the authors and do not necessarily represent those of their affiliated organizations, or those of the publisher, the editors and the reviewers. Any product that may be evaluated in this article, or claim that may be made by its manufacturer, is not guaranteed or endorsed by the publisher.

Supplementary material

The Supplementary Material for this article can be found online at: https://www.frontiersin.org/articles/10.3389/fspas.2023.1201625/full#supplementary-material

References

Barta, V., Natras, R., Srećković, V., Koronczay, D., Schmidt, M., and Šulic, D. (2022). Multi-instrumental investigation of the solar flares impact on the ionosphere on 05-06 December 2006. *Front. Environ. Sci.* 10, 904335. doi:10.3389/fenvs.2022.904335

Barta, V., Sátori, G., Berényi, K. A., Kis, Á., and Williams, E. (2019). Effects of solar flares on the ionosphere as shown by the dynamics of ionograms recorded in Europe and South Africa. *Ann. Geophys.* 37 (4), 747–761. doi:10.5194/angeo-37-747-2019

Berdermann, J., Kriegel, M., Banyś, D., Heymann, F., Hoque, M. M., Wilken, V., et al. (2018). Ionospheric response to the X9.3 Flare on 6 September 2017 and its implication for navigation services over Europe. *Space weather.* 16, 1604–1615. doi:10.1029/2018SW001933

Berényi, K. A., Barta, V., and Kis, Á. (2018). Midlatitude ionospheric F2-layer response to eruptive solar events-caused geomagnetic disturbances over Hungary during the maximum of the solar cycle 24: A case study. *Adv. Space Res.* 61 (5), 1230–1243. doi:10.1016/j.asr.2017.12.021

Bilitza, D., Altadill, D., Truhlik, V., Shubin, V., Galkin, I., Reinisch, B., et al. (2017). International Reference Ionosphere 2016: From ionospheric climate to real-time weather predictions. *Space weather.* 15, 418–429. doi:10.1002/2016sw001593

Bischoff, K., and Taubenheim, J. (1967). A study of ionospheric pulse absorption (A1) on 4 Mc/s during the solar eclipse of May 20, 1966. *J. Atmos. solar-terrestrial Phys.* 29 (9), 1063–1069. doi:10.1016/0021-9169(67)90140-7

Buresova, D., Lastovicka, J., Hejda, P., and Bochnicek, J. (2014). Ionospheric disturbances under low solar activity conditions. *Adv. Space Res.* 54, 185–196. doi:10.1016/j.asr.2014.04.007

Carrano, C. S., Bridgwood, C. T., and Groves, K. M. (2009). Impacts of the December 2006 solar radio bursts on the performance of GPS. *Radio Sci.* 44, RS0A25. doi:10.1029/2008RS004071

Chen, J., Lei, J., Wang, W., Liu, J., Maute, A., Qian, L., et al. (2021). Ionospheric electrodynamic response to solar flares in September 2017. *J. Geophys. Res. Space Phys.* 126, e2021JA029745. doi:10.1029/2021JA029745

Curto, J. J., Marsal, S., Blanch, E., and Altadill, D. (2018). Analysis of the solar flare effects of 6 September 2017 in the ionosphere and in the Earth's magnetic field using Spherical Elementary Current Systems. *Space weather. J.* 16, 1709–1720. doi:10.1029/2018sw001927

Davies, K. (1990). *Ionospheric radio*. London Peregrinus.

Denardini, C. M., Resende, L. C. A., Moro, J., and Chen, S. S. (2016). Occurrence of the blanketing sporadic E layer during the recovery phase of the October 2003 superstorm. *Earth Planets Space* 68, 80. doi:10.1186/s40623-016-0456-7

Friis, H. T. (1946). A note on a simple transmission formula. *Proc. IRE* 34, 254–256. doi:10.1109/jrproc.1946.234568

George, P. L., and Bradley, P. A. (1973) Relationship between HF absorption at vertical and oblique incidence. *Proc. Inst. Electr. Eng.* 120, 1355–1361. doi:10.1049/piee.1973.0273

Handzo, R., Forbes, J. M., and Reinisch, B. (2014). Ionospheric electron density response to solar flares as viewed by digisondes. *Space weather.* 12, 205–216. doi:10.1002/2013sw001020

Hazarika, R., Kalita, B. R., and Bhuyan, P. K. (2016). Ionospheric response to X-class solar flares in the ascending half of the subdued solar cycle 24. *J. Earth Syst. Sci.* 125, 1235–1244. doi:10.1007/s12040-016-0726-6

Hernández-Pajares, M., García-Rigo, A., Juan, J. M., Sanz, J., Monte, E., Aragón-Àngel, A., et al. (2012). GNSS measurement of EUV photons flux rate during strong and mid solar flares. *Space weather.* 10 (12). doi:10.1029/2012sw000826

Higashimura, M., Sinno, K., and Hirukawa, Y. (1969a). Analysis of long-term observations of ionospheric absorption measurement (I). Observations at kokubunji. *J. Radio Res. Lab.* 16, 131–138.

Higashimura, M., Sinno, K., and Hirukawa, Y. (1969b). Analysis of long-term observations of ionospheric absorption measurement (II). Observations in the northern hemisphere. *J. Radio Res. Lab.* 16, 139–147.

Kokourov, V. D., Vergasova, G. V., and Kazimirovsky, E. S. (2006). Longterm variations of ionospheric parameters as a basis for the study of the upper-atmospheric climate. *Phys. Chem. Earth, PartsA/B/C* 31.1, 54–58. doi:10.1016/j.pce.2005.03.002

Kolarski, A., Veselinović, N., Srećković, V. A., Mijić, Z., Savić, M., and Dragić, A. (2023). Impacts of extreme space weather events on september 6th, 2017 on ionosphere and primary cosmic rays. *Remote Sens.* 15 (5), 1403. doi:10.3390/rs15051403

Little, C. G. (1954). High latitude ionospheric observations using extra-terrestrial radio waves. *Proc. IRE* 42, 1700. doi:10.1016/0021-9169(95)00072-0

Liu, J., Qian, L., Maute, A., Wang, W., Richmond, A. D., Chen, J., et al. (2021a). Electrodynamical coupling of the geospace system during solar flares. *J. Geophys. Res. Space Phys.* 125, e2020JA028569. doi:10.1029/2020JA028569

Liu, J., Wang, W., Qian, L., Lotko, W., Burns, A. G., Pham, K., et al. (2021b). Solar flare effects in the Earth's magnetosphere. *Nat. Phys.* 17 (7), 807–812. doi:10.1038/s41567-021-01203-5

Liu, J. Y., Lin, C. H., Tsai, H. F., and Liou, Y. A. (2004). Ionospheric solar flare effects monitored by the ground-based GPS receivers: Theory and observation. *J. Geophys. Res.* 109, A01307. doi:10.1029/2003JA009931

Liu, X., Liu, J., Wang, W., Zhang, S.-R., Zhang, K., Lei, J., et al. (2022). Explaining solar flare-induced ionospheric ion upflow at Millstone Hill (42.6°N.). *J. Geophys. Res. Space Phys.* 127, e2021JA030185. doi:10.1029/2021JA030185

Mahajan, K. K., Lodhi, N. K., and Upadhayaya, A. K. (2010). Observations of X-ray and EUV fluxes during X-class solar flares and response of upper ionosphere. *J. Geophys. Res. Space Phys.* 115 (A12). doi:10.1029/2010ja015576

Mosna, Z., Kouba, D., Knizova, P. K., Buresova, D., Chum, J., Sindelarova, T., et al. (2020). Ionospheric storm of September 2017 observed at ionospheric station Pruhonice, the Czech Republic. *Adv. Space Res.* 65 (1), 115–128. doi:10.1016/j.asr.2019.09.024

Nogueira, P. A. B., Souza, J. R., Abdu, M. A., Paes, R. R., Sousasantos, J., Marques, M. S., et al. (2015). Modeling the equatorial and low-latitude ionospheric response to an intense X class solar flare. *J. Geophys. Res. Space Phys.* 120, 3021–3032. doi:10.1002/2014ja020823

Oksman, J., Wagner, C. U., Kaila, K., and Lauter, A. E. (1981). Post-storm mid-latitude green aurora and electron precipitation. *Planet. Space Sci.* 29, 405–413. doi:10.1016/0032-0633(81)90084-2

de Paula, V., Segarra, A., Altadill, D., Curto, J. J., and Blanch, E. (2022). Detection of solar flares from the analysis of signal-to-noise ratio recorded by Digisonde at mid-latitudes. *Remote Sens.* 14, 1898. doi:10.3390/rs14081898

Pedatella, N. M., and Liu, H.-L. (2018). The influence of internal atmospheric variability on the ionosphere response to a geomagnetic storm. *Geophys. Res. Lett.* 45, 4578–4585. doi:10.1029/2018GL077867

Ratcliffe, J. A. (1972). *An introduction to the ionosphere and magnetosphere*. Cambridge: The University Press.

Reinisch, B. W., and Galkin, I. A. (2011). Global ionospheric radio observatory (GIRO). *Earth Planet Sp.* 63, 377–381. doi:10.5047/eps.2011.03.001

Rishbeth, H., and Garriot, O. K. (1969). Introduction to ionospheric Physics, *Int. Geophys. Ser*, Vol. 14, Academic Press, NY, 87–120.

Rose, D. C., and Ziauddin, S. (1962). The polar cap absorption effect. *Space Sci. Rev.* 1, 115–134. doi:10.1007/bf00174638

Sales, G. S. (2011). *HF absorption measurements using routine digisonde data*, Conference material, XII. Lowell, MA: International Digisonde Forum, University of Massachusetts.

Sauer, H. H., and Wilkinson, D. C. (2008). Global mapping of ionospheric HF/VHF radio wave absorption due to solar energetic protons. *Space weather.* 6, 12002. doi:10.1029/2008SW000399

Schmitter, E. D. (2011). Remote sensing planetary waves in the midlatitude mesosphere using low frequency transmitter signals. *Ann. Geophys.* 29, 1287–1293. doi:10.5194/angeo-29-1287-2011

Scotto, C., and Settimi, A. (2014). The calculation of ionospheric absorption with modern computers. *Adv. Space Res.* 54 (8), 1642–1650. doi:10.1016/j.asr.2014.06.017

Sharma, S., Chandra, H., Vats, H. O., Pandya, N. Y., and Jain, R. (2010). Ionospheric modulations due to solar flares over Ahmedabad. *Indian J. Radio Space Phys.* 39, 296–301.

Srećković, V. A., Šulić, D. M., Ignjatović, L., and Vujčić, V. (2021). Low ionosphere under influence of strong solar radiation: Diagnostics and modeling. *Appl. Sci. (Basel).* 11 (16), 7194. doi:10.3390/app11167194

Sripathi, S., Balachandran, N., Veenadhari, B., Singh, R., and Emperumal, K. (2013). Response of the equatorial and low-latitude ionosphere to an intense X-class solar flare (X7/2B) as observed on 09 August 2011. *J. Geophys. Res. Space Phys.* 118, 2648–2659. doi:10.1002/jgra.50267

Stauning, P. (1996). Investigations of ionospheric radio wave absorption processes using imaging riometer techniques. *J. Atmos. solar-terrestrial Phys.* 58 (6), 753–764. doi:10.1016/0021-9169(95)00072-0

Šulić, D. M., and Srećković, V. A. (2014). A comparative study of measured amplitude and phase perturbations of VLF and LF radio signals induced by solar flares. *Serb. Astron. J.* 188, 45–54. doi:10.2298/saj1488045s

Šulić, D. M., Srećković, V. A., and Mihajlov, A. A. (2016). A study of VLF signals variations associated with the changes of ionization level in the D-region in consequence of solar conditions. *Adv. Space Res.* 57, 1029–1043. doi:10.1016/j.asr.2015.12.025 1029–

Tao, C., Nishioka, M., Saito, S., Shiota, D., Watanabe, K., Nishizuka, N., et al. (2020). Statistical analysis of short-wave fadeout for extreme space weather event estimation. *Earth, Planets Space* 72, 173. doi:10.1186/s40623-020-01278-z

Tsurutani, B. T., Verkhoglyadova, O. P., Mannucci, A. J., Lakhina, G. S., Li, G., Zank, G. P., et al. (2009). A brief review of "solar flare effects" on the ionosphere. *Radio Sci.* 44, 1–14. doi:10.1029/2008rs004029

Xiong, B., Wan, W., Ning, B., Ding, F., Hu, L., Yu, Y., et al. (2014). A statistic study of ionospheric solar flare activity indicator. *Space weather.* 12, 29–40. doi:10.1002/2013SW001000

Yasyukevich, Y., Astafyeva, E., Padokhin, A., Ivanova, V., Syrovatskii, S., and Podlesnyi, A. (2018). The 6 September 2017 X-class solar flares and their impacts on the ionosphere, GNSS, and HF radio wave propagation. *Space weather.* 16 (8), 1013–1027. doi:10.1029/2018sw001932

Zhang, D. H., Mo, X. H., Cai, L., Zhang, W., Feng, M., Hao, Y. Q., et al. (2011). Impact factor for the ionospheric total electron content response to solar flare irradiation. *J. Geophys. Res. Space Phys.* 116 (A4). doi:10.1029/2010ja016089

Zolesi, B., and Cander, L. (2014). *Ionospheric prediction and forecasting*. New York Dordrecht London: Springer Geophysics, Springer Heidelberg, 33–43.

frontiers | Frontiers in Astronomy and Space Sciences

TYPE Original Research
PUBLISHED 13 July 2023
DOI 10.3389/fspas.2023.1125950

OPEN ACCESS

EDITED BY
Christoph Jacobi,
Leipzig University, Germany

REVIEWED BY
Knut Jacobsen,
Norwegian Mapping Authority, Norway
Mogese Wassaie Mersha,
Bahir Dar University, Ethiopia

*CORRESPONDENCE
Ojochenemi Ikani,
ojochenemiikani@gmail.com

RECEIVED 16 December 2022
ACCEPTED 21 June 2023
PUBLISHED 13 July 2023

CITATION
Ikani O, Okeke FN, Okpala KC, Okoh D and Rabiu B (2023), Diurnal and seasonal variations of the occurrence of ionospheric irregularities over Nigeria from GNSS data.
Front. Astron. Space Sci. 10:1125950.
doi: 10.3389/fspas.2023.1125950

Diurnal and seasonal variations of the occurrence of ionospheric irregularities over Nigeria from GNSS data

Ojochenemi Ikani[1,2]*, Francisca Nneka Okeke[1], Kingsley Chukwudi Okpala[1], Daniel Okoh[3,4] and Babatunde Rabiu[3,4]

[1]Department of Physics and Astronomy, University of Nigeria, Nsukka, Nigeria, [2]Center for Atmospheric Research, National Space Research and Development Agency, Kogi State University Campus, Anyigba, Nigeria, [3]United Nations African Regional Centre for Space Science and Technology Education—English, Obafemi Awolowo University Campus, Ile Ife, Nigeria, [4]Institute for Space Science and Engineering, African University of Science and Technology, Abuja, Nigeria

We investigate the occurrence of ionospheric irregularities in Nigeria during 2014, using the Global Navigation Satellite System (GNSS) total electron content (TEC) rate of change index (ROTI). We categorized days with |Dst| < 30 nT as quiet days and days with |Dst| ≥ 50 nT as disturbed days, during both the daytime and nighttime periods. Our results reveal significant latitudinal differences in both quiet and disturbed conditions. The quiet-time observations indicate that irregularities were consistent across all the stations. The occurrence was strong and consistent at CLBR station in Calabar, Nigeria, which is located further away from the geomagnetic equator (and closer to the southern anomaly crest) than the other receivers. TEC variability is greatly influenced by the geographical location of the Earth's magnetic field, while its spatial patterns of variability are modulated by the Earth's diurnal rotation. Near the September equinox, the occurrence of irregularities was inhibited during disturbed periods, but an opposite pattern was observed during the March equinox across all stations. Two peaks of occurrence were observed: one in March and the other in September respectively. The strength of irregularities was generally greater in March equinox compared to September equinox, and they were more pronounced during pre-midnight hours. This pattern could be attributed to the suppressing role of the dynamo electric field, requiring further investigation.

KEYWORDS

equatorial ionosphere, ionospheric irregularities, TEC, Roti, fluctuation indices

1 Introduction

Trans-ionospheric electromagnetic Global Navigation Satellite System (GNSS) signals may experience fluctuation in amplitude and phase due to irregularities in the plasma density of the Earth's ionosphere. These fluctuations are referred to as ionospheric scintillation and are primarily generated by ionospheric plasma bubbles, which are also known as small-scale ionospheric depletions (Kintner et al., 2007).

The sudden change in amplitude and phase of the radio signal has consequent impacts on the overall performance of practical applications using trans-ionospheric electromagnetic signals. (Kintner et al., 2007; Oladipo and Schüler, 2013a). The coupling processes in the

upper atmosphere involve several factors that influence the uplift of the F-layer and the occurrence of ionospheric irregularities around the magnetic equator. The eastward electric field, also known as the pre-reversal enhancement (PRE), causes uplift of the F-layer after sunset, creating favorable conditions for Rayleigh-Taylor instabilities. This process is influenced by several factors, such as Sq circuit, equatorial electrojet (EEJ), and penetration electric fields. At the equator, the uplift caused by PRE can lead to the formation of plasma bubbles. (Abdu et al., 1983; Kil et al., 2009).

Furthermore, several studies have shown that ionospheric irregularities typically occur around the magnetic equator and are usually observed shortly after sunset (Oladipo and Schüler, 2013b; Sharma et al., 2018; Bolaji et al., 2019; Bolaji et al., 2020). The occurrence of ionospheric irregularities at the equatorial region has been linked to the enhancement of the eastward electric fields that is usually observed around the post-sunset hours (Rastogi, 1980; Abdu et al., 1983; Fejer et al., 1999). The R-T instability occurs in the ionosphere when tenuous plasma (due to plasma depletion associated with the absence of solar radiation at that period) at the bottom of the F2-layer is accelerated into dense plasma. The R-T instability is triggered by post-sunset enhancement of eastward electric field (EEF) (De Rezende et al., 2007). This is referred to as a plasma bubble.

Several studies on the ionospheric irregularities and occurrence frequency of plasma bubble at different sectors and the seasonal, local time, longitude, latitude, solar and magnetic activities dependence have been undertaken by different authors (e.g., Sobral et al., 2002; Chu et al., 2005; Muella et al., 2008; Seemala and Valladares, 2011; Oladipo and Schüler, 2013a; Oladipo and Schüler, 2013b; Ngwira et al., 2013; Mungufeni et al., 2016; Okoh et al., 2017; Amaechi et al., 2018a; Amaechi et al., 2018b; Bolaji et al., 2019; Dugassa et al., 2019).

In the American sector, Chu et al. (2005) studied ionospheric irregularities and ionospheric plasma bubbles over Brazil. Their results showed that ionospheric irregularities and ionospheric plasma bubbles are more pronounced between 20:00 and 01:00 LST in October to March. The results of Sobral et al. (2002) also reported similar trend of occurrence to those of Chu et al. (2005). The results showed that scintillation occurs consistently from September to March. Similarly, the study of Kintner et al. (2007) over the Brazilian sector, showed that irregularities exhibit seasonal dependency with a maximum in December to January and a minimum near May to June.

Oladipo and Schuler (2013a) conducted a study on large-scale ionospheric irregularities in Franceville, Gabon, an equatorial station in the African sector, during the last high solar activity. The study showed seasonal dependence of the occurrence of ionospheric irregularities. Irregularities occurred from March to November with a minimum around June. Oladipo et al. (2014) used ROTIAVE obtained from 30 s RINEX data to study the occurrence of large-scale ionospheric irregularities at Ilorin, Nigeria. The study showed that irregularities occur at Ilorin between March and November, with most occurrences between 1900 LST and 2400 LST.

Mungufeni et al. (2016) investigated the solar activity pattern of irregularities using four different stations spanning from east to west in the African region, employing TEC index derived from GNSS data. The study reported an asymmetry in the occurrence of irregularities during the two equinoxes over East Africa and an opposite trend over West Africa. Okoh et al. (2017) studied the occurrence frequency of equatorial plasma bubbles over West Africa using data from an all-sky airglow imager and GNSS receivers. The study found that most post-midnight plasma bubbles were observed around the months of December to March and that most plasma bubble occurrences were found during equinoxes and least during solstices.

Bolaji et al. (2020) used GPS data to investigate the latitudinal distribution of irregularities in the African region during quiet and storm periods. The study found that irregularities are mostly observed between 19:00 LST and 00:00 LST during quiet conditions regardless of the hemisphere. In contrast to quiet-time observations, irregularities were absent in all latitudes during the considered storm days.

It could be seen that most of these studies involving ionospheric irregularities in the African region largely consider data only during the geomagnetic storms and specific solar activity conditions within limited coverage in terms of geography or time in a particular month. It also appears that most studies have been carried out using a single station or few to investigate the several aspects of its variation. Furthermore, studies to characterize the ionospheric irregularities in the African equatorial region is yet to be exhaustive despite the growing need for the specification of their effect on critical GNSS technologies. The aim of this study is to investigate the occurrence characteristics of the irregularities in Nigeria, Africa. We employ data from ground-based GPS receivers at different longitudes under similar condition. This strategy can improve our current understanding on the physical mechanisms responsible for the development and evolution of ionospheric irregularities in the sector. The strategy of utilizing data from multiple ground-based GPS receivers situated at different longitudes under similar conditions can improve the existing understanding of ionospheric irregularities in several ways. Firstly, it can provide a more comprehensive picture of the spatial and temporal variations in ionospheric irregularities. Secondly, it can help identify and differentiate between the various physical mechanisms responsible for the development of ionospheric irregularities. Lastly, this strategy can improve the accuracy of models used for GNSS positioning and navigation by providing a more precise characterization of ionospheric irregularities.

Different fluctuation indices have been adopted by different researchers to study ionospheric irregularities. For example, Mendillo et al. (2000) and Lee et al. (2009) employed FP index, Li et al. (2007) used power spectral index (n) while Pi et al. (1997); Oladipo and Schuler 2013a; Oladipo and Schüler, 2013b), Li et al. (2010) and Deng et al. (2014) used the derived TEC fluctuations, commonly referred to as ionospheric irregularities—and—which is utilized by Rate of TEC (ROT) indices. In this study, we used GPS-TEC derived indices to detect ionospheric irregularities. The Rate of change of TEC index (ROTI) was employed. The observations of ground-based GPS receivers located in Nigeria are described in Section 2. The occurrence distributions of ionospheric irregularities detected by GPS over the region are presented and discussed in Sections 3 and 4 respectively. Finally, we offer concluding remarks in Section 5.

2 Data and analyses

We use GNSS data in Receiver Independent Exchange (RINEX) format obtained from the Nigerian GNSS Reference Network (NIGNET) server (http://www.nignet.net/data/). At the time of writing of this paper, the website was down. Figure 1 shows the geographical distribution of the GNSS receivers utilized in this research across Nigeria. The station names, codes, and the geodetic and geomagnetic information of the stations used are presented in Table 1. The GPS-TEC analysis software developed by Gopi Seemala of the Indian Institute of Geomagnetism was used to estimate the value of TEC from the GPS RINEX files. To eliminate any multipath effects an elevation cut-off mask of 45° is used. Different geomagnetic day conditions were considered using Disturbance storm time (Dst) index. The Dst index data were obtained from NASA's OMNIweb Service (https://omniweb.gsfc.nasa.gov). The monthly average value of TEC for each hour is calculated from the diurnal values of TEC for all the days in a month. Further, the means of the daily ROTI profiles for all of the quiet (or disturbed) days in the month were computed. The quiet days are days in which the absolute values of the |Dst| indices are consistently less than 30 nT (|Dst| < 30 nT) for all hours in the day, while disturbed days are days in which one or more hours in the day have absolute |Dst| indices greater than or equal to 50 nT (|Dst| ≥ 50 nT) for the year 2014 for both the daytime and nighttime period.

The months in the year were further grouped into four, namely, i) February, March and April to represent the March equinox (MEQU), ii) May, June and July as June solstice (JSOL), iii) August, September and October as September equinox (SEQU), and iv) November, December and January as December solstice (DSOL) for the seasonal study.

ROTI is a parameter derived from time variation of TEC [i.e., 30-s rate of change of TEC (ROT) given by Eq. 2.1].

$$ROT = \frac{dTEC}{dt} \tag{2.1}$$

The computation of ROT was performed using Eq. 2.2.

$$ROT(t) = \frac{STEC(t+\Delta t) - STEC(t)}{\Delta t} \times \cos\theta(t) \tag{2.2}$$

In this equation, "t" represents the instantaneous time, while Δt denotes the sampling interval, which was set at 30 s in our study. The inclusion of the term cos θ (t) in the formula aimed to compensate for the variations in signal path length caused by the changing zenith angle. When radio signals travel from satellites at lower elevations (resulting in higher zenith angles), they traverse a more extensive portion of the ionosphere. By incorporating the cos θ (t) term, we were able to eliminate the influence of these longer signal path changes in the ionosphere.

Pi et al. (1997) introduced ROTI as the standard deviation of ROT over 5-min period, and it is given by the expressionin Eq. 2.3.

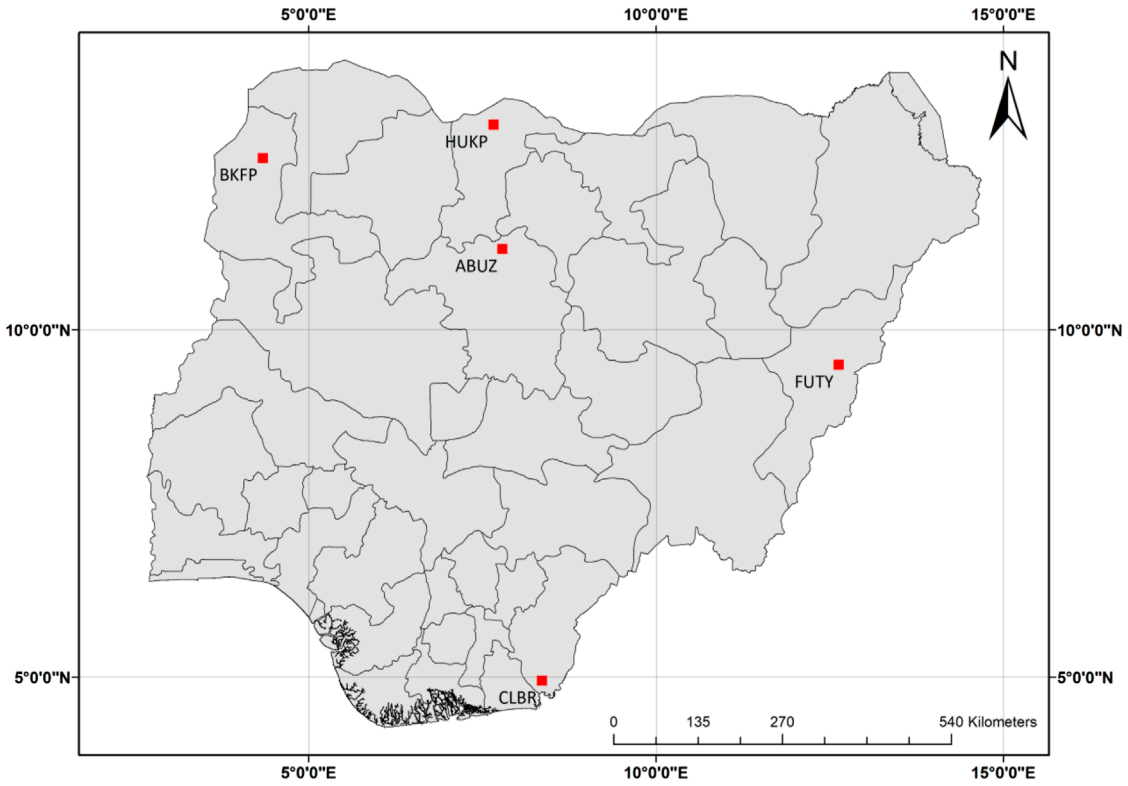

FIGURE 1
Locations of the GNSS receivers used in this study.

$$ROTI = \sqrt{< ROT^2 > - < ROT^2 >} \quad (2.3)$$

Mendillo et al. (2000), using the expression in Eq. 2.3 computed the average ROTI ($ROTI_{ave}$) ($ROTI_{ave}$ is a good proxy that indicate the 30-min phase fluctuation level over a location) as the average of ROTI over 30 min interval for a satellite and then the average over all satellites in view. This result gives the average level of irregularities (phase fluctuation) for half an hour over the station.

$$ROTI_{ave}(0.5h) = \frac{1}{nsat(0.5h)} \sum_{n}^{nsat} \cdot \sum_{i}^{k} \frac{ROTI(n, 0.5h, i)}{k} \quad (2.4)$$

where n is the satellite number, h is hour (0, 0.5, 1 … 23.5 UT), i is the 5 min section within half an hour (i = 1, 2, 3, 4, 5, and 6), nSat (0.5 h) is the number of satellites observed within half an hour, and k is the number of ROTI values available within half an hour for a particular satellite. To detect the presence of irregularities, the classification by Oladipo and Schuler (2013a) was adopted in this study. In this classification, $ROTI_{ave}$ < 0.4 TECU/min indicates the background irregularities (i.e., absence of irregularities), 0.4 < $ROTI_{ave}$ < 0.8 indicates the presence of moderate irregularities, and $ROTI_{ave}$ > 0.8 indicates the occurrence of severe irregularities. As stated earlier, the results and discussions of the study are presented in Section 3.

3 Results

Figures 2–5 show the diurnal plots of the rate of total electron content index (ROTI) over all the stations for the representative months (March, June, September and December) of the year 2014. The vertical axis shows the ROTI while the horizontal axis shows the days of the month. The white spaces show periods of data unavailability. The figures show presence of ionospheric irregularities across the entire stations with severe occurrence experienced at CLBR.

Figures 2–5 illustrate diurnal plots of the Rate of Total Electron Content Index (ROTI) over a 5-min interval, which is a valuable metric for quantifying short-term variability of ionospheric electron density. The analysis of these figures provides important information regarding the short-term variability of ROTI, highlighting the occurrence of spikes and extreme values. This information is critical

TABLE 1 GNSS receivers used in this study.

Station code	Station location	Geographic Lat. (deg.)	long. (deg.)	Geomagnetic Lat. (deg.)	long. (deg.)
ABUZ	Zaria	11.17	7.79	−0.62	79.88
BKFP	Birnin Kebbi	12.48	4.34	+0.72	76.72
CLBR	Calabar	4.95	8.36	−4.30	80.09
HUKP	Katsina	12.96	7.66	+1.08	79.84
FUTY	Yola	9.50	12.63	−1.17	84.44

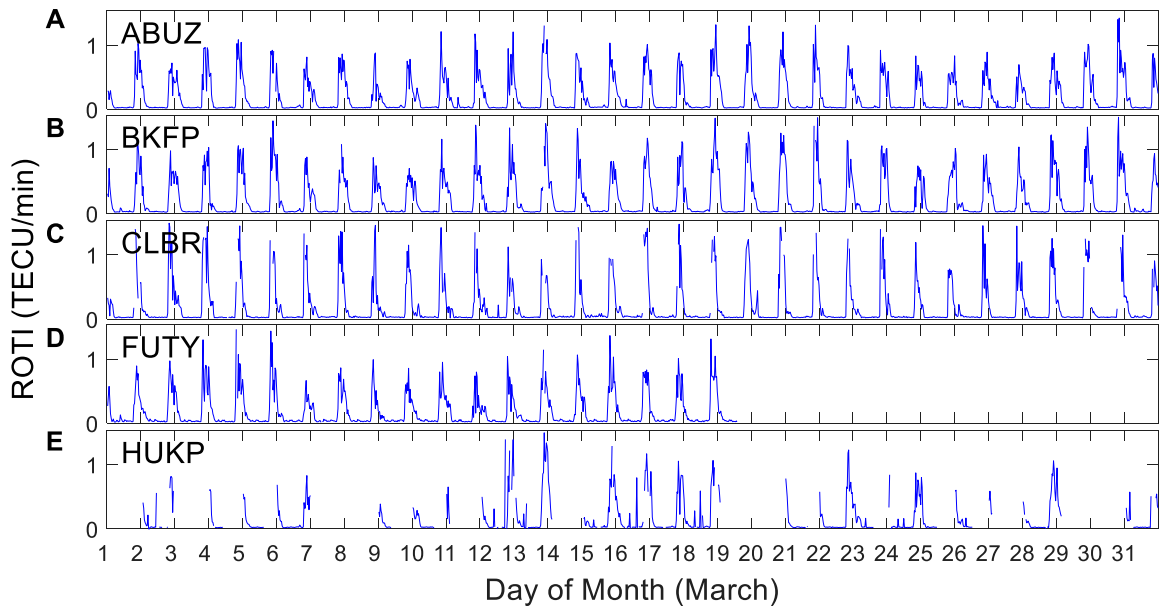

FIGURE 2
Diurnal plots of the rate of total electron content index (ROTI) for **(A)** ABUZ, **(B)** BKFP, **(C)** CLBR, **(D)** FUTY, and **(E)** HUKP, during March 2014.

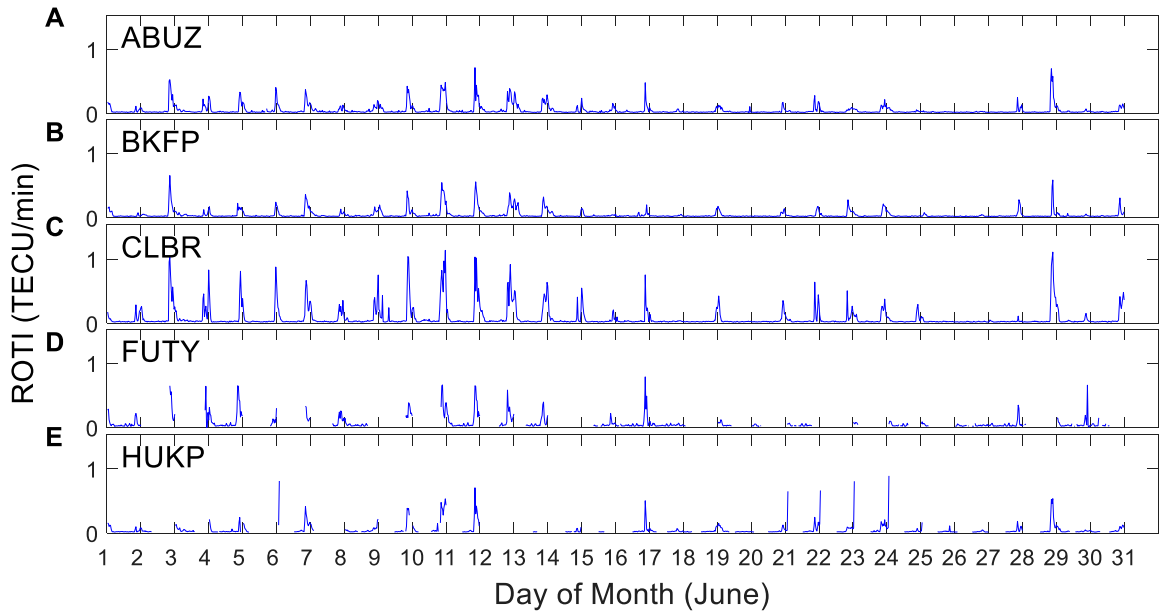

FIGURE 3
Diurnal plots of the rate of total electron content index (ROTI) for **(A)** ABUZ, **(B)** BKFP, **(C)** CLBR, **(D)** FUTY, and **(E)** HUKP, during June 2014.

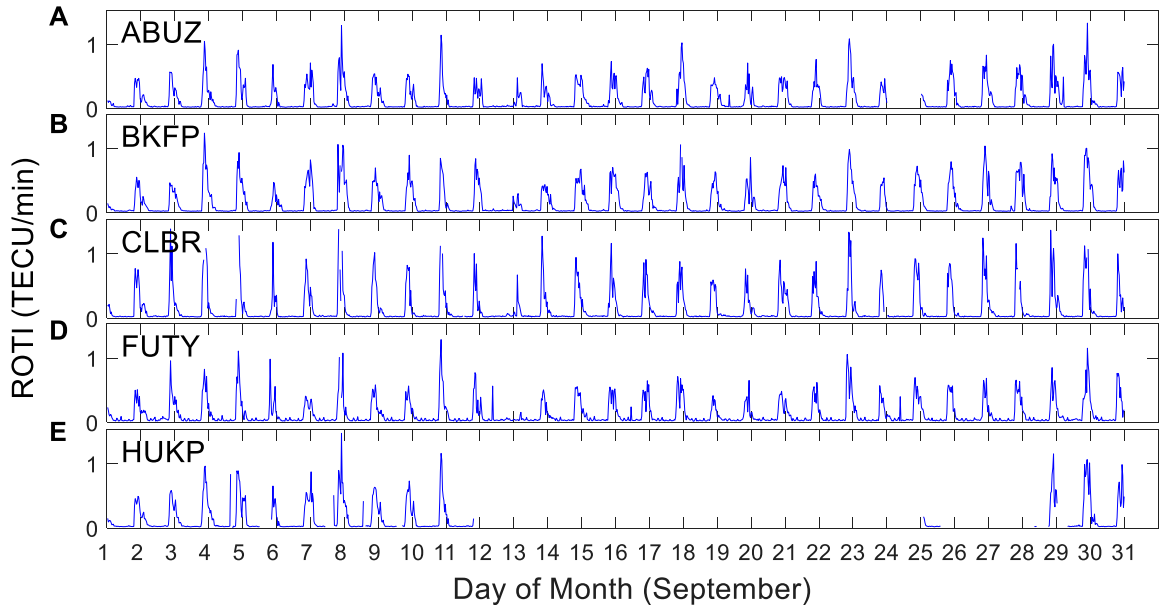

FIGURE 4
Diurnal plots of the rate of total electron content index (ROTI) for **(A)** ABUZ, **(B)** BKFP, **(C)** CLBR, **(D)** FUTY, and **(E)** HUKP, during September 2014.

in understanding the dynamics of the ionosphere and its impact on radio wave propagation.

To quantify the long-term trend of ROTI variation, we calculated the ROTIave, which represents the Rate of Total Electron Content Index Average over a 30-min interval. Figure 6 illustrates the results of this analysis. The computation of the ROTIave allows us to examine the long-term trends of ROTI variation and identify any systematic changes that may occur over time.

Figure 6 shows the annual contour plots of $ROTI_{ave}$ over all the five stations investigated in this study for the year 2014. The color bars indicate magnitudes of the $ROTI_{ave}$, and white spaces represent times when there are no available data from the stations. A common reason for why there may not be available data is power outage. As shown in the figure, occurrence of ionospheric irregularities is conspicuously observed during the hours from around 19:00 to 05:00 LST. High value of ROTI is observed during this time interval.

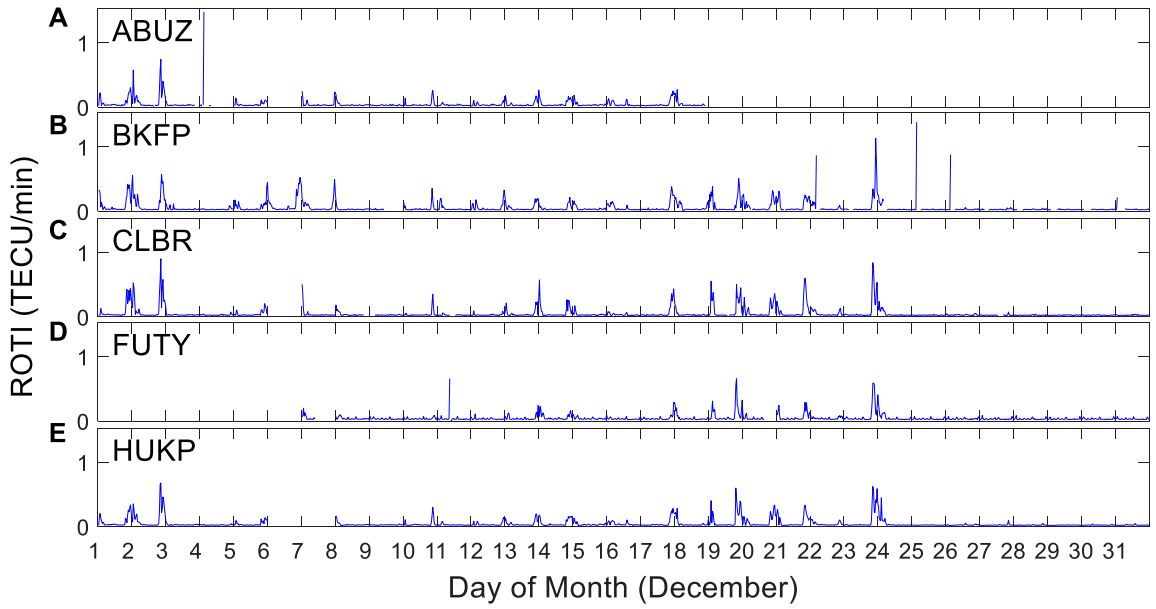

FIGURE 5
Diurnal plots of the rate of total electron content index (ROTI) for **(A)** ABUZ, **(B)** BKFP, **(C)** CLBR, **(D)** FUTY, and **(E)** HUKP, during December 2014.

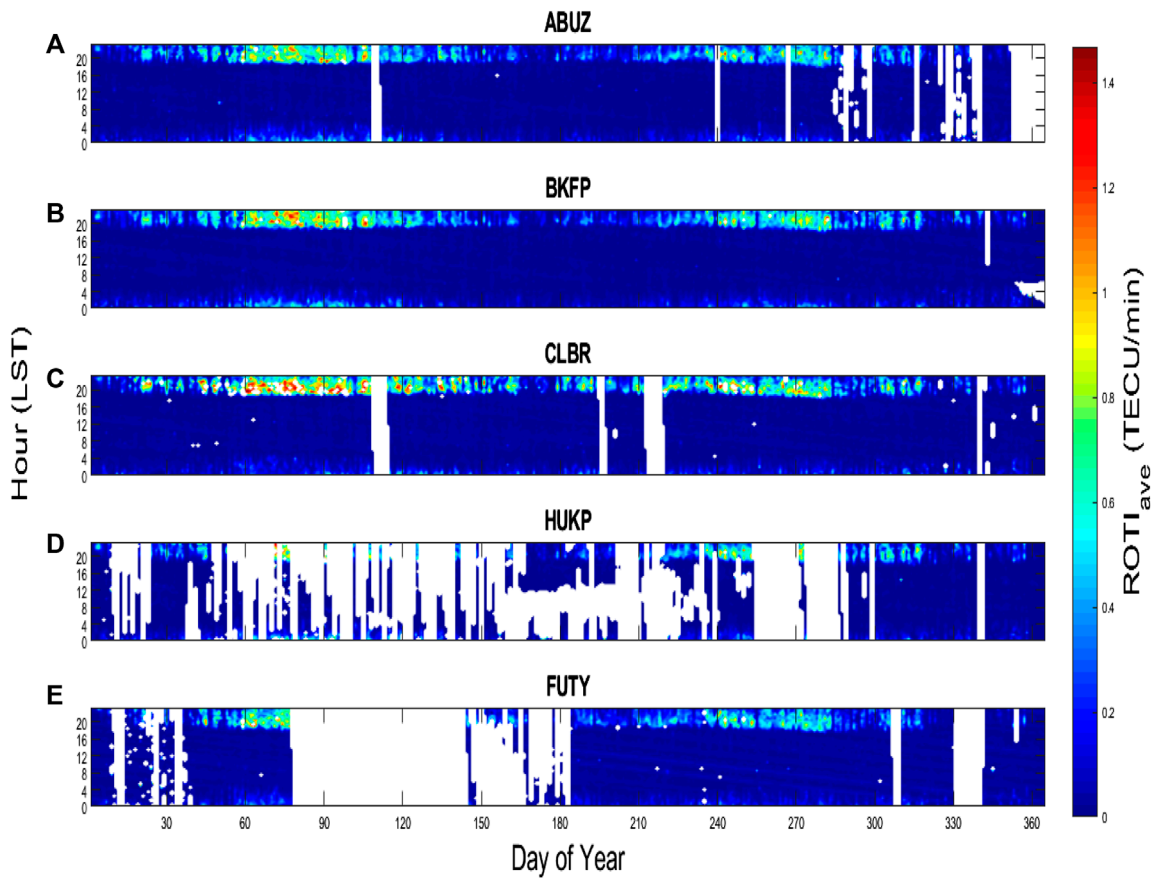

FIGURE 6
Contour plots showing the fluctuation occurrence over the entire stations, **(A)** ABUZ, **(B)** BKFP, **(C)** CLBR, **(D)** FUTY and **(E)** HUKP, during 2014, as a function of local solar time (LST) and day of the year 2014. The magnitude of the ROTI$_{ave}$ values is indicated by the color bar in which the colors range from blue (indicating low values) to red (indicating high values). The white spaces indicate periods of data unavailability.

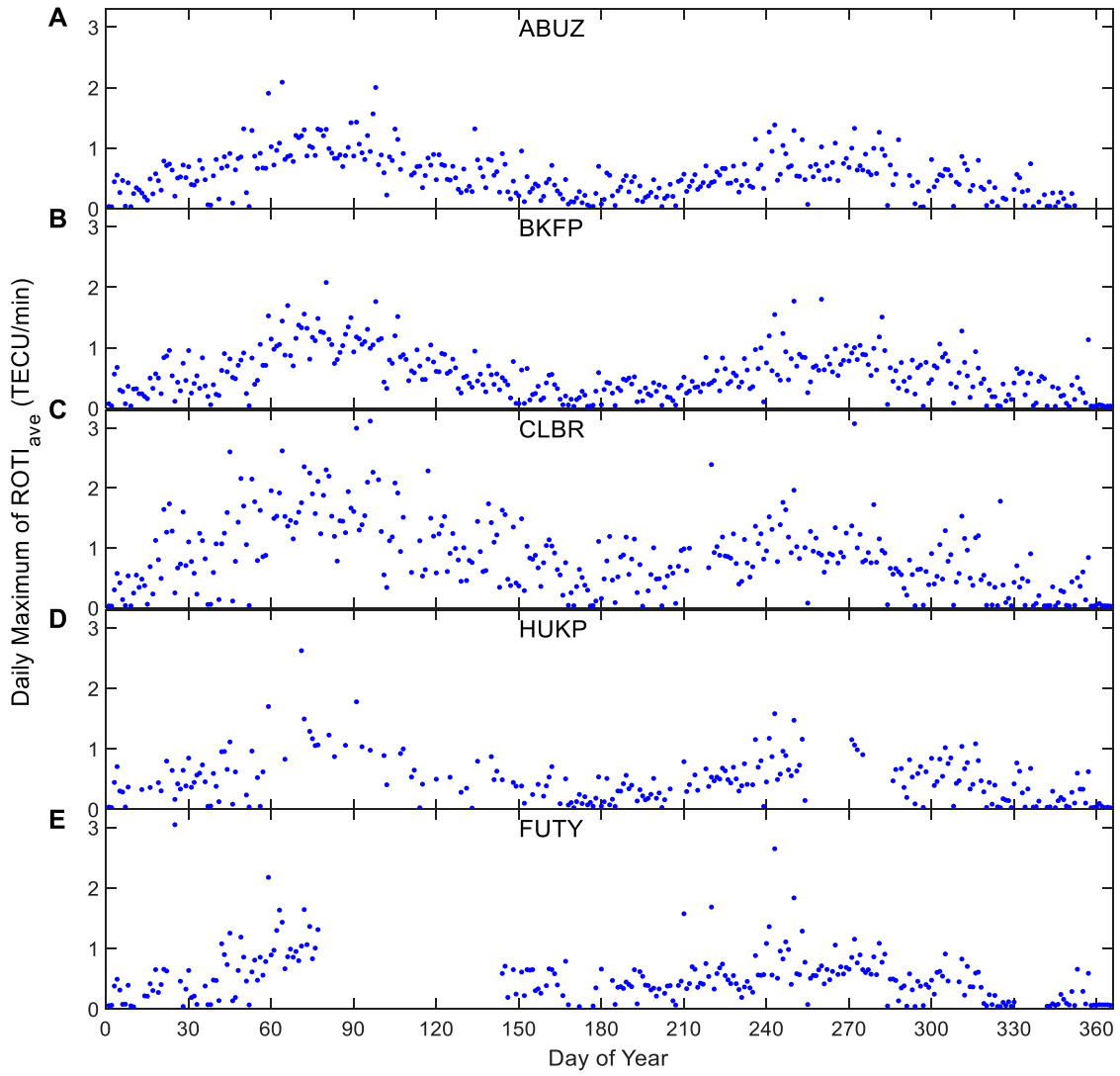

FIGURE 7
Daily maxima of ROTI$_{ave}$ values for ABUZ, BKFP, CLBR, HUKP, and FUTY, during year 2014.

To investigate the day-to-day peaks of ROTI, we obtained the maximum values of ROTI$_{ave}$ occurring after local sunset (18:00 LST) for each day. Figure 7 presents results of the daily maximum ROTI$_{ave}$ values. The results show that the highest values of ROTI are experienced at the CLBR station.

Figure 8 shows the monthly variation of ROTI during the quiet and disturbed days over the stations for March, September, and December respectively, during the year 2014. The vertical axis shows the ROTI values while the horizontal axis shows the LST(Hr). There was no data availability during June solstice and also during the disturbed days at both FUTY and HUKP respectively. High values of ROTI were recorded during March equinox than September equinox for both quiet and disturbed geomagnetic conditions. The Occurrence of irregularity was largely inhibited during the December solstice for both the quiet and disturbed geomagnetic conditions. This is opposite to the observations during the equinoxes.

4 Discussion

In this present study, the occurrence of ionospheric irregularities in Nigeria during 2014 was investigated using the Global Navigation Satellite System (GNSS) total electron content (TEC) rate of change index (ROTI). The figures show that there is a presence of ionospheric irregularities across all the stations, with severe occurrence experienced at CLBR. The high values of ROTI recorded at CLBR may be attributed to the difference in the values of the geomagnetic latitude of the stations, as described in Table 1. All the five stations considered in this study are around the geomagnetic equator, but CLBR is farther away from the geomagnetic equator (and closer to the southern anomaly crest) than the other stations. Adeniyi et al. (2021) stated that the occurrence probability of severe ionospheric irregularities is less likely around the magnetic equator than on both sides of the equator, particularly around the crest region.

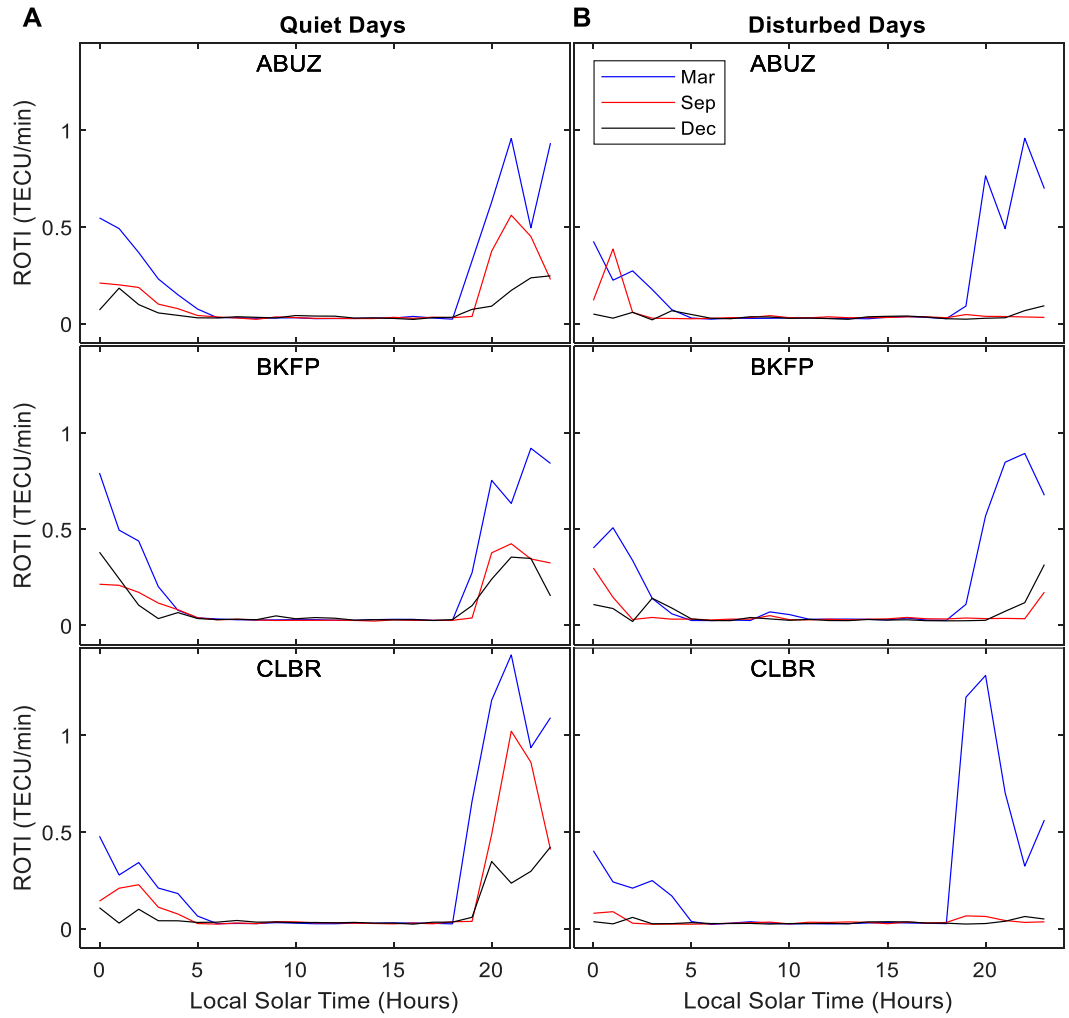

FIGURE 8
Monthly variation of ROTI during quiet and disturbed days (panel **(A)** quiet days and **(B)** for disturbed days) for ABUZ, BKFP, and CLBR, during March, September and December 2014.

The occurrence of irregularities was observed to be higher in equinoxes than in solstices with peak values of occurrence experienced in March and September respectively. As an explanation to why greater ROTI magnitudes are observed during the equinoxes than during the solstices, Tsunoda (1985) showed that the occurrence of plasma bubbles was maximum when sunsets in the conjugate E-region is simultaneous. Simultaneous sunset is expected to intensify prereversal enhancement (Nishioka et al., 2008). The angle between the geomagnetic declination and sunset terminator line, α, was introduced as a proxy of the simultaneous sunset in the conjugate points (Burke et al., 2004). The sunset times at conjugate E regions, south and north of the magnetic equator and along the magnetic meridian of each of the stations becomes close in equinox seasons, leading to increased conductivity gradient (Mungufeni et al., 2016). This might account for the severe ionospheric irregularities observed across all the stations during the equinoctial months.

Figure 6 shows that the appearance of irregularities typically begins very weakly around 19:00 LST, then the peak of ROTI magnitude is attained around 21:00 LST, and thereafter begin to decrease in magnitude until the irregularity finally disappears around 05:00 LST by the latest. This result is in agreement with previous studies involving individual locations in the region (e.g., Mungufeni et al., 2016; Bolaji et al., 2020 etc).

The occurrence of severe ionospheric irregularities at CLBR and the asymmetry in their magnitude between the equinoxes and solstices were investigated using the average rate of change of TEC index ($ROTI_{ave}$), which is a good proxy for phase fluctuation level over a location. Figure 7 shows the maximum $ROTI_{ave}$ values occurring after local sunset (18:00 LST) for each day. The strengths of ionospheric irregularities observed during the March equinox are greater than during the September equinox, and severe ionospheric irregularities are more pronounced during pre-midnight hours than during post-midnight hours, as seen in Figures 6, 7.

Moreover, ROTI magnitudes exhibit higher values during the equinoxes (March and September) compared to the solstices (June and December), a pattern observed in previous studies on ionospheric irregularities in the equatorial region of Africa

by Olwendo et al. (2013); Amabayo et al. (2014), Mungufeni et al. (2016 ab), and Okoh et al. (2017). This similarity is despite the fact that these works were conducted using observations made at different points in time and space. For example, Okoh et al. (2017) conducted their study using observations obtained during years 2015–2017, which is the declining phase of solar cycle 24, while the present study used observations from 2014, which is the peak phase of the solar cycle.

According to Rastogi (1980), one of the conditions for starting spread F over the equator is the existence of strong plasma density gradients. The production of the ionosphere is mainly dependent on the intensity of the ionising radiation from the sun, which varies with the elevation of the sun (Hargreaves, 1992). During equinox months, the elevation of the sun is high over the equatorial region, leading to increased ionization and the creation of the required plasma gradient.

The observed severe ionospheric irregularities occurring mostly during 20:00–00:00 LST (pre-midnight hours) over the stations are in line with the existing theory of the generation of ionospheric irregularities. During the nighttime, the uplift of the F-layer after the sunset by the eastward electric field at the equatorial region, known as the pre-reversal enhancement (PRE), creates favorable conditions for Rayleigh-Taylor instability (Adeniyi et al., 2021), where the depleted plasma at the bottomside F-region due to absence of solar radiation around that time rises up to the topside F-layer in the form of ionospheric irregularities or plasma bubbles (Basu et al., 1999; Fejer et al., 1999; Cervera and Thomas, 2006; Li et al., 2008; Mungufeni et al., 2016).

Figure 8 displays the monthly variation of Rate of TEC index (ROTI) at different stations during quiet and disturbed days in March, September, and December. Peak ROTI values were recorded at CLBR during both quiet and disturbed geomagnetic Irregularity occurrence was largely inhibited during December solstice for both quiet and disturbed conditions, opposite to the observations during the equinoxes. Most stations showed variations in irregularity strength and occurrence time. During September equinox, irregularity occurrence was largely inhibited, while an opposite pattern was observed during the March equinox across all stations.

The inhibition of the irregularities during the September equinox may be attributed to storm-induced disturbance dynamo mechanism, which may inhibit the occurrence of ionospheric irregularities in the region due to the action of disturbance electric fields. In the postsunset period, the equatorial F region rises to higher altitudes, where ion-neutral collision frequency is quite small, thereby creating conditions favorable for Rayleigh-Taylor (R-T) instability (Aarons, 1991). However, during magnetically disturbed days, the sunset-postsunset height rise is inhibited (Martyn, 1959; Jayachandran et al., 1987). Thus, the conditions may not be conducive for irregularity generation/growth during these periods (Aarons, 1991). It is well known that the Rayleigh-Taylor (R-T) and plasma density instabilities that cause the development of irregularities in the ionosphere are affected by some external driving forces such as electric fields, the magnetic field and neutral wind (Li et al., 2011). Due to the uniqueness of the magnetic orientation at the equatorial region, the ionosphere at the equatorial region is sensitive to any change in electric field. During geomagnetic storms, strong electric field which originate from the magnetosphere can penetrate down to the low latitudes (Buonsanto, 1999; Bolaji et at., 2018). An eastward (or westward) electric field during the daytime may favor (or impede) the upward drift of plasma (Bolaji et at., 2018). The injection of the eastward electric field during the disturbed days may have intensified the normal upward plasma drift and may have favored the development of irregularities during the march equinox.

5 Conclusion

In this study, we investigated occurrence and distributions of ionospheric irregularities over Nigeria, an equatorial region, using TEC derived indices (ROTI and $ROTI_{ave}$) from ground-based GNSS stations in Nigeria. Our findings revealed significant latitudinal differences in both quiet and disturbed conditions. During quiet periods, we observed consistent irregularities across all stations, with particularly strong and consistent occurrences at the CLBR station in Calabar, Nigeria. This station, located farther from the geomagnetic equator and closer to the southern anomaly crest, exhibited a higher occurrence of irregularities. It became evident that TEC variability is greatly influenced by the geographical location of the Earth's magnetic field, while the spatial patterns of variability are modulated by the Earth's diurnal rotation.

Our results show a level of consistency with previous studies that have employed different indices and various methods to study the occurrence of ionospheric irregularities over the African equatorial region. However, some new findings related to the African equatorial region are presented below:

1) This study reveal difference in the strength of ionospheric irregularities over stations located within the same equatorial region in Nigeria. This was attributed to the difference in the geomagnetic latitudes of the stations.
2) The variability of TEC is greatly influenced by the geographical location of the Earth's magnetic field, while its spatial patterns of variability are modulated by the Earth's diurnal rotation (Calabia, A., & Jin, S. 2020). At equatorial stations located on the north side of the magnetic equator, there is a significant depletion of TEC. This variation affects the accuracy of satellite-based communication and navigation systems. (Shah et al., 2022).
3) Significant quiet time diurnal and seasonal equatorial TEC irregularities (as shown in high values of ROTI) were observed during 2014. The diurnal irregularity was most noticeable during the night period with a peak at 21:00 LST.
4) Seasonal quiet time irregularities exhibited a bimodal feature showing equinoctial peaks. Observed Equinoctial asymmetry in the strength of ionospheric TEC irregularities confirm observations from earlier studies in other (near) equatorial regions in Africa (e.g., Olwendo et al., 2013).
5) The seasonal TEC irregularities during disturbed times were characterized by stronger TEC irregularities in the March equinox as compared with the September equinox season. The reduction of the ROTI and ROT during the September equinox could be attributed to the suppressing role of the dynamo electric field. This requires further investigation.

To improve the analysis of irregularities in Nigeria's statistics, a larger dataset from multiple years should be considered. Thus, it is

suggested that future studies on this topic collect and analyze data from multiple years (if possible) to gain a more detailed insight into the matter and provide a basis for evidence-based policy decisions.

Data availability statement

The raw data supporting the conclusion of this article will be made available by the authors, without undue reservation.

Author contributions

All authors listed have made a substantial, direct, and intellectual contribution to the work and approved it for publication.

Acknowledgments

The authors acknowledge the Nigerian GNSS Reference Network (NIGNET) (http://www.nignet.net/data/) for making the GPS data available to the public. The authors also thank Gopi Seemala of the Indian Institute of Geomagnetism, India, for providing the GPS TEC analysis software. The NASA-Space Physics Data Facility, Goddard Space Flight Center (https://omniweb.gsfc.nasa.gov/form/dx1.html) is acknowledged for the provision of the Dst|index. Ikani Ojochenemi would like to specially appreciate Center for Atmospheric Research's Space Environment Research Laboratory (SERL), Abuja, for the opportunity to have access to the research facility at the laboratory during which this study was carried out. Sincere appreciation to Christoph Jacobi and the reviewers for helping to improve the manuscript.

Conflict of interest

The authors declare that the research was conducted in the absence of any commercial or financial relationships that could be construed as a potential conflict of interest.

Publisher's note

References

Aarons, J. (1991). The role of the ring current in the generation or inhibition of equatorial F-layer irregularities during magnetic storms. *Radio Sci.* 26, 1131–1149. doi:10.1029/91rs00473

Abdu, M. A., Medeiros, R. T., Bittencourt, J. A., and Batista, I. S. (1983). Vertical ionization drift velocities and range type spread F in the evening equatorial ionosphere. *J. Geophys. Res.* 88, 399–402. doi:10.1029/JA088iA01p00399

Adebiyi, S. J., Ikubanni, S. O., Bolaji, O. S., Fashae, J., Adebesin, B., Joshua, B., et al. (2021). Equatorial F-region irregularities at different seasons in Africa. *Adv. Space Res.* 67 (3), 1850–1863. doi:10.1016/j.asr.2021.04.025

Amabayo, E. B., Edward, E., Cilliers, P. J., and Habarulema, J. B. (2014). Climatology of ionospheric scintillations and TEC trend over the Ugandan region. *Adv. Space Res.* 53 (5), 734–743. doi:10.1016/j.asr.2013.12.015

Amaechi, P. O., Oyeyemi, E. O., and Akala, A. O. (2018a). Geomagnetic storm effects on the occurrences of ionospheric irregularities over the African equatorial/low-latitude region. *Adv. Space Res.* 61 (8), 2074–2090. doi:10.1016/j.asr.2018.01.035

Amaechi, P. O., Oyeyemi, E. O., and Akala, A. O. (2018b). The response of African equatorial/low-latitude ionosphere to 2015 St. Patrick's Day geomagnetic storm. *Space weather* 16, 601–618. doi:10.1029/2017sw001751

Basu, S., Groves, K. M., Quinn, J. M., and Doherty, P. (1999). A comparison of TEC fluctuations and scintillations at Ascension Island. *J. Atmos. Solar-Terrestrial Phys.* 61 (15), 1219–1226. doi:10.1016/s1364-6826(99)00052-8

Bolaji, O. S., Adebiyi, S. J., and Fashae, J. B. (2019). Characterization of ionospheric irregularities at different longitudes during quiet and disturbed geomagnetic conditions. *J. Atmos. Solar-Terrestrial Phys.* 182, 93–100. doi:10.1016/j.jastp.2018.11.007

Bolaji, O. S., Adebiyi, S. J., Fashae, J. B., Ikubanni, S. O., Adenle, H. A., and Owolabi, C. (2020). Pattern of latitudinal distribution of ionospheric irregularities in the African region and the effect of March 2015 St. Patrick's Day storm. *J. Geophys. Res. Space Phys.* 125, e2019JA027641. doi:10.1029/2019JA027641

Buonsanto, M. J. (1999). Ionospheric storm – a review. *Space Sci. Rev.* 88, 563–601. doi:10.1023/a:1005107532631

Burke, W. J., Gentile, L. C., Huang, C. Y., Valladares, C. E., and Su, S. Y. (2004). Longitudinal variability of equatorial plasma bubbles observed by DMSP and ROCSAT-1. *J. Geophys. Res. Space Phys.* 109, A12301. doi:10.1029/2004ja010583

Calabia, A., and Jin, S. (2020). New modes and mechanisms of long-termionospheric TEC variations from globalionosphere maps. *J. Geophys. Res. Space Phys.* 125, e2019JA027703. doi:10.1029/2019JA027703

Cervera, M. A., and Thomas, R. M. (2006). Latitudinal and temporal variation of equatorial ionospheric irregularities determined from GPS scintillation observations. *Ann. Geophys.* 24, 3329–3341. doi:10.5194/angeo-24-3329-2006

Chu, F. D., Liu, J. Y., Takahashi, H., Sobral, J. H. A., Taylor, M. J., and Medeiros, A. F. (2005). The climatology of ionospheric plasma bubbles and irregularities over Brazil. *Ann. Geophys.* 23, 379–384. doi:10.5194/angeo-23-379-2005

De Rezende, L. F. C., De Paula, E. R., Batista, I. S., Kantor, I. J., and De Assis Honorato Muella, M. T. (2007). Study of ionospheric irregularities during intense magnetic storms. *Braz. J. Geophys.* 25, 151–158. doi:10.1590/s0102-261x2007000600017

Deng, B., Huang, J., Kong, D., Xu, J., Wan, D., and Lin, G. (2014). Temporal and spatial distributions of TEC depletions with scintillations and ROTI over south China. *Adv. Space Res.* 55 (1), 259–268. doi:10.1016/j.asr.2014.10.006

Dugassa, T., Habarulema, J. B., and Nigussie, M. (2019). Longitudinal variability of occurrence of ionospheric irregularities over the American, African and Indian regions during geomagnetic storms. *Adv. Space Res.* 63 (11), 2609–2622. doi:10.1016/j.asr.2019.01.001

Fejer, B. G., Scherliess, L., and de Paula, E. R. (1999). Effects of the vertical plasma drift velocity on the generation and evolution of equatorial spread F. *J. Geophys. Res.* 104, 19859–19869. doi:10.1029/1999ja900271

Hargreaves, J. K. (1992). *The solar-terrestrial environment*. The Pitt building, Trumpington Street, Cambridge: Cambridge University Press. doi:10.1017/CBO9780511564570

Jayachandran, B., Balan, N., Nampoothiri, S. P., and Rao, P. B. (1987). HF Doppler observations of vertical plasma drifts in the evening F region at the equator. *J. Geophys. Res.* 92 (11), 11253. doi:10.1029/JA092iA10p11253

Kil, H., Heelis, R. A., Paxton, L. J., and Oh, S. J. (2009). Formation of a plasma depletion shell in the equatorial ionosphere. *J. Geophys. Res. Space Phys.* 114 (A11), A11302. doi:10.1029/2009JA014369

Kintner, P. M., Ledvina, B. M., and de Paula, E. R. (2007). GPS and ionospheric scintillations. *Space weather* 5, S09003. doi:10.1029/2006SW000260

Lee, C. C., Chu, F. D., Chen, W. S., Liu, J. Y., Su, S. Y., Liou, Y. A., et al. (2009). Spread F, GPS phase fluctuations, and plasma bubbles near the crest of equatorial ionization anomaly during solar maximum. *J. Geophys. Res. Space Phys.* 114 (A8), A08307. doi:10.1029/2009ja014195

Li, G., Ning, B., Abdu, M. A., Yue, X., Liu, L., Wan, W., et al. (2011). On the occurrence of post-midnight equatorial F region irregularities during the June solstice. *J. Geophys. Res.* 116 (A4), A04318. doi:10.1029/2010JA016056

Li, G., Ning, B., Hu, L., Liu, L., Yue, X., Wan, W., et al. (2010). Longitudinal development of low-latitude ionospheric irregularities during the geomagnetic storms of July 2004. *J. Geophys. Res. Space Phys.* 115 (A4), 1978–2012. doi:10.1029/2009ja014830

Li, G., Ning, B., Liu, L., Ren, Z., Lei, J., and Su, S. Y. (2008). The correlation of longitudinal/seasonal variations of evening equatorial pre-reversal drift and of plasma bubbles. *Ann. Geophys.* 25 (9), 2571–2578. doi:10.5194/angeo-25-2571-2007

Li, G., Ning, B., and Yuan, H. (2007). Analysis of ionospheric scintillation spectra and TEC in the Chinese low latitude region. *Earth Planets Space* 59, 279–285. doi:10.1186/bf03353105

Martyn, D. F. (1959). The normal F region of the ionosphere. *Proc. IRE* 47, 147–155. doi:10.1109/jrproc.1959.287259

Mendillo, M., Lin, B., and Aarons, J. (2000). The application of GPS observations to equatorial aeronomy. *Radio Sci.* 35 (3), 885–904. doi:10.1029/1999rs002208

Muella, M. T. A. H., de Paula, E. R., Kantor, I. J., Batista, I. S., Sobral, J. H. A., Abdu, M. A., et al. (2008). GPS L-band scintillations and ionospheric irregularity zonal drifts inferred at equatorial and low-latitude regions. *J. Atmos. Solar-Terrestrial Phys.* 70, 1261–1272. doi:10.1016/j.jastp.2008.03.013

Mungufeni, P., Habarulema, J. B., and Jurua, E. (2016). Trends of ionospheric irregularities over African low latitude region during quiet geomagnetic conditions. *J. Atmos. Solar-Terrestrial Phys.* 138-139, 261–267. doi:10.1016/j.jastp.2016.01.015

Ngwira, C. M., Seemala, G. K., and Habarulema, J. B. (2013). Simultaneous observations of ionospheric irregularities in the African low-latitude region. *J. Atmos. Solar-Terrestrial Phys.* 97, 50–57. doi:10.1016/j.jastp.2013.02.014

Nishioka, M., Saito, A., and Tsugawa, T. (2008). Occurrence characteristics of plasma bubble derived from global ground-based GPS receiver networks. *J. Geophys. Res. Space Phys.* 113, A05301. doi:10.1029/2007JA012605

Okoh, D., Rabiu, B., Shiokawa, K., Otsuka, Y., Segun, B., Falayi, E., et al. (2017). First study on the occurrence frequency of equatorial plasma bubbles over West Africa using an all-sky airglow imager and GNSS receivers. *J. Geophys. Res. Space Phys.* 122, 12,430–12,444. doi:10.1002/2017JA024602

Oladipo, O. A., and Schüler, T. (2013a). Equatorial ionospheric irregularities using GPS TEC derived index. *J. Atmos. Solar-Terrestrial Phys.* 92, 78–82. doi:10.1016/j.jastp.2012.09.019

Oladipo, O. A., and Schüler, T. (2013b). Magnetic storm effect on the occurrence of ionospheric irregularities on an equatorial station in the African sector. *Ann. Geophys.* 56 (5), A0565. doi:10.4401/ag-6397

Olwendo, O. J., Baluku, T., Baki, P., Cilliers, P. J., Mito, C., and Doherty, P. (2013). Lowlatitude ionospheric scintillation and zonal irregularity drifts observed with GPS-SCINDA system and closely spaced VHF receivers in Kenya. *Adv. Space Res.* 51, 1715–1726. doi:10.1016/j.asr.2012.12.017

Pi, X., Mannucci, A. J., Lindqwister, U. J., and Ho, C. M. (1997). Monitoring of global ionospheric irregularities using the world-wide GPS network. *Geophys. Res. Lett.* 24 (18), 2283–2286. doi:10.1029/97GL02273

Rastogi, R. G. (1980). Seasonal variation of equatorial spread F in the American and Indian zones. *J. Geophys. Res. Space Phys.* 85 (A2), 722–726. doi:10.1029/JA085iA02p00722

Seemala, G., and Valladares, C. E. (2011). Statistics of total electron content depletions observed over the South American continent for the year 2008. *Radio Sci.* 46, 1. doi:10.1029/2011RS004722

Shah, M., Abbas, A., Ehsan, M., Calabia, A., Adhikari, B., Tariq, M., et al. (2022). Ionospheric–thermospheric responses in south America to the August 2018 geomagnetic storm based on multiple observations. *IEEE J. Sel. Top. Appl. Earth Observations Remote Sens.* 15, 261–269. doi:10.1109/JSTARS.2021.3134495

Sharma, A. K., Chavan, G. A., Gaikwad, H. P., Gurav, O. B., Nade, D. P., Nikte, S. S., et al. (2018). Study of ionospheric irregularities from Kolhapur (16.4°N, 74.2°E). *J. Atmos. Solar-Terrestrial Phys.* 173, 16–22. doi:10.1016/j.jastp.2017.12.019

Sobral, J. H. A., Abdu, M. A., Takahashi, H., Taylor, M. J., de Paula, E. R., Zamlutti, C. J., et al. (2002). Ionospheric plasma bubble climatology over Brazil based on 22 years (1977–1998) of airglow observations. *J. Atmos. Solar-Terrestrial Phys.* 64, 1517–1524. doi:10.1016/s1364-6826(02)00089-5

Tsunoda, R. T. (1985). Control of the seasonal and longitudinal occurrence of equatorial scintillations by the longitudinal gradient in integrated E region Pedersen conductivity. *J. Geophys. Res.* 90 (A1), 447–456. doi:10.1029/JA090iA01-p00447

frontiers | Frontiers in Astronomy and Space Sciences

TYPE Original Research
PUBLISHED 31 July 2023
DOI 10.3389/fspas.2023.1196231

OPEN ACCESS

EDITED BY
Dimitry Pokhotelov,
Institute for Solar-Terrestrial Physics, Germany

REVIEWED BY
Maosheng He,
Leibniz Institute of Atmospheric Physics (LG), Germany
Philip J. Erickson,
Massachusetts Institute of Technology, United States

*CORRESPONDENCE
Paul Prikryl,
paul.prikryl@unb.ca

RECEIVED 29 March 2023
ACCEPTED 06 July 2023
PUBLISHED 31 July 2023

CITATION
Prikryl P and Rušin V (2023), Occurrence of heavy precipitation influenced by solar wind high-speed streams through vertical atmospheric coupling. *Front. Astron. Space Sci.* 10:1196231. doi: 10.3389/fspas.2023.1196231

Occurrence of heavy precipitation influenced by solar wind high-speed streams through vertical atmospheric coupling

Paul Prikryl[1]* and Vojto Rušin[2]

[1]Physics Department, University of New Brunswick, Fredericton, NB, Canada, [2]Astronomical Institute, Slovak Academy of Sciences, Tatranská Lomnica, Slovakia

A tendency of heavy rainfall-induced floods in Canada to follow arrivals of solar wind high-speed streams (HSSs) from coronal holes is observed. Precipitation events during the winter, including extreme freezing rain events in the province of New Brunswick, also tend to occur following HSSs. More direct evidence is provided using the satellite-based gridded precipitation dataset Integrated Multi-satellitE Retrievals for GPM (IMERG) in the superposed epoch analysis of high-rate precipitation. The results show an increase in the high-rate daily precipitation occurrence over Canada following arrivals of major HSSs. This is consistent with previously published results for other mid-latitude geographic regions. The ERA5 meteorological reanalysis is used to evaluate the slantwise convective available potential energy (SCAPE) that is of importance in the development of storms. The role of the solar wind-magnetosphere-ionosphere-atmosphere coupling, mediated by globally propagating aurorally excited atmospheric gravity waves releasing the conditional symmetric instability in the troposphere leading to convection and precipitation, is proposed.

KEYWORDS

high-speed solar wind, magnetosphere–ionosphere–atmosphere coupling, atmospheric gravity waves, heavy rainfall-induced floods, high-rate precipitation, moist symmetric instability, slantwise convective available potential energy

1 Introduction

Solar influences on weather and climate through changes in total solar irradiance (Reid, 1997; Crowley, 2000), ultraviolet flux (Chandra and McPeters, 1994), and galactic and extragalactic cosmic rays modulated by solar activity (Harrison and Carslaw, 2003) have been extensively studied and reviewed (Gray et al., 2010).

A possible influence of solar wind and the resulting geomagnetic activity on the winter mid-latitude tropospheric circulation on the scale of days was suggested in the 1960s and 1970s. Wintertime deepening of 300-mb troughs has been found to be statistically related to geomagnetic activity (Macdonald and Roberts, 1960; Roberts and Olson, 1973). Wilcox et al. (1973) and Wilcox et al. (1974) discovered a relation (now referred to as the "Wilcox effect") between the solar magnetic sector structure and tropospheric vorticity using the upper-level tropospheric vorticity area index, which is a proxy for extratropical storminess. These results have been shown to be statistically significant (Hines and Halevy, 1977), raised a

lively discussion among scientists (Williams, 1978; Williams and Gerety, 1978; Burns et al., 1980; Rostoker and Sharma, 1980; Arora and Padgaonkar, 1981; Lundstedt, 1984), and prompted a search for a physical mechanism that could explain these results (Park, 1976; Wilcox et al., 1976; Wilcox, 1979; Wilcox and Scherrer, 1981). More recently, the dawn–dusk (B_y) component of the interplanetary magnetic field (IMF) and atmospheric electrical circuit influences on the ground-level atmospheric pressure have been shown (Burns et al., 2007; Burns et al., 2008; Tinsley, 2008; Lam et al., 2013; Lam et al., 2014; Lam and Tinsley, 2016), and Lam and Tinsley (2016) reviewed the connections of solar wind–atmospheric electricity–cloud microphysics to weather and climate. Owens et al. (2014) considered the polarity of the magnetic field modulating lightning in UK, and Scott et al. (2014) observed solar wind modulation of lightning in response to the arrival of solar wind high-speed streams coinciding with an increased flux of solar energetic protons.

A tendency of significant weather conditions, including explosive extratropical cyclones (Prikryl et al., 2016; Prikryl et al., 2018), rapid intensification of tropical cyclones (Prikryl et al., 2019), and heavy rainfall causing floods (Prikryl et al., 2021a; Prikryl et al., 2021b), to follow arrivals of solar wind high-speed streams from coronal holes has been observed. A possible physical mechanism that could explain these results was proposed (Prikryl et al., 2003; Prikryl et al., 2007; Prikryl et al., 2009a; Prikryl et al., 2009b).

Extreme weather events, such as heavy precipitation leading to floods or flash floods, particularly in summer, and snow- or ice-storms in winter, pose natural hazards with major socio-economic and environmental consequences (Brooks et al., 2001; Burn et al., 2016; Buttle et al., 2016). Despite the advances made in forecasting and improved understanding of mesoscale processes (Doswell and Bosart, 2001), predictions of extreme precipitation events continue to present difficult challenges (Doswell and Bosart, 2001; Villarini et al., 2010; Gourley et al., 2012). Such events are common in Canada, and with climate change affecting the stability of the Earth's atmosphere, their occurrence is expected to increase (Burn and Whitfield, 2016). Buttle et al. (2016) (Table 2) reviewed the key processes, classified as meteorological, hydrological, geomorphic, and human-induced, which generate floods in Canada.

In this paper, we focus on heavy precipitation events in Canada where the proximity of the auroral zone, the source region of atmospheric gravity waves (AGWs), makes it the most favorable geographic location to investigate the relationship between high-rate precipitation occurrence and solar wind high-speed streams.

2 Data sources and methods

A list of heavy rainfall-induced flood events in Canada between 1966 and 2020 is compiled from various other sources (https://www.for.gov.bc.ca/hfd/library/documents/, https://www.publicsafety.gc.ca/cnt/rsrcs/cndn-dsstr-dtbs/index-en.aspx). The initial days of heavy rainfall events (some lasting for a few days) that lead to these floods were checked and identified as the events' first days with significant rainfall by browsing historical weather data on the Environment and Climate Change Canada website (https://climate.weather.gc.ca/index_e.html).

Winter storm precipitation events, including extreme freezing rain, which caused power outages in the Province of New Brunswick have been studied by Chartrand and Thériault (2020) and Chartrand et al. (2022). These events were associated with a low-pressure system and were identified in sea-level pressure maps.

The Integrated Multi-satellitE Retrievals for GPM (IMERG) Final Precipitation L3 1 day 0.1° × 0.1° V06 (GPM_3IMERGDF) dataset (Huffman et al., 2019) is provided by the Goddard Earth Sciences Data and Information Services Center (https://disc.gsfc.nasa.gov/datasets/GPM_3IMERGDF_06/summary?keywords=IMERG).

For the analysis of moist symmetric instability in the troposphere, the latest hourly climate reanalysis produced by ECMWF, ERA5, at 0.25 × 0.25° is utilized (Hersbach et al., 2020). Following Chen et al. (2018), indices including convective available potential energy (CAPE), slantwise CAPE (SCAPE), and vertically integrated extent of realizable symmetric instability (VRS) are diagnosed, to assess the likelihood of slantwise convection in the observed precipitation events.

For the study of high-rate precipitation occurrence in the context of solar wind, the interplanetary magnetic field and solar wind plasma data are provided by the National Space Science Data Center (NSSDC), OMNIWeb (http://omniweb.gsfc.nasa.gov) (King and Papitashvili, 2005). The OMNI data also include geomagnetic indices, e.g., the *Dst* index that is used to characterize geomagnetic storms (Gonzalez et al., 1994). Solar wind plasma parameters are used to identify co-rotating interaction regions (CIRs) at the leading edge of high-speed streams (HSSs). As CIRs pass by a spacecraft, the solar wind density increases to a maximum and then decreases within a narrow stream interface while the magnetic field magnitude peaks. This interface between the fast and slow solar wind defines arrivals of HSSs. The high-density plasma ahead of CIRs (Tsurutani et al., 1995) and interplanetary coronal mass ejections (ICMEs) are also known to be highly geoeffective (Gopalswamy, 2016; Tsurutani et al., 2016). A catalog of near-Earth ICMEs was compiled by Richardson and Cane (2010) (https://izw1.caltech.edu/ACE/ASC/DATA/level3/icmetable2.html).

The sources of HSSs are coronal holes, open solar magnetic field regions that appear dark in the solar corona observed in the emission lines of ionized atoms, e.g., Fe XIV, 530.3 nm. Measurements of this green coronal emission by ground-based coronagraphs at high altitudes have been merged into a modified homogeneous coronal dataset (Dorotovič et al., 2014) (https://www.suh.sk/online-data), as a continuation of the original homogenized coronal dataset (Rybanský, 1975; Rybanský et al., 2005).

Super Dual Auroral Radar Network (SuperDARN) radars (Chisham et al., 2007) measure the line-of-sight velocity of ionospheric irregularities (ionospheric convection) and ground scatter power to observe traveling ionospheric disturbances, such as the ones caused by atmospheric gravity waves.

The superposed epoch analysis (SPE) method (Ambrož, 1979) is applied on the time series of green corona intensity, solar wind parameters and high-rate precipitation keyed to heavy rainfall events, arrivals of major HSSs/CIRs (Prikryl et al., 2021a; Prikryl et al., 2021b), or the maximum growth rate of extratropical cyclones (Prikryl et al., 2016).

3 The SPE analysis of high precipitation occurrences in the context of solar wind HSSs

Following the approach taken in previous studies (Prikryl et al., 2021a; Prikryl et al., 2021b), the SPE analysis (Figures 1A, B) of the time series of the green corona intensity and solar wind variables is keyed to the initial days of heavy rainfall events that lead to floods in Canada. For each epoch day, Figure 1C shows, for the IMERG data that are available since 2000, the cumulative number of IMERG grid cells over Canada up to 60° N of latitude where daily precipitation rates exceeded thresholds of 60, 80, 100, and 120 mm. Figure 1A shows a depletion in the mean green corona intensity at low heliographic latitudes before the epoch day −2, which is due to superposition of coronal holes that are sources of HSSs arriving a few days later, as shown by the mean solar wind variables in Figure 1B, with the mean velocity, V, ramping up to a maximum on epoch day +1. The broad peaks in the mean density and magnetic field are due to superposition of CIRs. The standard deviation, σ_{Bz}, of the IMF, $B_{Z,}$ component, which is a measure of

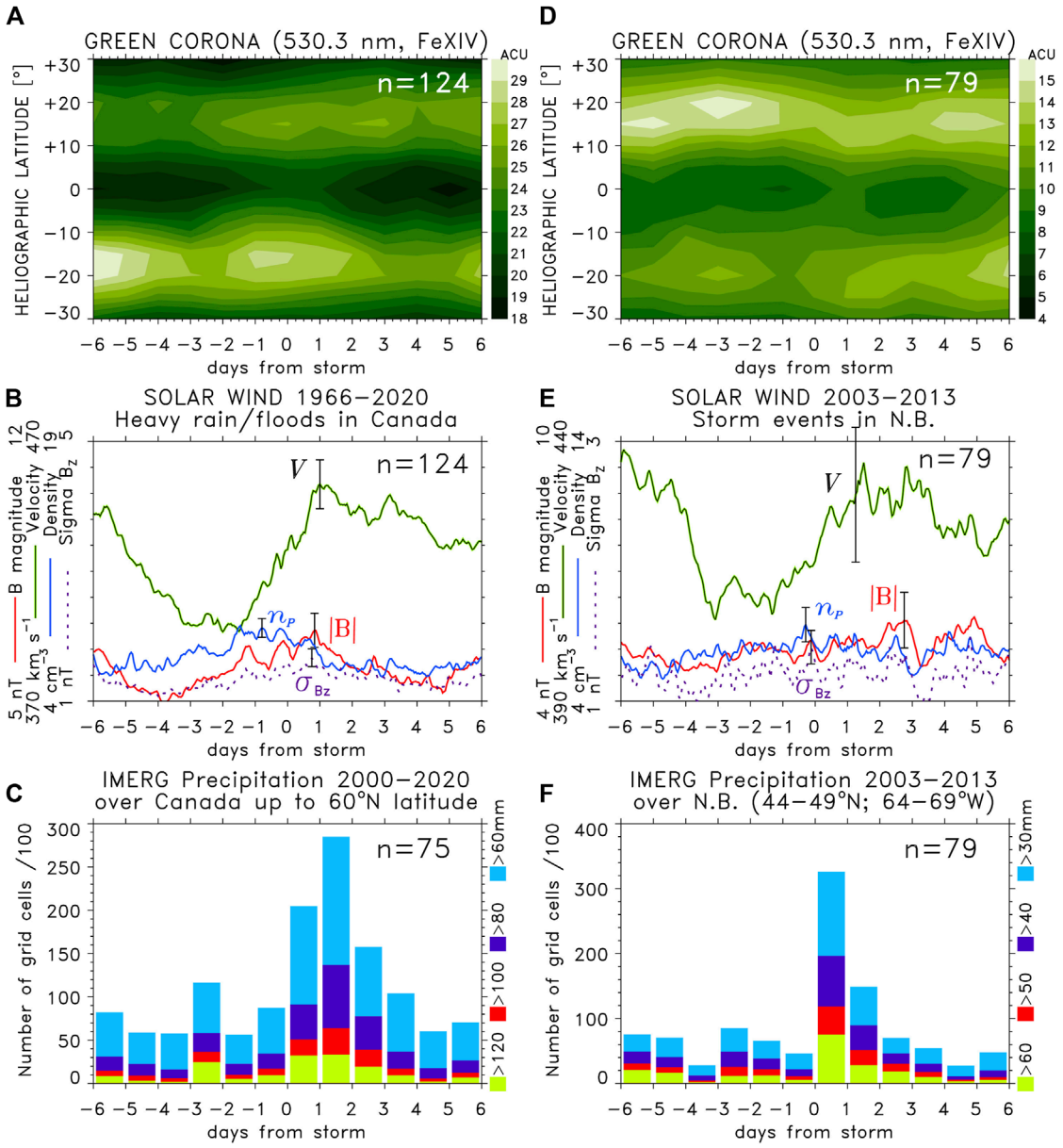

FIGURE 1
SPE analysis of the time series of **(A,D)** green corona intensity and **(B,E)** solar wind plasma variables keyed to start dates of (left panels) heavy rainfall-induced flood events in Canada and (right panels) significant precipitation events, including snow and freezing rain in New Brunswick (NB). The representative standard error bars for the mean values are shown. Bottom panels show cumulative numbers of grid cells with above-threshold daily precipitation rates **(C)** over Canada up to latitude 60° N and **(F)** over a rectangular area that includes NB.

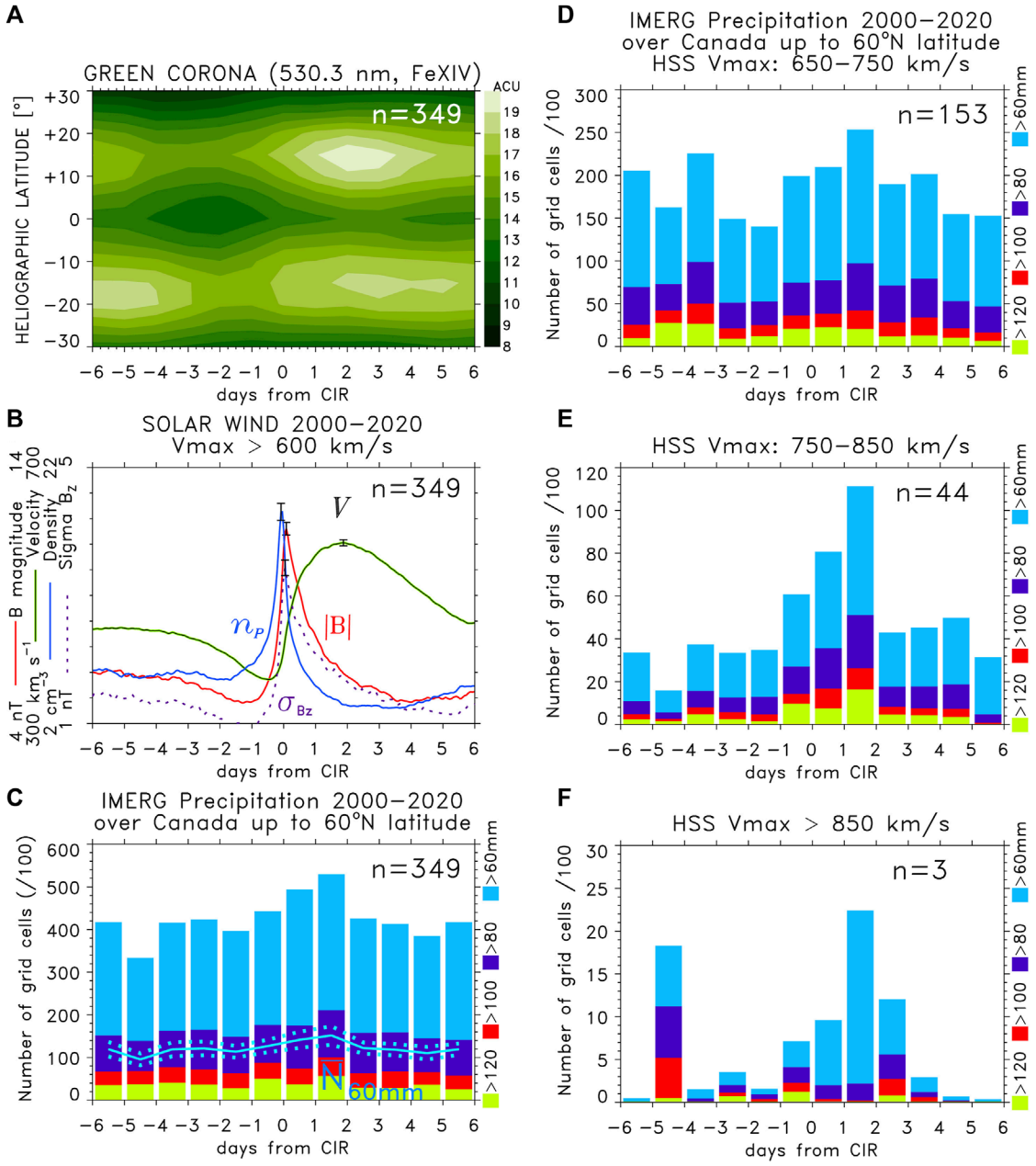

FIGURE 2
SPE analysis of the time series of **(A)** green corona intensity and **(B)** solar wind plasma variables keyed to arrivals of major HSSs/CIRs for solar wind streams that reached maximum velocity V_{max} >600 km/s. **(C)** Histograms show cumulative numbers of IMERG grid cells (divided by 100) over Canada up to 60° N latitude with above-threshold daily precipitation rates. Line plots (in the blue color) of the mean numbers of grid cells with the precipitation rate exceeding 60 mm/day, along with standard error bars for the mean that are superposed. **(D–F)** Cumulative numbers of IMERG grid cells for the SPE analysis performed for three ranges of V_{max}.

solar wind Alfvén wave amplitudes, also maximizes around the epoch day 0. These results suggest these heavy rainfall events tend to follow arrivals of HSSs/CIRs.

Figures 1D, E show the results of the SPE analysis keyed to start days of significant precipitation events, including snow and freezing rain (Chartrand et al., 2022) that caused power outages in New Brunswick (NB) during 2003–2013. Figure 1F shows the cumulative number of IMERG grid cells over a rectangular area that includes NB, where daily precipitation rates exceeded thresholds of 30, 40, 50, and 60 mm. Although the patterns of the mean V pattern and the depletion in the mean green corona intensity are similar to those in Figures 1A, B, the increase in the mean density, n_p, and magnetic field magnitude, B, around epoch day 0 is less prominent. The pattern still indicates that many NB events were associated with

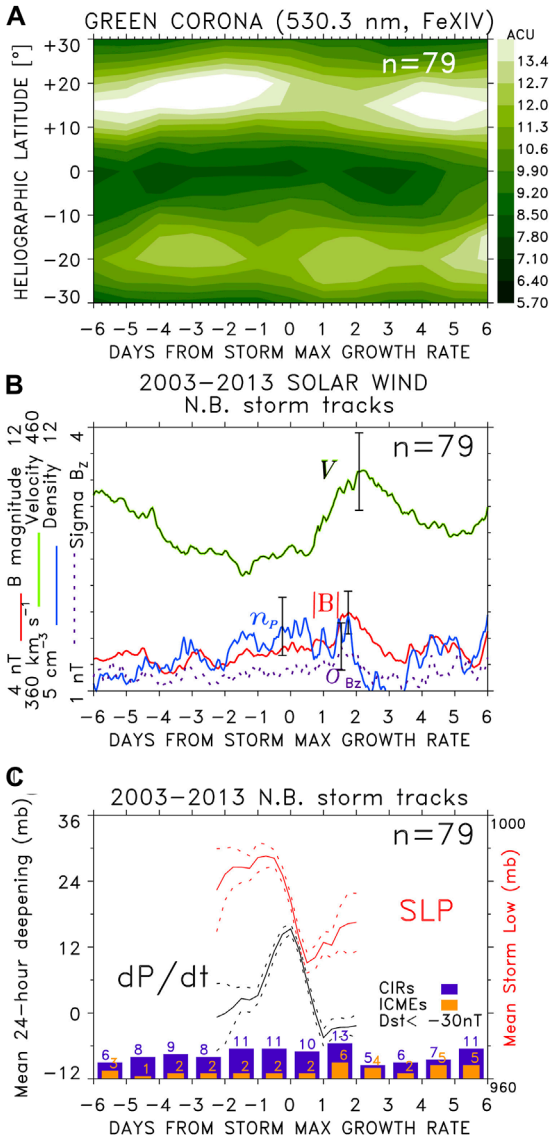

FIGURE 3
SPE analysis of the time series of **(A)** green corona intensity and **(B)** solar wind plasma variables keyed to the maximum growth (deepening) rate of extratropical cyclones that caused NB storm events. **(C)** Corresponding mean sea level pressure and mean deepening rate. The dotted lines show the standard error of the mean. Histograms of the number of CIRs (purple) and ICMEs (orange) are shown at the bottom.

arrivals of HSSs/CIRs. The peaks in B and n_p at later epoch days (+2 and +4) are due to superposition of ICMEs, as further discussed later.

In Figure 2, to examine the statistical occurrence of high-rate precipitation relative to arrivals of HSSs/CIRs, the approach is inverted by defining the key time in the SPE analysis as arrival times of major HSSs/CIRs. For the period of 2000–2020 and major HSSs reaching a maximum solar wind velocity V_{max} >600 km/s, Figures 2A, B show the SPE analysis results for the green corona intensity and solar wind parameters. As expected, the superposition of HSSs/CIRs relative to the well-defined interface between the fast and slow solar wind results in sharp peaks in the mean values of n_p, B, and σ_{Bz} close to the key time, while mean solar wind velocity V increases from a minimum before to a maximum after the key time (Figure 2B), with the mean coronal hole preceding it by about 4 days.

The main interest in this analysis is the total cumulative number of IMERG grid cells over Canada, up to 60° N latitude where daily precipitation rates exceeded given thresholds, summed up for each epoch day relative to the key time (Figure 2C). The occurrence of high-rate precipitation shows an increase starting at epoch day −1, to a maximum at epoch day +1 following the arrival of HSSs/CIRs. For the numbers of grid cells with the precipitation rate exceeding 60 mm/day, the mean ± standard error of the mean is shown. While the observed increase is relatively small, it is greater than the standard error of the mean. Furthermore, splitting the analysis into subperiods shows that the increase persists and becomes progressively more prominent for faster HSSs. The SPE analysis for three intervals of V_{max} (Figures 2D–F) shows the increase in the cumulative number of IMERG grid cells with above-threshold daily precipitation rates. In all three cases, high precipitation rates peak at epoch day +1. For progressively faster/stronger HSSs/CIRs, the relative increase in the high-rate precipitation occurrence following the key time is higher (Figures 2E, F). It is important to vary n and group the analysis by V_{max}. First, larger n should yield higher statistical significance for SPE results. Second, faster HSSs result in stronger MIA coupling. Third, the grouping into subperiods allows the consistency of SPE results to be checked.

In the case of NB events that caused power outages in the period of 2003–2013, we identified extratropical cyclones that caused the storms. Using global satellite images of clouds provided by the International Satellite Cloud Climatology Project (ISCCP), the Global ISCCP B1 Browse System (GIBBS) (https://www.ncdc.noaa.gov/gibbs/) and the mean sea level pressure (SLP) fields from the JRA-55 meteorological reanalysis data, the minima of central pressure of deepening extratropical cyclones were traced. Following the criterion introduced by Sanders and Gyakum (1980), the normalized central pressure deepening rate (NDR_c) [Lim and Simmonds 2002; their Eq. (1)] was computed. The maximum deepening rates of the cyclones are used as key times in the SPE analysis, with Figure 3C showing the mean SLP and deepening rate dP/dt. The results for the green corona intensity and solar wind plasma variables (Figures 3A, B) are similar to those in Figures 1D, E and to the previously published results linking the explosive development of extratropical cyclones to arrivals of HSSs/CIRs (Prikryl et al., 2016). The pattern of an increase in mean solar wind velocity V, from a minimum before the key time to a maximum at the epoch day + 2, with substantial increase in mean solar wind density n_p and magnetic field magnitude B starting from epoch day −2 is due to superposition of the number of CIRs that are shown in histograms between epoch days −2 and +1. This indicates a tendency of intensification of these cyclones to be associated with arrivals of HSSs/CIRs, which are often preceded by high-density plasma that is further discussed in the next section. In addition to CIRs, six ICMEs that are superposed on epoch day +1 contributed to peaks in B and n_p. However, as will be discussed in Section 6, HSSs/CIRs generate trains of AGWs. The impacts of ICMEs, while often resulting in geomagnetic storms, are more impulsive but short-lived.

4 Cases of high precipitation events leading to floods in the context of solar winds

4.1 Heavy rainfall-induced floods in Canada

The results of SPE analyses in Figures 1, 2 indicate a strong tendency of high-precipitation occurrence following arrivals of HSSs from coronal holes. We now examine cases of heavy rainfall events in the context of solar wind disturbances, including HSSs/CIRs (Gosling and Pizzo, 1999; Tsurutani et al., 2006a; Tsurutani et al., 2006b) and interplanetary coronal mass ejections (Gopalswamy, 2016). The solar wind magnetic sector boundaries, where the IMF direction switches its polarity between "away" and "toward" the Sun, that have been identified as heliospheric current sheets (HCSs; Smith et al., 1978; Hoeksema et al., 1983), usually closely precede or are imbedded within CIRs at the leading edge of HSSs. The high-density plasma (HDP) ahead of HCSs/CIRs leads to magnetic field compression, which is another geoeffective solar wind disturbance (Tsurutani et al., 1995). In the absence of IMF data, the magnetic sectors can be estimated from ground-based magnetograms (Svalgaard, 1975).

Figure 4 shows solar wind variables such as the IMF direction longitude (orange crosses) and the *Dst* index (green line). The symbols on the time axis indicate the times of HSS/CIR arrivals, impacts of ICMEs, and the IMF sector boundary/HCS crossings. Where available, the proxy magnetic field sectors (A: away; T: toward) are indicated below the time axis. Start dates of heavy rainfall events in Canada included in the SPE analysis are marked by symbols at the top. These are examples of events that occurred following arrivals of HSSs/HCSs/CIRs or impacts of ICMEs that caused geomagnetic storms. On 8 June 1999 (Figure 4A), White Rock, BC, experienced a sudden, intense storm with heavy rain that caused flash floods and mudslides. In July 1999 (Figure 4B), heavy snow and rain fell starting on July 2 caused flooding in Clearwater, AB. On September 22–23 (Figure 4C), Prince Edward Island experienced a severe rainstorm, causing flash flooding, damaging eight highways and bridges. The IMERG satellite-based precipitation data for June 2000 are obtained. At the top in

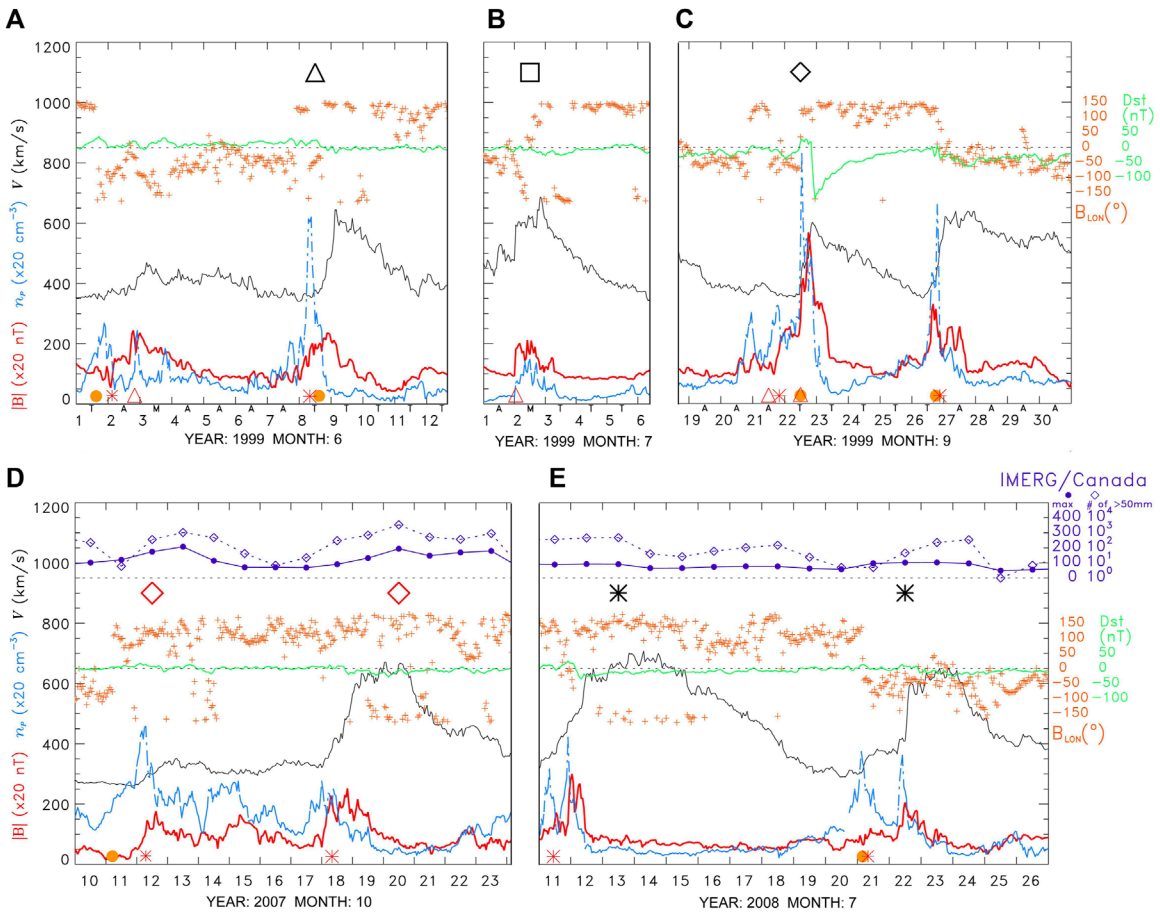

FIGURE 4
OMNI solar wind *V* (solid black line), *B* (red), and n_p (broken light blue line, with the *y*-axis scales shown on the left). The magnetic field direction longitude (orange crosses) and the *Dst* index (green line) with the *y*-axis are shown on the right. The symbols at the time axis indicate CIRs (✳), ICMEs (Δ), HCSs (●), and the proxy magnetic field sector (A: away; T: toward). **(A–E)** The symbols at the top mark the starting days of heavy rainfall-induced floods in Canada (Δ BC; □ AB/SK/MB; ✳ ON/QC; ◊ NS/PEI/NL; ◊ NB). **(D,E)** Maximum IMERG daily rates (solid purple line); the number of grid cells over Canada with precipitation rates exceeding 50 mm (dotted purple line) is shown at the top.

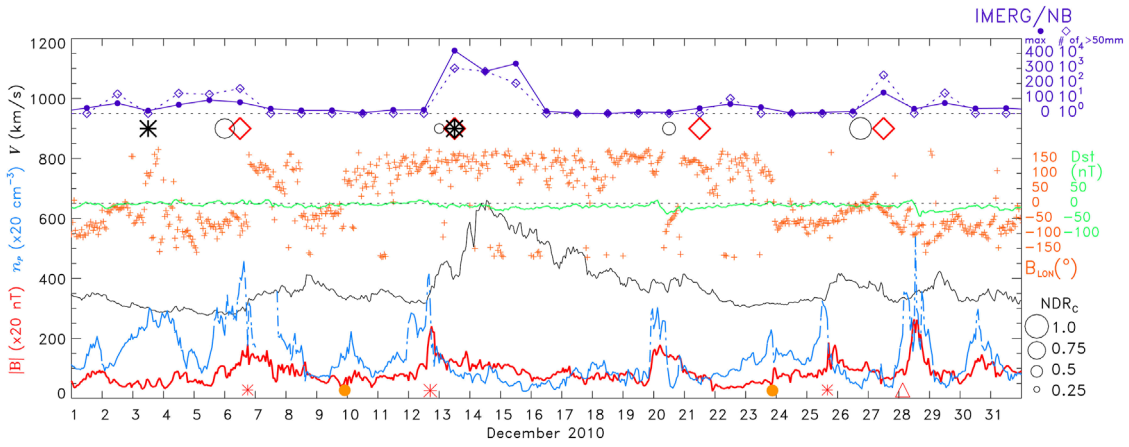

FIGURE 5
OMNI solar wind V (solid black line), B (red), and n_p (broken light blue line, with the y-axis scales shown on the left). The magnetic field direction longitude (orange crosses) and the Dst index (green line) with the y-axis shown on the right. The symbols at the time axis indicate CIRs (✳), ICMEs (Δ), and HCSs (●). Open circles scaled by the maximum normalized deepening rate (NDR_c) of the central mean SLP of extratropical cyclones that caused NB storms. The symbols mark the starting days of heavy rainfall-induced floods in Canada (Δ BC; □ AB/SK/MB; ∗ ON/QC; ◊ NS/PEI/NL; ◊ NB storms).

Figures 4D, E, the maximum IMERG daily rates at any grid cell over Canada (solid purple line) and the number of IMERG grid cells over Canada with precipitation rates exceeding 50 mm (dotted line) are shown. Figures 4C, D show cases of heavy rainfall events in New Brunswick and Quebec, respectively, and enhanced high-rate precipitation occurrence following HSSs/CIRs. More events in the context of solar wind can be viewed in the Supplementary Material.

4.2 Winter NB storm precipitation events in December 2010

Several heavy precipitation events affected eastern Canada in December 2010. Figure 5 shows the maximum IMERG daily rates and the number of grid cells over New Brunswick with precipitation rates exceeding 50 mm. The focus here is on the NB storms (marked by red diamonds) that followed rapid intensifications of extratropical cyclones (marked by open circles scaled by the maximum normalized deepening rate of the central mean SLP). On December 6, the storm that caused strong winds, heavy wet snow, and floods coincided with the arrival of a broad CIR on the leading edge of a moderate HSS that was preceded by high-density plasma adjacent to HCSs. While heavy precipitation and an extreme storm surge that caused floods occurred after the low pressure reached the east coast on December 6, this extratropical cyclone explosively deepened off the East Coast of the United States. Figure 6A shows the daily accumulated precipitation on December 6, overlaid with the storm track. The maximum deepening rate and the minimum central SLP reached are indicated in green and red colors, respectively. Another intense storm during December 13–14 resulted in extensive flood damages in New Brunswick and Quebec. It was caused by a rapidly deepening low-pressure system (Figure 6B) that closely followed the arrival of a major HSS/CIR (Figure 5). The cyclone brought heavy rain, wet snow, and strong winds, causing major power outages in New Brunswick. Heavy rain and floods also occurred in Gaspé, QC, when the high-rate IMERG precipitation peaked. Figure 6B shows the daily accumulated precipitation on December 13, overlaid with the storm track. Similarly, minor HSSs/CIRs on December 20 and 25 were followed by rapid intensifications of extratropical cyclones over the east coast, which brought heavy rain, wet snow, and strong winds to New Brunswick. The December 21 storm also caused a storm surge and flooding. In each case, there was an increase in the IMERG high-rate precipitation occurrence over New Brunswick (Figure 5).

5 Assessment of conditional symmetric instability and slantwise convection

Prikryl et al. (2009b) suggested that down-going aurorally-excited atmospheric gravity waves could contribute to release of moist symmetric instability, leading to slantwise convection (Schultz and Schumacher, 1999). Such a mechanism could explain the aforementioned results linking severe weather occurrences to solar wind events. In this section, the presence of slantwise convection in frontal zones is assessed for cases of extratropical cyclones using the method discussed by Chen et al. (2018).

Release of conditional symmetric instability (CSI; Schultz and Schumacher, 1999; Chen et al., 2018) has been known to initiate slantwise convection over frontal precipitation bands (Bennetts and Hoskins, 1979; Bluestein, 1993; Houze, 1993; Emanuel, 1994). The warm frontal cloud bands, in rapidly intensifying extratropical cyclones, were identified as "striated delta" clouds (Feren, 1995). Glinton et al. (2017) (Figures 1, 2) studied cases of CSI release contributing to precipitation in mature extratropical cyclones. Chen et al. (2018) (Figures 7, 10) investigated the evolution of slantwise convective available potential energy and CAPE in explosive and nonexplosive cyclones. They found that SCAPE

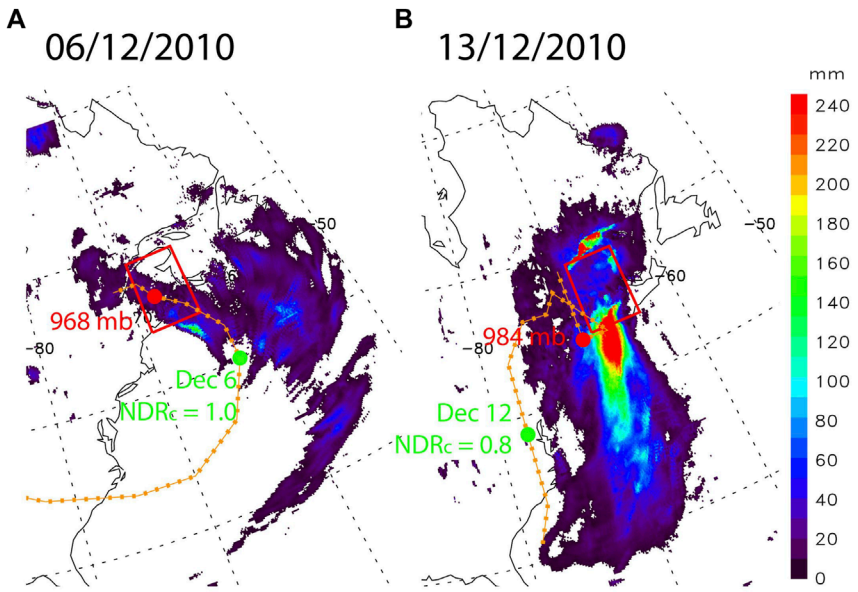

FIGURE 6
IMERG daily accumulated precipitation **(A)** on December 6 and **(B)** 13 December 2010. The rectangular area around New Brunswick is superposed. Tracks of central SLP of intensifying extratropical cyclones (orange line) with the maximum deepening rate and minimum central SLP are shown by green and red dots, respectively.

exhibits values greater than CAPE prior to the onset of the rapid intensification of explosive cyclones and then decreases sharply thereafter, thus pointing to the importance of CSI in the development of storms.

5.1 Case of the storm on 12–13 December 2010

The GOES-13 infrared images (https://www.ncdc.noaa.gov/gibbs/) of an intensifying extratropical cyclone showed "back building" convection cells along squall lines (Bluestein and Jain, 1985) off the East Coast of United States (Figure 7A). The CIMSS data archive (http://tropic.ssec.wisc.edu/archive/) provides overlay data products from wind analysis. The enhanced upper-level (150–300 mb) divergence (Figure 7B) indicates a region with rising air motion. There were strong mid-upper-level southwesterly winds (Figure 7C), low-level winds (Figure 7D) turning southerly over a string of convection cells, and large mid-level wind shear (Figure 7E). Furthermore, low-level winds and vertical wind shears based on the ERA5 reanalysis are also shown in Figure 8, discussed as follows. These conditions are conducive to over-reflection of down-going aurorally excited AGWs with a possibility of amplification (Section 6.3). The over-reflecting AGWs in the unstable frontal zone could contribute to the release of CSI, resulting in a series of convection cells forming the "back building" squall line. Similar cases of intensifying extratropical cyclones were discussed previously (Prikryl et al., 2018; including Supplementary Material).

Several indices are calculated using the ERA5 reanalysis to evaluate the likelihood of slantwise convection in this case. These indices that provide different but Supplementary Material, include SCAPE, fractional SCAPE residual (f_s = (SCAPE—CAPE)/SCAPE), and vertically integrated extent of realizable symmetric instability (Glinton et al., 2017; Chen et al., 2018). A high SCAPE, indicating high convective available potential energy for a slantwise ascending air parcel from low levels, is found but limited to the warm sector of the cyclone (Figure 8A). A closer-to-one f_s indicates the relative dominance of slantwise over upright convection, although such a condition is also scattered mostly in the south (Figure 8B). While the aforementioned two indicate the potential energy, VRS shows the thickness of the air layer (measured in pressure), where CSI, high relative humidity, and vertical motion coexist (Chen et al., 2018). Figure 8C shows that the cold front, where strings of "back building" convection cells (Figure 7A) produced high-rate precipitation co-located well with a high VRS value of above 150 hPa, shows a strong indication that CSI is being released actively there. Such high VRS values well-match the high precipitation band persisted for more than 1 day. As already noted previously, this was co-located with low-level southerly winds and wind shears evaluated between 900 and 1,000-hPa levels (Figure 8D), which is favorable for over-reflection of AGWs.

5.2 Case of the storm on 5–6 December 2010

The extratropical cyclone that caused heavy rain in New Brunswick on December 6 explosively intensified off the east coast (Figure 6A). This coincided with the arrival of the solar wind high-density plasma sheet on the leading edge of a moderate HSS/CIR (Figure 5). Figure 9A shows the GOES-13 infrared images (https://www.ncdc.noaa.gov/gibbs/) of an explosive extratropical cyclone showing development of a "striated delta" cloud in the cyclone vortex and "back building" bands in the cold front. They coincide

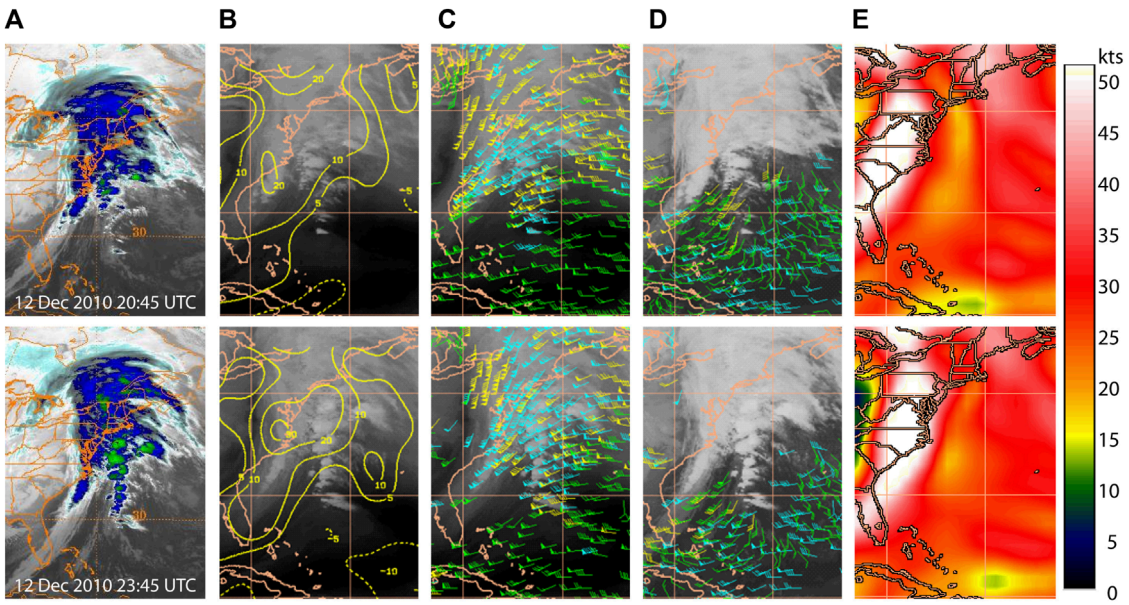

FIGURE 7
(A) GOES-13 infrared images (https://www.ncdc.noaa.gov/gibbs/) of an intensifying extratropical cyclone showing "back building" squall lines. Overlay data products from the CIMSS data archive (http://tropic.ssec.wisc.edu/archive/) of wind analysis show **(B)** upper-level (150–300 mb) divergence, **(C)** mid-upper-level winds, **(D)** low-level IR-cloud drift winds, and **(E)** mid-level wind shears.

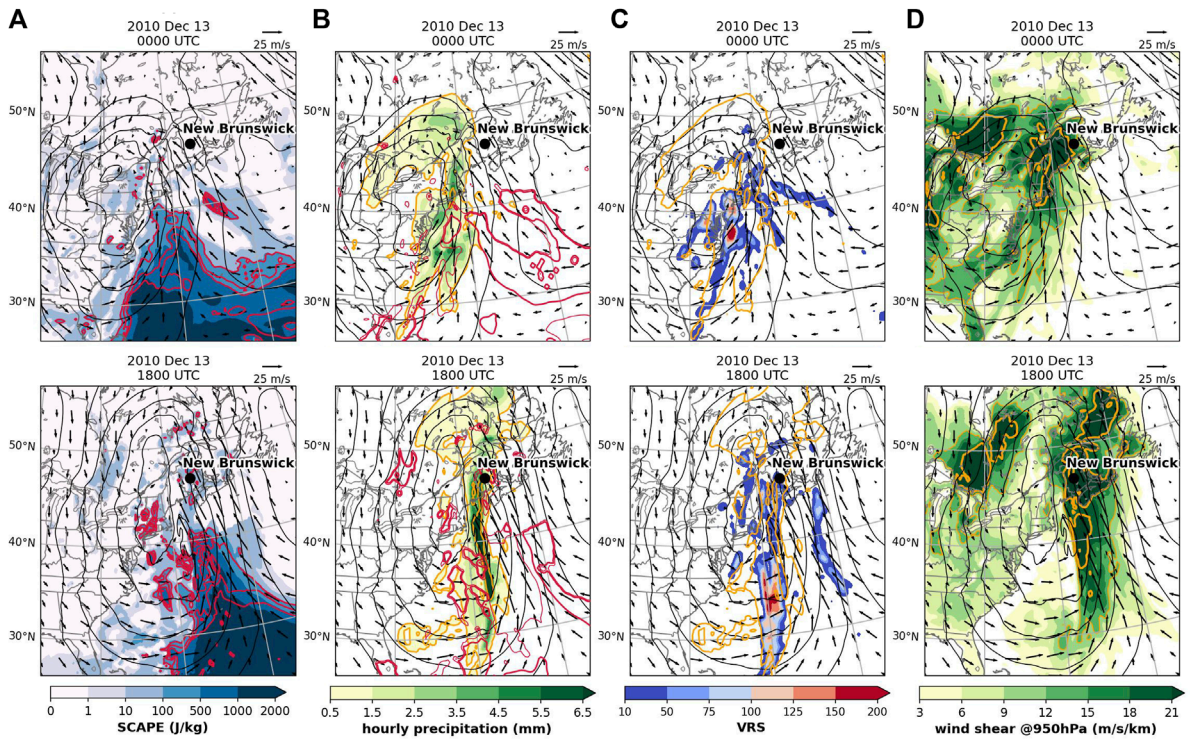

FIGURE 8
(A) SCAPE (shaded) and SCAPE−CAPE (red contours; 100, 300, and 500 J/kg), **(B)** 1-h accumulated precipitation (shaded) and f_s (red contours; thin for 0.5 and thick for 0.8), and **(C)** VRS (shaded) and precipitation (yellow contours; 0.5 and 5.5 mm), **(D)** low-level wind shear (yellow contour; 12, 21 m/s/km). **(A–D)** All overlapped with 950-hPa wind (vectors; m/s) and 950-hPa geopotential height (black contours; m; at intervals of 50 m).

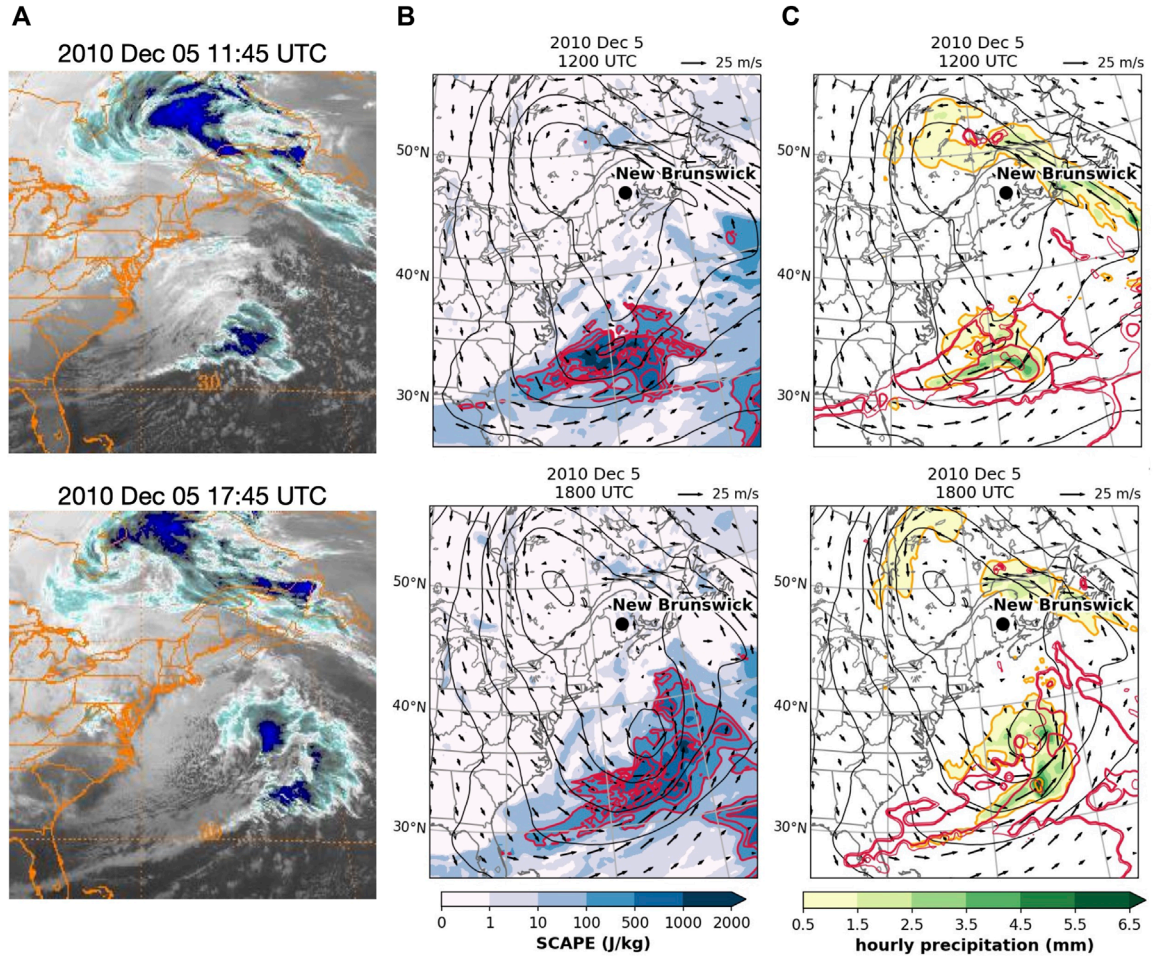

FIGURE 9
(A) GOES-13 infrared images (https://www.ncdc.noaa.gov/gibbs/) of an explosive extratropical cyclone showing a "striated delta" cloud in the cyclone vortex and "back building" bands in the cold front. **(B)** SCAPE (shaded) and SCAPE–CAPE (red contours; 100, 200, 300, and 400 J/kg), **(C)** 1-h accumulated precipitation (shaded) and f_s (red contours; thin for 0.5 and thick for 0.8). **(B,C)** All overlapped with the 950-hPa wind (vectors; m/s) and 950-hPa geopotential height (black contours; m; at intervals of 50 m).

with regions of high SCAPE and close-to-one f_s (Figure 9B). The resulting latent heat release could have contributed to the explosive development of the cyclone that later brought heavy rainfall to New Brunswick (Figure 6A).

While large SCAPE–CAPE residuals are mostly over the warm sector (to the south) of the extratropical cyclone, the heavy precipitation over New Brunswick on December 6, 00:06 UTC (Figure 10B), is co-located with some locally high VRS values (peak >150 hPa thickness at 03:00 UTC) that lasted more than 6 h over the "bent-back warm front" that wraps around the cyclone center. It should be noted that there exist other low-level forcing mechanisms for heavy precipitation, e.g., frontogenetical lifting and the strong low-level convergence of flows associated with two cyclone centers, which was likely the case when the cyclone was reaching New Brunswick (Figure 10B). Nevertheless, heavy precipitation and a storm surge that caused floods coincided with the arrival of a broad HSS/CIR with a dense HDP at its leading edge on December 6. Furthermore, similar to the observation on December 13, the high-rate precipitation was co-located with high low-level winds and wind shears at 950 hPa (Figure 10D). Equatorward propagating AGWs generated by solar wind coupling to the magnetosphere–ionosphere–atmosphere system could have reached the cyclone and contributed to the release of CSI, leading to cyclone intensification.

6 Solar wind coupling to the magnetosphere-ionosphere-atmosphere (MIA) system

6.1 High-latitude sources of AGWs in the lower thermosphere

At high latitudes, solar wind coupling to the magnetosphere-ionosphere-thermosphere system is the energy source of auroral heating, primarily Joule heating, due to collisions among electrons, positive ions, and neutral molecules (Brekke and Kamide, 1996; Knipp et al., 2004; Thayer and Semeter, 2004; Xu et al., 2013;

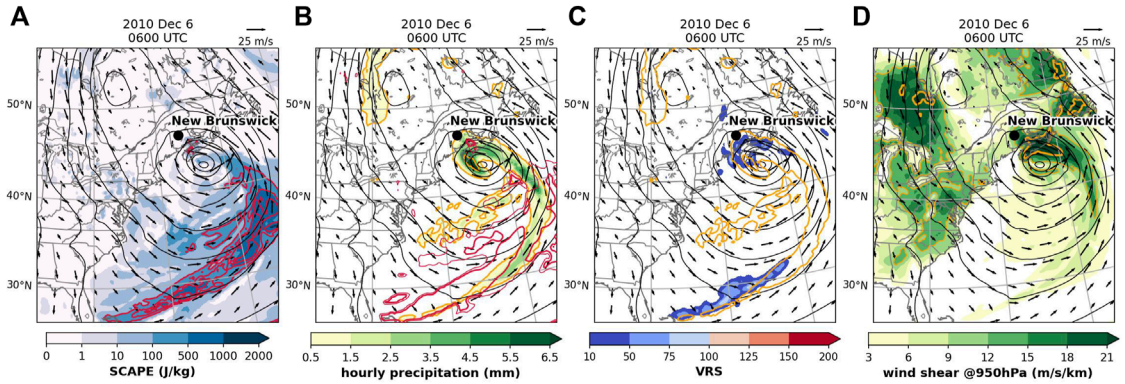

FIGURE 10
Same as Figure 8 but for December 6, 06:00 UTC.

Richmond, 2021), although its impact on the thermodynamics of the neutral atmosphere is thought to decrease below 100 km (Xu et al., 2013). Auroral heating is highly variable and often driven by ultra-low-frequency (ULF) waves.

The main source of ULF waves are HSSs emanating from coronal holes (Krieger et al., 1973). HSSs from polar coronal holes have speeds of ~750–800 km/s (Phillips et al., 1994; Phillips et al., 1995; Tsurutani et al., 2006a; Tsurutani et al., 2006b). However, coronal holes that affect the Earth by HSSs are either extensions of polar coronal holes (Phillips et al., 1994) to low latitudes or are self-contained coronal holes forming at low heliographic latitudes (de Toma, 2011). The high-density HCS plasma sheet ahead of CIRs leads to compression of the magnetic field that can cause recurring moderate-to-weak geomagnetic storms (Tsurutani et al., 1995). The high-density plasma sheet impinging onto the magnetosphere results in precipitation of magnetospheric relativistic electrons (Tsurutani et al., 2016). HSSs/CIRs have been shown (Tsurutani et al., 2006a; Tsurutani et al., 2006b) to be associated with high-intensity, long-duration continuous auroral electrojet activity (HILDCAAs) (Tsurutani and Gonzalez, 1987; Tsurutani et al., 1990; Tsurutani et al., 1995). HILDCAAs are caused by trains of solar wind Alfvén waves (Belcher and Davis, 1971) that couple to the magnetosphere–ionosphere system (Dungey, 1961; Dungey, 1995). Coupling produces pulses of Joule heating in the lower thermosphere that can launch AGWs with duration between tens of minutes to hours.

The theoretical understanding of gravity waves and their role in the ionosphere was developed by Hines (1960). The auroral sources of medium- to large-scale gravity waves have been recognized, and AGWs have been observed as traveling ionospheric disturbances (TIDs) for a long time (Chimonas and Hines, 1970; Testud, 1970; Richmond, 1978; Tanaka, 1979; Williams et al., 1993; Balthazor and Moffett, 1997; Oyama et al., 2001; Oyama and Watkins, 2012; Richmond, 2021). Francis (1974) theoretically described and distinguished between direct and Earth-reflected gravity waves and pointed out that the latter appear in the F-region as wave packets of nearly monochromatic waves, while the former induce isolated (nonperiodic) TIDs, which is consistent with the modeling of gravity waves generated by enhancements in the ionospheric electric field (Millward et al., 1993a; Millward et al., 1993b; Millward, 1994). Each electric field enhancement causes a Joule heating pulse, which in turn launches a single gravity wave propagating equatorward and poleward from the source region.

6.2 Global propagation of AGWs

The gravity wave dispersion relation (Hines, 1960) allows both upward (downward phase) and downward group (upward phase) propagation (Hocke and Schlegel, 1996). For clarity, we will refer to downward/upward group (wave energy) propagation as down/upgoing AGWs to distinguish them from upward/downward AGW phase propagation. Yeh and Liu (1974) used the ray theory approach and the WKB approximation and pointed out that a simplified ray tracing procedure based on Snell's law is applicable for a horizontally stratified atmosphere, e.g., (Bristow et al., 1996; Prikryl et al., 2005; and Prikryl et al., 2009b). A dispersion relation derived from Navier-Stokes equations (Bristow et al., 1996) with temperature gradients included by allowing the scale height to vary with altitude but not considering viscosity, thermal conductivity, and ion drag, showed results suggesting a seasonally dependent reflection of gravity waves due to the temperature gradient at mesospheric altitudes.

Based on a spectral model in terms of spherical harmonics, Mayr et al. (1984a) and Mayr et al. (1984b) described gravity wave response in the atmosphere and showed that propagating waves originating in the thermosphere can excite a spectrum of AGWs in the lower atmosphere, though with much smaller amplitudes. Their transfer function model (TFM), which describes global propagation of acoustic gravity waves in a dissipative and static atmosphere with globally uniform temperature and density variations, was reviewed (Mayr et al., 1990; Mayr et al., 2013). Globally propagating AGWs from sources in the lower thermosphere at high latitudes can be ducted in the lower atmosphere over long distances and reach the troposphere at mid-to-low latitudes. However, the amplitude of AGWs is known to decrease exponentially with decreasing height. At the top of the troposphere, the amplitude in velocity perturbation

is 3–4 orders of magnitude smaller than the amplitude of the wave launched in the E-region (Hines, 1965). In the lower thermosphere, large vertical wind velocities with magnitudes of 10–20 m/s are common at high latitudes (Larsen and Meriwether, 2012). Even larger vertical ion motions with amplitudes up to ± 50 m/s have been observed by incoherent scatter radars (Oyama et al., 2005) at altitudes of 95–111 km. Oyama et al. (2008) observed vertical winds exceeding 30 m/s at high-latitude altitudes of 110–120 km during moderately disturbed geomagnetic conditions. Hernandez (1982) observed periodic oscillations of vertical winds with amplitudes up to 50 m/s and a period of 40 min in the mid-latitude thermosphere, which were attributed to the passage of gravity waves from an auroral source. Rees et al. (1984) identified sources at high latitudes of strong vertical winds >100 m/s, resulting from local geomagnetic energy input and subsequent generation of thermospheric gravity waves. *In situ* measurements of large vertical motions of 100–250 m/s in the thermosphere were attributed to aurora-induced gravity waves (Spencer et al., 1976; Spencer et al., 1982), and vertical winds of 10–20 m/s are commonly observed in the lower thermosphere (Larsen and Meriwether, 2012). Such vertical motions scale down to a few cm/s at the tropospheric level, which is comparable to mean vertical motions in the troposphere (Fukao et al., 1991; Nastrom and Vanzandt, 1994) but less than typical instantaneous vertical motions of up to a few tens of cm/s associated with tropospheric gravity waves (Nastrom et al., 1990).

6.3 Initiation of tropospheric convection by aurorally excited AGWs

As already mentioned in Introduction, it has been suggested that aurorally excited AGWs can play a role in the CSI release, leading or contributing to explosive development of extratropical cyclones. When downgoing AGWs over-reflect in the warm frontal zone of extratropical cyclones, even a small lift that they would impart to a moist air parcel already rising over the cold air can initiate slantwise convection, forming a precipitation band. Extreme rainfall events often result from mesoscale convective systems producing convective rainfall regions that are sometimes nearly stationary. Bluestein and Jain (1985) (in Figure 1) introduced a concept of distinct kinds of mesoscale convective line (squall line) developments based on radar reflectivity and satellite observations of squall lines, with the two most commonly identified as "broken line" and "back building" formations. The squall lines form in a conditionally and convectively unstable atmosphere. The "broken line" forms typically along a cold front by probable development of "externally" forced multi-cells appearing at about the same time and transforming "into a solid line as the area of each existing cell expands and new cells develop" (Bluestein and Jain, 1985). The "back building" squall line "consists of the periodic appearance of a new cell upstream, relative to cell motion" and can form along different types of surface boundaries. The other types may include warm frontal bands and wide cold frontal bands (Bluestein and Jain, 1985). Similar to striated delta clouds (Prikryl et al., 2018; their Figure 9), the SPE analysis of solar wind data keyed to dates from the list of squall line cases (Bluestein and Jain, 1985; their Table 1) appears to show a tendency of such mesoscale convective line development to follow arrivals of HSSs/CIRs/ICMEs.

TFM simulations (Prikryl et al., 2018; their Figure 16) of propagation of the gravity wave launched by Joule heating with given vertical heating profiles in the lower thermosphere showed that they can produce vertical wind amplitudes of up to ~1 cm/s at 10 km altitude. The gravity wave ray tracing examples (Prikryl et al., 2018; their Figure 15) show that AGWs can reach lower troposphere altitudes, where they may at least seed the slantwise convection in a symmetrically unstable environment by providing a small lift to a parcel of air and contribute to the release of instability (Prikryl et al., 2009b; pp. 34 and 42–43). Cases of TIDs and/or their sources in the ionosphere followed several hours later by series of rain bands, or convective cells, indicated an approximately one-to-one correspondence (Prikryl et al., 2009b; Prikryl et al., 2018) that was consistent with the estimated AGW propagation time from the lower thermosphere to the upper troposphere. While even a very small amplitude of these AGWs at tropospheric levels may be sufficient to release the CSI, there is possibility of amplification of AGWs at the reflection point if waves encounter a wind shear or an opposing wind (Jones, 1968; Cowling et al., 1971; McKenzie, 1972; Eltayeb and McKenzie, 1975).

6.4 Observations of AGWs in the upper atmosphere

SuperDARN radars (Nishitani et al., 2019) measure the line-of-sight velocity component of $\mathbf{E} \times \mathbf{B}$ drift velocities of ionospheric irregularities in the F-region (at altitudes of ~350 km), with the electric field $\mathbf{E}$ mapping along equipotential magnetic field lines to the lower ionosphere. Velocity measurements are used to map ionospheric convection at mid-to-high latitudes. In addition to ionospheric scattering, the radars also observe the ground scatter power modulated by TIDs, including those that are driven by AGWs. To study the relevant geophysical context of the December 2010 storm event, we now examine *in situ* measurements of solar wind variables, ionospheric velocity and ground scatter power observed by the SuperDARN, and ground magnetometers sensing ionospheric currents.

On December 12, as in previously studied cases (Prikryl et al., 2009b; Prikryl et al., 2018), pulsed ionospheric flows (PIFs) observed over northern Greenland generated equatorward propagating AGWs/TIDs. Figure 11A shows ionospheric line-of-sight velocity V_{los} as a function of the magnetic latitude observed by the Iceland Stokkseyri radar beam 15. The ionospheric currents in the E-region at altitudes of ~110 km flow in the opposite direction to ionospheric convection (PIFs). It is the Joule heating caused by pulses of ionospheric currents that generated AGWs that were observed as TIDs by the Goose Bay radar in Labrador (Figure 11B). Similarly, on December 5, pulses of ionospheric convection/currents at high latitudes generated equatorward-propagating AGWs. Figure 11C shows TIDs in the ground scatter observed by the Pykkvibaer radar beam 7. Figures 11B, C show the ground scatter power focused/defocused by equatorward-propagating TIDs observed by radar beam 12. Rather than showing the ground scatter slant range, the ground scatter range is mapped to reflect the TID location in the ionosphere (Bristow et al., 1994). It is noted that PIFs and the consequent AGWs/TIDs were generated by solar wind Alfvén waves coupling with the dayside magnetosphere/ionosphere

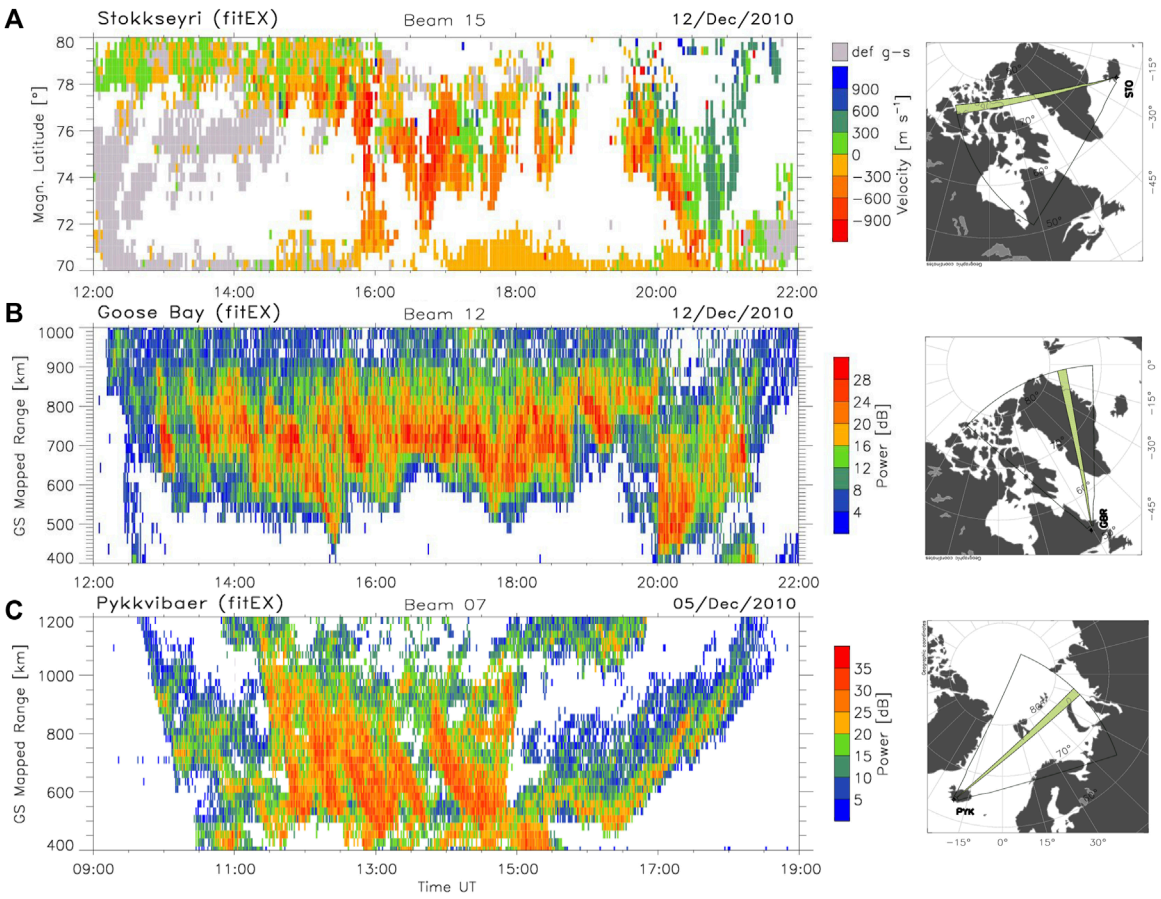

FIGURE 11
(A) Line-of-sight (LoS) velocity observed by the Stokkseyri radar beam 15. **(B)** Ground scatter power observed by the Goose Bay radar beam 12. **(C)** Ground scatter power observed by the Pykkvibaer radar beam 7.

by the pulsed magnetic reconnection at the subsolar magnetopause (Prikryl et al., 1998; Prikryl et al., 2002).

The magnetic reconnection is primarily driven by the southward IMF B_Z component, which is opposite to the Earth's magnetic field at the subsolar magnetopause. Figure 12A shows the IMF B_Z component in Geocentric Solar Ecliptic (GSE) coordinates (black line) measured by Wind spacecraft in the upstream solar wind. The dotted lines show detrended time series of IMF B_Z (red) and proton velocity V_Z (blue) components that are correlated. The correlation between the respective components of the solar wind magnetic field is the signature of anti-sunward propagating solar wind Alfvén waves (Belcher and Davis, 1971). The normalized fast Fourier transform (FFT) power spectra of the detrended time series of B_Z and V_Z show similar multiple peaks at frequencies of ~0.25, 0.4, and 0.6 mHz.

The north–south X component of the ground magnetic field (Figure 12B) was measured by a magnetometer on the west coast of Greenland in Upernavik (UPN), located in the field of view of the Stokkseyri radar beam 15. The perturbations of the ground magnetic field are caused by ionospheric currents at altitudes of ~110 km, with the north–south X component sensing east–west currents. The FFT power spectrum of the detrended time series (red dotted line) is very similar to those of the IMF B_Z and V_Z observed by the Wind spacecraft.

Figure 12C shows the time series of the Goose Bay radar ground scatter power for the range gate 30 showing variations that are due to equatorward-propagating TIDs. The main peak in the FFT power spectrum of the detrended time series (dotted line) is close 0.5 mHz (~30 min), representing the period of equatorward-propagating AGWs.

6.5 Ray tracing AGWs in a model atmosphere

Ray tracing of AGWs in a model atmosphere using the dispersion relation has been conducted (Prikryl et al., 2005) to show that downgoing AGWs launched by ionospheric currents at high latitudes can reach the troposphere. They can be ducted in the lower atmosphere to low latitudes, as shown by ray tracing and TFM methods (Prikryl et al., 2018).

Using the MSIS-90 model atmosphere, Figure 13 shows possible group paths from a source at 110 km altitudes of AGWs with a period of 30 min, including the ducted mode in the lower

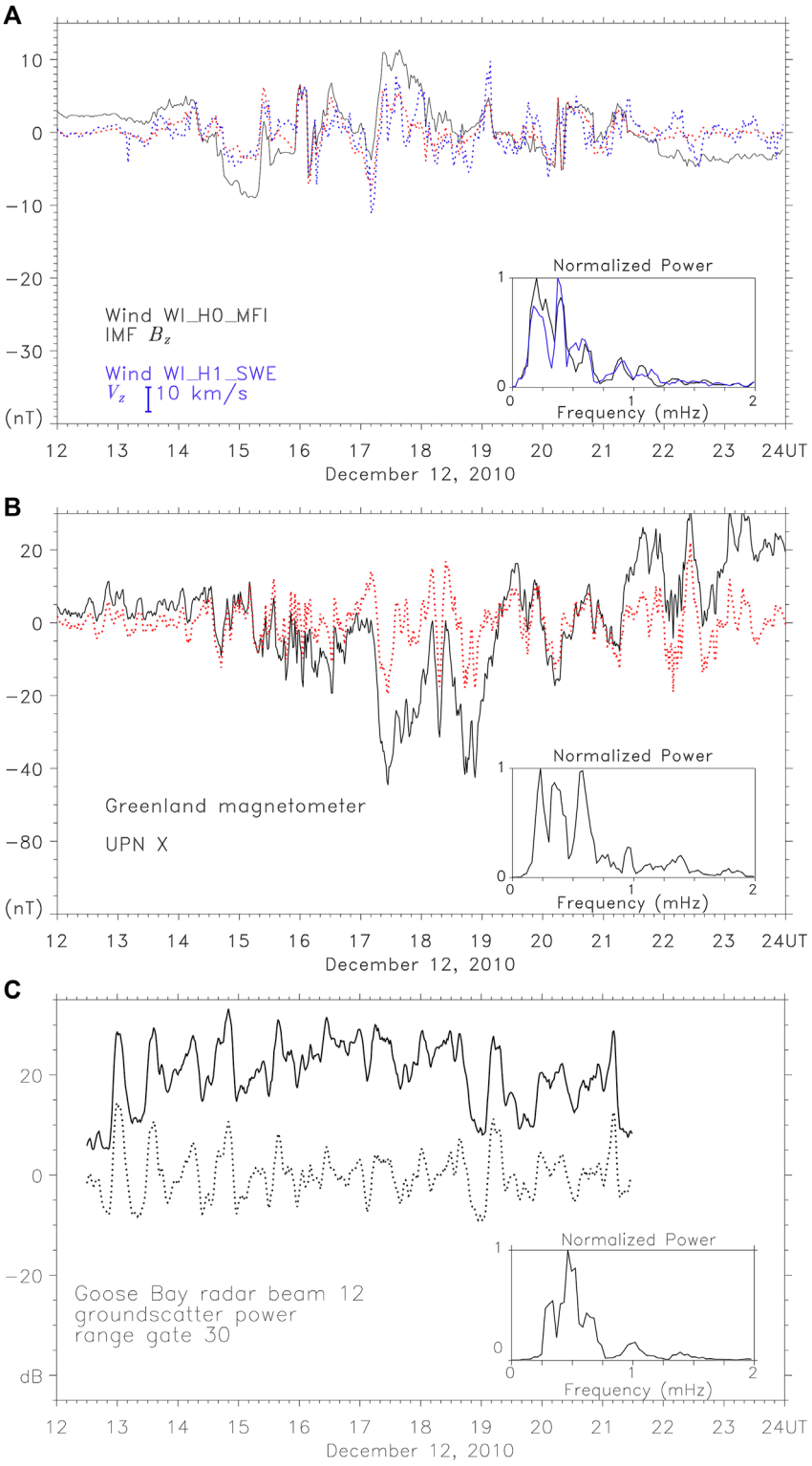

FIGURE 12
(A) Southward components of the magnetic field and proton velocity measured by the Wind spacecraft in the upstream solar wind. The normalized FFT power spectra of the detrended time series (dotted line) of IMF B_Z (red) and proton velocity V_Z (blue) components are shown. **(B)** The UPN X component of the ground magnetic field (black line) observed in Upernavik and the FFT spectrum of the detrended time series (dotted red line). **(C)** Ground scatter power observed by the Goose Bay radar beam 12 at range gate 30 and the FFT spectrum of the detrended time series (dotted line).

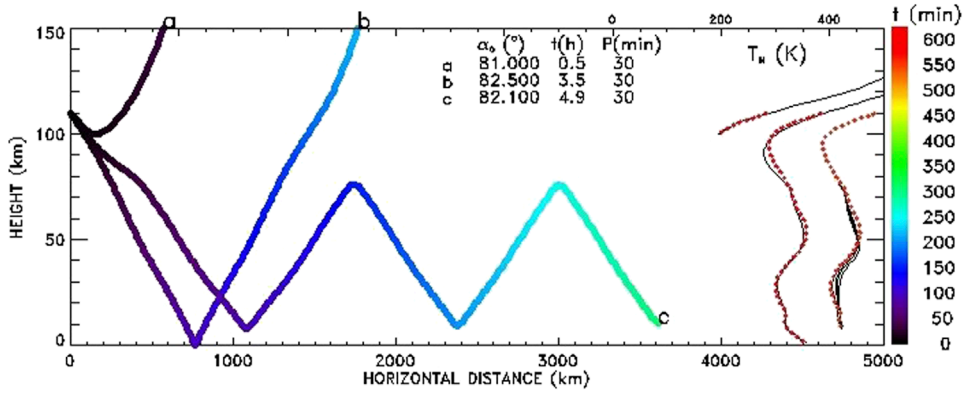

FIGURE 13
Ray tracing in the MSIS-90 model atmosphere of gravity waves with a 30-min period launched over Upernavik, Greenland. The rays are color-coded by group time, *t*. The neutral temperature $T_N(z)$ profiles for each ray are superposed. T_N for the first down-leg path is shown by the red dotted line. Multiple offsets of 100 K are applied to successive profiles for rays b and c. The initial values α_0 of wave vector k directions from the horizontal direction, wave period *P* and group time, are printed.

atmosphere. It is noted that group times for rays reaching the troposphere at distances past 3,000 km are greater than 4 h, which is approximately the time from the launch of AGWs to the appearance of "back building" convection cells (Figure 7A). Similar cases have been discussed previously (Prikryl et al., 2009a; Prikryl et al., 2018). Over-reflection of downgoing AGWs in unstable frontal zones could have contributed to the release of the instability, leading to a string of convection cells forming the "back building" squall line shown in Figure 7A.

Theoretical analysis of AGW propagation in the lower atmosphere using an expansion of three-dimensional normal mode functions was performed by Hagiwara and Tanaka (2020). These authors showed that the waves can propagate downward to the troposphere as attenuating gravity waves and "the wave propagations and reflections at the surface create an anti-node of geopotential at the bottom of the atmosphere corresponding to the vertical width of the initial state of the impact." On the other hand, "standing waves in temperature create a node at the ground surface." They suggested that standing waves generated in the lower troposphere could affect atmospheric stability through the passage of gravity waves, in turn affecting the development of cyclones.

These theoretical results propose the following question: could the strings of convective cells forming "back building" squall lines, as observed in Figure 7A, be caused by standing waves, as they are generated in the lower troposphere by downgoing AGWs? If so, the nodes (anti-nodes) of a standing wave would be separated by half a wavelength $\lambda/2$. While upgoing medium-scale AGWs/TIDs have typically horizontal wavelengths $\lambda \geq 400$ km, downgoing AGW packets would have shorter horizontal wavelengths $\lambda < 300$ km (Prikryl et al., 2005; their Figure 2B). Standing waves generated by such AGWs in the lower troposphere, as suggested previously, would have node spacing comparable with the spacing between the convective cells (~150 km or less). Furthermore, the two "back building" squall lines seem to have formed simultaneously (Figure 7A). This would be consistent with the notion that they were formed by equatorward-propagating AGWs at this time, although the one associated with the main cold front transformed more quickly into a solid squall line, while the convective cells forming the adjacent squall line persisted longer as they expanded.

7 Summary and conclusions

It is observed that heavy rainfall-induced floods in Canada tend to follow arrivals of solar wind high-speed streams from coronal holes. Cool season precipitation events, including extreme freezing rain events, that were caused by intensifying low-pressure systems and that resulted in power outages in the province of New Brunswick, also show this tendency. The superposed epoch analysis of solar wind variables keyed to the maximum deepening rate of the central sea-level pressure indicates that many of these extratropical cyclones intensified, some explosively, following arrivals of high-speed streams. Further evidence is provided by using a satellite-based gridded precipitation dataset. The superposed epoch analysis of high-rate precipitation over Canada shows a statistically significant increase in the high-rate precipitation occurrence following arrivals of major high-speed streams. These results support previously published results for other mid-latitude geographic regions. The link between solar wind high-speed streams and heavy precipitation occurrence points to solar wind–magnetosphere–ionosphere–atmosphere coupling mediated by aurorally excited globally propagating atmospheric gravity waves potentially contributing to convection by releasing the conditional symmetric instability in the troposphere. The latent heat release is often associated with intensification of storms. This is supported by the ERA5 reanalysis dataset used to diagnose SCAPE and the vertically integrated extent of realizable symmetric instability to assess the likelihood of slantwise convection. The assessment of conditional symmetric instability using the global ERA5 dataset will provide opportunities to study events when the proposed mechanism may be in action. The role of globally propagating aurorally excited gravity waves will be considered in future studies examining severe weather conditions, such as heavy rainfall-induced flash floods and large tornado outbreaks.

Data availability statement

The original contributions presented in the study are included in the article/Supplementary Material; further inquiries can be directed to the corresponding author.

Author contributions

PP and VR contributed to conception and design of the study. PP and VR contributed to the specific data analysis and organized the database. PP performed the statistical analysis and wrote the first draft of the manuscript. All authors contributed to the article and approved the submitted version.

Funding

This research was supported by the University of New Brunswick and by the VEGA project 2/0048/20 (Slovak Academy of Sciences).

Acknowledgments

The authors would like to thank T-C Chen at the Institute of Meteorology and Climate Research, Karlsruhe Institute of Technology, for providing the results of the analysis of moist symmetric instability and for many valuable comments and suggestions during the preparation of the manuscript. The contributions by ACE, Geotail, IMP-8, SOHO, and Wind spacecraft teams; the NSSDC OMNIWeb; and the SuperDARN project are acknowledged. The SuperDARN is a collection of radars funded by national scientific funding agencies of Australia, Canada, China, France, Italy, Japan, Norway, South Africa, the United Kingdom, and the United States. Meteorological data were accessed online at web pages provided by various institutions, including Environment Canada, the University of Wisconsin–Madison Space Science and Engineering Center, and the University of Washington, Department of Atmospheric Sciences. Satellite images and derived products were provided by the Cooperative Institute for Meteorological Satellite Studies, University of Wisconsin—Madison. The IMERG dataset is provided by the Goddard Earth Sciences Data and Information Services Center. The JRA-55 reanalysis is a product of the Japan Meteorological Agency (JMA). The reanalysis dataset ERA5 is a product of the European Centre for Medium-Range Weather Forecasts (ECMWF).

Conflict of interest

The authors declare that the research was conducted in the absence of any commercial or financial relationships that could be construed as a potential conflict of interest.

Publisher's note

Supplementary material

The Supplementary Material for this article can be found online at: https://www.frontiersin.org/articles/10.3389/fspas.2023.1196231/full#supplementary-material

References

Ambrož, P. (1979). Statistical method of superposition of epochs. I. Methodical analysis and some criteria of application. *B. Astron. Inst. Czechosl.* 30,114–121.

Arora, B. R., and Padgaonkar, A. D. (1981). Time-Variation of solar influence on tropospheric circulation. *J. Atmos. Terr. Phys.* 43, 91–95. doi:10.1016/0021-9169(81)90066-0

Balthazor, R. L., and Moffett, R. J. (1997). A study of atmospheric gravity waves and travelling iono-spheric disturbances at equatorial latitudes. *Ann. Geophys.* 15, 1048–1056. doi:10.1007/s00585-997-1048-4

Belcher, J. W., and Davis, L. (1971). Large- amplitude alfven waves in the interplanetary medium, 2. *J. Geophys. Res.* 76 (16), 3534–3563. doi:10.1029/ja076i016p03534

Bennetts, D. A., and Hoskins, B. J. (1979). Conditional symmetric instability – a possible explanation for frontal rainbands. *Quart. J. Roy. Meteor. Soc.* 105, 945–962. doi:10.1002/qj.49710544615

Bluestein, H. B., and Jain, M. H. (1985). Formation of mesoscale lines of pirecipitation: Severe squall lines in Oklahoma during the spring. *J. Atmos. Sci.* 42 (16), 1711–1732. doi:10.1175/1520-0469(1985)042<1711:FOMLOP>2.0.CO;2

Bluestein, H. B. (1993). *Synoptic-dynamic Meteorology in midlatitudes. Volume II: Observations and theory of weather systems*. Oxford University Press. doi:10.1016/0021-9169(94)90121-x

Brekke, A., and Kamide, Y. (1996). On the relationship between Joule and frictional heating in the polar ionosphere. *J. Atmos. Terr. Phys.* 58 (1–4), 139–143. doi:10.1016/0021-9169(95)00025-9

Bristow, W. A., Greenwald, R. A., and Samson, J. C. (1994). Identification of high-latitude acoustic gravity wave sources using the Goose Bay HF radar. *J. Geophys. Res.* 99 (A1), 319–331. doi:10.1029/93JA01470

Bristow, W. A., Greenwald, R. A., and Villain, J. P. (1996). On the seasonal dependence of medium-scale atmospheric gravity waves in the upper atmosphere at high latitudes. *J. Geophys. Res.* 101 (15), 15685–15699. doi:10.1029/96ja01010

Brooks, G. F., Evans, S. G., and Clague, J. J. (2001). Flooding. A synthesis of natural geological hazards in Canada. *Geol. Surv. Can. Bull.* 548, 101–143. doi:10.4095/212210

Burn, D. H., Caissie, D., Peters, D. L., Renzetti, S., St-Hilaire, A., and Whitfield, P. H. (2016). Preface to the special issue on floods in Canada. *Can. Water Resour. J./Revue Can. Des Ressources Hydriques* 41 (1–2), 2–6. doi:10.1080/07011784.2016.1142908

Burn, D. H., and Whitfield, P. H. (2016). Changes in floods and flood regimes in Canada. *Can. Water Resour. J./Revue Can. Des Ressources Hydriques* 41 (1–2), 139–150. doi:10.1080/07011784.2015.1026844

Burns, G. B., Bond, F. R., and Cole, K. D. (1980). An investigation of the southern hemisphere vorticity response to solar sector boundary crossings. *J. Atmos. Terr. Phys.* 42 (8), 765–769. doi:10.1016/0021-9169(80)90059-8

Burns, G. B., Tinsley, B. A., Frank-Kamenetsky, A. V., and Bering, E. A. (2007). Interplanetary magnetic field and atmospheric electric circuit influences on ground-level pressure at vostok. *J. Geophys. Res. Atmos.* 112 (4), D04103. doi:10.1029/2006JD007246

Burns, G. B., Tinsley, B. A., French, W. J. R., Troshichev, O. A., and Frank-Kamenetsky, A. V. (2008). Atmospheric circuit influences on ground-level pressure in the antarctic and arctic. *J. Geophys. Res. Atmos.* 113 (15), D15112. doi:10.1029/2007JD009618

Buttle, J. M., Allen, D. M., Caissie, D., Davison, B., Hayashi, M., Peters, D. L., et al. (2016). Flood processes in Canada: Regional and special aspects. *Can. Water Resour. J./Revue Can. Des Ressources Hydriques* 41 (1–2), 7–30. doi:10.1080/07011784.2015.1131629

Chandra, S., and McPeters, R. D. (1994). The solar cycle variation of ozone in the stratosphere inferred from Nimbus 7 and NOAA 11 satellites. *J. Geophys. Res.* 99 (D10), 20665–20671. doi:10.1029/94jd02010

Chartrand, J., Thériault, J. M., and Marinier, S. (2022). Freezing rain events that impacted the province of new Brunswick, Canada, and their evolution in a warmer climate. *Atmosphere-Ocean* 61 (1), 40–56. doi:10.1080/07055900.2022.2092444

Chartrand, J., and Thériault, J.~M. (2020). "Extreme freezing rain events in the province of new Brunswick, Canada, and their evolution in the future using convection-permitting simulations," in *AGU fall meeting abstracts*, A009–A0008.

Chen, T.-C., Yau, M. K., and Kirshbaum, D. J. (2018). Assessment of conditional symmetric instability from global reanalysis data. *J. Atmos. Sci.* 75 (7), 2425–2443. doi:10.1175/JAS-D-17-0221.1

Chimonas, G., and Hines, C. O. (1970). Atmospheric gravity waves launched by auroral currents. *Planet. Space Sci.* 18 (4), 565–582. doi:10.1016/0032-0633(70)90132-7

Chisham, G., Lester, M., Milan, S. E., Freeman, M. P., Bristow, W. A., Grocott, A., et al. (2007). A decade of the super dual auroral radar Network (SuperDARN): Scientific achievements, new techniques and future directions. *Surv. Geophys.* 28 (1), 33–109. doi:10.1007/s10712-007-9017-8

Cowling, D. H., Webb, H. D., and Yeh, K. C. (1971). Group rays of internal gravity waves in a wind-stratified atmosphere. *J. Geophys. Res.* 76 (1), 213–220. doi:10.1029/ja076i001p00213

Crowley, T. J. (2000). Causes of climate change over the past 1000 years. *Science* 289 (5477), 270–277. doi:10.1126/science.289.5477.270

de Toma, G. (2011). Evolution of coronal holes and implications for high-speed solar wind during the minimum between cycles 23 and 24. *Sol. Phys.* 274 (1–2), 195–217. doi:10.1007/s11207-010-9677-2

Dorotovič, I., Minarovjech, M., Lorenc, M., and Rybanský, M. (2014). Modified homogeneous data set of coronal intensities. *Sol. Phys.* 289 (7), 2697–2703. doi:10.1007/s11207-014-0501-2

Doswell, C. A., and Bosart, L. F. (2001). Extratropical synoptic-scale processes and severe convection. *Meteorol. Monogr.* 50 (50), 27–70. doi:10.1175/0065-9401-28.50.27

Dungey, J. W. (1961). Interplanetary magnetic field and the auroral zones. *Phys. Rev. Lett.* 6 (2), 47–48. doi:10.1103/PhysRevLett.6.47

Dungey, J. W. (1995). "Origins of the concept of reconnection and its application to the magnetopause: A historical view. Physics of the magnetopause," in *Geophysical monograph series*. Editor P. B. Song, U. O. Sonnerup, and M. F. Thomsen (Washington, D.C.: AGU), 17–19. doi:10.1029/GM090p0017

Eltayeb, I. A., and McKenzie, J. F. (1975). Critical-level behaviour and wave amplification of a gravity wave incident upon a shear layer. *J. Fluid Mech.* 72 (4), 661–671. doi:10.1017/S0022112075003217

Emanuel, K. (1994). *Atmospheric convection*. Oxford University Press.

Feren, G. (1995). The "striated delta" cloud system - a satellite imagery precursor to major cyclogenesis in the eastern Australian - weWesternasman Sea region. *Weather Forecast.* 10 (2), 286–309. doi:10.1175/1520-0434(1995)010<0286:TDCSSI>2.0.CO;2

Francis, S. H. (1974). A theory of medium-scale traveling ionospheric disturbances. *J. Geophys. Res.* 79 (34), 5245–5260. doi:10.1029/ja079i034p05245

Fukao, S., Larsen, M. F., Yamanaka, M. D., Furukawa, H., Tsuda, T., and Kato, S. (1991). Observations of a reversal in long-term average vertical velocities near the jet stream wind maximum. *Mon. Weather Rev.* 119 (6), 1479–1489. doi:10.1175/1520-0493(1991)119<1479:ooaril>2.0.co;2(1991)119<1479:OOARIL>2.0.CO;2

Glinton, M., Gray, S. L., Chagnon, J. M., and Morcrette, C. J. (2017). Modulation of precipitation by conditional symmetric instability release. *Atmos. Res.* 185, 186–201. doi:10.1016/j.atmosres.2016.10.013

Gonzalez, W. D., Joselyn, J. A., Kamide, Y., Kroehl, H. W., Rostoker, G., Tsurutani, B. T., et al. (1994). What is a geomagnetic storm?*J. Geophys. Res. Space Phys.* 99 (A4), 5771–5792. doi:10.1029/93ja02867

Gopalswamy, N. (2016). History and development of coronal mass ejections as a key player in solar terrestrial relationship. *Geosci. Lett.* 3 (1), 8. doi:10.1186/s40562-016-0039-2

Gosling, J. T., and Pizzo, V. J. (1999). Formation and evolution of corotating interaction regions and their three dimensional structure. *Space Sci. Rev.* 89, 21–52. doi:10.1023/A:1005291711900

Gourley, J. J., Erlingis, J. M., Hong, Y., and Wells, E. B. (2012). Evaluation of tools used for monitoring and forecasting flash floods in the United States. *Weather Forecast.* 27 (1), 158–173. doi:10.1175/WAF-D-10-05043.1

Gray, L. J., Beer, J., Geller, M., Haigh, J. D., Lockwood, M., Matthes, K., et al. (2010). Solar influences on climate. *Rev. Geophys.* 48 (4). doi:10.1029/2009RG-000282

Hagiwara, M., and Tanaka, H. L. (2020). A theoretical analysis of the atmospheric gravity wave that connects the thermosphere and the troposphere. *Tsukuba Geoenvironmental Sci.* 16, 1–14. doi:10.15068/00162379

Harrison, R. G., and Carslaw, K. S. (2003). Ion-aerosol-cloud processes in the lower atmosphere. *Rev. Geophys.* 41 (3), 1012. doi:10.1029/2002RG-000114

Hernandez, G. (1982). Vertical motions of the neutral thermosphere at midlatitude. *Geophys. Res. Lett.* 9 (5), 555–557. doi:10.1029/GL009i005p-00555

Hersbach, H., Bell, B., Berrisford, P., Hirahara, S., Horányi, A., Muñoz-Sabater, J., et al. (2020). The ERA5 global reanalysis. *Q. J. R. Meteorol. Soc.* 146, 1999–2049. doi:10.1002/qj.3803

Hines, C. O., and Halevy, I. (1977). On the reality and nature of a certain sun-weather correlation. *J. Atmos. Sci.* 34, 382–404. doi:10.1175/1520-0469(1977)034<0382:otrano>2.0.co;2

Hines, C. O. (1960). Internal atmospheric gravity waves at ionospheric heights. *Can. J. Phys.* 38 (11), 1441–1481. doi:10.1139/p60-150

Hines, C. O. (1965). "Motions of the neutral atmosphere," in *Canadian journal of Physics*. Editors J. A. F. C. O. Hines, I. Paghis, and T. R. Hartz (London: Prentice-Hall, Inc.).

Hocke, K., and Schlegel, K. (1996). A review of atmospheric gravity waves and travelling ionospheric disturbances: 1982-1995. *Ann. Geophys.* 14 (9), 917–940. doi:10.1007/s00585-996-0917-6

Houze, R. A. (1993). *Cloud dynamics*. Academic Press. doi:10.1016/0377-0265(87)90017-0

Huffman, G. J., Stocker, E. F., Bolvin, D. T., Nelkin, E. J., and Tan, J. (2019). *GPM IMERG final precipitation L3 1 day 0.1 degree x 0.1 degree V06*. Goddard Earth Sciences Data and Information Services Center (GES DISC. doi:10.5067./GPM/IMERGDL/DAY/06

Jones, W. L. (1968). Reflexion and stability of waves in stably stratified fluids with shear flow: A numerical study. *J. Fluid Mech.* 34 (3), 609–624. doi:10.1017/S0022112068002119

King, J. H., and Papitashvili, N. (2005). Solar wind spatial scales in and comparisons of hourly Wind and ACE plasma and magnetic field data. *J. Geophys. Res.* 110 (A2), A02104. doi:10.1029/2004JA010649

Knipp, D. J., Tobiska, W. K., and Emery, B. A. (2004). Direct and indirect thermospheric heating sources for solar cycles 21–23. *Sol. Phys.* 224 (1–2), 495–505. doi:10.1007/s11207-005-6393-4

Krieger, A. S., Timothy, A. F., and Roelof, E. C. (1973). A coronal hole and its identification as the source of a high velocity solar wind stream. *Sol. Phys.* 29 (2), 505–525. doi:10.1007/BF00150828

Lam, M. M., Chisham, G., and Freeman, M. P. (2014). Solar wind-driven geopotential height anomalies originate in the Antarctic lower troposphere. *Geophys. Res. Lett.* 41 (18), 6509–6514. doi:10.1002/2014GL061421

Lam, M. M., Chisham, G., and Freeman, M. P. (2013). The interplanetary magnetic field influences mid-latitude surface atmospheric pressure. *Environ. Res. Lett.* 8 (4), 045001. doi:10.1088/1748-9326/8/4/045001

Lam, M. M., and Tinsley, B. A. (2016). Solar wind-atmospheric electricity-cloud microphysics connections to weather and climate. *J. Atmos. Solar-Terrestrial Phys.* 149, 277–290. doi:10.1016/j.jastp.2015.10.019

Larsen, M. F., and Meriwether, J. W. (2012). Vertical winds in the thermosphere. *J. Geophys. Res. Space Phys.* 117 (A9), A09319. doi:10.1029/2012JA-017843

Lim, E.-P., and Simmonds, I. (2002). Explosive cyclone development in the southern hemisphere and a comparison with northern hemisphere events. *Mon. Weather Rev.* 130 (9), 2188–2209. doi:10.1175/1520-0493(2002)130<2188:ECDITS>2.0.CO;2

Lundstedt, H. (1984). Influence of interplanetary interaction regions on geomagnetic disturbances and tropospheric circulation. *Planet. Space Sci.* 32 (12), 1541–1545. doi:10.1016/0032-0633(84)90022-9

Macdonald, N. J., and Roberts, W. O. (1960). Further evidence of a solar corpuscular influence on large-scale circulation at 300 mb. *J. Geophys. Res.* 65 (2), 529–534. doi:10.1029/jz065i002p00529

Mayr, H. G., Harris, I., Herrero, F. A., Spencer, N. W., Varosi, F., and Pesnell, W. D. (1990). Thermospheric gravity waves: Observations and interpretation using the transfer function model (TFM). *Space Sci. Rev.* 54 (3–4), 297–375. doi:10.1007/BF00177800

Mayr, H. G., Harris, I., Varosi, F., and Herrero, F. A. (1984b). Global excitation of wave phenomena in a dissipative multiconstituent medium - 2. Impulsive perturbations in the earth'S thermosphere. *J. Geophys. Res.* 89 (A12), 10961–10986. doi:10.1029/JA089iA12p10961

Mayr, H. G., Harris, I., Varosi, F., and Herrero, F. A. (1984a). Global excitation of wave phenomena in a dissipative multiconstituent medium. 1. Transfer function of the earth'S thermosphere. *J. Geophys. Res.* 89 (A12), 10929–10959. doi:10.1029/JA089iA12p10929

Mayr, H. G., Talaat, E. R., and Wolven, B. C. (2013). Global propagation of gravity waves generated with the whole atmosphere transfer function model. *J. Atmos. Solar-Terrestrial Phys.* 104, 7–17. doi:10.1016/j.jastp.2013.08.001

McKenzie, J. F. (1972). Reflection and amplification of acoustic-gravity waves at a density and velocity discontinuity. *J. Geophys. Res.* 77 (16), 2915–2926. doi:10.1029/ja077i016p02915

Millward, G. (1994). A resonance effect in AGWs created by periodic recurrent bursts in the auroral electric field. *Ann. Geophysicae- Eur. Geophys. Soc.* 12 (1), 94.

Millward, G. H., Moffett, R. J., Quegan, S., and Fuller-Rowell, T. J. (1993a). Effects of an atmospheric gravity wave on the midlatitude ionospheric F layer. *J. Geophys. Res. Space Phys.* 98 (A11), 19173–19179. doi:10.1029/93ja02093

Millward, G. H., Quegan, S., Moffett, R. J., Fuller-Rowell, T. J., and Rees, D. (1993b). A modelling study of the coupled ionospheric and thermospheric response to an enhanced high-latitude electric field event. *Planet. Space Sci.* 41 (1), 45–56. doi:10.1016/0032-0633(93)90016-U

Nastrom, G. D., Peterson, M. R., Green, J. L., Gage, K. S., and Vanzandt, T. E. (1990). Sources of gravity wave activity seen in the vertical velocities observed by the Flatland VHF radar. *J. Appl. Meteorology* 29 (8), 783–792. doi:10.1175/1520-0450(1990)029<0783:SOGWAS>2.0.CO;2

Nastrom, G. D., and Vanzandt, T. E. (1994). Mean vertical motions seen by radar wind profilers. *J. Appl. Meteorology* 33 (8), 984–995. doi:10.1175/1520-0450(1994)033<0984:MVMSBR>2.0.CO;2

Nishitani, N., Ruohoniemi, J. M., Lester, M., Baker, J. B. H., Koustov, A. V., Shepherd, S. G., et al. (2019). Review of the accomplishments of mid-latitude super dual auroral radar Network (SuperDARN) HF radars. *Prog. Earth Planet. Sc.* 6, 27–52. doi:10.1186/s40645-019-0270-5

Owens, M. J., Scott, C. J., Lockwood, M., Barnard, L., Harrison, R. G., Nicoll, K., et al. (2014). Modulation of UK lightning by heliospheric magnetic field polarity. *Environ. Res. Lett.* 9 (11), 115009. doi:10.1088/1748-9326/9/11/115009

Oyama, S., Ishii, M., Murayama, Y., Shinagawa, H., Buchert, S. C., Fujii, R., et al. (2001). Generation of atmospheric gravity waves associated with auroral activity in the polar F region. *J. Geophys. Res. Space Phys.* 106 (A9), 18543–18554. doi:10.1029/2001ja900032

Oyama, S., and Watkins, B. J. (2012). Generation of atmospheric gravity waves in the polar thermosphere in response to auroral activity. *Space Sci. Rev.* 168 (1–4), 463–473. doi:10.1007/s11214-011-9847-z

Oyama, S., Watkins, B. J., Maeda, S., Shinagawa, H., Nozawa, S., Ogawa, Y., et al. (2008). Generation of the lower-thermospheric vertical wind estimated with the EISCAT KST radar at high latitudes during periods of moderate geomagnetic disturbance. *Ann. Geophys.* 26 (6), 1491–1505. doi:10.5194/angeo-26-1491-2008

Oyama, S., Watkins, B. J., Nozawa, S., Maeda, S., and Conde, M. (2005). Vertical ion motion observed with incoherent scatter radars in the polar lower ionosphere. *J. Geophys. Res. Space Phys.* 110 (A4). doi:10.1029/2004JA010705

Park, C. G. (1976). Solar magnetic sector effects on the vertical atmospheric electric field at Vostok, Antarctica. *Geophys. Res. Lett.* 3 (8), 475–478. doi:10.1029/GL003i008p00475

Phillips, J. L., Balogh, A., Bame, S. J., Goldstein, B. E., Gosling, J. T., Hoeksema, J. T., et al. (1994). Ulysses at 50° south: Constant immersion in the high-speed solar wind. *Geophys. Res. Lett.* 21 (12), 1105–1108. doi:10.1029/94GL01065

Phillips, J. L., Bame, S. J., Feldman, W. C., Goldstein, B. E., Gosling, J. T., Hammond, C. M., et al. (1995). Ulysses solar wind plasma observations at high southerly latitudes. *Science* 268 (5213), 1030–1033. doi:10.1126/science.268.5213.1030

Prikryl, P., Bruntz, R., Tsukijihara, T., Iwao, K., Muldrew, D. B., Rušin, V., et al. (2018). Tropospheric weather influenced by solar wind through atmospheric vertical coupling downward control. *J. Atmos. Solar-Terrestrial Phys.* 171, 94–110. doi:10.1016/j.jastp.2017.07.023

Prikryl, P., Greenwald, R. A., Sofko, G. J., Villain, J. P., Ziesolleck, C. W. S., and Friis-Christensen, E. (1998). Solar-wind-driven pulsed magnetic reconnection at the dayside magnetopause, Pc5 compressional oscillations, and field line resonances. *J. Geophys. Res. Space Phys.* 103 (A8), 17307–17322. doi:10.1029/97ja03595

Prikryl, P., Iwao, K., Muldrew, D. B., Rušin, V., Rybanský, M., and Bruntz, R. (2016). A link between high-speed solar wind streams and explosive extratropical cyclones. *J. Atmos. Solar-Terrestrial Phys.* 149, 219–231. doi:10.1016/j.jastp.2016.04.002

Prikryl, P., Muldrew, D. B., and Sofko, G. J. (2007). "Do auroral atmospheric gravity waves influence mesoscale processes, extratropical and tropical cyclones?," in *12th conference on mesoscale processes*, 11–15.

Prikryl, P., Muldrew, D. B., and Sofko, G. J. (2003). *High-speed solar wind, auroral electrojets and atmospheric gravity waves: A link to the earth's atmosphere*. European Space Agency, (Special Publication) ESA SP, 371–376.

Prikryl, P., Muldrew, D. B., Sofko, G. J., and Ruohoniemi, J. M. (2005). Solar wind Alfvén waves: A source of pulsed ionospheric convection and atmospheric gravity waves. *Ann. Geophys.* 23 (2), 401–417. doi:10.5194/angeo-23-401-2005

Prikryl, P., Muldrew, D. B., and Sofko, G. J. (2009b). The influence of solar wind on extratropical cyclones - Part 2: A link mediated by auroral atmospheric gravity waves?*Ann. Geophys.* 27 (1), 31–57. doi:10.5194/angeo-27-31-2009

Prikryl, P., Nikitina, L., and Rušin, V. (2019). Rapid intensification of tropical cyclones in the context of the solar wind-magnetosphere-ionosphere-atmosphere coupling. *J. Atmos. Solar-Terrestrial Phys.* 183, 36–60. doi:10.1016/j.jastp.2018.12.009

Prikryl, P., Provan, G., McWilliams, K. A., and Yeoman, T. K. (2002). Ionospheric cusp flows pulsed by solar wind Alfvén waves. *Ann. Geophys.* 20 (2), 161–174. doi:10.5194/angeo-20-161-2002

Prikryl, P., Rušin, V., and Prikryl, E. A. (2021a). High-rate precipitation occurrence modulated by solar wind high-speed streams. *Atmosphere* 12 (9), 1186. doi:10.3390/atmos12091186

Prikryl, P., Rušin, V., Prikryl, E. A., Šťastný, P., Turňa, M., and Zeleňáková, M. (2021b). Heavy rainfall, floods, and flash floods influenced by high-speed solar wind coupling to the magnetosphere–ionosphere–atmosphere system. *Ann. Geophys.* 39 (4), 769–793. doi:10.5194/angeo-39-769-2021

Prikryl, P., Rušin, V., and Rybanský, M. (2009a). The influence of solar wind on extratropical cyclones – Part 1: Wilcox effect revisited. *Ann. Geophys.* 27 (1), 1–30. doi:10.5194/angeo-27-1-2009

Rees, D., Smith, R. W., Charleton, P. J., McCormac, F. G., Lloyd, N., and Steen, Å. Å. (1984). The generation of vertical thermospheric winds and gravity waves at auroral latitudes I. Observations of vertical winds. *Planet. Space Sci.* 32 (6), 667–684. doi:10.1016/0032-0633(84)90092-8

Reid, G. C. (1997). Solar forcing of global climate change since the mid-17th century. *Clim. Change* 37 (2), 391–405. doi:10.1023/A:1005307009726

Richardson, I. G., and Cane, H. V. (2010). Near-earth interplanetary coronal mass ejections during solar cycle 23 (1996 – 2009): catalog and summary of properties. *Sol. Phys.* 264, 189–237. doi:10.1007/s11207-010-9568-6

Richmond, A. D. (1978). Gravity wave generation, propagation, and dissipation in the thermosphere. *J. Geophys. Res.* 83 (A9), 4131. doi:10.1029/ja083ia09p04131

Richmond, A. D. (2021). "Joule heating in the thermosphere. Space Physics and aeronomy collection volume 4: Upper atmosphere dynamics and energetics," in *Geophysical monograph. American geophysical union*. Editors W. Wang, and Y. Zhang (John Wiley and Sons, Inc.), 1–18. doi:10.1002/9781119815631.ch1

Roberts, W. O., and Olson, R. H. (1973). Geomagnetic storms and wintertime 300-mb trough development in the north pacific-north America area. *J. Atmos. Sci.* 30 (1), 135–140. doi:10.1175/1520-0469(1973)030<0135:GSAWMT>2.0.CO;2

Rostoker, G., and Sharma, R. P. (1980). Correlation of high latitude tropospheric pressure with the structure of the interplanetary magnetic field. *Can. J. Phys.* 58 (2), 255–269. doi:10.1139/p80-039

Rybanský, M. (1975). Coronal index of solar activity. *Bull. Astron. Inst. Czechoslov.* 28, 367–370.

Rybanský, M., Rušin, V., Minarovjech, M., Klocok, L., and Cliver, E. W. (2005). Reexamination of the coronal index of solar activity. *J. Geophys. Res. Space Phys.* 110 (A8), A08106. doi:10.1029/2005JA011146

Sanders, F., and Gyakum, J. R. (1980). Synoptic-dynamic Climatology of the "bomb". *Mon. Weather Rev.* 108 (10), 1589–1606. doi:10.1175/1520-0493(1980)108<1589:SDCOT>2.0.CO;2

Schultz, D. M., and Schumacher, P. N. (1999). The use and misuse of conditional symmetric instability. *Mon. Weather Rev.* 127 (12), 2709–2732. doi:10.1175/1520-0493(1999)127<2709:TUAMOC>2.0.CO;2

Scott, C. J., Harrison, R. G., Owens, M. J., Lockwood, M., and Barnard, L. (2014). Evidence for solar wind modulation of lightning. *Environ. Res. Lett.* 9 (5), 055004. doi:10.1088/1748-9326/9/5/055004

Smith, E. J., Tsurutani, B. T., and Rosenberg, R. L. (1978). Observations of the interplanetary sector structure up to heliographic latitudes of 16°: Pioneer 11. *J. Geophys. Res.* 83, 717–724.

Spencer, N. W., Theis, R. F., Wharton, L. E., and Carignan, G. R. (1976). Local vertical motions and kinetic temperature from AE-C as evidence for aurora-induced gravity waves. *Geophys. Res. Lett.* 3 (6), 313–316. doi:10.1029/GL003i006p00313

Spencer, N. W., Wharton, L. E., Carignan, G. R., and Maurer, J. C. (1982). Thermosphere zonal winds, vertical motions and temperature as measured from Dynamics Explorer. *Geophys. Res. Lett.* 9 (9), 953–956. doi:10.1029/GL009i009p00953

Svalgaard, L. (1975). On the use of Godhavn H component as an indicator of the interplanetary sector polarity. *J. Geophys. Res.* 80, 2717–2722. doi:10.1029/JA080i019p02717

Tanaka, T. (1979). Global structure and dynamics of the thermo-ionospheres. *Rev. Radio Res. Labs.* 25 (134), 265–309. (in Japanese).

Testud, J. (1970). Gravity waves generated during magnetic substorms. *J. Atmos. Terr. Phys.* 32 (11), 1793–1805. doi:10.1016/0021-9169(70)90137-6

Thayer, J. P., and Semeter, J. (2004). The convergence of magnetospheric energy flux in the polar atmosphere. *J. Atmos. Solar-Terrestrial Phys.* 66 (10), 807–824. doi:10.1016/j.jastp.2004.01.035

Tinsley, B. A. (2008). The global atmospheric electric circuit and its effects on cloud microphysics. *Rep. Prog. Phys.* 71 (6), 066801. doi:10.1088/0034-4885/71/6/066801

Tsurutani, B. T., McPherron, R. L., Gonzalez, W. D., Lu, G., Gopalswamy, N., and Guarnieri, F. (2006a). "Magnetic storms caused by corotating solar wind streams," in *Recurrent magnetic storms: Corotating solar wind streams*. Editors N. Tsurutani, R. McPherron, W. Gonzalez, G. Lu, and J. H. A. Sobral, (AGU monograph). doi:10.1029/GM167

Tsurutani, B. T., Gonzalez, W. D., Gonzalez, A. L. C., Guarnieri, F. L., Gopalswamy, N., Grande, M., et al. (2006b). Corotating solar wind streams and recurrent geomagnetic activity: A review. *J. Geophys. Res. Space Phys.* 111 (7), A07S01. doi:10.1029/2005JA011273

Tsurutani, B. T., Gonzalez, W. D., Gonzalez, A. L. C., Tang, F., Arballo, J. K., and Okada, M. (1995). Interplanetary origin of geomagnetic activity in the declining phase of the solar cycle. *J. Geophys. Res. Space Phys.* 100 (A11), 21717–21733. doi:10.1029/95ja01476

Tsurutani, B. T., and Gonzalez, W. D. (1987). The cause of high-intensity long-duration continuous AE activity (HILDCAAs): Interplanetary Alfvén wave trains. *Planet. Space Sci.* 35 (4), 405–412. doi:10.1016/0032-0633(87)90097-3

Tsurutani, B. T., Gould, T., Goldstein, B. E., Gonzalez, W. D., and Sugiura, M. (1990). Interplanetary Alfvén waves and auroral (substorm) activity: Imp 8. *J. Geophys. Res.* 95 (A3), 2241–2252. doi:10.1029/ja095ia03p02241

Tsurutani, B. T., Hajra, R., Tanimori, T., Takada, A., Remya, B., Mannucci, A. J., et al. (2016). Heliospheric plasma sheet (HPS) impingement onto the magnetosphere as a cause of relativistic electron dropouts (REDs) via coherent EMIC wave scattering with possible consequences for climate change mechanisms. *J. Geophys. Res. Space Phys.* , 121 (10), 10,130–10,156. doi:10.1002/2016JA-022499

Villarini, G., Krajewski, W. F., Ntelekos, A. A., Georgakakos, K. P., and Smith, J. A. (2010). Towards probabilistic forecasting of flash floods: The combined effects of uncertainty in radar-rainfall and flash flood guidance. *J. Hydrology* 394 (1–2), 275–284. doi:10.1016/j.jhydrol.2010.02.014

Wilcox, J. M., and Scherrer, P. H. (1981). On the nature of the apparent response of the vorticity area index to the solar magnetic field. *Sol. Phys.* 74 (2), 421–432. doi:10.1007/BF00154528

Wilcox, J. M., Scherrer, P. H., Svalgaard, L., Roberts, W. O., Olson, R. H., and Jenne, R. L. (1974). Influence of solar magnetic sector structure on terrestrial atmospheric vorticity. *J. Atmos. Sci.* 31 (2), 581–588. doi:10.1175/1520-0469(1974)031<0581:IOSMSS>2.0.CO;2

Wilcox, J. M., Scherrer, P. H., Svalgaard, L., Roberts, W. O., and Olson, R. H. (1973). Solar magnetic sector structure: Relation to circulation of the Earth's atmosphere. *Science* 180 (4082), 185–186. doi:10.1126/science.180.4082.185

Wilcox, J. M., Svalgaard, L., and Scherrer, P. H. (1976). On the reality of a sun-weather effect. *J. Atmos. Sci.* 33 (6), 1113–1116. doi:10.1175/1520-0469(1976)033<1113:OTROAS>2.0.CO;2

Wilcox, J. M. (1979). Tropospheric circulation and interplanetary magnetic sector boundaries followed by MeV proton streams. *Nature* 278 (5707), 840–841. doi:10.1038/278840a0

Williams, P. J. S., Virdi, T., Lewis, R., Lester, M., Rodger, A., McCrea, I., et al. (1993). Worldwide atmospheric gravity-wave study in the European sector 1985–1990. *J. Atmos. Terr. Phys.* 55 (4–5), 683–696. doi:10.1016/0021-9169(93)90014-P

Williams, R. G. (1978). A study of the energetics of a particular Sun-weather relation. *Geophys. Res. Lett.* 5 (6), 519–522. doi:10.1029/GL005i006p00519

Williams, R. G., and Gerety, E. J. (1978). Does the troposphere respond to day-to-day changes in solar magnetic field?*Nature* 275 (5677), 200–201. doi:10.1038/275-200b0

Xu, J., Smith, A. K., Wang, W., Jiang, G., Yuan, W., Gao, H., et al. (2013). An observational and theoretical study of the longitudinal variation in neutral temperature induced by aurora heating in the lower thermosphere. *J. Geophys. Res. Space Phys.* 118 (11), 7410–7425. doi:10.1002/2013JA019144

Yeh, K. C., and Liu, C. H. (1974). Acoustic-gravity waves in the upper atmosphere. *Rev. Geophys.* 12 (2), 193–216. doi:10.1029/RG012i002p00193

frontiers | Frontiers in Astronomy and Space Sciences

TYPE Original Research
PUBLISHED 07 August 2023
DOI 10.3389/fspas.2023.1198071

OPEN ACCESS

EDITED BY
Kazue Takahashi,
Johns Hopkins University, United States

REVIEWED BY
Sai Gowtam Valluri,
University of Alaska Fairbanks, United States
Catalin Negrea,
Space Science Institute, Romania

*CORRESPONDENCE
S. Sobhkhiz-Miandehi,
sahar@gfz-potsdam.de

RECEIVED 31 March 2023
ACCEPTED 17 July 2023
PUBLISHED 07 August 2023

CITATION
Sobhkhiz-Miandehi S, Yamazaki Y, Arras C and Themens D (2023), A comparison of FORMOSAT-3/COSMIC radio occultation and ionosonde measurements in sporadic E detection over mid- and low-latitude regions. *Front. Astron. Space Sci.* 10:1198071. doi: 10.3389/fspas.2023.1198071

A comparison of FORMOSAT-3/COSMIC radio occultation and ionosonde measurements in sporadic E detection over mid- and low-latitude regions

S. Sobhkhiz-Miandehi[1,2]*, Y. Yamazaki[3], C. Arras[4,5] and D. Themens[6,7]

[1]Department of Geophysics, GFZ German Research Centre for Geosciences, Potsdam, Germany, [2]Faculty of Mathematics and Natural Sciences, Institute of Geosciences, University of Potsdam, Potsdam, Germany, [3]Department Modelling of Atmospheric Processes, IAP Leibniz Institute of Atmospheric Physics, Kühlungsborn, Germany, [4]Department of Geodesy, GFZ German Research Centre for Geosciences, Potsdam, Germany, [5]Institute of Geodesy and Geoinformation Technology, Berlin University of Technology, Berlin, Germany, [6]School of Engineering, University of Birmingham, Birmingham, United Kingdom, [7]Department of Physics, University New Brunswick, Fredericton, NB, Canada

The investigation of sporadic E or Es layers typically relies on ground-based or satellite data. This study compares the Es layers recorded in ionograms with those detected using GNSS L1 signal-to-noise ratio data from FORMOSAT-3/COSMIC radio occultation at mid and low latitudes. GPS radio occultation measurements of Es layers, during an 11-year time span of 2007–2017, within a 2° latitude × 5° longitude grid around each ionosonde site are compared to the Es recordings of the ionosonde. By comparing multi-year radio occultation data with recordings from six ionosonde stations at mid and low latitudes, it was discovered that at least 20% of the Es layer detection results between each ionosonde and its crossing GPS radio occultation measurements did not agree. The results show that the agreement between the two methods in Es detection is highly dependent on the season and local time. This study suggests that Es layer recordings from ground-based ionosonde observations have the best agreement with the Es layers detected by radio occultation data during daytime and local summers. The difference in the Es detection mechanisms between the two methods can explain the inconsistency between Es events measured by these two methods. The detection of Es layers in ionograms relies on the high plasma concentration in the E region, whereas signal scintillations caused by a large vertical gradient of the plasma density in the E region are considered a sign of Es occurrence in satellite techniques.

KEYWORDS

sporadic E, radio occultation, ionosonde, FORMOSAT-3/COSMIC, ionogram

1 Introduction

Thin layers of enhanced electron density compared to the background ionization in the ionosphere's E region are referred to as sporadic E and abbreviated as Es (Whitehead, 1989; Mathews, 1998; Wu et al., 2005; Haldoupis, 2011). The Es layer is mainly known as a daytime and summer hemisphere phenomenon with higher occurrence rate at mid and low latitudes (Haldoupis et al., 2007; Christakis et al., 2009; Arras et al., 2010; Haldoupis, 2012).

Whitehead (1961) and Axford and Cunnold (1966) proposed that Es layers are formed by the wind shear mechanism. In subsequent studies, the wind shear theory has been confirmed as the physical mechanism responsible for the mid-latitude Es layer formation process (Whitehead, 1989; Haldoupis & Pancheva, 2002; Haldoupis, 2011; Yamazaki et al., 2022). According to the wind shear theory, metallic ions in the ionosphere dynamo region converge to thin layers of ionization by the vertical shears of neutral wind, mainly produced by atmospheric tides (Haldoupis, 2012; Chu et al., 2014; Shinagawa et al., 2017; Qiu et al., 2019; Sobhkhiz-Miandehi et al., 2022).

Es has been subject to many studies since the mid-twentieth century (Whitehead, 1961; 1970; 1989; Macleod, 1966) due to its potential disturbances on the radio signals in communication and navigation systems. Strong vertical electron density gradients of Es layers can cause severe radio wave propagation disruption and will directly influence the accuracy and reliability of satellite communication and navigation systems (Arras, 2010).

For many years, most of the observational studies of Es were performed using ionosonde recordings; there were also several investigations based on incoherent and coherent scatter radars and some through *in situ* measurements with rockets. These techniques have been documented in several review papers (Matsushita, 1962; Whitehead, 1989; Mathews, 1998; Haldoupis, 2011). However, with the development of the GPS radio occultation technique over the past two decades, satellite observations have become an increasingly popular tool for studying Es layers due to their ability to provide global data coverage (Igarashi et al., 2001; Wu et al., 2005; Arras et al., 2008).

First, Es occurrence global maps were introduced in the early 60s based on ionosonde measurements (Taguchi, 1961; Leighton et al., 1962). Reddy and Matsushita (1969) studied Es layers at mid and low latitudes utilizing the ionosonde to establish a more detailed understanding of temporal and latitudinal variations of them. Subsequently, until the 1990s, numerous studies typically focused on examining the diurnal and seasonal variations of Es by utilizing ionosonde observations (Axford & Cunnold, 1966; Harris and Taur, 1972; Chandra and Rastogi, 1975; Saksena, 1976; MacDougall, 1978; Baggaley, 1984).

In the 2000s, scientists started using GPS radio occultation measurements to study lower ionospheric irregularities such as Es. For the first time, Igarashi et al. (2001) conducted a study that used less than 6,000 occultation GPS/MET radio data from 1995 to examine the seasonal dependency of Es layers. Wickert et al. (2004) suggested that fluctuations in the CHAMP radio occultation amplitude data can be associated with ionospheric scintillations. Furthermore, Wu et al. (2005) presented a global climatology of the phase variances and signal-to-noise ratio (SNR) fluctuations using approximately 6000 GPS/CHAMP occultation in the E region.

Since the release of radio occultation measurements from FORMOSAT-3/COSMIC in the summer of 2006, our understanding of Es has significantly improved due to its global coverage. Arras et al. (2008) published the first Es occurrence rate global climatology using CHAMP, GRACE, and FORMOSAT-3/COSMIC radio occultation, which had a significantly better spatial and temporal resolution compared to previous studies. Subsequently, studies investigating Es on a global scale have been primarily based on radio occultation measurements (Wu et al., 2005; Chu et al., 2014; Qiu et al., 2019; Yu et al., 2019; Luo et al., 2021; Arras et al., 2022), while some literature has used ionosonde observations locally as an evaluation tool for their satellite-based investigations (Gooch et al., 2020; Carmona et al., 2022; Gan et al., 2022; Yu et al., 2022). Recently, Gan et al. (2022) used radio occultation data from the new China Seismo-Electromagnetic Satellite mission to derive Es events and used Wuhan ionosonde observations to assess the reliability of their research. Carmona et al. (2022) compared different GPS radio occultation techniques with ionosonde measurements over an 8-year period in order to identify the most accurate method for detecting Es occurrences using radio occultation data. Gooch et al. (2020) presented a global comparison of the intensity and height of mid-latitude and equatorial Es layers derived from FORMOSAT-3/COSMIC radio occultation and digital ionosonde measurements. All of these studies found a qualitative agreement between their satellite dataset and ionosonde measurements of the Es layer. However, they were limited by observations at a single ionosonde location during a restricted time frame and did not account for the diurnal, seasonal, and spatial dependence of Es layer detectability with satellite and ground-based techniques. In this paper, we have conducted a multi-year comparison of the mid- and low-latitude Es events recorded by an ionosonde ground-based technique to those observed using the satellite radio occultation method. Moreover, the diurnal, seasonal, and local dependence of the agreement between the two methods has been examined.

2 Data and methodology

2.1 Ionosonde

For decades, an ionosonde has remained the most commonly utilized instrument in ionospheric studies. Basically, an ionosonde transmits signals with increasing frequency from 0.1 to 30 MHz, and the frequency at which the initial signal is reflected completely will be recorded; it is known as critical frequency (fc). By measuring the frequency and reflection time of the transmitted signal, the electron density of the reflection point and the height of the ionization layer will be obtained. Two common frequency parameters used in Es layer studies are "foEs" and "fbEs." foEs represents the ordinary mode peak frequency of the layer, and technically, it shows the maximum frequency at which an Es layer will reflect a signal transmitted by the ionosonde. fbEs corresponds to the peak blanketing frequency of Es, representing the frequency at which the reflections from higher layers appear (Piggott, 1972; Wakai et al., 1987; Merriman et al., 2021).

In this study, we used the Digital Ionogram Database (DIDBase) repository of the Lowell Global Ionospheric Radio

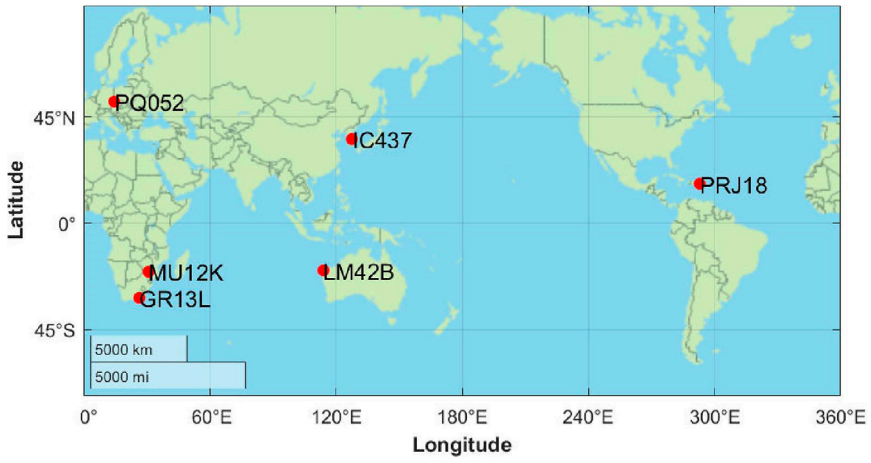

FIGURE 1
Map of the ionosonde stations.

TABLE 1 List of ionosonde stations.

Station code	Station name	Geographic latitude	Geographic longitude	Data of the year	Number of conjunction
PQ052	Pruhonice	50	14.6	2007–2017	4680
IC437	I-Cheon	37.1	127.5	2010–2017	1635
PRJ18	Ramey	18.5	293	2011–2017	2230
GR13L	Grahamstown	−33.3	26.5	2007–2017	3775
MU12K	Madimbo	−22.4	30.9	2007–2017	3150
LM42B	Learmonth	−21.8	114.1	2007–2017	3130

Observatory (GIRO) Data Center (Reinisch and Galkin, 2011). The Es events were derived from the ionograms manually. Six stations, as illustrated in Figure 1, were selected to encompass the mid- and low-latitude areas of both hemispheres across various longitudes. Additionally, the selection of ionosonde stations took into consideration the availability of sufficient data during the period when we have access to radio occultation observations. The ionosonde measurements used in this study were recorded with a time resolution of 15 min.

Table 1 provides details about the stations under investigation. Pruhonice and I-Cheon are situated at the mid-latitude region of the Northern Hemisphere, while Grahamstown serves as a representative of the mid-latitude region in the Southern Hemisphere. The Ramey station is located in the low-latitude region of the Northern Hemisphere, while the Madimbo and Learmonth stations are in the low-latitude region of the Southern Hemisphere, as investigated in our study.

2.2 FORMOSAT-3/COSMIC radio occultation

The GPS radio occultation technique is principally based on receiving GPS dual-frequency signals traveling through the atmosphere by a low earth-orbiting (LEO) satellite. GPS signals

TABLE 2 Confusion matrix of ~9,000 conjunction data points of ionograms and radio occultation profiles.

	$Es_{radio\text{-}occultation} = 1$	$Es_{radio\text{-}occultation} = 0$
$Es_{ionogram} = 1$	31.6% (Type 1)	20.4% (Type 2)
$Es_{ionogram} = 0$	10.6% (Type 3)	37.3% (Type 4)

are bent on their way through the atmosphere due to atmospheric refraction. The angle of this bending is the key observation and contains information on several atmospheric parameters, including electron density, temperature, pressure, and water vapor profiles (Hajj et al., 2002). The main advantages of radio occultation over ground-based techniques are its global coverage of atmospheric parameters and high spatial resolution. Nevertheless, the temporal resolution of radio occultation data is not as optimal as ground-based measurements at a specific location (Arras, 2010).

FORMOSAT-3/COSMIC stands for FORMOsa SATellite mission–3/Constellation Observing System for Meteorology, Ionosphere, and Climate. This American–Taiwanese mission has a constellation of six LEO satellites, which receive data from setting and rising occultations. Signal phase differences, ionospheric excess phase, and SNR values are three parameters that have been used in the literature to detect Es layers (Igarashi et al., 2001; Wu et al., 2005; Arras, 2010). According to the work of Arras (2010), utilizing L1

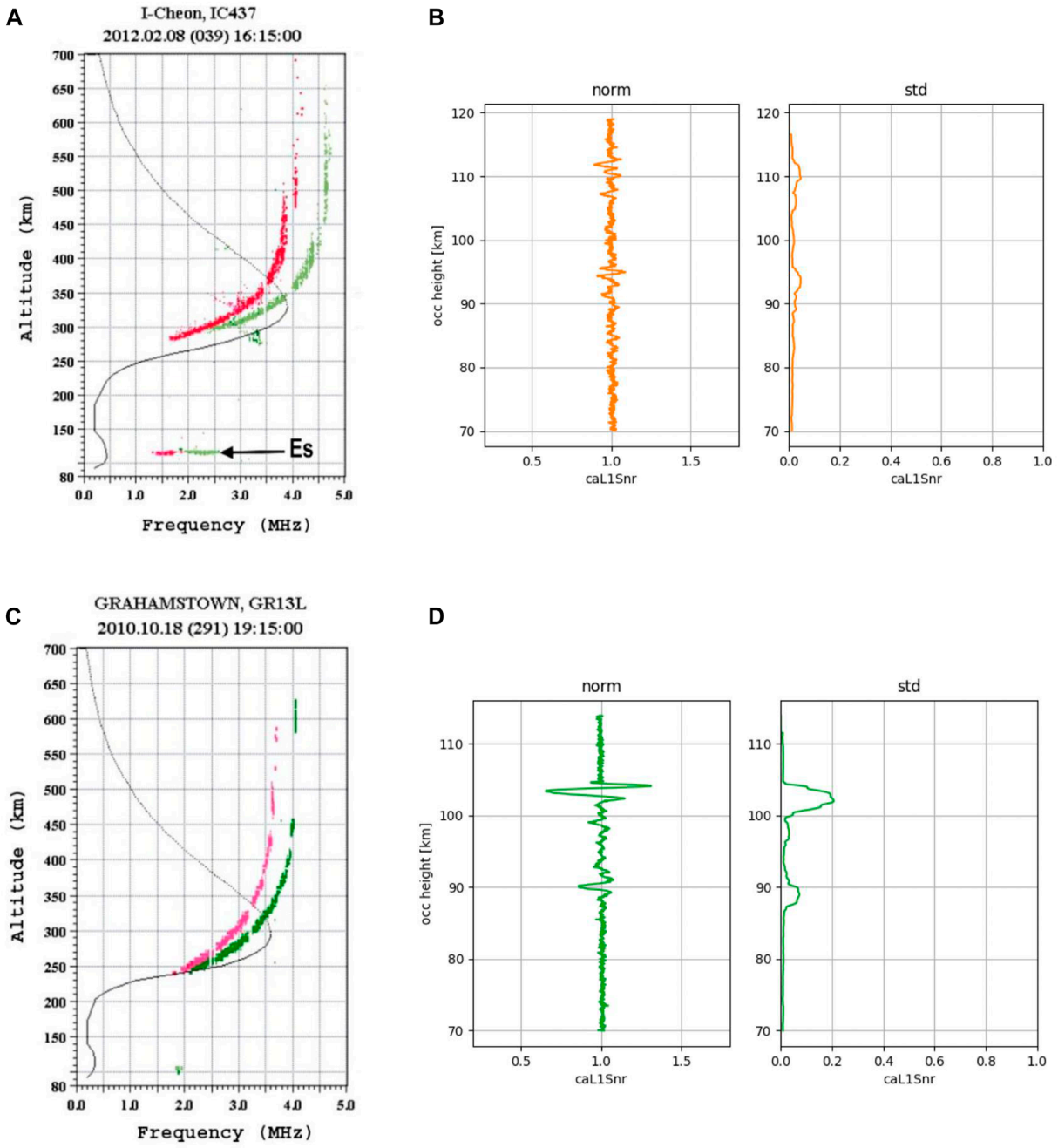

FIGURE 2
(A) Ionogram of the IC437 station (lat: 37.1° and lon: 127.5°) showing an Es layer on February 8, 2012, at 16:15. **(B)** SNR profile of a crossing radio occultation (lat: 37.3° and lon: 127.5°) showing no Es layer on February 8, 2012, at 16:12, and its corresponding standard deviation profile. **(C)** Ionogram of the GR13L station (lat: -33.3° and lon: 26.5°) showing no Es layer on October 18, 2010, at 19:15. **(D)** SNR profile of a crossing radio occultation (lat: -33.4° and lon: 26.6°) showing an Es layer on October 18, 2010, at 19:15, and its corresponding standard deviation profile.

signal SNR for Es detection offers advantages such as direct access to SNR profiles without the need for data smoothing, avoidance of noisy L2 data, and simplified analysis using raw GNSS L1 data, reducing errors in data analysis. This study relies on the Es detection method presented by Arras and Wickert (2018). They derived Es events from the SNR profiles of the GPS L1 signal of the 50 Hz level 1b atmPhs data product archived by the COSMIC Data Analysis and Archive Center (CDAAC). Empirical thresholds for SNR values were established by Arras and Wickert (2018) through manual examination of radio occultation profiles. SNR values were calculated at 2 km moving intervals and utilized to identify signal scintillations with an SNR standard deviation exceeding 0.2, provided that these large standard deviation values were concentrated within an altitude range of less than 10 km. This altitude criterion of 10 km was incorporated into the Es detection process to distinguish Es events from signal disruptions caused

TABLE 3 Latitudinal dependence of the agreement between ionosonde and radio occultation measurements in detecting the Es layer (lat_{st}: latitude of the Pruhonice station). Case 1 represents $Es_{radio\text{-}occultation} = 1$, while case 2 is $Es_{ionogram} = 1$.

(lat_{st}-2°, lat_{st}-1.5°)	(lat_{st}-1.5°, lat_{st}-1°)	(lat_{st}-1°, lat_{st}-0.5°)	(lat_{st}-0.5°, lat_{st})
Case 1: 85%	Case 1: 82%	Case 1: 91%	Case 1: 89%
Case 2: 54%	Case 2: 54.3%	Case 2: 62.2%	Case 2: 57.3%
(lat_{st}, lat_{st} + 0.5°)	(lat_{st} + 0.5°, lat_{st} + 1°)	(lat_{st} + 1°, lat_{st} + 1.5°)	(lat_{st} + 1.5°, lat_{st} + 2°)
Case 1: 86%	Case 1: 90%	Case 1: 90%	Case 1: 91%
Case 2: 53.7%	Case 2: 58.5%	Case 2: 61%	Case 2: 56.7%

TABLE 4 Longitudinal dependence of the agreement between ionosonde and radio occultation measurements in detecting the Es layer (lon_{st}: longitude of the Pruhonice station). Case 1 represents $Es_{radio\text{-}occultation} = 1$, while case 2 is $Es_{ionogram} = 1$.

(lon_{st}-5°, lon_{st}-4°)	(lon_{st}-4°, lon_{st}-3°)	(lon_{st}-3°, lon_{st}-2°)	(lon_{st}-2°, lon_{st}-1°)	(lon_{st}-1°, lon_{st})
Case 1: 84%	Case 1: 85%	Case 1: 92%	Case 1: 91%	Case 1: 87%
Case 2: 52.5%	Case 2: 53.1%	Case 2: 57.5%	Case 2: 59%	Case 2: 57.6%
(lon_{st}, lon_{st}+1°)	(lon_{st}+1°, lon_{st}+2°)	(lon_{st}+2°, lon_{st}+3°)	(lon_{st}+3°, lon_{st}+4°)	(lon_{st}+4°, lon_{st}+5°)
Case 1: 91%	Case 1: 84%	Case 1: 89%	Case 1: 89%	Case 1: 89%
Case 2: 63.6%	Case 2: 54.5%	Case 2: 62.6%	Case 2: 56.5%	Case 2: 58.6%

TABLE 5 Altitude dependence of the agreement between ionosonde and radio occultation measurements in detecting the Es layer. Case 1 represents $Es_{radio\text{-}occultation} = 1$, while case 2 is $Es_{ionogram} = 1$.

90–95 km	95–100 km	100–105 km	105–110 km	110–115 km	>115 km
Case 1: 81.5%	Case 1: 85.2%	Case 1: 89%	Case 1: 91.7%	Case 1: 93.1%	Case 1: 88.4%
Case 2: 48%	Case 2: 57.5%	Case 2: 60.1%	Case 2: 65.3%	Case 2: 66.5%	Case 2: 32.4%

TABLE 6 Seasonal dependence of the agreement between ionosonde and radio occultation measurements in detecting the Es layer. Case 1 represents $Es_{radio\text{-}occultation} = 1$, while case 2 is $Es_{ionogram} = 1$.

Local spring (Mar, Apr, and May)	Local summer (Jun, Jul, and Aug)	Local autumn (Sep, Oct, and Nov)	Local winter (Dec, Jan, and Feb)
Case 1: 87.3%	Case 1: 95.4%	Case 1: 83.5%	Case 1: 67.5%
Case 2: 47%	Case 2: 43.8%	Case 2: 50.5	Case 2: 40.5%

TABLE 7 Local time dependence of the agreement between ionosonde and radio occultation measurements in detecting the Es layer. Case 1 represents $Es_{radio\text{-}occultation} = 1$, while case 2 is $Es_{ionogram} = 1$.

0–3	3–6	6–9	9–12
Case 1: 66.1%	Case 1: 80.5%	Case 1: 98.7%	Case 1: 99%
Case 2: 55%	Case 2: 52.7%	Case 2: 51.4%	Case 2: 54%
12–15	15–18	18–21	21–24
Case 1: 97.5%	Case 1: 93.4%	Case 1: 79.6%	Case 1: 67.8%
Case 2: 52.7%	Case 2: 57.6%	Case 2: 57.8%	Case 2: 62.1%

TABLE 8 Solar zenith angle dependence of the agreement between ionosonde and radio occultation measurements in detecting the Es layer. Case 1 represents $Es_{radio\text{-}occultation} = 1$, while case 2 is $Es_{ionogram} = 1$.

Less than 45°	45°–90°	90°–135°	More than 135°
Case 1: 100%	Case 1: 98%	Case 1: 68.4%	Case 1: 47.5%
Case 2: 65.3%	Case 2: 51.2%	Case 2: 62%	Case 2: 63.3%

by technical issues or upper-layer effects like spread F from the ionospheric F layer. As SNR values are affected by the viewing angle of the GNSS satellite in relation to the LEO satellite antenna, normalized SNR values were used instead of SNR. This was carried out through the following formula (Arras, 2010):

$$SNR'(i) = \frac{SNR(i)}{\overline{SNR}},$$

where $SNR'(i)$ is the normalized SNR at profile i and $\overline{SNR}$ is the average SNR value of all profiles.

According to Wu et al. (2005), the Es layer typically extends horizontally for hundreds of kilometers, with a thickness of a few kilometers. Considering that approximately 1° corresponds to 100 km, a 2° latitude × 5° longitude grid was implemented around each ionosonde station to ensure simultaneous observations between ground-based and GPS radio occultation techniques. This grid size was intentionally chosen to be smaller than the average dimensions of the Es layer. Following the identification of all radio occultation crossings within a time difference of less than 15 min, all synchronous ionograms were inspected manually to find Es

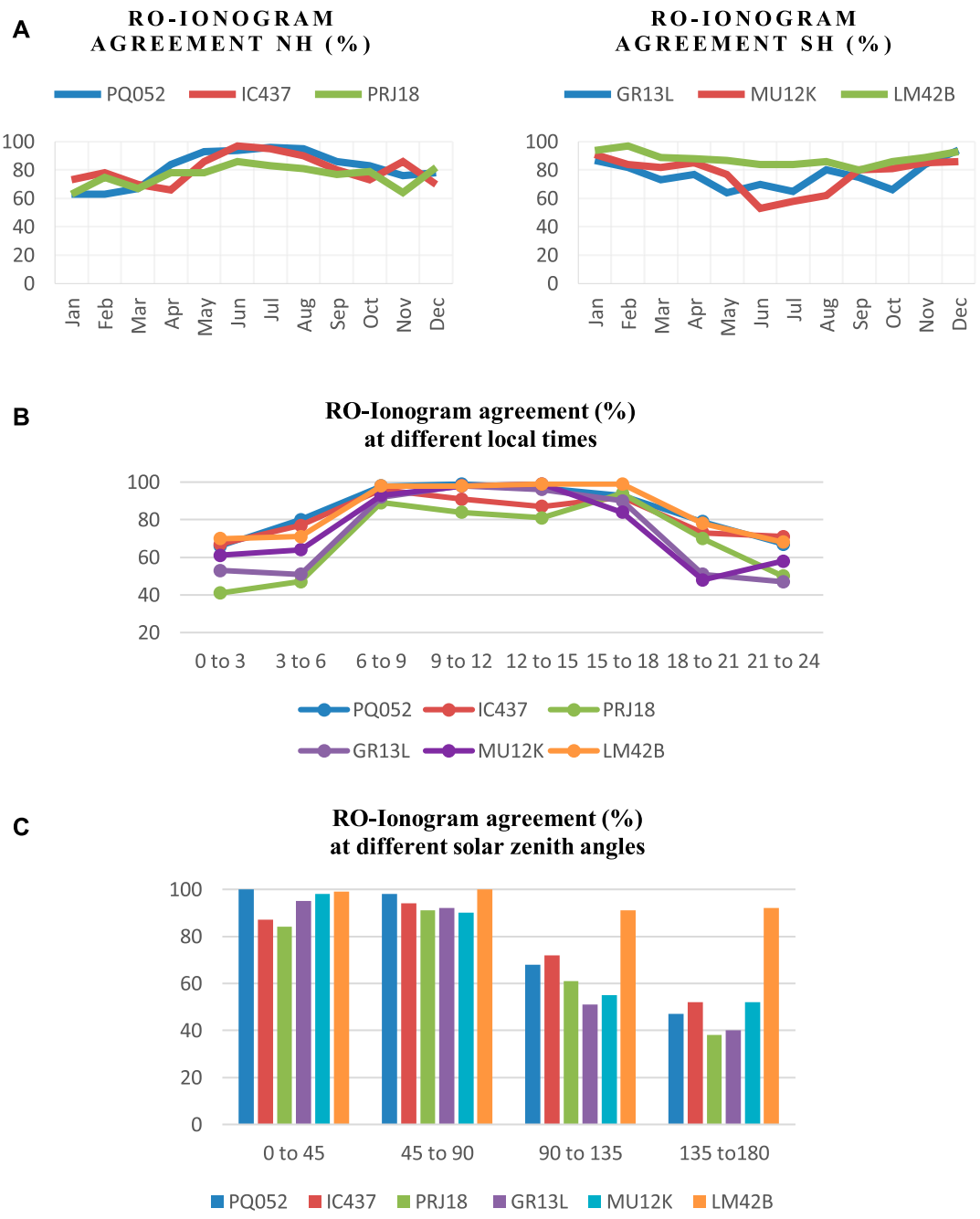

FIGURE 3
(A) Monthly dependence of the Es layer detection agreement when using radio occultation *versus* using ionosonde at the Northern Hemisphere (left) and Southern Hemisphere (right). **(B)** Local time dependence of the Es layer detection agreement when using radio occultation *versus* using ionosonde. **(C)** Solar zenith angle dependence of the Es layer detection agreement when using radio occultation *versus* using ionosonde. These results are related to case 1 ($Es_{radio-occultation}$ = 1).

events. The 15-min time interval was selected based on the sounding frequency of the ionosonde stations.

3 Results

Through a comparison of ionosonde recordings and GNSS radio occultation profiles, the results demonstrate that the agreement between the two methods in detecting Es layers ranged from 60% to 80% at different stations. We identified four possible outcomes when comparing the detection of Es layers using ionograms and GPS SNR profiles: 1) both methods detected the Es layer, 2) the Es layer was identified in ionograms but not in GPS SNR profiles, 3) GPS SNR profiles indicated the presence of an Es layer, but no signal reflection was recorded via the ionosonde in the corresponding epoch in the E region, and 4) neither method recorded the occurrence of

an Es layer. To gain a more comprehensive understanding of the distribution of these four types across all conjunction data points, we provided a confusion matrix of approximately 9,000 mid-latitude observations, presented in Table 2. It is important to note that in this paper, the notation Es = 1 signifies the presence of the Es layer, while Es = 0 denotes its absence. Furthermore, the detection of the Es layer using a specific technique is shown on the index. For instance, $Es_{ionogram} = 1$ indicates that the Es layer has been detected using an ionosonde.

Table 2 illustrates that the detection of Es layers is in agreement between ionograms and radio occultation observations in approximately 70% of the data points (summation of Type 1 and Type 4). The remaining observations are divided into two categories: Type 2 and Type 3, which account for approximately 30% of the observations. Type 2 represents approximately 65% of the remaining data, where the Es layer is observed in ionograms but not in radio occultation profiles. Conversely, Type 3, which represents almost 35% of the remaining observations, indicates the presence of an Es layer according to satellite data, but no signal reflection was recorded in ionograms. Examining similar tables for each station from 2007 to 2017, we observed that the disagreement rate between the two methods (summation of Type 2 and Type 3) varies between 20% and a maximum of 40%.

Figure 2 showcases two illustrative examples, specifically Type 2 and Type 3, that were examined in this study. In Figure 2A, we present an ionogram captured from the I-Cheon station on February 8, 2012, at 16:15. The station is located at 37.1° latitude and 127.5° longitude. The ionogram reveals the presence of an Es layer situated at an altitude of approximately 110 km. Notably, this Es layer appears relatively weak, characterized by an foEs value of 1.8 MHz and an fbEs value of 1.6 MHz. The subsequent ionogram taken at 16:30 does not display the presence of the Es layer observed earlier. This observation suggests the possibility that the I-Cheon station is located at the edge of the Es layer, where small horizontal displacements may influence the observations and result in the layer's intermittent visibility. In Figure 2B, we examine the GPS L1 SNR profile and its standard deviation for the same day. This profile was obtained using a 3-min time interval and a 0.2° difference in latitude at the same longitude. Upon closer analysis, we notice a slight increase in the signal standard deviation at altitudes approximately 95 km and 110 km. However, these deviations do not meet our predetermined criteria for detecting an Es layer. Despite the observed variations in signal standard deviation, they do not exhibit the necessary strength or magnitude to fulfill our detection criteria.

The ionogram displays two distinct ionospheric echo traces, namely, the ordinary (pink) and extraordinary (green) traces, which are attributed to the ionosphere's doubly refracting nature caused by the Earth's magnetic field (FengJuan et al., 2022).

As an illustrative example of Type 3, we present Figure 2C, which showcases an ionogram obtained from the Grahamstown ionosonde station on October 18th, 2010, at 19:15. Upon examining the ionogram, it is evident that there is no recording of the ordinary mode Es layer. This absence of a distinct Es layer signature indicates that the concentration of plasma in the E layer is insufficient to meet the criteria for classification as an Es layer in the ionogram. This observation suggests that the conditions necessary for the formation of a well-defined Es layer were not present during the time of the recording at the Grahamstown station. In contrast, Figure 2D provides further insights by presenting the GPS L1 signal data collected from a location situated approximately 0.1° in latitude and longitude from the ionosonde station, at the same time as the ionogram recording. Notably, the GPS signal data reveal distinct disturbances in the altitude range of 100–110 km. These disturbances are indicated by a standard deviation greater than 0.2, exceeding our predetermined criteria for detecting an Es layer in radio occultation data. Therefore, based on our criteria, we can confidently confirm the detection of an Es layer using the radio occultation technique.

In order to better understand the discrepancy between ground-based and satellite technique in Es layer detection, we performed a statistical analysis using a multi-year dataset of crossing observations at six stations. The analysis has been performed within different distances from the center station, at different seasons, and local times. The subsequent sections present statistical results of conjunctions at the Pruhonice station (50° N and 14.6°E) as an example of two separate cases: case 1 refers to conjunction data points in which an Es layer is detected through the radio occultation technique and is either confirmed by ionograms or not ($Es_{radio\text{-}occultation} = 1$); case 2 is characterized by the detection of an Es layer through ionograms while radio occultation signals may or may not be affected by the Es layer ($Es_{ionogram} = 1$). It is important to note that in all the following results, the agreement rate between the two methods in case 1 is always higher than in case 2. This can be simply explained by results in the confusion matrix presented in Table 2. The number of conjunction observations in which the Es layer is detected by an ionogram and not by radio occultation is almost half of those in the reverse type.

3.1 Local dependence of the ground/satellite Es agreement

The conjunction observations were classified into 0.5° latitude bands based on their distance from the Pruhonice station. The agreement between Es events derived from the ionosonde and radio occultation was then measured and presented in Table 3 for both cases. In case 1, each latitude band contained approximately 220 conjunction observations, while in case 2, there were approximately 330 observations in each latitude band. Similarly, the longitudinal dependence of the agreement between the two methods was examined in 1° longitude bands and presented in Table 4. For case 1, there were approximately 170 conjunction observations in each longitude band, while for case 2, there were approximately 260 observations.

The agreement between the ionosonde and radio occultation measurements of Es recordings was examined at various latitudinal and longitudinal distances from the base station. The results revealed that there is no significant dependence on the distance from the ionosonde station in both cases. This implies that the discrepancy in Es detection between ground-based and satellite techniques is hardly influenced by the distance from the ionosonde station, provided that a 2° latitude × 5° longitude grid around each ionosonde is considered.

As presented in Table 5, the altitude dependence of the agreement between ionogram and radio occultation observation

in detecting Es layers was studied in 5 km altitude bands. In both cases, the agreement between the two methods increased with the increase in altitude and reached its maximum at 105–115 km. However, beyond this height range, the agreement dropped. This trend is because the maximum amplitude of Es occurrence is found at heights between 95 and 115 km.

3.2 Temporal dependence of the ground/satellite Es agreement

To proceed, the conjunction data were sorted into various seasons and local times to investigate if the agreement in detecting Es through two methods varies with the local time and season. Table 6 presents that in case 1, the highest level of agreement was observed in the local summer, whereas the lowest was seen in local winter. However, in case 2, the agreement demonstrated almost no dependence on the season. The number of conjunction data points is rather equally distributed during different months, in each station. For case 1, there were at least 230 conjunction observations in each longitude band, while for case 2, the minimum number of conjunction observations was approximately 380. Additionally, the results in Table 7 indicate that for case 1, the agreement was highest during the daytime and remained at a nearly consistent level during different local times for case 2. The number of conjunction observations studied at each local time grid was at least 100.

The solar zenith angle dependence of the agreement between the ionosonde and radio occultation presented in Table 8 confirms our previous results.

According to the seasonal and local time dependence of the Es detection agreement between the two methods, we can conclude that in case of observing a radio occultation signal disturbance that meets the criteria of Es layer detection proposed by Arras & Wickert (2018), there is a higher likelihood of recording an ionogram Es layer echo in a nearby location during the daytime and local summer.

All stations show similar spatial, seasonal, and local-time dependence. An overview of the monthly dependence of the Es detection via two different methods in case 1 is demonstrated in Figure 3A. The month-to-month agreement of the Es detection between the ionosonde and radio occultation in Pruhonice, I-Cheon, and Ramey of the Northern Hemisphere station is maximum during May, June, July, and August; on the other hand, the maximum in Grahamstown, Madimbo, and Learmonth in the Southern Hemisphere occurs during November, December, January, and February. As shown in Figure 3A, Learmonth on the right panel shows a better agreement with radio occultation observations in recording Es occurrences. This can be due to different technical aspects or operating software being used at different ionosonde stations.

According to the results presented in Figure 3B, Es layers recorded in the ionogram agree largely with those in radio occultation measurements during local times between 6 and 18. During this time period, the agreement is greater than 80% in all stations. However, during night time, it can go down to 40% at some stations. Supporting that, as shown in Figure 3C, all ionosonde Es layer recordings have a greater agreement with Es layers detected in satellite observations when the solar zenith angle is less than 90°.

TABLE 9 S4 dependence of the agreement between ionosonde and radio occultation measurements in detecting the Es layer at IC437.

0–0.2	0.2–0.4	0.4–0.6	0.6–0.8	0.8–1
71%	81%	93%	97%	100%

TABLE 10 foEs dependence of the agreement between ionosonde and radio occultation measurements in detecting the Es layer at IC437.

foEs<2.5	2.5–3	3–3.5	3.5–4	4–4.5	4.5–5	5–5.5	foEs>5.5
47%	55%	63%	72%	74%	66%	55%	54%

TABLE 11 fbEs dependence of the agreement between ionosonde and radio occultation measurements in detecting the Es layer at IC437.

fbEs<2.5	2.5–3	3–3.5	3.5–4	4–4.5	4.5–5	5–5.5	fbEs>5.5
52%	50%	55%	78%	71%	61%	47%	43%

We conducted a similar study on other stations to examine the temporal dependence of the agreement between the two methods for case 2 in which all conjunction ionograms record an Es layer. However, no specific daily, monthly, or local dependence was discovered. Additionally, we analyzed the agreement year by year for each station to assess the influence of the 11-year solar cycle. The findings revealed that the agreement between the two methods remained relatively constant, with no significant differences indicating no solar cycle dependence.

3.3 Es intensity dependence of the ground/satellite Es agreement

We examined the dependence of the agreement between the two Es detection methods on the intensity of the Es layer by looking into the S4 index in case 1 and foEs and fbEs parameters in case 2. The agreement between Es events measured by the radio occultation technique with the Es layers recorded in the ionogram has been measured in 0.2 length S4 bands and presented in Table 9. As shown in the table, the agreement increases with the increase in S4. Therefore, the higher the Es intensity detected by the satellite is, the more probable it is to observe an Es layer in the conjunction ionogram.

In order to examine the Es intensity dependence in case 2, we studied the foEs dependence of the satellite and ground-based Es detection agreement. The results are presented in Table 10. In general, the agreement increases as the foEs becomes larger, but the agreement rate drops as foEs goes higher than 4.5–5 MHz.

Based on our analysis, more than 80% (i.e., 3798 blanketing Es events of the 9,000 conjunction points presented in Table 2) of the Es events in mid- and low-latitude regions were found to be blanketing Es. By taking into account only the blanketing-type Es and repeating all previous analyses, the temporal and spatial dependence of the Es detection method agreement stays the same. Therefore, we conducted an analysis to study the fbEs dependence of the ionosonde and satellite method agreement in detecting Es layers. The fbEs results presented in Table 11 were similar to the foEs.

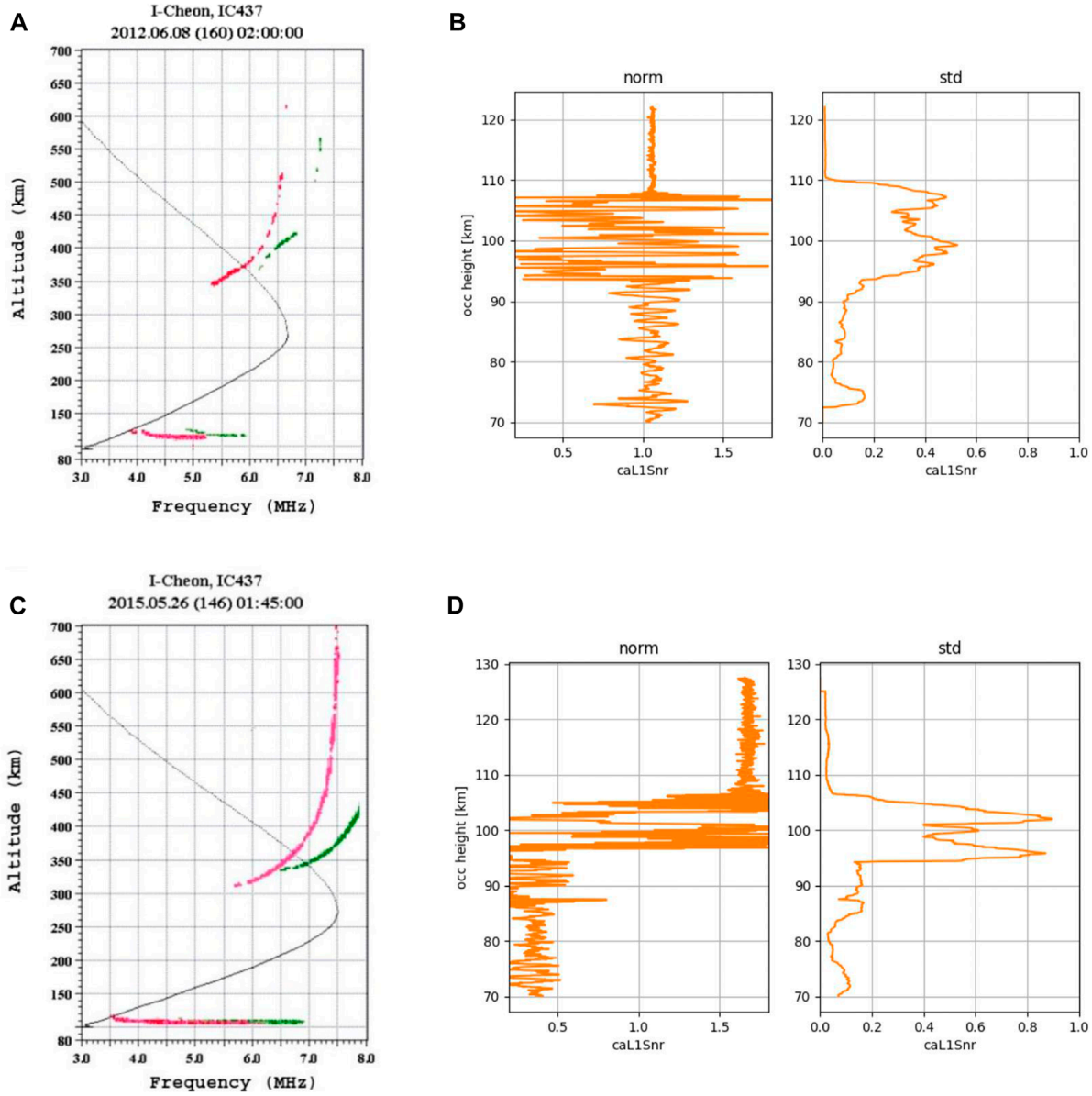

FIGURE 4
(A) Ionogram of the IC437 station (lat: 37.1° and lon: 127.5°), June 8, 2012, 2:00. **(B)** SNR profile of a crossing radio occultation (lat: 36.9° and lon: 130.7°) on June 8, 2012, at 1:55, and its corresponding standard deviation profile. **(C)** Ionogram of the IC437 station (lat: 37.1° and lon: 127.5°), May 26, 2015, 1:45. **(D)** SNR profile of a crossing radio occultation (lat: 36.9° and lon: 129.6°) on May 26, 2015, at 1:48, and its corresponding standard deviation profile.

4 Discussion

According to Table 10, when the foEs value is greater than average, the agreement between the two methods in detecting the Es layer decreases. We also noticed that 64.4% of these conjunction observations with a high fbEs value had an extremely large SNR value as well. Figure 4 provides two examples of such events. Figure 4A shows a strong blanketing Es, and in Figure 4B, there is a crossing radio occultation signal which is highly disturbed but not marked as an Es event. Arras and Wickert (2018) only showed tag signals with a standard deviation greater than 0.2 within the altitude range of 10 km as an Es layer. By applying these criteria, very strong Es layers, which cause very big standard deviation at a high-altitude band, will sometimes be overlooked.

Figure 4C is another example of a severe Es layer that blankets the echo from upper layers of ionosphere. As shown in Figure 4D, the radio occultation signal traveling from above reaches an Es layer at approximately 110 km and gets disturbed intensely. As a result of this disturbance, the normalized SNR reduces to less than one third of its initial amount. Such severe disruptions (in this case foEs = 6.3 MHz) caused by Es events can sometimes result in GNSS signal loss (Yue et al., 2016). Hence, despite the global Es data coverage that

radio occultation provides, it seems that further improvements can be applied to the Es detection criteria proposed by Arras and Wickert (2018).

The discrepancy between Es layers detected in ionograms and those observed in radio occultation might also exist due to limitations in the Es layer detection capability of the ground-based techniques. The ionosonde data used in this study are all derived from the Lowell data center. Nevertheless, it should be noted that the stations do not always utilize the same software. Furthermore, there are variations in hardware and technical aspects across different stations, including variations in antenna configurations from site to site. Factors such as sounding frequency, antenna type, system maintenance, and other technical considerations can potentially influence the detectability of Es layers. As demonstrated in Figures 3A, D, although the Learmonth station follows the same temporal dependence as other Southern Hemisphere stations, it has always a higher agreement rate with radio occultation observations in comparison to others. Ionosonde stations have different limits of density sensitivity, depending on their operating mode. Therefore, the detectability of the Es layer can depend on the ionosonde station and vary from one ionosonde to another based on their different software and technical facilities. Additionally, it is always possible to have human errors, when scaling ionograms manually.

Another potential factor contributing to the observed discrepancies between ground-based and satellite measurements of Es layers is the fundamental difference in the Es detection mechanisms employed by the two methods. It is important to recognize that ionosonde and satellite observations utilize distinct approaches to detect Es layers, which can yield divergent measurements of these atmospheric phenomena. These inherent dissimilarities in detection mechanisms may offer a plausible explanation for the contradictory findings observed between ground-based and satellite techniques. In ionosonde observations, Es layers are typically identified and recorded in ionograms by analyzing the electron density of the E layer, which is derived from the transmitted ionosonde signal. The ionogram provides information about the plasma density distribution within the ionosphere, allowing for the detection of Es layers based on their characteristic electron density patterns. However, in the radio occultation technique employed by satellites, the detection of Es layers relies on the observation of electron density gradients that induce scintillations in the global navigation satellite system (GNSS) signals. In this case, it is the presence and magnitude of these gradients that are indicative of the presence of Es layers. This fundamental disparity in the underlying mechanisms for Es detection between ground-based ionosondes and satellite-based radio occultation techniques can give rise to varying measurements of Es layers obtained through each method. For instance, there may be cases where an Es layer, such as the one depicted in Figure 2C, exhibits a plasma density that is too weak to be discerned and recorded in an ionogram. However, despite the lower plasma density, the associated electron density gradient can still be significant enough to cause disturbances in radio occultation signals, leading to their detection using satellite observations. This physical distinction in the detection approaches of the two methods may also provide an explanation for the observed maximum agreement between ground-based and satellite techniques during the daytime and local summer periods, as these conditions can favor the generation of notable electron density gradients within the Es layer.

5 Conclusion

In this study, we conducted a comprehensive comparison between the Es recordings obtained from six mid- and low-latitude ionosonde stations and the corresponding FORMOSAT-3/COSMIC radio occultation measurements, utilizing the method proposed by Arras & Wickert (2018). Our analysis focused on examining the local and temporal variations in the agreement between the ground-based and satellite techniques for detecting Es layers. The key findings of our investigation are summarized as follows:

1. At different ionosonde stations, we observed a noticeable disagreement of 20%–40% between the ground-based and satellite measurements of Es layer occurrence. The extent of this discrepancy varied depending on factors such as local time, season, and altitude at which an Es event occurred. These findings emphasize the importance of considering the specific conditions under which Es layers are detected.
2. Our results indicate that the agreement between ground-based and satellite measurements of Es layer occurrence is highest during local summer and daytime. When the Es detection method proposed by Arras & Wickert (2018) identifies an Es layer in radio occultation observations, it tends to align more closely with the ground-based measurements during these specific periods.
3. We observed that certain ionosonde stations demonstrated a consistently stronger agreement with satellite Es observations throughout the year. This observation suggests that differences in technical facilities and measurement software among ionosonde stations may influence their compatibility in Es detection. Further investigation into these variations can provide valuable insights into improving the overall consistency between ground-based and satellite techniques.
4. The detection capability of Es layers using radio occultation data is dependent on the specific criteria employed in the analysis of GNSS signals. For instance, our study identified instances where severe Es layers were not captured in the radio occultation data due to their high signal standard deviation across a wide range of altitudes. This observation underscores the need for careful consideration and refinement of the criteria used in analyzing GNSS signals to enhance the detection and characterization of Es layers.
5. A fundamental distinction exists between ground-based ionograms and satellite techniques in measuring Es layers. Ionograms record the E region plasma density, while satellite techniques focus on measuring the E region plasma density gradient, responsible for GNSS signal scintillations. This inherent difference contributes to observed discrepancies. Additionally, it explains the higher agreement during daytime and summer, characterized by more pronounced plasma density gradients. This information highlights that there is no single definition

of Es layers that can simultaneously satisfy both satellite and ground-based observations. In future studies, it is helpful to clearly define Es for each investigation and be mindful of the disparities between the chosen approaches.

In conclusion, our study conducts a comparison of ground-based and satellite measurements of Es layers, shedding light on the local and temporal factors influencing their agreement. While acknowledging the limitations and specific conditions of our study, further investigations can build upon these findings to refine the detection and characterization of Es layers and enhance the overall understanding of ionospheric dynamics. Future research should explore alternative data analysis techniques, incorporate a larger number of ionosonde stations, and consider additional factors that may impact the agreement between ground-based and satellite measurements. By addressing these aspects, we can advance our knowledge of Es layers and their impact on ionospheric behavior in different regions and seasons.

Data availability statement

Publicly available datasets were analyzed in this study. These data can be found at: The level 1b atmPhs radio occultation data from the F3/C mission are available at the COSMIC Data Analysis and Archive Center: https://www.cosmic.ucar.edu/what-we-do/cosmic-1/data/. Ionosonde recordings are available at GIRO: https://giro.uml.edu/didbase/.

Author contributions

SS-M performed the data analysis and wrote the paper. YY discussed the results and contributed to revise the paper. CA extracted the Es events from the SNR of the RO signal. DT provided guidance on ionogram scaling and supported the interpretation of the ionograms. All authors contributed to the article and approved the submitted version.

Funding

This study received partial support from JSPS and DFG (Grant YA-574-3-1) through the Joint Research Projects LEAD with DFG (JRPs-LEAD with DFG). Additionally, it was partly funded through the "Open-Access-Publikationskosten" program by DFG, Project Number 491075472.

Acknowledgments

SS-M would like to express gratitude to Dr. Veronika Barta for providing valuable insights on the interpretation of ground-based observations. CA acknowledges the support by Deutsche Forschungsgemeinschaft (DFG) under grant WI 2634/19-1.

Conflict of interest

The authors declare that the research was conducted in the absence of any commercial or financial relationships that could be construed as a potential conflict of interest.

Publisher's note

References

Arras, C. (2010). *A global survey of sporadic E layers based on GPS Radio occultations by CHAMP, GRACE and FORMOSAT–3/COSMIC, Deutsches GeoForschungsZentrum GFZ Potsdam]*.

Arras, C., Jacobi, C., Wickert, J., Heise, S., and Schmidt, T. (2010). Sporadic E signatures revealed from multi-satellite radio occultation measurements. *Adv. Radio Sci.* 8, 225–230. doi:10.5194/ars-8-225-2010

Arras, C., Resende, L. C. A., Kepkar, A., Senevirathna, G., and Wickert, J. (2022). Sporadic E layer characteristics at equatorial latitudes as observed by GNSS radio occultation measurements. *Earth, Planets Space* 74 (1), 163–215. doi:10.1186/s40623-022-01718-y

Arras, C., Wickert, J., Beyerle, G., Heise, S., Schmidt, T., and Jacobi, C. (2008). A global climatology of ionospheric irregularities derived from GPS radio occultation. *Geophys. Res. Lett.* 35 (14), L14809. doi:10.1029/2008gl034158

Arras, C., and Wickert, J. (2018). Estimation of ionospheric sporadic E intensities from GPS radio occultation measurements. *J. Atmos. Solar-Terrestrial Phys.* 171, 60–63. doi:10.1016/j.jastp.2017.08.006

Axford, W., and Cunnold, D. (1966). The wind-shear theory of temperate zone sporadic E. *Radio Sci.* 1 (2), 191–197. doi:10.1002/rds196612191

Baggaley, W. (1984). Ionospheric sporadic-E parameters: Long-term trends. *Science* 225 (4664), 830–833. doi:10.1126/science.225.4664.830

Carmona, R. A., Nava, O. A., Dao, E. V., and Emmons, D. J. (2022). A comparison of sporadic-E occurrence rates using GPS radio occultation and ionosonde measurements. *Remote Sens.* 14 (3), 581. doi:10.3390/rs14030581

Chandra, H., and Rastogi, R. (1975). Blanketing sporadic E layer near the magnetic equator. *J. Geophys. Res.* 80 (1), 149–153. doi:10.1029/ja080i001p00149

Christakis, N., Haldoupis, C., Zhou, Q., and Meek, C. (2009). Seasonal variability and descent of mid-latitude sporadic E layers at Arecibo. *Ann. Geophys.* 27 (3), 923–931. doi:10.5194/angeo-27-923-2009

Chu, Y.-H., Wang, C., Wu, K., Chen, K., Tzeng, K., Su, C.-L., et al. (2014). Morphology of sporadic E layer retrieved from COSMIC GPS radio occultation measurements: Wind shear theory examination. *J. Geophys. Res. Space Phys.* 119 (3), 2117–2136. doi:10.1002/2013ja019437

FengJuan, S., XianRong, W., HongBo, Z., Bao, Z., PanPan, B., and Hongyan, C. (2022). Statistical and simulation study on the separation in junction frequencies between ordinary (O) and extraordinary (X) wave in oblique ionograms. *Earth, Planets Space* 74 (1), 189–214. doi:10.1186/s40623-022-01755-7

Gan, C., Hu, J., Luo, X., Xiong, C., and Gu, S. (2022). Sounding of sporadic E layers from China Seismo-Electromagnetic Satellite (CSES) radio occultation and comparing with ionosonde measurements. *Ann. Geophys.* 40 (4), 463–474. doi:10.5194/angeo-40-463-2022

Gooch, J. Y., Colman, J. J., Nava, O. A., and Emmons, D. J. (2020). Global ionosonde and GPS radio occultation sporadic-E intensity and height comparison. *J. Atmos. Solar-Terrestrial Phys.* 199, 105200. doi:10.1016/j.jastp.2020.105200

Haldoupis, C. (2011). "A tutorial review on sporadic E layers," in *Aeronomy of the Earth's atmosphere and ionosphere* (Springer), 381–394.

Haldoupis, C. (2012). Midlatitude sporadic E. A typical paradigm of atmosphere-ionosphere coupling. *Space Sci. Rev.* 168 (1), 441–461. doi:10.1007/s11214-011-9786-8

Haldoupis, C., and Pancheva, D. (2002). Planetary waves and midlatitude sporadic E layers: Strong experimental evidence for a close relationship. *J. Geophys. Res. Space Phys.*, 107 (A6), 3–6. doi:10.1029/2001JA000212

Haldoupis, C., Pancheva, D., Singer, W., Meek, C., and MacDougall, J. (2007). An explanation for the seasonal dependence of midlatitude sporadic E layers. *J. Geophys. Res. Space Phys.* 112 (A6). doi:10.1029/2007ja012322

Harris, R., and Taur, R. (1972). Influence of the tidal wind system on the frequency of sporadic-E occurrence. *Radio Sci.* 7 (3), 405–410. doi:10.1029/rs007i003p00405

Igarashi, K., Nakamura, M., Wilkinson, P., Wu, J., Pavelyev, A., Wickert, J., et al. (2001). Global sounding of sporadic E layers by the GPS/MET radio occultation experiment. *J. Atmos. Solar-Terrestrial Phys.* 63 (18), 1973–1980. doi:10.1016/s1364-6826(01)00063-3

Leighton, H., Shapley, A., and Smith, E. (1962). *International series of monographs on electromagnetic waves*. Elsevier, 166–177.The occurrence of sporadic E during the IGY.

Luo, J., Liu, H., and Xu, X. (2021). Sporadic E morphology based on COSMIC radio occultation data and its relationship with wind shear theory. *Earth, Planets Space* 73 (1), 212–217. doi:10.1186/s40623-021-01550-w

MacDougall, J. (1978). Seasonal variation of semidiurnal winds in the dynamo region. *Planet. space Sci.* 26 (8), 705–714. doi:10.1016/0032-0633(78)90001-6

Macleod, M. A. (1966). Sporadic E theory. I. Collision-geomagnetic equilibrium. *J. Atmos. Sci.* 23 (1), 96–109. doi:10.1175/1520-0469(1966)023<0096:seticg>2.0.co;2

Mathews, J. (1998). Sporadic E: Current views and recent progress. *J. Atmos. Solar-Terrestrial Phys.* 60 (4), 413–435. doi:10.1016/s1364-6826(97)00043-6

Matsushita, S. (1962). "Lunar tidal variations of sporadic E," in *Ionospheric sporadic* (Elsevier), 194–214.

Merriman, D. K., Nava, O. A., Dao, E. V., and Emmons, D. J. (2021). Comparison of seasonal foEs and fbEs occurrence rates derived from global Digisonde measurements. *Atmosphere* 12 (12), 1558. doi:10.3390/atmos12121558

Piggott, W. (1972). *Handbook of Ionogram interpretation and reduction*. US Department of Commerce.

Qiu, L., Zuo, X., Yu, T., Sun, Y., and Qi, Y. (2019). Comparison of global morphologies of vertical ion convergence and sporadic E occurrence rate. *Adv. Space Res.* 63 (11), 3606–3611. doi:10.1016/j.asr.2019.02.024

Reddy, C., and Matsushita, S. (1969). Time and latitude variations of blanketing sporadic E of different intensities. *J. Geophys. Res.* 74 (3), 824–843. doi:10.1029/ja074i003p00824

Saksena, R. (1976). Possible effect of small and large wind shears on temperate latitude sporadic E. *Indian J. Radio and Space Phys.* 5, 235–239.

Shinagawa, H., Miyoshi, Y., Jin, H., and Fujiwara, H. (2017). Global distribution of neutral wind shear associated with sporadic E layers derived from GAIA. *J. Geophys. Res. Space Phys.* 122 (4), 4450–4465. doi:10.1002/2016ja023778

Sobhkhiz-Miandehi, S., Yamazaki, Y., Arras, C., Miyoshi, Y., and Shinagawa, H. (2022). Comparison of the tidal signatures in sporadic E and vertical ion convergence rate, using FORMOSAT-3/COSMIC radio occultation observations and GAIA model. *Earth, Planets Space* 74 (1), 88–13. doi:10.1186/s40623-022-01637-y

Taguchi, S. (1961). World maps of foEs. *J. Radio Res. Laboratory* 8 (38).

Wakai, N., Ohyama, H., and Koizumi, T. (1987). *Manual of ionogram scaling*. Japan: Radio Research Laboratory, Ministry of Posts and Telecommunications.

Whitehead, J. (1970). Production and prediction of sporadic E. *Rev. Geophys.* 8 (1), 65–144. doi:10.1029/rg008i001p00065

Whitehead, J. (1989). Recent work on mid-latitude and equatorial sporadic-E. *J. Atmos. Terr. Phys.* 51 (5), 401–424. doi:10.1016/0021-9169(89)90122-0

Whitehead, J. (1961). The formation of the sporadic-E layer in the temperate zones. *J. Atmos. Terr. Phys.* 20 (1), 49–58. doi:10.1016/0021-9169(61)90097-6

Wickert, J., Pavelyev, A., Liou, Y., Schmidt, T., Reigber, C., Igarashi, K., et al. (2004). Amplitude variations in GPS signals as a possible indicator of ionospheric structures. *Geophys. Res. Lett.* 31 (24), L24801. doi:10.1029/2004gl020607

Wu, D. L., Ao, C. O., Hajj, G. A., de La Torre Juarez, M., and Mannucci, A. J. (2005). Sporadic E morphology from GPS-CHAMP radio occultation. *J. Geophys. Res. Space Phys.* 110 (A1), A01306. doi:10.1029/2004ja010701

Yamazaki, Y., Arras, C., Andoh, S., Miyoshi, Y., Shinagawa, H., Harding, B., et al. (2022). Examining the wind shear theory of sporadic E with ICON/MIGHTI winds and COSMIC-2 radio occultation data. *Geophys. Res. Lett.* 49 (1), e2021GL096202. doi:10.1029/2021gl096202

Yu, B., Xue, X., Scott, C. J., Yue, X., and Dou, X. (2022). An empirical model of the ionospheric sporadic E layer based on GNSS radio occultation data. *Space weather.* 20 (8), e2022SW003113. doi:10.1029/2022sw003113

Yu, B., Xue, X., Yue, X. a., Yang, C., Yu, C., Dou, X., et al. (2019). The global climatology of the intensity of the ionospheric sporadic E layer. *Atmos. Chem. Phys.* 19 (6), 4139–4151. doi:10.5194/acp-19-4139-2019

Yue, X., Schreiner, W. S., Pedatella, N. M., and Kuo, Y. H. (2016). Characterizing GPS radio occultation loss of lock due to ionospheric weather. *Space weather.* 14 (4), 285–299. doi:10.1002/2015sw001340

frontiers | Frontiers in Astronomy and Space Sciences

TYPE Original Research
PUBLISHED 14 September 2023
DOI 10.3389/fspas.2023.1214591

OPEN ACCESS

EDITED BY
Han-Li Liu,
National Center for Atmospheric Research (UCAR), United States

REVIEWED BY
Eelco Doornbos,
Royal Netherlands Meteorological Institute, Netherlands
Andrés Calabia,
University of Alcalá, Spain

*CORRESPONDENCE
Ludger Scherliess,
ludger.scherliess@usu.edu

RECEIVED 30 April 2023
ACCEPTED 21 June 2023
PUBLISHED 14 September 2023

CITATION
Molina I and Scherliess L (2023), Spatial and temporal correlations of thermospheric zonal winds from GOCE satellite observations.
Front. Astron. Space Sci. 10:1214591.
doi: 10.3389/fspas.2023.1214591

Spatial and temporal correlations of thermospheric zonal winds from GOCE satellite observations

Ivana Molina and Ludger Scherliess*

Center for Atmospheric and Space Sciences, Utah State University, Logan, UT, United States

Winds in the thermosphere play an important role in the transport of momentum and energy in the upper atmosphere and affect the composition, dynamics and morphology of the ionospheric plasma. Although the general morphology of the winds is well understood, we are only starting to understand its variability. During the last decade it has become inherently clear that in addition to solar forcing of the thermosphere, the lower atmosphere also is an important driver of thermospheric variability. Therefore, an understanding of thermospheric variability and its spatial and temporal correlations is critical for an improved understanding of the coupled ionosphere-thermosphere system and the coupling to the lower atmosphere. The Gravity Field and Steady-State Ocean Explorer (GOCE) provided zonal winds near dawn and dusk at an altitude of around 260 km from November 2009 to October 2013. We have used GOCE zonal wind observations from low- to mid-latitudes obtained during geomagnetically quiet times to investigate spatial and temporal correlations in the zonal winds near dawn and dusk. Latitudinal correlations were calculated for the GOCE zonal winds for December solstice separately for each year from 2009 to 2012 and their year-to-year variation was established. Correlations between hemispheric conjugate points were found at mid latitudes during the latter years. Latitudinal correlations for December solstice 2009 and June solstice 2010 were compared and the correlation length was found to be consistently larger in the winter hemisphere during dawn and in the summer hemisphere during dusk. Zonal wind longitudinal/temporal correlations were also determined for December 2009 and 2011 and for June 2010 and found to be periodic in longitude/time. The temporal evolution of the temporal/longitudinal correlations were found to gradually decrease over the course of several days. The maxima in the correlation coefficients were always located in the winter hemisphere during dawn and in the summer hemisphere during dusk. During dawn, the largest contributors to the temporal/longitudinal correlations were found to be nonmigrating tides, whereas during dusk, additional waves appear to play important roles.

KEYWORDS

neutral wind, thermosphere, ionosphere, tides, upper atmosphere dynamics, GOCE

1 Introduction

Neutral winds affect the composition in the thermosphere as well as the motion of the charged particles by dragging the plasma up and down magnetic field lines, changing rates of production and recombination (Kelley, 2009) and by creating electric fields via the neutral wind dynamo (Maute and Richmond, 2017). Thermospheric neutral winds are

known to be affected by geomagnetic conditions, seasons, local time and atmospheric tides, among others (Wang et al., 2021) and vary over large temporal scales ranging from minutes to years. Understanding their variability becomes critical, as they transfer energy and momentum in the upper atmosphere and directly or indirectly affect the dynamics, morphology and composition of the ionosphere, which can disrupt radio communication and navigation systems (e.g., Calabia et al., 2023).

A powerful approach to quantify the variability in thermospheric winds is to calculate spatial and temporal correlations, which indicate a statistical relationship between variations in the winds at different times and locations on the globe. Spatial and temporal correlations are also important for model validations, which involve comparisons of correlations obtained from observations with those obtained from the models (e.g., Bruinsma et al., 2014). Correlations can also help to gain insight into physical processes that produce variability seen in observations (e.g., Forbes et al., 2005) and provide critical constraints for model error covariances used in various data assimilation schemes.

Correlations of different physical parameters are widely used to study the global morphology and variability in the atmosphere. Alken and Maus (2007) studied correlation lengths in the equatorial electrojet using CHAMP, Ørsted and SAC-C magnetic observations; Shim et al. (2008) studied the spatial correlations of day-to-day GPS Total Electron Content variations; Garcia et al. (2016) used correlations from GOCE density and cross-wind variations for gravity wave detection and characterization; Bruinsma et al. (2021) used density correlations as part of model assessments during geomagnetic storms. Liu (2014) and Liu (2016) investigated the correlation time of the zonal mean zonal wind, as well as the amplitudes of four main tidal components (DW1, SW2, DE3 and SW1) with winter stratospheric temperature anomalies using detrended time series of these quantities from a 20-year model simulation of the Whole Atmosphere Community Climate Model with thermosphere extension (WACCM-X).

In this paper, latitudinal and longitudinal/temporal correlations are presented for the GOCE zonal wind data at low- and mid-latitudes, and the results are discussed. In a companion paper Molina and Scherliess (2023) have used the same GOCE zonal wind observations to determine the zonal wave structures associated with nonmigrating tides.

This paper is organized as follows. Initially, the data and the methodology are described. Next the GOCE zonal wind latitudinal correlations are presented for December solstice 2009–2012 and June solstice 2010 followed by the longitudinal/temporal correlations for December solstice 2009 and June solstice 2010. Finally, the results are summarized and discussed.

2 Data

The Gravity Field and Steady-State Ocean Explorer (GOCE) mission provided cross-track thermospheric (zonal) neutral winds from November 2009 to October 2013. The satellite was launched on 17 March 2009 into a dawn-dusk Sun-synchronous orbit with an inclination of 96.7° (near-polar orbit). The mean altitude of the satellite was near 270 km during the initial years of the mission and gradually decreased to about 250 km during 2012 and 2013, with variations in the height of the satellite within one orbit of about 20 km. Although the main objective of GOCE was to investigate the gravitational field of the Earth, thermospheric parameters, including the densities and winds were also provided in 10-s increments by combining the accelerometer and ion thruster data, together with GPS tracking and star camera data (Doornbos et al., 2013). For the current study we used data set version 2.0.

Due to the very small orbital precession, the local solar time corresponding to the equatorial crossing of the satellite only slightly changed throughout the mission by about 20 min/year from initially 06:15/18:15 LT to 07:30/19:30 LT by the end of the mission. As a result, GOCE produced a large data set of zonal winds in the dawn-dusk sectors.

The errors in the GOCE zonal wind are of the order of ~10%–20%, with the dominant source of errors being biases due to instrument calibration and external models used in the calculation of the winds (Doornbos et al., 2010).

3 Methodology

To investigate the correlations in the GOCE zonal winds, we focused on geomagnetically quiet 27-day periods (one solar rotation) that were centered as close as possible to the December solstice for the years 2009, 2010, 2011, and 2012 and the June solstice for the year 2010. These periods were chosen due to data availability and geomagnetic activity. The selected windows are:

- December 2009: 12 December 2009 to 07 January 2010
- December 2010: 05 December 2010 to 31 December 2010
- December 2011: 08 December 2011 to 03 January 2012
- December 2012: 08 December 2012 to 03 January 2013
- June 2010: 04 June 2010 to 30 June 2010
- June 2011: 08 June 2011 to 04 July 2011 (in Supplementary Material)

Figure 1 shows the daily F10.7 cm radio flux (1A) and daily Kp index (1B) for the span of the GOCE thermospheric data set. The December and June solstice periods selected for this study are indicated by yellow and purple vertical bars, respectively. During 2009 and 2010 the solar flux was significantly lower than during 2011 and 2012. The average F10.7 value for the selected window in December 2009 was 76 sfu and 81 sfu for the corresponding 2010 period. The average values for the 2011 and 2012 periods, on the other hand, were 132 sfu and 109 sfu, respectively. The average F10.7 value for the June 2010 period was 75 sfu and 95 sfu for the June 2011 window. Geomagnetic activity was generally very low during all selected periods with average Kp values over the individual 27-day periods not exceeding 1^0 for each of the December solstice periods and below 2^- for the June solstice periods. Figure 1B shows that the daily Kp reaches a value of 3 only once during December 2011 and a value of 3.3 once during each June period. The total number of 10-s observations at low- and mid-latitudes for each 27-day time period is about 60,000.

We employ a methodology similar to Shim et al. (2008) to investigate spatio-temporal variability. The data was first separated according to the local time of the observation into dawn and dusk bins. The data along a given orbit was then binned and

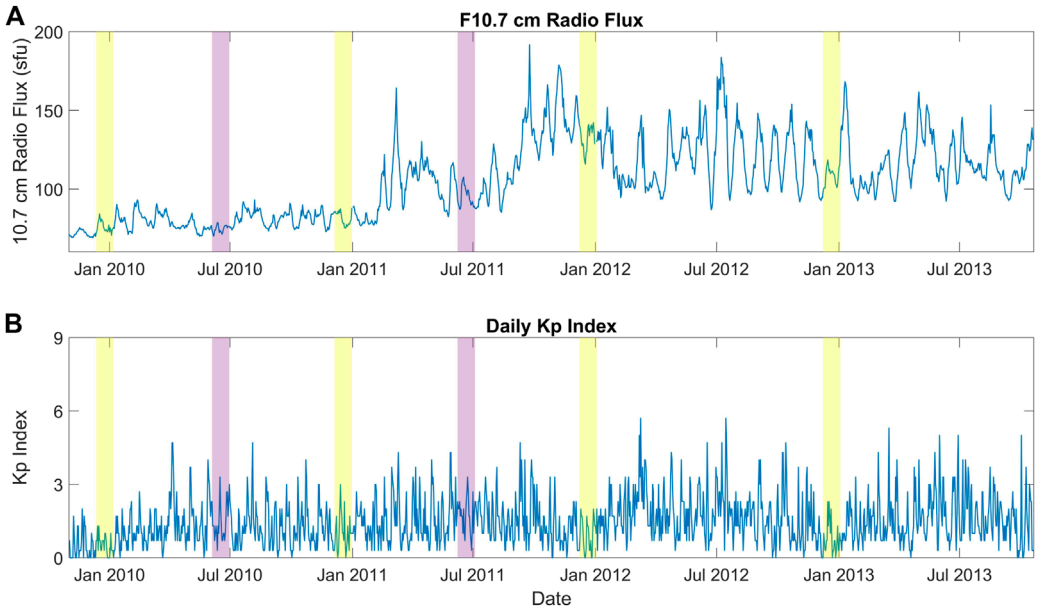

FIGURE 1
F10.7 cm radio flux **(A)** and daily Kp index **(B)** for the span of the GOCE thermospheric data set. The December and June solstice periods selected for this study are indicated by yellow and purple vertical bars, respectively.

averaged in 1°-wide geographic latitude bands from −60° to 60° geographic latitude. Next, the median value was calculated for each latitude band from all orbits in each 27-day period. Finally, the corresponding median value, m, was subtracted from the binned and averaged measurements, u, to calculate the correlation as follows:

$$r_{i,j,\Delta Orbit} = \frac{\sum_{k=1}^{norbit}(u_i - m_i)_k \cdot (u_j - m_j)_{k+\Delta Orbit}}{\left\{\sum_{k=1}^{norbit}(u_i - m_i)_k^2\right\}^{\frac{1}{2}} \cdot \left\{\sum_{k=1}^{norbit}(u_j - m_j)_{k+\Delta Orbit}^2\right\}^{\frac{1}{2}}}$$

Here, i and j correspond to the reference and comparison points, respectively and the summation is executed over all orbits during the given 27-day period ($norbit$ = 16 orbits/day *27 days = 432 orbits). Due to the orbit of the GOCE satellite longitude and time are intimately coupled and longitudinal/temporal correlations cannot be calculated by using pairs of observations along a given orbit. Instead, data pairs obtained from different orbits need to be used. This is accomplished by introducing the index $\Delta Orbit$, which indicates the difference in orbit number from a given orbit to all other orbits. Hence, a value of $\Delta Orbit = 0$ indicates that u_i and u_j are taken along the same orbit whereas positive/negative values of $\Delta Orbit$ indicate that u_j was obtained from temporally later/earlier orbits, respectively. Note that consecutive orbits differ by about 90 min and 22° in longitude. Therefore, values of $\Delta Orbit = 16, 32, 48, \ldots$ correspond to observations taken approximately one, two, three, … days later at the same longitude. Similarly, values of $\Delta Orbit = 8, 24, 42, \ldots$ correspond to correlations between observations with time differences of about half a day, one and a half day, two and a half days, etc., that are located 180° apart in longitude.

Latitudinal correlations are calculated by setting $\Delta Orbit = 0$. GOCE takes about 30 min to cross from 60°N to 60°S and vice versa and therefore, the latitudinal correlations do not correspond to perfectly synchronous observations but instead are smeared out by up to 30 min. Furthermore, GOCE does not exactly return to its position after 16 orbits, but instead advances by about 1° in longitude over a 1-day period. This again leads to a slight smearing of our longitudinal/temporal correlations.

So far, our approach will eliminate correlations associated with deterministic variations in solar cycle, season and local time and focuses on stochastic and tidal variations. The results of this analysis will be shown in Sections 4.1–4.3. To investigate correlations not associated with tides (Section 4.4) we subsequently eliminated their contribution from the zonal winds before calculating the longitude/time correlation coefficients. For this, we have used the results presented in Molina (2022), Molina and Scherliess (2023), who have used the same GOCE zonal wind observations to determine the zonal wave structures associated with nonmigrating tides by applying a longitudinal Fast Fourier Transform to the binned and averaged GOCE zonal wind data. We have used their results by subtracting their deterministic monthly-mean wave-1 to wave-5 structures from the GOCE zonal wind observations before calculating the longitude/time correlation coefficients.

4 Results

4.1 Latitudinal correlations

Figure 2 shows the December solstice latitude correlations in the GOCE zonal winds from mid to low latitudes during dawn. The results are separately shown for each year from 2009 to 2012 (Figures 2A–D) and correspond to correlations in the zonal

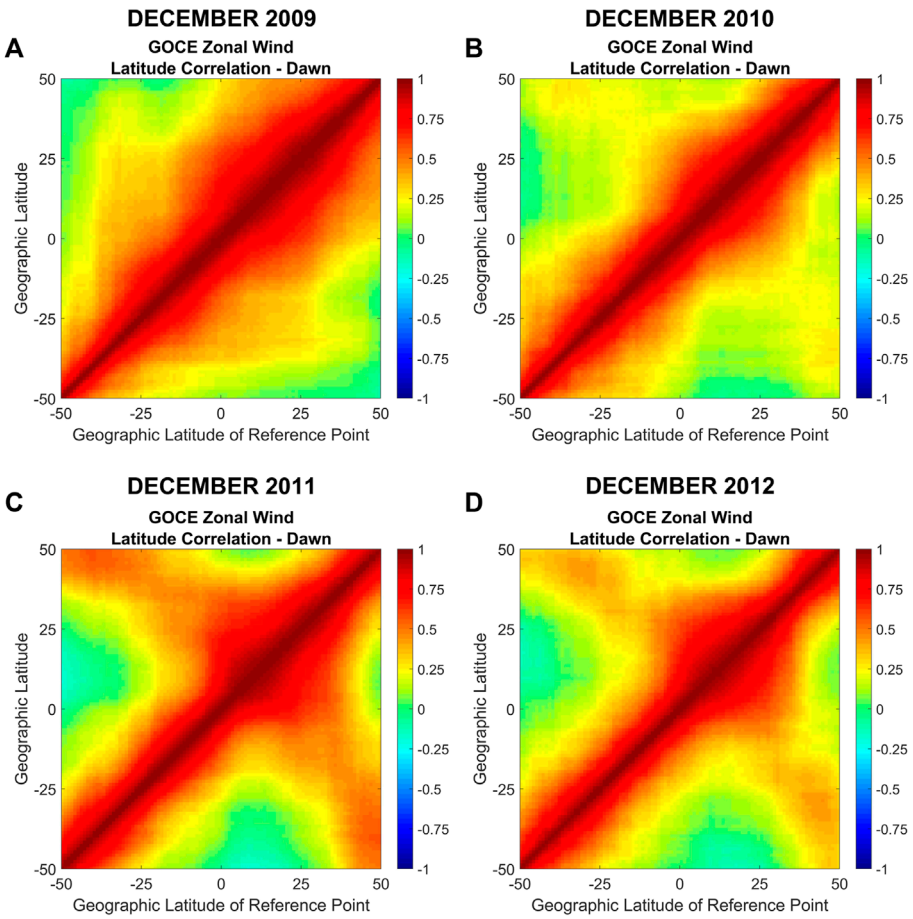

FIGURE 2
GOCE zonal wind latitudinal correlations during dawn for December solstice for years 2009–2012 **(A–D)**. The x-axis corresponds to the latitude of the reference point and the y-axis to the latitude of the comparison point.

wind between data pairs along a GOCE orbit characterized by the geographic latitude of a reference point and the geographic latitude of a comparison point. In general, during all four December solstice periods the correlations are larger and more extended in latitude in the northern hemisphere compared to the southern hemisphere. A year-to-year progression can also be observed in the correlations. From 2009 to 2010 the correlation lengths become generally smaller, and some localized correlations start to appear between near-conjugate points near ±40°- ±50° latitude. During 2011 this hemispheric conjugacy is even more evident, reaching correlation values of about 0.5. Finally, in 2012 it becomes weaker, with values of 0.3–0.4. Generally, the observed near-conjugacy is shifted towards the northern hemisphere. We have performed the same analysis using geomagnetic instead of geographic coordinates which resulted in a much cleaner presentation of the conjugacy (see Supplementary Figure S1). Therefore, the observed year-to-year variation in the conjugacy might be related to the variations in the solar flux from year to year with larger values during periods of enhanced solar activity. As mentioned above, the average F10.7 values changes from 76 sfu in 2009 to 81 sfu in 2010, 132 sfu in 2011 and 109 sfu in 2012.

Figures 3A–D show the GOCE zonal wind latitude correlations during dusk for December solstice 2009 to 2012. In this case, it is observed that 2009 and 2010 exhibit significantly larger and more extended correlations for reference latitudes located in the southern hemisphere and in the northern hemisphere up to ~20° latitude. In contrast, during 2011 the latitudinal extension of the correlations is much reduced and then increases again in 2012. This variation might also be related to the aforementioned variation in the solar activity from year to year.

Figure 4 shows the GOCE zonal wind latitude correlations during dawn and dusk for December 2009 (Figures 4A,B) and for June 2010 (Figures 4C,D). The average solar flux during June 2010 was very similar to the corresponding value during December 2009. Figure 4 shows that the extend of the latitudinal correlations during dawn is larger in the winter hemisphere (northern/southern hemisphere during December/June solstice) and larger in the summer hemisphere (southern/northern hemisphere during December/June solstice) during dusk. This is also observed for June 2011 (see Supplementary Figure S2).

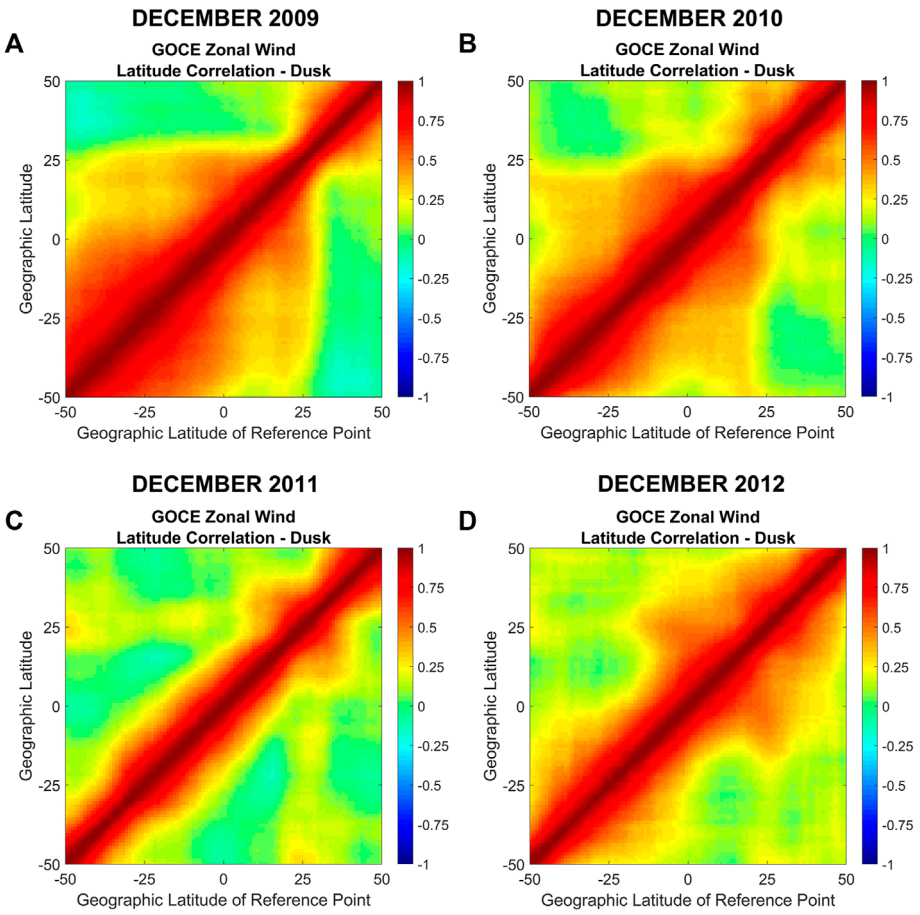

FIGURE 3
Same as Figure 2 but during dusk.

4.2 Latitudinal correlation lengths

Figure 5 shows the correlation lengths for the GOCE zonal wind for December solstice 2009 and June 2010 as a function of the latitude of the reference point for dawn (Figure 5A) and dusk (Figure 5B). Results are shown for reference points extending from −50° to 50° latitude, in steps of 5°. Here, the correlation length for a given reference latitude is defined as the latitudinal separation between that reference and the comparison point at which the correlation coefficient drops to 0.7, indicating that 50% of the variability at the comparison point can be explained by the variability seen at the reference point (the square of the correlation coefficient is ~0.5). During dawn the correlation lengths for December solstice have their largest values in the northern hemisphere with a maximum of about 18° located at a reference latitude of about 25°. During dusk, the December solstice correlation lengths show larger values in the southern hemisphere and peak near a reference latitude of about −35° with a value of approximately 17°. In contrast, during June 2010, the larger correlation lengths are found in the southern hemisphere during dawn and in the northern hemisphere during dusk. During this season, the maximum correlation lengths during dawn are found near a reference latitude of −20° with a value of about 22° and a broader maximum extending from about 20° to 45° in reference latitude is found during dusk with peak values of 20°–21°. Note that during both solstice periods, the correlation lengths exhibit their largest values consistently in the winter hemisphere during dawn and in the summer hemisphere during dusk.

4.3 Longitudinal/temporal correlations

Figure 6 shows the longitudinal/temporal GOCE zonal wind correlation coefficients for December 2009 (Figures 6A,B) and June 2010 (Figures 6C,D) separately for dawn (top) and dusk (bottom). The correlation coefficients correspond to reference and comparison points with the same latitude ($i = j$) but separated in longitude/time by a given number of orbits ($\Delta Orbit$). The correlation values are shown for latitudes ranging from −50° to 50° in steps of 1° and a longitudinal/temporal window of 96 orbits from the reference orbit. Due to the symmetry in the correlation coefficient for positive and negative values of $\Delta Orbit$, the correlation coefficients for the same values of $|\Delta Orbit|$ were averaged. For the interpretation of the results seen in Figure 6 note that the satellite revisits approximately the same location every 16 orbits corresponding to a time difference of 1 day; Figure 6 shows that every 16 orbits (dashed vertical lines)

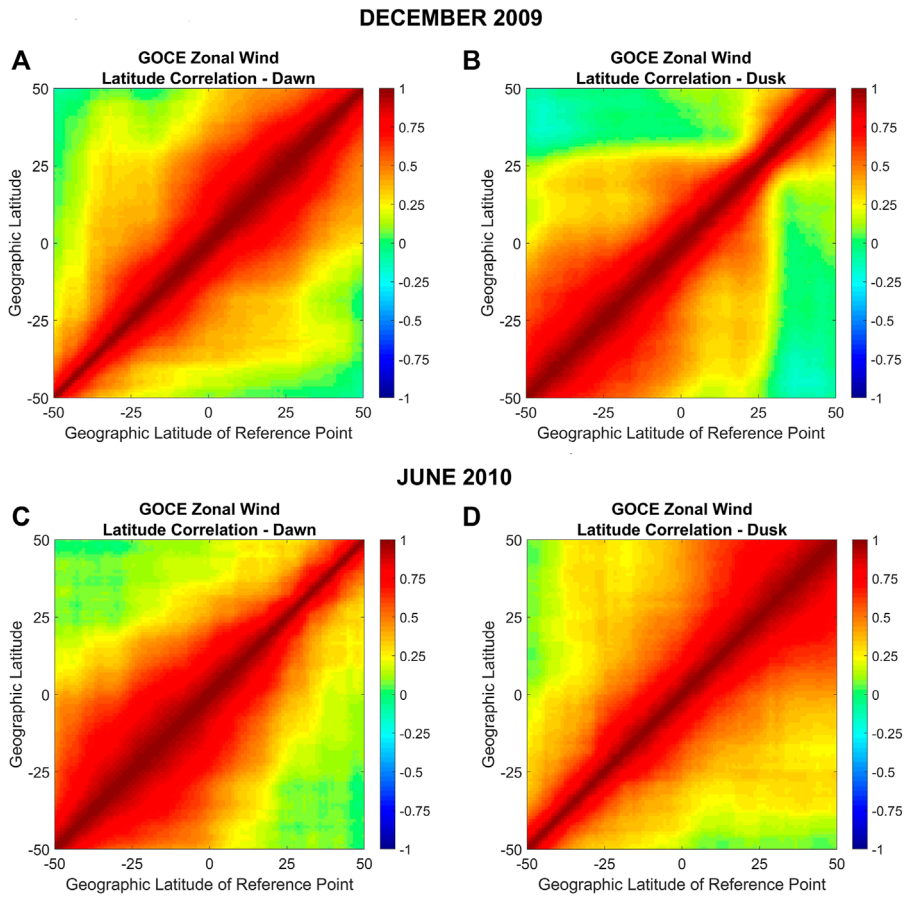

FIGURE 4
GOCE zonal wind latitudinal correlations during dawn and dusk for December solstice 2009 **(A,B)** and June solstice 2010 **(C,D)**. The x-axis corresponds to the latitude of the reference point and the y-axis to the latitude of the comparison point.

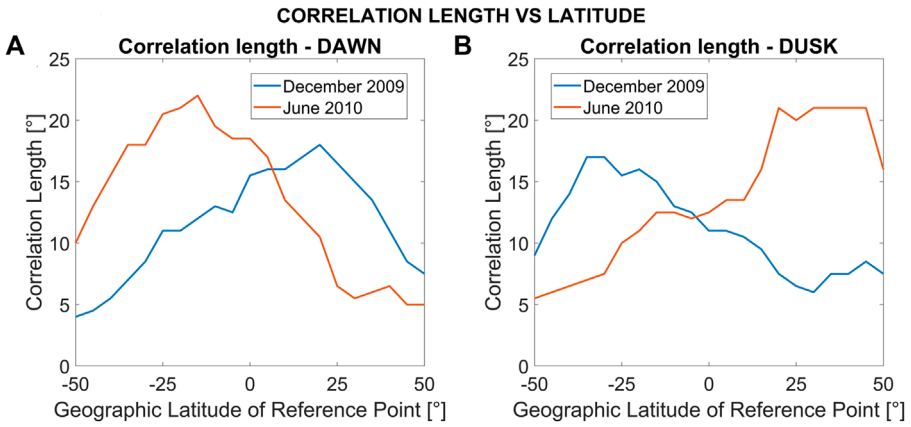

FIGURE 5
Latitudinal correlation lengths vs. latitude for the GOCE zonal wind for December solstice 2009 (blue) and June solstice 2010 (orange) during dawn **(A)** and dusk **(B)**. The correlation lengths are calculated every 5°.

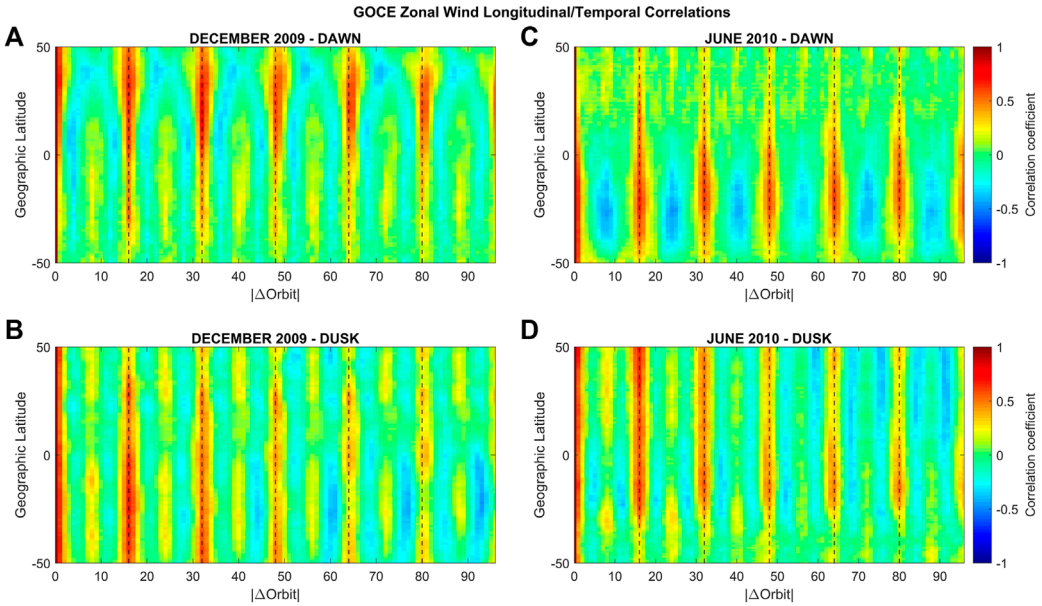

FIGURE 6
Longitudinal/temporal GOCE zonal wind correlation coefficients for December 2009 **(A,B)** and June 2010 **(C,D)** during dawn (top) and dusk (bottom). The correlation coefficients correspond to reference and comparison points with the same latitude, but separated in longitude/time by a given number of orbits ($\Delta Orbit$). The correlations are calculated in steps of 1° in latitude and a longitudinal/temporal window of 96 orbits from the reference orbit ($\Delta Orbit = 0$).

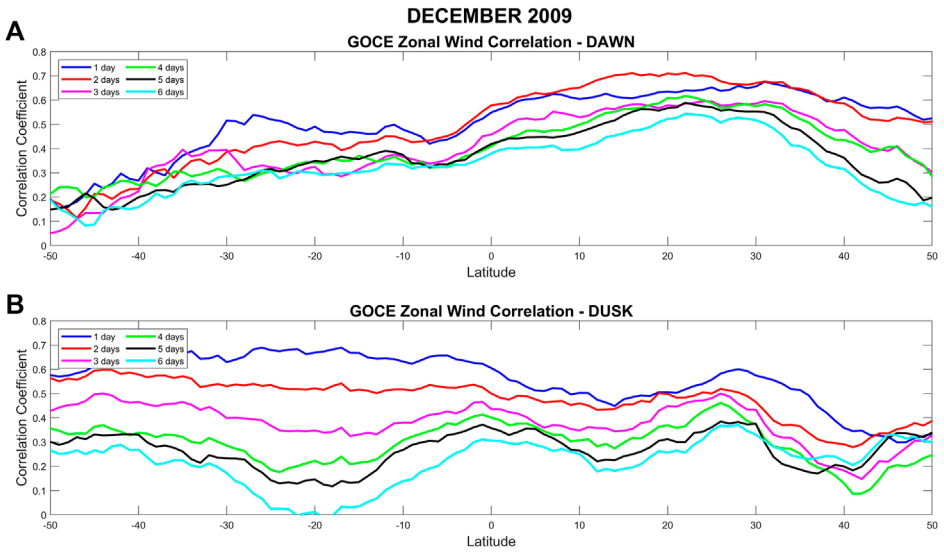

FIGURE 7
Temporal evolution of the longitudinal/temporal correlation coefficients for latitudes from −50° to 50° for December solstice 2009 during dawn **(A)** and dusk **(B)** for $|\Delta Orbit| = 16, 32, 48, 64, 80, 96$. These values of $|\Delta Orbit|$ have a correspondence in time of 1, 2, 3, 4, 5, and 6 days respectively.

the values of the correlations are positive and exhibit their largest values, irrespective of latitude, season, and local time. Note that $\Delta Orbit$ represents a change in both longitude and time. Therefore, a periodic structure in $\Delta Orbit$ could be produced by a wind structure that is either periodic in time or in longitude. For example, if positive correlations are observed every 16 orbits and negative correlations at $|\Delta Orbit| = 8, 24, 40, \ldots$, this could be produced by a structure that is either diurnal or that presents a zonal wave-1 periodicity.

For December solstice 2009, the magnitudes of the correlation coefficients are generally larger in the northern hemisphere during dawn and larger in the southern hemisphere during dusk. Specifically, at dawn, in addition to the positive correlations every 16 orbits, negative correlations are observed poleward of

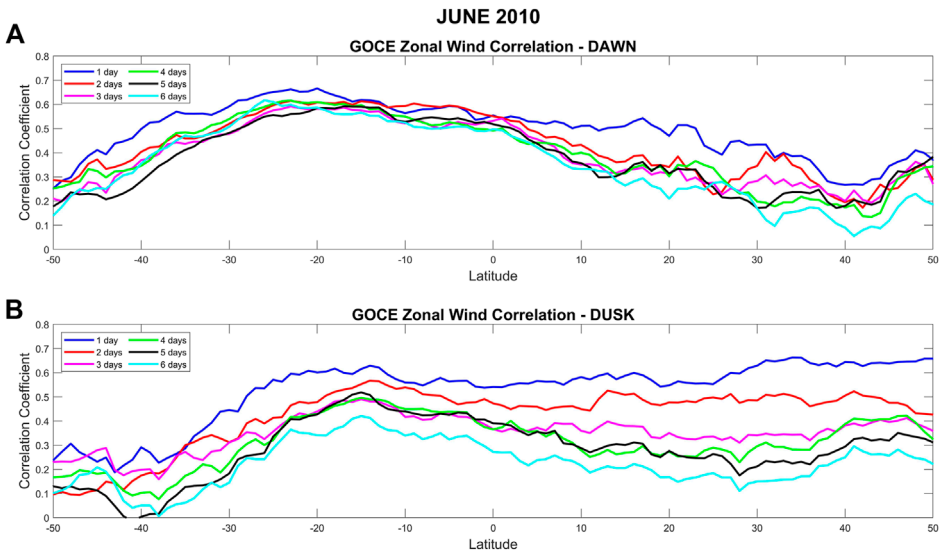

FIGURE 8
Same as Figure 7 but for June solstice 2010.

about 40° latitude at $|\Delta Orbit| = 8, 24, 40, 56, 72, 88$ with values of ~-0.3. These variations correspond to an anticorrelation between locations 180°/12 h apart and can be interpreted as the presence of a diurnal/wave-1 structure. Equatorward of about 40° latitude (and throughout the entire southern hemisphere) additional troughs are observed at $|\Delta Orbit| = 4, 12, 20, \ldots$ and crests at $|\Delta Orbit| = 8, 24, 40, \ldots$, indicating the presence of a semidiurnal/wave-2 structure at these latitudes. The correlation values in the troughs range from about −0.2 to 0 and the crest values range from about 0.2 to 0.3. During dusk, the semidiurnal/wave-2 structure is observed at all latitudes with similar correlation values as those observed during dawn.

During June solstice 2010 at dawn, a diurnal/wave-1 periodicity is observed in the southern hemisphere, while in the northern hemisphere a semidiurnal/wave-2 structure can be seen, albeit not as clearly. The values in the southern hemisphere (~-0.4 for peak negative correlations and ~0.5 to 0.6 for the positive correlations) are significantly higher than in the northern hemisphere (~-0.1 for peak negative correlations and ~0.2 to 0.3 for the positive correlations).

During dusk, a semidiurnal/wave-2 structure is present for all latitudes. Higher correlation values (0.4–0.6) are present for $|\Delta Orbit| = 16, 32, 48, \ldots$ and lower values (~0.2–0.3) for $|\Delta Orbit| = 8, 24, 40, \ldots$. In contrast to the December 2009 results, during this season the higher absolute correlation values are observed in the southern hemisphere during dawn and in the northern hemisphere during dusk.

Figure 7 shows the temporal evolution of the correlation coefficients for latitudes from −50° to 50° for December 2009 during dawn (Figure 7A) and dusk (Figure 7B) for $|\Delta Orbit| = 16, 32, 48, 64, 80, 96$. These values of $|\Delta Orbit|$ correspond to a difference in time of 1, 2, 3, 4, 5 and 6 days between the reference and comparison orbits. Generally, it can be seen that the correlation coefficients are largest for a time difference of 1 day and gradually decrease with increasing time difference. Specifically, during dawn, the correlation coefficients for the same location reduce by approximately 0.2 from day 1 to day 6. During dusk, the difference is larger, with correlation coefficients reducing from about 0.6 to 0.5 for a time difference of 1 day, to 0–0.2 for a difference of 6 days.

Figure 8 shows the same as Figure 7, but for June solstice 2010. During dawn, the correlation coefficients are reduced by ~0.1 from 1–2 days–6 days for the same location. During dusk, the difference is again larger, with correlation coefficients of about 0.6–0.5 for 1 day later, to 0.2–0.3 for 6 days later.

Comparing the correlation coefficients shown in Figures 7, 8, we observe that during dawn the maxima in the correlation coefficients are always located in the winter hemisphere, i.e., for December 2009, the maximum is located in the northern hemisphere and for June 2010, it is located in the southern hemisphere. This hemispheric "flip" can also be seen during dusk in the summer hemisphere, albeit not as clearly. To evaluate changes in the longitudinal/temporal correlations between different years, Figure 9 shows, similar to Figure 6, longitudinal/temporal GOCE zonal wind correlations, but this time for December 2009 (Figures 9A,B) and December 2011 (Figures 9C,D). These 2 years were chosen as they represent the lowest (76 sfu for December 2009) and highest (132 sfu for December 2011) solar flux values in the data analyzed. During dawn, the general structure observed in the correlations in 2009 can also be seen in 2011, with the exception in the southern mid-latitudes (~-35° to −45°), where a clear diurnal/wave-1 structure is observed during 2011, with trough values ranging from −0.3 to −0.4. During dusk the differences between the 2 years are more pronounced. While the correlation coefficients at dusk exhibit a clear semidiurnal/wave-2 periodicity at all latitudes during December 2009, this is only the case from about −40° to −50° latitude during 2011. Instead, a terdiurnal/wave-3 structure emerges for latitudes from −5° to 35°, with correlation

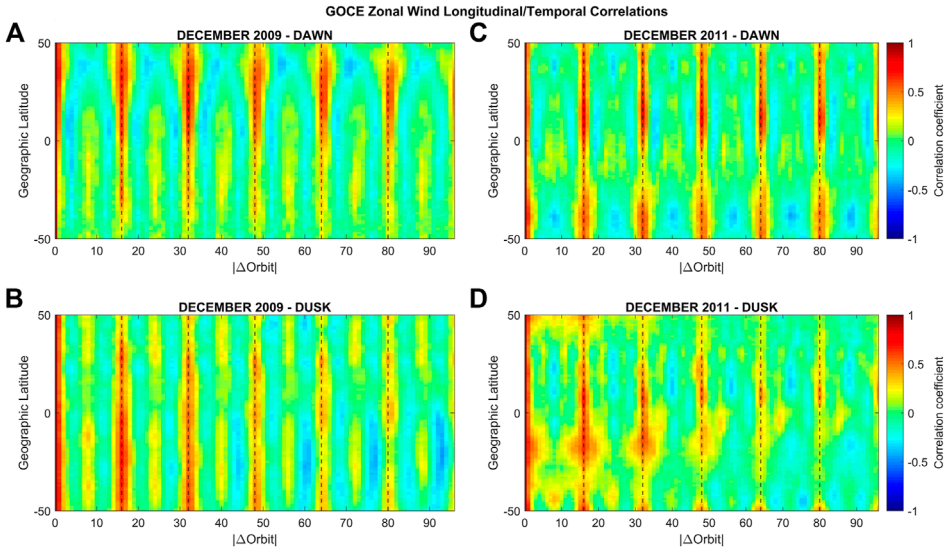

FIGURE 9
Same as Figure 6 but for December 2009 **(A,B)** and December 2011 **(C,D)**.

values at the troughs of ~-0.3. An additional structure of positive correlations centered around −15° of latitude can also be seen every 16 orbits up to 48 orbits. Supplementary Figure S3 shows the comparison of longitudinal/temporal GOCE zonal wind correlations, for June 2010 (Supplementary Figures S3A, B) and June 2011 (Supplementary Figures S3C, D). These two periods also differ significantly in their average solar flux. During dawn, the same structure can be seen for both years, but with enhanced values during 2011. This is also the case during dusk, but this time the correlation values are diminished during the later year.

The global pattern of the correlation coefficients of GOCE zonal winds for December solstice 2009 at dawn are shown in Figure 10, separately for reference points located at ±40°, ±20° and 0° latitude. In each panel the correlation coefficients correspond to a temporal/longitudinal window of ±96 orbits from the reference orbit and latitudes of the comparison orbit from −50° to 50°. Clearly, the main morphology and longitudinal/temporal structures observed in Figure 6 are present.

It is interesting to note that the longitudinal structures seen in Figure 10 are slightly slanted and lean towards the right side of the graph. This indicates a phase shift in latitude of the periodic longitudinal/temporal structures and a corresponding north-west orientation. This can be seen by realizing that a positive value of $\Delta Orbit$ indicates that the corresponding measurements were obtained at a location located to the west of the reference orbit ($\Delta Orbit = 0$) and were taken at a later time. Similarly, negative values of $\Delta Orbit$ correspond to measurements taken at earlier times toward the east of the location of the reference orbit. As a result, the observed slant of the periodic structures toward the right of the graph (higher $\Delta Orbit$ with higher latitudes) translates into a north-west orientation of the structures.

Figure 11 shows the longitudinal/temporal correlation coefficients of GOCE zonal winds for December 2009 during dusk. Again, the main morphology and longitudinal/temporal structures observed in Figure 6 are present. The slant of the longitudinal structures in this case is leaning towards the left side of the graph corresponding to a north-east orientation.

Similar figures were also generated for June solstice 2010 (Supplementary Figures S3, S4). For this season, during dawn, the slant of the longitudinal structures in this case is leaning towards the right side of the graph indicating, as discussed before, a general north-west orientation. During dusk, the slant of the longitudinal structures is leaning towards the left side of the graph indicating a general north-east orientation.

4.4 GOCE zonal wind longitudinal correlations after removal of tides

Figure 12 shows the longitudinal/temporal correlation coefficients of GOCE zonal winds for December solstice 2009 during dawn after the removal of the tides. Most of the correlation coefficients that were presented in Figure 10 are strongly attenuated. The same attenuation can be observed at dawn for December solstice 2011 (see Supplementary Figure S11) and in Figure 13 and in Supplementary Figure S7 for the June 2010 and June 2011 dawn time period, respectively. This might suggest that most of the periodic structures during dawn are indeed the result of nonmigrating tides irrespective of season and solar flux.

During dusk, however, clear residual structures can be seen in the correlations after removing the tides. This can be seen in Figure 14 for December solstice 2009 where in the southern hemisphere a periodic structure emerges with positive correlation coefficients of about 0.5 for $|\Delta Orbit| < 52$ and negative correlation coefficients of about −0.4 for $|\Delta Orbit| > 40$. A similar structure can also be seen in Supplementary Figure S8 for December solstice 2011 dusk conditions. Figure 15 shows that residual structures are also present for June 2010 during dusk, however, in this case, the

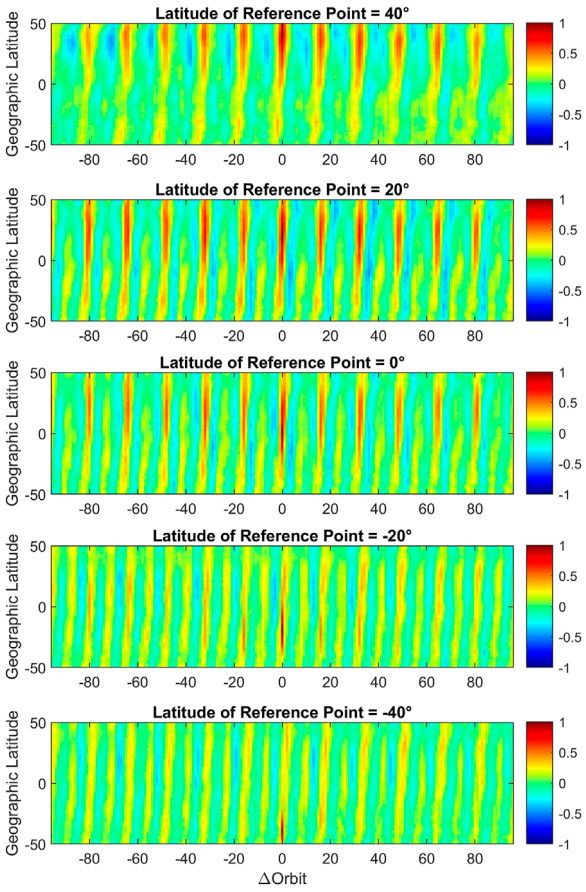

FIGURE 10
Longitudinal/temporal correlation coefficients of GOCE zonal winds for December solstice 2009 during dawn. The x-axis shows the orbit difference between the comparison point and the reference point ($\Delta Orbit$) up to ±96 orbits from the reference. The y-axis corresponds to the geographic latitude of the comparison point. Plots are shown for a reference point at ±40°, ±20° and 0°.

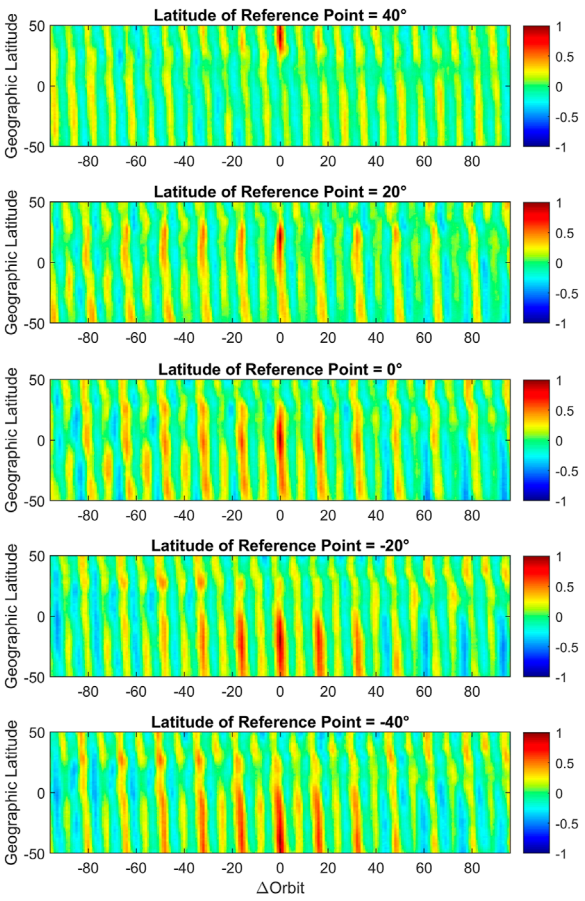

FIGURE 11
Same as Figure 10 but during dusk.

structure is largely confined to the northern hemisphere and consist of positive correlation values (between 0.3 and 0.4) for $|\Delta Orbit| < 20$ and negative correlation coefficients (~-0.3) for $|\Delta Orbit| > 60$. The same characteristics can also be seen in Supplementary Figure S9 for June 2011.

5 Summary and discussion

We have analyzed GOCE zonal wind observations from low- to mid-latitudes to investigate their spatial and temporal correlations. The year-to-year variations as well as the inter-seasonal differences were established for dawn and dusk. We have focused on geomagnetically quiet 27-day periods (one solar rotation) centered as close as possible to the December solstice for the years 2009, 2010, 2011 and 2012 and the June solstice for the years 2010 and 2011. For the calculation of the latitude and longitude/temporal correlations an approach similar to the one described in Shim et al. (2008) was followed. Our results represent zonally averaged values and do not correspond to a particular location/longitude on the globe. Furthermore, our approach eliminated correlations associated with deterministic variation in solar cycle, season and local time and instead focused on stochastic and tidal variations. Additionally, due to the orbit of GOCE longitudinal/temporal correlations could not be separately analyzed.

We found that for all four December solstice periods the latitude correlations during dawn were larger and more extended in latitude in the northern hemisphere compared to the southern hemisphere.

During dusk for December solstice 2009 and 2010 significantly larger and more extended correlations were found for reference latitudes located in the southern hemisphere and in the northern hemisphere up to ~20° latitude. During December 2011 the extension of the latitudinal correlations in latitude were seen to be much reduced before increasing again in 2012. The cause of this year-to-year progression is not known at this point but might be related to similar variations, albeit anticorrelated, in the solar activity throughout these years.

We have also evaluated the zonal wind latitudinal correlations for June solstice 2010 and the larger correlation lengths during

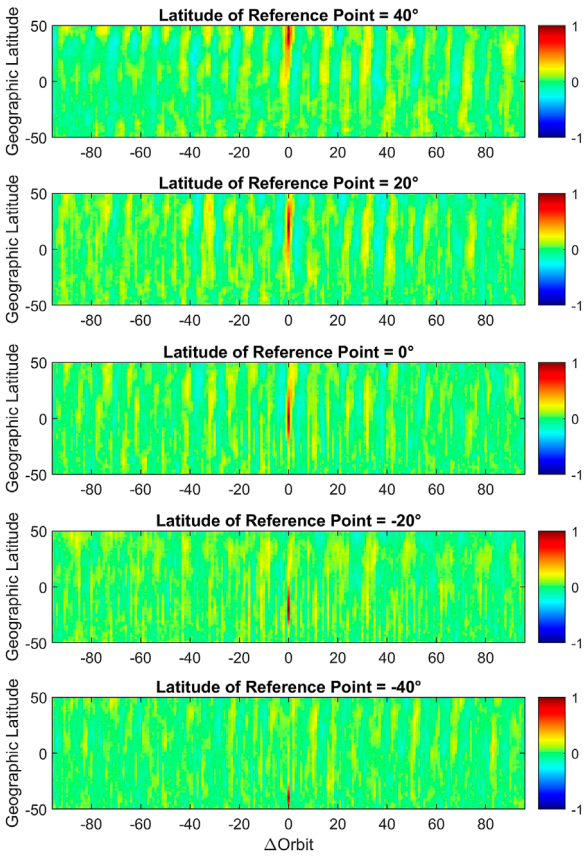

FIGURE 12
Same as Figure 10 but after the removal of tides.

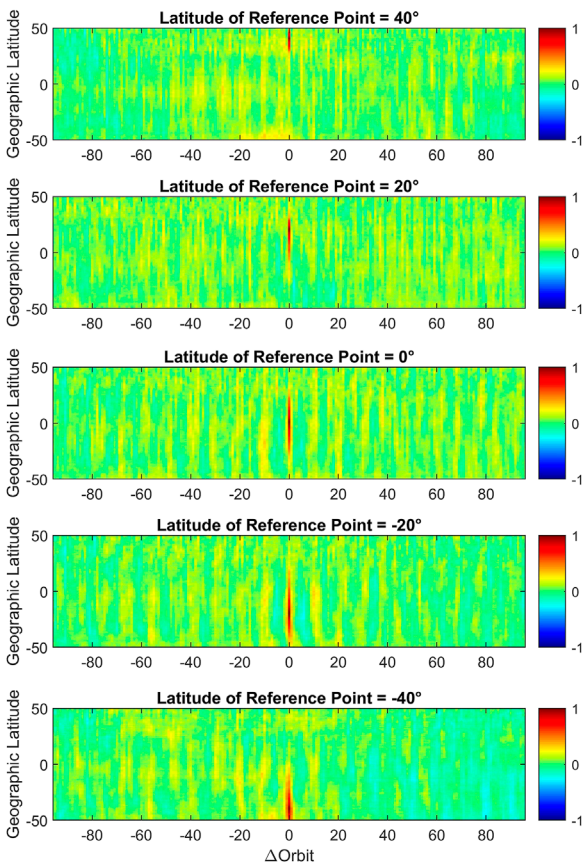

FIGURE 13
Same as Figure 12 but for June solstice 2010.

dawn were found in the southern hemisphere and during dusk in the northern hemisphere. This indicates that during both solstice periods, the latitudinal correlation lengths exhibit their largest values consistently in the winter hemisphere during dawn and in the summer hemisphere during dusk.

Of particular interest are the observed latitudinal correlations at dawn between hemispheric conjugate points observed at mid latitudes during the later December solstice periods. The strength of this conjugacy also appeared to follow similar variations in the solar activity throughout these years, i.e., during December 2009 it was not observed, started to appear in 2010, strengthened in 2011, before weakening again in 2012. This conjugacy was also examined in geomagnetic instead of geographic coordinates which resulted in a much cleaner presentation of the conjugacy. The physical cause for the observed conjugacy, however, is not clear at this point. We speculate that it might be related to midlatitude nighttime MSTIDs, also named electro-buoyancy waves, which map into the opposite hemisphere (Valladares et al., 2016). These waves are found to be magnetically conjugate and preferentially occur during the solstices (Makela et al., 2010; Martinis et al., 2010; Duly et al., 2013). However, Martinis et al. (2010) found that MSTIDs follow an inverse occurrence rate with solar activity conditions in contrast to our observation of the variation of the strength of the conjugate correlation coefficients.

In addition to electro-buoyancy waves, the observed conjugacy at mid-latitudes might also be related to conjugate variations in the high latitude electrodynamics. Wu et al. (2014) reported they observed conjugacy in thermospheric zonal winds in the American sector with varying degrees depending on geomagnetic conditions. They found that conjugacy is highest under moderate geomagnetic conditions, but it is observed for all geomagnetic activity levels, including geomagnetically quiet times. In our case, the average Kp values did not exceed 1^0 for each of the December solstice periods, but the variation seems to follow the solar activity. Clearly further studies are needed to elucidate the underlying causes of the observed conjugacy.

We have also analyzed the dawn and dusk longitudinal/temporal correlations of zonal wind for December 2009 and 2011 and for June 2010 and found that they exhibit periodic structures with the largest positive correlations every 16 orbits (every 1 day) during all geophysical conditions, albeit with different characteristics. The temporal evolution of the temporal/longitudinal correlations were found to gradually decrease over the course of several days. Based on a 20-model year simulation of WACCM-X, Liu (2016) reported

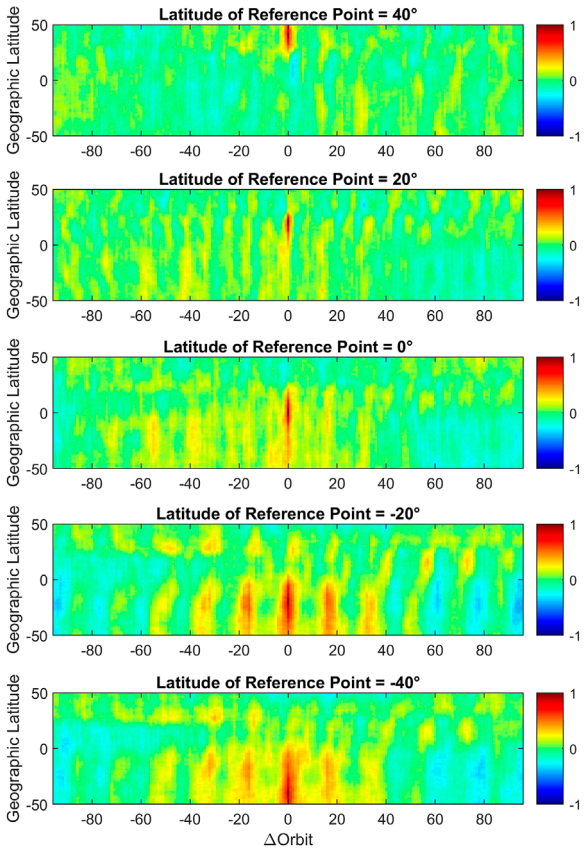

FIGURE 14
Same as Figure 12 but during dusk.

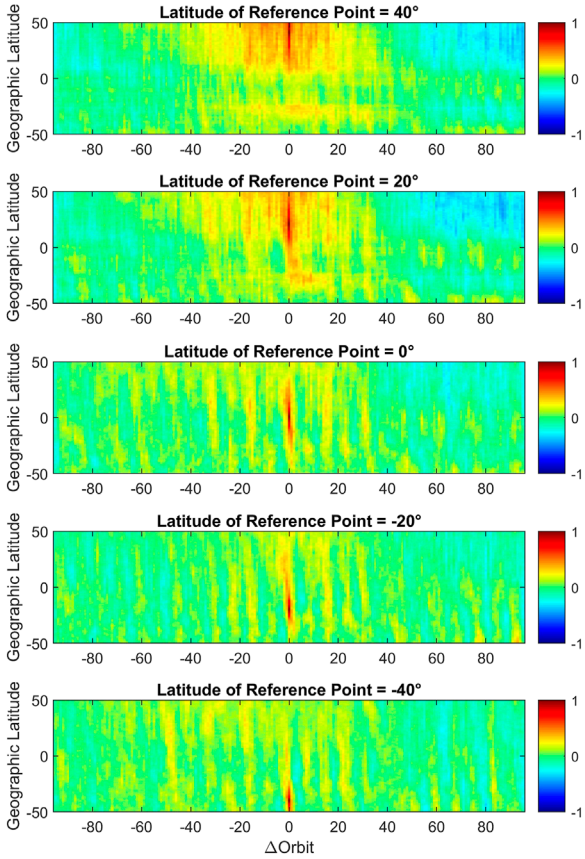

FIGURE 15
Same as Figure 14 but for June solstice 2010.

correlation times of zonal mean zonal winds in the thermosphere of the order of days, in agreement with our results. We found that the correlation coefficients for the same location decreased more slowly during dawn and much faster during dusk for both December and June solstice conditions. We also observed that during dawn the maxima in the correlation coefficients were always located in the winter hemisphere. This hemispheric "flip" was also seen during dusk in the summer hemisphere, but not as clearly.

The temporal/longitudinal correlation coefficients for December solstice 2009 were found to be generally larger in the northern hemisphere during dawn and larger in the southern hemisphere during dusk. Specifically, during dawn the temporal/longitudinal correlation for December 2009 displayed a diurnal/wave-1 periodicity in the northern mid-latitudes and a semidiurnal/wave-2 periodicity for lower latitudes and the southern hemisphere. The orientation of these structures was found to be in the north-west direction. During dusk, a semidiurnal/wave-2 structure was observed for all latitudes, with a north-east orientation. The general structure observed during dawn in the correlations in December solstice 2009 could also be seen in December solstice 2011 but larger differences between the 2 years were found during dusk.

The temporal/longitudinal correlation coefficients for June 2010 at dawn displayed a diurnal/wave-1 periodicity in the southern hemisphere and a semidiurnal/wave-2 periodicity in the northern hemisphere. Here, the orientation of the structures was found to be in the north-west direction. During June solstice dusk, a semidiurnal/wave-2 structure was observed for all latitudes, with a north-east orientation. This time, however, the larger correlation values were observed in the northern hemisphere, in contrast to our December solstice results.

Although our study does not allow for a detailed analysis of the underlying causes of the observed periodic structures, we speculate that they are the result of the presence of atmospheric tides, and in particular nonmigrating tides. To investigate correlations not associated with tides we have eliminated their contribution up to zonal wave-5 from the zonal winds before calculating the longitude/time correlation coefficients. The results show that the longitudinal/temporal correlations were strongly attenuated during dawn for both December and June solstices, suggesting that indeed the main structures observed before were the result of nonmigrating tides during this time of the day, irrespective of season and solar flux. Some smaller localized correlations are still apparent in the remaining correlations at dawn, which might be related to the presence of gravity waves that have been reported to be present in GOCE observations (Garcia et al., 2016; Vadas et al., 2019) and/or variations in the phase and amplitude of the tides. A modeling study

by Liu (2014), for example, suggests that there is an irregular or stochastic aspect of the day-to-day tidal variability.

In contrast, during dusk, a previously masked structure appears after the removal of the tidal effects that follows a multi-day period for both December (in the southern hemisphere) and June (in the northern hemisphere). Although more investigation is needed, these correlations might be the result of the presence of other waves that we have not included in our analysis. Gasperini et al. (2015), for example, reported the presence of ultra-fast Kelvin waves in the GOCE zonal wind observations with a period of 3.5 days.

Finally, note that our analysis only pertains to geomagnetically quiet conditions at dawn and dusk and an investigation of the correlation coefficients of the zonal winds for other local times and geomagnetically active conditions needs to be performed in the future.

Data availability statement

Publicly available datasets were analyzed in this study. This data can be found here: The GOCE data used in this work are publicly available and provided by the European Space Agency (ESA) and can be found at https://earth.esa.int/eogateway/catalog/goce-thermosphere-data. The F10.7 cm radio flux and Kp index were obtained through NASA/GSFC's Space Physics Data Facility's OMNIWeb service, which can be found at https://omniweb.gsfc.nasa.gov/form/dx1.html.

Author contributions

IM and LS contributed to the conception and design of the study. IM conducted the analysis. All authors contributed to the article and approved the submitted version.

Funding

This research was partially supported by NASA Headquarters under the NASA Earth and Space Science Fellowship Program (NESSF/FINESST), GRANT 80NSSC17K0431; National Science Foundation grant AGS-1651461 to Utah State University and NASA grant 80NSSC20K0191 to Utah State University.

Acknowledgments

We acknowledge the use of the GOCE data provided by the European Space Agency (ESA). We acknowledge use of NASA/GSFC's Space Physics Data Facility's OMNIWeb service to obtain the F10.7 cm radio flux and Kp index. Part of this work is included in IM's PhD dissertation, which can be found at https://digitalcommons.usu.edu/etd/8671/.

Conflict of interest

The authors declare that the research was conducted in the absence of any commercial or financial relationships that could be construed as a potential conflict of interest.

Publisher's note

All claims expressed in this article are solely those of the authors and do not necessarily represent those of their affiliated organizations, or those of the publisher, the editors and the reviewers. Any product that may be evaluated in this article, or claim that may be made by its manufacturer, is not guaranteed or endorsed by the publisher.

Supplementary material

The Supplementary Material for this article can be found online at: https://www.frontiersin.org/articles/10.3389/fspas.2023.1214591/full#supplementary-material

References

Alken, P., and Maus, S. (2007). Spatio-temporal characterization of the equatorial electrojet from CHAMP, Ørsted, and SAC-C satellite magnetic measurements. *J. Geophys. Res. Space Phys.* 112 (A9). doi:10.1029/2007ja012524

Bruinsma, S. L., Doornbos, E., and Bowman, B. R. (2014). Validation of GOCE densities and evaluation of thermosphere models. *Adv. Space Res.* 54 (4), 576–585. doi:10.1016/j.asr.2014.04.008

Bruinsma, S., Boniface, C., Sutton, E. K., and Fedrizzi, M. (2021). Thermosphere modeling capabilities assessment: Geomagnetic storms. *J. Space Weather Space Clim.* 11, 12. doi:10.1051/swsc/2021002

Calabia, A., Lu, G., and Bolaji, O. S. (2023). Advances on upper-atmosphere characterization for geodetic space weather research and applications. *Front. Astronomy Space Sci.* 10, 141. doi:10.3389/fspas.2023.1211582

Doornbos, E., Bruinsma, S., Fritsche, B., Visser, P. N. A. M., Van Den Ijssel, J., Encarnacao, J. T., et al. (2013). Air density and wind retrieval using GOCE data. *In ESA Living Planet Symp.* 722, 7.

Doornbos, E., Van Den Ijssel, J., Luhr, H., Forster, M., and Koppenwallner, G. (2010). Neutral density and crosswind determination from arbitrarily oriented multiaxis accelerometers on satellites. *J. Spacecr. Rockets* 47 (4), 580–589. doi:10.2514/1.48114

Duly, T. M., Chapagain, N. P., and Makela, J. J. (2013). Climatology of nighttime medium-scale traveling ionospheric disturbances (MSTIDs) in the Central Pacific and South American sectors. *Ann. Geophys.* (Göttingen, Germany: Copernicus Publications), 31 (12), 2229–2237.

Forbes, J. M., Lu, G., Bruinsma, S., Nerem, S., and Zhang, X. (2005). Thermosphere density variations due to the 15–24 April 2002 solar events from CHAMP/STAR accelerometer measurements. *J. Geophys. Res. Space Phys.* 110 (A12), A12S27. doi:10.1029/2004ja010856

Garcia, R. F., Bruinsma, S., Massarweh, L., and Doornbos, E. (2016). Medium-scale gravity wave activity in the thermosphere inferred from GOCE data. *J. Geophys. Res. Space Phys.* 121 (8), 8089–8102. doi:10.1002/2016ja022797

Gasperini, F., Forbes, J. M., Doornbos, E. N., and Bruinsma, S. L. (2015). Wave coupling between the lower and middle thermosphere as viewed from TIMED and GOCE. *J. Geophys. Res. Space Phys.* 120 (7), 5788–5804. doi:10.1002/2015ja021300

Kelley, M. C. (2009). *The Earth's ionosphere: Plasma physics and electrodynamics*. Cambridge, MA, USA: Academic Press.

Liu, H. L. (2016). Variability and predictability of the space environment as related to lower atmosphere forcing. *Space weather*. 14 (9), 634–658. doi:10.1002/2016sw001450

Liu, H. L. (2014). "WACCM-X simulation of tidal and planetary wave variability in the upper atmosphere," in *Modeling the ionosphere–thermosphere system* (Hoboken, NJ, USA: Wiley), 181–199.

Makela, J. J., Miller, E. S., and Talaat, E. R. (2010). Nighttime medium-scale traveling ionospheric disturbances at low geomagnetic latitudes. *Geophys. Res. Lett.* 37 (24). doi:10.1029/2010gl045922

Martinis, C., Baumgardner, J., Wroten, J., and Mendillo, M. (2010). Seasonal dependence of MSTIDs obtained from 630.0 nm airglow imaging at Arecibo. *Geophys. Res. Lett.* 37 (11). doi:10.1029/2010gl043569

Maute, A., and Richmond, A. D. (2017). F-Region dynamo simulations at low and mid-latitude. *Space Sci. Rev.* 206 (1-4), 471–493. doi:10.1007/s11214-016-0262-3

Molina, I. (2022). *Variability of thermospheric zonal winds near Dawn and dusk (PhD dissertation)*. Logan, Utah: Utah State University.

Molina, I., and Scherliess, L. (2023). Longitudinal variability of thermospheric zonal winds near dawn and dusk. *Front. Astron. Space Sci.* 10, 1214612. doi:10.3389/fspas.2023.1214612

Shim, J. S., Scherliess, L., Schunk, R. W., and Thompson, D. C. (2008). Spatial correlations of day-to-day ionospheric total electron content variability obtained from ground-based GPS. *J. Geophys. Res. Space Phys.* 113 (A9). doi:10.1029/2007ja012635

Vadas, S. L., Xu, S., Yue, J., Bossert, K., Becker, E., and Baumgarten, G. (2019). Characteristics of the quiet-time hot spot gravity waves observed by GOCE over the Southern Andes on 5 July 2010. *J. Geophys. Res. Space Phys.* 124 (8), 7034–7061. doi:10.1029/2019ja026693

Valladares, C. E., and Sheehan, R. (2016). Observations of conjugate MSTIDs using networks of GPS receivers in the American sector. *Radio Sci.* 51 (9), 1470–1488. doi:10.1002/2016rs005967

Wang, W., Burns, A. G., and Liu, J. (2021). Upper thermospheric winds: Forcing, variability, and effects. *Up. Atmos. Dyn. energetics*, 41–63. doi:10.1002/9781119815631.ch3

Wu, Q., Noto, J., Kerr, R., Kapali, S., Riccobono, J., and Wang, W. (2014). First Palmer and Millstone Hill midlatitude conjugate observation of thermospheric winds. *J. Geophys. Res. Space Phys.* 119 (4), 3016–3028.

frontiers | Frontiers in Astronomy and Space Sciences

TYPE Original Research
PUBLISHED 18 September 2023
DOI 10.3389/fspas.2023.1217737

OPEN ACCESS

EDITED BY
Huixin Liu,
Kyushu University, Japan

REVIEWED BY
John Bosco Habarulema,
South African National Space Agency, South Africa
Larisa Goncharenko,
Massachusetts Institute of Technology, United States
McArthur Jones Jr,
Naval Research Laboratory, United States

*CORRESPONDENCE
Federico Gasperini,
federico.gasperini@orionspace.com

RECEIVED 05 May 2023
ACCEPTED 04 September 2023
PUBLISHED 18 September 2023

CITATION
Gasperini F, Harding BJ, Crowley G and Immel TJ (2023), Ionosphere-thermosphere coupling via global-scale waves: new insights from two-years of concurrent *in situ* and remotely-sensed satellite observations. *Front. Astron. Space Sci.* 10:1217737. doi: 10.3389/fspas.2023.1217737

Ionosphere-thermosphere coupling via global-scale waves: new insights from two-years of concurrent *in situ* and remotely-sensed satellite observations

Federico Gasperini[1]*, Brian J. Harding[2], Geoffrey Crowley[1] and Thomas J. Immel[2]

[1]Orion Space Solution, Louisville, CO, United States, [2]Space Sciences Laboratory, University of California, Berkeley, CA, United States

Growing evidence indicates that a selected group of global-scale waves from the lower atmosphere constitute a significant source of ionosphere-thermosphere (IT, 100–600 km) variability. Due to the geometry of the magnetic field lines, this IT coupling occurs mainly at low latitudes (< 30°) and is driven by waves originating in the tropical troposphere such as the diurnal eastward propagating tide with zonal wave number s = −3 (DE3) and the quasi-3-day ultra-fast Kelvin wave with s = −1 (UFKW1). In this work, over 2 years of simultaneous *in situ* ion densities from Ion Velocity Meters (IVMs) onboard the Ionospheric Connection Explorer (ICON) near 590 km and the Scintillation Observations and Response of the Ionosphere to Electrodynamics (SORTIE) CubeSat near 420 km, along with remotely-sensed lower (ca. 105 km) and middle (ca. 220 km) thermospheric horizontal winds from ICON's Michelson Interferometer for Global High-resolution Thermospheric Imaging (MIGHTI) are employed to demonstrate a rich spectrum of waves coupling these IT regions. Strong DE3 and UFKW1 topside ionospheric variations are traced to lower thermospheric zonal winds, while large diurnal s = 2 (DW2) and zonally symmetric (D0) variations are traced to middle thermospheric winds generated *in situ*. Analyses of diurnal tides from the Climatological Tidal Model of the Thermosphere (CTMT) reveal general agreement near 105 km, with larger discrepancies near 220 km due to *in situ* tidal generation not captured by CTMT. This study highlights the utility of simultaneous satellite measurements for studies of IT coupling via global-scale waves.

KEYWORDS

IT coupling, global-scale waves, ICON, SORTIE, CTMT, DE3, UFKW

1 Introduction

The generation and propagation of atmospheric waves with different spatiotemporal scales represent the primary mechanism through which energy and momentum are carried from the lower atmosphere to the ionosphere-thermosphere (IT) system. Solar tides are

primarily generated by the periodic absorption of solar radiation in longitude and localtime (LT) by tropospheric water vapor, stratospheric ozone, and latent heat release in deep tropical clouds. Planetary waves (PWs), Kelvin waves (KWs), and gravity waves (GWs) are mainly excited by surface topography, unstable shear flows, and convection. The subset of this wave spectrum that can effectively propagate upward grows exponentially with height into the less dense atmosphere. As a result, the waves achieve their largest amplitudes in the dissipative region between about 100 km and 150 km known as the mesosphere-lower-thermosphere (MLT) (e.g., Yiğit and Medvedev, 2015; Liu, 2016; Yiğit et al., 2016). A fraction of the wave spectrum can reach the upper thermosphere and exosphere (e.g., Forbes et al., 2009; Oberheide et al., 2009; Gasperini et al., 2015; 2018; 2020; 2022). As part of their vertical propagation, nonlinear wave-wave interactions can occur that contribute to modifying the interacting waves and generating secondary waves (Palo et al., 1999; Chang et al., 2011; Liu, 2016; Gasperini et al., 2015; 2021; Forbes et al., 2021a; b). The wave-driven IT wind variations can redistribute ionospheric plasma through the electric fields generated via the dynamo mechanism in the MLT or directly by moving plasma along magnetic field lines at higher levels (e.g., Liu, 2016).

The global IT coupling described above occurs primarily at low latitudes (<30°) as a result of the geometry of the magnetic field lines near the equator and is largely driven by waves of tropical tropospheric origin. Two prominent examples of such large-scale waves from the tropical wave spectrum that preferentially propagate into the IT system are the well-known diurnal eastward propagating with zonal wavenumber s = −3 (DE3), and the eastward-propagating ~2.5–4-day period ultra-fast Kelvin wave (UFKW) with zonal wavenumber s = −1, hereafter UFKW1 (e.g., Forbes et al., 2009; 2020a; b; Oberheide et al., 2009; Gasperini et al., 2015; 2021; 2022; Chang et al., 2011; Gu et al., 2014a; Pedatella and Forbes, 2009; Yamasaki et al., 2020; Liu et al., 2013). As discussed by Gasperini et al. (2022), these so-called 'ultra-fast tropical waves' that include DE3 and UFKWs, are known to preferentially propagate into the IT system and significantly alter thermospheric winds (Gasperini et al., 2015; 2020) and ionospheric densities (Pedatella and Forbes, 2009; Chang et al., 2011; He et al., 2011; Gu et al., 2014a; Gasperini et al., 2021). DE3 originates primarily in the tropical troposphere by latent heat release in deep convective clouds (e.g., Hagan, 1996; Lieberman et al., 2007), and its equatorially symmetric mode is the largest component in the lower thermosphere (e.g., Truskowski et al., 2014) and can propagate into the middle thermosphere (e.g., Oberheide et al., 2011; Gasperini et al., 2015; 2018) and ionosphere (e.g., Gasperini et al., 2021) due to its long vertical wavelength of about 56 km. UFKWs are a special kind of GW trapped in equatorial and low-latitude regions, where the Coriolis force is negligible (Salby et al., 1984; Andrews et al., 1987). Similarly to DE3, UFKWs originate primarily from latent heat release in the tropical troposphere and are the largest in the zonal wind component. UFKWs are characterized by the longest vertical wavelength (~51 km) of all Kelvin waves and thus can penetrate well into the lower and middle thermosphere (e.g., Forbes et al., 2020a; b), with amplitudes of upwards of 30 m/s in the MLT zonal wind (Gu et al., 2014a), and middle thermospheric zonal wind amplitudes exceeding 10 m/s (Gasperini et al., 2015; 2018; 2020). The focus of this study is on diurnal tides and UFKWs, however, semidiurnal tides (and terdiurnal tides) can also play a large role in IT coupling and connections to the lower atmosphere, as recently demonstrated observationally by Forbes et al. (2022).

Using concurrent satellite observations from Ionospheric Connection Explorer (ICON; Immel et al., 2018; Immel et al., 2021) observatory, the Scintillation Observations and Response of The Ionosphere to Electrodynamics (SORTIE; Crowley et al., 2016) CubeSat, and the Thermosphere Ionosphere Mesosphere Energetics Dynamics (TIMED) Sounding of the Atmosphere using Broadband Emission Radiometry (SABER) instrument (Mertens et al., 2001), along with Specified-Dynamics Whole Atmosphere Community Climate Model with thermosphere and ionosphere eXtension (SD/WACCM-X; Liu et al., 2018; Gasperini et al., 2020) modeling, Gasperini et al. (2021) demonstrated a pronounced zonal wavenumber 4 (WN4) structure in the global low-latitude ionosphere due to the DE3 propagating through the lower thermosphere. More recently, Gasperini et al. (2022) revealed a rich spectrum of waves coupling the lower (~90–105 km) and middle (~200–270 km) thermosphere with the upper F-region (~540 and ~590 km) ionosphere through analyses of simultaneous ICON and Constellation Observing System for Meteorology, Ionosphere and Climate 2 (COSMIC-2) observations. These and other recent studies (e.g., Heelis R. A. et al., 2022; Lieberman et al., 2022; Harding et al., 2022; Yamazaki et al., 2022; Forbes et al., 2021a; b; Immel et al., 2021; Liu et al., 2021; Wautelet et al., 2021), demonstrate the utility of employing a diverse set of contemporaneous satellite observations to characterize and better understand the origin of large-scale variability occurring in the tightly-coupled IT system.

Despite some improved understanding of IT connections involving global-scale waves afforded by recent ICON, Global-scale Observations of the Limb and Disk (GOLD), and COSMIC-2 satellite observations, there are many unresolved questions regarding the variability of the wave spectrum and its impacts on the low-latitude IT system. Availability of simultaneous lower (i.e., ~90–110 km) and middle (i.e., ~200–300 km) thermospheric winds and topside F-region (i.e., ~590 km) ion density from the ICON mission (Immel et al., 2018; 2021), combined with periods of concurrent ionospheric observations from the SORTIE CubeSat (Crowley et al., 2016) near 420 km, during the solar minimum and generally geomagnetic-quiescent period (Kp>4 on only about 8.7% of the days) between January 2020 and March 2022 provides a unique opportunity to develop an improved experimental understanding of how global-scale waves couple lower thermospheric variability with IT variability. This study evaluates, for the first time, the simultaneous diurnal tidal spectrum and other high-impact global-scale waves in the lower and middle thermosphere and topside F-region ion density using the most recent version of the data publicly available at the time of writing. This is accomplished through spectral analyses of the recently-released version 5 (v05) of ICON MIGHTI wind data over the height ranges ~93–106 km and ~200–270 km, where wind measurements are made during both day and night, and in-situ-measured topside F-region ion density from IVM instruments onboard ICON (v06) and SORTIE (v02).

This paper is organized as follows: Section 2 briefly describes the satellite data, modeling, and methodologies, Section 3 contains the results and related discussions, while Section 4 provides a summary and the main conclusions.

2 Satellite observations, modeling, and methods

This study employs simultaneous ICON MIGHTI horizontal wind, ICON IVM ion density, and SORTIE IVM ion density satellite observations, along with diurnal tidal output from the Climatological Tidal Model of the Thermosphere (CTMT). A brief overview of these observational datasets, CTMT, and the spectral methods herein adopted are provided below. This summary provides the necessary context for the interpretation of the global-scale wave analyses presented in Section 3.

2.1 Satellite data

ICON is a NASA Heliophysics System Observatory (HSO) mission launched on 10 October 2019 on a nearly circular ~27° inclination orbit at an altitude near 590 km (Immel et al., 2018). The ICON mission aims to directly measure the processes of ionospheric modification by the dynamics of the neutral atmosphere (Immel et al., 2018; 2021; Immel and Eastes, 2019). As a single satellite, ICON only covers two local solar times (LST) a day, each precessing by about 29.8 min toward earlier LST each day.

This study employs MIGHTI Level 2 Version 5 (V05) green-line vector winds (~95–106 km) and red-line vector winds (~200–270 km) that provide coverage during both daytime and nighttime. Dhadly et al. (2021) showed agreement between MIGHTI and Thermosphere, Ionosphere, Mesosphere Energetics and Dynamics Doppler Interferometer (TIMED/TIDI) zonal wind observations, with correlations around 0.6 and root mean square (RMS) differences of ~56 m/s, and similar large amplitude longitudinal variations. RMS differences between MIGHTI winds and ground-based radars and interferometers are on the order of 20 m/s (Harding et al., 2021; Makela et al., 2021). Characterization of the mean horizontal winds and the associated circulation by ICON/MIGHTI for Northern Hemisphere summer solstice conditions was also studied by Yiğit et al. (2022). While the aforementioned studies employed previous data versions, a new calibration method for the so-called 'zero wind' was developed for V05 MIGHTI winds that uses a long-term comparison of the ascending- and descending-orbit data to perform a self-calibration of the zero baselines, which is independent of external data or models (Englert et al., 2023). The estimated accuracy of the V05 wind data is generally 10–25 m/s (Englert et al., 2023). Such uncertainties are negligible in tidal/wave fits when a sufficiently large number of data points are used. Recent work by Yamazaki et al. (2023) shows general agreement between MIGHTI V05 mean winds and Horizontal Wind Model 14 (HWM14) winds.

Along with the MIGHTI thermospheric wind observations described above, this study utilizes ICON IVM-A L2-7 V06 ion densities (Heelis et al., 2017; 2022a; b; Huba et al., 2021; Park et al., 2021a; Park et al., 2021b). The IVM is comprised of two instruments, the Retarding Potential Analyzer (RPA) and the Drift Meter (DM). The IVM data are down-selected by including data only for times where the two 'RPA' and 'DM' flags are both less than 1. Heelis et al. (2017) reported ICON/IVM ion densities to have an accuracy exceeding $10^3 cm^{-3}$ based on mission requirement considerations. Total ion concentrations measured by ICON IVM (primarily O+ and H+) are considered equivalent to electron density and hereafter referred to as 'Ne'. Gasperini et al. (2021) found strong agreement (r>0.8) between nearly-coincident independent Ne observations from IVM instruments onboard ICON and COSMIC-2 during a period of similar LT coverage. Similar results were obtained in the recent study by Choi et al. (2023), wherein comparisons of *in situ* ion density measurements from IVMs onboard COSMIC-2 and ICON using observations during geomagnetic quiet days at solar minimum showed strong agreement.

SORTIE is a NASA HSO 6U CubeSat mission launched onboard Dragon CRS-19 to the International Space Station, from where it deployed on 19 February 2020 in a nearly circular ~51.6° inclination orbit near 420 km (Crowley et al., 2016). SORTIE reentered Earth's orbit around 8 September 2022. The primary objective of the SORTIE mission is to discover the sources of wave-like plasma perturbations in the F-region ionosphere, including the relative role of dynamo action *versus* direct mechanical forcing in their formation. The SORTIE sensor suite consists of two components; a micro planar Langmuir probe (μPLP) and an IVM. The temperature, composition, and vector velocity of the ionospheric plasma are measured by the IVM. Gasperini et al. (2021) used concurrent ICON and SORTIE IVM ion density observations to demonstrate coupling from the lower thermosphere to the topside ionosphere from the DE3 tide during a period of similar local time coverage. Azeem et al. (2022) showed the first observation of Traveling Ionospheric Disturbances (TIDs) by SORTIE above a deep convection system over Texas and used model simulation and corroborating satellite and ground-based data to demonstrate their connection to vertically propagating GWs. This study uses the *in situ* L2 total ion density product from the miniature IVM (day and night) from 27 May 2020–8 October 2020 (i.e., days 148–282) and 8 April 2021–21 October 2021 (i.e., days 464–660).

2.2 Climatological Tidal Model of the thermosphere (CTMT)

The CTMT (Oberheide et al., 2011) characterizes the global behavior of vertically propagating tides in the thermosphere (90–400 km; pole to pole). CTMT is based on tidal temperatures and winds in the mesosphere-lower-thermosphere (MLT) region from the Sounding of the Atmosphere using Broadband Emission Radiometer (SABER) and TIMED Doppler Interferometer (TIDI) instruments onboard the Thermosphere Ionosphere Mesosphere Energetics Dynamics (TIMED) satellite extended into the thermosphere using Hough Mode Extension (HME) modeling.

In brief, HMEs represent global solutions (pole-to-pole, 0- to 400-km altitude) to the linearized dynamical equations of the atmosphere for an oscillation of a given frequency and zonal wavenumber, taking into account dissipative effects (including radiative cooling, eddy and molecular diffusion of heat and momentum) above the forcing region (Lindzen and Hong, 1974; Forbes and Hagan, 1988). These perturbations are computed for a background windless atmosphere characterized by a single climatological height profile of temperature. HMEs can be thought of as a latitude *versus* height table of self-consistent amplitudes

and phases for the velocity, temperature, and density perturbation fields of an oscillation with a particular frequency and zonal wavenumber (e.g., Forbes et al., 1994; 2017; 2022). More details on HMEs and CTMT can be found in the recent study by Forbes et al. (2022), which focuses on the vertical evolution of the non-migrating semidiurnal tidal spectrum and their relationship to viscous dissipation and *in situ* thermospheric sources.

As detailed in Oberheide et al. (2011), monthly tidal climatologies for CTMT are obtained from averaging about 6 years (2002–2008) of TIMED SABER and TIDI observations. CTMT accounts for contributions from solar radiation absorption in the troposphere and stratosphere, tropospheric latent heat release, and nonlinear wave-wave interactions occurring within and below the MLT and is valid for low-to-medium solar radio flux conditions (F10.7 = 110 SFU). One should keep in mind that thermospheric tidal forcing occurring above the MLT is not accounted for by CTMT. As a result, this model is not able to capture migrating tides forced *in situ* by the absorption of solar EUV radiation and nonmigrating tides forced in the thermosphere (e.g., Jones et al., 2013).

This study employs zonal and meridional wind diurnal tidal amplitudes from CTMT for comparison with ICON MIGHTI. Given the observationally-based climatological height-latitude tidal information provided by CTMT for solar low-to-medium conditions (F10.7 = 110 SFU), CTMT is an excellent model for the interpretation of the MIGHTI-derived tidal amplitudes during 2020–2021.

2.3 Spectral analyses and nomenclature

As noted in Section 2.1, ICON only covers two LSTs each day which prohibits the reliable extraction of tidal variability on a daily or quasi-daily basis. Cullens et al. (2020) showed that at least 35 days of data have to be combined into a composite day to obtain LST coverage sufficient for tidal diagnostics at all latitudes observed by MIGHTI (~10°S to ~40°N). Similar considerations can be made for ICON IVM. The tidal diagnostics of the composite data is further explained in Forbes et al. (2022) and Gasperini et al. (2022) and follows a similar procedure as that adopted by Gasperini et al. (2015, 2017, 2020) in the analyses of GOCE and CHAMP tidal winds and densities.

Only data collected during the period between 1 January 2020 and 23 March 2022 were used in this study. This period was selected because it occurs near solar minimum and is and generally geomagnetic-quiescent. The daily Kp index reaches Kp ≥ 6 (Kp ≥ 5) only on 4 (17) out of the 813 days examined. Data collected during days with Kp > 5 are excluded from the analysis. Note that during the period under investigation, ~25.3% of days have Kp>3, ~8.7% of days have Kp>4, ~2.1% of days have Kp>5, and ~0.5% of days have Kp>6. It is pertinent to note that recent investigations (e.g., Cai et al., 2020; 2021) elucidate that even modest levels of geomagnetic activity (Kp<3) have the potential to generate large IT perturbations, which can penetrate the equatorial regions. Nonetheless, the low-latitude protracted oscillations in IT parameters investigated in this study and the composite 40-day moving means involved in the tidal fitting, are likely to significantly reduce any impact from any underlying fluctuations in geomagnetic activity. The effect of solar and geomagnetic preconditioning in IT coupling via global-scale waves is an important topic of research that will be investigated further in future work.

The green-line winds are given every ~2.5 km for the height range ~91–112 km, while the red-line winds are given every ~10 km between ~203–301 km. Diurnal tidal fits are performed using 40-day moving windows on winds averaged in 6° latitude, 40° longitude, and 2-h UT bins extending from 10°S to 40°N using the native ~2.5 km (green-line) and ~10 km (red-line) altitude sampling. To determine the spatiotemporal evolution of the waves, a linear 2-dimensional least squares fit is performed to waves propagating in time and longitudes. A moving window of 40 days is chosen instead of 35 days to alleviate negative effects associated with the occurrence of occasional gaps, data quality issues, and instrument calibrations. As noted by Forbes et al. (2022), this binning effectively removes the effects of small-scale variations and improves the statistics while also leading to smoother visual depictions. The fits are performed for diurnal (24-h period), semidiurnal (12-h period), terdiurnal (8-h period), and quarterdiurnal (6-h period) tides with zonal wave numbers s = ±4. Note that quarterdiurnal tides were recently demonstrated to play a non-negligible role in the lower thermosphere (Pancheva and mukhtarov, 2023). The primary reason for using the same averaging window for both greenline and redline wind data, despite the different dynamic and electrodynamic processes at play, is consistency in the wave retrieval at the two altitudes, including averaging nearly identical local times, which is a preferred condition for comparing tidal winds between these two different altitude regions. The fitting method allows for robustness in the statistics as the 40-day wave fits are assumed to be valid only when at least 35 days of data are available.

For ICON MIGHTI, only the data that are flagged as 'Good' or (Wind Quality = 1) and 'Caution' (Wind Quality = 0.5) are used. This data quality selection criterion largely eliminates observations near the South Atlantic Anomaly (SAA) where the retrieval of wind velocities is difficult due to increased radiation, observations with small airglow signals, and observations from the day-night terminators where mode changes of the instrument take place. Their removal primarily eliminates data near 270°–330° longitude in the Southern Hemisphere, which are away from the primary latitude regions of interest for the wind results contained in this study (i.e., 0°–40°N). Occasional data gaps in the V05 MIGHTI winds are largely removed by the 40-day averaging. Data gaps may be a source of uncertainty in the retrieval of wave amplitudes due to incomplete local time sampling, especially during more extensive data gaps in mid-2021. Future data releases that improve coverage are expected to alleviate any potential detrimental effects of missing data. For ICON IVM, the 'RPA' and 'DM' flags are less than 1 when the data is of the highest quality and greater than 1 when it should be used with caution or rejected (see the data product documentation in the University of California at Berkely (UCB) ICON's public FTP site provided in the Data Availability Statement for further details). This data quality selection criterion (flags <1) is adopted for ICON IVM.

The tidal nomenclature used here is standard (e.g., Hagan et al., 1995; Hagan and Forbes, 2002): DWs or DEs is a westward or eastward propagating diurnal tide, respectively, with zonal wavenumber s. For semidiurnal tides, D is replaced by S. D0 is the zonally symmetric diurnal tide, while S0 is the zonally symmetric

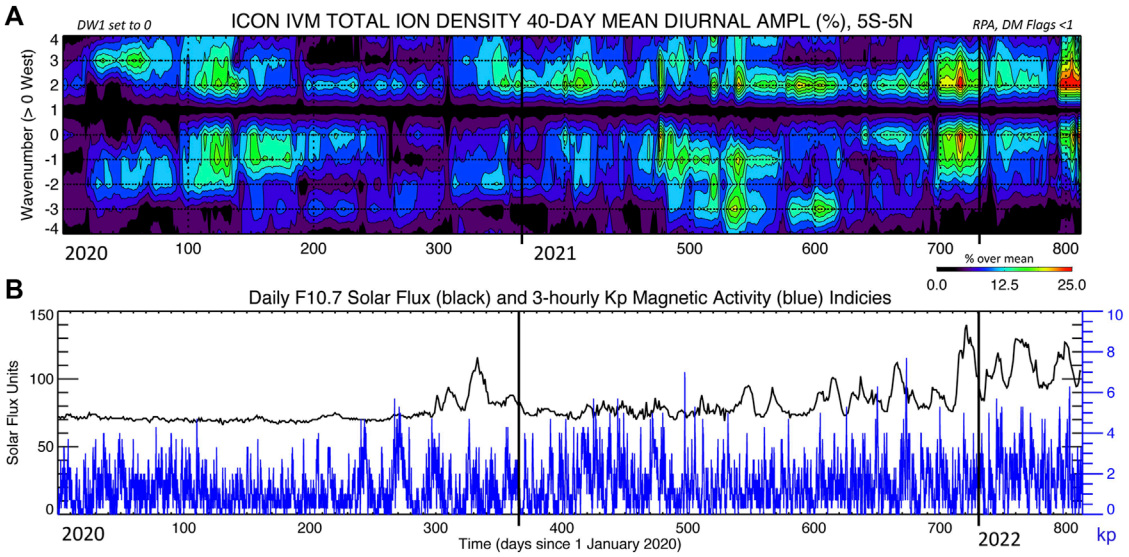

FIGURE 1
(A) Diurnal spectrum of ICON IVM total ion density (i.e., Ne, electron density) during 1 January 2020–23 March 2022 near the geomagnetic equator (±5° MLAT) near 590 km showing zonal wavenumbers 's' (positive for westward propagation) within ±4. The spectrum is obtained by applying 2-dimensional spectral fitting on 40-day moving windows and including only data with RPA and DM flags <1 occurring on 3-hourly intervals with kp < 6. DW1 is set to 0. The amplitudes are shown as percentage variations with respect to the zonal mean. Contours are shown from 0% to 25% in 2.5% intervals. **(B)** Time series of the daily F10.7 solar radio flux (black line) and 3-hourly kp geomagnetic (blue line) indices.

semidiurnal tide. Stationary PWs with zonal wavenumber m are denoted 'SPWm'.

3 Results and discussion

Figure 1A shows the diurnal non-migrating tidal spectrum of ICON IVM Ne near the geomagnetic equator (±5° MLAT) and 590 km altitude covering zonal wavenumbers s = ±4 and extending from 1 January 2020 to 23 March 2022 (days 1–813). The strong day-night Ne difference 'aliased' into DW1 is removed to highlight non-migrating diurnal tidal variability. The tidal variations are shown as percentages relative to the zonal mean. The time series of the solar (daily F10.7 solar radio flux) and geomagnetic (3-hourly kp) indices is shown in Figure 1B. This ~2-year period is characterized by solar flux that increases from about 70 SFU in early 2020 to about 100–130 SFU in early 2022, and by geomagnetic activity that is generally below kp = 6. For the period examined, the daily Kp index exceeded Kp = 5 (Kp = 6) during 17 (4) days. The 17 days with Kp>5 were excluded from the analysis. Only 3 days or less occurred in the same 40-day windows, thus their removal generated no significant gaps in the analysis. This method assumes that any deviations related to enhanced geomagnetic activity are averaged out. It is important to keep in mind that due to the 40-day averaging required to derive the full zonal wavenumber tidal spectrum from ICON observations, day-to-day tidal variability is largely absent in the tidal spectra herein presented. Moreover, tidal amplitudes are likely to appear reduced due to the 40-day averaging (see, e.g., related discussions in Forbes et al. (2017); Hausler et al. (2014)).

Strong Ne variability associated with DE3 is observed around days 510–630 (i.e., June-September 2021), with amplitudes upward of 20%. Smaller (~10%–15%) DE3 Ne variability is observed around days 150–280 (i.e., June-September 2020) in agreement with the well-known seasonal and inter-annual variations in the thermospheric DE3. Large D0 and DW2 Ne variability, exceeding 20% is several occasions, is observed throughout the ~820 days displayed. A close relationship between the temporal variations of D0 and DW2 Ne variations can be seen by a close inspection of Figure 1A. Larger D0 and DW2 can be seen during days 700–820 corresponding to increased solar flux in early 2022. Note also some remarkable correspondence between prominent quasi-27-day solar rotation variations in flux (see the black curve in Figure 1B) and D0 and DW2 Ne variability, further suggesting a connection to solar forcing for these tidal components that will be discussed in further detail below. Shown in Figure 1A are also large (up to 15%–20%) DE1 Ne amplitudes around days ~100–200 and ~460–580 and occasionally enhanced DE2 and DW3 (e.g., days ~20–80) Ne amplitudes.

Next, we examine the concurrent diurnal non-migrating tidal spectrum from ICON MIGHTI zonal winds in the lower (i.e., ~105 km) and middle (i.e., ~220 km) thermosphere near the geographic equator and at 10°N-20°N geographic latitude (GLAT), as shown in Figure 2. The lower thermospheric diurnal non-migrating tidal spectrum is dominated by DE3 with amplitude variations upward of 25 m/s during days 180–320 and 540–690 corresponding to early July through mid-November 2020 and 2021, respectively. In the middle thermosphere, DE3 still retains significant amplitudes up to around 15 m/s in agreement with the vertical propagation of this wave component to higher thermospheric altitudes. For both altitudes shown in Figure 2, DE3 attains the largest amplitudes near the geographic equator in accordance with the Kelvin wave equatorially-trapped nature of

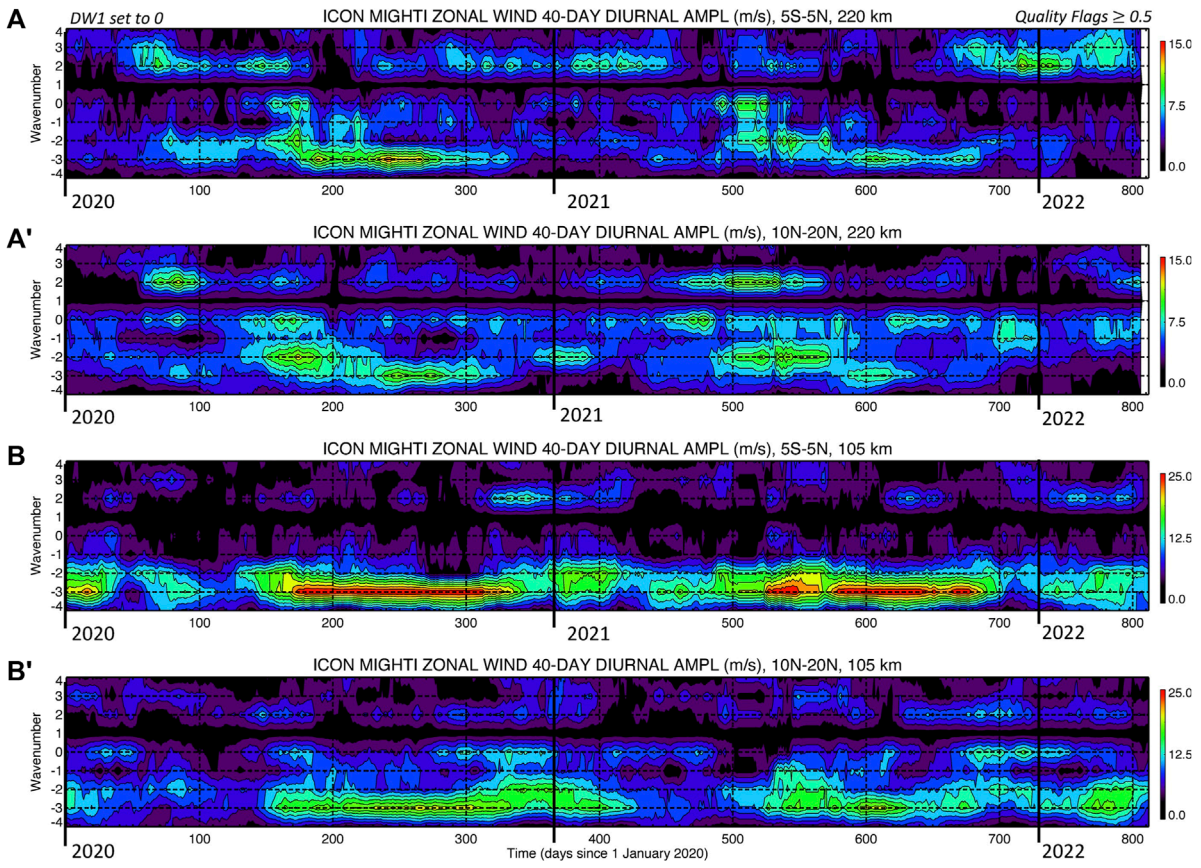

FIGURE 2
(A-A′) Diurnal non-migrating tidal spectrum (s ± 4, positive to the west) of ICON MIGHTI red-line middle thermospheric (~220 km) zonal winds during 1 January 2020–23 March 2022 near the geographic equator (±5° GLAT) and between 10°N and 20°N GLAT, respectively. **(B-B′)** same as **(A-A′)** but in the lower thermosphere near 105 km. The wind tidal amplitudes are shown as m/s, with maxima set to 15 m/s near 220 km and 25 m/s near 105 km. Different color scale ranges are chosen for the lower and middle thermospheric wind spectra to facilitate visual representation. Contours at ~220 km (~105 km) are shown from 0 m/s to 15 m/s (25 m/s) in ~1.7 m/s (~2.8 m/s) intervals. Quality flags ≥0.5 are adopted. As for Figure 1, the tidal spectrum is obtained by applying 2-dimensional spectral fitting on 40-day moving windows, and DW1 is set equal to 0.

the dominant thermospheric Hough mode of DE3 with a vertical wavelength of about 56 km (e.g., Gasperini et al., 2015; 2017). Remarkable correspondence is also found between the seasonal variations in the thermospheric zonal wind DE3 and the ionospheric Ne DE3 concurrently measured by ICON IVM and shown in Figure 1A. Given the significantly larger DE3 amplitudes observed in the lower thermosphere, the primary coupling process is likely to be associated with the E-region dynamo. Nonetheless, direct propagation to the middle thermosphere is also likely to constitute a non-negligible source of ionospheric DE3 (e.g., Gasperini et al., 2021). More work needed to be done to understand possible ion-neutral coupling effects in the zonal wind DE3 near 220 km due to the component of DE3 associated with E-region dynamo processes.

Hagan and Forbes (2002) demonstrated that DE3 and DE2 are mostly forced by latent heat release in persistent large-scale tropical rainfall systems and provide a direct coupling mechanism between tropospheric weather and upper thermospheric variability via upward propagation. These and other nonmigrating tides were also shown to induce a significant longitudinal and local time variation in the low-latitude F-region plasma, as discovered by Sagawa et al. (2005) and Immel et al. (2006), and more recently shown by Gasperini et al. (2021) using concurrent ICON, SORTIE, and TIMED satellite data, along with SD/WACCM-X modeling. An important neutral-plasma coupling process is the longitudinal modulation of E-region dynamo electric fields by nonmigrating zonal wind tides (Hagan et al., 2007; Jin et al., 2008) although F-region meridional tidal winds and thermospheric tidal O/N2 variations also play an important role (England et al., 2010).

Figure 2 also shows large zonal wind DW2, DE2, and D0 amplitudes with maxima near 15–20 m/s and larger amplitudes generally occurring in the middle thermosphere. Closer comparisons between Figures 2A,B near the equator and between Figure 2A′ and Figure 2B′ near 10°N-20°N GLAT reveal that significant middle thermospheric variability associated with DW2, DE2, and D0 is not traceable to lower thermospheric variability. This result is a strong indication of *in situ* generation in the thermosphere for these wave components. As hypothesized by Oberheide et al. (2011) and later demonstrated by Jones et al. (2013) using Thermosphere-Ionosphere-Mesosphere-Electrodynamics General Circulation Model (TIME-GCM) simulations, D0 and

DW2 can originate via nonlinear interaction between the *in-situ* EUV-generated DW1 and the stationary planetary wave with s = 1 (SPW1) resulting from the geographic and geomagnetic field offset driven by plasma-neutral interactions. Similar D0 and DW2 variability is also observed in Ne measured *in situ* by ICON IVM near 590 km (see Figure 1A). Using TIME-GCM, Jones et al. (2013) distinguished between diurnal and semidiurnal migrating and non-migrating tidal components generated locally in the thermosphere from those that originate in the troposphere. They found that at low and middle latitudes both migrating and nonmigrating tides can be generated *in situ* through ion-neutral interactions due to the longitude-dependent ionosphere imposed by the realistic magnetic field configuration. Specifically, Jones et al. (2013) found that during solar maximum, non-migrating diurnal and semidiurnal tides forced by ion-neutral interactions are responsible for the majority of the longitude-dependent tidal structure seen in the low and middle latitude upper thermosphere, with D0 and DW2 arising from hydromagnetic coupling between SPW1 (i.e., modified ionosphere) and DW1 (i.e., idealized wind circulation) that can reach amplitudes of up to 20 m/s near 500 km. More discussion on this important finding and discrepancies with the modeling results by Jones et al. (2013) is provided in the later part of this study.

Note that the geographic coordinate system is the more natural and effective frame for diagnosing the origins of tidal dynamics. Therefore, in the present study, zonal winds near 105 km (typically corresponding to the peak height of the Hall conductivity) and 220 km are ordered in geographic coordinates to diagnose the lower-to-middle thermospheric connection. This allows us to understand what component of the thermospheric DE3 can propagate to the middle thermosphere. A geomagnetic reference frame may be appropriate to study connections between the middle thermospheric wave amplitudes and those observed in the topside F-region ionosphere. A geomagnetic frame will certainly generate some distortions in the structures. This is due to the way that a wind field ordered in geographic coordinates interacts with a magnetic field whose inclination, declination, and magnitude vary with longitude (see, e.g., Maute et al., 2012; Forbes et al., 2021b). However, magnetic coordinates are most appropriate for diagnosing global-scale waves in ionospheric parameters, as shown in many IT wave coupling studies (e.g., see references in Forbes et al., 2021b). A geomagnetic reference frame may be appropriate to study connections to the topside ionosphere DE3, however, the distortions in the structures due to the way that a wind field ordered in geographic coordinates interacts with a magnetic field whose

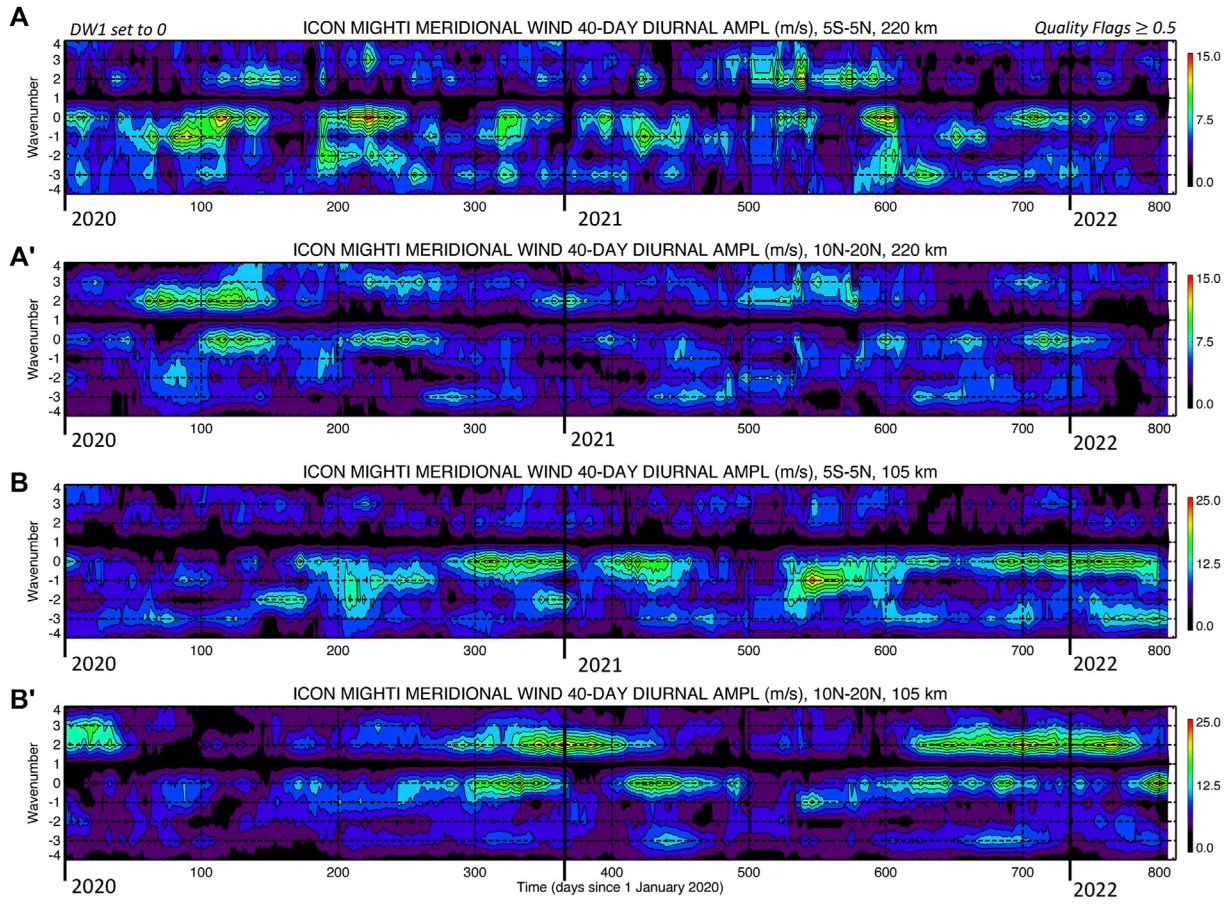

FIGURE 3
Same as Figure 2 **(A–B′)** but for ICON MIGHTI meridional winds. As for Figure 2, contours at ~220 km (~105 km) are shown from 0 m/s to 15 m/s (25 m/s) in ~1.7 m/s (~2.8 m/s) intervals.

inclination, declination, and magnitude vary with longitude are not the primary focus of this study and will be subject of follow-on work.

We now turn our attention to the diurnal non-migrating tidal spectrum in meridional winds measured by ICON MIGHTI. Figure 3 shows the same spectral depictions of MIGHTI winds as Figure 2 but for the meridional wind component. Clearly, the spectra are dominated by D0 and DW2 variability in both the lower and middle thermosphere with meridional wind amplitudes exceeding 20 m/s on several occasions. In the lower thermosphere (i.e., ~105 km), particularly striking are the DW2 variations around days 255–415 (i.e., mid-September 2020—mid-February 2021) and 620–780 (i.e., mid-September 2021 - mid-Feruary 2022) and 10°N-20°N GLAT and D0 variations around days 255–450 (i.e., mid-September 2020 - late-March 2021) and 520–780 (i.e., early-June 2021 - mid-February 2022) near the geographic equator and 10°N-20°N GLAT. In the middle thermosphere (i.e., ~220 km), significant D0 and DW2 variations are observed throughout 2020–2022 with amplitude maxima near 15 m/s a little correspondence with the lower thermospheric D0 and DW2. This finding suggests, similar to what was discussed in the context of Figure 2, that these wave components are likely to be generated *in situ* likely from the nonlinear interaction between *in-situ* EUV-generated DW1 and the SPW1. More discussion on this topic is provided below.

Next, we compare the ionospheric diurnal tidal spectrum observed at two different ionospheric heights to investigate the persistence of certain features through different altitude regions in the topside F-region ionosphere. For this purpose, we compare tidal results from concurrent IVM measurements onboard the SORTIE CubeSat near 420 km and ICON near 590 km. Due to their different altitudes, SORTIE IVM observes an O + -dominated ionosphere while ICON IVM samples nonnegligible H+ (especially during nighttime). Thus, to best interpret the ionospheric tidal signatures observed concurrently by ICON and SORTIE, Figure 4 compares ICON O+ density with SORTIE total ion density (i.e., Ne). Gasperini et al. (2021) already demonstrated a strong correlation between the WN4 structure seen in SORTIE Ne and ICON O+ density during May 2020, with Pearson correlation coefficients as high as 0.87.

Figure 4A, A′ show the diurnal nonmigrating tidal spectrum as a function of time near the geomagnetic equator (5°S-5°N MLAT) of ICON IVM O+ density and SORTIE IVM Ne, respectively. For SORTIE, IVM data is sufficiently continuous to allow 40-day

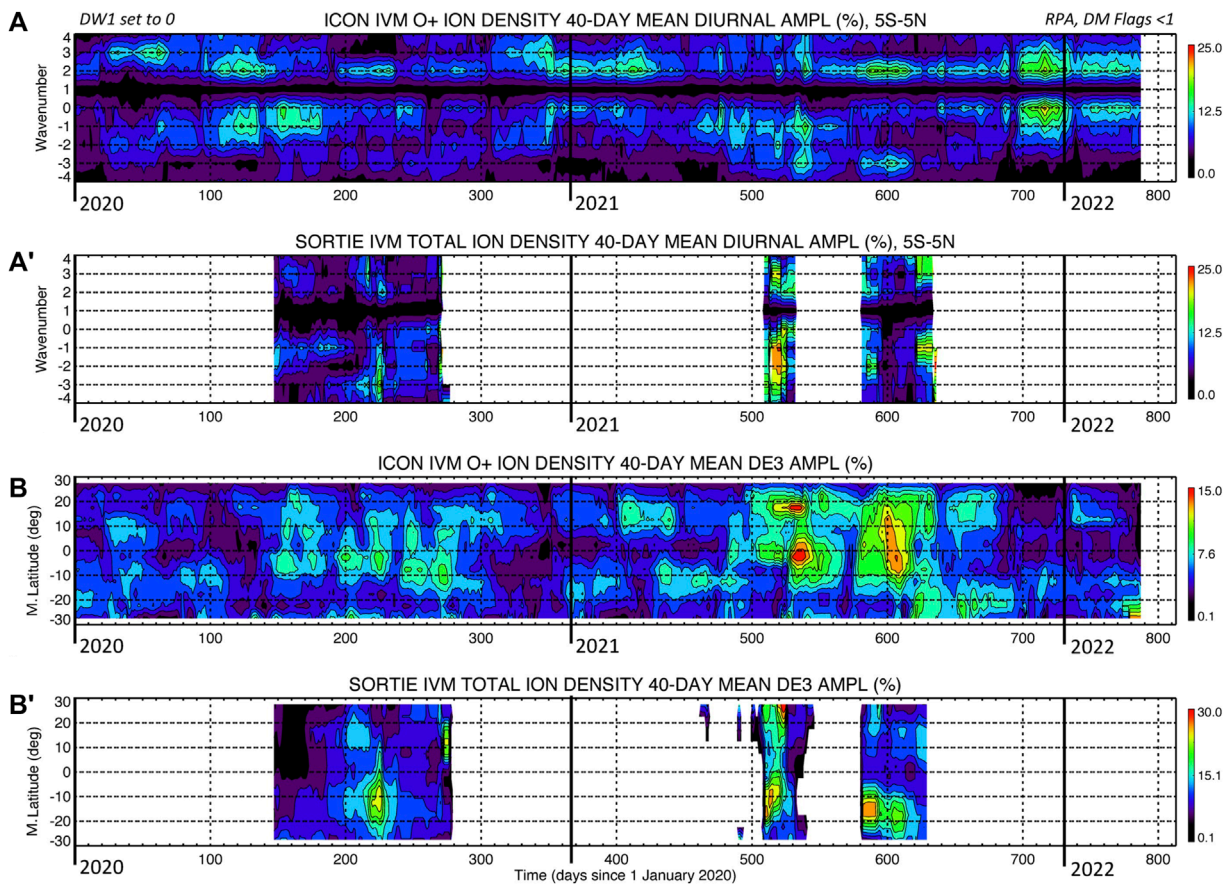

FIGURE 4
(A-A′) Wavenumber-DOY diurnal spectrum of O^+ ion density near the geomagnetic equator (5°S-5°N MLAT) from ICON IVM near 590 km and SORTIE IVM near 420 km, respectively. **(B-B′)** MLAT-DOY depiction of ICON IVM and SORTIE IVM DE3 O^+ amplitudes. The amplitudes (shown as percentages over the zonal mean) are obtained by applying 2-dimensional spectral fitting on 40-day moving windows. Note the different color scales for SORTIE and ICON DE3. SORTIE (ICON) DE3 maxima near 30% (15%). Contours for ICON (SORTIE) are shown from 0% to 15% (25%) in 1.5% (2.5%) intervals.

spectral fitting during the two periods: 27 May 2020–8 October 2020 (i.e., days 148–282) and 8 April 2021–21 October 2021 (i.e., days 464–660). Comparisons between the diurnal spectra of ICON IVM Ne near 590 km and SORTIE IVM Ne near 420 km suggest the presence of similar wave components, with large DE3, D0, DE2, and DW2 (note that the enhancements are not concurrent for all times and wave components). Near the geomagnetic equator, Ne tidal amplitudes near 420 km are about 40% larger than those observed near 590 km (note the different color scales between Figures 4A,B). This result is evidence that the prominent D0 and DW2 Ne variations previously discussed are not isolated to 590 km but are a common feature throughout the topside ionosphere.

Further, Figure 4B, B′ elucidate the MLAT-temporal structure of DE3 amplitudes (as percentages over the zonal mean) of ICON O+ density and SORTIE Ne, respectively. Effects from the equatorial ionization anomaly (EIA) in DE3 appear evident at both altitudes, although at ~420 km the peaks occur near ±20° MLAT while at ~590 km the peaks are near ±10° MLAT. This effect is likely due to SORTIE's lower mean altitude in accordance with the well-known ionospheric fountain effect (e.g., Andrews et al., 1987). Important equatorial asymmetries exist in DE3 Ne amplitudes near 420 km that are not as clearly present near 590 km.

We now focus on the latitudinal-temporal amplitude structure of a few dominant wave components in the lower and middle thermospheric and topside ionospheric diurnal spectra, specifically DW1, SPW1, D0, and DW2 as shown in Figure 5. Prominent variability in the nonmigrating tidal components is observed in both lower and middle thermospheric zonal winds with amplitudes up to ~18 m/s. The lower thermospheric DW1 shows little resemblance with the middle thermospheric DW1, as expected since the latter is largely driven *in situ* in the thermosphere by the absorption of solar EUV radiation. The DW1 Ne appears to be rather equatorially symmetric and shows a closer association with the middle thermospheric DW1 than the lower thermospheric DW1. A closer inspection of Figure 5 reveals strong similarities in the timing and latitude structure of the middle thermospheric zonal wind SPW1 and D0 (particularly in the northern hemisphere around days 150–220 and 480–610), and some correspondence with DW1 and DW2. Similar considerations can be made for the latitudinal-temporal of these 4 wave components in Ne. A more detailed discussion on DW2 and D0 is provided below in the context of previous studies and CTMT results.

Next, we investigate diurnal tidal variability in the zonal winds from the CTMT model. The focus is on latitude-temporal and altitude-temporal structures and comparisons with those observed by MIGHTI. As already discussed in Section 2.2, tidal forcing occurring *in situ* in the thermosphere is not accounted for in CTMT. In other words, CTMT is not capable of reproducing in-situ-forced migrating tides resulting from EUV forcing (e.g., the middle thermospheric DW1), and in-situ-forced nonmigrating tides in the middle thermosphere due to nonlinear interactions, most notably the diurnal nonmigrating tidal components DW2 and D0. For context, Table 1 contains information on the peak height, peak latitudes, and vertical wavelengths for zonal wind HME1 and HME2 for DW2, DW1, D0, DE1, DE2, and DE3 that are at the basis of CTMT. Also included in Table 1 are HME1 and

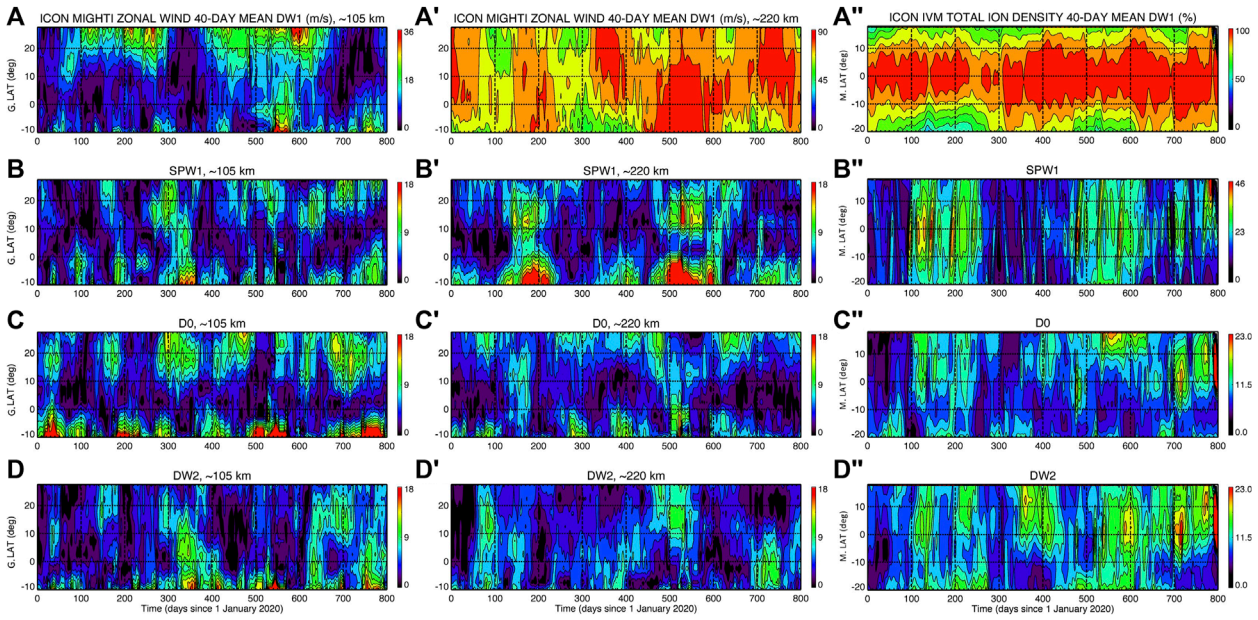

FIGURE 5
Geographic latitude (GLAT) *versus* DOY structure of ICON MIGHTI zonal wind DW1 **(A)**, SPW1 **(B)**, D0 **(C)**, and DW2 **(D)** amplitudes in the lower thermosphere near 105 km. **(A″–D″)** Same as **(A–D)**, but in the middle thermosphere near 220 km. **(A″–D″)** Same as **(A–D)**, but from ICON IVM Ne near 590 km. All the spectra are obtained by least squares fitting data in 40-day moving windows. Contours for DW1 at ~105 km, ~220 km, and ~590 km are shown up from 0 m/s/% to 36 m/s, 90 m/s, and 100% in ~3.2 m/s, ~8.2 m/s, and 9.1% intervals, respectively. Contours for SPW1 at ~105 km, ~220 km, and ~590 km are shown from 0 m/s/% to 18 m/s, 18 m/s, and 46% in ~1.6 m/s, ~1.6 m/s, and 4.2% intervals, respectively. Contours for D0 and DW2 at ~105 km, ~220 km, and ~590 km are shown from 0 m/s or 0% to 18 m/s, 18 m/s, and 23% in ~1.6 m/s, ~1.6 m/s, and 2.1% intervals, respectively.

HME2 of the 3-day UFKW1. HME1 and HME2 correspond to the first symmetric and first antisymmetric Hough modes with symmetric and antisymmetric referring to the relative phasing across the equator. Note that meridional wind HMEs always have the opposite symmetry. As shown in previous studies (e.g., Oberheide and Forbes, 2008; Oberheide et al., 2009; 2011) non-equatorial tidal peaks in the middle/upper thermosphere tend to shift toward higher latitudes due to molecular diffusion. Gasperini et al. (2017) studied the effects of mean winds and dissipation on both DE3 and a 3-day UFKW1 in a general circulation model for solar minimum conditions, reporting that the effects of asymmetric mean winds are to distort the horizontal shapes of these waves and shifting their peaks toward westward wind regimes.

The latitude *versus* month-of-the-year structure of the major (DW2, DW1, D0, DE2, and DE3) diurnal tidal amplitudes from CTMT near 105 km (220 km) altitude in zonal and meridional winds are contained in Figure 6 (Figure 7). While Figure 8 shows the latitude-height structure of the annual-mean diurnal tidal amplitudes also from CTMT. As already discussed by Oberheide et al. (2011) in the context of comparisons between CTMT and neutral density and wind observations from the Challenging Minisatellite Payload (CHAMP) satellite, the presence of strong middle/upper thermospheric DW2 and D0 and their absence in CTMT suggests the presence of additional forcing mechanisms in the thermosphere. For tides, the time constants of eddy and molecular diffusion are proportional to the square of their vertical wavelengths (e.g., Oberheide et al., 2011). As such, the short vertical wavelength characterizing DW2 (~33 km) makes it not capable of effectively propagating into higher thermospheric altitudes. As shown in Table 1, for the zonal winds only the antisymmetric HME (HME2) of D0 has a sufficiently long vertical wavelength (~69 km) to propagate into the thermosphere. Note that for the meridional winds (not shown in Table 1) only the symmetric HME (HME1) of D0 can effectively propagate to the thermosphere. HME2 is responsible for generating prominent antisymmetric signals in the lower (partly shown by Figure 6C) and middle (partly shown in Figure 7C) thermospheric D0 zonal winds, while HME1 is responsible for producing symmetric signals in the lower (Figure 6C′) and middle (Figure 7C′) thermospheric D0 meridional winds. These tidal signatures (and latitude structures)

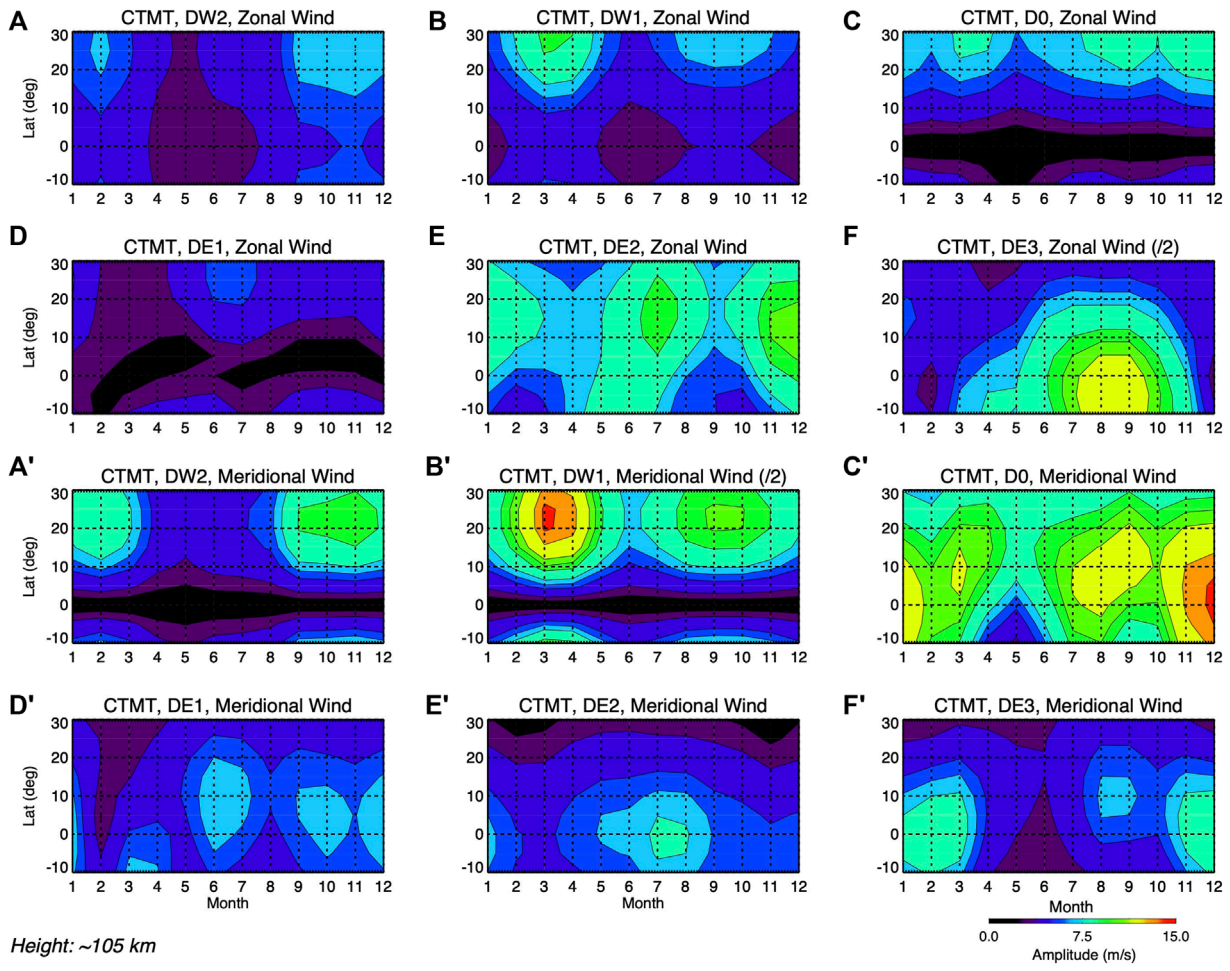

FIGURE 6
Latitude *versus* month zonal wind amplitude structure of DW2 **(A)**, DW1 **(B)**, D0 **(C)**, DE1 **(D)**, DE2 **(E)**, and DE3 **(F)** near 105 km altitude from the Climatological Tidal Model of the Thermosphere (CTMT) model. **(A′–F′)** Same as **(A–F)**, but for the meridional wind component. Contours are shown from 0 m/s to 15 m/s in 1.5 m/s intervals. The zonal (meridional) wind DE3 (DW1) amplitudes are divided in half to facilitate visual representation.

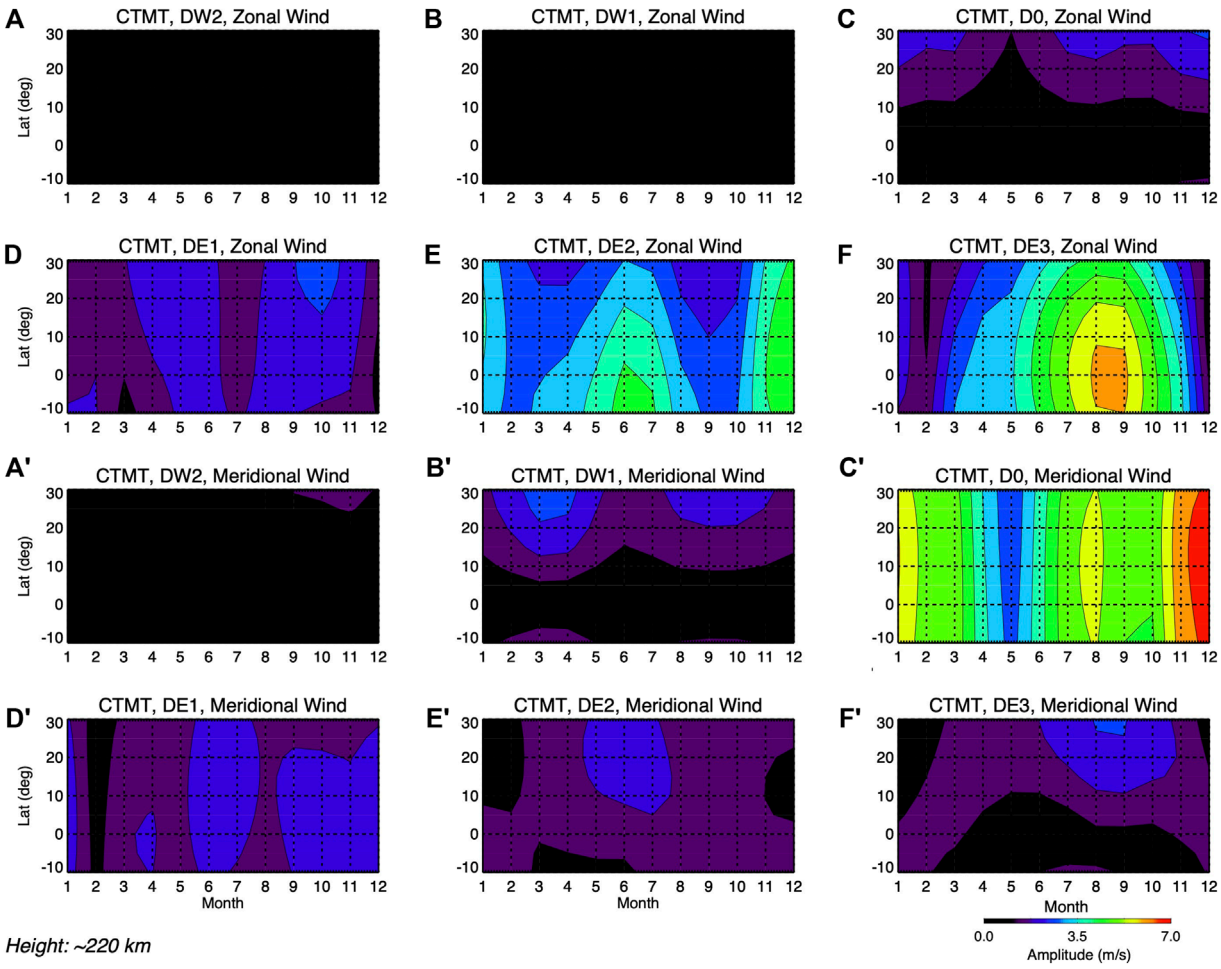

FIGURE 7
Same as Figure 6 **(A–F′)**, but near 220 km altitude. Contours are shown from 0 m/s to 7 m/s in ~0.7 m/s intervals.

in D0 are also found in the MIGHTI observations (Figure 5 for the zonal wind component), although CTMT underestimates the amplitudes by up to ~75% in the middle thermosphere (i.e., near 20 m/s in MIGHTI and near 5 m/s in CTMT, depending on latitude and month of the year) due to lack on *in situ* generation. DW2 meridional and zonal winds are very large below about 100 km (not shown), small near 105 km (Figure 6A, A′, respectively), and nearly absent in the middle thermosphere (Figure 7A, A′, respectively) as the zonal wind component is associated with the first symmetric HME. DW2 zonal wind amplitudes in the lower thermosphere are underestimated by CTMT by up to ~67%(12 m/s *versus* 4 m/s), while the strong (15 m/s) middle thermospheric DW2 observed by MIGHTI is nearly absent in CTMT likely due to *in situ* generation not reproduced by CTMT.

To summarize, diagnostics of MIGHTI red-line winds (Figure 5A′–D′) indicate middle thermospheric diurnal tidal amplitudes exceeding 15 m/s with D0, DW2, and SPW1 often the largest nonmigrating diurnal tides present. This finding, already suggested by Oberheide et al. (2011) and confirmed numerically by Jones et al. (2013), demonstrates that the nonmigrating components DW2 and D0 have an upper thermospheric source. This source is most likely associated with the nonlinear interaction occurring *in situ* in the middle/upper thermosphere of the in-situ-generated DW1 and SPW1, as clearly demonstrated by the close association between the latitude-temporal structure of these 4 wave components (Figure 5). A strong and somewhat prominent finding from Figure 5 that is different than what was modeled by Jones et al. (2013) is the presence of D0 and DW2 with prominent amplitudes even during weak solar flux conditions. Jones et al. (2013) showed that these non-migrating tides were less likely to be strong under solar minimum/maximum conditions, which is not in agreement with the MIGHTI results shown in Figure 5.

The HME2 of DW2 does not play a significant role here since DW2 is fully symmetric below about 100 km altitude. As one can see from Figure 8, the eastward propagating DE2 and DE3 zonal wind tides can propagate directly into the thermosphere without substantial changes to their latitudinal structures as a result of their relatively longer vertical wavelengths (70 km and 56 km, respectively, as shown in Table 1) that correspond to reduced molecular dissipation for their first symmetric modes. In general, the MIGHTI latitude-temporal structures at 220 km are significantly different than those shown by the CTMT. In the case of D0,

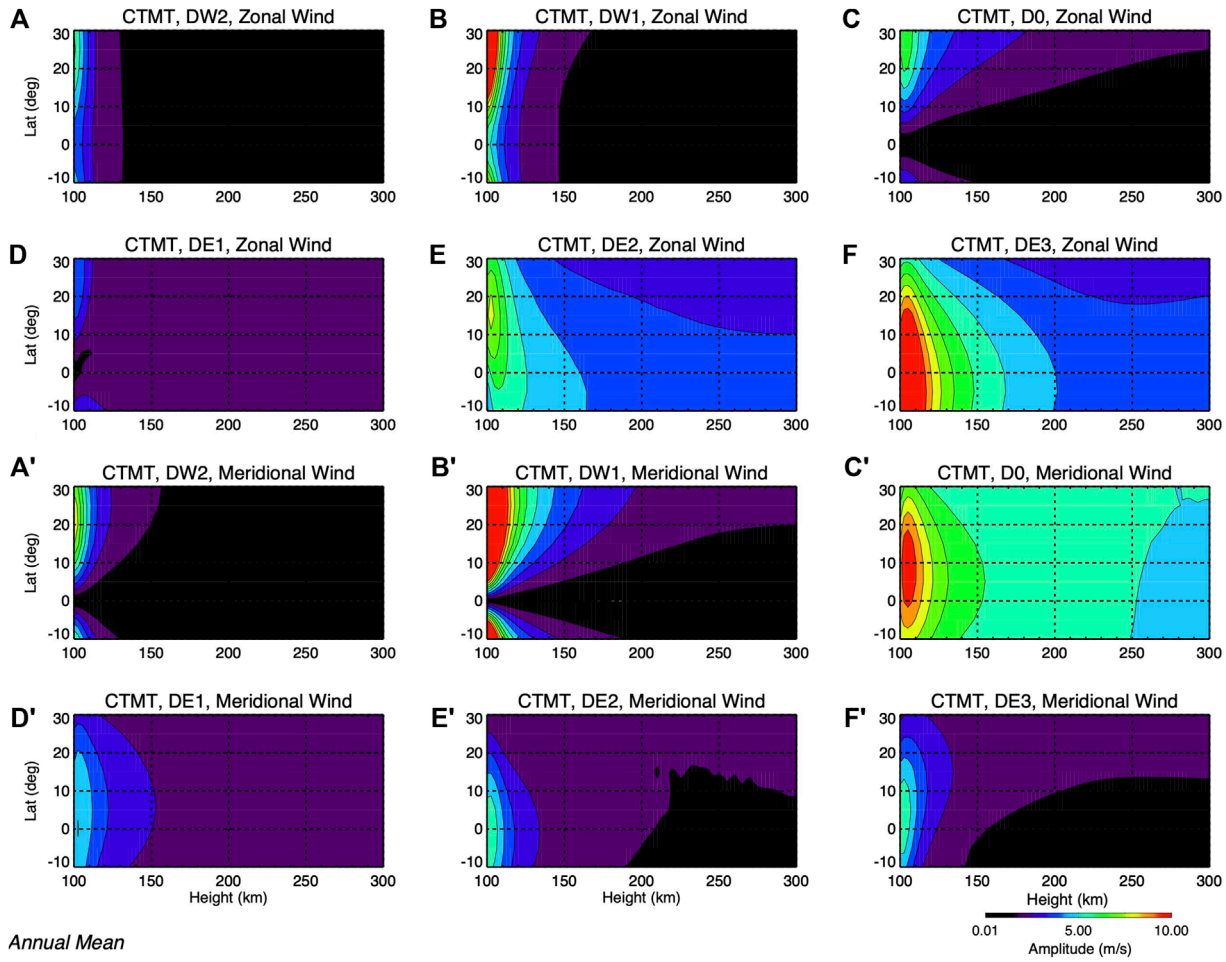

FIGURE 8
Latitude (10°S-40°N, y-axis) *versus* height (100–300 km, x-axis) zonal wind amplitude structure of DW2 **(A)**, DW1 **(B)**, D0 **(C)**, DE1 **(D)**, DE2 **(E)**, and DE3 **(F)** as annual means from the CTMT model. **(A′–F′)** Same as **(A–F)**, but for the meridional wind component. Contours are shown from 0 m/s to 10 m/s in 1 m/s intervals.

TABLE 1 Zonal wind HMEs for diurnal tides and the 3-day UFKW1. '*z*' is the altitude of maximum amplitude, 'λ_z' denotes the vertical wavelength between 90 and 120 km for F10.7 = 125, while 'lat_z' the latitudes of zonal wind peaks at '*z*'.

	HME1		HME2	
Component	$z(km)/\lambda_z(km)$	$lat_z(°)$	$z(km)/\lambda_z(km)$	$lat_z(°)$
DW2	94/33	±24	*unstable*	—
DW1	93/35	±30	*unstable*	—
D0	94/32	±30	105/69	±30
DE1	164/149	0	101/45	±24
DE2	105/70	0	101/35	±24
DE3	106/56	0	102/30	±18
UFKW1 (3d)	110/51	0	101/7	±15

DW1, and DW2 this is due to the presence of in situ-generated components in the MIGHTI tides which are not included in the CTMT. Comparisons between MIGHTI and CTMT diurnal tides reveal discrepancies connected with differences in tides with longer vertical wavelengths that are more capable of propagating from ~105 km to ~220 km. Lower (middle) thermospheric zonal wind DE3 amplitudes from CTMT maximizing near 15 m/s (~7 m/s) are largely underestimated (by about 50%) compared to those observed by MIGHTI with maxima near 30 ~ m/s (~15 m/s). Note that the MIGHTI-observed DE3 zonal wind amplitudes are generally consistent with previous observations (e.g., Gasperini et al., 2015; 2018; 2021). Some model-data differences not ascribed to *in situ* generation in the thermosphere may be ascribed to lower solar flux in the observations (70–100 SFU for MIGHTI *versus* ~110 SFU for CTMT) that favors wave propagation to the middle thermosphere and by the well-known inter-annual variability in the waves (note that CTMT is a 'climatology' of the tidal spectrum obtained combining over 6 years of TIMED data).

Seminal theoretical studies (e.g., Lindzen, 1967; Lindzen and Hong, 1974; Volland, 1974; Volland and Mayr, 1977; Forbes and Garrett, 1979; Forbes and Hagan, 1988; Forbes and Vincent, 1989) reported on some basic characteristics of waves propagating into the thermosphere, where the dissipative time scales increase roughly as

the inverse of density. Entering the thermosphere, tidal amplitudes generally increase up to a region where dissipation is important and then (case 1) asymptotically approach constant values (with no significant decrease in amplitude with increasing altitude), or can increase up to a region where dissipation is important but then (case 2) decrease considerably before asymptotically reaching a constant value. In previous work, Gasperini et al. (2017) examined the vertical propagation of DE3 (and UFKW1) to the thermosphere using TIME-GCM with the lower boundary based on Modern-Era Retrospective analysis for Research and Applications (MERRA) reanalysis data. This study found that (a) the effect of molecular dissipation is to broaden the latitudinal structures in accord with prior theoretical predictions and satellite observations (e.g., Gasperini et al., 2015); (b) the main effect of background zonal mean winds is to distort the height-latitude structures; (c) the altitude where upward propagating waves maximize is related to the ratio between the timescale for dissipation and the wave's Doppler-shifted frequency.

Figure 9 contains the vertical structure of CTMT equatorial DE3 zonal wind amplitudes (panel a) and phases (panel b) during September, which shows a behavior largely consistent with a significant reduction in wave amplitudes in the thermosphere. As previously noted, careful analysis of the observational results contained in Figure 2 reveals DE3 zonal wind amplitudes that are reduced by about 50% near 220 km compared to ~105 km. This result suggests that the MIGHTI-observed DE3 in the middle thermosphere is undergoing dissipation more closely resembling case (2). It is important to note that while the DE3 may still have appreciable amplitudes near 220 km, there is likely only some small phase progression with altitude, i.e., dissipative effects have made its vertical wavelength extremely long. As such, one may argue that the DE3 is no longer propagating vertically.

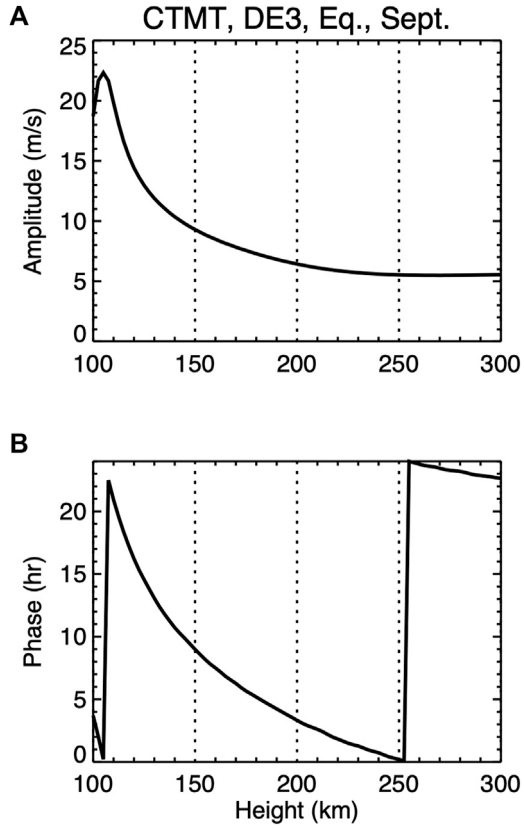

FIGURE 9
Vertical structure (100–300 km, x-axis) of CTMT equatorial DE3 zonal wind amplitudes **(A)** and phases **(B)** during September.

Finally, we examine the global-scale wave spectrum extending from 0.5 days to 7 days as revealed by 2-dimensional least-squares fitting of remotely-sensed MIGHTI lower (i.e., 105 km) and middle (i.e., 220 km) thermospheric zonal winds and we compare it with the one inferred by in-situ-measured IVM Ne near 590 km. These spectral results near the equator (10°S-10°N GLAT for the winds and 10°S-10°N MLAT for Ne) that combine over 800 days of data are shown in Figures 10A–C, respectively. The migrating tides are set to 0 to facilitate visual representation. The dominant diurnal tidal periodicities present near 105 km are DE3, DE2, D0, and DW2 (already extensively discussed in Figures 2, 5).

Figure 10A reveals the existence of a prominent and persistent ~3-day UFKW1 in the lower thermosphere, with ~2-year mean amplitudes near 10 m/s. UFKWs constitute the subset of Kelvin waves with faster horizontal phase speeds (~150 m/s) enabling their propagation to MLT heights and above (e.g., Salby et al., 1984; Forbes, 2000; Gu et al., 2014; Gasperini et al., 2015; 2018; Forbes et al., 2020). In the MLT the most frequent and longest-lasting UFKW events have s = −1 and ~2–4-day periods. UFKWs can effectively drive F-region ionospheric variability (Liu et al., 2013; 2015; Gu et al., 2014; Abdu et al., 2015) primarily through the E-region dynamo processes (e.g., Chang et al., 2010) but also *in situ* via F-region winds and field-aligned drifts (e.g., Forbes et al., 2020).

The lower thermospheric zonal wind wave spectrum in Figure 10A also demonstrates a strong s = +1 ~6-day variation associated with the westward quasi-6-day planetary wave with zonal wavenumber 1 (Q6DW). The Q6DW is a prominent and recurrent planetary wave in the MLT region (e.g., Talaat et al., 2002; 2001; Lieberman et al., 2003; Riggin et al., 2006; Forbes and Zhang, 2017). A number of recent studies demonstrated impacts on F-region ionospheric variability from Q6DWs (Gan et al., 2016; 2017; Gu et al., 2014b; 2018a; b; Qin et al., 2019; Yamazaki, 2018). As noted by Forbes et al. (2020c), changes in F-region electron densities at Q6DW periods result from transport by ExB drifts, where the electric field E is generated in the ionospheric E-region through dynamo action of Q6DW winds and possibly Q6DW modulation of tides and/or gravity waves. The spatial structure of Q6DW in the MLT region is highly consistent with the theoretical Rossby (1, 1) normal mode (Talaat et al., 2001), with Q6DW amplitudes in the zonal wind maximizing around the equator (e.g., Qin et al., 2019; 2021; Forbes et al., 2020c).

Spectral analyses of MIGHTI middle thermospheric winds indicate significantly reduced amplitudes (by ~50%–80%) for both the UFKW1 and Q6DW near 220 km (see Figure 10B″ for UFKW1). This result suggests that both these wave components undergo strong dissipation in their propagation between ~105 km and ~220 km. It is important to realize that the wave spectra in Figures 10A–C are averages of over 2 years of MIGHTI and IVM observations. However, previous modeling and observational evidence indicate that thermospheric UFKW and Q6DW occur mainly in limited events lasting from about 10 days to 30 days.

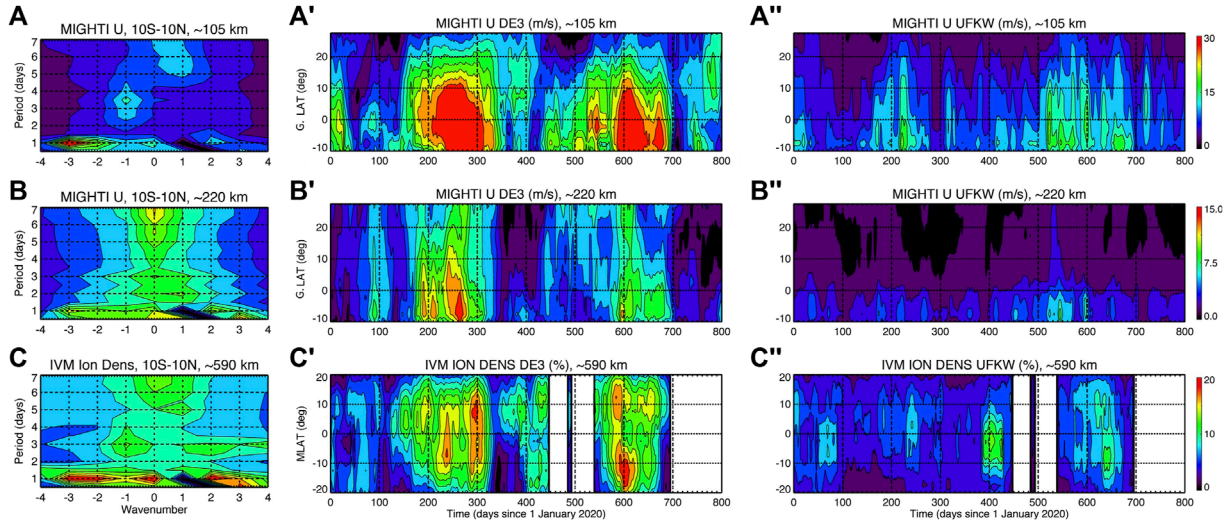

FIGURE 10
(A) Period-wavenumber spectrum of ICON MIGHTI green-line zonal winds near the geographic equator (10°S-10°N GLAT) and 105 km altitude, obtained by combining all data from 1 January 2020 through 23 March 2022. The migrating DW1 and SW2 tidal amplitudes are set to 0. **(A′)** GLAT-DOY amplitude structure of DE3 zonal winds near 105 km. **(A′′)** GLAT-DOY amplitude structure of UFKW1 zonal winds near 105 km. **(B–B″)** Same as **(A–A″)**, but for ICON MIGHTI red-line zonal winds near 220 km. **(C–C″)** Same as **(A–A″)**, but for ICON IVM Ne near 590 km. Contours are shown from 0 m/s or 0% to 30 m/s, 15 m/s, 20% in 3 m/s, 1.5 m/s, and 2% intervals at ~105 km, ~220 km, and ~590 km, respectively.

Hence, the UFKW1 and Q6DW amplitudes in Figures 10A–C are likely to be significantly suppressed by the averaging involved.

Closer examination of the middle thermospheric wave spectrum reveals dominant s = 0 variations with periods of 12 h (i.e., S0, as recently shown by Forbes et al., 2022), 1-day (i.e., D0, previously discussed), and 7 days; and other notable s = 0 variations near 2 and 3 days. Remarkably, along with the expected strong DE3, DE2, D0, and DW2 variations, the Ne wave spectrum (Figure 10C) shows prominent variability near 3 days and s = −1 associated with the lower thermospheric UFKW1 and near 6 days and s = +1 associated with the Q6DW (Figure 10A). Figure 10C also shows strong SW3 variability (similar to that discussed by Forbes et al., 2022), westward propagating 3-day variations, and prominent s = 0 variability near 7 days that closely resembles the variability in zonal winds near 220 km (Figure 10B). These latter two variations have not been reported before in ICON data and will be the subject of future work. Comparison between Figures 10A–C, allowed by contemporaneous MIGHTI and IVM observations, demonstrates how the short-term large-scale variability of ionospheric density is mostly driven by lower and middle thermospheric waves, at least at low latitudes for low solar activity and relatively quiet geomagnetic conditions. The similarities between the ~2-year-averaged lower thermospheric zonal wind and ionospheric Ne wave spectra in Figures 10A–C are quite remarkable.

Similar to DE3 which is known to be primarily generated in the tropical troposphere by latent heat release in deep convective clouds (e.g., Hagan, 1996; Lieberman et al., 2007), UFKWs also originate primarily from latent heat release in the tropical troposphere and have a predominance of the kinetic energy in the zonal wind component (e.g., Forbes, 2000). As previously discussed, UFKWs are a special kind of gravity waves modified by the Earth's rotation and trapped in the equatorial and low-latitude regions, where the Coriolis force is negligible (Salby et al., 1984; Andrews et al., 1987), and have a long vertical wavelength (>50 km) that allow them to propagate into the lower and middle thermosphere, with zonal wind amplitudes exceeding 30 m/s near 110 km (Gu et al., 2014a) and 10 m/s near 260 km (Gasperini et al., 2015). Using HMEs, Forbes et al. (2023) recently showed that UFKWs with periods shorter than about 4 days can effectively penetrate above the lower thermosphere, and dissipation broadens UFKW latitude structures with increasing height and lengthens vertical wavelengths with increasing latitude, whereas ion drag effectively dampens UFKW amplitudes with increasing efficiency at higher solar activity levels.

Figures 10A–C demonstrate the prominence of the thermospheric DE3 and UFKW1 and their ability to effectively couple into the ionosphere. Next, we focus our attention on their latitude-temporal structures in MIGHTI zonal winds near 105 km (Figure 10A′ and Figure 10A″, respectively) and 220 km (Figure 10B′ and Figure 10B″, respectively) and in IVM Ne near 590 km (Figure 10C′ and Figure 10C″, respectively). After the exact UFKW1 period is determined using spectral analysis, simultaneous least-squares fits are performed on these 40-day windows to derive DE3 and UFKW1 amplitudes and phases. UFKW1 amplitudes are derived using 40-day moving windows for consistency with the tidal diagnostics. As discussed in detail for Figure 2, the lower thermospheric zonal wind DE3 shows prominent amplitudes upward of ~25 m/s during days 180–320 and 540–690 (early July through mid-November 2020 and 2021), while the middle thermospheric DE3 retains large amplitudes up to about 15 m/s.

The latitude-temporal structure of the DE3 zonal winds is similar between the two heights in agreement with the primarily first symmetric mode of DE3 (with vertical wavelengths of ~56 km, see Table 1) that dominates at both heights compared to the second

antisymmetric mode (with vertical wavelengths of ~30 km, see Table 1) that peaks near 102 km, and is thus likely to be already mostly dissipated by about 105 km altitude. The UFKW1 shows similar seasonal behavior to DE3 with large amplitudes upward of 18 m/s during days 180–320 and 540–690 corresponding to early July through mid-November 2020 and 2021. While this finding is not surprising considering that both DE3 and UFKWs are known to be generated via similar processes in the lower thermosphere (i.e., latent head in tropical convective systems), various previous studies (e.g., Gasperini et al., 2015; 2018) noted lack of a defined seasonal variation for UFKWs. While it is possible that the 40-day averaging would hide some of the variability, Figure 10A″ suggests that some recurrent seasonal pattern in the lower thermospheric UFKW may be present. This finding may require further verification that will necessitate additional analyses and longer observational datasets. UFKW1 middle thermospheric amplitudes show maxima near 8 m/s, i.e., about 50% less than their corresponding amplitudes near 105 km. Significant latitudinal asymmetry is found in both DE3 and UFKW1 at both thermospheric heights. Using a general circulation model, Gasperini et al. (2017) showed notable effects from mean winds on DE3 and UFKW amplitudes. These effects are significantly more severe for DE3 than for the UFKW despite the fact that they share the same phase speed and that their full latitudinal widths at half-maximum are both near 30° thus making them subject to effectively the same mean winds. Similar conclusions can be made by close inspection of Figure 10. Note that UFKWs are not included in CTMT, hence no comparisons can be made for these wave components.

4 Conclusion

This study evaluates the simultaneous diurnal tidal spectrum and other high-impact waves in the lower and middle thermosphere and topside F-region ion density (i.e., Ne) from ICON and SORTIE. This is accomplished through spectral analyses of recently-released version 5 (v05) ICON MIGHTI wind data over the height ranges ~93–106 km and ~200–270 km (with day and night coverage), and *in-situ* topside F-region ion densities from IVMs onboard ICON (v06) near 590 km and the SORTIE CubeSat (v02) near 420 km. Results are presented during the solar minimum and generally geomagnetic-quiescent period (Kp>4 on only about 8.7% of the days) extending from January 2020 to March 2022 which provides a unique opportunity to better understand how a selected group of global-scale waves couple lower thermospheric variability with IT variability. Comparisons with the CTMT tidal model are also presented. These analyses of remotely-sensed horizontal thermospheric winds from ICON MIGHTI and in-situ-measured F-region Ne from ICON and SORTIE IVMs, along with comparisons with tidal output from CTMT, reveal the following.

1. ICON IVM diurnal spectral analyses reveal large D0-and DW2-induced ion density variability, exceeding 20% on several occasions, throughout January 2020 - March 2022. A close relationship between the D0 and DW2 Ne variations is found consistent with strong quasi-27-day variations in the amplitudes during later 2021 likely induced by corresponding solar rotation variations in flux. Strong Ne variability associated with DE3 is observed around July-October 2021 with amplitudes upward of 20%. Smaller (~10%–15%) DE3 Ne variability is observed around July-October 2020 in agreement with the well-known seasonal and inter-annual variations in the thermospheric DE3.
2. The lower thermospheric diurnal non-migrating tidal spectrum is dominated by DE3 with amplitude variations upward of 25 m/s from early July to mid-November 2020 and 2021. The middle thermospheric DE3 retains significant amplitudes up to around 15 m/s near the equator in agreement with the vertical propagation of this wave component to higher thermospheric altitudes. Remarkable correspondence is also found between the latitude-temporal variations of the lower thermospheric zonal wind DE3 and corresponding variation in the ionospheric DE3, consistent with primary coupling through E-region dynamo processes.
3. Large zonal wind DW2, DE2, and D0 amplitudes with maxima near 15–20 m/s and larger amplitudes generally occur in the middle thermosphere. Significant DW2, DE2, and D0 middle thermospheric variability is not traceable to lower thermospheric variability in these wave components, indicating *in situ* generation in the thermosphere for these wave components (as hypothesized by Oberheide et al., 2011 and later demonstrated numerically by Jones et al., 2013). Results indicate that D0 and DW2 are likely to originate via nonlinear interaction between *in-situ* EUV-generated DW1 and the stationary planetary wave with s = 1 (SPW1) resulting from the geographic and geomagnetic field offset, driven by plasma-neutral interactions. Similar D0 and DW2 variability is also observed in Ne near 590 km. An important finding from MIGHTI different than what was modeled by Jones et al. (2013) is the presence of prominent D0 and DW2 even during weak solar flux conditions.
4. The diurnal non-migrating tidal spectrum in meridional winds measured by ICON MIGHTI is dominated by D0 and DW2 variability in both the lower and middle thermosphere with meridional wind amplitudes exceeding 20 m/s on several occasions. In the lower thermosphere particularly striking are the DW2 variations and D0 variations consistent with their *in-situ* generation from the nonlinear interaction between *in-situ* EUV-generated DW1 and the SPW1. Detailed diagnostics of MIGHTI red-line winds indicate middle thermospheric diurnal amplitudes exceeding 15 m/s with D0, DW2, and SPW1 often the largest nonmigrating diurnal tides present. This source is most likely associated with the nonlinear interaction occurring *in situ* in the middle/upper thermosphere of the in-situ-generated DW1 and SPW1, as clearly demonstrated by the close association between the latitude-temporal structure of these 4 wave components. The middle/upper thermospheric DW1 is largely due to *in-situ* EUV forcing, while SPW1 is the result of the geographic/geomagnetic pole displacement.
5. Comparisons between the diurnal spectra of ICON IVM Ne near 590 km and SORTIE IVM Ne near 420 km suggest the presence of similar wave components, with large DE3, D0, DE2, and DW2 (with enhancements that are not concurrent for all times and wave components). Near the geomagnetic equator, Ne tidal amplitudes

near 420 km are about 40% larger than 590 km, indicating that the prominent D0 and DW2 Ne variations previously discussed are a common feature throughout the topside ionosphere and not limited to the altitudes sampled by ICON IVM near 590 km. EIA-induced effects are evident in DE3 with peaks occurring near ±20° MLAT near 420 km while the peaks are near ±10° MLAT near ~590 km, likely due to SORTIE's lower mean altitude. Important equatorial asymmetries exist in DE3 Ne amplitudes near 420 km that are not present near 590 km, possibly due to vertically changing mean winds in the 420–590 km region.

6. The latitude-temporal and altitude-temporal diurnal non-migrating tidal structures from the CTMT model are analyzed and compared with MIGHTI observations. The lower thermospheric spectra are in general agreement, while large discrepancies are found in the middle thermosphere due to *in situ* tidal generation not captured by CTMT. The presence of strong middle thermospheric DW2 and D0 and their absence in CTMT is consistent with the presence of additional forcing mechanisms in the thermosphere. For the zonal winds, only the antisymmetric HME (HME2) of D0 has a sufficiently long vertical wavelength to propagate into the thermosphere; while for the meridional winds only the symmetric HME (HME1) of D0 can effectively propagate to the thermosphere. HME2 is responsible for generating antisymmetric signals in the lower and middle thermospheric D0 zonal winds, while HME1 is responsible for producing symmetric signals in the lower and middle thermospheric D0 meridional winds. The D0 amplitudes in CTMT are underestimated by up to ~75% near 220 km, and DW2 zonal wind amplitudes in the lower thermosphere are underestimated by CTMT by up to ~67%, while the strong (~15 m/s) middle thermospheric DW2 observed by MIGHTI is nearly absent in CTMT due to the lack of *in situ* generation in CTMT. These results suggest that CTMT (and any tidal model of the thermosphere) would strongly benefit from the assimilation of concurrent satellite measurements, including those from ICON and SORTIE.
7. The MIGHTI lower and middle thermospheric zonal wind wave spectra with periods from 0.5 days to 7 days are analyzed and compared with that of Ne inferred from IVM near 590 km. Prominent and persistent ~3-day UFKW1 lower thermospheric zonal wind variability with ~2-year mean amplitudes near 10 m/s is found to be consistent with ionospheric Ne signatures. Given the greatly reduced UFKW1 amplitudes near 220 km, we surmise that the F-region UFKW1 ionospheric Ne variability is primarily driven by E-region dynamo processes, while *in situ* driving via F-region winds and field-aligned drifts are likely to play a smaller role. The UFKW1 shows similar seasonal behavior to DE3 with large amplitudes upward of 18 m/s during early July through mid-November 2020 and 2021. UFKW1 middle thermospheric amplitudes show maxima near 8 m/s, i.e., about 50% less than their corresponding amplitudes near 105 km. Significant latitudinal asymmetry is found in both DE3 and the UFKW1 at both thermospheric heights, similar to previous modeling studies (e.g., Gasperini et al., 2017). These effects are significantly more severe for DE3 than for the UFKW despite the fact that they share the same phase speed and that their full latitudinal widths at half-maximum are both near 30° thus making them subject to effectively the same mean winds that warrant further investigations.
8. The lower thermospheric zonal wind wave spectrum also reveals marked Q6DW variability during 2020–2021. Spectral analyses of MIGHTI middle thermospheric winds show significantly reduced amplitudes (by ~50%–80%) for both the UFKW1 and Q6DW near 220 km. This result suggests that both these wave components undergo strong dissipation in their propagation between 105 km and 220 km.
9. The middle thermospheric zonal wind wave spectrum reveals dominant s = +0 variations with periods of 0.5 days (i.e., S0, as recently shown by Forbes et al., 2022), 1-day (i.e., D0, discussed in Section 3), and 7 days; and other notable s = 0 variations near 2 and 3 days. These middle thermospheric s = 0 variations (including large s = 0 IT variability near 9 days not shown or discussed in this article) are reflecting prominent topside F-region ion density variability that will be the subject of follow on work.

Despite improved observational capabilities afforded by recent satellite missions, our ability to attain a comprehensive physical understanding of the relevant processes is significantly impaired by data sparsity in the IT system. This study highlights the importance of simultaneous satellite measurements to provide much-needed day/night wind, temperature, and composition observations throughout the thermosphere and ionosphere that will enable the investigation of wave-mean flow interactions, ion-neutral interactions, and dynamo processes critical for improvided nowcasting and forecasting capabilities of IT phenomena.

Data availability statement

The original contributions presented in the study are included in the article/supplementary material, further inquiries can be directed to the corresponding author. ICON data were obtained from https://icon.ssl.berkeley.edu/Data/. Post-processed SORTIE IVM Level 2 ion density data can be accessed on Zenodo at https://zenodo.org/record/6811341. The 3-hourly Kp index was obtained from GFZ Potsdam at https://www.gfz-potsdam.de/en/kp-index/, the F10.7 cm radio flux from NASA/GSFC OMNIWeb at https://omniweb.gsfc.nasa.gov/form/dx1.html. We gratefully acknowledge J. Oberheide for making the Climatological Tidal Model of the Thermosphere (CTMT) model freely available at: https://doi.org/10.5281/zenodo.5541913.

Author contributions

FG performed the analyses, made the interpretations, and wrote the manuscript. BH, GC, and TI supported the interpretation and reviewed the draft. GC and TI supported the funding acquisition. All authors contributed to the article and approved the submitted version.

Acknowledgments

FG acknowledges support from NASA grants No. 80NSSC22K0019 and 80NSSC22K1010, AFOSR grant No. FA9550-22-1-0328, and NSF grant No. 2113411. The SORTIE mission is supported by NASA grant No. 80NSSC18K0094. ICON is supported by NASA's Explorers Program through contracts NNG12FA45C and NNG12FA42I.

Conflict of interest

Authors FG and GC were employed by Orion Space Solutions.

The remaining authors declare that the research was conducted in the absence of any commercial or financial relationships that could be construed as a potential conflict of interest.

Publisher's note

All claims expressed in this article are solely those of the authors and do not necessarily represent those of their affiliated organizations, or those of the publisher, the editors and the reviewers. Any product that may be evaluated in this article, or claim that may be made by its manufacturer, is not guaranteed or endorsed by the publisher.

References

Abdu, M. A., Brum, C., Batista, P. P., Gurubaran, S., Pancheva, D., Bageston, J. V., et al. (2015). Fast and ultrafast Kelvin wave modulations of the equatorial evening F region vertical drift and spread F development. *Earth, Planets Space* 67, 1. doi:10.1186/s40623-014-0143-5

Andrews, D. G., Holton, J. R., and Leovy, C. B. (1987). *Middle atmospheric dynamics*. Academic Press, 489.

Azeem, I., Crowley, G., Wu, W., Randall, C. E., Harvey, V. L., Sharon, S. L., et al. (2022). Travelling ionospheric Disturbances detected by the scintillation observations and response of the ionosphere to electrodynamics (SORTIE) CubeSat at 420 km altitude. *Authorea*. doi:10.1002/essoar.10511395.1

Cai, X., Burns, A. G., Wang, W., Qian, L., Pedatella, N., Coster, A., et al. (2021). Variations in thermosphere composi-tion and ionosphere total electron content under 'geomagnetically quiet' conditions at solar-minimum. *Geophys Res. Lett.* 48, e2021GL093300. doi:10.1029/2021GL093300

Cai, X., Burns, A. G., Wang, W., Qian, L., Solomon, S. C., Eastes, R. W., et al. (2020). The two-dimensional evolution of thermospheric O/N2 response to weak geomagnetic activity during solar-minimum observed by GOLD. *Geophys Res. Lett.* 47, e2020GL088838. doi:10.1029/2020GL088838

Chang, L. C., Liu, J. Y., and Palo, S. E. (2011). Propagating planetary wave coupling in SABER MLT temperatures and GPS TEC during the 2005/2006 austral summer. *J. Geophys Res.* 116, A10324. doi:10.1029/2011JA016687

Chang, L. C., Palo, S. E., Liu, H.-L., Fang, T.-W., and Lin, C. S. (2010). Response of the thermosphere and ionosphere to an ultra fast Kelvin wave. *J. Geophys. Res.* 115, A00G04. doi:10.1029/2010JA015453

Choi, J. M., Lin, C. C. H., Panthalingal Krishanunni, R., Park, J., Kwak, Y. S., Chen, S. P., et al. (2023). Comparisons of *in situ* ionospheric density using ion velocity meters onboard FORMOSAT-7/COSMIC-2 and ICON missions. *Earth Planets Space* 75, 15. doi:10.1186/s40623-022-01759-3

Cullens, C. Y., Immel, T. J., Triplett, C. C., Wu, Y. J., England, S. L., Forbes, J. M., et al. (2020). Sensitivity study for ICON tidal analysis. *Prog. Earth Planet Sci.* 7, 18. doi:10.1186/s40645-020-00330-6

England, S. L., Immel, T. J., Huba, J. D., Hagan, M. E., Maute, A., and DeMajistre, R. (2010). Modeling of multiple effects of atmospheric tides on the ionosphere: an examination of possible coupling mechanisms responsible for the longitudinal structure of the equatorial ionosphere. *J. Geophys. Res.* 115, A05308. doi:10.1029/2009JA014894

Englert, C. R., Harlander, J. M., Marr, K. D., Harding, B. J., Makela, J. J., Fae, T., et al. (2023). Michelson interferometer for global high-resolution thermospheric imaging (MIGHTI) on-orbit wind observations: data analysis and instrument performance. *Space Sci. Rev.* 219, 27. doi:10.1007/s11214-023-00971-1

Forbes, J. M., Bruinsma, S. L., Zhang, X., and Oberheide, J. (2009). Surface-exosphere coupling due to thermal tides. *Geophys Res. Lett.* 36, L15812. doi:10.1029/2009GL038748

Forbes, J. M., He, M., Maute, A., and Zhang, X. (2020a). Ultrafast Kelvin wave variations in the surface magnetic field. *J. Geophys Res. Space Phys.* 125, e2020JA028488. doi:10.1029/2020JA028488

Forbes, J. M., Heelis, R., Zhang, X., Englert, C. R., Harding, B. J., He, M., et al. (2021a). Q2DW-tide and-ionosphere interactions as observed from ICON and ground-based radars. *J. Geophys Res. Space Phys.* 126, e2021JA029961. doi:10.1029/2021JA029961

Forbes, J. M., Manson, A. H., Vincent, R. A., Fraser, G. J., Vial, F., Wand, R., et al. (1994). Semidiurnal tide in the 80-150 km region: an assimilative data analysis. *J. Atmos. Terr. Phys.* 56, 1237–1249. doi:10.1016/0021-9169(94)90062-0

Forbes, J. M., Maute, A., and Zhang, X. (2020b). Dynamics and electrodynamics of an ultra-fast Kelvin wave (UFKW) packet in the ionosphere-thermosphere (IT). *J. Geophys Res. Space Phys.* 125, e2020JA027856. doi:10.1029/2020JA027856

Forbes, J. M., Zhang, X., Heelis, R., Stoneback, R., Englert, C. R., Harlander, J. M., et al. (2021b). Atmosphere-ionosphere (A-I) coupling as viewed by ICON: day-to-day variability due to planetary wave (PW)-tide interactions. *J. Geophys Res. Space Phys.* 126, e2020JA028927. doi:10.1029/2020JA028927

Forbes, J. M., Zhang, X., and Maute, A. (2020c). Planetary wave (PW) generation in the thermosphere driven by the PW-modulated tidal spectrum. *J. Geophys Res. Space Phys.* 125, e2019JA027704. doi:10.1029/2019JA027704

Forbes, J. M., and Garrett, H. B. (1979). Theoretical studies of atmospheric tides. *Rev. Geophys.* 17 (8), 1951–1981. doi:10.1029/RG017i008p01951

Forbes, J. M., and Hagan, M. E. (1988). Diurnal propagating tide in the presence of mean winds and dissipation: a numerical investigation. *Space Sci.* 36 (6), 579–590. doi:10.1016/0032-0633(88)90027-x

Forbes, J. M., Oberheide, J., Zhang, X., Cullens, C., Englert, C. R., Harding, B. J., et al. (2022). Vertical coupling by solar semidiurnal tides in the thermosphere from ICON/MIGHTI measurements. *J. Geophys. Res. space Phys.* 127, e2022JA030288. doi:10.1029/2022JA030288

Forbes, J. M., and Vincent, R. A. (1989). Effects of mean winds and dissipation on the diurnal propagating tide: an analytic approach. *Planet. Space Sci.* 37, 197–209. doi:10.1016/0032-0633(89)90007-x

Forbes, J. M. (2000). Wave coupling between the lower and upper atmosphere: case study of an ultra-fast Kelvin wave. *J. Atmos. Solar-Terrestrial Phys.* 62, 1603–1621. doi:10.1016/s1364-6826(00)00115-2

Forbes, J. M., Zhang, X., Hagan, M. E., England, S. L., Liu, G., and Gasperini, F. (2017). On the specification of upward-propagating tides for ICON science investigations. *Space Sci. Rev.* 212, 697–713. doi:10.1007/s11214-017-0401-5

Forbes, J. M., Zhang, X., and Palo, S. E. (2023b). UFKW propagation in the dissipative thermosphere. *J. Geophys. Res. space Phys.* 128 (1), e2022JA030921. doi:10.1029/2022JA030921

Forbes, J. M., and Zhang, X. (2017). The quasi-6-day wave and its interactions with solar tides. *J. Geophys. Res. space Phys.* 122, 4764–4776. doi:10.1002/2017JA023954

Gan, Q., Oberheide, J., Yue, J., and Wang, W. (2017). Short-term variability in the ionosphere due to the nonlinear interaction between the 6-day wave and migrating tides. *J. Geophys. Res. Space Phys.* 122, 8831–8846. doi:10.1002/2017JA023947

Gan, Q., Wang, W., Yue, J., Liu, H., Chang, L. C., Zhang, S., et al. (2016). Numerical simulation of the 6 day wave effects on the ionosphere: dynamo modulation. *J. Geophys. Res. Space Phys.* 121 (10), 116. 103–10. doi:10.1002/2016JA022907

Gasperini, F., Azeem, I., Crowley, G., Perdue, M., Depew, M., Immel, T., et al. (2021). Dynamical coupling between the low-latitude lower thermosphere and ionosphere via the non-migrating diurnal tide as revealed by concurrent satellite observations and numerical modeling. *Geophys Res. Lett.* 48, e2021GL093277. doi:10.1029/2021GL093277

Gasperini, F., Forbes, J. M., Doornbos, E. N., and Bruinsma, S. L. (2018). Kelvin wave coupling from TIMED and GOCE: inter/intra-annual variability and solar activity effects. *J. Atmos. Sol-Terr Phys.* 171, 176–187. doi:10.1016/j.jastp.2017.08.034

Gasperini, F., Forbes, J. M., Doornbos, E. N., and Bruinsma, S. L. (2015). Wave coupling between the lower and middle thermosphere as viewed from TIMED and GOCE. *J. Geophys Res.* 120, 5788–5804. doi:10.1002/2015JA021300

Gasperini, F., Forbes, J. M., and Hagan, M. E. (2017). Wave coupling from the lower to the middle thermosphere: effects of mean winds and dissipation. *J. Geophys Res.* 122, 7781–7797. doi:10.1002/2017JA024317

Gasperini, F., Liu, H., and McInerney, J. (2020). Preliminary evidence of Madden-Julian oscillation effects on ultra-fast tropical waves in the thermosphere. *J. Geophys Res.* 125, e2019JA027649. doi:10.1029/2019JA027649

Gasperini, F., Crowley, G., Immel, T. J., and Harding, B. J. (2022). Vertical wave coupling in the low-latitude ionosphere-thermosphere as revealed by concurrent ICON and COSMIC-2 observations. *Space Sci. Rev.* 218, 55. doi:10.1007/s11214-022-00923-1

Gu, S-Y., Dou, X., Lei, J., Li, T., Luan, X., Wan, W., et al. (2014a). Ionospheric response to the ultrafast Kelvin wave in the MLT region. *J. Geophys Res. Space Phys.* 119, 1369–1380. doi:10.1002/2013JA019086

Gu, S-Y., Liu, H. L., Li, T., Dou, X. K., Wu, Q., and Russell, J. M. (2014b). Observation of the neutral-ion coupling through 6 day planetary wave. *J. Geophys Res. Space Phys.* 119, 10376–10383. doi:10.1002/2014JA020530

Gu, S.-Y., Dou, X., Lei, J., Li, T., Luan, L., Wan, W., et al. (2014). Ionospheric response to the ultrafast Kelvin wave in the MLT region. *J. Geophys. Res. Space Phys.* 119, 1369–1380. doi:10.1002/2013JA019086

Gu, S.-Y., Liu, H.-L., Dou, X., and Jia, M. (2018a). Ionospheric variability due to tides and quasi-two day wave interactions. *J. Geophys. Res. Space Phys.* 123, 1554–1565. doi:10.1002/2017JA025105

Gu, S.-Y., Ruan, H., Yang, C.-Y., Gan, Q., Dou, X., and Wang, N. (2018b). The morphology of the 6-day wave in both the neutral atmosphere and F region ionosphere under solar minimum conditions. *J. Geophys. Res. Space Phys.* 123, 4232–4240. doi:10.1029/2018JA025302

Hagan, M. E. (1996). Comparative effects of migrating solar sources on tidal signatures in the middle and upper atmosphere. *J. Geophys Res.* 101, 21213–21222. doi:10.1029/96jd01374

Hagan, M. E., and Forbes, J. M. (2002). Migrating and nonmigrating diurnal tides in the middle and upper atmosphere excited by tropospher-ic latent heat release. *J. Geophys. Res.* 107 (D24), 4754. doi:10.1029/2001JD001236

Hagan, M. E., Maute, A., Roble, R. G., Richmond, A. D., Immel, T. J., and England, S. L. (2007). Connections between deep tropical clouds and the Earth's ionosphere. *Geophys. Res. Lett.* 34, L20109. doi:10.1029/2007GL030142

Hagan, M., Forbes, J., and Vial, F. (1995). On modeling migrating solar tides. *Geophys. Res. Lett.* 22 (8), 893–896. doi:10.1029/95GL00783

Harding, B. J., Chau, J. L., He, M., Englert, C. R., Harlander, J. M., Marr, K. D., et al. (2021). Validation of ICON-MIGHTI thermospheric wind observations: 2. Green-Line comparisons to specular meteor radars. *J. Geophys. Res. Space Phys.* 126, e2020JA028947. doi:10.1029/2020JA028947

Harding, B. J., Wu, Y.-J. J., Alken, P., Yamazaki, Y., Triplett, C. C., Immel, T. J., et al. (2022). Impacts of the january 2022 Tonga volcanic eruption on the ionospheric dynamo: ICON-MIGHTI and swarm observations of extreme neutral winds and currents. *Geophys. Res. Lett.* 49, e2022GL098577. doi:10.1029/2022GL098577

Hausler, K., Hagan, M. E., Baumgaertner, A. J. G., Maute, A., Lu, G., Doornbos, E., et al. (2014). Improved short-term variability in the thermosphere-ionosphere-mesosphere-electrodynamics general circulation model. *J. Geophys. Res. Space Phys.* 119, 6623–6630. doi:10.1002/2014JA020006

He, M., Liu, L., Wan, W., and Wei, Y. (2011). Strong evidence for couplings between the ionospheric wave-4 structure and atmospheric tides. *Geophys Res. Lett.* 38, L14101. doi:10.1029/2011GL047855

Heelis, R. A., Chen, Y.-J., Depew, M. D., Harding, B. J., Immel, T. J., Wu, Y.-J., et al. (2022b). Topside plasma flows in the equatorial ionosphere and their relationships to F-region winds near 250 km. *J. Geophys. Res. Space Phys.* 127. e2022JA030415. doi:10.1029/2022JA030415

Heelis, R. A., Depew, M. D., Chen, Y. J., and Perdue, M. D. (2022a). Ionospheric connections (ICON) ion velocity meter (IVM) observations of the equatorial ionosphere at solar minimum. *Space Sci. Rev.* 218 (8), 68–16. Public access. doi:10.1007/s11214-022-00936-w

Heelis, R. A., Stoneback, R. A., Perdue, M. D., Depew, M. D., Morgan, W. A., Mankey, M. W., et al. (2017). Ion velocity measurements for the ionospheric connections explorer. *Space Sci. Rev.* 212, 615–629. doi:10.1007/s11214-017-0383-3

Huba, J. D., Heelis, R., and Maute, A. (2021). Large-scale O+ depletions observed by ICON in the post-midnight topside ionosphere: data/model comparison. *Geophys. Res. Lett.* 48, e2020GL092061. doi:10.1029/2020GL092061

Immel, T. J., and Eastes, R. W. (2019). New NASA missions focus on terrestrial forc-ing of the space environment. *Bull. Am. Meteorol. Soc.* 100, 2153–2156. doi:10.1175/BAMS-D-19-0066.1

Immel, T. J., England, S. L., Mende, S. B., Heelis, R. A., Englert, C. R., Edelstein, J., et al. (2018). The ionospheric connection explorer mission: mission goals and design. *Space Sci. Rev.* 214, 13. doi:10.1007/s11214-017-0449-2

Immel, T. J., Harding, B. J., Heelis, R. A., Maute, A., Forbes, J. M., England, S. L., et al. (2021). Regulation of ionospheric plasma velocities by thermospheric winds. *Nat. Geosci.* 14, 893–898. doi:10.1038/s41561-021-00848-4

Immel, T. J., Sagawa, E., England, S. L., Henderson, S. B., Hagan, M. E., Mende, S. B., et al. (2006). Control of equatorial ionospheric morphology by atmospheric tides. *Geophys. Res. Lett.* 33 (15), L15108. doi:10.1029/2006GL026161

Jin, H., Miyoshi, Y., Fujiwara, H., and Shinagawa, H. (2008). Electrodynamics of the formation of ionospheric wave number 4 longitudinal structure. *J. Geophys. Res.* 113, A09307. doi:10.1029/2008JA013301

Jones, M., Forbes, J. M., Hagan, M. E., and Maute, A. (2013). Non-migrating tides in the ionosphere-thermosphere: *in situ* versus tropospheric sources. *J. Geophys. Res. Space Phys.* 118, 2438–2451. doi:10.1002/jgra.50257

Lieberman, R. S., Riggin, D. M., Ortland, D. A., Nesbitt, S. W., and Vincent, R. A. (2007). Variability of mesospheric diurnal tides and tropospheric diurnal heating during 1997-1998. *J. Geophys Res.* 112, D20110. doi:10.1029/2007JD008578

Lieberman, R. S., Harding, B. J., Heelis, R. A., Pedatella, N. M., Forbes, J. M., and Oberheide, J. (2022). Atmospheric lunar tide in the low latitude thermosphere-ionosphere. *Geophys. Res. Lett.* 49, e2022GL098078. doi:10.1029/2022GL098078

Lieberman, R. S., Riggin, D. M., Franke, S. J., Manson, A. H., Meek, C., Nakamura, T., et al. (2003). The 6.5-day wave in the mesosphere and lower thermosphere: evidence for baroclinic/barotropic instability. *J. Geophys. Res.* 108 (D20), 4640. doi:10.1029/2002JD003349

Lindzen, R. S., and Hong, S. S. (1974). Effects of mean winds and horizontal temperature gradients on solar and lunar semidiurnal tides in the atmosphere. *J. Atmos. Sci.* 31, 1421–1446. doi:10.1175/1520-0469(1974)031<1421:eomwah>2.0.co;2

Lindzen, R. S. (1967). Thermally driven diurnal tide in the atmosphere. *Q. J. R. Meteorol. Soc.* 93, 18–42. doi:10.1002/qj.49709339503

Liu, G., England, S. L., Immel, T. J., Frey, H. U., Mannucci, A. J., and Mitchell, N. J. (2015). A comprehensive survey of atmospheric quasi 3-day planetary-scale waves and their impacts on the day-to-day variations of the equatorial ionosphere. *J. Geophys. Res. Space Phys.* 120, 2979–2992. doi:10.1002/2014JA020805

Liu, G., England, S. L., Lin, C. S., Pedatella, N. M., Klenzing, J. H., Englert, C. R., et al. (2021). Evaluation of atmospheric 3-day waves as a source of day-to-day variation of the ionospheric longitudinal structure. *Geophys. Res. Lett.* 48, e2021GL094877. doi:10.1029/2021GL094877

Liu, G., Immel, T. J., England, S. L., Frey, H. U., Mende, S. B., Kumar, K. K., et al. (2013). Impacts of atmospheric ultrafast Kelvin waves on radio scintillations in the equatorial ionosphere. *J. Geophys. Res. space Phys.* 118, 885–891. doi:10.1002/jgra.50139

Liu, H-L., Yudin, V. A., and Roble, R. G. (2013). Day-to-day ionospheric variability due to lower atmosphere perturbations. *Geophys Res. Lett.* 40, 665–670. doi:10.1002/grl.50125

Liu, H.-L., Bardeen, C. G., Foster, B. T., Lauritzen, P., Liu, J., Lu, G., et al. (2018). Development and validation of the Whole atmosphere community climate model with thermosphere and ionosphere extension (WACCM-X 2.0). *J. Adv. Model. Earth Syst.* 10, 381–402. doi:10.1002/2017MS001232

Liu, H.-L. (2016). Variability and predictability of the space environment as related to lower atmosphere forcing. *Space weather.* 14, 634–658. doi:10.1002/2016SW001450

Makela, J. J., Baughman, M., Navarro, L. A., Harding, B. J., Englert, C. R., Harlander, J. M., et al. (2021). Validation of ICON-MIGHTI thermospheric wind observations: 1. Nighttime red-line ground-based fabry-perot interferometers. *J. Geophys. Res. Space Phys.* 126, e2020JA028726. doi:10.1029/2020JA028726

Maute, A., Richmond, A. D., and Roble, R. G. (2012). Sources of low-latitude ionospheric E × B drifts and their variability. *J. Geophys. Res.* 117, A06312. doi:10.1029/2011JA017502

Oberheide, J., Forbes, J., Hausler, K., Wu, Q., and Bruinsma, S. L. (2009). Tropospheric tides from 80 to 400 km: propagation, interannual variability, and solar cycle effects. *J. Geophys Res.* 114. doi:10.1029/2009JD012388

Oberheide, J., Forbes, J. M., Zhang, X., and Bruinsma, S. L. (2011). Climatology of upward propagating diurnal and semidiurnal tides in the thermosphere. *J. Geophys Res.* 116, A11306. doi:10.1029/2011JA016784

Oberheide, J., and Forbes, J. M. (2008). Tidal propagation of deep tropical cloud signatures into the thermosphere from TIMED observations. *Geophys. Res. Lett.* 35, L04816. doi:10.1029/2007GL032397

Palo, S. E., Roble, R. G., and Hagan, M. E. (1999). Middle atmosphere effects of the quasi-two-day wave determined from a General Circulation Model. *Earth Planets Space* 51, 629–647. doi:10.1186/bf03353221

Pancheva, D., and Mukhtarov, P. (2023). Climatology and interannual variability of the migrating quarterdiurnal tide (QW4) seen in the SABER/TIMED temperatures (2002–2022). *J. Atmos. Solar-Terrestrial Phys.* 250, 106111. doi:10.1016/j.jastp.2023.106111

Park, J., Evans, J. S., Eastes, R. W., Lumpe, J. D., van den Ijssel, J., Englert, C. R., et al. (2022a). Exospheric temperature measured by NASA-GOLD under low solar activity: comparison with other data sets. *J. Geophys. Res. Space Phys.* 127, e2021JA030041. doi:10.1029/2021JA030041

Park, J., Mende, S. B., Eastes, R. W., and Frey, H. U. (2022b). Climatology of equatorial plasma bubbles in ionospheric connection explorer/far-UltraViolet (ICON/FUV)

Limb images. *J. Astronomy Space Sci.* 39 (3), 87–98. doi:10.5140/JASS.2022.39.3.87

Pedatella, N. M., and Forbes, J. M. (2009). Interannual variability in the longitudinal structure of the low-latitude iono-sphere due to the El Niño–southern oscillation. *J. Geophys Res.* 114, A12316. doi:10.1029/2009JA014494

Qin, Y., Gu, S.-Y., Dou, X., Gong, Y., Chen, G., Zhang, S., et al. (2019). Climatology of the quasi-6-day wave in the mesopause region and its modulations on total electron content during 2003–2017. *J. Geophys. Res. Space Phys.* 124, 573–583. doi:10.1029/2018JA025981

Qin, Y., Gu, S-Y., Teng, C-K-M., Dou, X-K., Yu, Y., and Li, N. (2021). Comprehensive study of the climatology of the quasi-6-day wave in the MLT region based on aura/MLS observations and SD-WACCM-X simulations. *J. Geophys. Res. Space Phys.* 126, e2020JA028454. doi:10.1029/2020JA028454

Riggin, D. M., Hays, P. B., Skinner, W. R., Roble, R. G., Russell III, J. M., Mertens, C. J., et al. (2006). Observations of the 5-day wave in the mesosphere and lower thermosphere. *J. Atmos. Solar-Terrestrial Phys.* 68, 323–339. doi:10.1016/j.jastp.2005.05.010

Sagawa, E., Immel, T. J., Frey, H. U., and Mende, S. B. (2005). Longitudinal structure of the equatorial anomaly in the nighttime ionosphere observed by IMAGE/FUV. *J. Geophys. Res.* 110, A11302. doi:10.1029/2004JA010848

Salby, M. L., Hartmann, D. L., Bailey, P. L., and Gille, J. C. (1984). Evidence for equatorial Kelvin modes in nimbus-7 LIMS. *J. Atmos. Sci.* 41, 220–235. doi:10.1175/1520-0469(1984)041<0220:efekmi>2.0.co;2

Stromberg, E., Crowley, G., Azeem, I., Fish, C., Frazier, C., Reynolds, A., et al. (2016). "Scintillation observations and response of the ionosphere to electrodynamics (SORTIE)," in *Proceedings of the 30th annual AIAA/USU SmallSat conference*. paper: SSC16-VI-3.

Talaat, E. R., Yee, J.-H., and Zhu, X. (2002). The 6.5-day wave in the tropical stratosphere and mesosphere. *J. Geophys. Res.* 107 (D12), 4133. doi:10.1029/2001JD000822

Talaat, E. R., Yee, J. H., and Zhu, X. (2001). Observations of the 6.5-day wave in the mesosphere and lower thermosphere. *J. Geophys. Res.* 106, 20,715–20,723. doi:10.1029/2001jd900227

Truskowski, A. O., Forbes, J. M., Zhang, X., and Palo, S. E. (2014). New perspectives on thermosphere tides - 1. Lower thermosphere spectra and seasonal-latitudinal structures. *Earth Planets Space* 66, 136. doi:10.1186/s40623-014-0136-4

Volland, H., and Mayr, H. G. (1977). Theoretical aspects of tidal and planetary wave propagation at thermospheric heights. *Rev. Geophys.* 15 (2), 203–226. doi:10.1029/RG015i002p00203

Volland, H., and Mayr, H. G. (1974). Theoretical aspects of tidal and planetary wave propagation at thermospheric heights. *J. Atmos. Sol. Terr. Phys.* 36, 203–460. doi:10.1029/RG015i002p00203

Wautelet, G., Hubert, B., Gérard, J.-C., Immel, T. J., Frey, H. U., Mende, S. B., et al. (2021). First ICON-FUV nighttime NmF2 and hmF2 comparison to ground and space-based measurements. *J. Geophys. Res. Space Phys.* 126, e2021JA029360. doi:10.1029/2021JA029360

Yamazaki, Y., Arras, C., Andoh, S., Miyoshi, Y., Shinagawa, H., Harding, B. J., et al. (2022). Examining the wind shear theory of sporadic E with ICON/MIGHTI winds and COSMIC-2 radio occultation data. *Geophys. Res. Lett.* 49, e2021GL096202. doi:10.1029/2021GL096202

Yamazaki, Y., Harding, B. J., Qiu, L., Stolle, C., Siddiqui, T. A., Miyoshi, Y., et al. (2023). Monthly climatologies of zonal-mean and tidal winds in the thermosphere as observed by ICON/MIGHTI during April 2020-March 2022. *Authorea*. doi:10.22541/essoar.168056794.43452415/v1

Yamazaki, Y., Miyoshi, Y., Xiong, C., Stolle, C., Soares, G., and Yoshikawa, A. (2020). Whole atmosphere model simulations of ultra-fast Kelvin wave effects in the ionosphere and thermosphere. *J. Geophys. Res. Space Phys.* 125, e2020JA027939. doi:10.1029/2020JA027939

Yamazaki, Y. (2018). Quasi-6-day wave effects on the equatorial ionization anomaly over a solar cycle. *J. Geophys. Res. Space Phys.* 123, 9881–9892. doi:10.1029/2018JA026014

Yiğit, E., and Medvedev, A. S. (2015). Internal wave coupling processes in Earth's atmosphere. *Adv. Space Res.* 55, 983–1003. doi:10.1016/j.asr.2014.11.020

Yiğit, E., Dhadly, M., Medvedev, A. S., Harding, B. J., Englert, C. R., Wu, Q., et al. (2022). Characterization of the thermospheric mean winds and circulation during solstice using ICON/MIGHTI observations. *J. Geophys. Res. Space Phys.* 127. e2022JA030851. doi:10.1029/2022JA030851

Yiğit, E., Knízova, P. K., Georgieva, K., and Ward, W. (2016). A review of vertical coupling in the atmosphere-ionosphere system: effects of waves, sudden stratospheric warmings, space weather, and of solar activity. *J. Atmos. Sol. Terr. Phys.* 141, 1–12. doi:10.1016/j.jastp.2016.02.011

frontiers | Frontiers in Astronomy and Space Sciences

TYPE Original Research
PUBLISHED 29 September 2023
DOI 10.3389/fspas.2023.1214612

OPEN ACCESS

EDITED BY
Han-Li Liu,
National Center for Atmospheric Research (UCAR), United States

REVIEWED BY
Federico Gasperini,
Orion Space Solutions LLC, United States
Hidekatsu Jin,
National Institute of Information and Communications Technology, Japan

*CORRESPONDENCE
Ludger Scherliess,
ludger.scherliess@usu.edu

RECEIVED 30 April 2023
ACCEPTED 07 September 2023
PUBLISHED 29 September 2023

CITATION
Molina I and Scherliess L (2023), Longitudinal variability of thermospheric zonal winds near dawn and dusk. *Front. Astron. Space Sci.* 10:1214612. doi: 10.3389/fspas.2023.1214612

Longitudinal variability of thermospheric zonal winds near dawn and dusk

Ivana Molina and Ludger Scherliess*

Center for Atmospheric and Space Sciences, Utah State University, Logan, UT, United States

Understanding the morphology and dynamics of the thermosphere is key to understanding the Earth's upper atmosphere as a whole. Thermospheric winds play an important role in this process by transporting momentum and energy and affecting the composition, dynamics and morphology of not only the thermosphere but also of the ionosphere. The general morphology of the winds has been well established over the past decades, but we are only starting to understand its variability. In this process the lower atmosphere plays an important role due to direct penetration of waves from the lower atmosphere into the ionosphere/thermosphere, secondary waves generated on the way, or internal feedback mechanisms in the coupled ionosphere-thermosphere system. Therefore, knowledge about thermospheric variability and its causes is critical for an improved understanding of the global ionosphere-thermosphere system and its coupling to the lower atmosphere. We have used low-to mid-latitude zonal wind observations obtained by the Gravity Field and Steady-State Ocean Explorer (GOCE) satellite near 260 km altitude during geomagnetically quiet times to investigate the interannual and spatial zonal wind variability near dawn and dusk, during December solstice. The temporal and spatial variability is presented as a variation about the zonal mean values and decomposed into its underlying wavenumbers using a Fourier analysis. The obtained wave features are compared between different years and clear interannual changes are observed in the individual wave components, which appear to align with changes in the solar flux but do not correlate with variations in either El Niño Southern Oscillation or the Quasi Biennial Oscillation. The obtained wave features are compared and contrasted with results from the Climatological Tidal Model of the Thermosphere (CTMT) and revealed a very good agreement between CTMT and the 2009 and 2010 December GOCE zonal wind perturbations at dawn. However, during dusk, the CTMT zonal wind perturbations and in particular the zonal wave-1 component show significant differences with those observed by GOCE.

KEYWORDS

neutral wind, thermosphere, ionosphere, tides, upper atmosphere dynamics, GOCE

1 Introduction

Thermospheric neutral winds present a highly dynamic behavior with changing geophysical conditions. Understanding their variability becomes critical, as they transfer energy and momentum in the upper atmosphere and directly or indirectly affect the dynamics, morphology and composition of the ionosphere, which can disrupt radiocommunication and navigation systems (e.g., Wang et al., 2021).

Waves present in the thermosphere play a particular role and add significant variability in the wind system. Generally, these waves are classified as (i) planetary waves, which are global in scale with periods of up to several days to a month (Forbes, 1996); (ii) tides, which are also global in scale but with periods that are sub-harmonics of solar and lunar days (Oberheide et al., 2015); and (iii) gravity waves, which are medium-to small-scale oscillations with periods ranging from a few minutes to several hours (Fritts and Alexander, 2003).

Migrating and non-migrating tides originating from the lower atmosphere are recognized as important players in the vertical coupling between the lower and upper atmosphere. The general morphology of these tides has been studied extensively over the past decades (e.g., Lindzen, 1981; Teitelbaum and Vial, 1981; Miyahara et al., 1993; Liu et al., 2010; Forbes et al., 2017) and can be observed as global oscillations in winds, density, temperature and other atmospheric fields. In general, they transfer energy and momentum from the lower regions of the atmosphere into the upper atmosphere and generate longitudinal variations in the various atmospheric state parameters and can modify the global ionosphere-thermosphere (I-T) system (e.g., Immel et al., 2006; Forbes, 2007). Therefore, it is important to understand the spatial and temporal variability they generate in the upper atmosphere.

Thermospheric data derived from satellite accelerometers (e.g., Bruinsma and Biancale, 2003; Sutton et al., 2007; Doornbos et al., 2010) has been used to study global longitudinal structures produced by non-migrating tides. For example, Forbes et al. (2012) used densities from the SETA, CHAMP and GRACE satellites to investigate vertical tidal propagation and to identify the tidal oscillations in the longitudinal structures present in the data; Häusler and Lühr (2009) investigated the non-migrating tidal spectra in zonal wind data at equatorial latitudes obtained from the CHAMP accelerometer with an emphasis on the annual variation of the wave-4 structure at 400 km altitude; Lieberman et al. (2013a) investigated tidal variations in longitudinally averaged CHAMP global zonal winds; Gasperini et al. (2015) used GOCE neutral densities and zonal winds and TIMED-SABER temperatures to study vertical coupling in the thermosphere; Liu et al. (2016) found the presence of wind jets aligned with the magnetic equator in GOCE zonal winds; Dhadly et al. (2020) studied the latitudinal variation in intra-annual oscillations in the GOCE cross-track neutral winds.

This study focuses on longitudinal structures present in zonal winds produced by non-migrating atmospheric tides and observed by the GOCE satellite during dawn and dusk. The year-to-year progression during December solstice is investigated and the contributions from zonal wave-1 to wave-5 structures is studied. The GOCE results are compared to the Climatological Tidal Model of the Thermosphere (CTMT) (Oberheide et al., 2011).

Throughout this paper, the standard nomenclature for tides is used; DEs (DWs) is an eastward (westward) propagating diurnal tide with zonal wavenumber s. For semidiurnal tides, an S is used in place of the D.

This paper is organized in the following manner. Section 2 describes the data used in the study, while Section 3 describes the methodology. In Section 4 the combined contributions of zonal wave-1 to wave-5 structures are presented, and their individual contributions are shown in Section 5. In Section 6, the GOCE results are compared to the CTMT model. Finally, Section 7 provides a summary and discussion of the results.

2 GOCE data

The Gravity field and steady-state Ocean Circulation Explorer (GOCE) satellite was launched on 17 March 2009 into a dawn-dusk Sun-synchronous orbit with an inclination of 96.7° (near-polar orbit) and an altitude of ~260 km. Its main objective was to study Earth's gravity field, with thermospheric densities and winds calculated later combining accelerometer and ion thruster data, together with GPS tracking and star camera data. For a description of the determination algorithm see Doornbos et al., 2010. The data set version 2.0 was used for this study, which had been reprocessed with a new implementation of the algorithms (Visser et al., 2019). The algorithm uses a new satellite geometry and aerodynamic model representation (March et al., 2019a), with a new setting of the aerodynamic energy accommodation coefficient (March et al., 2019b).

Even though the GOCE satellite altitude is on the average ~260 km, it varies with time, starting initially at ~270 km in 2009 and decreasing to ~250 km in 2013. The local time corresponding to dawn and dusk also varies. In 2009 the local solar time at the equator crossing for dusk is ~18 h and by the end of the mission it reaches ~19 h.

The errors in the GOCE zonal wind are of the order of ~10%–20%, with the dominant source of errors being biases due to instrument calibration and external models used in the calculation of the winds (Doornbos et al., 2010). In this work, the errors will be attenuated by using residuals, which account for these biases.

Due to the availability of geomagnetically quiet-time data, the December solstice was selected to study the year-to-year progression of the longitudinal variability in the GOCE zonal winds. In order to calculate the perturbations in the GOCE zonal wind measurements, a 27-day window of data was selected for each year; this helps to minimize the effect of the Sun's rotation. These selected windows are centered as close as possible to the December solstice for the years 2009, 2010, 2011, and 2012, taking into account gaps in the data and geomagnetically active periods. For reference, figures for June 2010 and 2011 are also included in the Supplementary Material. The selected windows are:

- December solstice 2009: 12 December 2009 to 07 January 2010
- December solstice 2010: 05 December 2010 to 31 December 2010
- December solstice 2011: 08 December 2011 to 03 January 2012
- December solstice 2012: 08 December 2012 to 03 January 2013
- June 2010: 04 June 2010 to 30 June 2010 (in Supplementary Material)
- June 2011: 08 June 2011 to 04 July 2011 (in Supplementary Material)

Figure 1A shows the daily F10.7 cm radio flux for the duration of the GOCE wind data set. The periods selected are indicated by green (December solstices) and purple (June solstices) vertical

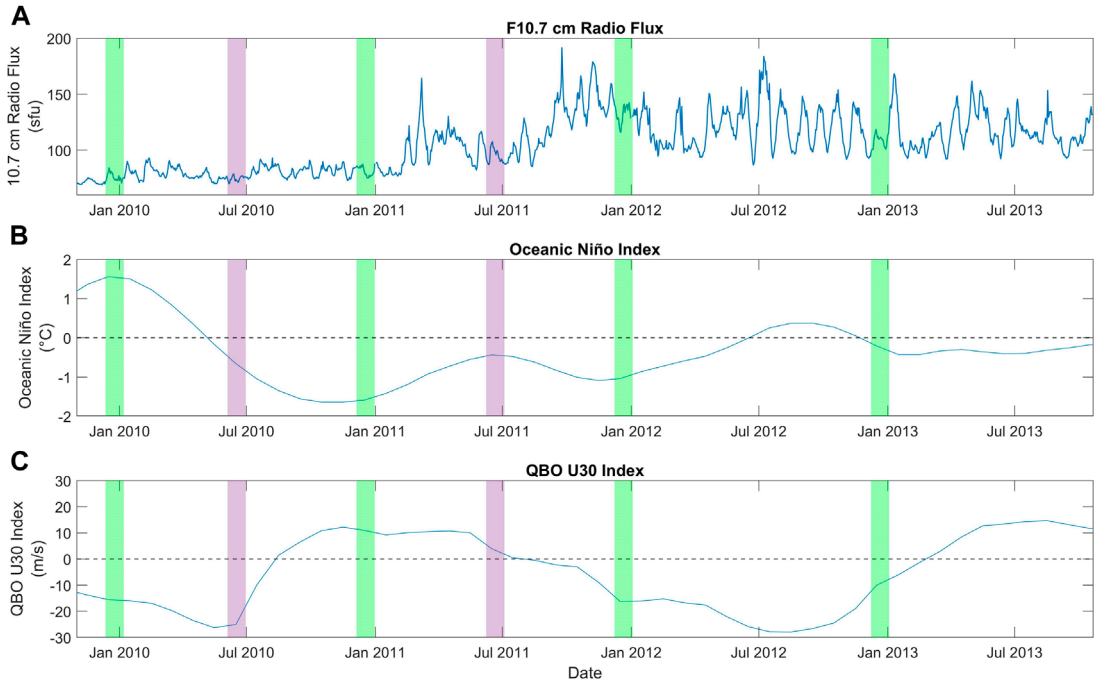

FIGURE 1
F10.7 cm radio flux **(A)**, Oceanic Niño Index (ONI) **(B)** and Quasi-Biennial Oscillation at 30 hPa (QBO U30) index **(C)**, during the span of the GOCE thermospheric data set. The ONI and QBO indices are 3-month averages plotted at the mid-point of each period. The December and June solstice periods selected are indicated with green and purple vertical bars, respectively.

bars. The average F10.7 value for the selected window in December 2009 was 76 sfu. For 2010 that value was 81 sfu. The averages for 2011 and 2012 were higher, at 132 sfu and 109 sfu respectively. The mean F10.7 value for June 2010 was 75 sfu and for June 2011 it was 95 sfu. The geomagnetic activity in these periods was, in general, very low. The average Kp values did not exceed 1^0 during the December solstice windows and it was below 2^- for the June periods. With the exception of one day in December 2011, the daily Kp index is always below a value of 3 for all of the December periods, and reaches 3.3 once during each of the selected June periods. The reason for not including June 2012 and June 2013 in our analysis is due to data gaps and the presence of geomagnetic storms during these periods which precluded us from finding suitable 27-day windows. Figure 1B shows, for the same period as above, the Oceanic Niño Index (ONI), a 3-month running mean of sea-surface temperature anomalies (Bamston et al., 1997) with respect to the mean from 1971 to 2000 in the region 120 to 170°W and 5°N to 5°S. The ONI is used to classify El Niño Southern Oscillation (ENSO). El Niño conditions are present when ONI exceeds +0.5K for 5 consecutive months whereas La Niña conditions correspond to values of ONI of −0.5K or lower. ENSO is categorized into weak (ONI values of 0.5–0.9), moderate (ONI 1.0-1.4), strong (ONI 1.5-1.9) and extreme (values of ONI 2 or higher). Figure 1C shows the Quasi Biennial Oscillation (QBO) U30 index, which corresponds to the zonally averaged wind at 30 hPa over the Equator. It is observed that throughout the span of the GOCE thermospheric data set both of these indices exhibit strong variations which will be discussed in Section 7.

3 Methodology

Following a similar approach as outlined in Molina (2022) as well as in the companion paper by Molina and Scherliess (2023) the data corresponding to each 27-day window were separately analyzed for dawn (~06 h local time) and dusk (~18 h local time) conditions and sorted into bands of 1° of geographic latitude from −50° to 50° N. In each latitude band the median value was calculated. Next, the zonal wind perturbations (to be called dWind) were obtained for every GOCE zonal wind observation by computing: $dWind = Wind - Median$, where the median subtracted from each wind measurement is the value that corresponds to the latitude band where the measurement is located.

For the longitudinal analysis the spatial resolution of the data was further reduced by organizing the dWind values into bins of 5° of latitude and 2° of longitude. In each bin, data points that fell beyond two standard deviations from the corresponding mean were filtered out and the remaining data points were averaged. Figure 2 shows, as an example, a global map of the calculated dWind for the December 2009 period. Figures 2A, B show each individual dWind data point whereas Figures 2C, D show the binned and averaged data. It can be seen that our binning and averaging preserves the main characteristics of the perturbations but attenuates the noise in the data. A longitudinal structure can be recognized from the plots as well, both in the dawn and the dusk perturbations. This structure presents alternating bands of positive (eastward) and negative (westward) wind perturbations that are the main focus of this paper.

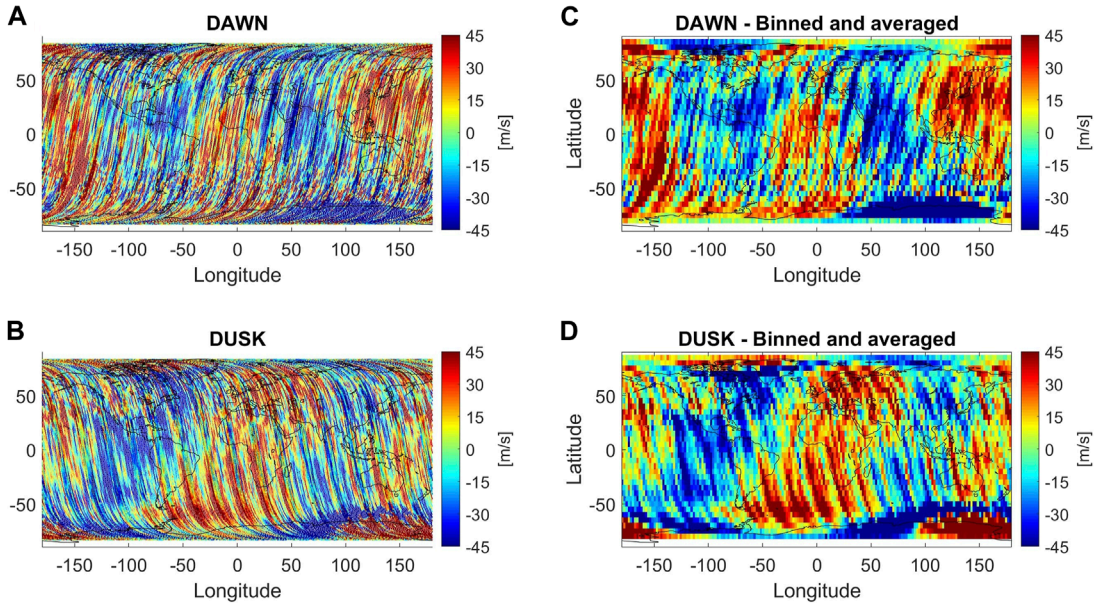

FIGURE 2
GOCE Eastward dWind for December 2009 for dawn **(A,C)** and dusk **(B,D)**. dWind values calculated for each individual wind measurement are shown on the left, and the right shows the results after binning and averaging. Positive (negative) values correspond to eastward (westward) perturbations.

In order to analyze the longitudinal structures and to elucidate their underlying wave characteristics, a 1-D Fast Fourier Transform (FFT) was applied to the binned and averaged deviations separately in each latitude band. Here, the 1-D FFT will provide the different longitudinal frequencies present in the zonal wind perturbations. Because the 1-D FFT is applied separately in each 5° latitude band, the results for each band will be independent from each other.

For a fixed local solar time, the tidal perturbations $\tilde{T}$ can be expressed as (Oberheide et al., 2003):

$$\tilde{T} = \sum_{s,n} T_{s,n} \cos[\omega_n (t - t_{s,n}) - \lambda(s+n)]$$

where $T_{s,n}$ is the amplitude, ω_n is the wave frequency, t is the local solar time, $t_{s,n}$ is the time of maximum amplitude with respect to 0° longitude, λ is the longitude, s is the zonal wavenumber and n is the number of cycles per day ($n = 1$ for the diurnal components, $n = 2$ for the semidiurnal). This equation implies that when observing at a constant local time, the observed zonal wavenumber corresponds to $s' = |s + n|$. Depending on the sign of s, the wave propagation is eastward for positive values of s and westward for negative values of s.

Since the GOCE data are analyzed separately for dawn and dusk and thus correspond approximately to a fixed local time of ~06 h for dawn and ~18 h for dusk, the longitudinal variations in the GOCE data will appear as waves where the contributions from individual tides cannot be separated. Therefore, for example, both SE2 and DE3 will appear as part of a zonal wave-4 structure in the data, and their contributions will be combined in the FFT results. Since for migrating tides $= -n$, and consequently $s' = 0$, their contribution appears as a constant in the tidal perturbations and becomes part of the median that we had subtracted from the zonal winds in our analysis. Consequently, the contribution of migrating tides is largely eliminated, and our results pertain to only non-migrating tides.

Figure 3 shows an example of the amplitude spectrum obtained from the FFT for the December 2011 period. Shown are the wave-m components up to wave-9. As already noted, these wave-m components do not pertain to a certain tidal wave, but instead are a combination of multiple tides. It is evident from Figure 3 that in this case the largest amplitudes are found in the first three wave components.

Figure 4 shows the wave amplitudes for December dawn conditions separately for each year from 2009 to 2012 (Figures 4A–D). Shown are the amplitudes for wave-1 to wave-9 as a global average (blue bars), averaged over the northern hemisphere (red bars), and averaged over the southern hemisphere (yellow bars). Here, the global values were obtained by averaging the individual wave-amplitudes in each latitude bin from −45° to 45° geographic latitude, and the northern/southern hemisphere averages were obtained by averaging the corresponding values from 0° to 45° and from 0° to −45°, respectively. It is interesting to note that during December 2009 the wave-1 amplitude in the northern hemisphere is more than twice the value found in the southern hemisphere. A similar hemispheric asymmetry can also be seen for wave-2 and wave-3 during December 2012. Figure 5 shows the same as Figure 4, but for dusk conditions. During this time, hemispheric asymmetries are present for wave-3 for December 2011 and for wave-2 and wave-3 during December 2012. Otherwise, the northern and southern averaged amplitudes are comparable to each other.

Figures 4, 5 also show that most of the wave amplitudes are concentrated in the first few wave numbers. In fact, our analysis

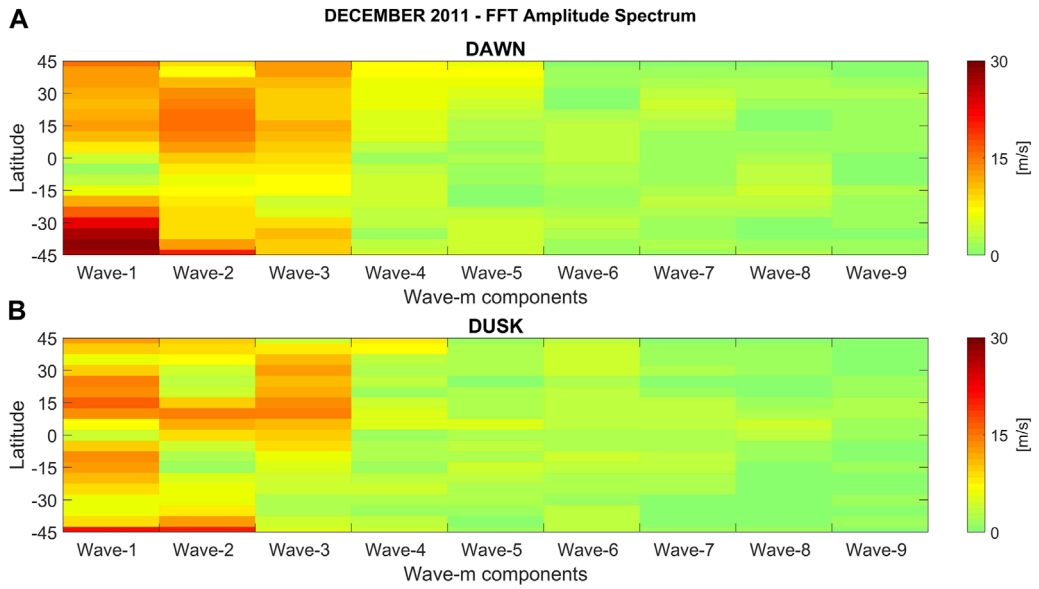

FIGURE 3
FFT amplitude spectrum for zonal wave-1 through wave-9 for GOCE zonal dWind for December 2011 during dawn **(A)** and dusk **(B)**.

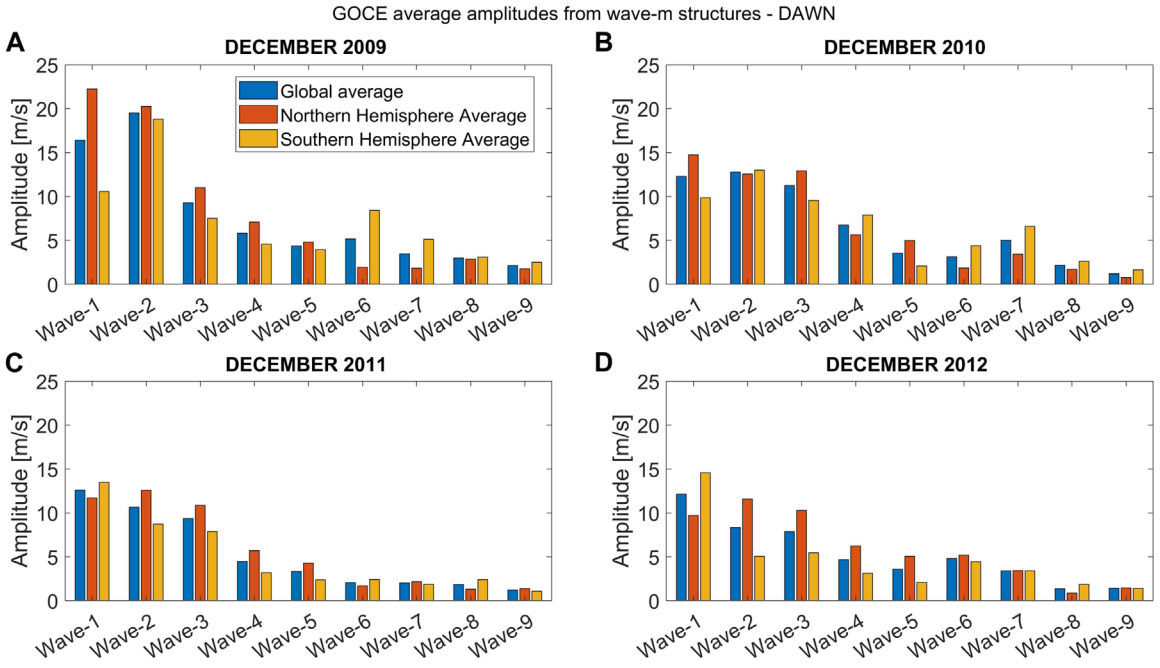

FIGURE 4
Average wave-m amplitudes for GOCE zonal dWind during dawn for wave-1 to wave-9 for December solstice 2009-2012 **(A–D)**. The blue bars correspond to a global average (from -45° to 45° geographic latitude), the red bars represent the average for the northern hemisphere (0° to 45°) and the yellow bars correspond to the average in the southern hemisphere (0° to -45°).

shows that 75%–85% of the variability is represented by the first five components. As a consequence, we have limited our further analysis to only consider these first five wave-numbers.

Specifically, we have initially investigated the combined effect of wave-1 to wave-5 applying an inverse FFT (IFFT) after filtering out all contributions with zonal wavenumbers higher than 5. This was followed by a study of the individual effect of each wave-m component up to wave-5. For this all components of the FFT except the one corresponding to that particular wavenumber were filtered before the IFFT was performed. This step was repeated for all wave components from wave-1 through wave-5. In the following the combined contributions from wave-1 to wave-5 will be presented

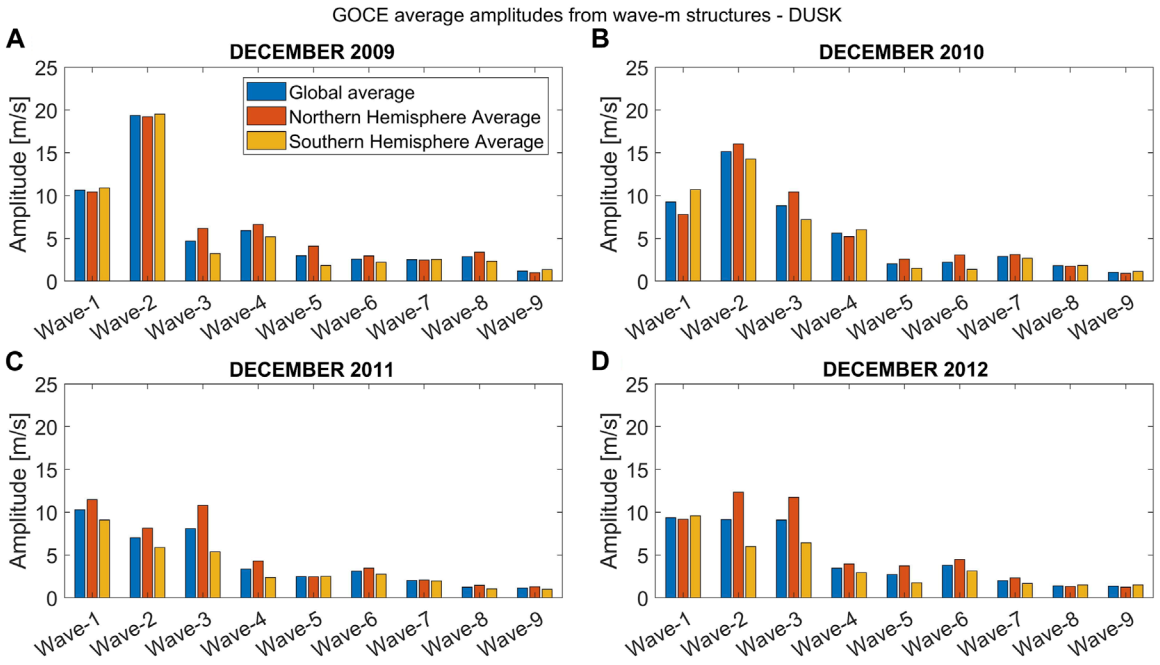

FIGURE 5
Same as Figure 4 but for dusk.

followed by a presentation of the individual contributions from wave-1 to wave-5.

4 Total zonal wind perturbations from wave-1 to wave-5

The total December GOCE zonal wind perturbations (dWind) obtained from the IFFT produced by the contributions from wave-1 through wave-5 are separately shown for each year from 2009 to 2012 as a function of latitude and longitude in the first four rows of Figure 6. Figures 6A–D correspond to dawn and Figures 6E–H to dusk conditions. Positive (negative) values are shown as red (blue) colors and correspond to eastward (westward) perturbations. Figures 6I, J show the corresponding model results obtained from CTMT that will be discussed in Section 6.

In general, the total GOCE zonal wind perturbations at dawn remarkably resemble each other from one year to the next. During dusk, the GOCE zonal wind perturbations also show a good agreement for the low solar flux years 2009 and 2010 and as well as for the higher solar flux years 2011 and 2012. However, a clear change in the global pattern can be seen from 2010 to 2011. In the following sections, the global perturbation patterns are presented and agreements and differences from year to year are described in more detail.

4.1 Total zonal wind perturbations during dawn

The total December 2009 GOCE zonal wind perturbations at low- and mid-latitudes during dawn are shown in Figure 6A. The perturbations range from about −40 m/s to 50 m/s and exhibit a clear longitudinal structure consisting of four distinct bands. These bands alternate between eastward and westward perturbations and are generally tilted westward with increasing latitude (north-west alignment).

The first band exhibits eastward perturbations and is centered at about −160° longitude. The band shows two local maxima near 35° and −35° latitude that reach peak values of ~45 m/s and ~40 m/s, respectively.

The second band (westward perturbations) extends in the northern hemisphere from about −130° to about −30° longitude and forks into two branches resembling a Y-shaped structure centered at about −80° longitude. The peak values in this structure range from −10 m/s to −30 m/s. In the southern hemisphere, the band becomes narrower, extending from ~-100° to ~-50° with wind perturbations ranging from about −10 m/s to −30 m/s between about −10° and −50° latitude. Near the equator, from about 0° to −10° latitude, the wind perturbations in this band are small, with values of about −10 m/s.

The third band (eastward perturbations) is centered at about −10° longitude and depicts a more localized structure extending between ~±30° latitude and −35° and 15° longitude. This structure exhibits wind perturbations ranging from about 10 m/s to 30 m/s.

The fourth band (westward perturbations) is centered at about 50° with wind perturbations between about −20 m/s to −40 m/s.

An additional eastward structure can be seen, centered at about 130° longitude. This structure, which is most apparent in the northern hemisphere, appears to be connected to the first band described above. The structure is located between 100° and 160°

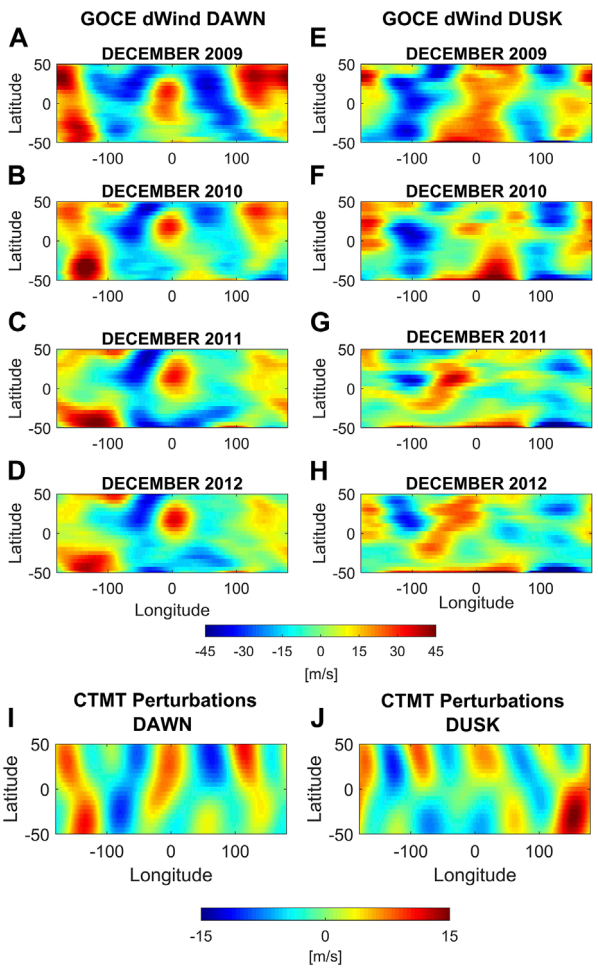

FIGURE 6
GOCE zonal dWind for December solstice for years 2009 to 2012 **(A–H)**, and CTMT zonal wind perturbations **(I,J)** for December solstice 2011, during dawn (left column) and dusk (right column). Values correspond to the combined contributions from zonal wave-1 through wave-5. Positive (negative) values correspond to eastward (westward) perturbations.

longitude and shows wind perturbations ranging from about 10 m/s to 40 m/s. In the southern hemisphere, the wind perturbations associated with this structure decrease to values of about 5 m/s.

The dawn GOCE wind perturbations for December 2010 for low- and mid-latitudes are shown in Figure 6B and also range from about −40 m/s to 50 m/s. A similar range of values is also found during December 2011 (Figure 6C), while during December 2012 (Figure 6D) the eastward peak values slightly reduce to about 40 m/s. The longitudinal structure observed in December 2009 can be identified in the subsequent years, but with noticeable changes.

The first eastward band, centered at around −160° longitude, is still present in 2010, but contrary to the 2009 results, the peak wind perturbations in the southern hemisphere are larger (~50 m/s) compared to the northern hemisphere (~27 m/s). These two maxima are also present in 2011 and 2012 but are no longer part of a distinct continuous band, but instead break into two isolated peaks. These isolated structures do not exhibit significant changes from 2011 to 2012. The peak values in 2011 are 30 m/s for the northern hemisphere peak and 45 m/s for the southern hemisphere maximum. For 2012 these peaks slightly reduce with values of 25 m/s and 40 m/s, respectively.

The second longitudinal band, which consists of westward perturbations, is present in 2010 as well, but significant differences are observed. The values in the northern hemisphere reach ~ −40 m/s and the band is tilted eastward with increasing latitude (north-east alignment). This portion of the structure persists through 2011 and 2012, maintaining a remarkably similar shape and magnitude. In the southern hemisphere the zonal wind perturbations for 2010 are around −15 m/s, whereas in 2011 their magnitudes become much higher, reaching values of about −40 m/s. In 2012 they decrease again to about −15 m/s.

The third band (eastward perturbations) becomes more localized in 2010 and is only present in the northern hemisphere between 0° and 40° latitude, with magnitudes near 30 m/s. During 2011 and 2012 this structure remains nearly unchanged.

The fourth band (westward perturbations) is still present in 2010, but with smaller magnitudes overall. In the northern hemisphere it reaches values of −20 m/s and in the southern hemisphere the values are reduced to about −10 m/s to −15 m/s. In 2011 and 2012 this band nearly disappears at low latitudes (peak values of about −5 m/s) but is present at mid-latitudes in the southern hemisphere with values of the order of −20 m/s, connecting with the second longitudinal band at these latitudes.

The additional eastward structure that appeared connected to the first eastward band for 2009 gradually fades in the subsequent years, reducing from about 30 m/s in 2010 to about 15 m/s in 2011 and 2012.

4.2 Total zonal wind perturbations during dusk

The low and mid-latitude GOCE zonal wind perturbations for December 2009 during dusk are shown in Figure 6E and range from −40 m/s to 45 m/s. Similar to dawn, a clear longitudinal banded structure can also be identified during dusk with four bands alternating between eastward and westward perturbations. This time, however, the bands are generally tilted eastward with increasing latitude (north-east alignment).

The first band presents westward perturbations, and it is centered at about −90° longitude. The wind perturbations range from −20 m/s to −40 m/s. Although the width of the band changes with latitude, it spans on average approximately 65° of longitude.

The second band (eastward perturbations) is centered around 10° longitude, with the zonal wind perturbations ranging from 20 m/s to 40 m/s.

The third band presents westward perturbations and is composed of one localized maximum in each hemisphere. The northern hemisphere peak is located between 30° and 50° latitude and 90° to 135° longitude with peak values of about −20 m/s to −30 m/s. The southern hemisphere maximum is located between −5° and −50° latitude and 60° to 100° longitude. Here, the perturbations are of the order of −20 m/s. It is interesting to note that even though the general orientation of the bands is north-east, this particular structure exhibits a north-west orientation.

The fourth band presents eastward perturbations consisting of three maxima. The first peak is centered at about 180° longitude and 35° latitude and has a width of 20° in latitude and 50° in longitude. It has the highest values of perturbations within the band, ranging from 30 m/s to 40 m/s. The second maximum presents perturbations of about 15 m/s and is located between 135° and 175° longitude and −15° to −5° latitude. The third maximum has magnitudes of the order of 20 m/s and is present from 125° to 160° longitude and −30° to −40° latitude.

The dusk GOCE zonal wind perturbations for December 2010 (Figure 6F) are very similar to the corresponding 2009 results and also range from −40 m/s to 45 m/s. Some differences between the two years can be seen in the first band (westward perturbations) with smaller perturbation values (less than 5 m/s) during 2010 in the latitude range from 30° to 35° latitude and generally smaller westward perturbations in the southern hemisphere. Furthermore, although the second band (eastward perturbations) is still present in the southern hemisphere in December 2010 with wind perturbations of about 20 m/s to 45 m/s, a break-up into separate structures is seen in the northern hemisphere with overall lower perturbation values of about 20 m/s. The third band (westward perturbations) is also observed in the 2010 wind perturbations, with many of the same characteristics present in 2009. The band consists of two peaks, one in each hemisphere. The northern hemisphere maximum is located between 20° and 60° latitude and wind perturbations of about −20 m/s to −35 m/s. In the southern hemisphere the peak extends from about −40° to −5° latitude with wind perturbations ranging from −15 m/s to −20 m/s. Finally, the fourth band (eastward perturbations) is more continuous in 2010 where it extends from −20° to 50° latitude with wind perturbations ranging from 20 m/s to 35 m/s.

The dusk GOCE zonal wind perturbations for December 2011 and 2012 (Figures 6G, H) also range from −40 m/s to 45 m/s. The longitudinal structures observed during these later years, however, considerably differ from those observed during the earlier years and the banded structure is not as clearly defined in 2011 and 2012.

In particular, the first westward band that was observed during the earlier years, is not present in the southern hemisphere and consists in the northern hemisphere of localized peaks with wind perturbations that range from −20 m/s to −40 m/s in 2011 and from −20 m/s to −35 m/s in 2012. The second band (eastward perturbations) has shifted westward when compared to the earlier years and is now centered at about −50° longitude with magnitudes that range from 20 m/s to 40 m/s in 2011 to values of 20 m/s to 25 m/s in 2012. This band also exhibits a strong north-east alignment in contrast to the earlier years. The third band (westward perturbations) has become more localized in latitude during 2011 and 2012 with peaks approximately located between 20° and 40° and −5° and −25° latitude, respectively. Here, the peak wind perturbations are about −20 m/s to −30 m/s in the northern hemisphere and −15 m/s to −20 m/s in the southern hemisphere. Finally, the fourth band (eastward perturbations) is only present in 2011 for latitudes northward of about 20° latitude with wind perturbations of about 15 m/s to 20 m/s. During 2012 the band stretches from −5° to 50° of latitude, with wind perturbations of about 15 m/s to 25 m/s.

5 Individual contributions from wave-1 to wave-5

In the following sections the individual contributions of wave-1 to wave-5 to the total zonal wind perturbations are analyzed separately. The results are first shown for dawn followed by the corresponding results for dusk.

5.1 Individual contributions during dawn

The rows A through D of Figure 7 show the result of the separation of the dawn December 2009-2012 (top to bottom) GOCE zonal wind perturbations into their individual wave-m components with m ranging from *1* to *5* (left to right). Each wave-m structure is shown as a function of latitude and longitude. In general, the individual wave-m structures are remarkably similar from year to year in both phase and magnitude, but also exhibit differences in particular when comparing the individual wind perturbations for the low solar flux years (2009-2010) to those of the higher solar flux years (2011-2012).

The zonal wind perturbation associated with wave-1 during dawn is shown in the first column and shows clear maxima (25–30 m/s) in the northern mid-latitudes (20°–50°) in 2009 and 2010. During 2011 and 2012 these structures gradually decrease to about 10–15 m/s and develop a banded structure with north-east alignment. In the southern hemisphere, from 2009 to 2012 the reverse process is observed.

Wave-2 (second column) presents a clear change from year-to-year. 2009 shows a banded structure with north-west alignment with magnitudes ranging from 15 to 25 m/s. In 2010, this structure evolves into more localized peaks in the northern (from 0° to 35° latitude) and southern hemisphere (−15° to −50° latitude) with slightly lower wind perturbation values when compared to 2009 (about 10 m/s to 20 m/s). In 2011 and 2012 the northern hemisphere peaks remain, but the alignment changes into a north-east direction for 2011 and more localized peaks in 2012. The southern hemisphere zonal wind perturbations diminish in magnitude progressively from 2009 to 2012, maintaining the north-west alignment, but nearly disappearing from −5° to −35° latitude in 2012.

The wave-3 component for 2009 (third column) exhibits localized peaks in the northern hemisphere, which evolve into a more banded structure with north-east alignment from 2010 to 2012. The phase of these structures is maintained for all years. The peak wind perturbations, however, change from 12 to 15 m/s in 2009, to 10–12 m/s in 2010 and 7–10 m/s in 2011 and 2012.

The 2009 wave-4 component presents bands (~10 m/s) in the northern hemisphere (20°–40°). In the southern hemisphere the bands are located between −15° and 50° and the magnitudes are smaller (5–7 m/s). From 2010 to 2012 the bands are continuous for all latitudes with values ranging from 3 m/s to 7 m/s. In 2010 localized peaks can also be seen with magnitudes up to 10 m/s in the northern hemisphere (between 35° and 45°) and up to 12 m/s in the southern hemisphere (between −20° and −40°).

The zonal wind perturbations associated with wave-5 present a mostly north-aligned banded structure for all years (magnitudes ~3–5 m/s), with more intense peaks (~6 m/s) in the northern

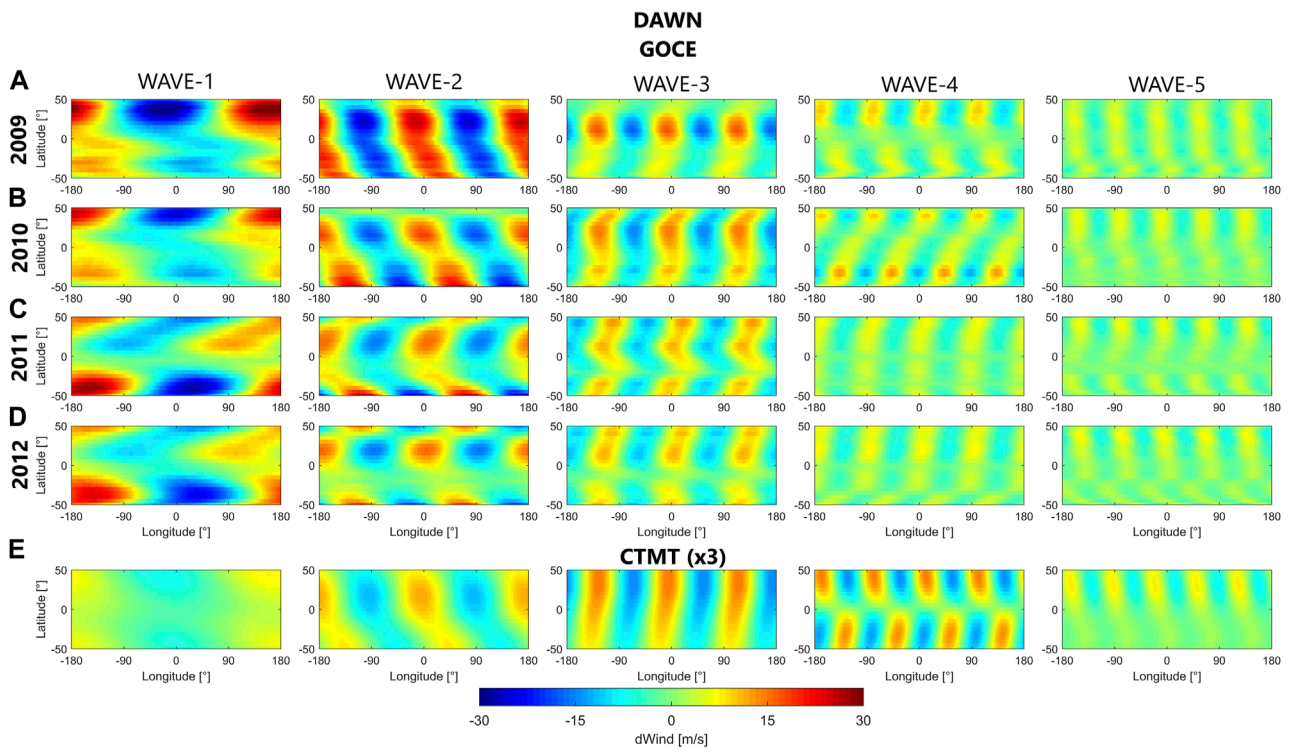

FIGURE 7
Individual zonal wave-1 to wave-5 zonal wind perturbations (left to right) during dawn. Rows **(A–D)** correspond to GOCE zonal dWind for December 2009 to 2012. Row **(E)** corresponds to CTMT zonal wind perturbations with the magnitudes multiplied by a factor of 3. Positive (negative) values correspond to eastward (westward) perturbations.

hemisphere for years 2010–2012. The amplitudes of these bands for 2009 are the same for both the northern and the southern hemisphere (~3–5 m/s).

5.2 Individual contributions during dusk

The rows A through D of Figure 8 show the result of the separation of the dusk December 2009-2012 (top to bottom) GOCE zonal wind perturbations into their individual wave-m components with m ranging from *1* to *5* (left to right). Similar to the general morphology during dawn, the individual wave-m structures are again similar from year to year in both phase and magnitude, but this time the differences between the individual wind perturbations for the low solar flux years (2009-2010) and those for the higher solar flux years (2011-2012) become even more evident.

The zonal wind perturbations associated with wave-1 for 2009 during dusk are generally north-east aligned and show a banded structure with peaks (10–14 m/s) in the northern low and mid-latitudes and higher peaks (15–20 m/s) in the southern mid-latitudes. In 2010, the wave-1 zonal wind perturbations are very similar to the 2009 results, with some exceptions in the northern hemisphere where the peaks become more localized at low latitudes but maintaining similar magnitudes. The wave-1 responses in 2011 and 2012 are also very similar to each other but show significant differences to the prior years. In the southern mid-latitude, the maxima (10–12 m/s) are still present but exhibit a phase shift with respect to 2009 and 2010. Separate peaks are also observed in the higher southern (~20 m/s) and northern latitudes (10–14 m/s).

The wave-2 response for 2009 shows a band structure with slight north-east alignment (~20–25 m/s), which is also seen in 2010 but with smaller magnitudes (~15–20 m/s). In 2011 and 2012 a banded structure is still present, but again significant differences to the prior years can be seen. In particular, more localized peaks with smaller amplitudes (~10–12 m/s) and a stronger north-east alignment are observed. In 2011, the peaks are localized in the low (0°–20°) latitudes for the northern hemisphere and in the mid to higher (35°–50°) northern and southern latitudes. In 2012 larger amplitudes (12–15 m/s) are observed around 0°–40° in the northern hemisphere and −40° to −50° in the southern hemisphere.

The wave-3 zonal wind perturbations are very similar during the years from 2010 to 2012 but differ from the 2009 response. For 2009 localized peaks are present (~10 m/s) in the northern hemisphere mid latitudes that become more extended toward the lower latitudes and stronger in magnitude during the subsequent years (10–16 m/s).

The wave-4 response for 2009, 2010, and 2012 exhibits a banded structure with north-west alignment. In 2011, the wave-4 response is more reminiscent of checkerboard pattern. The magnitudes of the

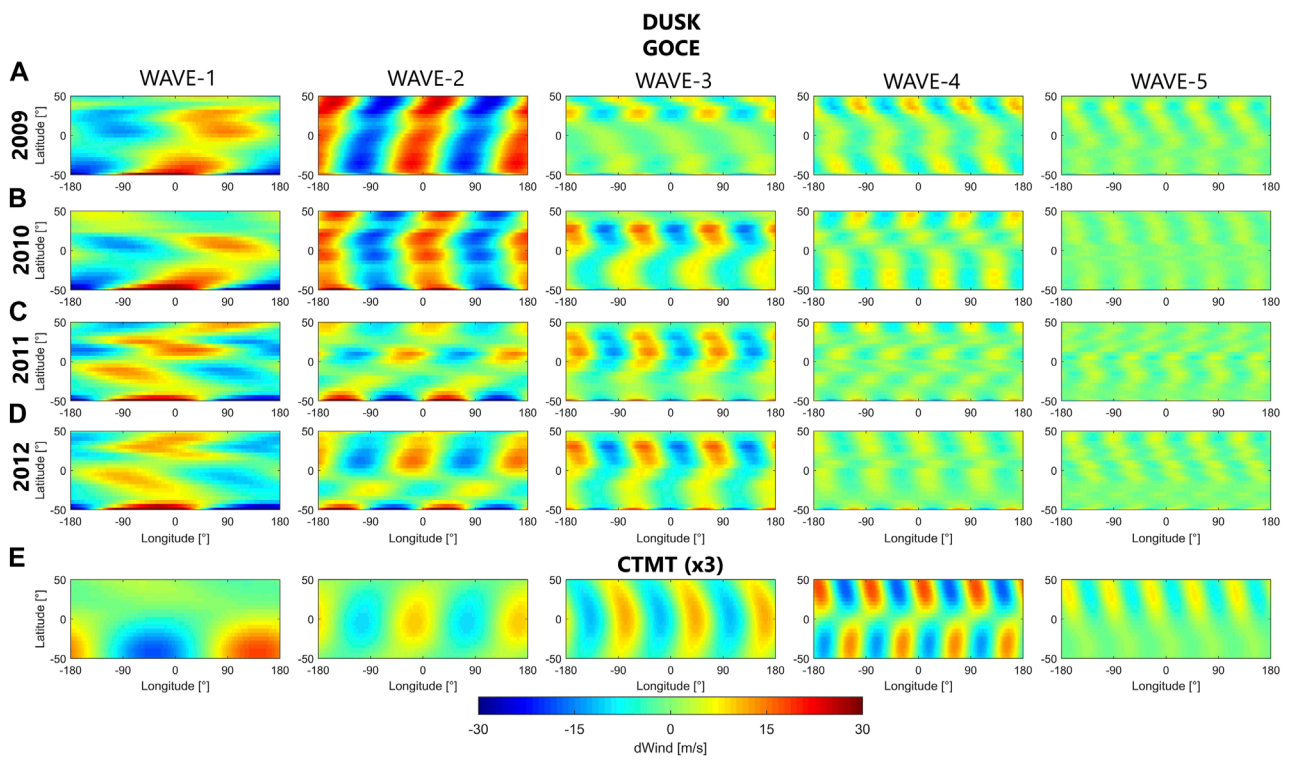

FIGURE 8
Same as Figure 7 but for dusk.

wave-4 wind perturbations progressively decrease from 2009 to 2012 (from 5 to 10 m/s to 3–5 m/s).

The wave-5 responses for 2009, 2010, and 2012 are very similar to each other and show a banded structure with northwest alignment. In 2011, a checkerboard pattern can be seen in the northern hemisphere. The magnitudes are similar for all years (2–4 m/s).

6 Comparison with CTMT

In this section we will compare the GOCE results with simulations obtained from the Climatological Tidal Model of the Thermosphere (CTMT) (Oberheide et al., 2011) model. CTMT is an observation-based model that includes amplitudes and phases for six diurnal (DW2, DW1, D0, DE1, DE2, DE3) and eight semidiurnal (SW4, SW3, SW2, SW1, S0, SE1, SE2, SE3) tidal components for temperature, density, zonal, meridional and vertical winds from 80 to 400 km of altitude, pole-to-pole, and for moderate (F10.7 = 110 sfu) solar flux conditions. The model is based on Hough Mode Extensions to mean tidal diagnostics obtained from the TIMED Doppler Interferometer (TIDI) and the Sounding the Atmosphere using Broadband Emission Radiometry (SABER) instruments onboard the Thermosphere, Ionosphere, Mesosphere Energetics and Dynamics (TIMED) satellite. CTMT perturbations have been compared to satellite observations (Forbes et al., 2012; Lieberman et al., 2013b; Forbes et al., 2014; Forbes et al., 2022), used as boundary conditions for numerical experiments (e.g., Jones Jr et al., 2019) and to interpret and explain ground-based observations (e.g., Yuan et al., 2014).

The monthly CTMT amplitudes and phases are provided on a latitude/altitude grid with 5° latitude and 2.5 km altitude resolution. For our comparison of the GOCE zonal wind perturbations with those predicted by CTMT we have calculated for each individual GOCE data point the corresponding CTMT value. Specifically, we have interpolated the provided amplitude and phase data to the same days and locations of each individual GOCE observation using a linear interpolation in each dimension. Once the corresponding CTMT amplitudes and phases were obtained, the corresponding CTMT zonal wind perturbation for each individual tide was calculated using:

$$\tilde{T}_{n,s} = A_{n,s}\cos\left[n\Omega t_L - (s+n)\lambda - \phi_{n,s}\right]$$

where $\tilde{T}_{n,s}$ is the tidal perturbation, n is the subharmonic of a solar day ($n = 1$ for diurnal tides and $n = 2$ for semidiurnal tides), s is the zonal wavenumber, $A_{n,s}$ is the amplitude, Ω is the rotation rate of the Earth, t_L is the local solar time, λ is the longitude and $\phi_{n,s}$ is the phase. Finally, the individual tidal components were added to obtain the total simulated zonal wind perturbation.

When investigating the longitudinal variations in the CTMT simulated zonal wind perturbations at a fixed local time the contributions from migrating tides appear as a constant and longitudinal variations are only due to non-migrating tidal components that will appear as a wave-m structures spanning from

wave-1 to wave-5. In particular, D0, DW2, SW1 and SW3 will appear as a wave-1. Wave-2 will be comprised of DE1, S0 and SW4. Wave-3 will be composed of DE2 and SE1. DE3 and SE2 will appear as a wave-4. SE3 is the only component in CTMT that will appear as a wave-5.

Once the CTMT perturbations were calculated, the same steps performed on the GOCE zonal wind perturbations described in Section 3 were applied to the simulated CTMT zonal wind perturbations.

6.1 Comparison of combined contributions from wave-1 to wave-5

The top four rows of Figure 6 show the GOCE zonal wind perturbations for December 2009 to 2012 as already described in Section 4. Figures 6I, J show the corresponding CTMT zonal wind perturbations for dawn and dusk, respectively. The CTMT model results correspond to the December 2011 time period, which is used as a proxy for all four years. CTMT is a climatological model and does not vary with solar flux or geomagnetic activity. Consequently, differences between the CTMT results for the other years are only due to the small difference in the individual 27-day time period (differences of a few days) and the small shift in local time of the GOCE orbit from year to year (about 20 min/year). As a result, the CTMT results for the different years only display a longitudinal shift that does not exceed 4° and differ by at most 20%.

A visual inspection of the left column of Figure 6 shows the very good agreement in the general morphology of the structures at dawn between the CTMT and the 2009 and 2010 GOCE zonal wind perturbations, especially in the northern hemisphere, where the observed longitudinal bands align within 10° of those seen in the model results. In particular, the two peaks that were observed in the first band of eastward perturbations in GOCE during December 2009 and 2010 are also present in the CTMT model results. Furthermore, the Y-shape structure seen in the second band of westward perturbations in GOCE are closely resembled in the CTMT results. And finally, the inverted Y-shaped structure seen in the CTMT results as the fourth band (westward perturbations) is similar to the one observed in the 2010 GOCE perturbations. This band presents a peak in the northern hemisphere and smaller values in the southern hemisphere.

However, even though there are striking similarities between the general morphology of the GOCE and CTMT zonal wind perturbations, there are also noticeable differences. Foremost, the magnitudes of the CTMT wind perturbations are only about one-third of the corresponding GOCE values (note the difference in the color scale for GOCE and CTMT in Figure 6). Also, one additional band with westward zonal wind perturbations that is not present in the GOCE observations can be seen in the CTMT results centered near 170° longitude. Additional noticeable differences are a peak in the second band in the CTMT results in the southern hemisphere that is not as clearly seen in the GOCE zonal perturbations, and the existence of a more continuous third band (eastward perturbations) spanning latitudes from 50° to −25, where the GOCE wind perturbations were more localized.

During dusk, the CTMT zonal wind perturbations (Figure 6J) show significant differences with the observed GOCE zonal wind perturbations. The structures present in the CTMT perturbations do not resemble the general morphology of the GOCE results for any of the years. This will be further discussed in Section 6.2 and Section 7.

6.2 Comparison of individual contributions from wave-1 to wave-5

In order to further compare and contrast the GOCE and CTMT zonal wind perturbations, we have calculated for each individual wave-1 through wave-5 the corresponding CTMT result as described in Section 3.

Row E in Figures 7, 8 shows the result of the separation into wave-m components of the CTMT zonal wind perturbations and the GOCE zonal wind perturbations up to wave-5 during dawn and dusk respectively, for December 2009 to 2012. In order for GOCE and CTMT results to display similar magnitudes, the CTMT results have been multiplied by a factor of three.

Figure 7 shows that the dawn CTMT wave-1 component (bottom left panel) exhibits a very similar general structure when compared to the corresponding GOCE wave-1 variations. This includes a very similar phase and alignment of the longitudinal structures. However, the magnitudes of the CTMT wave-1 perturbations are significantly smaller when compared to the corresponding GOCE values. This comparison also holds when evaluating the relative importance of the wave-1 structures to the total zonal wind perturbations. For CTMT, the wave-1 perturbations only constitute about ~14%–20% of the total zonal wind perturbations whereas the GOCE wave-1 perturbations constitute about 50%–60%. This difference will be further discussed in Section 7.

The wave-2 component shows a good agreement between the CTMT and the GOCE zonal wind perturbations for all years, especially in the northern hemisphere. The CTMT zonal wind perturbations present a structure of localized peaks (~4 m/s) in the northern hemisphere between 0° and 50° of latitude with smaller perturbations (~2 m/s) in the southern hemisphere forming a band that has a north-west orientation. The CTMT zonal wind perturbations are mostly aligned in longitude during all GOCE years (within ±10°).

The CTMT wave-3 component during dawn shows good agreement with the GOCE results in the northern hemisphere for 2010, 2011, and 2012, presenting a banded structure with north-east alignment. The model results present magnitudes of 3–5 m/s and the phase is also within ±5° of the GOCE 2010 results and within ±10°of the 2011 and 2012 results.

The CTMT wave-4 components show a checkered pattern of eastward and westward perturbations with magnitudes of about 4–5 m/s, with a separation (from −5° to 5°) near the geographic equator where the magnitudes get close to zero. This general structure agrees well with the 2009 wave-4 GOCE zonal wind perturbations.

For wave-5, the CTMT wind perturbations only consist of one tidal component, namely, SE3. For this component, CTMT agrees well with the corresponding GOCE zonal wind perturbations in the northern hemisphere where it presents a banded structure with values of ~2.5 m/s. In the southern hemisphere, the wave-5 CTMT

perturbations become very small with values less than 0.5 m/s. A similar hemispheric variation can also be seen in the wave-5 GOCE zonal wind perturbations during the years 2010–2012, with higher values in the northern hemisphere (~5–6 m/s) than in the southern hemisphere (magnitudes up to ~3 m/s).

As noted above, the total CTMT perturbations at dusk, as shown in Figure 6, did not resemble the corresponding GOCE perturbations. Figure 8 reveals that, in particular, the wave-1 component for dusk displays large differences from the corresponding GOCE wave-1 structure. In the southern hemisphere, CTMT presents large eastward and westward perturbations that maximize near −45° and 135° longitude, respectively, which appear nearly entirely out of phase with the corresponding GOCE pattern. In the northern hemisphere, the CTMT wave-1 structure practically vanishes, whereas GOCE shows significant perturbation values.

For wave-2, the CTMT results show a banded structure, albeit with smaller relative amplitudes, that agrees reasonably well with the GOCE pattern especially during the years 2009 and 2010. However, the CTMT values maximize at lower latitudes (between −20° and 20° latitude) whereas the GOCE perturbations during these years are uniformly extended over the entire latitude range. For the years 2011 and 2012 the phase of the CTMT and GOCE wave-2 pattern agrees well in the northern hemisphere, but the structures are out of phase in the southern hemisphere.

The dusk wave-3 component for CTMT presents structures with semicircular shapes centered at the equator that do not agree well with the GOCE results. Similarly, the CTMT wave-4 presents a checkered pattern, with a separation (from −5° to 5°) at the geographic equator, which also does not agree well with GOCE. However, the CTMT wave-5 pattern agrees well with GOCE during the years 2009, 2010 and 2012.

7 Summary and discussion

We have used low-to mid-latitude zonal wind observations from 2009 to 2012 obtained by the GOCE satellite near 260 km altitude during geomagnetically quiet times to investigate the interannual variation of the longitudinal variability of the zonal wind near dawn and dusk. The focus of the study was to investigate the year-to-year progression of the longitudinal variability in the GOCE zonal winds during December solstice produced by nonmigrating atmospheric tides. For each year the contributions from zonal wave-1 to wave-5 structures were separately determined and compared. The GOCE longitudinal zonal wind variations were also compared with corresponding results obtained from the CTMT model.

To determine the longitudinal variation in the GOCE zonal wind measurements, a 27-day window (one solar rotation) was selected for each year and the data were separately analyzed for dawn and dusk from −50° to 50° geographic latitude. The temporal and spatial variability of the zonal winds was then presented as a variation about the zonal mean values and decomposed into its underlying wave-m structures using a Fourier analysis. This approach largely eliminated the contribution of migrating tides from our analysis but also precluded us from separating the longitudinal variations into their individual tidal components. Consequently, our zonal wind perturbations appear as zonal wave-m structures that result from the superposition of individual non-migrating tidal components. It is important to highlight that in this methodology, the Fourier analysis is applied to each latitude band individually; therefore, the results for each one of these bands are independent of each other. The coherence between the adjacent latitude bands presented in Figures 6–8 gives confidence in the structures observed.

It was found that 75%–85% of the longitudinal zonal wind variability could be explained as due to waves that generate zonal wave-m structures with m up to 5, and therefore, this was the cutoff used in our Fourier analysis. A clear interannual progression of the individual wave components could be observed in the resulting structures.

In general, the total GOCE zonal wind perturbations at dawn remarkably resemble each other from one year to the next. During dusk, the GOCE zonal wind perturbations also show a good agreement for the low solar flux years 2009 and 2010 as well as for the higher solar flux years 2011 and 2012. However, a clear change in the global pattern can be seen from 2010 to 2011. Note that the F10.7 solar flux values during 2009 and 2010 were lower than during 2011 and 2012 and the change in the pattern might be related to the change in solar flux. A similar good agreement in the total GOCE zonal wind perturbations can also be observed for June 2010 and June 2011 (shown in Supplementary Figure S1). As pointed out above, the average F10.7 solar flux during these two June periods also only differs by 20 sfu.

Both ENSO and the QBO are also known to produce year-to-year variability on atmospheric tides (e.g., Oberheide et al., 2009; Warner and Oberheide, 2014). As mentioned above, the GOCE results for each December pair 2009-2010 and 2011-2012 are similar. Figure 1B shows, however, that the ONI values for 2009 and 2010 are very different and correspond to moderate El Niño and strong La Niña conditions, respectively. December 2011 presents moderate La Niña conditions, and December 2012 does not present either. From Figure 1C, it is also evident that the QBO U30 index is different for the December 2009 and 2010 pair. Differences are also observed in the index for the June 2010 and 2011 pair. Based on these observations, it appears that the year-to-year variations seen in GOCE are not the result of either variations in ENSO or the QBO. During dawn, the total December solstice GOCE zonal wind perturbations at low- and mid-latitudes range from about −40 m/s to 50 m/s and exhibit a clear longitudinal structure consisting of four distinct bands. These bands alternate between eastward and westward perturbations and are generally tilted westward with increasing latitude (north-west alignment). The individual wave-m structures during dawn are also remarkably similar from year to year in both phase and magnitude, but also exhibit differences when comparing the individual wind perturbations for the low solar flux years (2009-2010) to those of the higher solar flux years (2011-2012).

During dusk, the low and mid-latitude GOCE zonal wind perturbations for December solstice also range from −40 m/s to 45 m/s. Like dawn, a clear longitudinal banded structure can be identified at with four bands alternating between eastward and westward perturbations. This time, however, the bands are generally tilted eastward with increasing latitude (north-east alignment). Similar to the general morphology during dawn,

the individual wave-m structures are again similar from year to year in both phase and magnitude, but this time the differences between the individual wind perturbations for the low solar flux years (2009-2010) and those for the higher solar flux years (2011-2012) become even more evident. Here again, a similar result is found for the two June periods where the individual wave-m structures resemble each other year-to-year (see Supplementary Figure S2 for dawn and Supplementary Figure S3 for dusk).

Some of the characteristics just described are observed in a companion paper by Molina and Scherliess (2023), who have used the same GOCE zonal wind observations to determine their spatial and temporal correlations. In particular, it is mentioned that the longitudinal/temporal correlations for December 2009 indicate that the structures that generate them have a north-west orientation during dawn (Figure 10 in their paper) and north-east orientation during dusk (their Figure 11). It is noteworthy that this is observed in Figure 6 of this paper as the general orientation of the longitudinal bands for December 2009 for dawn and dusk, respectively. The zonal wave structures up to wave-5 obtained in this work were also subtracted from the associated perturbations, and the longitude/time correlation coefficients were subsequently calculated for their study. The resulting correlation coefficients (Figures 12 to 15 in their paper) suggest that the zonal wave-m structures described in this paper are largely responsible for the original patterns observed in their longitudinal/temporal correlations.

A comparison of the GOCE results with simulations obtained from the CTMT model has revealed a very good agreement between the CTMT and the December 2009 and 2010 GOCE zonal wind perturbations at dawn, especially in the northern hemisphere, where the observed longitudinal bands align within 10° of those seen in the model results. However, even though there are striking similarities between the general morphology of the GOCE and CTMT zonal wind perturbations, there are also noticeable differences. During dusk the CTMT zonal wind perturbations show significant differences with the observed GOCE zonal wind perturbations. The structures present in the CTMT perturbations do not resemble the general morphology of the GOCE results for any of the years. In particular, the CTMT wave-1 component significantly differs from the GOCE results (this can also be seen in Supplementary Figures S2, S3 for June solstice). There could be several reasons for this discrepancy. Oberheide et al. (2011) compared the CTMT densities near 400 km altitude with those obtained from the CHAMP satellite and found that the agreement with the tidal components DW2, D0, SW1, and SW3 was poor. As mentioned before, these are also the components that constitute the wave-1 structure. They suggest that the observed differences are the result of the generation mechanisms of these tidal components, which are believed to be generated by hydromagnetic coupling between various waves (Jones et al., 2013) which is not captured by the CTMT formulation. Part of the discrepancy between GOCE and CTMT at dusk might also be the result of our use of a geographic coordinate system in our analysis. Liu et al. (2016) found the presence of wind jets aligned with the magnetic equator in GOCE zonal winds. Zhang et al. (2018) used CHAMP zonal winds together with TIEGCM model simulations to investigate the effect of the geomagnetic field on longitudinal variations observed in zonal winds. They conclude that the large-scale longitudinal variations are produced by the geomagnetic field structure and might be the result of temporal variations of ion drag and pressure gradient forces. Indeed, the variation captured by TIEGCM in their Figure 10 is reminiscent of a wave-1 structure for both dawn and dusk.

Regarding the differences in magnitudes of the CTMT wind perturbations, which are only about one-third of the corresponding GOCE values, it needs to be noted that it is not clear whether this difference is the result of an underestimation of zonal wind perturbations by CTMT or due to a systematic overestimation of the GOCE wind data or both. Jiang et al. (2021) for example, compared GOCE zonal winds with wind observations obtained from ground-based Fabry-Perot Interferometer (FPI) measurements at low and mid latitudes and reported an overall overestimation of the GOCE winds when compared to the ground-based data. They found that the magnitudes from GOCE are generally larger than the FPI winds by a factor of 1.37–1.69, consistent with FPI comparisons at high latitudes where factors of 1.2–2.0 were reported by Kärräng (2015), albeit using an earlier version of the GOCE data. An earlier version of the data was also used by Dhadly et al. (2017, Dhadly et al., 2019) who reported a magnetic latitude-depended bias in the GOCE data when compared to WINDII, SDI and FPI observations at high latitudes. The possible presence of a bias in the GOCE data, however, would have only affected our zonal mean values and consequently would have been eliminated when calculating the wind perturbations. A factor difference, however, would also affect our perturbation values and consequently our reported values should be scaled by this factor.

Finally, it should be noted that our analysis only pertains to December and June solstice conditions at dawn and dusk and an investigation of the year-to-year progression of the longitudinal variability of the zonal wind during other seasons and local times needs to be performed in the future.

Data availability statement

Publicly available datasets were analyzed in this study. This data can be found here: https://earth.esa.int/eogateway/catalog/goce-thermosphere-data, https://doi.org/10.5281/zenodo.5541913, https://omniweb.gsfc.nasa.gov/form/dx1.html, https://www.cpc.ncep.noaa.gov/data/indices/.

Author contributions

IM and LS contributed to the conception and design of the study. IM conducted the analysis. All authors contributed to the article and approved the submitted version.

Funding

This research was partially supported by NASA Headquarters under the NASA Earth and Space Science Fellowship

Program (NESSF/FINESST), GRANT 80NSSC17K0431; National Science Foundation grant AGS-1651461 to Utah State University and NASA grant 80NSSC20K0191 to Utah State University.

Acknowledgments

The GOCE data used in this work are publicly available and provided by the European Space Agency (ESA) and can be found at https://earth.esa.int/eogateway/catalog/goce-thermosphere-data. We acknowledge use of NASA/GSFC's Space Physics Data Facility's OMNIWeb service to obtain the F10.7 cm radio flux and Kp index. We acknowledge the use of the ONI and QBO U30 index provided by the National Weather Service Climate Prediction Center. We gratefully acknowledge Dr J. Oberheide for making the Climatological Tidal Model of the Thermosphere freely available. The CTMT netCDF data files can be found at https://doi.org/10.5281/zenodo.5541913. Part of this work is included in IM's PhD dissertation, which can be found at https://digitalcommons.usu.edu/etd/8671/.

Conflict of interest

The authors declare that the research was conducted in the absence of any commercial or financial relationships that could be construed as a potential conflict of interest.

Publisher's note

Supplementary material

The Supplementary Material for this article can be found online at: https://www.frontiersin.org/articles/10.3389/fspas.2023.1214612/full#supplementary-material

References

Bamston, A. G., Chelliah, M., and Goldenberg, S. B. (1997). Documentation of a highly ENSO-related SST region in the equatorial pacific: research note. *Atmosphere-ocean* 35 (3), 367–383. doi:10.1080/07055900.1997.9649597

Bruinsma, S., and Biancale, R. (2003). Total densities derived from accelerometer data. *J. Spacecr. Rockets* 40 (2), 230–236. doi:10.2514/2.3937

Dhadly, M., Emmert, J., Drob, D., Conde, M., Doornbos, E., Shepherd, G., et al. (2017). Seasonal dependence of northern high-latitude upper thermospheric winds: A quiet time climatological study based on ground-based and space-based measurements. *J. Geophys. Res. Space Phys.* 122 (2), 2619–2644. doi:10.1002/2016ja023688

Dhadly, M. S., Emmert, J. T., Drob, D. P., Conde, M. G., Aruliah, A., Doornbos, E., et al. (2019). HL-TWiM empirical model of high-latitude upper thermospheric winds. *J. Geophys. Res. Space Phys.* 124 (12), 10592–10618. doi:10.1029/2019ja027188

Dhadly, M. S., Emmert, J. T., Jones, M., Jr, Doornbos, E., Zawdie, K. A., Drob, D. P., et al. (2020). Oscillations in neutral winds observed by GOCE. *Geophys. Res. Lett.* 47 (17), e2020GL089339. doi:10.1029/2020gl089339

Doornbos, E., Van Den Ijssel, J., Luhr, H., Forster, M., and Koppenwallner, G. (2010). Neutral density and crosswind determination from arbitrarily oriented multiaxis accelerometers on satellites. *J. Spacecr. Rockets* 47 (4), 580–589. doi:10.2514/1.48114

Forbes, J. M. (2007). Dynamics of the thermosphere. *J. Meteorological Soc. Jpn. Ser. II* 85, 193–213. doi:10.2151/jmsj.85b.193

Forbes, J. M., Oberheide, J., Zhang, X., Cullens, C., Englert, C. R., Harding, B. J., et al. (2022). Vertical coupling by solar semidiurnal tides in the thermosphere from ICON/MIGHTI measurements. *J. Geophys. Res. Space Phys.* 127 (5), e2022JA030288. doi:10.1029/2022ja030288

Forbes, J. M. (1996). Planetary waves in the thermosphere-ionosphere system. *J. geomagnetism Geoelectr.* 48 (1), 91–98. doi:10.5636/jgg.48.91

Forbes, J. M., Zhang, X., and Bruinsma, S. L. (2014). New perspectives on thermosphere tides: 2. Penetration to the upper thermosphere. *Earth, Planets Space* 66 (1), 122–211. doi:10.1186/1880-5981-66-122

Forbes, J. M., Zhang, X., and Bruinsma, S. (2012). Middle and upper thermosphere density structures due to nonmigrating tides. *J. Geophys. Res. Space Phys.* 117 (A11). doi:10.1029/2012ja018087

Forbes, J. M., Zhang, X., Hagan, M. E., England, S. L., Liu, G., and Gasperini, F. (2017). On the specification of upward-propagating tides for ICON science investigations. *Space Sci. Rev.* 212, 697–713. doi:10.1007/s11214-017-0401-5

Fritts, D. C., and Alexander, M. J. (2003). Gravity wave dynamics and effects in the middle atmosphere. *Rev. Geophys.* 41 (1). doi:10.1029/2001rg000106

Gasperini, F., Forbes, J. M., Doornbos, E. N., and Bruinsma, S. L. (2015). Wave coupling between the lower and middle thermosphere as viewed from TIMED and GOCE. *J. Geophys. Res. Space Phys.* 120 (7), 5788–5804. doi:10.1002/2015ja021300

Häusler, K., and Lühr, H. (2009). Nonmigrating tidal signals in the upper thermospheric zonal wind at equatorial latitudes as observed by CHAMP. *Ann. Geophys.* 27, 2643–2652. doi:10.5194/angeo-27-2643-2009

Immel, T. J., Sagawa, E., England, S. L., Henderson, S. B., Hagan, M. E., Mende, S. B., et al. (2006). Control of equatorial ionospheric morphology by atmospheric tides. *Geophys. Res. Lett.* 33 (15), L15108. doi:10.1029/2006gl026161

Jiang, , Guoying, , Xiong, C., Stolle, C., Xu, J., and Yuan, W. (2021). Comparison of thermospheric winds measured by GOCE and ground-based FPIs at low and middle latitudes. *J. Geophys. Res. Space Phys.* 126 (2), e2020JA028182.

Jones, M., Jr, Forbes, J. M., Hagan, M. E., and Maute, A. (2013). Non-migrating tides in the ionosphere-thermosphere: *in situ* versus tropospheric sources. *J. Geophys. Res. Space Phys.* 118 (5), 2438–2451. doi:10.1002/jgra.50257

Jones, M., Jr, Forbes, J. M., and Sassi, F. (2019). The effects of vertically propagating tides on the mean dynamical structure of the lower thermosphere. *J. Geophys. Res. Space Phys.* 124 (8), 7202–7219. doi:10.1029/2019ja026934

Kärräng, P. (2015). *Comparison of thermospheric parameters from space-and ground-based instruments (MS thesis)*. Kiruna, Sweden: Luleå University of Technology.

Lieberman, R. S., Akmaev, R. A., Fuller-Rowell, T. J., and Doornbos, E. (2013a). Thermospheric zonal mean winds and tides revealed by CHAMP. *Geophys. Res. Lett.* 40 (10), 2439–2443. doi:10.1002/grl.50481

Lieberman, R. S., Oberheide, J., and Talaat, E. R. (2013b). Nonmigrating diurnal tides observed in global thermospheric winds. *J. Geophys. Res. Space Phys.* 118 (11), 7384–7397. doi:10.1002/2013ja018975

Lindzen, R. S. (1981). Turbulence and stress owing to gravity wave and tidal breakdown. *J. Geophys. Res. Oceans* 86 (C10), 9707–9714. doi:10.1029/jc086ic10p09707

Liu, H., Doornbos, E., and Nakashima, J. (2016). Thermospheric wind observed by GOCE: wind jets and seasonal variations. *J. Geophys. Res. Space Phys.* 121 (7), 6901–6913. doi:10.1002/2016ja022938

Liu, H. L., Wang, W., Richmond, A. D., and Roble, R. G. (2010). Ionospheric variability due to planetary waves and tides for solar minimum conditions. *J. Geophys. Res. Space Phys.* 115 (A6). doi:10.1029/2009ja015188

March, G., Doornbos, E. N., and Visser, P. N. A. M. (2019a). High-fidelity geometry models for improving the consistency of CHAMP, GRACE, GOCE and Swarm thermospheric density data sets. *Adv. Space Res.* 63 (1), 213–238. doi:10.1016/j.asr.2018.07.009

March, G., Visser, T., Visser, P. N. A. M., and Doornbos, E. N. (2019b). CHAMP and GOCE thermospheric wind characterization with improved gas-surface interactions modelling. *Adv. Space Res.* 64 (6), 1225–1242. doi:10.1016/j.asr.2019.06.023

Miyahara, S., Yoshida, Y., and Miyoshi, Y. (1993). Dynamic coupling between the lower and upper atmosphere by tides and gravity waves. *J. Atmos. Terr. Phys.* 55 (7), 1039–1053. doi:10.1016/0021-9169(93)90096-h

Molina, I. (2022). *Variability of thermospheric zonal winds near dawn and dusk (PhD dissertation)*. Logan, Utah: Utah State University.

Molina, I., and Scherliess, L. (2023). Spatial and temporal correlations of thermospheric zonal winds from GOCE satellite observations. *Frontiers in Astronomy and Space Sciences* 10, 1214591.

Oberheide, J., Forbes, J. M., Häusler, K., Wu, Q., and Bruinsma, S. L. (2009). Tropospheric tides from 80 to 400 km: propagation, interannual variability, and solar cycle effects. *J. Geophys. Res. Atmos.* 114 (D1). doi:10.1029/2009jd012388

Oberheide, J., Forbes, J. M., Zhang, X., and Bruinsma, S. (2011). Climatology of upward propagating diurnal and semidiurnal tides in the thermosphere. *J. Geophys. Res. Space Phys.* 116 (A11). doi:10.1029/2011ja016784

Oberheide, J., Hagan, M. E., Richmond, A. D., and Forbes, J. M. (2015). "Atmospheric tides," in *Encyclopedia of atmospheric Sciences*. Second ed. China, (Academic Press), 287–297.

Oberheide, J., Hagan, M. E., and Roble, R. G. (2003). Tidal signatures and aliasing in temperature data from slowly precessing satellites. *J. Geophys. Res. Space Phys.* 108 (A2). doi:10.1029/2002ja009585

Sutton, E. K., Nerem, R. S., and Forbes, J. M. (2007). Density and winds in the thermosphere deduced from accelerometer data. *J. Spacecr. Rockets* 44 (6), 1210–1219. doi:10.2514/1.28641

Teitelbaum, H., and Vial, F. (1981). Momentum transfer to the thermosphere by atmospheric tides. *J. Geophys. Res. Oceans* 86 (C10), 9693–9697. doi:10.1029/jc086ic10p09693

Visser, T., March, G., Doornbos, E., De Visser, C., and Visser, P. (2019). Horizontal and vertical thermospheric cross-wind from GOCE linear and angular accelerations. *Adv. Space Res.* 63 (10), 3139–3153. doi:10.1016/j.asr.2019.01.030

Wang, W., Burns, A. G., and Liu, J. (2021). Upper thermospheric winds: forcing, variability, and effects. *Up. Atmos. Dyn. energetics*, 41–63. doi:10.1002/9781119815631.ch3

Warner, K., and Oberheide, J. (2014). Nonmigrating tidal heating and MLT tidal wind variability due to the El Niño–Southern Oscillation. *J. Geophys. Res. Atmos.* 119 (3), 1249–1265. doi:10.1002/2013jd020407

Yuan, T., Wang, J., Cai, X., Sojka, J., Rice, D., Oberheide, J., et al. (2014). Investigation of the seasonal and local time variations of the high-altitude sporadic Na layer (Nas) formation and the associated midlatitude descending E layer (Es) in lower E region. *J. Geophys. Res. Space Phys.* 119 (7), 5985–5999. doi:10.1002/2014ja019942

Zhang, K., Wang, W., Wang, H., Dang, T., Liu, J., and Wu, Q. (2018). The longitudinal variations of upper thermospheric zonal winds observed by the CHAMP satellite at low and midlatitudes. *J. Geophys. Res. Space Phys.* 123 (11), 9652–9668. doi:10.1029/2018ja025463

frontiers | Frontiers in Astronomy and Space Sciences

TYPE Opinion
PUBLISHED 10 October 2023
DOI 10.3389/fspas.2023.1200959

OPEN ACCESS

EDITED BY
Jaroslav Chum,
Institute of Atmospheric Physics (ASCR), Czechia

REVIEWED BY
Nickolay Ivchenko,
Royal Institute of Technology, Sweden

*CORRESPONDENCE
Dmytro Kotov,
dmitrykotoff@gmail.com

RECEIVED 05 April 2023
ACCEPTED 27 September 2023
PUBLISHED 10 October 2023

CITATION
Kotov D and Bogomaz O (2023), Hydrogen atoms near the exobase are cold: independent observations do not support the hot exosphere concept. *Front. Astron. Space Sci.* 10:1200959. doi: 10.3389/fspas.2023.1200959

Hydrogen atoms near the exobase are cold: independent observations do not support the hot exosphere concept

Dmytro Kotov[1]* and Oleksandr Bogomaz[1,2]

[1]Institute of Ionosphere, Kharkiv, Ukraine, [2]State Institution National Antarctic Scientific Center of the Ministry of Education and Science of Ukraine, Kyiv, Ukraine

KEYWORDS

atomic hydrogen, exobase, hot atoms, cold atoms, independent observations

1 Introduction

Atomic hydrogen (H) near the exobase (above ~500 km) is the primary source of neutral and charged particles for the two largest systems of near-Earth space–the geocorona and plasmasphere.

The H atoms near the exobase have long been considered to be in thermal equilibrium with the dense ambient atomic oxygen thermosphere. However, in their analysis of the GUVI satellite observations of dayside Lyman-α emission at low solar activity, Qin and Waldrop (2016) concluded that the exobase hydrogen atoms are extremely hot (~20,000 K), which is more than 20 times hotter than the oxygen thermosphere. This result contradicts the fundamental assumptions of existing geocoronal theories. Qin and Waldrop listed several possible sources of the hot H atoms and postulated that the high temperature is a consequence of incomplete collisional thermalization due to the low thermospheric oxygen density at solar minimum.

Here, we question the Qin and Waldrop conclusions on the basis of comparison with results from numerous different independent observations of temperature and density of atomic hydrogen and of hydrogen ion and electron densities. We show that those observations provide comprehensive evidence in favour of validity of classic cold hydrogen concept.

2 Comparison to observations by independent techniques

Obviously, the most solid evidence pro or contra hot hydrogen concept could be provided by independent measurements of the hydrogen atoms temperature near the exobase. Such observations were conducted for typical mid-latitudes during magnetically quiet periods and medium-to-high solar activity conditions by Mierkiewicz et al. (2012). The authors retrieved the atomic hydrogen temperatures near the exobase from the Balmer-α spectra data within 2 years for all the seasons. Their hydrogen temperature estimates (range from 710 K to 975 K) are two to three times smaller than one of Qin and Waldrop (~2200 K) and are close to the temperature of the ambient oxygen provided for the same location, dates, and altitudes by the well-tested NRLMSISE-00 model (Picone et al., 2002). This closeness evidences against the existence of a notable amount of much hotter H atoms near the exobase during medium-to-high solar activity conditions with a caveat that Mierkiewicz et al. temperatures were obtained for dawn and dusk while Qin and Waldrop estimates are for near-noon time. It

should be noted that no significant change of the H atoms temperature is expected from the noon towards dusk because (1) the ambient oxygen thermosphere changes are small from the noon towards the dusk (the temperature and density decrease by only several tens percent) and (2) lifetime of the exospheric H atoms is ~ 1 day as estimated by Hodges (1994) for the daytime hydrogen temperatures of the same order of magnitude as the estimates of Qin and Waldrop. These imply that, even if the hypothetical hotter H atoms are originated during the daytime, they do not leave the exosphere through the night and their chance to be cooled is not larger than during the day.

Another sensitive indicator of the correctness or incorrectness of the hot hydrogen concept is the H density at high altitudes in the exosphere. It is seen from Figure 2 b, e of the Qin and Waldrop paper that change of the classic cold hydrogen concept on the hot hydrogen concept increases the H density at an altitude of 20,000 km by a factor of ~ 5 for medium-to-high solar activity. For such conditions, H density at altitudes of ~ 20,000 km was retrieved from Lyman-α observations by the Dynamics Explorer 1 satellite (Rairden et al., 1986) and TWINS satellite (Zoennchen et al., 2015) and those estimates are close to ones obtained by Qin and Waldrop using cold hydrogen approach. It should be noted that both the analyses by Rairden et al. and Zoennchen et al. were also conducted assuming the cold hydrogen concept, i.e., the equality of the exobase hydrogen temperature to the temperature of oxygen thermosphere. Since this equality is supported by the above discussed H temperature observations of Mierkiewicz et al., the Dynamics Explorer 1 and TWINS H density estimates provides further support for correctness of the classical cold hydrogen concept.

For the solar minimum, for which Qin and Waldrop retrieved the largest temperatures of the H atom (~20,000 K), there are no independent observations of the H temperature. Thus, despite extreme sensitivity of the high-altitude exospheric H density to change of cold hydrogen assumption to hot one (see Figure 2 b, e of Qin and Waldrop paper), comparison with other observations employing cold hydrogen approach (Zoennchen et al., 2011; Zoennchen et al., 2013) cannot be useful to refute or support hot hydrogen concept.

Indirect support of validity of the classic cold hydrogen concept for solar minimum comes from numerous comparisons of the observed H^+ ion and electron densities in the topside ionosphere and plasmasphere with the results of simulations using physical model of the ionosphere-plasmasphere system (Kotov et al., 2015; Kotov et al., 2016; Kotov et al., 2018; Kotov et al., 2019; Panasenko et al., 2021; Kotov et al., 2023). Those plasma densities are quite sensitive to the H density near the exobase (Kotov et al., 2023) but insensitive to the H temperature because the O^++H reaction responsible to the densities is near thermo neutral (Fox and Sung, 2001). Comparison of the plasma density observations conducted using independent techniques and facilities for all seasons of two solar minima with the simulations shows that the physical model which uses the near-exobase H density corresponding to the classic cold hydrogen approach provides excellent agreement with the observations. Applying the hot hydrogen concept reduces the near-exobase H density by a factor of a ~ 3 to 4 at solar minimum (Figure 2 b, e of Qin and Waldrop paper). As follows from Kotov et al. (2023), with such small H density, simulated H^+ ion and electron density in the topside ionosphere and plasmasphere would be at least twice smaller than the observations.

3 Conclusion

The existence of large amounts of hot H atoms near the exobase is not supported either by independent observations of H atom temperature and density or by numerous observations of hydrogen ion and electron densities conducted with different independent techniques.

Conducted near the exobase, in the exosphere, ionosphere, and plasmasphere for various levels of solar activity, seasons, and geographical regions, these independent observations provide comprehensive support for the classic cold hydrogen concept.

Author contributions

DK proposed the idea and wrote the first draft of the manuscript. OB participated in the manuscript editing. All authors contributed to the article and approved the submitted version.

Funding

DK was supported by the National Academy of Sciences of Ukraine (project 0122U000187 “Investigation of variations in the ion composition of the topside ionosphere during the weak maximum of the 25th solar cycle”). OB was supported by the State Institution National Antarctic Scientific Center of the Ministry of Education and Science of Ukraine (project 0121U112420 “Investigation of machine learning applicability for detection of traveling ionospheric disturbances”).

Acknowledgments

The authors are grateful to every Ukrainian soldier, volunteer, medic, and personnel of the emergency and municipal services, and to all the Ukrainians whose fearless resistance to the genocidal war conducted by Russia allows Ukrainian scientists to do their usual peaceful job. DK says great thank you to: The dedicated team at the Institute of Ionosphere for their excellent research and important findings despite the war conditions. Phil Richards, University of Alabama in Huntsville, for his continuous support, and for sharing his expertise and the Field Line Interhemispheric Plasma model. Richard Hodges, Laboratory for Atmospheric and Space Physics, University of Colorado Boulder, for providing expert advice on the exosphere and for his unique works that helped to argue key explanation in this paper. Edwin Mierkiewicz, Embry-Riddle Aeronautical University, and Susan Nossal, University of Wisconsin-Madison, for their support and for the unique investigations that provided key support for the conclusions in this paper. NI whose thorough analysis of the manuscript

greatly improved the paper and made it more convincing and interesting.

Conflict of interest

The authors declare that the research was conducted in the absence of any commercial or financial relationships that could be construed as a potential conflict of interest.

Publisher's note

References

Fox, J. L., and Sung, K. Y. (2001). Solar activity variations of the Venus thermosphere/ionosphere. *J. Geophys. Res.* 106 (A10), 21305–21335. doi:10.1029/2001JA000069

Hodges, R. R. (1994). Monte Carlo simulation of the terrestrial hydrogen exosphere. *J. Geophys. Res. Space Phys*. doi:10.1029/94JA02183

Kotov, D., Richards, P. G., Reznychenko, M., Bogomaz, O., Truhlík, V., Nossal, S., et al. (2023). Interhemispheric ionosphere-plasmasphere system shows a high sensitivity to the exospheric neutral hydrogen density: A caution of the global reference atmospheric model hydrogen density. *Front. Astron. Space Sci.* 10, 1113706. doi:10.3389/fspas.2023.1113706

Kotov, D. V., Richards, P. G., Bogomaz, O. V., Chernogor, L. F., Truhlík, V., Emelyanov, L. Y., et al. (2016). The importance of neutral hydrogen for the maintenance of the midlatitude winter nighttime ionosphere: evidence from IS observations at Kharkiv, Ukraine, and field line interhemispheric plasma model simulations. *J. Geophys. Res. Space Phys.* 121, 7013–7025. doi:10.1002/2016JA022442

Kotov, D. V., Richards, P. G., Truhlík, V., Bogomaz, O. V., Shulha, M. O., Maruyama, N., et al. (2018). Coincident observations by the kharkiv IS radar and ionosonde, DMSP and arase (ERG) satellites, and FLIP model simulations: implications for the NRLMSISE-00 hydrogen density, plasmasphere, and ionosphere. *Geophys. Res. Lett.* 45, 8062–8071. doi:10.1029/2018GL079206

Kotov, D. V., Richards, P. G., Truhlík, V., Maruyama, N., Fedrizzi, M., Shulha, M. O., et al. (2019). Weak magnetic storms can modulate ionosphere-plasmasphere interaction significantly: mechanisms and manifestations at mid-latitudes. *J. Geophys. Res. Space Phys.* 124, 9665–9675. doi:10.1029/2019JA027076

Kotov, D. V., Truhlík, V., Richards, P. G., Stankov, S., Bogomaz, O. V., Chernogor, L. F., et al. (2015). Night-time light ion transition height behaviour over the Kharkiv (50°N, 36°E) IS radar during the equinoxes of 2006–2010. *J. Atmos. Sol. Terr. Phys.* 132, 1–12. doi:10.1016/j.jastp.2015.06.004

Mierkiewicz, E. J., Roesler, F. L., and Nossal, S. M. (2012). Observed seasonal variations in exospheric effective temperatures. *J. Geophys. Res.* 117, A06313. doi:10.1029/2011JA017123

Panasenko, S. V., Kotov, D. V., Otsuka, Y., Yamamoto, M., Hashiguchi, H., Richards, P. G., et al. (2021). Coupled investigations of ionosphere variations over European and Japanese regions: observations, comparative analysis, and validation of models and facilities. *Prog. Earth Planet Sci.* 8, 45. doi:10.1186/s40645-021-00441-8

Picone, J. M., Hedin, A. E., Drob, D. P., and Aikin, A. C. (2002). NRLMSISE-00 empirical model of the atmosphere: statistical comparisons and scientific issues. *J. Geophys. Res.* 107 (12), SIA. doi:10.1029/2002JA009430

Qin, J., and Waldrop, L. (2016). Non-thermal hydrogen atoms in the terrestrial upper thermosphere. *Nat. Commun.* 7, 13655. doi:10.1038/ncomms13655

Rairden, R. L., Frank, L. A., and Craven, J. D. (1986). Geocoronal imaging with Dynamics explorer. *J. Geophys. Res.* 91 (A12), 13613–13630. doi:10.1029/JA091iA12p13613

Zoennchen, J. H., Nass, U., and Fahr, H. J. (2015). Terrestrial exospheric hydrogen density distributions under solar minimum and solar maximum conditions observed by the TWINS stereo mission. *Ann. Geophys.* 33, 413–426. doi:10.5194/angeo-33-413-2015

Zoennchen, J. H., Bailey, J. J., Nass, U., Gruntman, M., Fahr, H. J., and Goldstein, J. (2011). The TWINS exospheric neutral H-density distribution under solar minimum conditions. *Ann. Geophys* 29, 2211–2217. doi:10.5194/angeo-29-2211-2011

Zoennchen, J. H., Nass, U., and Fahr, H. J. (2013). Exospheric hydrogen density distributions for equinox and summer solstice observed with TWINS1/2 during solar minimum. *Ann. Geophys.* 31, 513–527. doi:10.5194/angeo-31-513-2013

frontiers | Frontiers in Astronomy and Space Sciences

TYPE Correction
PUBLISHED 07 November 2023
DOI 10.3389/fspas.2023.1320143

OPEN ACCESS

EDITED AND REVIEWED BY
Jaroslav Chum,
Institute of Atmospheric Physics (ASCR), Czechia

*CORRESPONDENCE
Dmytro Kotov,
dmitrykotoff@gmail.com

RECEIVED 11 October 2023
ACCEPTED 27 October 2023
PUBLISHED 07 November 2023

CITATION
Kotov D and Bogomaz O (2023), Corrigendum: Hydrogen atoms near the exobase are cold: independent observations do not support the hot exosphere concept.
Front. Astron. Space Sci. 10:1320143.
doi: 10.3389/fspas.2023.1320143

Corrigendum: Hydrogen atoms near the exobase are cold: independent observations do not support the hot exosphere concept

Dmytro Kotov[1]* and Oleksandr Bogomaz[1,2]

[1]Institute of Ionosphere, Kharkiv, Ukraine, [2]State Institution National Antarctic Scientific Center of the Ministry of Education and Science of Ukraine, Kyiv, Ukraine

KEYWORDS

atomic hydrogen, exobase, hot atoms, cold atoms, independent observations

A Corrigendum on
Hydrogen atoms near the exobase are cold: independent observations do not support the hot exosphere concept

by Kotov D and Bogomaz O (2023). Front. Astron. Space Sci. 10:1200959. doi: 10.3389/fspas.2023.1200959

In the published article, there was an error. There was a typo in **2 Comparison to observations by independent techniques**, paragraph 2, in which "hot" was used instead of "cold". The correct sentence appears below:

"It should be noted that both the analyses by Rairden et al. and Zoennchen et al. were also conducted assuming the cold hydrogen concept, i.e., the equality of the exobase hydrogen temperature to the temperature of oxygen thermosphere."

In the published article, there was an error. There was a typo in **2 Comparison to observations by independent techniques**, paragraph 3 in which the word "of" was used instead of "or". The corrected sentence appears below:

"Thus, despite extreme sensitivity of the high-altitude exospheric H density to change of cold hydrogen assumption to hot one (see Figure 2 b, e of Qin and Waldrop paper), comparison with other observations employing cold hydrogen approach (**Zoennchen et al., 2011**; **Zoennchen et al., 2013**) cannot be useful to refute or support hot hydrogen concept."

The authors apologize for these errors and state that this does not change the scientific conclusions of the article in any way. The original article has been updated.

Publisher's note

All claims expressed in this article are solely those of the authors and do not necessarily represent those of their affiliated organizations, or those of the publisher, the editors and the reviewers. Any product that may be evaluated in this article, or claim that may be made by its manufacturer, is not guaranteed or endorsed by the publisher.

frontiers | Frontiers in Astronomy and Space Sciences

TYPE Original Research
PUBLISHED 13 October 2023
DOI 10.3389/fspas.2023.1240081

OPEN ACCESS

EDITED BY
Dimitry Pokhotelov,
German Aerospace Center (DLR),
Germany

REVIEWED BY
Joachim Vogt,
Jacobs University Bremen, Germany
Ildiko Horvath,
The University of Queensland, Australia

*CORRESPONDENCE
Elena A. Kronberg,
kronberg@geophysik.uni-muenchen.de

RECEIVED 14 June 2023
ACCEPTED 26 September 2023
PUBLISHED 13 October 2023

CITATION
Maetschke KN, Kronberg EA, Partamies N and Grigorenko EE (2023), A possible mechanism for the formation of an eastward moving auroral spiral.
Front. Astron. Space Sci. 10:1240081.
doi: 10.3389/fspas.2023.1240081

A possible mechanism for the formation of an eastward moving auroral spiral

Katharina N. Maetschke[1], Elena A. Kronberg[1]*, Noora Partamies[2] and Elena E. Grigorenko[3,4]

[1]Department of Earth and Environmental Sciences, Ludwig-Maximilians-Universität München, Munich, Germany, [2]Department of Arctic Geophysics, University Centre in Svalbard (UNIS), Longyearbyen, Norway, [3]Space Research Institute, Russian Academy of Sciences, Moscow, Russia, [4]Moscow Institute of Physics and Technology, Moscow, Russia

The generation process of auroral spirals is described by different theories varying for their morphology and surrounding conditions. Here, a possible mechanism is proposed for an eastward moving auroral spiral, which was observed in Tromsø, Norway, during the expansion phase of a substorm on 18 September 2013. Measurements from the THEMIS-A and Cluster spacecraft were analyzed, which were located up to ~10 R_E duskward from the spiral generator region in the magnetosphere. Precursory to the spiral observation, concurrent magnetic field dipolarizations, flow bursts and electron injections were measured by the Cluster satellites between 13.6 and 14.2 R_E radial distance from Earth. A local Kelvin-Helmholtz-like vortex street in the magnetic field was detected at the same time, which was likely caused by bursty bulk flows. The vortex street was oriented approximately in the X-Y (GSE) plane and presumably propagated towards the source region of the spiral due to a high dawnward velocity component in the flow bursts. The observations suggest that the spiral can have been generated by an associated vortex in the magnetotail and then mapped along the magnetic field lines to the ionosphere. To better understand the role of the ionosphere in auroral spiral generation, in future more mesoscale observations are required.

KEYWORDS

auroral spiral, bursty bulk flows, Kelvin-Helmholtz instability, substorm, aurora

1 Introduction

As the optical manifestation of atmospheric ionization through precipitating electrons from the magnetosphere, auroral arcs are commonly observed as narrow bands in the nightside auroral oval. They can, however, reshape and distort into numerous small- and meso-scale structures, among those auroral spirals (Paschmann et al., 2003). An auroral spiral can occur as an individual structure or in a vortex street with multiple spirals (Hallinan, 1976). On average they have diameters of 25–75 km (Partamies et al., 2001b), but can reach sizes up to 1,300 km and thereby they are the largest vortical forms found in an auroral arc (Davis and Hallinan, 1976). As stated by Partamies et al. (2001b), spirals develop primarily during quiet magnetospheric conditions. In the course of a substorm, they occur mainly during the expansion and beginning of the recovery phase (Hallinan, 1976).

Partamies et al. (2001b) observed that the drift motion of auroral spirals coincides with the direction of the ionospheric convection. As viewed from above in the northern

hemisphere, auroral spirals wind in a counterclockwise direction around upward field-aligned currents (FACs). Increased auroral precipitation in the FACs connected to brighter aurora is correlated with the winding of the spiral, while its brightness decreases with unwinding (Partamies et al., 2001b). Instead of unwinding, spirals can also decay into patchy auroral structures (Davis and Hallinan, 1976). While the auroral spiral was subject to several ground observations (Davis and Hallinan, 1976; Partamies et al., 2001b) and theoretical approaches (Hallinan, 1976; Partamies et al., 2001a), correlated space and ground measurements as performed by Keiling et al. (2009b) have rarely been done. This is due to a lack of events during which satellites were positioned in a magnetospheric region conjunct by magnetic field lines with the region of a spiral observation. Therefore, the exact generation mechanism and location, which may also vary for different magnetospheric states, is not yet established. In this paper we study an eastward moving spiral event with space measurements and propose a spiral generation mechanism following from the theory by Keiling et al. (2009b).

2 Observations

2.1 Ground-based

2.1.1 Auroral spiral

At 22:58 UT on 18 September 2013, an auroral spiral (see Figure 1 22:58 UT) was observed in Tromsø, Norway (67.176° and 115.627° geomagnetic latitude and longitude). The auroral arc along with the spiral was moving approximately towards east (see Figure 1) with the spiral itself exhibiting anti-clockwise rotation. The sense of rotation here is defined as viewed from above. From Figure 1 22:58 UT, the spiral was estimated to have a diameter of approximately 189 ± 45 km. This estimation was made by determining the zenith angle for the far (72 ± 3°) and near end (50 ± 2°) of the spiral by comparing the positions of star constellations in the photograph with the astronomy software Stellarium (Version 23.2, Zotti et al. (2021)). These angles were then used for trigonometric calculations, taking the auroral spiral to be in an approximate height of 100 km and thus reaching a diameter value of 189 ± 45 km. The spiral was observed during the expansion phase of a substorm. The onset of this substorm was taking place at approximately 22:20 UT, marked by a sharp growth of the AE index to values of ~500 nT. The expansion phase lasted until about 23:40 UT, when the IMF turned from an entirely southward orientation to exhibiting northward peaks and the AE index decreased rapidly. No records of the duration of the spiral display or its development and decay could be obtained. At 23:27 and 23:34 UT, the photographs in Figure 1 show east-west aligned decreasing auroral activity coinciding with the end of the expansion phase.

2.1.2 Equivalent ionospheric currents

Equivalent ionospheric currents ($\mathbf{J}_{eq}$) here are defined as sheet currents that generate magnetic field variations at the Earth's surface that are equivalent to the measured ground horizontal field perturbations (Untiedt and Baumjohann, 1993). With the simplified assumptions that the currents flow near the Earth's surface, approximated as a plane, the equivalent ionospheric currents can be defined as $\mathbf{J}_{eq} = \hat{\mathbf{z}} \times \mathbf{B}_h$ times unit surface area. The vector $\mathbf{B}_h$ represents the horizontal magnetic disturbance and $\hat{\mathbf{z}}$ is the unit vector that points vertically downward. This equation then corresponds to $\mathbf{J}_{eq}$ being equal to the horizontal magnetic field vector rotated 90° clockwise (Untiedt and Baumjohann, 1993).

$\mathbf{J}_{eq}$ directions as seen in Figure 2 were retrieved from 10 s IMAGE magnetometer data by the Spherical Elementary Current System (SECS) method as described by Juusola et al. (2016). Three time steps around the observation of the auroral spiral (22:58 UT) are shown. Tromsø was located in the westward current region with magnitudes of ~500 A km^{-1}. The field of view from Tromsø with a zenith angle of 72° is marked by a green dotted ellipse in the middle panel of Figure 2. There, the solid green ellipse shows an estimate of the spiral size with 189 ± 45 km in diameter. The spiral thus occurred in the region of downward field-aligned currents. During the occurrence of the optical auroral spiral, no equivalent ionospheric current vortices could be identified and the currents did not vary much in strength or direction throughout the shown time interval.

2.2 Cluster and THEMIS measurements

Measurements from three of the Cluster spacecraft (in the following called Cl1, Cl2 and Cl4) and the THEMIS-A (TH-A) satellite were obtained from Cluster Science Archive (Laakso et al., 2010) and NASA CDAweb, respectively. At the time of the spiral observation the Cluster and THEMIS-A spacecraft were positioned in the magnetotail (see Figure 3). The retrieved magnetic field measurements, plasma flow velocity and electron **flux, temperature and density** are displayed in Figure 4 for the time period of 22:40 UT to 23:10 UT.

The magnetic field (see Figures 4A–D) measured by FGM instruments shows dipolarization signatures for the Cluster spacecraft starting from ~22:54 UT. The Cl1 data show a short peak in the B_Z component around 22:55 UT, then a longer lasting increase with further peaks of the B_Z component at 22:57 UT. These signatures known as dipolarizations are understood as the change of the magnetotail field from a stretched to a more dipolar configuration. Cl4 shows less distinct signatures than Cl1 around 22:55 UT, but also a peak of the B_Z component at 22:57 UT. The satellite located farthest from Earth, Cl2, shows less variation than the other Cluster spacecraft in all magnetic field components, but also enhancements at 22:57 UT. In the TH-A magnetic field data no large perturbations are visible over the whole regarded time period. The Y component is near zero for the whole interval with a slight increase at ~22:53 UT. The X and Z components constantly decrease from 22:40 UT to 23:10 UT.

The plasma flow velocities (see Figures 4E, F) were obtained from measurements by the Cl4 CIS-CODIF instrument and the TH-A ESA instrument. For the examined time interval, only the Cl4 CIS-CODIF instrument was operational. Enhanced quasi-periodical plasma flows can be discerned in its data from ~22:50 to ~22:58 UT. With a period of ~2 min, the velocity in X direction (GSE) increases repeatedly to over ~500 km s^{-1} before receding to ~0 km s^{-1}. The Y component shows the same development, with peak velocities of up to ~500 km s^{-1} in negative Y direction (GSE). From about 2 min before the development of the optical auroral spiral in Tromsø, the deviations in X and negative Y direction (GSE)

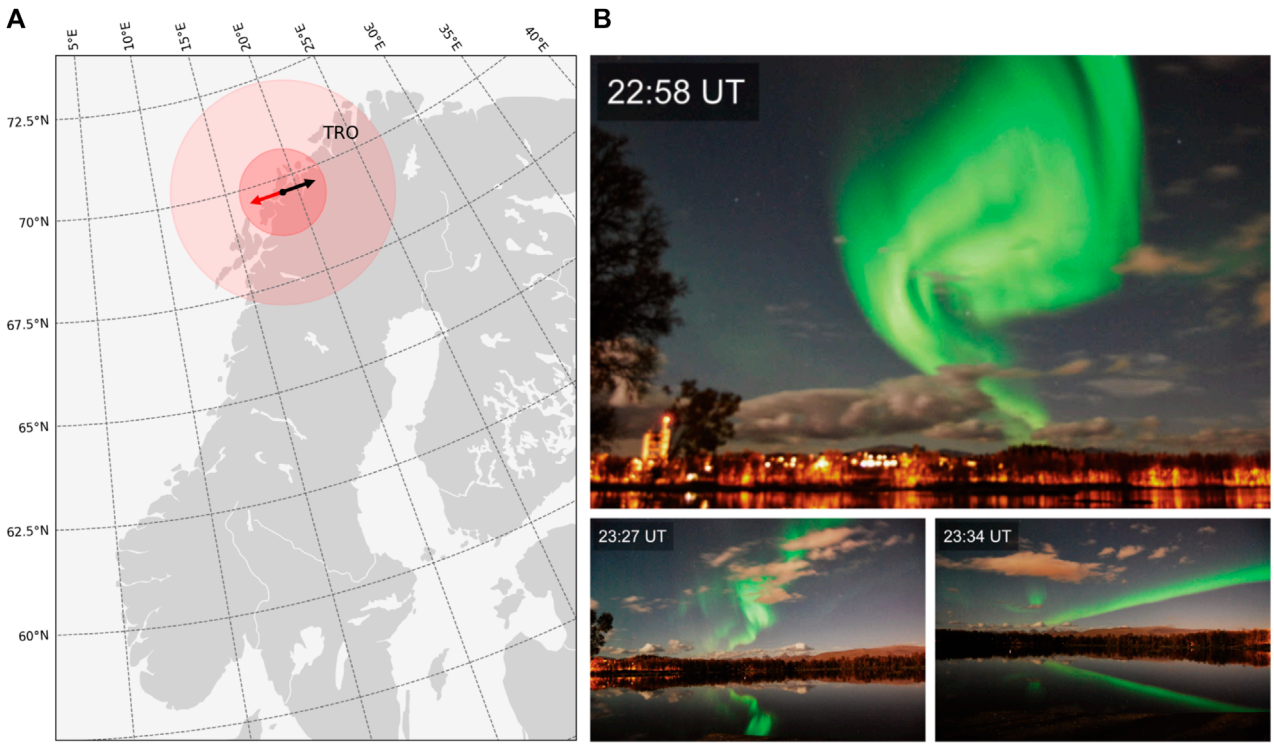

FIGURE 1
(A) Map showing the location of the spiral observation with the red circles marking the field of view from Tromsø with zenith angles of 50° and 72° mapped to an altitude of 100 km. The approximate line of sight is shown by the red arrow, while the direction of auroral movement is marked with the black arrow. The map was made using *cartopy* (Met Office, 2010 - 2015). **(B)** Photographs of the aurora taken in Tromsø on 18 September 2013 (E. Kronberg, personal communication, 22 March 2021). **22:58 UT:** Auroral spiral formation. **23:27 UT** and **23:34 UT:** decreasing auroral activity with increasingly quiet auroral arcs.

were most pronounced and the Z component showed enhanced flows of up to ~500 km s^{-1}. TH-A measured plasma flow that was slower than the Cl4 flow by one order of magnitude. Flow enhancements in the TH-A data starting at ~22:49 UT can be seen in Figure 4F, which approximately concurs with the start of the high-speed flows visible in the Cluster data. The TH-A plasma velocity fluctuated between ~40 km/s in positive and negative X directions (GSE). The Y component also fluctuated with peak velocities of ~40 km s^{-1} and ~70 km s^{-1} in dawn and dusk direction, respectively. These deviations in the TH-A flow velocity last only up to ~22:56 UT.

The electron flux data from the Cluster RAPID instrument and the TH-A SST instrument is shown in Figures 4G–J. In the Cl2 data plots, strong signatures of dispersionless electron injections are discernible around 22:57 UT. Only the TH-A electron flux measurements with good data quality are displayed. The presented energy levels are not equal, but comparable to the Cluster energy channels. In the intervals where data with good quality was available, no variations in electron flux can be observed, while for the time of most interest no measurements are available.

In the interval between 22:49—22:56 UT the Cl1 electron total temperature and density (Figures 4J, K) measured by the PEACE instrument show quasi-periodical spikes in the electron density at the same time as sharp dips in the temperature. This dense and cold plasma alternates periodically with depleted and hot plasma, which is a typical signature of Kelvin-Helmholtz vortices (Hasegawa et al., 2009).

Overall, the Cluster data show deviations in all observed parameters up to 9 min precursory of the development of the visible auroral spiral in Tromsø.

3 Methods

3.1 Mapping

To correlate the spiral observations with their respective source regions in the magnetosphere, magnetic field line mapping was applied. Firstly, to determine the ionospheric footprints of the Cluster and TH-A satellites for the 18 September 2013 substorm, and, in particular, the time of the auroral spiral observation (22:58 UT). Secondly, a possible source region of the spiral was determined to evaluate if the structures observed by the spacecraft can have been correlated with the auroral spiral.

For these processes, the Python-based module *IrbemPy*, which is based on the *IRBEM-lib* library (Boscher et al., 2010) was used. It is part of the Python package *SpacePy* (Morley et al., 2010). As input options for the computation, the International Geomagnetic Reference Field (Erwan et al., 2015) was chosen as the internal magnetic field model and set to be updated on 18 September 2013.

10.3389/fspas.2023.1240081

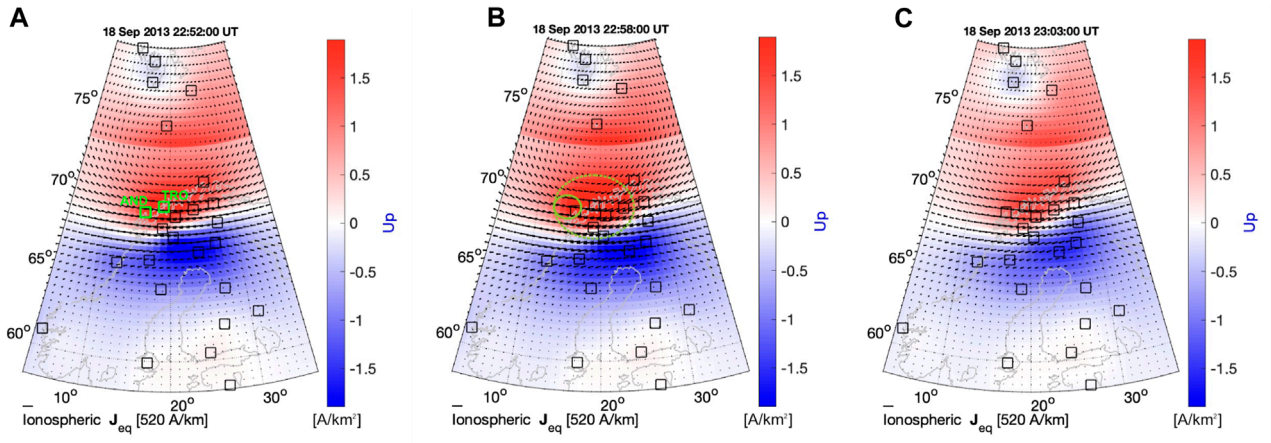

FIGURE 2
Direction of equivalent ionospheric currents ($\mathbf{J}_{eq}$) shown as black arrows derived from IMAGE magnetometer stations (black squares) around the time of the auroral spiral. Colors depict the curl of equivalent currents, which is an estimate for field-aligned currents (FAC). **(A)** 22:52 UT, **(B)** 22:58 UT and **(C)** 23:03 UT. The dotted green ellipse marks the region of field of view from Tromsø with zenith angle 72°. The solid green ellipse shows an estimate for the size of the optical auroral spiral.

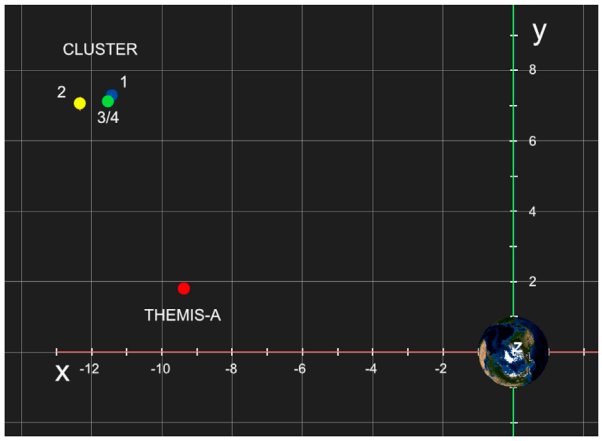

FIGURE 3
Position of the Cluster and THEMIS-A satellites at the time of the auroral spiral observation.

As the external magnetic field model, the Tsyganenko 1996 (T96) (Tsyganenko, 1995; Tsyganenko, 1996) magnetospheric model as stated below was selected. It was chosen above newer models, because it is also used in similar research (e.g., Keiling et al. (2009a)) and the T02 and T05 models primarily represent stormy or quiet conditions, while the here regarded event occurred during a substorm (Tsyganenko, 2002; Tsyganenko and Sitnov, 2005). For the mapping, the hourly values of the Kp, Dst and AL indices, as well as the solar wind density, velocity and dynamic pressure and the IMF B_Y and B_Z components were obtained from the NASA/GSFC's OMNI data set through the *OMNI* module (Morley et al., 2010).

3.1.1 Ionospheric footprints

The footprints of the magnetic field lines conjunct with the Cluster and TH-A spacecraft were derived using *IrbemPy* and position data retrieved from the Cluster Science Archive and NASA CDAweb. They are defined here as intercept points of these field lines and the ionosphere at an altitude of 100 km in the northern hemisphere. From 21:00 UT to 02:00 UT, the footprints lie in the area of the auroral oval in the dusk sector (see Figure 5). At 22:58 UT, the time of the auroral spiral observation, the footprints are located at longitudinal distances from Tromsø of ~68° for Cluster and ~34° for TH-A. The results from T96 were compared with newer models for quiet and stormy conditions (T02 and T05). These models delivered no footprints for the northern hemisphere for the time interval of 21 UT to ~23 UT, placing the satellites on open field lines that were only connected to the southern hemisphere. These different results can be due to all these models not well representing substorm conditions of the magnetosphere and the area in which the satellites were located.

3.1.2 Spiral generator region

A possible magnetospheric generator region of the auroral spiral was derived with the constraint of it being conjunct with Tromsø by a magnetic field line. As explained below, the Cluster satellites observed Kelvin-Helmholtz vortices and it is suggested that after encountering the satellites these vortices possibly traveled to the generator region mentioned here, where they mapped down to the ionosphere to produce the optical spiral. Starting from the location of the Cl4 satellite at 22:58 UT, the coordinates were iteratively varied until their footprint was located in a radius of less than 50 km around Tromsø using the T96 model and *IrbemPy*. A potential source region of the spiral is thus located at around $X_{GSE} = -3.8\ R_E$, $Y_{GSE} = -1.7\ R_E$ and $Z_{GSE} = 2.4\ R_E$. The absolute distance of this area to the Cluster satellites amounts to ~12.1 R_E.

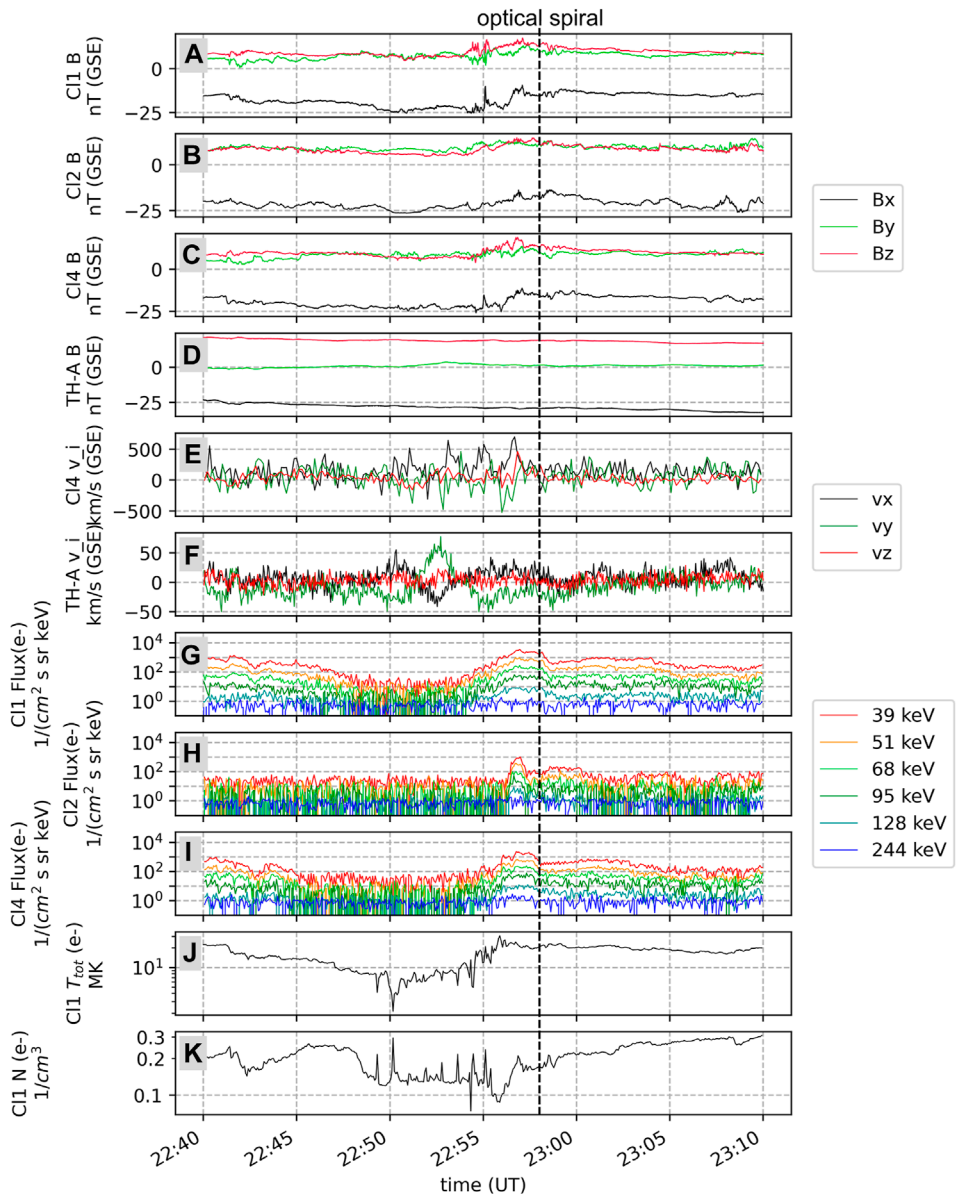

FIGURE 4
Data from Cl1, Cl2, Cl4 and TH-A on 18 September 2013 from 22:40 to 23:10 UT. **(A–D)** magnetic field measured by FGM instruments. **(E, F)** plasma flow velocities derived from data from CIS (Cluster) and ESA (TH-A) instruments. **(G–I)** electron flux for a range of energies measured by the Cluster RAPID instruments. **(J, K)** total electron temperature and density from the Cl1 PEACE instrument. The vertical dotted line shows the time of the spiral observation on the ground (22:58 UT). The data was retrieved from the Cluster Science Archive and NASA CDAweb.

3.2 Minimum variance analysis

To suitably display and analyze the spacecraft data in a local spacecraft coordinate system, Minimum Variance Analysis (MVA) as first proposed by Sonnerup and Cahill Jr (1967), was performed on the magnetic field and ion velocity data sets of Cl1, Cl2, Cl4 and TH-A. For TH-A the results of this method are not presented in the following, because the weak structures it detected were better displayed in the GSE coordinate system.

The method of MVA used here was derived from Sonnerup and Scheible (1998); Dunlop et al. (1995). In the time interval from 22:40 UT to 23:10 UT, the times of the maximum in the B_Z (GSE) component of the Cluster magnetic field measurements were identified. For Cl1 the maximum was at 22:57:06 UT, for Cl2 at 22:57:37 UT and for Cl4 at 22:56:45 UT. A time period of 10 min symmetrically around 22:57:26 UT was selected for all Cluster satellites, this being the medium point in time between the Cl4 and Cl2 B_Z maximum values. This interval was used for MVA calculations for each satellite to enable comparisons and showed reasonably good results for all three spacecraft.

The calculated eigenvalues and eigenvectors of the magnetic variance matrix (Dunlop et al. (1995); Sonnerup and Scheible, 1998)

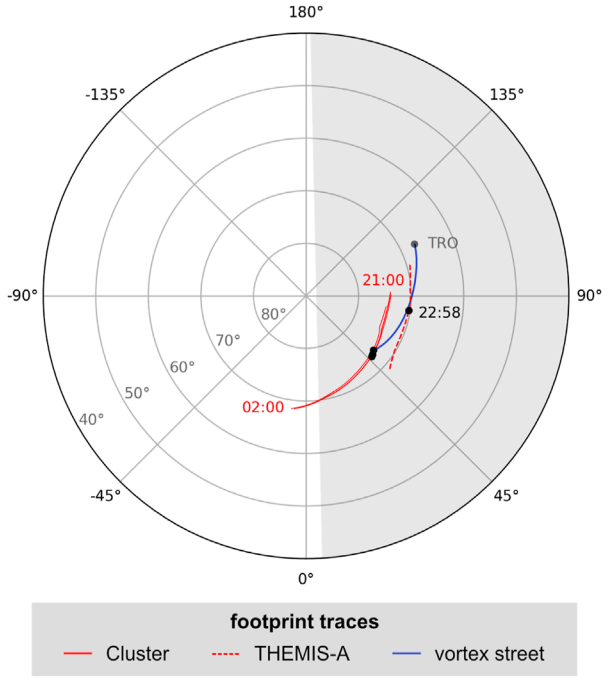

FIGURE 5
Ionospheric footprints of the Cl1, Cl2, Cl4 and TH-A spacecraft on 18/19 September 2013 plotted onto a geomagnetic grid with marked terminator for 22:58 UT. The red lines show the ionospheric footprints from 21:00 UT to 02:00 UT. For the time of the visible auroral spiral (22:58 UT) the footprints are designated with a black dot. Tromsø is marked with a gray dot. The blue line marks the propagation of the observed vortex street toward the spiral source region.

TABLE 1 Values from the Minimum Variance Analysis for an interval of 10 min around 22:57:26 UT performed on the Cluster magnetic field data.

Spacecraft	Eigenvalues	λ_2/λ_3	Eigenvectors
	$\lambda_1 = 20.903$		$\mathbf{l} = (-0.90135, -0.24720, -0.35561)^\top$
Cluster 1	$\lambda_2 = 3.7416$	1.9957	$\mathbf{m} = (-0.34066, -0.10234, 0.93460)^\top$
	$\lambda_3 = 1.8748$		$\mathbf{n} = (0.267429, -0.96354, -0.008031)^\top$
	$\lambda_1 = 13.487$		$\mathbf{l} = (-0.71043, -0.26996, -0.64993)^\top$
Cluster 2	$\lambda_2 = 2.2337$	3.4934	$\mathbf{m} = (-0.60200, 0.71145, 0.36252)^\top$
	$\lambda_3 = 0.63941$		$\mathbf{n} = (-0.36453, -0.64881, 0.66796)^\top$
	$\lambda_1 = 18.686$		$\mathbf{l} = (-0.80643, -0.14959, -0.57210)^\top$
Cluster 4	$\lambda_2 = 2.8776$	2.5889	$\mathbf{m} = (-0.59093, 0.16811, 0.78901)^\top$
	$\lambda_3 = 1.1115$		$\mathbf{n} = (-0.02185, 0.97435, -0.22396)^\top$

are listed in Table 1. The eigenvalues of the variance matrix describe the deviations of the field in the respective field directions, with the eigenvector **n** of the smallest eigenvalue (λ_3) pointing in the expected direction of the boundary normal (Sonnerup and Scheible, 1998). The ratio λ_2/λ_3 is a measure for the quality of the direction estimates. Dunlop et al. (1995) give values of two to three for the λ_2/λ_3 ratio as a typical guideline. Here, the λ_2/λ_3 ratios were ~2.0 for Cl1, ~3.5 for Cl2 and ~2.6 for Cl4 (see Table 1). As can be seen, the variance matrix is nearly degenerate for the three satellites, i.e., $\lambda_3 \simeq \lambda_2$. The boundary normal **n** is therefore not very well defined, although the eigenvector **l** is a good representation of a tangential direction to the boundary layer (Sonnerup and Scheible, 1998). According to Sonnerup and Scheible (1998), for near-degenerate cases, the eigenvectors **m** and **n** are prone to permute when modifying the time period for the calculation. As stated by Sonnerup and Scheible (1998) and Song and Russell (1999), this can be analyzed by executing the above method with different nested time intervals between 22:40 and 23:10 UT. All other time periods essentially showed similar λ_2/λ_3 ratios and highly changing directions of the eigenvectors **m** and **n** implying that the observed structure is 3-dimensional. The MVA in this case is not applicable.

For identification of the vortical structures in the magnetic field and ion flow velocity we can use an arbitrary orthogonal coordinate system. We have decided to use the one obtained above because it is orthogonal according to the dot product between the eigenvectors.

The axes of the resulting LMN system are shown in Figure 6 with respect to the GSE coordinate system. The axes are defined so that the basis vectors **l**, **m** and **n** are parallel to the equivalent L, M and N axes. As can be seen, the direction of maximum variance **l** coincides approximately with the X (GSE) direction for all three Cluster satellites. However, the orientation of **m** and **n** varies for the satellites because the moving structure is 3D.

The transformed magnetic field and ion flow velocity were projected to the L-M plane of the LMN coordinate system (see Figure 7). The TH-A data was accordingly projected to the X-Y (GSE) plane for the whole time period of 22:40 to 23:10 UT (see Figure 8). The Cluster magnetic field vector projections show rotational signatures in the time interval of 22:56 to 22:59 UT. Cl2, the most remote satellite, shows three major variations in sign of the B_L component. Cl1 and Cl4, which were located closer together and nearer to Earth than Cl2, show one rotational signature coinciding with the first change of sign for the Cl2 B_L component. For Cl1, which was closest to Earth, the signature is weaker than for Cl4. The vector projection of the plasma velocity does not show changes in sign for the v_L component, but a change in the predominant v_M direction in the time interval from 22:57 to 22:59 UT. The TH-A magnetic field data shows a change of sign of the B_Y component around 22:57 UT. Its plasma velocity also shows major variations of the v_Y component to positive and then negative values in the time period of 22:52 to 22:55 UT.

4 Discussion

On 18 September 2013 at 22:58 UT, an auroral spiral was observed in Tromsø during the expansion phase of a substorm. Simultaneously, measurements in the magnetotail by three Cluster and the THEMIS-A spacecraft were obtained.

The three Cluster spacecraft measured strong variations in the magnetic field components, the plasma flow velocity and the electron flux approximately 1–2 min prior to the spiral development in Tromsø (see Figure 4). The plasma flow velocity from Cl4 over a time interval of 8 min showed quasi-periodic peaks in velocity up to ~500 km s^{-1} in X and Y directions.

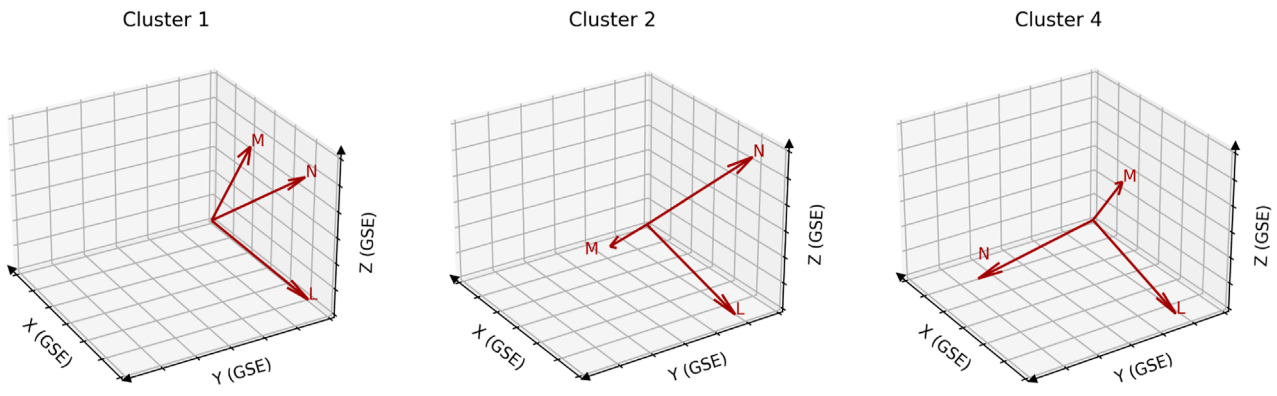

FIGURE 6
Axes of the LMN coordinate system (shown in red) with respect to the GSE coordinate system for the three used Cluster spacecraft.

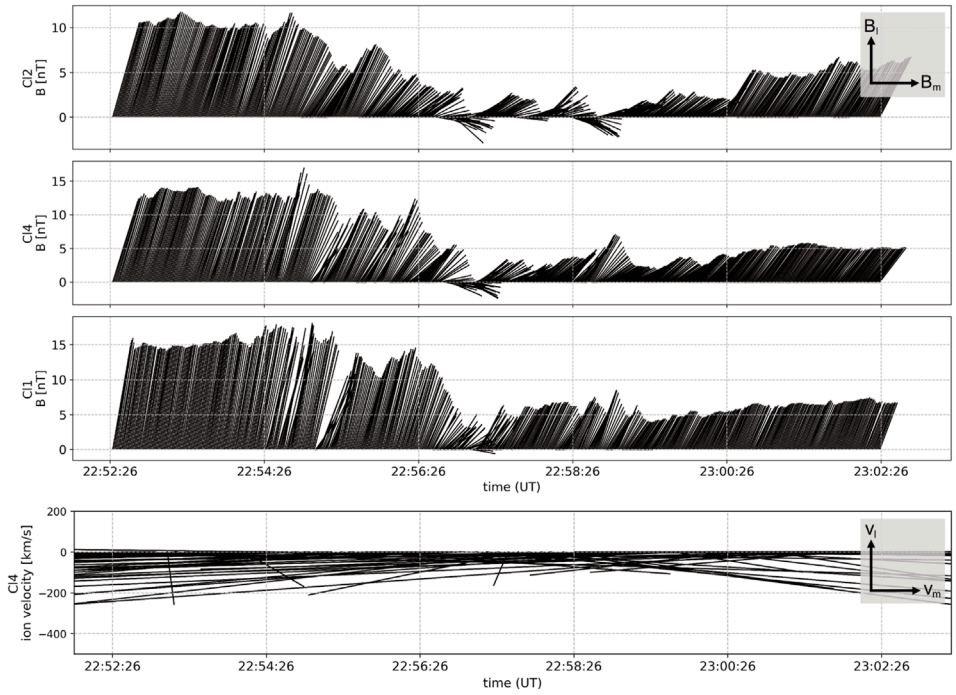

FIGURE 7
Magnetic field vectors of Cl2, Cl4 and Cl1 in this order and plasma velocity vectors from Cl4 projected onto the L-M plane of the LMN coordinate system *versus* time for a time interval containing the observation of the optical auroral spiral.

These measurements correspond to the signatures of bursty bulk flows with intermittent flow bursts (Angelopoulos et al., 1992). As they commonly are (Paschmann et al., 2003), these bursty bulk flows were accompanied by dipolarization signatures seen in the B_Z magnetic field components. The vector plots of the Cluster magnetic field projected onto the L-M plane of the local LMN coordinate system, which varies for each spacecraft, also show vortical signatures (see Figure 7). Cl2 encountered a magnetic field vortex street approximately oriented in the X-Y plane (GSE) with opposed rotating vortices on either side of its trajectory, as shown in Figure 9. Cl1 and Cl4 only measured a pair of opposed rotating vortices located roughly in the X-Z plane (GSE). Cl1 and Cl4 were positioned close together, so it is likely that they observed the same pair of magnetic field vortices.

If the frozen-in condition is valid, it is expected that the magnetic field vortices are connected to plasma flow vortices. The plasma flow velocity observed by Cl4 exhibited a change of direction at the occurrence of the magnetic field vortices, which suggests a vortical structure. Clear signatures of plasma vortices were not detected by the Cl4 spacecraft, likely because the CIS instrument used to measure the plasma velocity has a time resolution of ~4 s. The

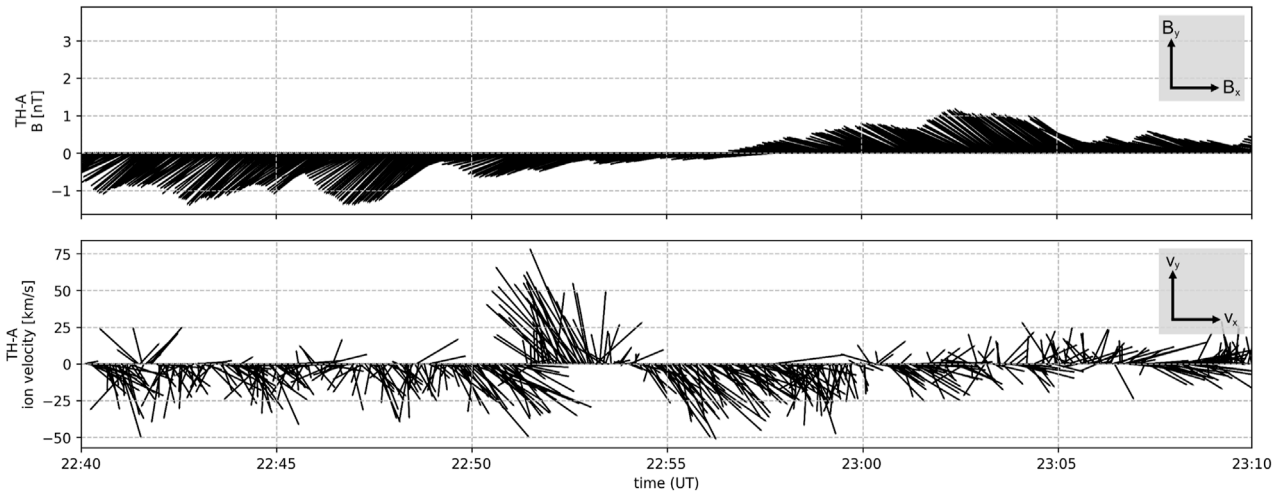

FIGURE 8
Magnetic field vectors and plasma velocity vectors from TH-A projected onto the X-Y plane (GSE) *versus* time for a time interval containing the observation of the optical auroral spiral.

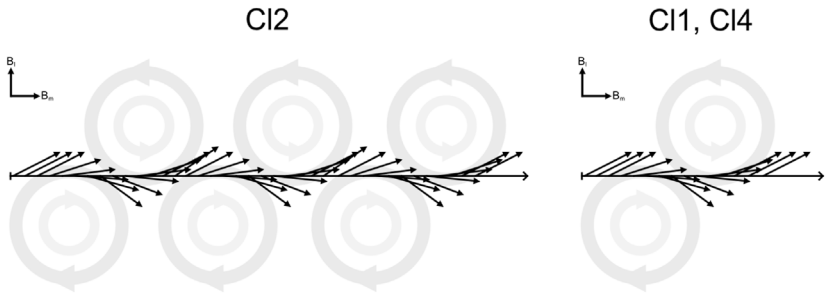

FIGURE 9
Illustration of the magnetic field vortices that can have caused the obtained vector measurements from Cl2, Cl1 and Cl4 shown in the L-M plane of the local spacecraft coordinate system LMN and along an idealized satellite trajectory.

magnetic field vortices however occurred at a temporal scale of ~30 s.

These magnetic field vortices were probably associated with the bursty bulk flows that were also measured by Cl4. Bursty bulk flows are known to cause vortical structures in plasma flow in the X-Y (GSM) plane, when they encounter the dipolarized region of the inner magnetosphere (e.g., Panov et al., 2010; Birn et al., 2011). It was also observed by e.g., Volwerk et al. (2007) that Kelvin-Helmholtz instabilities appear together with bursty bulk flows. Hasegawa et al. (2004) detected plasma flow and magnetic field signatures caused by a Kelvin-Helmholtz instability at the magnetopause. Their magnetic field perturbations are different than shown in Figure 7, because the perturbations in our study are probably caused by pairs of oppositely rotating vortices, not by a single vortex street. TH-A was located closer to Earth and did not measure any vortical structures (see Figure 8). As seen in Figures 4J, K, Cl1 observed signatures in the electron temperature and density that are typical for Kelvin-Helmholtz instability, similar to Cluster observations described by Hasegawa et al. (2009). Therefore, the Cluster satellites likely observed a Kelvin-Helmholtz-like vortex street in the magnetic field induced locally by the measured bursty bulk flows. It has however to be taken into account that part of these results are based on the MVA, which produced results that were not ideally reliable.

Keiling et al. (2009b) observed short-lived equivalent ionospheric current vortices of 600–800 km size associated with the appearance of auroral spirals. In this study, such short-lived vortical $\mathbf{J}_{eq}$ structures could not be resolved. This can be due to the size of the auroral spiral (189 ± 45 km) and the comparative spatial resolution of the IMAGE magnetometer network. The stations in the vicinity of Tromsø have an average calculated distance of ~140 km to Tromsø, but the coverage in this area is limited by the ocean to the north and west. Therefore, the only station in the spiral region (marked by the green solid ellipse in the middle panel of Figure 2) is Andenes (AND). According to the estimates of the spiral location and size at the time of the photograph in Figure 1 the spiral was not located in the zenith over Tromsø, and only marginally over Andenes. This can potentially lead to the missing deflection of the

ionospheric currents during the optical spiral. To better resolve such structures, more mesoscale observations as described by, e.g., Gabrielse et al. (2023) would be helpful. Another possibility for the absence of vortical J_{eq} structures is that the particle precipitation during this observed spiral event can have been too weak to deflect E-region plasma flows.

To be able to correlate the ground observations and space measurements, the ionospheric footprints of the satellites were derived with the T96 external magnetic field model. They were located in the pre-midnight sector of the auroral oval (see Figure 5). The footprints lay at a distance from Tromsø of ~68° and ~34° in longitude for Cluster and TH-A, respectively. Since the spiral was developing up to ~5° in longitude west of Tromsø, as inferred from the field of view from Tromsø (Figure 1), the longitudinal distance of the footprints to the visible spiral may have been smaller than their distance to Tromsø. In the magnetosphere, the possible source region of the auroral spiral was located ~10.1 R_E in Y (GSE) direction from the Cluster satellites. It has to be taken into account that topological magnetic mapping is not very reliable during substorm conditions in particular (Paschmann et al., 2003). The T96 model may describe the overall conditions of this event better than the newer models, but it does not specifically represent substorms (Tsyganenko, 1996). For a strongly disturbed magnetosphere, it is known not to display the dawn-dusk asymmetry of the inner magnetosphere and to overstretch the field lines (Tsyganenko, 2001). Also, the discrepancy between the results of the newer models T02 and T05 and the T96 model is very high, since the newer models generate an entirely different field line topology in placing the spacecraft on open field lines. This shows the high uncertainty in the mapping and therefore also in the interpretations. With these aspects considered, the footprints calculated with the T96 magnetospheric model are regarded only as an approximation for the real ionospheric footprints of the spacecraft. The derivation of the magnetospheric source region of the auroral spiral is treated equally. Due to the uncertainty of magnetic mapping during substorm conditions, the Cluster satellites may have been located closer to or further from the source region of the spiral than the computations suggest. Also, the plasma velocity measurements discussed above exhibited significant flow bursts and the electron temperature and density showed signatures typical for KHI. Approximately 2 min before the spiral development, the plasma velocity started to increase to an absolute value of $v \simeq 960$ km s^{-1}. The flow bursts could have produced the vortices in the magnetic field and plasma. With a distance d = 12.1 R_E between the spacecraft and the possible source region and $t = d/v$, a propagation time t ≃ 80 s of the vortex street observed by Cl2 to the generator region can be estimated. A schematic illustration of this movement is given in Figure 10. It is assumed that the propagation of the plasma flow in X direction is slowed due to the dipolarized magnetic field near the Earth. In Figure 5, the ionospheric footprints of this motion are depicted.

Following from the above calculation it can be possible that the magnetic field vortices, associated bursty bulk flows, KHI and dipolarizations detected by the spacecraft and described above were correlated with the spiral formation. What must be emphasized again, however, is the high uncertainty in the field line mapping during substorm conditions. This makes these interpretations mostly suggestions for a generation mechanism of the auroral spiral,

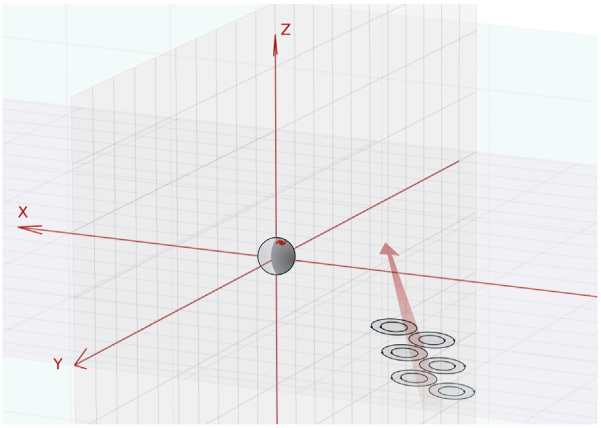

FIGURE 10
Schematic illustration of the vortex street oriented roughly in the X-Y (GSE) plane observed by Cl2 and its propagation towards the spiral source region (not to scale).

based more on the temporal correlation of the vortices in the magnetotail and the optical spiral than on the exact spatial positions.

This suggestion proposes the spiral formation taking place already in the magnetosphere, not only in the ionosphere. Therefore, taking into account the available data, the spiral generation theory presented by Hallinan (1976) is not applicable to this event, since it states that the spiral only fully develops in the ionosphere.

According to a theory by Keiling et al. (2009b), plasma flow vortices in the magnetosphere are the initiator of a spiral, which then maps to ionospheric altitudes. These vortex structures can in turn be caused by either ballooning instabilities (e.g., Voronkov et al. (1997)) or bursty bulk flows (Keiling et al., 2009a; Panov et al., 2010). On encountering the dipolarized magnetic field in the inner magnetosphere, the high-speed plasma flows are decelerated (Panov et al., 2010; Birn et al., 2011). By their deflection around the dipolar magnetic field, vortices with opposed sense of rotation form on both sides of the flows (Panov et al., 2010).

5 Conclusion

The observations of dipolarizations and bursty bulk flows in this study coincide with the theory by Keiling et al. (2009b). In contrast to the detected structures of this event, Keiling et al. (2009b) also observed opposed rotating $\mathbf{J}_{eq}$ vortices that developed and decayed concomitant with auroral spirals. They associated these vortices with upward and downward field-aligned currents, which were driven in the magnetosphere by a pair of vortical plasma flows. According to Keiling et al. (2009b), the generation of the auroral spiral was likely initiated in the region of strong plasma flows between the plasma flow vortices in the magnetosphere. Here, such conclusions can not be drawn in the same way, because there were no equivalent ionospheric current vortices detected. The evidence of a vortex pair of $\mathbf{J}_{eq}$ in the ionosphere connected to plasma flow vortices in the magnetosphere was also not given. This can be due to the lack of mesoscale observations that can resolve these structures. However,

with ~500 A km^{-1} the westward electrojet current observed was stronger than an average substorm expansion current (Juusola et al., 2015), which may have helped establish an the instability for the spiral formation. Also, the magnetic field and possibly plasma vortices observed in the magnetotail caused by the eastward bursty bulk flows can have propagated toward the spiral source region and then mapped to the ionosphere as proposed similarly by Keiling et al. (2009b).

For future research on the interaction of magnetosphere and ionosphere in the generation of auroral spirals extended mesoscale observations in the ionosphere are needed. Also, for optical detection of auroral spiral events complementary to all sky cameras, citizen science projects like Aurorasaurus (MacDonald et al., 2015) are helpful.

Data availability statement

The datasets presented in this study can be found in online repositories. The names of the repository/repositories and accession number(s) can be found below: https://csa.esac.esa.int/csa-web/ (Cluster Science Archive) https://cdaweb.gsfc.nasa.gov (NASA CDAweb) https://space.fmi.fi/image/www/index.php? (IMAGE magnetometers).

Author contributions

EK provided the idea for this study and took the original photograph of the auroral spiral. KM made the plots and wrote the manuscript. NP provided the plots for equivalent ionospheric currents. All authors contributed to the article and approved the submitted version.

Funding

The work of EK and KM is supported by German Research Foundation (DFG) under number KR 4375/2-1 within SPP "Dynamic Earth." EK also acknowledges the support by Volkswagen foundation under the number AZ 97 742.

Acknowledgments

We thank the institutes who maintain the IMAGE Magnetometer Array: Tromsø Geophysical Observatory of UiT the Arctic University of Norway (Norway), Finnish Meteorological Institute (Finland), Institute of Geophysics Polish Academy of Sciences (Poland), GFZ German Research Centre for Geosciences (Germany), Geological Survey of Sweden (Sweden), Swedish Institute of Space Physics (Sweden), Sodankylä Geophysical Observatory of the University of Oulu (Finland), Polar Geophysical Institute (Russia), DTU Technical University of Denmark (Denmark), and Science Institute of the University of Iceland (Iceland). The provisioning of data from AAL, GOT, HAS, NRA, VXJ, FKP, ROE, BFE, BOR, HOV, SCO, KUL, and NAQ is supported by the ESA contracts number 4000128139/19/D/CT as well as 4000138064/22/D/KS. We acknowledge use of NASA/GSFC's Space Physics Data Facility's CDAWeb service, and OMNI data. We acknowledge the use of the IRBEM library (V.4.3), the latest version of which can be found at https://doi.org/10.5281/zenodo.6867552.

Conflict of interest

The authors declare that the research was conducted in the absence of any commercial or financial relationships that could be construed as a potential conflict of interest.

Publisher's note

References

Angelopoulos, V., Baumjohann, W., Kennel, C. F., Coroniti, F. V., Kivelson, M. G., Pellat, R., et al. (1992). Bursty bulk flows in the inner central plasma sheet. *J. Geophys. Res. Space Phys.* 97, 4027–4039. doi:10.1029/91JA02701

Birn, J., Nakamura, R., Panov, E. V., and Hesse, M. (2011). Bursty bulk flows and dipolarization in MHD simulations of magnetotail reconnection. *J. Geophys. Res. Space Phys.* 116. doi:10.1029/2010JA016083

Boscher, D., Bourdarie, S., O'Brien, P., and Guild, T. (2010). *IRBEM library V4.3, 2004-2008*. Toulouse France: ONERA-DESP.

Davis, T. N., and Hallinan, T. J. (1976). Auroral spirals, 1. Observations. *J. Geophys. Res.* 81, 3953–3958. doi:10.1029/JA081i022p03953

Dunlop, M., Woodward, T., and Farrugia, C. (1995). "Minimum variance analysis: Cluster themes," in *Proceedings of the cluster workshops*. Editors K.-H. Glassmeier, U. Motschmann, and R. Schmidt (Braunschweig, Germany: ESA Special Publication), 33.

Erwan, T., Finlay, C., Beggan, C., Alken, P., Aubert, J., Barrois, O., et al. (2015). International geomagnetic reference field: the 12th generation. *Earth, Planets Space* 67, 79. doi:10.1186/s40623-015-0228-9

Gabrielse, C., Gkioulidou, M., Merkin, S., Malaspina, D., Turner, D., Chen, M., et al. (2023). Mesoscale phenomena and their contribution to the global response: a focus on the magnetotail transition region and magnetosphere-ionosphere coupling. *Front. Astronomy Space Sci.* 10, 1151339. doi:10.3389/fspas.2023.1151339

Hallinan, T. J. (1976). Auroral spirals, 2. Theory. *J. Geophys. Res.* 81, 3959–3965. doi:10.1029/JA081i022p03959

Hasegawa, H., Fujimoto, M., Phan, T.-D., Rème, H., Balogh, A., Dunlop, M., et al. (2004). Transport of solar wind into Earth's magnetosphere through rolled-up Kelvin–Helmholtz vortices. *Nature* 430, 755–758. doi:10.1038/nature02799

Hasegawa, H., Retinò, A., Vaivads, A., Khotyaintsev, Y., André, M., Nakamura, T., et al. (2009). Kelvin-helmholtz waves at the earth's magnetopause: multiscale development and associated reconnection. *J. Geophys. Res.* 114. doi:10.1029/2009JA014042

Juusola, L., Kauristie, K., van de Kamp, M., Tanskanen, E. I., Mursula, K., Asikainen, T., et al. (2015). Solar wind control of ionospheric equivalent currents and their time derivatives. *J. Geophys. Res. Space Phys.* 120, 4971–4992. doi:10.1002/2015JA021204

Juusola, L., Kauristie, K., Vanhamäki, H., Aikio, A., and van de Kamp, M. (2016). Comparison of auroral ionospheric and field-aligned currents derived from swarm and ground magnetic field measurements. *J. Geophys. Res. Space Phys.* 121, 9256–9283. doi:10.1002/2016JA022961

Keiling, A., Angelopoulos, V., Runov, A., Weygand, J., Apatenkov, S. V., Mende, S., et al. (2009a). Substorm current wedge driven by plasma flow vortices: THEMIS observations. *J. Geophys. Res. Space Phys.* 114. doi:10.1029/2009JA014114

Keiling, A., Angelopoulos, V., Weygand, J. M., Amm, O., Spanswick, E., Donovan, E., et al. (2009b). THEMIS ground-space observations during the development of auroral spirals. *Ann. Geophys.* 27, 4317–4332. doi:10.5194/angeo-27-4317-2009

Laakso, H., Perry, C., McCaffrey, S., Herment, D., Allen, A., Harvey, C., et al. (2010). "Cluster active archive: overview," in *The cluster active archive*. Editors H. Laakso, M. Taylor, and C. Escoubet (Dordrecht: Springer), 3–37.

MacDonald, E. A., Case, N. A., Clayton, J. H., Hall, M. K., Heavner, M., Lalone, N., et al. (2015). Aurorasaurus: A citizen science platform for viewing and reporting the aurora. *Space Weather.* 13, 548–559. doi:10.1002/2015SW001214

Met Office (2010-2015). Cartopy: a cartographic python library with a matplotlib interface. *Exeter, Devon*. Available at: https://scitools.org.uk/cartopy

Morley, S., Welling, D., Koller, J., Larsen, B., Henderson, M., and Niehof, J. (2010). "Spacepy - a python-based library of tools for the space sciences," in *Proceedings of the 9th Python in science conference*. Editors S. van der Walt, and J. Millman Austin, TX, 67–72.

Panov, E. V., Nakamura, R., Baumjohann, W., Angelopoulos, V., Petrukovich, A. A., Retinò, A., et al. (2010). Multiple overshoot and rebound of a bursty bulk flow. *Geophys. Res. Lett.* 37. doi:10.1029/2009GL041971

Partamies, N., Freeman, M. P., and Kauristie, K. (2001a). On the winding of auroral spirals: interhemispheric observations and hallinan's theory revisited. *J. Geophys. Res. Space Phys.* 106, 28913–28924. doi:10.1029/2001JA900093

Partamies, N., Kauristie, K., Pulkkinen, T. I., and Brittnacher, M. (2001b). Statistical study of auroral spirals. *J. Geophys. Res. Space Phys.* 106, 15415–15428. doi:10.1029/2000JA900172

Paschmann, G., Haaland, S., and Treumann, R. (2003). *Auroral plasma Physics*. Dordrecht: Springer Science+Business Media. doi:10.1007/978-94-007-1086-3

Song, P., and Russell, C. (1999). Time series data analyses in space Physics. *Space Sci. Res.* 87, 387–463. doi:10.1023/A:1005035800454

Sonnerup, B. U. O., and Cahill, L. J., Jr. (1967). Magnetopause structure and attitude from Explorer 12 observations. *J. Geophys. Res.* 72, 171–183. doi:10.1029/JZ072i001p00171

Sonnerup, B. U. Ö., and Scheible, M. (1998). Minimum and maximum variance analysis. *ISSI Sci. Rep. Ser.* 1, 185–220. Available at: https://api.semanticscholar.org/CorpusID:118577335

Tsyganenko, N. A. (2002). A model of the near magnetosphere with a dawn-dusk asymmetry 2. Parameterization and fitting to observations. *J. Geophys. Res. Space Phys.* 107, SMP 10-11–SMP 10-17. doi:10.1029/2001JA000220

Tsyganenko, N. A. (1996). "Effects of the solar wind conditions in the global magnetospheric configurations as deduced from data-based field models," in *International conference on substorms*. Editors E. J. Rolfe, and B. Kaldeich (ESA Special Publication), 181.

Tsyganenko, N. A. (2001). "Empirical magnetic field models for the space weather program," in *Space weather*. Editors H. S. P. Song, and G. Siscoe (Washington, D. C: American Geophysical Union), 273–280.

Tsyganenko, N. A. (1995). Modeling the Earth's magnetospheric magnetic field confined within a realistic magnetopause. *J. Geophys. Res. Space Phys.* 100, 5599–5612. doi:10.1029/94JA03193

Tsyganenko, N. A., and Sitnov, M. I. (2005). Modeling the dynamics of the inner magnetosphere during strong geomagnetic storms. *J. Geophys. Res. Space Phys.* 110, A03208. doi:10.1029/2004JA010798

Untiedt, J., and Baumjohann, W. (1993). Studies of polar current systems using the IMS Scandinavian magnetometer array. *Space Sci. Rev.* 63, 245–390. doi:10.1007/BF00750770

Volwerk, M., Glassmeier, K.-H., Nakamura, R., Takada, T., Baumjohann, W., Klecker, B., et al. (2007). Flow burst-induced Kelvin-Helmholtz waves in the terrestrial magnetotail. *Geophys. Res. Lett.* 34, L10102. doi:10.1029/2007GL029459

Voronkov, I., Rankin, R., Frycz, P., Tikhonchuk, V. T., and Samson, J. C. (1997). Coupling of shear flow and pressure gradient instabilities. *J. Geophys. Res. Space Phys.* 102, 9639–9650. doi:10.1029/97JA00386

Zotti, G., Hoffmann, S. M., Wolf, A., Chéreau, F., and Chéreau, G. (2021). The simulated sky: Stellarium for cultural astronomy research. *J. Skyscape Archaeol.* 6, 221–258. doi:10.1558/jsa.17822

frontiers | Frontiers in Astronomy and Space Sciences

TYPE Original Research
PUBLISHED 23 November 2023
DOI 10.3389/fspas.2023.1197430

OPEN ACCESS

EDITED BY
Tatsuhiro Yokoyama,
Kyoto University, Japan

REVIEWED BY
Alexei V. Dmitriev,
Lomonosov Moscow State University, Russia
Scott Alan Thaller,
Atmospheric and Space Technology Research Associates, United States

*CORRESPONDENCE
L. A. Da Silva,
ligia.alves01@gmail.com,
ligia.silva@inpe.br

RECEIVED 31 March 2023
ACCEPTED 02 November 2023
PUBLISHED 23 November 2023

CITATION
Da Silva LA, Shi J, Vieira LE, Agapitov OV, Resende LCA, Alves LR, Sibeck D, Deggeroni V, Marchezi JP, Chen S, Moro J, Arras C, Wang C, Andrioli VF, Li H and Liu Z (2023), Why can the auroral-type sporadic E layer be detected over the South America Magnetic Anomaly (SAMA) region? An investigation of a case study under the influence of the high-speed solar wind stream.
Front. Astron. Space Sci. 10:1197430.
doi: 10.3389/fspas.2023.1197430

Why can the auroral-type sporadic E layer be detected over the South America Magnetic Anomaly (SAMA) region? An investigation of a case study under the influence of the high-speed solar wind stream

L. A. Da Silva[1,2]*, J. Shi[1], L. E. Vieira[2], O. V. Agapitov[3], L. C. A. Resende[1,2], L. R. Alves[2], D. Sibeck[4], V. Deggeroni[2], J. P. Marchezi[5], S. Chen[2], J. Moro[1,2], C. Arras[6,7], C. Wang[1], V. F. Andrioli[1,2], H. Li[1] and Z. Liu[1]

[1]State Key Laboratory of Space Weather, National Space Science Center, Chinese Academy of Sciences, Beijing, China, [2]National Institute for Space Research—INPE, São José dos Campos, Brazil, [3]Berkeley—UCB—Space Sciences Laboratory, University of California, Berkeley, CA, United States, [4]NASA Goddard Space Flight Center, Greenbelt, MD, United States, [5]Institute for the Study of Earth, Oceans and Space, University of New Hampshire, Durham, NH, United States, [6]German Research Centre for Geosciences—GFZ, Potsdam, Germany, [7]Institute of Geodesy and Geoinformation Science, Technische Universität Berlin, Berlin, Germany

The low-electron flux variability (increase/decrease) in the Earth's radiation belts could cause low-energy Electron Precipitation (EP) to the atmosphere over auroral and South American Magnetic Anomaly (SAMA) regions. This EP into the atmosphere can cause an extra upper atmosphere's ionization, forming the auroral-type sporadic E layers (Esa) over these regions. The dynamic mechanisms responsible for developing this Esa layer over the auroral region have been established in the literature since the 1960s. In contrast, there are several open questions over the SAMA region, principally due to the absence (or contamination) of the inner radiation belt and EP parameter measurements over this region. Generally, the Esa layer is detected under the influence of geomagnetic storms during the recovery phase, associated with solar wind structures, in which the time duration over the auroral region is considerably greater than the time duration over the SAMA region. The inner radiation belt's dynamic is investigated during a High-speed Solar wind Stream (September 24-25, 2017), and the hiss wave-particle interactions are the main dynamic mechanism able to trigger the Esa layer's generation outside the auroral oval. This result is compared with the dynamic mechanisms that can cause particle precipitation in the auroral region, showing that each region presents different physical mechanisms. Additionally, the difference between the time duration

of the hiss wave activities and the Esa layers is discussed, highlighting other ingredients mandatory to generate the Esa layer in the SAMA region.

KEYWORDS

inner radiation belt, South America Magnetic Anomaly, auroral-type sporadic E-layers, particle precipitation, hiss waves, pitch angle scattering

Highlights

- The low-energy electron injections (≤100 keV) between L* = 2.8 and 3.0 are observed during the conjunction between VAP-B and Santa Maria station.
- The level of low-energy electron precipitation (EP) predominant defines the base height of the Esa layer.
- The maximum peak of the ionization rate integrated defines the maximum critical frequency of the Esa layer.

1 Introduction

The generating mechanism of the auroral-type sporadic E (Esa) layers detected in the auroral oval has been well understood since the 1960s (Rees, 1963). In the auroral oval, low energy electron precipitation (EP) originating from the magnetosphere and Solar Energetic Particles (SEPs) are primarily responsible for producing auroral-type sporadic E. These mechanisms operate exclusively in the auroral regions (Whitehead, 1970). In addition, Esa layers can be generated in the low/middle-latitude, specifically over South America, due to the presence of the South American Magnetic Anomaly (SAMA) (Batista and Abdu, 1977; Moro et al., 2022a; Da Silva et al., 2022). Esa layers over South America have a different generating mechanism from those in the auroral zone, which is thought to be related to the geometric configuration of the geomagnetic field (Pinto and Gonzalez, 1989) that contributes to the inner boundary of the inner radiation belt being deeper compared to the other point of the same latitude around the globe (Roederer, 1967). These pronounced departures in geomagnetic field symmetry promote proton contamination in the electron measurements, as well as the low-energy electron precipitation over the SAMA region, which results in a significant impact on the local ionosphere, such as the generation of the auroral-type sporadic E layer, detected since the 1970s (Batista and Abdu, 1977). The electron energy range able to generate the Esa layers over the auroral oval is ≥1 keV (Rees, 1963; Cai and Ma, 2007), while over the SAMA region, it is between 0.5 keV and tens keV (see Da Silva et al., 2022). The dynamic mechanisms responsible for electron precipitation in both auroral ovals and the SAMA region are completely different (Da Silva et al., 2022). Therefore, they can generate different characteristics in these Esa layers when detected in these distinct regions, such as the time duration, intensity, position in altitude, as well as frequency range (Resende et al., 2022b).

The low-energy EP over the auroral oval can be originated in the outer radiation belt. They can occur through the wave-particle resonances driven by the whistler-mode chorus, plume, and magnetosonic waves. Generally, the low-energy EP over the auroral oval occurs during the geomagnetic storms and substorms under the influence of the different solar wind structures (Horne et al., 2009; Rodger et a., 2010; Meredith et al., 2011). The generator mechanisms of the Esa layer over the auroral oval regions are well known, principally due to the exclusive dependence on low-energy EP of this kind of sporadic E layer in these regions (Resende et al., 2022b).

Conversely, the main dynamic mechanism responsible for causing the low-energy EP over the SAMA region under the influence of an Interplanetary Coronal Mass Ejection (ICME) is the pitch angle scattering driven by hiss waves (Da Silva et al., 2022). Therefore, this low-energy EP can trigger the generator mechanisms of the Esa layer over this peculiar region during the recovery phase of the geomagnetic storm (Batista and Abdu, 1977; Moro et al., 2022a; Da Silva et al., 2022). On the other hand, the dynamic mechanism over the SAMA region able to trigger the generator mechanisms of the Esa layer under the influence of a High-Speed solar wind Stream (HSS) needs to be identified, including the role of the magnetospheric waves in the low-energy EP over this region. Thus, the inner radiation belt dynamic and its impact on the local ionosphere will be discussed to answer the question in the title of this paper, considering the influence of an HSS.

The low-energy EP is not a unique ingredient in developing the sporadic E layer over SAMA. The wind shear mechanism is fundamental to the Es layer development at low and middle latitudes. These Es layer occurrences are classified as blanketing (Esb) layers. In this process, the molecular and the metallic ions are converged in thin layers due to the tidal wind components. In fact, the zonal and meridional winds in opposite directions carry the ions, and due to the magnetic field, the Lorentz force causes a vertical movement of these ions. Thus, there is an accumulation of the ions in the null points of the tidal winds generating a dense thin ionization layer compared to the background (Chimonas and Axford 1968). Therefore, the upper atmospheric wind conditions are also important and must be considered (Rees, 1963; Cai and Ma, 2007; Resende et al., 2022b; Resende et al., 2022c).

2 Data set and methodology

A case study under the influence of an HSS was selected to analyze and to compare the physical processes related to the auroral-type sporadic E (Esa) layers detected over the low/middle-latitude and auroral regions. This comparison between the physical processes in the outer and inner radiation belt will answer the questions about this kind of sporadic E layer detected outside the auroral region. The satellite and ground-based data are employed to develop these analyses. The interplanetary medium conditions, the dynamic mechanisms, such as the wave-particle interaction in the radiation

belts, and their impact on the ionosphere over the SAMA region will be discussed to be better understood.

The HSS's characteristics are discussed from parameters measured by the Magnetic Field Experiment (MAG) and Solar Wind Electron, Proton, and Alpha Monitor (SWEPAM) onboard the Advanced Composition Explorer (ACE) satellite, which provides the solar wind parameters at the L1 Lagrangian point (Stone et al., 1998). The geomagnetic index (Auroral electrojet - AE) available at OMNIWeb (https://omniweb.gsfc.nasa.gov/) is used to describe the different substorm periods. The Esa layers are detected over the SAMA's center using the ionosonde installed at Santa Maria (29.7°S, 53.8°W, dip (*I*): ~-37°, L: 1.16). The ionosonde measurements at Tromso (69.7°N, 18°E, dip (*I*): ~78°, L: 6.45) will be used only for the comparison with the SAMA's results. The dip, or geomagnetic inclination (*I*), is the angle between the horizontal plane and the total field vector (e.g., Chulliat et al., 2020).

The low-energy EP over the SAMA's center and auroral oval regions are discussed using the measurements *in situ* (radiation belts) of the low-energy electron injections from the Magnetic Electron Ion Spectrometer (MagEIS) instrument (Blake et al., 2013), and Helium, Oxygen, Proton, and Electron (HOPE) instrument (Funsten et al., 2013) onboard Van Allen Probe B (Mauk et al., 2013). The MagEIS data has been reprocessed by Claudepierre et al. (2015) to correct for proton contamination close to perigee. The SAMA region is significantly contaminated by protons, and it is impossible to use the available low-orbit satellite data to measure low-energy EP directly. The low-energy electron injections are also analyzed through the time evolution of phase space density (PhSD [c/(cm MeV))^3 sr^{-1}]), which PSD data was obtained from MagEIS instrument onboard Van Allen Probe B available at https://rbspgway.jhuapl.edu/psd.

The whistler mode chorus waves outside the plasmapause (hundreds of Hz up to about 10 kHz) (Gurnett and O'Brien, 1964), plume whistler mode waves in plasmaspheric plumes (Su et al., 2018; Li et al., 2019), and whistler mode hiss waves inside the plasmasphere (20 Hz to a few kHz) (Meredith et al., 2004) are analyzed. The whistler waves are plasma waves, right circularly polarized, observed in the magnetosphere (Helliwell, 1965), in which can interact resonantly with the low-energy electron to launch these particles to the loss cone, followed by the precipitation into the atmosphere in the auroral oval and SAMA regions (Horne et al., 2009; Rodger et al., 2010; Li et al., 2019; Da Silva et al., 2022). Therefore, the power spectral densities of the magnetic field and total electron density are used to detect these whistler mode waves and the plasmapause position (Lpp), respectively. The polarization properties, such as the wave Normal Angle (WNA), ellipticity, and planarity, are calculated through the singular value decomposition method (Santolík et al., 2003). These parameters are obtained from the Electric and Magnetic Field Instrument Suite and Integrated Science (EMFISIS) (Kletzing et al., 2013) onboard Van Allen Probes (Mauk et al., 2012).

3 Interplanetary medium parameters during the influence of a HSS

The solar wind parameters, interplanetary magnetic field (IMF), and AE index are presented in Figure 1. The interplanetary medium conditions are here described, emphasizing the substorms duration associated with an HSS that reached L1 Lagrangian point on 24 September 2017. Panel (a) and (b) shows the solar wind velocity (Vp) and proton density (particles/cm-3), respectively, in which solar wind velocity reached the maximum value (420 km s^{-1}) close to 04:00 UT and 08:30 UT, respectively, on September 25. The proton density reached values above 30 particles/cm^{-3}, followed by a decrease in a few hours. The maximum proton density value is almost concurrent with the negative Bz component of the IMF (panel d - red line). Bx (panel c - red line) and By (panel c - blue line) components of the IMF are not so strong and remain preferentially positive and negative, respectively, in which the Alfvenic fluctuations are observed in Vx component during some periods as shown in Supplementary Figure S1 (Supporting Information). The concept of Alfvénicity in the context of solar wind refers to the degree to which the solar wind plasma and magnetic field exhibit characteristics associated with Alfvén waves. The Alfvénic fluctuations of the IMF are commonly observed during the long recovery phases of the HSS (Da Silva et al., 2019; Da Silva et al., 2021b). This behavior in IMF, generally is observed simultaneously with moderate substorms activities, followed by intermittent intervals of enhanced magnetospheric convection that contribute to the low-energy electron injections into the radiation belts (e.g., Forsyth et al., 2016).

The auroral electrojet (AE) index (panel e) reached the maximum value close to 450 nT almost simultaneously with the strong value of the proton density. The subsequent AE index peaks are not strong, reaching values from 75 nT to 345 nT. It means that the substorms associated with this HSS are considerably weak. It suggests that the low-energy electron injections in the inner magnetosphere under the influence of these substorms may also be weak both in flux intensity and in-depth that the particles reach in the radiation belts, compared to the low-energy electron injections in the inner magnetosphere under the influence of ICMEs (e.g., Da Silva et al., 2022). In subsequent sections, this behavior will be discussed to highlight the different physical processes at the L1 Lagrangian point and their impact on the inner magnetosphere and ionosphere.

4 Auroral-type sporadic E layer detected over the SAMA region

The ionograms from the Digisonde located at Santa Maria station detected the auroral-type sporadic E layer (Esa) over the SAMA region only during two periods (06:00 UT—07:00 UT and 22:05 UT—22:25 UT on 25 September 2017, in which are under the influence of the HSS that reached at L1 Lagrangian point on 24 September 2017. Figures 2A, B shows the Esa layers detected during the first and second periods, which are indicated through the red arrows. Curiously, these Esa Layers detected over the SAMA region are generated under the influence of Alfvenic fluctuations in the Vx component, as shown in Supplementary Figure S1 (Supporting Information), which illustrates the linear correlation coefficients between Solar wind and Alfvén velocities. A high correlation coefficient can be associated to an Alfvenic nature of the solar wind, in which this observation is particularly evident in the top and bottom panels of the first row in Supplementary Figure S1, showing

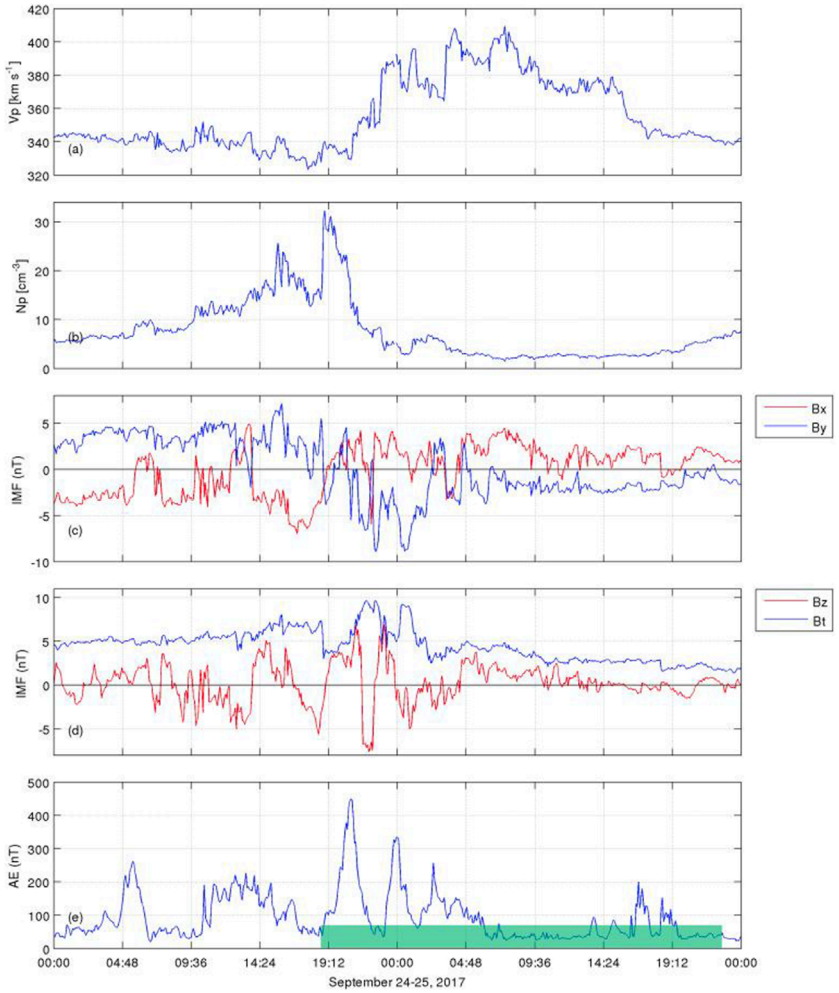

FIGURE 1
(A) Solar wind velocity (Vp); **(B)** Proton density (Np); **(C)** Bx component and By component of the Interplanetary Magnetic Field (IMF); **(D)** B total (Bt) and Bz component of the IMF; and **(E)** Auroral electrojet (AE) index. The IMF components are in GSM coordinates. The green box is referent to the period of analysis. The HSS reached L1 Lagrangian point on 24 September 2017.

a high correlation between the fluctuations in the x component indicating a high Alfvenic solar wind (e.g., Da Silva et al., 2019; Da Silva et al., 2021b). The Esa Layers detected over the SAMA region under the influence of ICMEs were not previously observed concurrent with Alfvenic fluctuations but simultaneously with the recovery phase of the storm (see Batista and Abdu, 1977; Moro et al., 2022a; Da Silva et al., 2022). As discussed in the following sections, these different behaviors at L1 Lagrangian point trigger different physical processes in the magnetosphere and, consequently, in the ionosphere.

Two types of Es layers over Santa Maria are observed, the Esa layer, formed due to particle precipitation, and the blanketing (Esb) layer, formed by wind shear. In fact, as Santa Maria is a transition region between the low and middle latitudes, the winds have high amplitudes, forming the Esb layers (Moro et al., 2022b). Generally, these winds are driven by the diurnal, semidiurnal, and terdiurnal tides present in the E region. Unfortunately, Santa Maria has no wind measurements during this related event. However, Andrioli et al. (2009) studied the mean winds and tides over Santa Maria from 2005 to 2007, and they showed a dominance of the diurnal tide in September with a maximum occurrence around 6:00 UT (zonal) and 12:00 UT (meridional) at around 100 km. Thus, the wind shear significantly influences the Es layer development over Santa Maria.

The competition between the particle precipitation and wind shear is seen mainly in panel (b) of Figure 2. It is noticed that the beginning of the F region trace is higher than 3 MHz. This behavior means that the Es layer blocked the F region in these hours, proving the action of the winds. Additionally, the maximum frequency in the cases of Figure 2B reached high values (more than 5 MHz, shown in red arrows). On the other hand, this fact was not observed in panel (a) of Figure 2, which is indicative that the particle precipitation was the principal mechanism of the Es layer formation at hours around 06:00 UT.

The ionograms from Digisonde located at Tromso station are presented and compared with the ionograms from Santa Maria

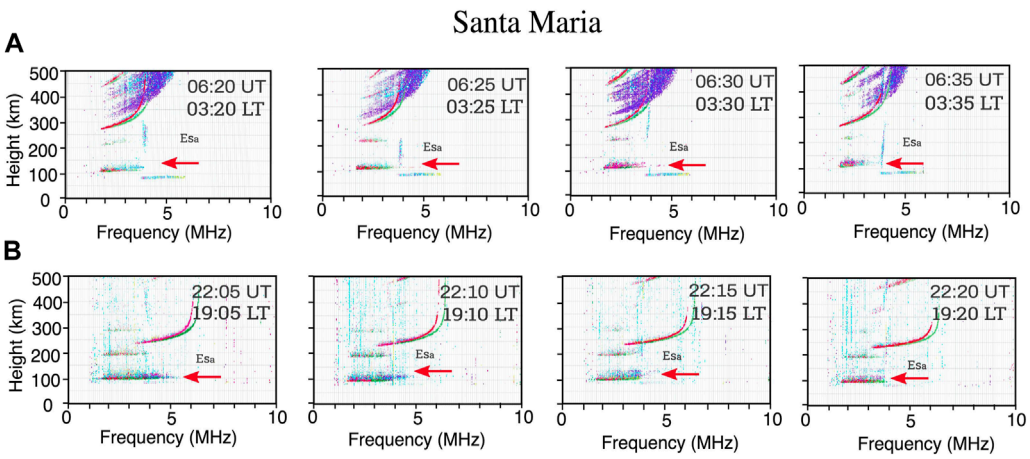

FIGURE 2
Ionograms from Digisonde located at Santa Maria station, which detected Esa layers only during the periods between 06:20 UT - 06:35 UT (03:30-03:35 LT, panel **(A)**, and 22:05 UT - 22:20 UT (19:05 LT - 19:20 LT panel **(B)** on September, 25. The red arrows indicate the presence of the Esa layers. The color code in these ionograms represents the echo direction of the received signal. The thin "trace" at approximately 80 km is a technical artifact resulting from an error in the Digisonde processor.

station. The Tromso station detected Esa layers almost the entire period of the HSS influence, except close 06:00 UT on 25 September 2017. Supplementary Figure S2 (Supporting Information) shows the Esa layer detected between 21:00–23:30 UT on 24 September 2017 (panel a), and 22:00–22:45 UT on 25 September 2017 (panel b). The explanation of the absence of the Esa layer close 06:00 UT is directly related to the lack of plasma waves in the outer radiation belt at this period, which will be observed in Section 6. The Esa layers have a spreading trace over Tromso, as observed in Santa Maria. This behavior was discussed in Resende et al. (2022c), in which the pitch angle scattering driven by whistler mode chorus waves can cause low-energy EP (Da Silva et al., 2021a) over the auroral region. It is important to emphasize that the low-energy EP is a unique ingredient for developing the Esa layer over the auroral region. In contrast, the pitch angle scattering driven by plasmaspheric hiss waves (in the inner radiation belt) contributes to the particle precipitation over the SAMA (Da Silva et al., 2022), and there is a competition between the EP and the winds during the formation of the Esa layer over this region, which is observed in Figure 2B.

5 Conjunction between the Van Allen Probes and the ionosonde station over the SAMA's center

The mechanisms responsible for the low-energy EP over auroral regions are widely studied, and the literature is well established (Rees, 1963; Whitehead, 1970), which means the generator mechanism of the Esa layer over this region is also well understood. The low-energy EP originated in the outer radiation belt can be analyzed here to discuss one crucial kind of physical process responsible for causing the EP over the auroral region, so it is not necessary to do the conjunction with the auroral region in the study because the behavior observed over Tromso station is similar to the other areas in the auroral oval. Another point is the measurements from the VAP-AB in the outer radiation belt are for a long time (apogee orbit). In contrast, the measurements in the inner radiation belt are brief (perigee orbit), in which the main analyses here will be concentrated in detail to explain the dynamic mechanisms responsible for causing the low-energy EP over the SAMA region.

These dynamic mechanisms within the inner radiation belt can cause electron particle precipitation over the SAMA region. They can trigger the physical processes responsible for generating the auroral-type sporadic E layer in this low-latitude (Da Silva et al., 2022). Thereby, using the Van Allen Probes data during their perigee orbit, it is possible to study the inner radiation belt conditions and their impact in the atmosphere for low L-shells (Da Silva et al., 2022) around the Earth. The interest here is in low L-shells over the SAMA region, which is necessary to find the conjunctions between the Van Allen Probes and Santa Maria station during the Esa layers detected on 25 September 2017.

Figure 3 shows the magnetic equator (red line) at 150 km of altitude, Van Allen probes orbit (blue line), and their footprint (blue dashed line) on 25 September 2017. The conjunctions can be observed when the blue dashed line crosses the Santa Maria station (red triangle), which is installed in the central region of the SAMA (white iso-intensity lines with 23,000 nT). Panel (a) shows the VAP-B orbit (6:00–6:30 UT) and panel (b) presents the VAP-A orbit (21:30–22:30 UT), periods of the Esa layers' detection over SAMA. The conjunction between VAP-B and Santa Maria station (red triangle) was observed at 06:22 UT on 25 September 2017, in which the Magnetic Local Time (MLT) from VAP-B (MLT = 2.298) and Santa Maria station (MLT = 2.326) were almost coincident. The L values for both VAP-B and Santa Maria station were also almost coincident, presenting L = 1.23 and L = 1.16, respectively. On the

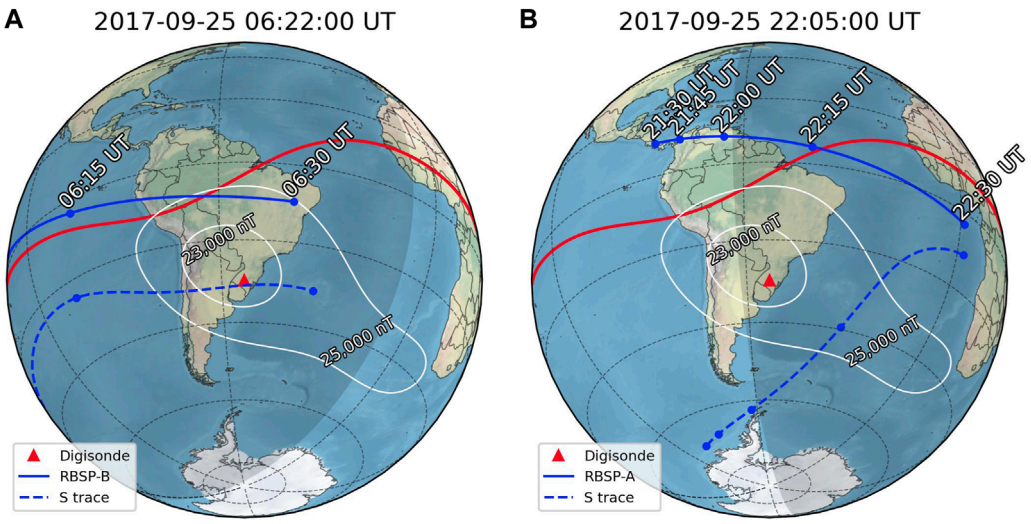

FIGURE 3
Magnetic equator (red line) at 150 km altitude, Van Allen probes orbit (blue line) and their footprint (blue dashed line) on 25 September 2017, for the two periods of the Esa layers detected. Panel **(A)** 06:22 UT and Panel **(B)** 22:05 UT. Santa Maria stations (red triangle) and the central region of the SAMA (white iso-intensity lines with 23,000 nT).

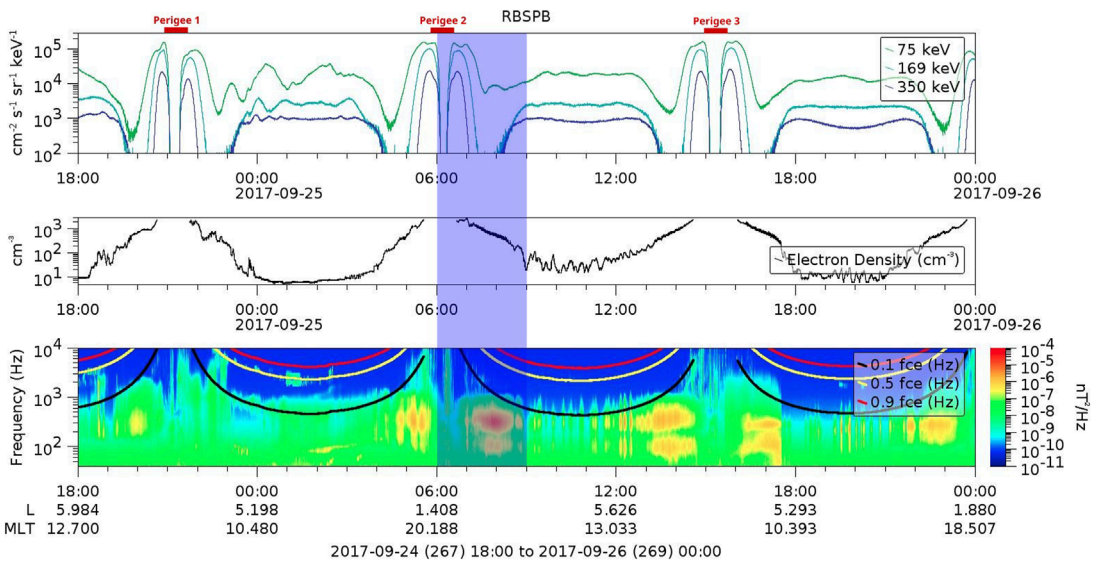

FIGURE 4
(top panel) the low-energy electron flux (energy channels: 75 and 169 keV) obtained from MagEIS instrument. (medium panel) the total electron density obtained from the EMFISIS instrument. (bottom panel) the power spectral density of the magnetic field obtained from the EMFISIS instrument, in which the red, yellow and black lines represent 0.9 fce, 0.5 fce and 0.1 fce. Blue box is referent to the conjunction period between VAP-B and Santa Maria station. MagEIS and EMFISIS instruments are onboard the Van Allen Probe B.

other hand, the second period analyzed during this HSS observed a coincidence between VAP-A and Santa Maria station at 22:05 UT only in MLT, in which both show MLT = 18.029 and 18.032, respectively.

The discussions regarding the dynamic mechanisms inside the radiation belts will use only the data from the VAP-B due to the non-perfect conjunction using VAP-A and the proton contamination of the MagEIS instrument onboard VAP-A at the perigee.

6 Low-energy electron injections/precipitations and whistler mode wave activities within the radiation belts

The flux injections in this paper means the flux enhancements in different energy ranges (e.g., Sarris et al., 1976; Gabrielse et al., 2014) into the inner radiation belt (L-shell <2), which has been

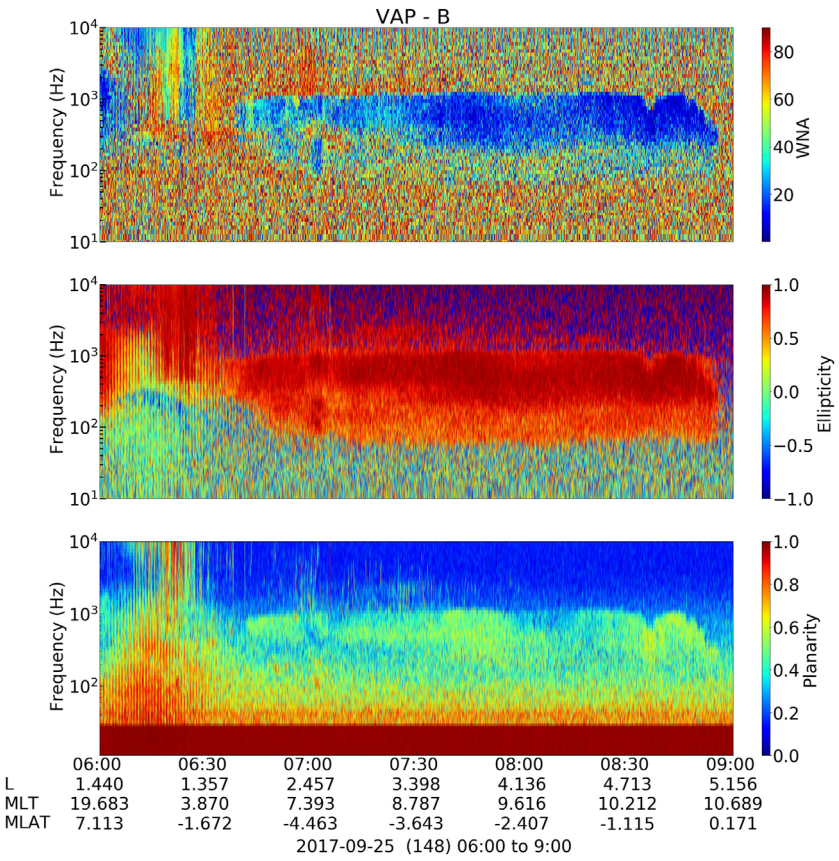

FIGURE 5
(top panel) Wave Normal Angle, (medium panel) ellipticity, and (bottom panel) Planarity are obtained from the EMFISIS instrument onboard Van Allen probe B at 6:00-9:00 UT on September 2017 (blue box period in Figure 4). These parameters are calculated through the singular value decomposition method (Santolík et al., 2003).

observed since 1990 decade, e.g., in Vampola and Korth, (1992), Baker et al. (1994), Xiao et al. (2009), and Shi et al. (2016), based on CRESS, SAMPEX, POLAR, and Van Allen Probes data mission, respectively. Cosmic Ray Albedo Neutron Decay (CRAND) is an important process to produce electrons locally in the inner radiation belt region during quiet geomagnetic periods (see Xiang et al., 2019; Li et al., 2023), although the decay rate of neutrons is considered relatively constant, in which could not explain the fast variability of the low-energy electrons flux in the inner radiation belt during the perturbed geomagnetic periods. High-energy electrons injections, i.e., > 100 keV are due to radial transport (see Li et al., 2023 and references therein) and magnetotail dipolarizations under substorms (Kim et al., 2021). The inner belt low energy electrons (<100 keV) dynamics can also follow processes similar to the higher energy populations. The enhancements of low energy electrons are observed more often (Reeves et al., 2015) and it can be related to fast magnetosonic wave interacting (Turner et al., 2015) under geomagnetic storms (Zhang et al., 2021).

Therefore, the main physical processes to explain the electrons flux injections in the inner radiation belt during the perturbed geomagnetic periods are interactions of the electrons with the fast magnetosonic waves, specifically in the Pi2 frequency range inside the plasmasphere (e.g., Zhao et al., 2014; Turner et al., 2015; Zhang et al., 2021; Li et al., 2023). The Pi2 cavity mode waves can explain the sudden enhancements of low-energy electrons at low L shells because this mode presents the electric field as an antinode within the plasmasphere, as discussed by Takahashi et al. (2003), in which the azimuthal electric field oscillation can interact resonantly with drifting energetic electrons, violating the third adiabatic invariant, and resulting in acceleration and radial injections crossing magnetic field lines (conserving the first and second adiabatic invariants) (e.g., Li et al., 1998; Turner et al., 2015).

On the other hand, three types of waves can scatter in low-energy electron resulting in loss of inner radiation belt electrons through resonance interactions (Li et al., 2015; Green et al., 2020; Hua et al., 2020; Li et al., 2023). Green et al. (2020) suggests that the lightning-generated whistlers (2–12 kHz) are important for scattering electrons from several hundred keV to several MeV at L ~1.5. VLF transmitter waves play an important role in electron loss (e.g., Wang et al., 2018). The plasmaspheric hiss waves (~50–10 kHz) can be responsible for the electron precipitation at the outer plasmasphere of tens to hundreds keV, as observed by Reeves et al. (2016), and below tens keV, as observed by Khazanov and Ma (2021). Therefore, the hiss waves are analyzed in this work due the interest in the scattering in energy level below 10 keV.

Figure 4 shows the low-energy electron injections for the energy channels of 75 keV and 169 keV (top panel) and the power spectral density (PSD) of the magnetic field (bottom panel)

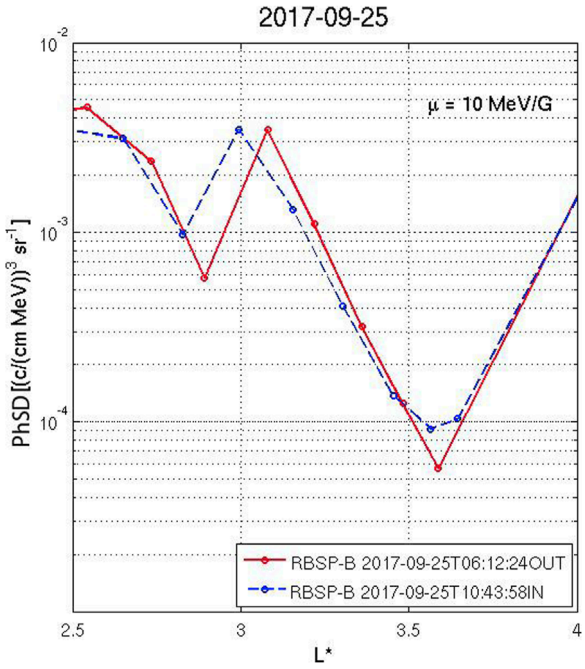

FIGURE 6
The Phase Space Density (PhSD) as a function of L* at μ = 10 MeV/G and K = 0.11 $G^{1/2}R_E$ during the conjunction between VAP-B and Santa Maria station. PSD data was obtained from MagEIS instrument onboard Van Allen Probe B available in https://rbspgway.jhuapl.edu/psd.

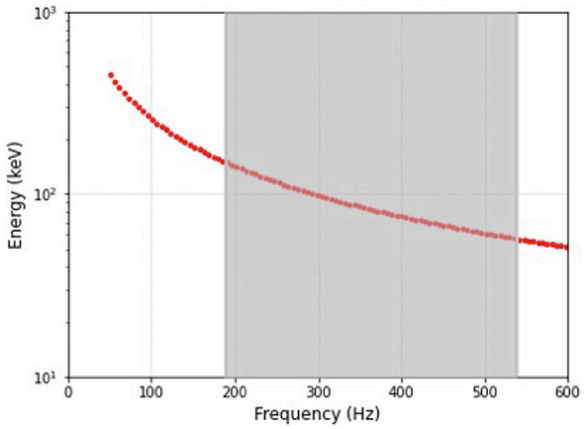

FIGURE 7
Resonant kinetic energy (in keV) for electrons as a function of hiss wave frequency propagating in a high-density plasmasphere. The gray vertical lines corresponds to the hiss wave frequency (in Hz) interval band observed in the plasmasphere at 08:00 UT on September 25 (shown in Figure 4; Supplementary Figure S3).

obtained from MagEIS and EMFISIS instruments, respectively, onboard Van Allen Probe B. Red, yellow and black lines represent 0.9 fce, 0.5 fce, 0.1 fce, in which fce is electron cyclotron frequency. The total electron density (medium panel) is used to identify the plasmapause position (Lpp). Plasmapause is a boundary between the low-density and high-density plasma regions, represented by the ratio variation between the maximum and minimum electron density (e.g., Lemaire, 1975; Thomas et al., 2021). Their position is essential to confirm the plasmaspheric wave activities.

The whistler mode chorus, plume, and plasmaspheric hiss waves are observed in Figure 4 (bottom panel) for almost the entire substorms period. The hiss waves are detected at all perigees, in which the low power (~10^{-8} nT^2/Hz) is observed only during the first perigee. The polarization properties, such as the wave Normal Angle (WNA), ellipticity, and planarity, are presented in Figure 5. They are calculated through the singular value decomposition method (Santolík et al., 2003) to confirm the presence of the hiss waves inside the plasmasphere (e.g., Li et al., 2015; 2019). WNA ≤40° (Figure 5 - top panel), ellipticity ≥0.5 (Figure 5 - medium panel), and planarity close to 0.5 (Figure 5 - bottom panel) are observed between 6:45-8:50 UT on September 2017, which are the same values observed by Li et al. (2015) and Da Silva et al. (2022) during the detection of the hiss waves.

The low-energy electron injections (Figures 4 top panel) are observed during all periods of analyzed along all L-shells and are considerably more intense at the first 9 hours, which coincides with the first AE index peaks (Figure 1E). The low-energy electron injection peaks at high L-shells are concurrent with the whistler mode chorus and plume waves (bottom panel), suggesting the possible wave-particle interactions inside the outer radiation belt that may cause the low-energy EP to the atmosphere of the auroral regions.

The low-energy electron injection peaks (Figure 4 top panel) between 06:15 UT and 08:30 UT (blue box) are observed with more detail in Supplementary Figure S9. The concomitance between the power of whistler mode hiss waves of ~10^{-5} nT^2/Hz (Figure 4 - bottom panel) and electron injection peaks is observed from 6:57 UT in Supplementary Figure S8. These results are similar to those observed by Moro et al. (2022a) and Da Silva et al. (2022) during the low-energy electron precipitation over the SAMA region that contributed to the generator mechanism of the Esa layers. Although the presence of the hiss waves power of ~10^{-5} nT^2/Hz is evident from 6:57 UT (L-shell = 2.47), values of the hiss power below 10^{-5} nT^2/Hz are observed inside the inner radiation belt (L-shell <2). Over the SAMA region, the power spectral density values of ~10^{-5} nT^2/Hz are also observed just above 500 Hz.

The electron injections over the SAMA region are observed close to 6:30 UT for the energy levels 75 keV and 350 keV in Supplementary Figure S9 and energy levels <10 keV in Supplementary Figure S10. It is essential to highlight that 6:30 UT is a time during the passage of the Van Allen Probe B over the SAMA region. The electron injection peaks <0.5 keV are also observed in Supplementary Figure S10, almost simultaneously with the Esa layer detected in Santa Maria station. This behavior observed in the electron flux injections within the inner radiation belt over the SAMA region concomitant with hiss wave activities suggests the possible wave-particle interactions that may cause the low-energy EP to the atmosphere of this region.

Although the whistler-mode hiss waves power of ~10^{-5} nT^2/Hz is similar during the influence of this HSS and the ICMEs (Moro et al., 2022a; Da Silva et al., 2022), the generator mechanisms of the hiss waves inside the inner radiation belt are completely

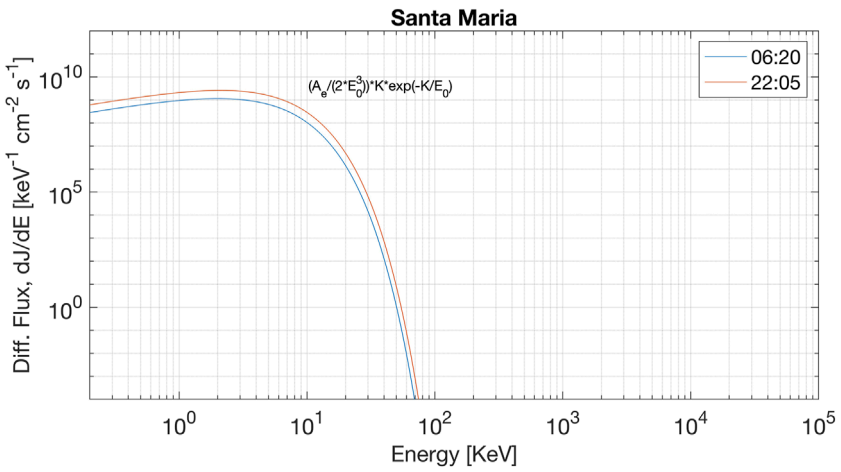

FIGURE 8
Total incident energy of electrons between 100 eV and hundreds of keV for Santa Maria station during the first (6:20 UT—blue line) and second (22:05 UT—red line) conjunction on 25 September 2017.

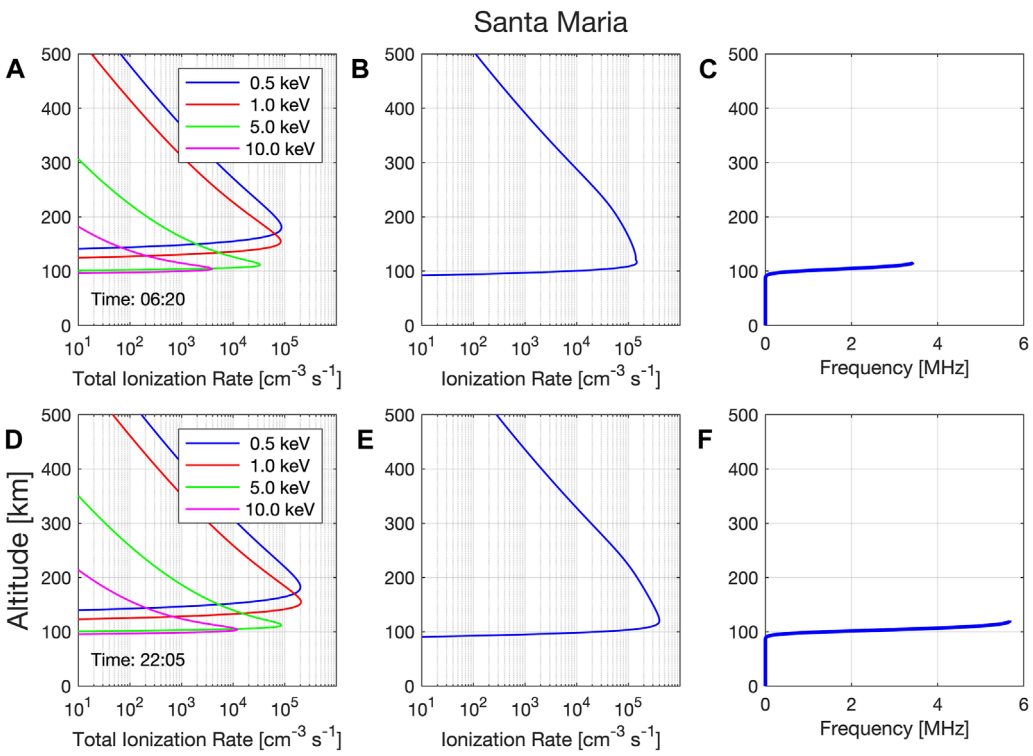

FIGURE 9
Ionization rate altitude profiles panels **(A,D)**; ionization rate altitude integrated panels **(B,E)**; and frequency range altitude for Santa Maria station panels **(C,F)**. The time analyzed refers to the period of the conjunctions between VAP-AB and Santa Maria station.

different for each solar wind structure. For example, the plasmapause position generally is compressed during the recovery phase of the storms associated with the ICMEs and relaxed under the influence of the HSSs, which directly impacts the time duration and position of this kind of wave activity. Consequently, it can cause different impacts on the behavior of electron precipitation in the atmosphere.

Using the time evolution of the radial Phase Space Density (PhSD) profiles at inbound/outbound regions of the Van Allen Probe B it is possible to identify the electron injections energy levels and local (L*) of the injections. Therefore, the PhSD as a function of L*, calculated using a magnetic field model (TS04) (Tsyganenko & Sitnov, 2005), at fixed first (μ = 10 MeV/G) and second (K = 0.11 G1/2RE) adiabatic invariants (e.g., Hartley

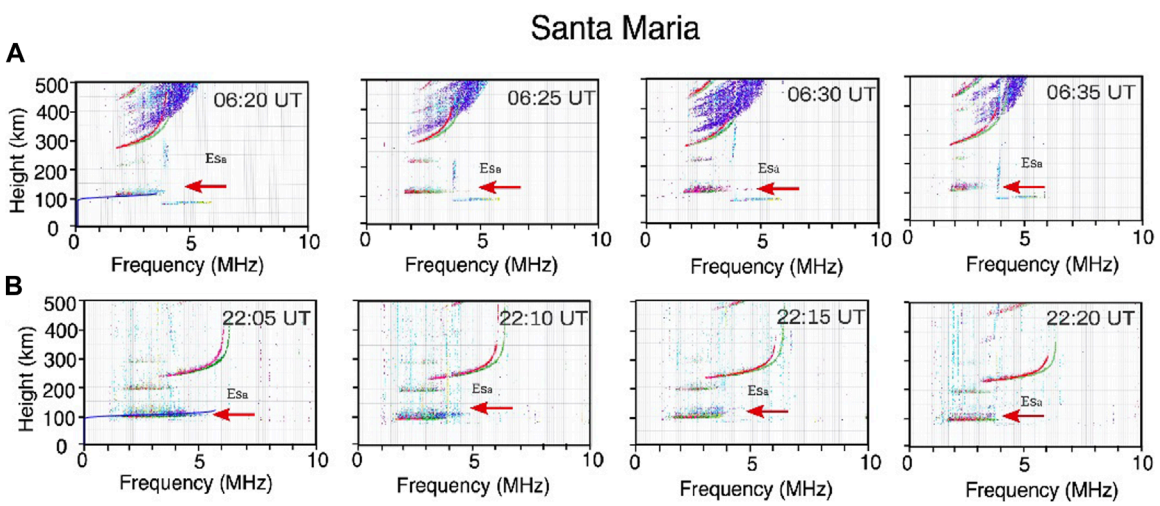

FIGURE 10
Ionograms from Digisonde located at Santa Maria station, which detected Esa layers only between 06:20 UT - 06:35 UT panel **(A)**, and 22:05 UT - 22:20 UT panel **(B)** on September, 25. The red arrows show the Es_a layer presence, and the blue line (6:20 UT and 22:05 UT) is referent the critical modeled frequency (MHz) altitude.

and Denton, 2014; Da Silva et al., 2019; Da Silva et al., 2021a) are presented in Figure 6. The PhSD profiles confirm the low-energy electron injections (~100 keV) between L* = 2.8 and 3.0 (close to the inner radiation belt) during the conjunction between VAP-B and Santa Maria station, which was also observed in the blue box of Figure 4. It suggests the occurrence of the low-energy EP close to the SAMA region.

The electron resonant kinetic energy is calculated using the dispersion relation presented in Eq. 1 (see Helliwell, 1965; Bittencourt, 1995; Alves et al., 2023) without the Lorentz factor.

$$\omega - \vec{k}.\vec{v_e} = n\Omega_{ce} \tag{1}$$

Where:

$\vec{k}$ is the wave number vector

ω is the frequency

$\vec{v_e}$ is the electron velocity vector

Ω_{ce} is the electron gyrofrequency

The gyrofrequency low-order harmonics $n = \pm 1, 2, 3\ldots$

The range of electron kinetic energy able to resonantly interact with hiss waves is calculated using PSD of hiss waves in the time interval shown in the blue box (Figure 4), specifically at 08:00 UT on September 25. The second harmonic number is considered in the calculation, besides the ambient magnetic field at 379 nT and the electron density of 470 cm^{-3}. In the selected time instant, the hiss emission occurred in broadband from 190 to 540 Hz (Supplementary Figure S3 - Supporting Information), leading to a resonant kinetic energy of ~150 keV–60 keV, as shown in the gray area in Figure 7.

Although most studies regarding the interaction between hiss and electrons have shown strong efficiency in scattering electrons of 10 keV - 1 MeV energies, recently, studies presented by Khazanov and Ma (2021) have shown that the hiss waves can scatter electrons of energies below 10 keV down to tens of eV, which are coincident with the main energy range of interest in this work.

7 Atmospheric ionization over the SAMA and auroral oval regions (100–200 km)

The ionization rate altitude profiles over the SAMA region are calculated using an empirical model, which considers the isotropically precipitating electrons (100 eV–1 MeV) (Fang et al., 2010). The computed atmospheric ionization assumes that the incident particles (differential number flux, $cm^{-2}\ s^{-1}\ keV^{-1}$) have a Maxwellian distribution (e.g., Da Silva et al., 2022). The atmospheric ionization model (Fang et al., 2010) also can estimate the critical ionospheric frequency (MHz) altitude profile, which may be associated with the peak electron concentration [N_e (electrons/m^3)] of the Es layer by the relation $F_c = c\sqrt{N_e}$, where c = 8.98 (e.g., Nikolaeva et al., 2021; Da Silva et al., 2022).

The atmospheric ionization is calculated assuming that the incident particles, given by the differential number flux ($cm^{-2}\ s^{-1}\ keV^{-1}$) have a Maxwellian distribution, as defined by the function:

$$\Phi_M(E) = \frac{Q_0}{2E_0^3} E \exp\left(-\frac{E}{E_0}\right), \tag{2}$$

Where the free parameters are:

Q_0 is the total energy flux in keV $cm^{-2}\ s^{-1}$

E_0 is the characteristic energy in keV

Φ_M is the differential number flux in $cm^{-2}\ s^{-1}\ keV^{-1}$

To estimate the incident energies and the atmospheric conditions is necessary to consider the variation of the days of the year and location, in which the geographic location (latitude and longitude), geomagnetic indices (F10.7 and Ap) and height scale (Supplementary Figure S4) are included in the model.

Initially, the total incident energy of electrons between 100 eV and hundreds of keV and the height scale (km) is estimated for Santa Maria station at 6:20 UT (first conjunction) and 22:05 UT (second conjunction) on 25 September 2017, as presented Figure 8;

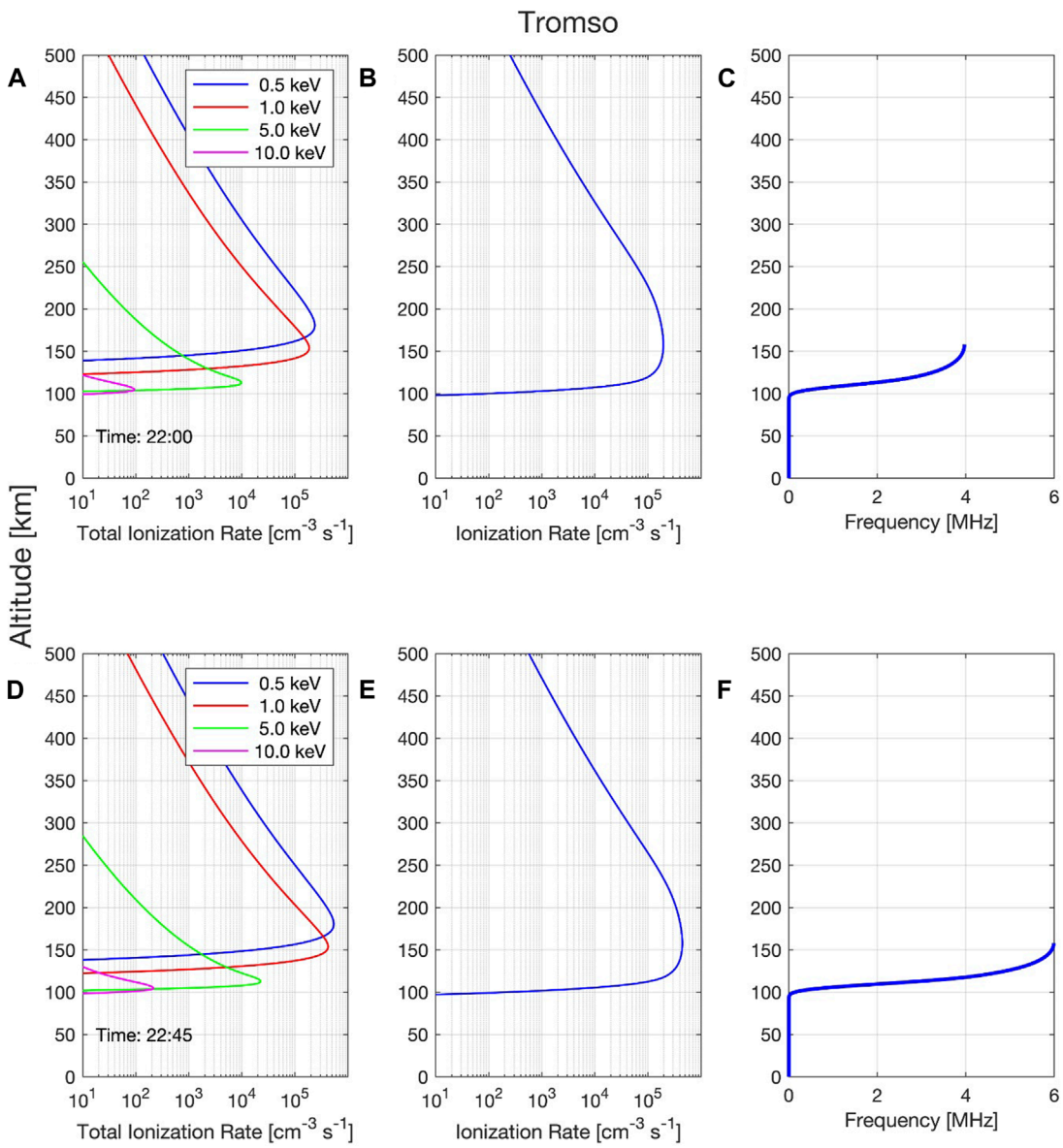

FIGURE 11
Ionization rate altitude profiles panels **(A,D)**; ionization rate altitude integrated panels **(B,E)**; and frequency range altitude for Tromso station panels **(C,F)** at 22:00 UT and 22:45 UT on 25 September 2017.

Supplementary Figure S6 (top panel - Supporting Information), respectively. The total incident energy of electrons during the second conjunction (Figure 8 red line) is slightly higher than the values during the first conjunction (Figures 8 blue line), which can cause influence the formation mechanisms of the Esa layer close to 100 km of altitude.

Figure 9 shows the total ionization rate altitude profiles (panels a and d), ionization rate altitude integrated (panels b and e), and critical ionospheric frequency (MHz) altitude, named here as frequency range altitude (panels c and f) for Santa Maria station during the first (6:20 UT—blue line) and second (22:05 UT—red line) conjunctions. The total ionization rate altitude profiles (panels a and d) presented significant values of the low-energy electrons (0.5 keV–10 keV) between 100 km–200 km of altitude for both analysis times. The previous sections suggested that the hiss waves have caused the precipitation of low-energy electrons to the atmosphere over the SAMA region through the pitch angle scattering mechanism (Li et al., 2019; Khazanov and Ma, 2021; Da Silva et al., 2022). However, the total ionization rate (panels a and d) and integrated (panels b and e) at the second conjunction is slightly more significant than the ionization rate at the first conjunction. This result caused a direct impact on frequency range altitude (panels c and f), in which the values above 3 MHz were reached during the first conjunction (panel c) and above 5 MHz during the second conjunction (panel f), which can trigger different generator mechanisms of the Esa layer in these periods.

The different values of the ionization rate during these conjunctions were expected due to the behavior of the total incident

energy of the electron presented in Figure 8. On the other hand, the range of the low-energy electrons observed between 100 km–200 km of altitude is far above the results presented in Da Silva et al. (2022) for the same ionosonde station, principally due to the low/absence values of the 5 keV and the absence of the 10 keV, which contributed to the displacement of the Esa layer reaching values close to 150 km of altitude. Therefore, the level of low-energy electron precipitation (EP) predominant defines the base height of the Esa layer.

The critical modeled frequencies at 6:20 UT and 22:05 UT are included in the ionograms (Figure 10), and the relationship between the critical modeled frequencies and the maximum frequency reached by the Esa layer can be observed. The Esa layer at 22:05 UT reached a frequency greater than at 6:20 UT (Figure 11 first panels). It suggests a direct relationship exists between the ionization rate altitude profiles and the characteristics of the Esa layer. The electron energy levels ≥5 keV contributed to defining the Esa layer base height close to 100 km of altitude at 22:05 UT and 6:20 UT (Figures 10A, B - first panels). Conversely, the values of the ionization rate contributed to defining the maximum frequency reached by the Esa layer, > 5 MHz at 22:05 UT (Figure 10B first panel) and >3 MHz at 6:20 UT (Figure 10A first panel). Therefore, knowing the dynamic mechanisms responsible for causing the EP over the SAMA region, principally to estimate the range of electron energy levels that will precipitate is crucial to understanding the generator mechanisms of the Esa layer over this region.

The ionization rate altitude profiles, ionization rate altitude integrated, and frequency range altitude to Tromso station are presented in Figure 11. The time of analysis is 22:00 UT (panels a, b and c) on 25 September 2017, to compare with the results observed in Santa Maria station at 22:05 UT (Figures 9D, E, F). Although the dynamic mechanisms that cause the EP over Tromso to be different from the mechanisms over SAMA, at the ionosphere, the formation mechanism of Esa layer in both regions has the EP as a main ingredient. It means that the electron energy levels, and the values of the ionization rate define the characteristics of the Esa layers in both regions, such as the Esa layer base height and the maximum frequency reached by Esa layer. Figure 9B (first panels) and Supplementary Figure S5 (top panel - Supporting Information) show that the Esa layer base height in Santa Maria is close to 100 km of altitude and in Tromso is >130 km of altitude, respectively, while the maximum frequency reached by Esa layer in Santa Maria is > 3 MHz and in Tromso is ~ 4 MHz.

8 Concluding remarks

The dynamic mechanisms inside the inner radiation belt, generally under the influence of the solar wind structures, can cause the low-energy EP (0.5 keV–10 keV) into the atmosphere (100–200 km) over the SAMA region. The pitch angle scattering driven by plasmaspheric hiss waves is responsible for this range of EP in this altitude over this region, which generally contributes to the generation of the Esa layer during the recovery phase period of the geomagnetic storm, associated with ICMEs (Batista and Abdu, 1977; Moro et al., 2022a; Da Silva et al., 2022).

The environment here is under the influence of an HSS. This solar wind structure triggered the dynamic mechanisms able to cause the low-energy electron injections (seed and source populations) inside the radiation belts, followed by the low-energy EP in the auroral and SAMA region. These dynamic mechanisms also contributed to generating the plasma waves inside the radiation belts under the influence of the Alfvenic fluctuations. Although the substorms driven by this HSS were considered weak, the total ionization rate altitude profiles in Santa Maria station presented significant energy levels between 0.5 and 10 keV, which are greater than the energy levels showed in Tromso station and presented by Da Silva et al. (2022) Santa Maria station. It means that the level of low-energy electron precipitation (EP) predominant defines the base height of the Esa layer, which is close to 100 km at Santa Maria station and 130 km at Tromso station. Additionally, the ionization rate integrated defines the maximum critical frequency of the Esa layer, which reached values > 3 MHz in Santa Maria and ~ 4 MHz in Tromso. This behavior suggests that the storm's intensity is not crucial to define the EP levels over the SAMA region once the Esa layers were generated without high values of the AE index.

Therefore, the main ingredients responsible for generating the Esa layer over the SAMA region are related directly to the total and integrated ionization rate at the interest's altitude. They are essential to define the base height and the maximum critical frequency of the Esa layer. Thereby, it is important to highlight that they are dependent on several factors, such as the amount, period, and levels of the electron flux injections in the inner radiation belt, the power spectral density of the hiss waves, the period of the hiss wave activities, and the resonance condition, which can have different behaviors under the influence of the different solar wind structures.

Data availability statement

The datasets presented in this study can be found in online repositories. The names of the repository/repositories and accession number(s) can be found in the article/Supplementary Material. All the data used are available at: ECT: https://cdaweb.gsfc.nasa.gov/pub/data/rbsp/ EMFISIS: https://emfisis.physics.uiowa.edu/Flight ACE: http://www.srl.caltech.edu/ACE/ASC/DATA/browse-data Digisonde (Santa Maria): http://www2.inpe.br/climaespacial/portal/ionossondas-inicio/ Digisonde (Tromso): https://lgdc.uml.edu/common/DIDBYearListForStation?ursiCode=TR169 IGRF-13: https://www.ngdc.noaa.gov/geomag/calculators/igrfgridForm.shtml VAP-AB orbit and foot print: https://sscweb.gsfc.nasa.gov/cgi-bin/Locator.cgi.

Author contributions

LS: Develop the idea of the article; make Figures 1, 4, 5; Supplementary Figure S1 and write all sections. JS: Revision of the manuscript and discussions about the results. LV. Runs the ionization rate model (make Figures 8, 9, 11; Supplementary Figures S4, S5, S6). OA: Calculate the electron lifetime based on the hiss model (make Figure 7). LR: Make Figure 2; Supplementary Figure S2, revision of the manuscript, and discussions about the Esa layers over SAMA. LA: Calculate the resonance kinetic energy (Make Figure 6; Supplementary Figure S3). DS: Revision of the manuscript and discussions about the results. VD: Revision of the manuscript and

discussions about the results. JPM: Revision of the manuscript and discussions about the results. SC: Make Figure 3. JM: Download the data for making Figure 2; Supplementary Figure S2, revision of the manuscript, and discussions about the Esa layer over the SAMA region. CA: Revision of the manuscript and discussions about the results. CW: Revision of the manuscript and discussions about the results. VA: Discuss the atmospheric Wind conditions and their influences on Es layers over SAMA. HL: Revision of the manuscript and discussions about the results. ZL: Revision of the manuscript and discussions about the results. All authors contributed to the article and approved the submitted version.

Funding

This research was supported by the International Partnership Program of Chinese Academy of Sciences (grants 183311KYSB20200003 and 183311KYSB20200017). OA was supported by NASA grants 80NNSC19K0264, 80NNSC19K0848, 80NSSC20K0218, 80NSSC22K0522, and NSF grant 1914670. LV was supported by CNPq/MCTIC (Grant 307404/2016-1), TED-004/2020-AEB and PO-20VB.0009. LA was supported by CNPq/MCTIC (Grant 301476/2018-7).

Acknowledgments

LS, JM, LR, and VA are grateful for financial support from China-Brazil Joint Laboratory for Space Weather (CBJLSW), National Space Science Center (NSSC), and the Chinese Academy of Science (CAS). LS also thanks the autoplot platform. We acknowledge the NASA Van Allen Probes, Harlan E. Spence [PI ECT; University of New Hampshire] and Craig Kletzing [PI EMFISIS; University of Iowa] for use of data. We acknowledge the NASA ACE satellite, Edward Stone [PI ACE; Caltech]. LV thanks CNPq/MCTIC (Grant 307404/2016-1), TED-004/2020-AEB and PO-20VB.0009. LA thanks to CNPq/MCTIC (Grant 301476/2018-7).

Conflict of interest

The authors declare that the research was conducted in the absence of any commercial or financial relationships that could be construed as a potential conflict of interest.

Publisher's note

All claims expressed in this article are solely those of the authors and do not necessarily represent those of their affiliated organizations, or those of the publisher, the editors and the reviewers. Any product that may be evaluated in this article, or claim that may be made by its manufacturer, is not guaranteed or endorsed by the publisher.

Supplementary material

The Supplementary Material for this article can be found online at: https://www.frontiersin.org/articles/10.3389/fspas.2023.1197430/full#supplementary-material

References

Alves, L. R., Alves, M. E. S., da Silva, L. A., Deggeroni, V., Jauer, P. R., and Sibeck, D. G. (2023). Relativistic kinematic effects in the interaction time of whistler-mode chorus waves and electrons in the outer radiation belt. *Ann. Geophys. Discuss*. doi:10.5194/angeo-2023-6

Andrioli, V., Clemesha, B., Batista, P., and Schuch, N. (2009). Atmospheric tides and mean winds in the meteor region over Santa Maria (29.7°S; 53.8°W). *J. Atmos. Solar-Terrestrial Phys.* 71 (17-18), 1864–1876. doi:10.1016/j.jastp.2009.07.005

Baker, D. N., Blake, J. B., Callis, L. B., Cummings, J. R., Hovestadt, D., Klecker, B. S., et al. (1994). Relativistic electron acceleration and decay time scales in the inner and outer radiation belts: SAMPEX. *Geophys. Res. Lett.* 21, 409–412. doi:10.1029/93GL03532

Batista, I. S., and Abdu, M. A. (1977). Magnetic storm associated delayed sporadic E enhancements in the Brazilian Geomagnetic Anomaly. *J. Geophys. Res.* 82 (29), 4777–4783. doi:10.1029/JA082i029p04777

Bittencourt, J. A. (1995). *Fundamentals of plasma Physics*. Edition 3. New York, NY: Springer. doi:10.1007/978-1-4757-4030-1

Blake, J. B., Carranza, P. A., Claudepierre, S. G., Clemmons, J. H., Crain, W. R., Jr, Dotan, Y., et al. (2013). The magnetic electron ion spectrometer (MagEIS) instruments aboard the radiation belt storm probes (RBSP) spacecraft. *Space Sci. Rev.* 179, 383–421. doi:10.1007/s11214-013-9991-8

Cai, H.-T., and Ma, S.-Y. (2007). Initial study of inversion method for estimating energy spectra of auroral precipitating particles from ground-based is radar observations. *Chin. J. Geophys.* 50 (1), 12–21. doi:10.1002/cjg2.1005

Chulliat, A., Brown, W., Alken, P., Beggan, C., Nair, M., Cox, G., et al. (2020). *The US/UK world magnetic model for 2020-2025: technical report*. Great Britain, United States: NOAA. doi:10.25923/ytk1-yx35

Claudepierre, S. G., O'Brien, T. P., Blake, J. B., Fennell, J. F., Roeder, J. L., Clemmons, J. H., et al. (2015). A background correction algorithm for Van Allen Probes MagEIS electron flux measurements. *J. Geophys. Res. Space Phys.* 120, 5703–5727. doi:10.1002/2015JA021171

Da Silva, L. A., Shi, J., Alves, L. R., Sibeck, D., Marchezi, J. P., Medeiros, C., et al. (2021b). High-energy electron flux enhancement pattern in the outer radiation belt in response to the Alfvenic fluctuations within high-speed solar wind stream: a statistical analysis. *J. Geophys. Res. Space Phys.* 126. doi:10.1029/2021JA029363

Da Silva, L. A., Shi, J., Alves, L. R., Sibeck, D., Souza, V. M., Marchezi, J. P., et al. (2021a). Dynamic mechanisms associated with high-energy electron flux dropout in the Earth's outer radiation belt under the influence of a coronal mass ejection sheath region. *J. Geophys. Res. Space Phys.* 126, e2020JA028492. doi:10.1029/2020JA028492

Da Silva, L. A., Shi, J., Resende, L. C. A., Agapitov, O. V., Alves, L. R., Batista, I. S., et al. (2022). The role of the inner radiation belt dynamic in the generation of auroral-type sporadic E-layers over south American magnetic anomaly. *Front. Astronomy Space Sci.* 9, 1–23. doi:10.3389/fspas.2022.970308

Da Silva, L. A., Sibeck, D., Alves, L. R., Souza, V. M., Jauer, P. R., Claudepierre, S. G., et al. (2019). Contribution of ULF wave activity to the global recovery of the outer radiation belt during the passage of a high-speed solar wind stream observed in September 2014. *J. of Geophys. Research-Space Phys.* 124, 1660–1678. doi:10.1029/2018ja026184

Fang, X., Randall, C. E., Lummerzheim, D., Wang, W., Lu, G., Solomon, S. C., et al. (2010). Parameterization of monoenergetic electron impact ionization. *Geophys. Res. Lett.* 37, L22106. doi:10.1029/2010GL045406

Funsten, H. O., Skoug, R. M., Guthrie, A. A., MacDonald, E. A., Baldonado, J. R., Harper, R. W., et al. (2013). Helium, oxygen, proton, and electron (HOPE) mass spectrometer for the radiation belt storm probes mission. *Space Sci. Rev.* 179, 423–484. doi:10.1007/s11214-013-9968-7

Gabrielse, C., Angelopoulos, V., Runov, A., and Turner, D. L. (2014). Statistical characteristics of particle injections throughout the equatorial magnetotail. *J. Geophys. Res. Space Phys.* 119, 2512–2535. doi:10.1002/2013JA019638

Green, A., Li, W., Ma, Q., Shen, X. C., Bortnik, J., and Hospodarsky, G. B. (2020). Properties of lightning generated whistlers based on Van Allen Probes observations and their global effects on radiation belt electron loss. *Geophys. Res. Lett.* 47 (17), e2020GL089584. doi:10.1029/2020GL089584

Gurnett, D. A., and O'Brien, B. J. (1964). High-latitude geophysical studies with satellite Injun 3: 5. Very-low-frequency electromagnetic radiation. *J. Geophys. Res.* 69 (1), 65–89. doi:10.1029/JZ069i001p00065

Hartley, D. P., and Denton, M. H. (2014). Solving the radiation belt riddle. *Astronomy Geophys.* 55 (6), 17–20. doi:10.1093/astrogeo/atu247

Helliwell, R. A. (1965). *Whistlers and related ionospheric phenomena*. Stanford University Press.

Horne, R. B., Lam, M. M., and Green, J. C. (2009). Energetic electron precipitation from the outer radiation belt duringgeomagnetic storms. *Geophys. Res. Lett.* 36, L19104. doi:10.1029/2009GL040236

Hua, M., Li, W., Ni, B. B., Ma, Q. L., Green, A., Shen, X. C., et al. (2020). Very-low-frequency transmitters bifurcate energetic electron belt in near-Earth space. *Nat. Commun.* 11, 4847. doi:10.1038/s41467-020-18545-y

Khazanov, G. V., and Ma, Q. (2021). Dayside low energy electron precipitation driven by hiss waves in the presence of ionospheric photoelectrons. *J. Geophys. Res. Space Phys.* 126, e2021JA030048. doi:10.1029/2021JA030048

Kletzing, C. A., Kurth, W. S., Acuna, M., MacDowall, R. J., Torbert, R. B., Averkamp, T., et al. (2013). The electric and magnetic field instrument suite and integrated science (EMFISIS) on RBSP. *Space Sci. Rev.* 179 (1–4), 127–181. doi:10.1007/s11214-013-9993-6

Lemaire, J. (1975). The mechanics of formation of the plasmapause. *Ann. Geophys.* 31 (1), 175–189.

Li, W., Ma, Q., Thorne, R. M., Bortnik, J., Kletzing, C. A., Kurth, W. S., et al. (2015). Statistical properties of plasmaspheric hiss derived from Van Allen Probes data and their effects on radiation belt electron dynamics. *J. Geophys. Res. Space Phys.* 120 (5), 3393–3405. doi:10.1002/2015JA021048

Li, W., Shen, X.-C., Ma, Q., Capannolo, L., Shi, R., Redmon, R. J., et al. (2019). Quantification of energetic Electron precipitation driven by plume whistler mode waves, Plasmaspheric hiss, and exohiss. *Geophys. Res. Lett.* 46, 3615–3624. doi:10.1029/2019GL082095

Li, Y. X., Yue, C., Liu, Y., Zong, Q.-G., Zou, H., and Ye, Y. G. (2023). Dynamics of the inner electron radiation belt: a review. *Earth Planet. Phys.* 7 (1), 109–118. doi:10.26464/epp2023009

Mauk, B. H., Fox, N. J., Kanekal, S. G., Kessel, R. L., Sibeck, D. G., and Ukhorskiy, A. (2013). Science objectives and rationale for the radiation belt storm probes mission. *Space Sci. Rev.* 179 (1–4), 3–27. doi:10.1007/s11214-012-9908-y

Meredith, N. P., Horne, R. B., Thorne, R. M., Summers, D., and Anderson, R. R. (2004). Substorm dependence of plasmaspheric hiss. *J. Geophys. Res. Space Phys.* 109 (A6), 6209. doi:10.1029/2004JA010387

Meredith, N. P., Horne, R. B., Lam, M. M., Denton, M. H., Borovsky, J. E., and Green, J. C. (2011). Energetic electron precipitation during high-speed solar wind stream driven storms. *J. Geophys. Res.* 116 (A5), A05223. doi:10.1029/2010JA016293

Moro, J., Xu, J., Denardini, C. M., Resende, L. C. A., Silva, L. A., Chen, S. S., et al. (2022a). Different sporadic-E (Es) layer types development during the August 2018 geomagnetic storm: evidence of auroral type (Es) over the SAMA region. *J. of Geophys. Research-Space Phys. V.*, 1. doi:10.1029/2021JA029701

Moro, J., Xu, J., Denardini, C. M., Stefani, G., Resende, L. C. A., Santos, A. M., et al. (2022b). Blanketing sporadic-E layer occurrences over Santa Maria, A transition station from low to middle latitude in the South American magnetic anomaly (sama). *J. Geophys. Research-Space Phys.* 127, E2022ja030900. doi:10.1029/2022ja030900

Nikolaeva, V., Gordeev, E., Sergienko, T., Makarova, L., and Kotikov, A. (2021). AIM-E: E-region auroral ionosphere model. *Atmosphere* 12, 748. doi:10.3390/atmos12060748

Pinto, O., and Gonzalez, W. D. (1989). Energetic electron precipitation at the South atlantic magnetic anomaly: a review. *J. Atmos. Terr. Phys.* 51 (5), 351–365. doi:10.1016/0021-9169(89)90117-7

Rees, M. H. (1963). Auroral ionization and excitation by incident energetic electrons. *Planet. Space Sci.* 11 (10), 1209–1218. doi:10.1016/0032-0633(63)90252-6

Reeves, G. D., Friedel, R. H. W., Larsen, B. A., Skoug, R. M., Funsten, H. O., laudepierre, S. G., et al. (2016). Energy-dependent dynamics of keV to MeV electrons in the inner zone, outer zone, and slot regions. *J. Geophys. Res. Space Phys.* 121 (1), 397–412. doi:10.1002/2015JA021569

Resende, L. C. A., Zhu, Y., Arras, C., Denardini, C. M., Chen, S. S., Moro, J., et al. (2022b). Analysis of the sporadic-E layer behavior in different American stations during the days around the september 2017 geomagnetic storm. *Atmosphere* 13, 1714. doi:10.3390/atmos13101714

Resende, L. C. A., Zhu, Y., Denardini, C. M., Moro, J., Arras, C., Chagas, R. A. J., et al. (2022c). Worldwide study of the Sporadic E (Es) layer development during a space weather event. *J. Atmos. Solar-Terrestrial Phys.* 241, 105966. doi:10.1016/j.jastp.2022.105966

Rodger, C. J., Clilverd, M. A., Seppälä, A., Thomson, N. R., Gamble, R. J., Parrot, M., et al. (2010). Radiation belt electron precipitation due to geomagnetic storms: significance to middle atmosphere ozone chemistry. *J. Geophys. Res.* 115, A11320. doi:10.1029/2010JA015599

Roederer, J. G. (1967). On the adiabatic motion of energetic particles in a model magnetosphere. *J. Geophys. Res.* 72 (3), 981–992. doi:10.1029/jz072i003p00981

Santolík, O., Parrot, M., and Lefeuvre, F. (2003). Singular value decomposition methods for wave propagation analysis. *Radio Sci.* 38 (1), 1010. doi:10.1029/2000RS002523

Sarris, E. T., Krimigis, S. M., and Armstrong, T. P. (1976). Observations of magnetospheric bursts of high-energy protons and electrons at ~35$R_E$with Imp 7. *J. Geophys. Res.* 81 (13), 2341–2355. doi:10.1029/JA081i013p02341

Shi, R., Summers, D., Ni, B., Fennell, J. F., Blake, J. B., Spence, H. E., et al. (2016). Survey of radiation belt energetic electron pitch angle distributions based on the Van Allen Probes MagEIS measurements. *J. Geophys. Res. Space Phys.* 121, 1078–1090. doi:10.1002/2015JA021724

Stone, E. C., Frandsen, A. M., Mewaldt, R. A., Christian, E. R., Margolies, D., Ormes, J. F., et al. (1998). The advanced composition explorer. *Space Sci. Rev.* 86 (1/4), 1–22. doi:10.1023/A:1005082526237

Su, Z., Liu, N., Zheng, H., Wang, Y., and Wang, S. (2018). Large-amplitude extremely low frequency hiss waves in plasmaspheric plumes. *Geophys. Res. Lett.* 45 (2), 565–577. doi:10.1002/2017GL076754

Takahashi, K., Lee, D.-H., Nosé, M., Anderson, R. R., and Hughes, W. J. (2003). CRRES electric field study of the radial mode structure of Pi2 pulsations. *J. Geophys. Res.* 108 (A5), 1210. doi:10.1029/2002JA009761

Thomas, N., Shiokawa, K., Miyoshi, Y., Kasahara, Y., Shinohara, I., Kumamoto, A., et al. (2021). Investigation of small scale electron density irregularities observed by the Arase and Van Allen Probes satellites inside and outside the plasmasphere. *J. Geophys. Res. Space Phys.* 126, e2020JA027917. doi:10.1029/2020JA027917

Tsyganenko, N. A., and Sitnov, M. I. (2005). Modeling the dynamics of the inner magnetosphere during strong geomagnetic storms. *J. Geophys. Res.* 110, A03208. doi:10.1029/2004JA010798

Turner, D. L., Claudepierre, S. G., Fennell, J. F., O'Brien, T. P., Blake, J. B., Lemon, C., et al. (2015). Energetic electron injections deep into the inner magnetosphere associated with substorm activity. *Geophys. Res. Lett.* 42 (7), 2079–2087. doi:10.1002/2015GL063225

Vampola, A. L., and Korth, A. (1992). Electron drift echoes in the inner magnetosphere. *Geophys. Res. Lett.* 19, 625–628. doi:10.1029/92GL00121

Whitehead, J. D. (1970). Production and prediction of sporadic E. *Rev. Geophys.* 8 (1), 65–144. doi:10.1029/RG008i001p00065

Xiang, Z., Li, X. L., Selesnick, R., Temerin, M. A., Ni, B. B., Zhao, H., et al. (2019). Modeling the quasi-trapped electron fluxes from cosmic ray albedo neutron decay (CRAND). *Geophys. Res. Lett.* 46 (4), 1919–1928. doi:10.1029/2018GL081730

Xiao, F., Zong, Q.-G., and Chen, L. (2009). Pitch-angle distribution evolution of energetic electrons in the inner radiation belt and slot region during the 2003 Halloween storm. *J. Geophys. Res.* 114, A01215. doi:10.1029/2008JA013068

Zhang, Z. X., Xiang, Z., Wang, Y. F., Ni, B. B., and Li, X. Q. (2021). Electron acceleration by magnetosonic waves in the deep inner belt (L = 1.5-2) region during geomagnetic storm of August 2018. *J. Geophys. Res. Space Phys.* 126 (12), e2021JA029797. doi:10.1029/2021JA029797

Zhao, H., Li, X., Blake, J. B., Fennell, J. F., Claudepierre, S. G., Baker, D. N., et al. (2014). Peculiar pitch angle distribution of relativistic electrons in the inner radiation belt and slot region. *Geophys. Res. Lett.* 41 (7), 2250–2257. doi:10.1002/2014GL059725

Frontiers in
Astronomy and Space Sciences

Explores planetary science and extragalactic astronomy in all wavelengths

Advances the understanding of our universe - from planetary science to extragalactic astronomy, to high-energy and astroparticle physics.

Discover the latest Research Topics

See more →

Frontiers

Avenue du Tribunal-Fédéral 34
1005 Lausanne, Switzerland
frontiersin.org

Contact us

+41 (0)21 510 17 00
frontiersin.org/about/contact